Doctoral Thesis

Surface-modified oxygen electrodes for reduced temperature SOFC applications

---

Author:
Ana Isabel Casas Hidalgo

Supervisor:
Dr Denis Cumming

A thesis submitted in fulfilment of the requirements for the degree of
Doctor of Philosophy in the

Department of Chemical and Biological Engineering

February 2022

Abstract

As population and its energy demand increased, fossil fuels became a requirement for sustainment of daily life. However, their extended use has brought along several unwanted consequences that are now a subject of concern, for example global warming, increase to greenhouse gasses emissions, and changes to major meteorological events. Out of these concerns, the emergence of alternative energy devices, such as fuel cells, have attracted a significant amount of attention due to their superior efficiency and reduced dependency on fossil fuels.

Out of the many fuel cells, solid oxide fuel cells (SOFC) are a specific type of fuel cell that operates at high temperatures (600 – 1000°C). Their inherently high operation temperatures broaden the spectra of potential fuel sources, and their excess heat can be integrated into other processes, further increasing the overall efficiency of the system. In recent years, SOFC technology has leaned towards reducing the operation temperature (600-800°C). However, at lower temperatures the oxygen reduction reaction (ORR) kinetics become increasingly sluggish, challenging the use of traditional cathode materials, hence, the need for highly active cathodes, like LSCF-6428 ($La_{0.6}Sr_{0.4}Co_{0.2}Fe_{0.8}O_{3-\delta}$).

One of the major drawbacks of LSCF is its inherent tendency to degrade due to Sr-surface segregation (SSS), phenomena driven by elastic and electrostatic forces within the material structure that results in hindered ORR activity. Infiltration of a secondary phases has been reported to suppress SSS while enhancing ORR activity for Sr-containing electrodes. This work investigated $Gd_{0.1}Ce_{0.9}O_{1.95}$ (GDC) and HfO_2 at various concentrations as surface-modifiers on porous LSCF-6428 electrodes as well as dense substrates to evaluate their effect electrode performance and SSS prevention when compared to unmodified LSCF when all materials are subjected to typical IT-SOFC operation conditions.

It was observed from experimental results of unmodified electrodes that degradation rate for electrodes (dRp%) decreased for electrodes that were stored before testing (~31% and ~4%) in contrast to electrodes that were tested closer to their fabrication date (~60%). Additionally, SEM images showed the appearance of particles along the grain boundaries that grew with increasing ageing time, consistent with SSS in literature. The absence of SSS signs on the rest of the samples was theorised to be caused by a *calendar ageing effect*, that has yet to be reported in literature to the authors knowledge.

When analysing surface-modified electrodes and substrates, it was observed that both surface modifications produced more stable, *i.e.* less degradable, and better performing electrodes as proved by EIS and Rp monitoring for 50h. GDC proved to be most effective when using 0.125M and 0.250M, while for HfO_2 13.16 and 26.32 mg mL^{-1} concentrations worked best to produce electrodes with better ORR performance, this is lower Rp values, than non-infiltrated ones. Additionally, no surface particles that could be associated with SSS were identified using XRD nor SEM on flat substrates when surface modifications were used, suggesting that even the lowest concentrations were effective in preventing Sr-segregation.

Although the previously identified *calendar ageing effect* on bare samples could also be identified on surface-modified measurements, it was ultimately concluded that due to time constraints and limitations, more research into this subject is necessary to elucidate the causes behind these observations.

Acknowledgements

I would like to dedicate this work to:

My family, for providing me with all the love and support to pursue this goal regardless of the time and distance. I am particularly grateful to my mom and dad, who have always encouraged me to follow my dreams.

My *abuelitos* Chabelita and Manuel, who never failed to let me know how proud they are of me and keep watching over me.

Valeria, Carlos, Ale, Ana, David, Itzel, and Celia for sharing their warmth and becoming my Mexican family away from home.

Ed, Gareth, Tori, and Jen for welcoming with open arms, becoming a new family for me and keeping me sane during my darkest hours.

My loving partner, Rubén, for believing in me even when I didn’t, being the greatest cheerleader in all the ventures that brought me here and willingly sharing his life with me.

Finally, a heartfelt thanks to Dr Denis Cumming and Dr Ge Wang, for sharing their knowledge, guidance, and supporting me in my journey towards becoming an independent researcher.

Additionally, I would like to thank all University of Sheffield technical and administrative staff for all their assistance during my PhD.

“While it is always best to believe in oneself, a little help from others can be a great blessing”

Uncle Iroh, AtLA (S02, EP15)

This is not who I am, this is just something that I did

Contents

List of Figures

List of Tables

List of symbols and abbreviations

2PB	Two phase boundaries
3PB	Triple phase boundary
AFC	Alkaline fuel cell
BSEs	Backscattered electrons
CGO	Ceria gadolinium oxide, $Ce_{1-x}Gd_xO_2$
CT	X – ray computed tomography
DMFC	Direct methanol fuel cell
dRp	Change in Rp value
EC	Equivalent circuit
ECF	Equivalent circuit fitting
ECM	Equivalent circuit model
EDS	Energy – dispersive X – ray spectroscopy
EDX	Energy dispersive X-ray analysis
EIS	Electrochemical impedance spectroscopy
EISA	Evaporation-induced self-assembly
FC	Fuel cell
FRA	Frequency response analyser
GDC	Gadolinium doped ceria, $Gd_xCe_{1-x}O_{2-\delta}$
HT–SOFC	High temperature solid oxide fuel cell
ICDD	International Centre for Diffraction Data
IPA	Isopropyl alcohol
IT–SOFC	Intermediate temperature solid oxide fuel cell
LBF	$La_{0.8}Ba_{0.2}FeO_3$
LC	$LaCoO_3$
LCaF	$La_{0.8}Ca_{0.2}FeO_3$
LCC	$La_{0.4875}Ca_{0.0125}Ce_{0.5}O_{2-\delta}$
LGO	$LaGaO_3$
LNF	$LaNi_{0.6}Fe_{0.4}O_3$
LSC	$La_{1-x}Sr_xCoO_{3-\delta}$
LSCF	$La_{1-x}Sr_xCo_{1-y}Fe_y O_{3-\delta}$
LSCF–6428	Lanthanum strontium cobalt iron ferrite of specific composition $La_{0.6}Sr_{0.4}Co_{0.2}Fe_{0.8} O_{3-\delta}$
LSCN	$La_{0.8}Sr_{0.2}Co_{0.8}Ni_{0.2}O_{3-\delta}$
LSF	$La_{1-x}Sr_xFeO_{3-\delta}$
LSFSc	$La_{0.6}Sr_{0.4}Fe_{0.9}Sc_{0.1}O_{3-\delta}$

LSGM	Lanthanum gallate doped with strontium and magnesium, $La_{1-x}Sr_xMg_yGa_{1-y}O_{3-x/2-y/2}$
LSM	$La_{1-x}Sr_xMnO_3$
LST	$La_{0.3}Sr_{0.7}TiO_{3-\delta}$
LSTM	$La_{0.4}Sr_{0.6}Ti_{0.4}Mn_{0.6}O_{3-\delta}$
LT–SOFC	Low temperature solid oxide fuel cell
M	Unit of concentration, mol L^{-1}
MCFC	Molten carbonate fuel cell
MIEC	Mixed ionic and electronic conductivity
NP	Nanoparticles
ORR	Oxygen reduction reaction
PAFC	Phosphoric acid fuel cell
PCO	$Pr_{0.2}Ce_{0.8}O_2$
PDF	Powder diffraction file
PEMFC	Proton exchange membrane fuel cell
P_{O2}	Oxygen partial pressure
PSCM	$PrSrCoMnO_{3-\delta}$
PSM	$Pr_{0.75}Sr_{0.2}MnO_{3-\delta}$
Rp	Polarisation resistance ($\Omega \cdot cm^2$)
Rs	Electrolyte resistance
SDC	Samarium doped ceria, $Sm_xCe_{1-x}O_{2-\delta}$
SEM	Scanning electron microscopy
SEM – EBSD	Scanning electron microscopy and Electron backscatter diffraction
SEs	Secondary electrons
SOFCs	Solid oxide fuel cell
SSC	$Sm_{1-x}Sr_xCoO_3$
SSS	Sr-surface segregation
TEC	Thermal expansion coefficient
XRD	X – ray diffraction
YSZ	Yttrium – stabilized zirconia, ZrO_2 doped with 8% mol Y_2O_3

1 Introduction

As mankind grew and evolved it became clear that their needs evolved along with them. Since the beginning of the industrial revolution, wood was replaced by fossil fuels as the main energy source. Fossil fuels have been used for a multitude of applications ranging from transport, electricity generation, heat generation, and as the basis for many manufacturing processes. As population and its energy demand increased, fossil fuels became a requirement for sustainment. However, their extended use has brought along several unwanted consequences that are now a subject of concern [1].

For starters, the average temperature of earth has been steadily rising ever since the industrial revolution at an average rate of ~0.08°C per decade, *i.e.* temperature today is 1.06°C warmer than it was in the pre-industrial period [2]. This rise in temperature is commonly known as *global warming*. Additionally, the escalating emission of greenhouse gasses such as carbon dioxide, methane, nitrous oxide, etc., has also contributed to global warming, which in turn has other concerning effects like the rise in sea levels, significant changes to meteorological events like El Niño, extreme precipitations or draughts that could potentially have devastating effects if left undealt with [1].

Among some of the alternative sources for energy, fuel cells (FC) have received a significant amount of attention due to their ability to transform fuels into electricity in an efficient manner whilst reducing the dependency to fossil fuels and the emission of greenhouse gases. In this sense, FCs are devices very similar to batteries and engines; however, unlike batteries, FCs work continuously as long as a fuel is supplied and do not need to be recharged; additionally, in contrast to thermal engines, their efficiency is not limited by the *Carnot cycle* [3, 4].

The first FC prototype was invented by Sir William Grove in 1839, it was known as the *gaseous voltaic battery* and it was a fragile assembly filled with dilute sulphuric acid that acted as the electrolyte, platinum as the electrodes, as well as hydrogen and oxygen as the reactants. It would be later determined by Christian Friedrich Schoenbein in 1843 that the produced current was the result of a chemical reaction between hydrogen and oxygen caused by platinum [5].

In 1899, Wilhem Nernst was investigating solid conductors as potential filaments for lamps. He then realised that the conductivities of mixed oxides, particularly the mixture with a 85% mol ZrO_2 and 15% mol Y_2O_3 was significantly higher than sulphuric acid. This specific mix of oxides would be later be known as the *"Nernst mass"* and it would also become the base for the development of several materials that would then serve as electrolytes for SOFC devices in present day [1].

The basic concept of SOFCs was demonstrated for the first time in 1937 by Emil Bauer and Hans Preis using an assembly comprising of zirconia ceramic as the electrolyte, Fe_3O_4 as a cathode, and C as an anode. The proof of this concept would set the basis for Joseph Weissbart and Roswell Ruka, from Westinghouse Electric Corporation, that reported their findings for the measuring of oxygen concentration of gaseous phase using a solid electrolyte fuel cell in 1961. These efforts successfully culminated in a patent and the fabrication of the first “bell and spigot” SOFC stack by Westinghouse/Siemens [3],

As it was previously mentioned, since FCs convert the chemical energy stored in fuels into electrical energy through electrochemical reactions. The major advantages of these devices are that their efficiency is not limited by the Carnot cycle, and they are capable of producing lower or no greenhouse emissions (depending on fuel of choice). Additionally, FCs as power generators are quieter and produce less vibrations than traditional heat engines, which makes them a prime candidate for stationary power applications [1].

Furthermore, the high operation temperatures (600 – 1000°C) of SOFCs provide other advantages, *e.g.* the effective activation of fuel reforming (transformation of the fuel into a CO_2 and H_2-rich stream), thus broadening the spectra of usable fuels in both liquid and gas state; high-quality waste heat that can be integrated into other processes known as the co-production of heat and power (CHP), which in turn increases the overall efficiency of the system to a 85 – 90% range [3].

The inherently demanding operation conditions for SOFCs make the use of specialised materials a necessity, which also represents an increase in production cost potentially limiting the high scale utilisation of SOFC due to electricity being produced at a higher cost, potential interfacial reactions between the components, densification of the electrodes, and potential cracks due to thermal shock from thermal cycling or from input streams not being at the right temperature [6].

Since the 90’s, lowering the operation temperature of SOFCs became a topic of particular interest and with the intentions to [7]:

- Introduce cheaper materials with better mechanical and conductive properties,
- Allow faster start-up/shut-down protocols,
- Reducing the interfacial interactions between components and effectively extending the lifespan of the device.

Nevertheless, new challenges arise from these new operation conditions, mainly that the electrolyte and the cathode struggle to perform at reduced temperatures, *i.e.* the reaction kinetics for the oxygen reduction reaction (ORR) at the cathode become sluggish whilst the ionic conductivity of the electrode tends drops as well.

The current state of the art SOFC materials for high temperature operation (850-1000°C) are yttrium-stabilised zirconia (YSZ) as the electrolyte, Ni-YSZ as the anode, and a $La_{0.8}Sr_{0.2}MnO_3$ (LSM) as the cathode. These ceramics, offer the necessary mechanical strength to the device, whilst still providing all the necessary conductive and catalytic properties required to carry out the electrochemical reactions required to produce energy from the oxidation of a wide range of fuels [8].

For cells that operate a reduced temperature (anything between 500 – 700 °C), the commonly used electrolyte materials tend to be doped ceria-based oxides due to their superior ionic conductivity at $T<800°C$ and lack of chemical interactions with the preferred cathode material in comparison to YSZ [9]. The most popular dopants for ceria are gadolinium and samarium, to produce $Gd_xCe_{1-x}O_{2-\delta}$ (GDC) or $Sm_xCe_{1-x}O_{2-\delta}$ (SDC), respectively.

In terms of the cathode material, the mixed ionic and electronic conductive material, $La_{0.6}Sr_{0.4}Co_{0.2}Fe_{0.8}\ O_{3-\delta}$ (LSCF-6428, as commonly known in the literature) has proved to be one of the best candidates due to the balance between conductive properties and thermal compatibility with doper-ceria electrolytes [9]. However, one of the major drawbacks for this material is the tendency of the Sr atoms in the bulk structure to migrate to the surface, a phenomenon known as Sr-surface segregation or SSS [10-12] .

Since SSS has a negative effect on electrode, and thus cell performance, researchers have turned their attention into trying to figure out why this occurs and how can it be prevented. A number of computational and practical studies have determined that there are some driving forces for the SSS [13-17]. Firstly, the elastic energy caused by cation size mismatch between the dopant Sr^{2+} and host La^{3+} cations [17]; alternatively, the charge interactions between positively charged oxygen vacancies and negatively charged defects [16, 18] have been found to be the main driving forces for SSS in Sr-containing perovskite materials.

As a countermeasure to SSS, Tsvetkov *et al.* [19, 20] investigated the effect of modifying the surface of LSC with less reducible cations as a way to control oxygen vacancies on the material surface. They reported that 16% Hf effectively prevented SSS and also enhanced the oxygen surface exchange kinetics (a key factor for cathode performance) [21]. Given the similarities between LSC and LSCF materials, it would be safe to assume that similar results could be obtained when applied to LSCF, which to the best knowledge of the author has not been yet reported.

Many different infiltrates have been tested on LSCF, which will be discussed in depth in future sections of this work. Nevertheless, it has been suggested by Kiebach *et al*. [22] that the cause of performance enhancement on modified electrodes is mainly attributed to a significant increase in sites for the ORR to take place and not dependent to the conductive nature of the infiltrate, *i.e.* ionic, electronic or mixed conducting. However, this study also concluded that particularly for the case where GDC was the infiltrate, the modified electrodes showed less degradation after 100h.

Finally, although the basic protocol for infiltration is generally the same for most of the reported literature, some key factors, such as concentration, use of surfactants or different solvents, are not a fixed parameters and can be fine-tuned to produce a coating or surface modification of specific characteristics, *i.g.* nanoparticles (NPs) clusters or continuous coatings, varied thickness, etc.(most of these subjects and their impact on performance is further discussed in Section 2.6.2 of this thesis)

1.1 Research aims and objectives

The aim of this work is to investigate the effect on Sr-surface segregation (SSS) and electrode performance of two different surface modifications, namely HfO_2 and $Gd_{0.1}Ce_{0.9}O_{1.95}$ (GDC) on $La_{0.6}Sr_{0.4}Co_{0.2}Fe_{0.8}O_{3-\delta}$, (LSCF-6458) materials under IT-SOFC operation conditions. It is hoped that the results of this work can be used to produce more stable electrodes that are less prone to SSS and with enhanced ORR performance. To achieve this the following objectives have been formulated:

- Fabricate two types of LSCF-6428 configurations for analysis; *i.e* flat and dense LSCF substrates and porous LSCF electrodes on GDC electrolytes to conform symmetrical test cells. The different configurations will provide different information regarding SSS after thermal ageing treatment, and electrode performance after 50h of testing in their coated/infiltrated and bare states.
- Monitor the performance via electrochemical impedance spectroscopy (EIS) of symmetric, non-infiltrated LSCF/GDC/LSCF cells for a period of 50h. Obtained data will be fitted to an appropriate equivalent circuit model (ECM) to extract electrode polarisation (Rp) values as a benchmark for performance and degradation for infiltrated cells.
- Monitor the performance via EIS of infiltrated LSCF/GDC/LSCF cells for a period of 50h. Infiltration will be performed using two different precursors ($Gd_{0.1}Ce_{0.9}O_{1.95}$, and HfO_2) at varying concentrations to observe its effect on electrode performance/degradation. Obtained data will be fitted to an appropriate equivalent circuit model (ECM) to extract electrode polarisation (Rp) values for comparison

against literature and benchmark values. Particularly for the case of HfO_2 infiltration on LSCF, no other similar data is present in the literature using this method.

- Flat and dense LSCF substrates with no surface modification will be thermally treated (800°C) for prolonged time to promote SSS that will be analysed using scanning electron microscopy (SEM) and X-ray diffraction (XRD) as a benchmark.
- Flat and dense LSCF substrates with HfO_2 and GDC surface modifications at various concentrations will be thermally treated (800°C) for prolonged time to observe their effect in preventing SSS. Samples will be analysed using SEM and XRD to observe the presence or absence of SSS. Obtained data will be compared against benchmark data and literature. Once again, for the case of HfO_2 modification on LSCF, no other similar data is present in the literature, to the authors knowledge.

2 Literature Review

2.1 Fuel cells, principles, and basic operation

A f*uel cell* (FC) is a device capable of producing electrical energy from a chemical feed via electrochemical reactions. The basic elements in FCs are the two electrodes (commonly named anode and cathode) located on each side of an electrolyte. The fuel and oxygen are constantly being supplied to the anode and cathode, respectively [4]. Meanwhile, the ions and electrons produced from the electrochemical reactions taking place on each electrode (Equation 1 –Equation 3, in which the consumed fuel is hydrogen) [5], migrate to the opposite electrode following different paths:

Anode reaction $$H_2 + O^{2-} \rightarrow H_2O + 2e^-$$ $E^0 = 0$ V *Equation 1*

Cathode reaction $$\frac{1}{2}O_2 + 2e^- \rightarrow O^{2-}$$ $E^0 = 0.89$ V *Equation 2*

Net reaction $$H_2 + \frac{1}{2}O_2 \rightarrow H_2O$$ $E^0 = 0.89$ V *Equation 3*

Whilst the oxygen ions (O^{2-}) generated on the cathode make their way through the electrolyte, the electrons (e^-) produced on the anode travel through an external circuit generating a current flow. Finally, they reach the opposite electrode to complete the reactions and close the circuit, as shown in Figure 2-1 [23].

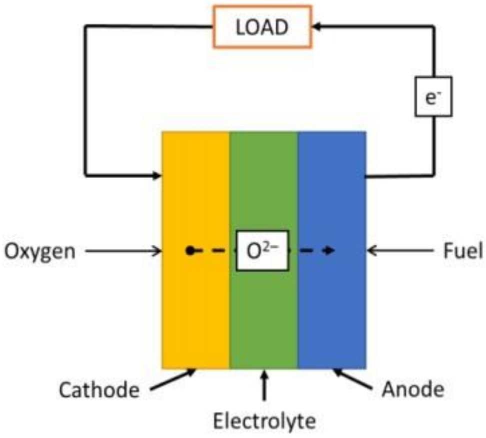

Figure 2-1 A simple schematic of a fuel cell

FCs can operate over a wide range of parameters, such as different temperatures, electrolyte, or fuel type. Based on these characteristics clear distinctions can be made to further classify these devices into more specific categories. For the purposes of this text, the broader distinction considered will be working temperature as depicted in Table 2-1:

Table 2-1 Different types of FCs classified in terms of their working temperature [4]

Temperature range	**Fuel cells**
Low temperature (<150°C)	• Proton exchange membrane fuel cell (PEMFC) • Alkaline fuel cell (AFC) • Direct methanol fuel cell (DMFC)
Intermediate temperature (150 – 200°C)	• Phosphoric acid fuel cell (PAFC)
High temperature (600 – 1100°C)	• Molten carbonate fuel cell (MCFC) • Solid oxide fuel cell (SOFC)

Among the various FCs listed above, PEMFCs and SOFCs have received the most attention. Although PEMFCs operate at low temperatures, the use of expensive and sometimes scarce materials, such as Pt and Pt-based catalytic materials for both the oxygen reduction reaction and hydrogen oxidation reaction is necessary to achieve good performance [24, 25]. In contrast, the high operation temperature of SOFCs promotes faster reaction kinetics on the electrodes, thus yielding a higher power density with more compact units that can be constructed with less expensive materials. This trade of SOFC is of special interest for the large-scale exploitation of these kind of devices [3, 5, 23].

2.2 Solid oxide fuel cells

As previously stated, FCs will produce electricity while being supplied with oxygen (generally from the air) and an appropriate fuel source. A solid oxide fuel cell (SOFC, Figure 2-2) consists of a dense ceramic oxide electrolyte with ion conducting properties separating the porous electrodes. The *oxygen reduction reaction* (ORR), described in Equation 2, and the fuel oxidation, described in Equation 1, occur on the cathode and anode, respectively [26].

Multiple cells can be stacked and connected to generate a larger power output by using an *interconnect material*, which is generally a ceramic material with conducting properties. Because of their characteristics, SOFCs are suitable for applications like stationary power supply, heat generation and as auxiliary power units for transportation.

Although the characteristic high operation temperature (800 – 1000 °C) of SOFC confers them significant advantages such as: flexibility in fuel selection, faster reaction kinetics and heat generation; there is a considerable interest in lowering these values to intermediate (600 – 800 °C) and low (400 – 600°C) temperatures. This would help to widen the range of usable materials for fabrication, reduce costs and extend lifetime of these devices [3, 5].

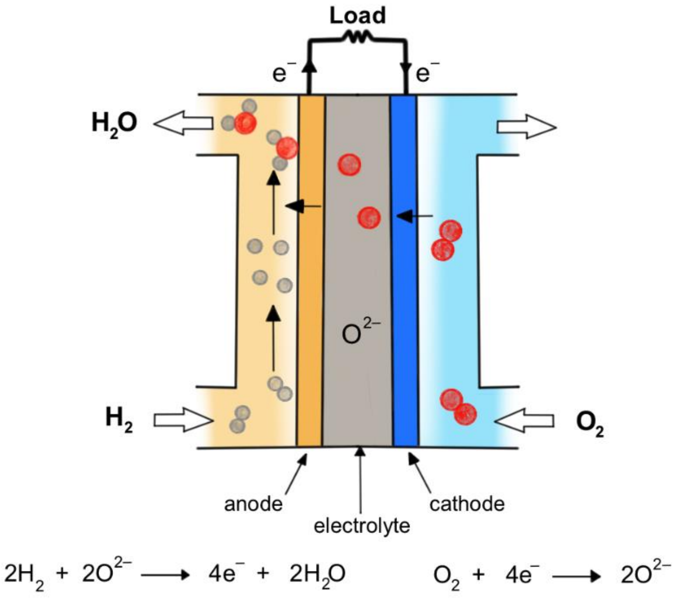

Figure 2-2 Schematic of operating SOFC

In summary, SOFCs are a simple and straightforward two-phase system where gaseous reactants interact with a solid matrix to produce energy with low CO_2 emissions. However, each cell component must meet a specific criterion and perform one or more specific functions. In the following sections, the individual components, and generalities of SOFC materials will be discussed in more detail.

2.2.1 Solid electrolytes

The electrolyte is composed of a crystalline ceramic oxide material with mostly pure ionic specific conductivity (generally O^{2-}) and negligible electronic conductivity. The electrolyte component is fabricated as a dense and nonporous layer to prevent the fuel and oxygen streams from mixing or trespassing to the opposite electrode. Electrolyte thickness has been identified as one of the causes of voltage loss due to the dependence between resistance and thickness, *i.e.*, cells with thicker electrolytes present higher resistance.

For a material to be considered a suitable candidate as SOFC electrolyte, the following criteria must be observed:

- Stability: Mechanical and chemical stability is required since this component is constantly exposed to extreme conditions (elevated temperatures, reducing and oxidising atmospheres) during fabrication and operation.

- Conductivity: Ionic conductivity should be high and stable over time. On the other hand, electronic conductivity must be negligible to prevent short circuit.
- Compatibility: Chemical interactions between cell components must be avoided to prevent the formation of insulating phases or any changes in material properties, such as thermal expansion coefficient (TEC), ionic or electronic conductivity [3, 27].

Fluorite type AO_2 materials, where A is a tetravalent cation, are the most representative conductive materials. Stabilized zirconia (ZrO_2), specifically yttrium-stabilized zirconia (8% mol Y_2O_3, commonly known as YSZ) is the state-of-art electrolyte material for *high temperature* SOFC (HT–SOFC) applications. Although zirconia can be stabilised with other oxide dopants to produce materials with higher ionic conductivities, yttria is widely used because of its availability, stability in both oxidising and reducing atmospheres, chemical compatibility with other cell components and reasonable cost [3, 7, 9, 27].

During YSZ fabrication some impurity phases are introduced to the electrolyte structure either from natural occurrence or intentionally by the manufacturer [28]. Naturally, zirconia is largely abundant in $ZrSiO_4$ form found in large deposits in Australia, Africa, Asia, and America. However, it is particularly difficult and cost intensive to remove SiO_2 from this natural form. Intentional impurities like alumina, titania, and hafnia are sometimes added to zirconia by the manufacturer in order to lower the sintering temperature, and improve density or strength [29].The presence of these impurities tends to be minimal (less than 0.1%wt.) and their possible detrimental effects in performance are negligible when the cell operates at high temperature (above 850°C). In contrast, these impurities have a significant negative effect when the operation temperature is reduced. In consequence, YSZ-based cells have good performance only when operated at high temperature [7].

The operating temperature of SOFCs is dominated by the nature and thickness of the electrolyte. Hence, to lower the operation temperature of these devices there are two possible pathways: (1) to reduce the thickness of the electrolyte and (2) to develop new and enhanced materials with increased O^{2-} conductivity.

The main problem with thin films electrolytes (15 – 20 µm approximately) is the difficulty to produce a film that is dense enough, with good mechanical stability and defect-free to withstand the harsh operation conditions after prolonged time periods. Therefore, to achieve the goal of lowering operation temperature of SOFCs, the research and developments of alternative materials has gained significant interest [27].

On this matter, doped ceria (CeO_2) is probably one of the most promising candidates for IT–SOFC applications, showing better conductivity and lower conduction activation energy compared to YSZ. Ceria is often doped with gadolinium ($Gd_xCe_{1-x}O_2$ abbreviated GDC or

CGO) or samarium ($Sm_xCe_{1-x}O_2$ also known as SDC) to introduce oxygen vacancies and enhance ionic conductivity.

Moreover, doped ceria is rather chemically stable and capable of avoiding undesirable interactions with electrode materials. Nonetheless, one important disadvantage of the material is the development of electronic conductivity derived from the partial ceria reduction from Ce^{4+} to Ce^{3+} close to the fuel electrode-electrolyte interface. To prevent this, an additional ultra-thin electrolyte layer is often used, creating bi-layered electrolyte and thus, a more complex SOFC assembly [3].

Alternatively to doped ceria materials, there are lanthanum gallate ($LaGaO_3$ or LGO) doped with strontium and/or magnesium ($La_{1-x}Sr_xMg_yGa_{1-y}O_{3-x/2-y/2}$ abbreviated LSGM) materials. LSGM has a slightly lower ionic conductivity at low temperatures than doped cerias, but the electronic conductivity remains unaltered. However, the main problems regarding this material are the complicated fabrication method and difficulty to obtain a pure phase, which raise concerns over the material's long-term durability [30, 31].

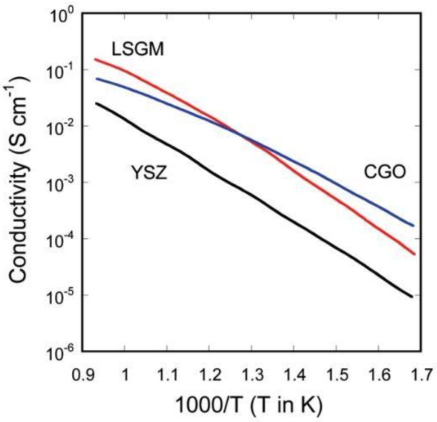

Figure 2-3 Ionic conductivity data for YSZ, CGO and LSGM (Note that GCO is an alternative name to GDC. Image source [31]

Parasitic effects of electronic conduction in the electrolyte can be neglected if operating temperature of SOFCs can be lowered enough. In this case, the main problem becomes the fact that ORR kinetics becomes sluggish, requiring a more active oxygen electrode to catalyse the reaction.

2.2.2 Anode

On one side of the electrolyte, the anode must be porous to allow the diffusion of the gaseous fuel stream. The prospective electrode materials should meet the following criteria [3, 7, 27]:

- Be active for the catalytic oxidation of the selected fuel.

- Possess carbon tolerance, specifically when using carbon-containing fuels when carbon accumulation is possible.
- Have tolerance to other possible contaminants associated with the selected fuel (*e.g.,* sulphur, chlorine, tars, etc.).
- Be chemically stable to prevent undesirable interactions with the electrolyte and/or interconnect material.
- Redox tolerance during start-up and shut-down procedures.
- Stable under oxidising atmospheres (conditions during operation).
- Thermally stable to avoid phase transition and TEC mismatch during production and operation.
- Porosity >30 vol% to enable gas diffusion into the triple phase boundary (3PB).
- Good electronic conductivity that remains stable over time.

The conventional anode electrode material in SOFCs is a cermet (ceramic-metal composite) fabricated by mixing NiO and YSZ powders. Then, the NiO is reduced *in situ* to form Ni nanoparticles uniformly distributed onto the electrolyte, which then is known as the cermet Ni-YSZ. Conductivity of this electrode is strongly dependant of two important factors: Ni content (which must be at least 30 vol%) and microstructure (particle size, size distribution and connectivity between Ni particles and the cermet). A solely metallic Ni anode would not be suitable because of the great TEC difference between the metal and the commonly used YSZ electrolyte. Therefore, Ni content must be thoroughly adjusted to ensure compatibility between the components [27].

The Ni-YSZ electrode works well when H_2 is the fuel. However, when using C-containing fuels some carbon formation and accumulation is expected. This phenomenon is linked to metal dusting and electrode structural damage, leading to a significant decrease in lifetime and cell performance. To inhibit or prevent carbon formation on the Ni-YSZ cermet the following strategies have been adopted [3, 7, 27, 32]:

1) Replace Ni in the electrode with ceramic perovskite materials of the type ABO_3. For this purpose, materials like $La_{0.3}Sr_{0.7}TiO_{3-\delta}$ (LST) and $La_{0.4}Sr_{0.6}Ti_{0.4}Mn_{0.6}O_{3-\delta}$ (LSTM) have shown to have a good combination of all the desired properties.
2) Promote Ni with the addition of other species such as Ru, Pd, Pt, Au, Ag, Sn and alkaline earth oxides (BaO, CaO, SrO), in dopant levels to help prevent carbon accumulation.
3) Re-engineer the electrode with non-Ni materials.

Regardless of the selected strategy, more research is needed to find suitable and more stable materials capable of efficient long-term operation that can be produced at a reasonable cost.

2.2.3 Cathode

On the opposite side, electrodes for the oxygen reduction reaction must observe the following criteria [3, 7, 27]:

- Be active for the catalysis of ORR at selected operation temperature.
- Chemically stable to prevent undesirable interactions with the electrolyte and/or interconnect.
- Redox tolerance during start-up and shut-down system procedures.
- Stable in reducing atmosphere (conditions during operation).
- Thermally stable to avoid phase transition and TEC mismatch during production and operation.
- Porous to enable O_2 or air diffusion into the electrode's phase boundary.
- Good electronic or *mixed ionic-electronic conductivity* (MIEC) that remains stable over time.

Reduction of oxygen from air occur on the electrode as described in the following electrochemical reaction [27]:

$$O_2 + 4e^- + 2V_O^{\bullet\bullet} \rightarrow 2O_O^X \quad \text{Equation 4}$$

Where O_2 is molecular oxygen from air, e^- are electrons in the electrode material, $V_O^{\bullet\bullet}$ represents vacant oxygen sites either on the electrode or electrolyte material, and $O_O{}^X$ represents oxygen ions in the electrolyte material.

As described in Equation 4, ORR requires the presence of both electrons and oxygen vacancies, so depending on the material characteristics, two case scenarios can present. When the electrode material is an electronic conductor with little or non-ionic conductivity, the pores in the structure will serve as O_2 carriers, the material as e^- carrier, and the electrolyte will provide the vacant oxygen sites. Therefore, restricting the ORR process to the 3PB lines (Figure 2-4a).

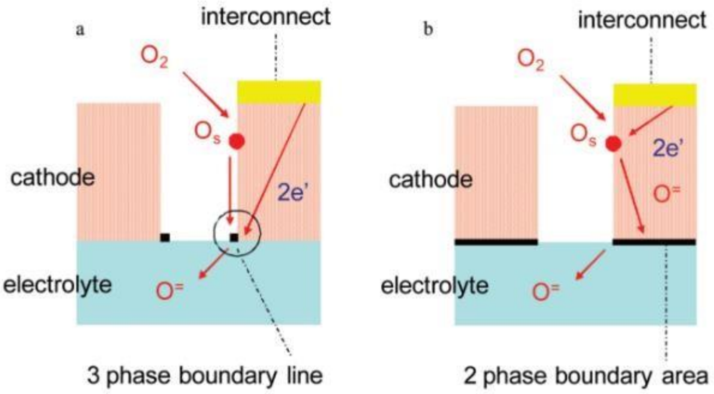

Figure 2-4 Schematic representations of cathode (or oxygen electrode) structures when the material is (a) poor or (b) good ionic conductor. Image source [31]

Alternatively, when the electrode material exhibits mixed conductivity, the ORR occurring at 3PB is also effectively extended to the electrode's surface to form oxygen ions when in contact with air [33, 34]. The formed ions are transferred to the electrolyte through the electrode/electrolyte interface (2 phase boundary or 2PB) or at the vicinity of the 3PB (Figure 2-4b) [27, 31].

Cathodes are often fabricated from manganites or cobaltites of lanthanum ($LaMnO_3$ and $LaCoO_3$, respectively) doped with divalent metals. Besides their inherent ionic conduction, they also possess some electronic conductivity that helps to provide more uniform current distribution on the electrode. Electrodes are often prepared from mixtures of the corresponding metal nitrates salts, then thermally treated at high temperatures to remove the nitrate component to achieve a pure phase material [3].

Material selection for the oxygen electrode is strongly based on thermomechanical properties and affinity with the electrolyte material. While some materials may possess better ionic conductivity than others, their thermal expansion coefficient (TEC) mismatch with the electrolyte makes them difficult to use.

Despite the extensive research on the subject, there are still considerable disagreements on the exact reaction sites for ORR on a MIEC electrode [34]. Generally speaking, the oxygen reduction reaction comprises the adsorption, incorporation, charge transfer and transport of O-species from the air stream to the electrode and/or electrolyte materials. Three main pathways have been identified for the ORR, a simple summary of these is presented on Figure 2-5.

Pathway 1 is known as the electrode bulk process, oxygen from air is adsorbed onto the electrode surface and then incorporated to the electrode bulk and transferred from the electrode to the electrolyte. This pathway is limited by the oxygen diffusion through the bulk of the electrode. On pathway 2, or electrode surface process, oxygen is adsorbed onto the electrode surface but not incorporated into the bulk, instead, it diffuses through the material surface and finally is incorporated to the electrolyte. This pathway is limited by the dissociative adsorption and diffusion on the electrode surface, Finally, pathway 3 or electrolyte process, consists of the direct electrochemical reduction of oxygen on the electrolyte surface, which can occur on electrolytes with some electronic conduction, such as the case of CeO_2–based materials. All three of these pathways can occur simultaneously, however, the contribution from pathway 3 the overall process is negligible when compared to 1 and 2, thus is generally not considered during experimental discussions [35].

The limiting step for ORR is highly dependent on the nature and characteristics of the cathode material, hence, more research is needed in this area to fully understand the process [36].

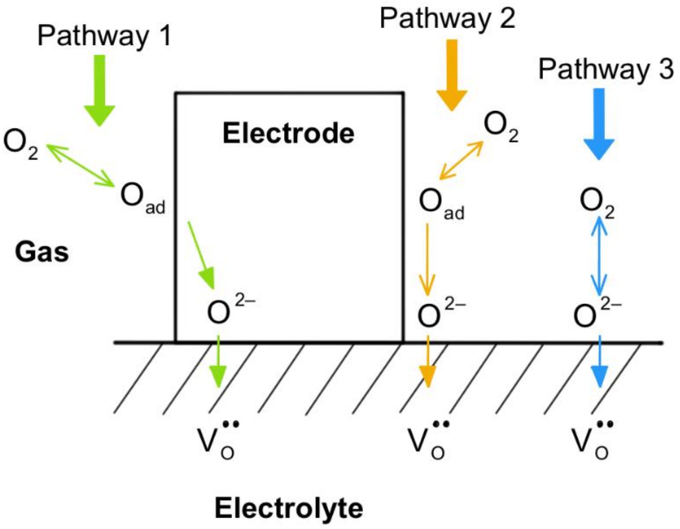

Figure 2-5 The three main possible pathways for ORR on SOFC electrodes

2.2.3.1 Electron conducting electrodes

Lanthanum manganite ($LaMnO_3$) based perovskites (ABO_3-type compounds) are intrinsic p-type conductors. The electronic conductivity can be improved by replacing La^{3+} with lower valence cations, such as Ca^{2+} or Sr^{2+}. In terms of SOFC applications, Sr substitution is preferred due to the higher stability, conductivity, and compatibility with YSZ of the resulting material [27, 30].

Common problems with $La_{1-x}Sr_xMnO_3$ (LSM) include undesirable interactions with YSZ at elevated temperatures during fabrication or operation processes and oxygen-stoichiometry dependence to oxygen partial pressure (P_{O_2}). At high temperatures LSM and YSZ can react to produce the insulating phases $La_2Zr_2O_7$ and $SrZrO_3$; alternatively, manganese from LSM can diffuse into the electrolyte layer. Properties of LSM itself can also be affected by operation conditions, oxygen stoichiometry becomes dependant to oxygen partial pressure (P_{O_2}) at high temperatures, affecting its conductive properties [3, 27, 30].

Nonetheless, these problems can be disregarded if processing and operating temperatures are kept under acceptable levels. Therefore, LSM with a Sr content between ~0.1 – 0.2 is the practical choice as oxygen electrode material in YSZ-electrolyte based SOFCs operating .in the 700 – 900°C range; mainly because of its high electronic conductivity, electrochemical activity towards ORR, high thermal stability, excellent microstructural and long-term performance stability, as well as good compatibility with the electrolytes YSZ, GDC and LSGM at their respective operation conditions [3, 7, 27].

2.2.3.2 Mixed oxygen ion-electron conducting electrodes

These perovskite oxide materials (ABO_3 compounds) have been widely investigated as electrode materials because of their MIEC characteristics. Their properties can be further enhanced by substitutions on the A or B-sites to tailor the thermal expansion coefficient (TEC) and/or to introduce oxygen vacancies [27].

The first candidate is lanthanum cobaltite ($LaCoO_3$) which exhibits better electronic conductivity than $LaMnO_3$ under the same conditions. Unfortunately, TEC mismatch with YSZ is significantly higher and they are more prone to produce insulating phases, particularly at high temperatures. Additionally, reproducible measurements of conductive properties are difficult to obtain due to the material's low thermodynamic stability. Nevertheless, cobaltites have exceptional electrochemical activity for ORR and the preferred operation range is 500-700°C [3].

$LaCoO_3$ can be improved with A-site substitution using Sr to give $La_{1-x}Sr_xCoO_{3-\delta}$ (LSC), a material with increased oxygen vacancy concentration and improved ionic conductive properties. It has been found that the ionic conductivity of LSC is directly correlated to Sr content, reaching its maximum value at the optimal content level of $x = 0.5$ when measured at 1 atm oxygen pressure at a temperature range from 100 to approximately 600°C [7, 31].

Additional enhancement can be achieved by subsequent B-site substitution with Fe to produce $La_{1-x}Sr_xCo_{1-y}Fe_yO_{3-\delta}$ (LSCF). Addition of Fe helps to minimise thermal mismatch with the electrolyte, whilst Sr substitution increases ionic conductivity. The composition $\mathbf{La_{0.6}Sr_{0.4}Co_{0.2}Fe_{0.8}O_3}$ (LSCF–6428) has attracted significant attention for IT-SOFC applications due to its great balance of catalytic activity, compatibility, and stability characteristics; especially when used with GDC or LGO electrolytes [3, 30].

Strontium-doped lanthanum ferrite $La_{1-x}Sr_xFeO_{3-\delta}$ (LSF) is another suitable option for reduced temperature SOFC applications. The electronic configuration of Fe^{3+} in LSF produces a highly stable and less reactive material, even at high operation temperatures. However, when LSF is sintered at temperatures above 1200°C, doped with other cations in A/B sites, or the original A/B-ratio is modified, its stability becomes compromised and undesired reactions can occur affecting cell performance. To prevent these adverse effects, a layer of SDC or GDC is often used as a protective barrier which also improves electrochemical behaviour due to the enhanced oxygen surface exchange kinetics of ceria [7, 31].

2.2.4 Interconnect

In order to generate a larger power output, it is possible to arrange SOFCs in stacks of two or more units connected to one another using a specialised component known as *interconnect* [30].

This material serves as an electrical connector between two adjacent cells whilst separating the fuel and air feed stream for each unit. To perform this task, the interconnect material must be: (1) a good electronic conductor and oxide ion insulator, (2) chemically stable under both oxidising and reducing environments, (3) thermally stable to match the adjacent electrodes and (4) gas impermeable to prevent streams mixing [7].

Considering the requirements only a few materials such as Cr_2O_3 alloys, alkaline-doped $LaCrO_3$ or other Cr-containing ceramic perovskites are suitable candidates for the conventional high operation temperature (~1000°C) of SOFC stacks. Nevertheless, ceramic interconnects are expensive, difficult to process and prone to developing O^{2-} ion conduction under certain conditions, which is an undesirable trait for these materials [27].

Furthermore, for ceramic interconnects, microstructure, doping effect, electronic conductivity, TEC and fabrication process need to be carefully evaluated during material selection. In practice, all commercially available cell designs use a small amount of interconnect material.

With the further advances in lowering operation temperatures, the use of already available high-temperature metallic alloys can be enabled. Besides being a more cost-effective option, metallic interconnect materials are preferable to ceramic materials mainly because of their true nature as electronic conductors and oxide ion insulators. Moreover, they are mechanically stable, durable, conduct heat more efficiently and are easier to fabricate [3].

Whatever the choice in material, more research is needed to enhance stability of the overall system without compromising the performance.

2.3 Fabrication of SOFC electrodes

Electrodes are generally made using simple powder processing routes. Powders are obtained from either solid-state reaction between the oxides of the desired components or precipitation of a gel from nitrate salt precursor solutions [9, 26, 37-39].

Nitrates are usually selected as solution precursors due to their high purity and clean burn-out (meaning no carbon residue) which in consequence, produce highly pure powder material [40]. The resulting powder is then dried,calcined, and finally pulverized to give particles in the 1 –10 μm size range. Electrode deposition is done using one of the following methods:

- Slurry coating,
- Screen printing,
- Tape casting or
- Wet powder spraying.

The proper selection of the fabrication method will depend on cell design and desired electrode characteristics. After deposition, the next step is to dry and finally sinter the material. The sintering temperature must be carefully chosen to ensure proper connection between components and stable microstructure while avoiding undesirable interactions [9, 41].

2.3.1 Electrode degradation and performance decay

SOFC systems are constantly under extreme conditions and being supplied with oxidants (generally air) and fuel streams. Therefore, degradation of individual components and detrimental effects on performance are expected. For oxygen electrodes the principal sources for contaminants are the SO_2 and Cr present in air feed streams or raw materials and interconnect materials, respectively [9].

Metallic components and interconnects in SOFC systems can become a source of Cr-containing vapours, which can cause *poisoning* of the oxygen electrode at operation conditions. However, this phenomenon is sensitive to electrode material, presenting different mechanisms. For LSM, Cr is deposited at the 3PB, whereas for LSCF is deposited on its surface with possible formation of $SrCrO_4$ [3].

Other well-known and expected contaminant related to material impurities is sulphur; considered a major contaminant in raw ceramic powders and some metallic materials due to its proclivity to form insulating phases. In a similar way to Cr, sulphur poisoning mechanisms differ among materials. LSM has shown better tolerance S-poisoning and little surface modification in comparison to LSCF under similar operation conditions [7, 42].

Degradation derived from microstructure coarsening and shrinkage of the active working surface on electrodes are consequences of the high operation temperature and long-time operation periods. In general terms, the microstructure of the electrode undergoes significant changes that ultimately lead to gradual increase in polarisation resistance of the electrode and overall voltage loss. Some of the observed changes in microstructure are *agglomeration, segregation, or diffusion of individual components from one neighbouring phase to another, change in material porosity and secondary phases formation* [17, 27, 43-47].

High temperature operation can also be prejudicial to cell structure. Thermal shock and sharp temperature gradients cause severe mechanical stress. These gradients may be the result of *cold* feed streams entering the cell or during start/shutdown procedures. Many of these challenges could be eliminated by reducing the operation temperature without undermining the system’s advantages and performance. To do so, the ideal range for temperature operation would be 600–700°C [5] or even lower.

To achieve this goal there are two challenges that need to be addressed: (1) conductivity of YSZ-based electrolytes drops significantly at low temperatures and (2) the kinetics of the reactions on the electrodes, particularly for the ORR, are severely affected [48].

The first challenged can be resolved using alternative electrolyte materials like doped ceria. Lastly, it is clear that development of suitable *oxygen electrodes* is the key to reducing SOFCs operation temperature and possibly accelerating the commercialisation process of this type of technology.

The use of MIEC materials as porous scaffolds enhanced using infiltration is, perhaps, the most promising option to achieve this goal; but there are still many technical issues that require further improvement.

2.4 Surface–modified electrodes through infiltration

In general terms, the infiltration method is a four-step process that involves: (1) the pre-fabrication of a porous backbone layer onto a dense electrolyte layer, (2) co-sintering of the components, (3) infiltration of a second phase and (4) calcination of the infiltrated electrode [49, 50]. Screen-printing or tape casting techniques are frequently used to deposit an ink containing the electrode material. Next, the two components are co-sintered at high temperatures to enhance the connectivity and conductivity. Afterwards, the secondary phase is infiltrated in the form of a precursor solution, usually from nitrate salts of the selected metals.

This step can be completed solely contacting the solution with the scaffold and letting the infiltration occur due to capillary action or using vacuum to accelerate the process. A specific infiltrate microstructure and/or loading can be achieved by either performed infiltration in one or many cycles. For such purpose, the infiltrating solution's properties can be tailored.

Finally, the infiltrated electrode is calcined at a temperature lower than required for traditional ceramic fabrication (*e.g.* ~800°C) promoting the secondary phase formation. The full process is summarised in Figure 2-6, exemplifying the fabrication of an infiltrated YSZ electrode [3, 26].

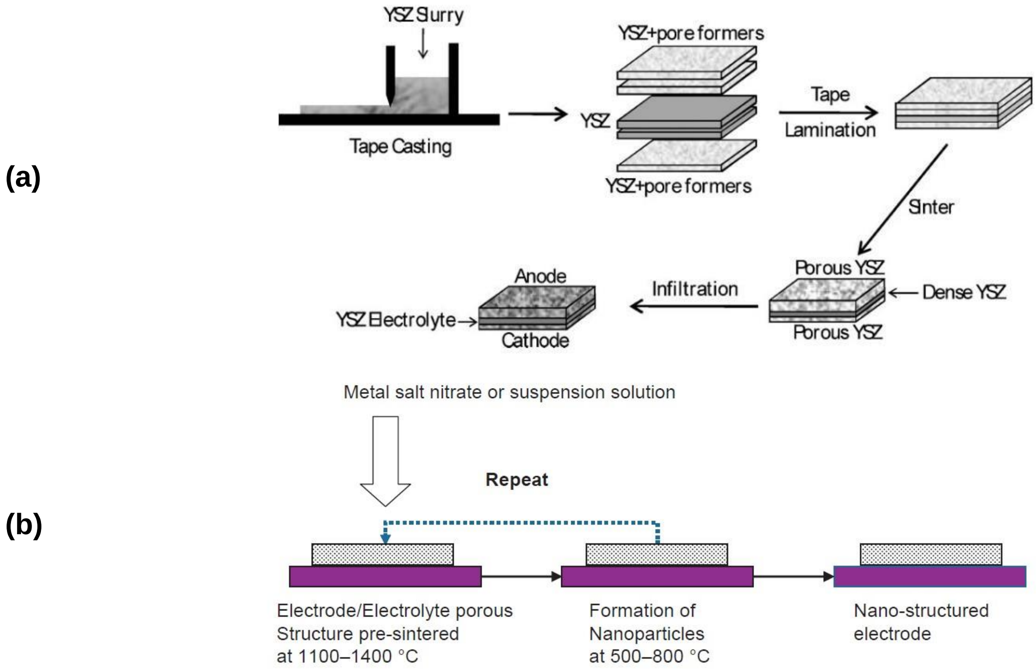

Figure 2-6 Diagrams showing (a) the general fabrication procedure for infiltrated electrodes and (b) detailed procedure for infiltration process. Image source [3, 26]

The multiple-step approach of this methodology allows the incorporation of materials that otherwise would be omitted because of their chemical or thermal incompatibility with the electrolyte or electrode material [48].

2.4.1 Factors affecting the Infiltration process and microstructure

Performance of the fabricated electrode is strongly dependant on the resulting loading and morphological aspects of the infiltrated phase, as well as final microstructure of the electrode scaffold; therefore, it is necessary to identify the variables that can be modified to tailor the final product.

For the construction of the scaffold: porosity, surface area and connectivity to the electrolyte are the most important parameters to optimise. The use of pore formers (either organic or polymeric) mixed with the scaffold powder in the ink is an effective strategy t\794o achieve a good porosity. The firing temperature of the scaffold as well as the heating and cooling ramps during fabrication should also be carefully considered. A high enough firing temperature must be achieved ensure complete sintering and adherence to the electrolyte without detriment to the porosity or promoting undesirable reactions between the components [3, 51], whilst both heating and cooling ramps must be within an appropriate range that prevents thermal shock from occurring and thus prevent any physical damage to the fabricated device. Usual heating/cooling ramps using during device fabrication are in the range between 3 – 20 °C min^{-1} [52].

For the infiltration step, the solution's properties can be altered to promote uniform distribution, phase formation and particle size of the infiltrate. Solution concentration, solvent choice and added surfactants or complexing agents are the usual modifiable variables [53].

While low concentrations yield a smaller particle size, a greater number of infiltration cycles might be required to obtain the target material load [22]. Nonetheless, low concentrations are less likely to affect the intrinsic liquid's properties like viscosity and wettability, which also play a key role during infiltration. On the other hand, surfactants or solvent mixtures, usually Triton X–100 (polyethylene glycol p-(1,1,3,3-tetramethylbutyl)-phenyl ether, which is a nonionic surfactant) or water/alcohols mixtures, are used to facilitate the infiltration by modifying the liquid's superficial tension and contact angle with the scaffold. Some surfactants and complexing agents have proved to be helpful in achieving pure phase formation of the infiltrate. Nevertheless, evidence suggests that the effectiveness of the process is related to the nature of the backbone and infiltrated phase [53-55].

The final calcination step is carried at a lower temperature to remove residual nitrates, humidity and to promote phase formation of the infiltrate. This temperature is also one of the main factors responsible of resulting microstructure, as coarsening and agglomeration of the infiltrate can occur during this step [56].

2.5 Nanostructured oxygen electrodes

Infiltration of oxygen electrodes enhances performance by either (1) enlarging the 3PB surface area for ORR, (2) increasing electronic and/or (3) ionic conductivity. The final improvement mechanism and effect is dependant of the scaffold's microstructure and nature, as well as the microstructure of the infiltrated phase [49, 50, 57]. The different possibilities will be discussed in more detail in the following sections.

2.5.1 Infiltration of ionic–conducting scaffolds

The use of ionic conducting materials as scaffolds has the advantage that this same material can be used as the electrolyte; therefore, excellent electrode/electrolyte bonding and complete TEC match can be guaranteed. In this case the infiltrated phase must be an active ORR electrocatalyst and provide an electronic conduction path. LSM or MIEC materials are usually infiltrated for this purpose [58-61].

LSM-infiltrated electrodes are the most reported materials and experimental results show enhanced performance over traditional LSM/electrolyte composite electrodes under similar operation conditions [62]; in their book Meng and Zhao [3]. compare a LSM-infiltrated YSZ electrode against a conventional LSM-YSZ composite electrode, both synthesized and tested under similar conditions, obtaining polarisation resistance (Rp) values of 0.66 $\Omega\cdot cm^2$ and 5.2 $\Omega\cdot cm^2$ at 700°C for the infiltrated and conventional electrode, respectively.

Calcination temperature used to produce the infiltrated electrodes has been identified as one the main factors affecting electrode microstructure, heavily influencing the infiltrate's particle size, electrode porosity and 3PB surface area [26]. Other studies have linked the effectiveness of infiltration to the conductive properties of the scaffold [63, 64] and even a couple of different models capable of predicting the expected electrode performance (specifically referring to its resistance) from its physical and electrochemical characteristics have been developed.

The *surface resistance* (SR) model describes situations where the electrode surface kinetics dominate the cathode performance, this is, polarisation resistance depends entirely on oxygen surface exchange resistance [65].

The Tanner, Fung and Virkar model (TVF) considers both the surface and bulk ionic effects contributing to the overall electrode performance, *i.e.* oxygen surface exchange and posterior ionic conduction [65, 66].

Finally, the Simple Infiltrated Microstructure Polarisation Loss Estimation, otherwise known as the SIMPLE model, that is based on the TVF model. Resistances from oxygen being incorporated to the electro-catalyst surface and being transported through the ionic-conducting scaffold are considered; however, this model operates under the assumptions that bulk oxygen transport only occurs through the scaffold, that its microstructure can be approximated as a series of columns, and that oxygen is only incorporated at the infiltrated electrocatalyst [67].

Due to the low calcination temperature (between 500 – 800 °C) used after the infiltration step, MIECs such as LSF [68, 69], LSC [70, 71], $La_{0.8}Ca_{0.2}FeO_3$ (LCaF),

$La_{0.8}Ba_{0.2}FeO_3$ (LBF) [72], LSCF [43, 73-75] and $La_{0.6}Sr_{0.4}Fe_{0.9}Sc_{0.1}O_{3-\delta}$ (LSFSc) [76] have been successfully incorporated into YSZ scaffolds undesired reactions or TEC mismatch, whilst achieving good performances associated with increased 3PB area [74]. Nonetheless, the long-term stability of these materials needs to be further investigated and improved since performance tends to decay derived from phase segregation, coarsening and agglomeration of the infiltrate [43, 69, 72, 77].

Moreover, LSCF [78-84], LSF [55], LSC [55, 85], $La_{0.8}Sr_{0.2}Co_{0.8}Ni_{0.2}O_{3-\delta}$ (LSCN) [86] and Pr oxides [87, 88] have been effectively infiltrated into other electrolyte scaffolds such as GDC, a more suitable option for IT–SOFC and LT–SOFC, with the benefit of avoiding formation of insulating phases.

Despite the inherent benefits of this approach to electrode infiltration, pure phase formation, size and distribution of the infiltrate becomes an issue of particular concern. The use of complexing agents, dispersants, or pre-infiltration of a secondary phase have proved to be effective strategies to promote pure phase formation, good particle dispersion and narrow size distribution, respectively.

Particularly for the case of LSF, LSC and LSCF infiltrated into GDC scaffolds, Burye *et al.* [53-55] have effectively demonstrated that particle size of the infiltrate can be significantly reduced, and its distribution improved by: (1) pre infiltrating the scaffold with GDC, (2) chemically desiccating the precursor before calcination, (3) adding Triton X-100 as dispersing or citric acid as complexing agent to precursor solution.

The use of desiccants after electrode infiltration and GDC pre-infiltrated electrodes produced smaller and more uniformly distributed nanoparticles (NP) for each case in comparison to unmodified and non-desiccated precursor. Through controlling desiccation of the infiltrated precursor by using different desiccants is possible to control the particle size and distribution of the NP to be produced in large part due to the evaporation-induced self-assembly (EISA) process, which has been extensively researched as a way to obtain mesoporous and patterned thin films, especially when paired with other organic additives. GDC pre-infiltration showed to be the most effective method to obtain the smallest infiltrated NP. All modified electrodes performed better than non-infiltrated electrodes.

However, these features tend to make the overall process more complex. Furthermore, some studies link the effectiveness of these agents to the specific nature of the infiltrate [73].

2.5.2 Infiltration of electronic–conducting scaffolds

In this case, the scaffold functions as the ORR catalyst and electronic conductor, LSM is the most common material. To enhance the performance an ionic conductor is infiltrated to enlarge the 3PB surface area; usually, doped ceria and MIECs are used for this purpose [89-91].

In practice, LSM scaffolds are infiltrated with either GDC or SDC to provide an ionic conducting pathway. Reports by Xu *et al.* [92], suggest that the optimum level of infiltration is 50%, at this level 3PB is effectively extended clearly promoting ORR over bare LSM electrodes.

SDC impregnation has also proved to enhance the fuel electrode performance. Data by Tian *et al.* [93] shows that resistance for an uncoated (Ni-SDC/SDC/LSM) cell measured at 600°C was 1.15 $\Omega\cdot cm^2$. After infiltrating the oxygen electrode, the resistance decreased to 0.58 $\Omega\cdot cm^2$, after infiltrating both electrodes the final resistance was 0.36 $\Omega\cdot cm^2$; meaning that cell resistance decreased ~3.2 times.

Similarly, GDC modification also improves electrode performance by increasing 3PB, inhibiting LSM grain growth and reducing Rp [51]. LSM has also been infiltrated with LSC, $LaCoO_3$ (LC), $LaNi_{0.6}Fe_{0.4}O_3$ (LNF) [94], YSZ [95] and LSM-YSZ [96]. In all cases, increase in 3PB has been reported as the mechanism for electrode improvement.

In this case, desired phase formation is not a problem due to GDC being a fluorite type material, hence crystals will form in a face-centred cubic arrangement. Nonetheless, some of the challenges for this infiltration rely on the fact that: (1) there's a TEC mismatch risk when dealing with different components and (2) a high number of infiltration cycles might be necessary to obtain enough loading to enable proper ionic conduction. Nevertheless, evidence suggest that infiltration is an effective way to further enhance the performance on this type of electrodes and prevent degradation over moderate periods of time (~500 h); evaluations for long–term operation periods are necessary to determine electrode stability.

2.5.3 Infiltration of MIEC scaffolds

As has been previously discussed in section 2.5, infiltration was used to either enlarge 3PB surfacearea or enhance ionic/electronic conductivity. Infiltration of MIEC scaffolds is a strategy primarily used to achieve one or more of the following objectives:

- Enhance O_2 surface exchange kinetics,
- Prevent phase segregation or surface enrichment,
- Further enhance conductive properties.

Mixed ionic and electronic conduction are not limited to ABO_3 perovskite materials, the same benefits can be obtained via fabrication of composite electrodes with an electronic and an ionic conductor, like in the case of LSM-YSZ composite electrodes. In a study by Kiebach *et al.* [97] a commercially available stack of 10 cells was infiltrated with GDC; the uniformly deposited thin film enhanced performance when operating at temperatures below 780°C because of the superior ionic conductivity of GDC. However, after exposure at higher temperatures (*i.e.* 860°C) the initial cell voltage improvement of 2% significantly decreased (~53%). Other studies looking into infiltration of the same type of composite materials using GDC [98] and $Pd_{0.95}Mn_{0.05}O$ [99] corroborated that the performance of the electrodes was enhanced thanks to the infiltrated phase. Ultimately, it was demonstrated that infiltration is a useful tool not only for self-fabricated electrodes, but also for commercially available ones.

Another interesting study by Kiebach, *et al.* [22] tried to correlate the enhancement in electrode performance to the specific conductive nature of the infiltrate. To observe this, the base composite LSM-YSZ electrode was infiltrated with LSM, GDC or LCN ($LaCo_{0.6}Ni_{0.4}O_{3-\delta}$), which are electronic, ionic (O^{2-}), and mixed conducting materials, respectively. All infiltrates showed improved performance effectively reducing Rp during heating and cooling processes. A clear tendency in performance degradation was also observed after high temperature treatment. When testing at 550°C, the LCN infiltrated electrode exhibited the highest improvement over LSM and GDC. However, with increasing operation temperature, LCN is less capable of reducing Rp compared to LSM or GDC. In contrast, during the cooling down section of the test, only LSM and concentrated GDC remain capable or effectively reducing Rp. LSM and GDC infiltrated electrodes presented a lower degradation rate, 66% and 20% respectively, being GDC the most effective of the two. The intrinsic conduction properties of the infiltrates seemed to have no influence over the resulting electrochemical performance, but further improvement is expected upon increasing the number of infiltration cycles [100] or precursor concentration [101].

As previously stated, MIEC materials are a suitable option as oxygen electrodes for IT–SOFC and LT–SOFC applications. Although MIECs are more chemically and thermally compatible with doped cerias, it is possible to use them in YSZ electrolyte-based cells. The preferred material for this purpose is LSCF mainly because of its chemical stability and TEC compatibility [3]. Reports by Cheng *et al.* [100] have demonstrated that as little as two infiltration cycles are enough to drastically reduce electrode Rp, observing maximum performance after 10 infiltration cycles without detrimental effects on performance or microstructure.

LSCF faces other challenges that need to be considered, such as Sr-surface segregation and limited O_2 surface exchange kinetics which are the most common causes of electrode degradation [17, 43-45, 78].

As previously mentioned, LSCF–6428 with the specific composition $La_{0.6}Sr_{0.4}Co_{0.2}Fe_{0.8}O_3$ has the best balance of catalytic activity and compatibility with commonly used electrolyte materials. Surface modification of LSCF–6428 via infiltration has proved to be an effective way to produce a more stable electrode with enhanced performance and resistant to degradation by SSS, as presented in Table 2-2.

In nanoparticle infiltration cases, R*p* values tend to decrease from blank electrodes associated with an increase in 3PB surface area or enhanced ionic conductivity; however, rapid degradation due to infiltrate coarsening and SSS can occur especially when electrode is exposed to high temperatures (>800 °C).

Thin (<100 nm) network of interconnected NP produced a porous coating modification that effectively decreased R*p* and prevented SSS. Depending on the infiltrate's properties either oxygen conduction and oxygen vacancies increase (SDC, GDC, SSC, PSM and PSCM) or electronic conduction and 3PB increase (LSM, LCC and LSCF). Coatings are less prone to coarsening and therefore are more stable than scattered NP. However, data also showed that dense coatings produced adverse effects on electrode performance derived from reduced active surface area and poor oxygen diffusion.

Interesting findings by Lee *et al.* [17] have suggested that dopant segregation in perovskites is directly associated with cation size mismatch and electrostatic interactions with oxygen vacancies. Based on this, Tsvetkov *et al.* [19, 20] have reported that modifying the surface of LSC dense films with less reducible cations, like Hf, can enhance the oxygen surface exchange kinetics and prevent Sr– surface segregation by tuning the oxygen vacancies at the surface. This modification has a 'volcano effect' meaning that there is an ideal Hf% value to achieve enhanced performance and stability; for the particular case of LSC this value is 16%. Due to the similarities between LSC and LSCF this strategy could also be adopted to modify LSCF electrodes expecting to have similar results, thus producing an enhanced electrode with extended lifespan under IT-SOFC operation conditions.

2.6 $La_{0.6}Sr_{0.4}Co_{0.2}Fe_{0.8}O_{3-\delta}$ (LSCF-6428) as cathode material

As previously mentioned in Chapter 1, as the operation temperature of SOFCs gets lowered from typical values, the oxygen reduction reaction (ORR) becomes the most important reaction in the system, mainly due to the reaction kinetics becoming sluggish with the temperature decrease [34, 102]. As a countermeasure to this problem, the use of alternative cathode materials with enhanced ORR catalytic activity and conductive properties under these conditions has been extensively researched and reported on [103].

One of the prime candidates for SOFCs operating at reduced temperatures is LSCF. LSCF is a perovskite type material (ABO_3) resulting from the doping on both the A and B site of base material $LaCoO_3$ (LC) with Sr and Fe respectively. Although many molar doping proportions could be used to produce a variety of LSCF ($La_{1-x}Sr_xCo_{1-y}Fe_yO_{3-\delta}$) materials, it has been reported that when $x = 0.4$ and $y = 0.8$, the resulting material (commonly referred to as LSCF6428) displays the best balance of conducting and thermomechanical properties for its use as cathode on SOFCs, particularly when paired with doped ceria electrolytes, such as GDC [104].

For LSCF-6428, conductivity values in air are 210, 282 and 332 Scm^{-1} at 900, 800, and 600°C respectively; while its thermal expansion coefficient (TEC) value is $15.3 \times 10^{-6}\ K^{-1}$ (compared to GDC's, which is $11.5 – 11.9 \times 10^{-6}\ K^{-1}$).

LSCF belongs to the $R\overline{3}c$ space group with a near cubic crystal structure. For this material Sr-solubility is limited to $x \leq 0.4$ and the rhombohedral and orthorhombic phases are stable for $x \geq 0.4$ and $x \leq 0.2$, respectively. Specifically for the $x = 0.4$, the theoretical density for the single-phase perovskite has been calculated as 6.37 gcm^{-3} [8]. Changes in material composition can induce strain in the crystal lattice of LSCF; regardless of this, oxygen vacancies are the primary defect present in LSCF.

The inherent mixed conductive behaviour of LSCF is a combination of the localised hopping holes between Fe^{3+} and Fe^{4+} characteristic of LSF, and the charge compensation by reduction of Co^{3+} to Co^{2+}, characteristic of LSC [105].

Two main pathways for the ORR on SOFCs cathodes have been identified [36]. On pathway 1, bulk diffusion to the two-phase boundary occurs; on pathway 2, oxygen adsorption and desorption occur at the electrode surface followed by surface diffusion to the triple phase boundary (TPB). Depending on the electrode material, the ORR can be dominated by one of the pathways or they can occur in parallel. In either case, oxygen vacancies are the key factor that influences the ORR mechanism. (Figure 2-7).

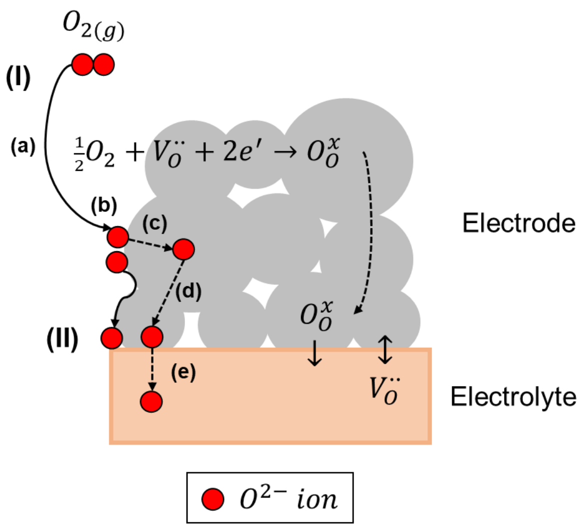

Figure 2-7 A simple schematic showing the ORR reaction via two possible pathways on SOFC cathodes. On pathway (I) bulk diffusion consisting of (a) dissociative oxygen adsorption, (b) ionisation of oxygen atom, (c) incorporation of adsorbed oxygen atom in electrode bulk, (d) bulk diffusion and (e) oxygen atom transfer at the electrode/electrolyte interface; pathway (II) surface diffusion to the TPB.

Despite its advantages one of the major concerns with LSCF as a cathode material is its stability and long-term degradation under SOFC operating temperatures and working conditions. Numerous studies have determined that when LSCF is prepared via conventional ceramic methods eventually suffer from Sr segregation, which in turn has a highly detrimental effect on the kinetics of ORR [12]. Some of the identified phenomena responsible for cathode degradation are reaction between the cathode and the electrolyte [106], coarsening or changes in microstructure [81], deposition/poisoning by contaminants [107], and Sr surface segregation (SSS) [11, 108].

As the name describes it, when Sr migrates from the bulk to the surface of the material, *i.e.* it segregates to the surface and forms insulating phases such as SrO, $Sr(OH)_2$, and $SrCO_3$; leading to the blocking of ORR active sites and changing electrode composition, which then results in decreased oxygen surface diffusion kinetics [109].

SSS on LSCF electrodes and its detrimental effect on cell performance has been extensively reported in literature. When investigated in dense bar samples [110], the original smooth surface presented a large number of submicron particles with some isolated micron-sized particles only after thermal ageing at 800°C for 96h.

Causes for cation segregation have been extensively investigated. Elastic energy and electrostatic charge interaction were identified as driving forces for SSS [13]. The elastic energy is related to the lattice mismatch between the dopant and host as the former is introduced to the structure on the A-site (Sr^{2+} as the dopant and La^{3+} as the host) [111], whilst charge interaction is derived from the interactions between the positively charged oxygen vacancies and the negatively charged A-site defects resulting from substituting a trivalent La^{3+} with a bivalent Sr^{2+} [111].

Through computational first principle studies, it has also been found that SrO-terminated surfaces in LSCF are the basic thermodynamic driving force for SSS. Unfortunately, ceramic processing methods are most likely to produce a SrO- terminated surface rather than a LaO- terminated one. Additionally, even though oxygen vacancies are crucial to improve ORR, their presence also reduces the stability of the structure by weakening the attractive forces and increasing the repulsive ones [16].

Furthermore, it was discovered that Sr-containing species are volatile. To assess this, SrO and LSCF powders were covered by a YSZ sheet and heated at 1000°C for 200h, it was found that for the SrO powder, some of it had been deposited onto the YSZ sheet. Alternatively, for the LSCF powder, no Sr deposition was observed, possibly due to a lower degree of activity of this material. Nevertheless, when investigating the Sr distribution on cathodes after long term operation, it was found that Sr systematically concentrated along the gas flow direction; strongly suggesting that Sr species from LSCF cathode are volatile and can be transported via gas phase evaporation and deposition [112].

2.6.1 Reactivity of LSCF with contaminants

2.6.1.1 Chromium

Cr based materials are by far the preferred interconnect material due to their economic and easy processing characteristics, particularly for IT-SOFCs. However, at high temperatures, the interconnect becomes a source of volatile Cr species that can get deposited on the cathode, which can rapidly deteriorate ORR activity by reducing active sites and blocking pores limiting gas diffusion. Additionally, it has been reported that Cr deposition occurs preferentially on segregated SrO, which in turn accelerates SSS [113].

2.6.1.2 Boron

Glass materials are often used as seals in SOFCs structures thanks to their flexibility in structure and properties. Introducing boron oxide (B_2O_3) in glass is a well-recognised way of tailoring some of the glass properties, like viscosity and softening temperature. However, one of the main concerns when using boron is the high volatility of B-containing species under SOFC operation conditions which can poison the electrodes.

When discussing specifically LSCF electrodes, the presence of borosilicate glass has a major detrimental effect on microstructure and electrode performance due to the formation of borates, particularly $LaBO_3$, that deteriorate oxygen exchange and diffusion on the electrode [114].

2.6.1.3 Sulphur

Sulphur readily exists as an impurity in hydrocarbon fuels, and the major challenge with is undoubtably the poisoning of Ni-based anodes. Additionally, its detrimental effect can be extended to the cathode, where SOx present in air can be accumulated and react with LSCF to produce $SrSO_4$. Studies have shown that sulphur deposition exhibits a characteristic volcano effect dependent on temperature [115]; meaning that reactions between SrO and SO_2 are most pronounced at 700°C. Other studies have also shown that sulphur deposition is random, irreversible, and becomes predominant as operation temperature is reduced [116].

2.6.1.4 CO_2, water vapour and other contaminants

Both CO_2 and water vapor exist in the air that circulate in SOFC stack systems, hence the importance of studying their effect on electrochemical performance of the cathode.

Through several studies it was found that CO_2 and H_2O had a more severe detrimental effect on LSCF at lower temperatures [117]. Whilst at 750°C, no microstructural changes or inhibition to ORR was observed, below said temperature and high humidity, SSS was found to be increased, Cr-contamination was accelerated, and it was hypothesised that water vapour decreased ORR by competitive adsorption with oxygen [118].

2.6.2 Development of LSCF-based cathodes

2.6.2.1 SSS suppression and enhanced ORR activity

As already mentioned, when the operation temperatures of SOFC systems get reduced, the reaction kinetics for ORR become more sluggish and increasingly predominant with decreasing temperatures. The characteristic MIEC properties and ORR catalytic activity under these conditions make LSCF an excellent cathode material for this type of applications. However, despite the obvious benefits of LSCF, Sr surface segregation (SSS) has been identified as the intrinsic degradation mechanism for this material, leading to performance decay. Said degradation is driven by cation size mismatch between doping and host atoms, and electrostatic attractions [13, 17, 111]. Thus, research has heavily focused in minimising or entirely preventing SSS via surface modification or tailoring the electrode structure to enhance ORR activity [119].

Doping the B-site with high valence cations proved to stabilise the perovskite structure with a trade-off of slightly reduced ORR [120]. Based on systematic first principle calculations, surface coatings, applying a compressive strain via doping with larger elements or higher valence elements on the B-site, or lower valence elements on the A-site and introducing A-site vacancies have proven to be effective ways to prevent SSS in LSCF [121]

Tsvetkov *et. al.* [19] studied the effect of surface modification on LSC with less reducible cations and observed a dramatic SSS suppression via the reduction of oxygen vacancies. Given the similarities between LSC and LSCF, is possible that the same approach with LSCF would yield similar results.

It is notable that surface modification of LSCF has been found to aid in both SSS prevention and enhancement of ORR activity.

Although surface modification with catalytically active nanoparticles (NPs) has been widely used in SOFC electrodes, the effect of discrete NPs on SSS it's still debatable. In a study conducted by Chen *et.al.* [18] a PNM ($PrNi_{0.5}Mn_{0.5}O_3$) thin film with exosoluted PrO_x NPs has been studied and found that the PNM film helped with the reduction of SSS whilst the PrO_x significantly accelerated ORR kinetics and effectively reduced electrode Rp form ~0.134 Ωcm^{-2} to ~0.022 Ωcm^{-2}.

Work by Ascolani-Yael *et.al.* [122] showed that infiltration of a secondary catalytically active phase into LSCF is another way to enhance the performance of these electrodes . Particularly for the cases where doped ceria (either with Gd or Sm) was infiltrated, the increase in electrode performance is related to the oxygen surface exchange properties of the ceria infiltrates.

When infiltrating $Sm_{0.2}Ce_{0.8}O_{1.95-\delta}$ (SDC) at various concentrations into porous LSCF electrodes, NP of varying sizes and morphologies were obtained [123]. Scattered 20 and 40 nm NPs, NPs in 60 nm clusters, and continuous 80 nm film. All infiltrated electrodes performed better than the bare LSCF electrode in the 650–700°C temperature range. At 700°C, bare LSCF electrodes exhibited and Rp of 0.40 Ωcm^{-2} compared to 0.17 Ωcm^{-2} for an electrode infiltrated with a 0.25 mol L^{-1} SDC precursor solution. Coated electrodes also exhibited better stability during long term testing (100h for this study) when compared with bare LSCF electrodes. However, no detailed mechanism for this improvement was proposed by the authors. Another study by dos Santos-Gomez *et al.* [44] showed that infiltrated $Gd_{0.2}Ce_{0.8}O_{1.9}$ (GDC) deposited onto LSCF-GDC scaffolds via spray pyrolysis at two different deposition times produced two types of coatings, NP and NP porous coating. These surface coatings significantly lowered the resistance of LSCF electrodes by a factor of 8 whilst also preventing SSS. The proposed mechanism for performance enhancement was related to the significant increase in TPB sites for ORR to take place. The porous coating displayed a lower degradation rate than the NP surface modification as demonstrated by prolonged testing, 400 h at 600°C were GDC infiltrated electrodes presented minimal Rp change (0.27 to 0.30 Ωcm^{-2}) oppositely to bare electrodes where the Rp change was more prominent (2.8 to 5.8 Ωcm^{-2}).

The use of Pr-doped ceria has attracted a significant amount of attention. Chen *et al.* [119] used $Pr_{0.2}Ce_{0.8}O_2$ (PCO), CeO_2, and PrO_2 to produce coatings of two different thicknesses, 2 and 6 nm, showed that the activity and durability of LSCF electrodes was improved. It was also concluded that whilst PrO_2 showed the most enhancement for ORR activity due to its high concentration of oxygen vacancies, CeO_2 was better at reducing SSS mainly due to Sr being less soluble in CeO_2 than PCO.

Liu *et al.* [124] studied $La_{0.4875}Ca_{0.0125}Ce_{0.5}O_{2-\delta}$ (LCC) as another type of doped ceria for electrode infiltration. In their work it's discussed how the La dopant into the Ce site significantly enhances the compounds oxygen transfer capability whilst Ca doping in conjunction with La provides enough oxygen vacancies to facilitate the ORR. By varying the concentration of the precursor NPs, thin and thick coatings were obtained. This study concluded that NPs and the thin coating lowered Rp values to ~0.076 Ωcm^{-2}, a reduction of ~60% when compared to bare LSCF whilst the thick coating had an adverse effect on Rp, possibly due to low bulk diffusion kinetics on LCC.

Although $La_{0.8}Sr_{0.2}MnO_3$ (LSM) remains as the state-of-the-art cathode material for SOFCs operating at temperatures above 800°C, its low ionic conductivity at lower temperatures severely affects its effectiveness as a cathode [8]. Nevertheless, LSM and some derivates have proven to significantly enhance LSCF electrode performance and effectively prevent SSS from happening. Ding *et al.* [125] infiltrated an LSCF electrode scaffold with 3 different infiltrates in thin coatings, $La_{0.8}Sr_{0.2}MnO_3$ (LSM), $Pr_{0.75}Sr_{0.2}MnO_{3-\delta}$ (PSM), and $PrSrCoMnO_{6-\delta}$ (PSCM). It was found that Pr-containing infiltrates performed better than LSM at enhancing electrode performance, *i.e.* lowering cathode Rp and producing a higher cell voltage/power density. For example, Rp measured at 750°C was 0.107, 0.093, 0.126 and 0.197 Ωcm^{-2}, for PSM, PSCM, blank and, LSM infiltrated cathodes, respectively. Furthermore, PSCM showed the best performance after 500h of operation. Since infiltrate coatings were very thin (10 – 50 nm), it makes the use of expensive materials like Pr, Pt or Pt more feasible as an infiltrate than as the bulk cathode material.

$La_{0.85}Sr_{0.15}MnO_{3\text{-}\pm\delta}$ (LSM) in a thin 50 nm film was used in the work of Lynch *et al.* [126]. Modified electrodes initially had lower performance than the unmodified ones. However, under prolonged testing (500h), the LSM-modified electrodes exhibited a time-dependent activation phenomenon which then resulted in a better performing electrode within the first 200h of operation. Liu *et al.* [127] also investigated the effect of $La_{0.85}Sr_{0.15}MnO_{3-\delta}$ (LSM) coatings on LSCF performance. Different thicknesses were evaluated by changing the concentration of the infiltrated solution giving the following morphologies: NP, thin, porous coating, and thick coating. The best performance was achieved by the thin coating while the thick coating increased Rp value when compared to bare LSCF. Rp value trend was 0.25 M> 0.125 M≥ 0.06 M> blank LSCF > 0.015 M> 0.03 M, where only lower infiltrate concentrations achieved lower Rp values than bare LSCF at similar testing conditions (~0.41 Ωcm^{-2} for blank LSCF versus 0.30 Ωcm^{-2} for LSM infiltrated electrode). Additionally, electrode modification also made the electrodes more stable through extended periods of testing (~120h). Choi *et al.* [128] also tested the A-deficient $(La_{0.8}Sr_{0.2})_{0.95}MnO_3$ (LSM) via sol-gel deposition of precursors at different concentrations on dense LSCF. Their results showed that LSM-thickness can be controlled within a specific 5 – 60 nm range by selecting the appropriate precursor concentration. Additionally, they concluded that after annealing at 850°C for 900h, bare LSCF samples showed signs of Sr-surface segregation (SSS), opposite to modified electrodes, suggesting that SSS was effectively prevented by the LSM coatings.

Infiltration of other mixed conductors like $Sm_{1-x}Sr_xCoO_3$ (SSC) and even LSCF into porous LSCF electrodes has also been studied. Even though SSC possess excellent oxygen surface exchange, bulk ion diffusion and electrical conductivity properties its use is limited by its high cost and insufficient thermal compatibility to electrolyte materials [129]. M. Liu's group Lou *et al.* [130] investigated the wetting properties of the precursors and their results showed that the ethanol addition to the solution lowered its surface tension allowing the formation of continuous and uniform $Sm_{0.6}Sr_{0.4}CoO_{3-\delta}$ (SSC) coatings in the form of disperse NP of 40 – 80 nm and NP clusters. All the modified electrodes exhibited lower Rp than bare LSCF enhancing the performance 30%, and when testing lower temperatures, the disperse coatings performed better than the NP clusters. Similar results were obtained by the same group when analysing the infiltration of [131] $Sm_{0.6}Sr_{0.4}CoO_{3-\delta}$ and LSCF-6428 as surface modifications. SSC was infiltrated in disperse 30 nm NP, thin 50 nm film and particulate coating of 50 -100 nm; while LSCF was used as a 50 nm film. All surface modifications exhibited a lower Rp value (~0.071 Ωcm^{-2} for LSCF and ~0.043 Ωcm^{-2} for SSC) in contrast with bare electrode (~0.103 Ωcm^{-2}), nevertheless, SSC performed better than LSCF as surface modification. It was concluded that a thin layer of SSC, significantly enhanced electrode performance and stability during the testing period (100h). F. Si *et al.* [132] also investigated the effect of infiltrating LSCF-6428 NPs as catalysts into a porous LSCF cathode at different weight percentages (3, 5, 10 and 15%). They concluded that even a 3%wt infiltration produced a significant decrease in Rp, from 2.136 Ωcm^{-2} as a baseline for blank LSCF to 0.229 Ωcm^{-2}, corresponding to a 89% reduction. It was also concluded that increasing NP loading resulted in further Rp deduction but not as significant.

Alternatively, an adequate tailoring and optimisation of the impregnation protocol can also result in better performing electrodes, as demonstrated by the comprehensive work by Burye *et.al.* where the effects of preinfiltration [53], precursor desiccation [55] and precursor additives [54] on electrode performance were evaluated, showing that precursor desiccation using chemical agents and GDC preinfiltration reduced the particle size of the infiltrated phase without compromising phase purity. Furthermore, the addition of other chemical additives, such as citric acid, also produced smaller infiltrated particles which were identified to be responsible for electrode performance enhancement.

Table 2-2 summarises some of the most relevant studies and their findings discussed above.

2.6.3 Concluding remarks

The popularity of fuel cells (FC) has increased significantly in recent years thanks to their ability to transform the chemical energy stored in fuels in electrical energy via electrochemical reactions. Furthermore, the energetic conversion is more efficient than traditional heat engines since FCs are not limited by the Carnot cycle.

Out of the many types of FCs, solid oxide fuel cells (SOFCs), which are a type of cell that operates at a high temperature range (600 – 1000°C), have a few added bonuses. The elevated temperatures facilitate the use of a wide range of fuels in either liquid or gas state and the waste heat can be repurposed or integrated to other processes that can increase their efficiency up to 90%.

Due to the extreme operation conditions and costly materials, the recent trends lean towards lowering the operation temperature of SOFCs (600 – 800°C). However, in doing so researchers face new challenges that require the development of more active cathode materials to overcome slow oxygen reduction reaction (ORR) kinetics. In this regard, LSCF has emerged as a popular material mainly due to its mixed ionic and electronic conductive properties, reasonable oxygen surface exchange, and good thermal compatibility with electrolyte materials.

Despite all the good qualities of LSCF, one of the materials major drawbacks is Sr-surface segregation (SSS), which is considered a degradation mechanism that tends to form insulating phases that greatly hinders the ORR. Numerous studies suggest *infiltration* as a viable strategy to prevent SSS whilst enhancing electrode performance.

Even though the production of high-performing and durable LSCF electrodes for IT-SOFC application still faces many challenges, there are also several areas of opportunity for improvement. Thus, more research in this subject will surely culminate in more durable, better performing, and cheaper electrodes.

Table 2-2 Different surface modifications for LSCF and their findings on electrode performance (LSCF–6428 was used as electrode scaffold material unless stated otherwise)

Infiltrate	**Electrolyte**	**Surface modification**	**Findings**	**Ref.**
$Sm_{0.2}Ce_{0.8}O_{1.95}$ (SDC)	YSZ with $Sm_{0.2}Ce_{0.8}O_{1.9}$ buffer layer	NP (~20 nm SDC 20, ~40 nm SDC40) NP coating (~60 nm SDC60) and continuous film (~80 nm SDC80)	Rp at 750 °C were 0.15, 0.13, 0.12, 0.074 and 0.085 Ω cm^{-2} for the blank LSCF, SDC20/LSC, SDC40/LSCF, SDC60/LSCF and SDC80/LSCF, respectively. Rp for coating and nanoparticles was similar at 800°C. However, at low operation temperatures (650 and 700 °C) coatings exhibited the lowest Rp values	[126]
$Gd_{0.2}Ce_{0.8}O_{1.9}$ (GDC)	GDC $Gd_{0.2}Ce_{0.8}O_{1.9}$	NP and NP porous coating (40 – 100 nm)	After annealing for 400 h at 600 and 800 °C coated samples showed less degradation than blank samples and SSS was prevented	[44]
$La_{0.4875}Ca_{0.0125}Ce_{0.5}O_{2-\delta}$ (LCC)	YSZ with $Sm_{0.2}Ce_{0.85}O_{2-\delta}$ buffer layer	NP, agglomerated clusters, thin, porous coatings, and thick coatings	Thin coatings showed the best performance, while thicker films produced increased Rp values. At 750 °C Rp for blank LSCF, LCC(NP)/LSCF, LCC (thin film)/LSCF and LCC (thick film)/LSCF were 0.130, 0.115, 0.076 and 0.148 Ω cm^{-2}, respectively	[124]
$Pr_{0.75}Sr_{0.2}MnO_{3-\delta}$ (PSM)	YSZ with $Sm_{0.2}Ce_{0.8}O_{1.9}$ buffer layer	Thin coating 10 – 50 nm	Rp values at 750 °C. for PSM, PSCM, blank LSCF and LSM infiltrated electrodes were 0.107, 0.093, 0.126 and 0.197 Ω cm^{-2}. Observed performance as anode supported cell PSCM/LSCF>PSM/LSCF>LSM/LSCF>Blank LSC, tendency remained constant for 500 h operation	[125]
$PrSrCoMnO_{3-\delta}$ (PSCM)				
$La_{1-x}Sr_{x}MnO_{3-\delta}$ (LSM)				
$La_{0.85}Sr_{0.15}MnO_{3}$ (LSM)	GDC $Gd_{0.1}Ce_{0.9}O_{1.95}$	Thin film (~50 nm)	LSM/LSCF electrodes exhibited lower resistance than blank LSCF electrodes. Full cell tests with an LSM/LSCF yielded better current density and higher voltage output even after ~500 h of testing	[126]
$La_{0.85}Sr_{0.15}MnO_{3}$ (LSM)	GDC $Gd_{0.1}Ce_{0.9}O_{1.95}$	NP, thin and porous coatings, and thick coatings	Best performance achieved by producing a thin coating, while thicker films produced increased Rp values. Test in full cell at 650°C blank LSCF ~0.41 Ω cm^{-2} and LSM/LSCF ~0.30 Ω cm^{-2}	[127]

Continued from previous page

$(La_{0.8}Sr_{0.2})_{0.95}MnO_3$ (LSM) on a dense LSCF–6428	N/A	Thin film (~50 nm)	After annealing at 850°C for 900 h, Sr-enriched superficial areas were detected on a bare dense LSCF pellet. No Sr-enriched areas were detected for the LSM/LSCF sample	[128]
$Sm_{0.6}Sr_{0.4}CoO_3$ (SSC)	GDC $Gd_{0.1}Ce_{0.9}O_{1.95}$	NP coating (40 – 80 nm) and NP clusters	At 750°C both modified electrodes showed ~0.036 Ω cm^{-2}, lower resistance than the blank LSCF. At 550°C resistances were 0.69, 1.0 and 3.52 Ω cm^{-2} for the coated, discrete nanoparticle and blank LSCF electrodes, respectively	[130]
$Sm_{0.6}Sr_{0.4}CoO_3$ (SSC)	GDC $Gd_{0.1}Ce_{0.9}O_{1.95}$	NP coating (~30 nm SSC30), thin film (~50 nm SSC50) and continuous particulate coating (50 – 100 nm SSC100)	Rp values at 750 °C were ~0.103, 0.071, 0.047, 0.043, 0.036 Ω cm^{-2} for the blank, LSCF/LSCF, SSC30/LSC, SSC50/LSC and SSC100/LSCF, respectively	[131]
$La_{0.6}Sr_{0.4}Co_{0.2}Fe_{0.8}O_{3-\delta}$ (LSCF)	GDC $Gd_{0.1}Ce_{0.9}O_{1.95}$	Thin film (~50 nm)		
$La_{0.6}Sr_{0.4}Co_{0.2}Fe_{0.8}O_{3-\delta}$ NP into $(La_{0.60}Sr_{0.40})_{0.95}(Co_{0.20}Fe_{0.80})O_{3-\delta}$	GDC $Gd_{0.2}Ce_{0.8}O_{1.9}$	NP	Infiltrated NP (3, 5, 10 and 15 wt%) critically enlarged the electrode surface area and enhanced performance. Rp at 650 °C for a blank LSCF electrode and the 3 %wt -infiltrated electrode were 2.136 Ω cm^{-2}, and 0.229 Ω cm^{-2} respectively; decease by one order of magnitude. Small cumulative increments were obtained with higher infiltrations.	[132]

2.7 Electrode characterisation techniques

In the following sections, a few of many available analytical techniques used to characterise SOFC electrodes are discussed. The particular interest in the following techniques derives from the fact that these were the ones used during the experimental stages of this research work.

2.7.1 Electrochemical impedance spectroscopy (EIS)

Electrochemical impedance spectroscopy (EIS) is well known and established tool for the investigation of mechanisms for electrochemical reactions, measuring the transport properties of materials and analysing the properties of porous electrodes [133-137].

One of the greatest strengths of EIS is the fact that it relies on small-signal perturbation reveals the relaxation times and amplitudes of various processes occurring in the system over a wide range of frequencies. Additionally, many different types of equipment have been developed for both benchtop and mobile measurements. Nevertheless, the need to acquire software to operate and analyse obtained data can increase the cost of performing this technique [138].

Ohmic polarisation or loss is associated to the resistivity if the materials to transport ions (ionic resistivity of the electrolyte) or electrons (electronic resistivity of the electrode). This contribution becomes significantly important especially for the electrolyte in the cases where its thickness is considerably larger than for that of the electrodes and when the electronic resistivity of the material used is significantly larger than the electronic resistivity of the electrode materials (check for ionic resistivity of GDC at operation temp vs electronic resistivity of LSCF at the same temperature). Derived from resistance to electron and ion flow in materials. Major contributor is the electrolyte resistance, especially if electrolyte layer is on the thicker side [139].

Concentration polarisation. Since the reacting species at the electrodes are gaseous and must be transported from the feed stream to the porous electrode to the 2PB or 3PB. The physical resistance to the transport of the gases through the electrode structure, which is a function of the gas's diffusivity and electrode microstructure, is reflected as an electrical voltage loss, also known as concentration polarisation. Resistance to mass transport through electrodes and interfaces, it's generally larger at the cathode, particularly if cathode–supported cells are employed [138].

Activation polarisation. All electrode reactions intrinsically involve charge transfer as a fundamental step (either convert neutral species to ions or vice versa); thus, involving electron transfer. In the case of oxygen electrodes, the charge transfer reaction consists of converting oxygen molecules into oxygen ions. In the cases where the material exhibits mixed conductive properties, pinpointing the specific mechanisms under which charge transfer occurs is a field open for discussion. When MIEC materials are used as electrode materials, electrochemical reactions can occur over the entire electrode surface (2PB) making this a great advantage for the use of these materials. Nevertheless, defect chemistry needs to be carefully manipulated to ensure that both ionic and electronic conductivities are sufficiently high. [8] voltage drop due to the sluggishness of reactions occurring at the electrode – electrolyte interfaces [133, 138].

In contrast to other classical electrochemical techniques that present measurements as a function of time, EIS presents a signal as a function of frequency at a constant potential, which demands some knowledge of mathematics for its understanding.

The biggest advantages for the use of EIS as a characterisation technique include the ability to obtain information on several processes (ohmic losses, electrochemical kinetics and mass transfer processes) can be individually characterised using a single experiment, since the different polarisations will have different time dependences.

EIS is usually measured by applying an ac potential to a system (the cell in this case) and measuring the current through it. On the *frequency response analysis* (FRA) impedance method, a small ac potential wave of 5 – 15 mV of a given frequency is applied to the working electrode, an ac current measurement is then made, and this same process is repeated by scanning along a desired frequency range. The impedances from the ac voltage and current (typically 5 – 10 measurements for a decade change in frequency) are registered and computed to obtain a visual representation of the data [133, 136].

The plotting of the imaginary part of the impedance, $-\mathrm{Im}Z(\omega)$, on the y – axis and the real part, $\mathrm{Re}Z(\omega)$, on the x – axis will produce a Nyquist plot. In an ideal case, the plot will show a series of semi–circles and quarter–circles that sometimes may be distorted or overlapped. Intercepts with the x – axis represent resistive losses due to various physical processes, whilst the positions of the arcs will provide information on the non – ohmic terms [7].

In addition to provide information regarding polarisations, EIS is also useful in simulating reaction mechanisms and it’s particularly useful when several coupled processes are involved in determining the system’s performance. Nevertheless, because EIS is measured at a limited range of frequencies, this method is useful only for studying processes with relaxation times from µs up to tens of seconds [133, 137, 139].

2.7.1.1 Equivalent Circuit Model (ECM)

Posterior to acquisition, data can be analysed based on a series of hypotheses involving the several possible physicochemical processes occurring in the system. In order to do this, measurements are fitted to certain mathematical formalisms of electrical circuits to form an *electrical circuit mode*l (ECM) with various components such as: inductors (L), resistors (R), constant phase elements (CPE) and other more complex elements [140].

Since the resulting electrical circuit and the calculated parameters do not have a clear physicochemical significance, often, the construction of an appropriate model is considered one of the most difficult parts of data analysis and is subject to misinterpretation [134].

2.7.2 X-ray diffraction (XRD)

X – ray diffraction is a non-destructive and bulk sensitive analytical method widely used for materials that are partly or mostly crystalline, where is most effective. Once the diffraction pattern for any given sample is obtained, this is later compared to database of known patterns for identification [141].

X – rays are short wavelength energy beams of electromagnetic radiation and are usually characterised by its wavelength or photon energy; and are produced when high speed electrons accelerated by a high voltage field, collide with a metal target. The kinetic energy from the electrons is converted to X – ray radiation. When an incident electron with enough energy excites an electron from the inner K shell to a higher energy state, the resulting vacancy will be filled by an electron from the outer shells (either L or M) to stabilise the atom. When an outer electron takes the vacancy at an inner shell, this leaves a new vacancy at the corresponding level that will be filled as well, thus inducing a cascade to fill occurring vacancies.

When the resulting transition goes from shell L to K, *Kα* radiation is produced, when the transition geos from shell M to K, *Kβ* radiation is produced. The same notation will be used for transitions from the M to L shell (*Lα)* and N to L shell (*Lβ*). When an outer shell electron transitions to an inner shell, it releases energy in the form of X – rays with specific energy. In the following example (Figure 2-8), a *K* – shell vacancy can be filled by an electron from either *L* or *M* shell, which results in the emission of characteristic *Kα* or *Kβ* X – rays, respectively.

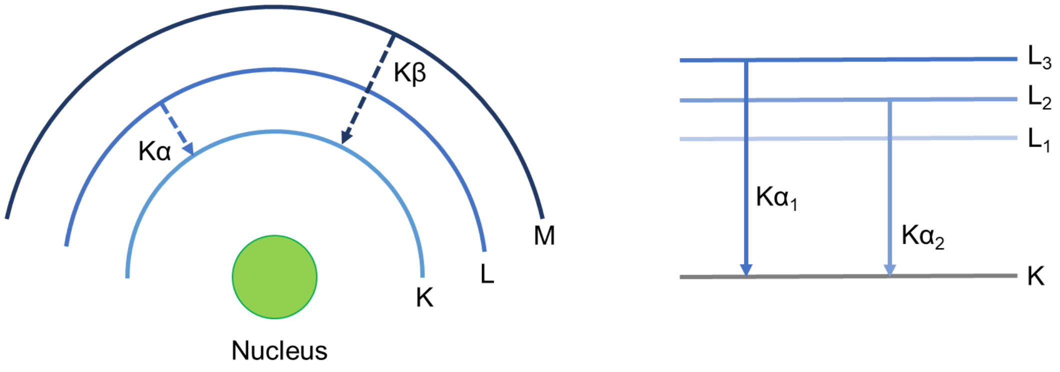

Figure 2-8 Schematic of how X-rays are produced

Since electrons from the immediate higher shell fill the low energy vacancies with more frequency than electrons from higher and further away shells, α rays are more intense than β rays. For the example above, $K\alpha$ rays are more intense than $K\beta$ since electrons from shell L will fill the vacancies on the K shell with more frequency when compared to M shell electrons. Additionally, Kα rays contain two characteristic lines: $K\alpha_1$ and $K\alpha_2$, with the wavelength for $K\alpha_2$ being slightly longer than for $K\alpha_1$, derived from the sub shell structure of the L shell, represented by L_1, L_2 and L_3.

$K\alpha_1$, $K\alpha_2$ and $K\beta$ are the strongest characteristic X – rays used for diffraction; when they hit the surface of the sample, they will be scattered by the regularly spaced atoms conforming the crystallographic planes, as shown in Figure 2-9. The scattered beams may interact with each other via constructive or destructive interference, when constructive interference occurs the beams satisfy Equation 5, known as Bragg's Law, and this effect is called *diffraction*.

$$n\lambda = 2d\sin\theta \qquad \textit{Equation 5}$$

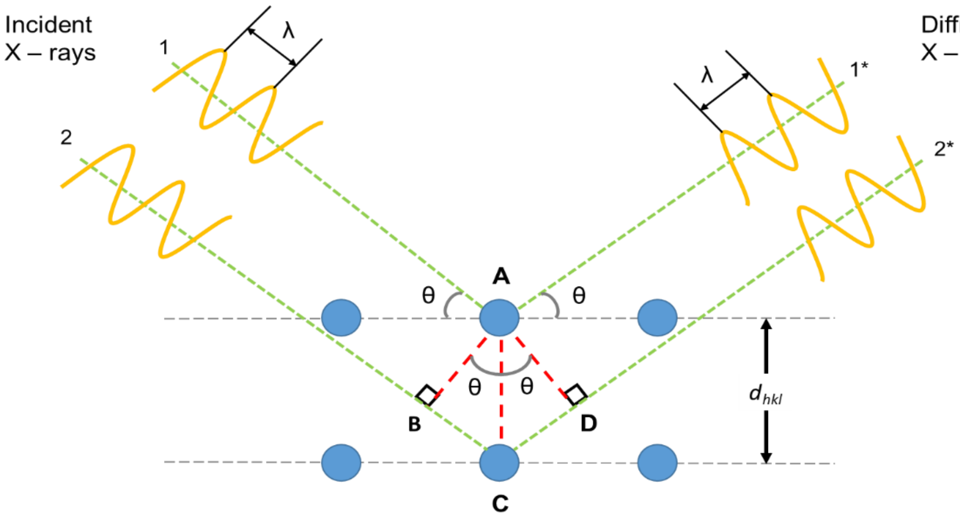

Figure 2-9 Schematic for Bragg's Law for XRD analysis

From Bragg's law, information about the spacing between atomic planes at a given incidence angle and wavelength can be obtained, and thus, the crystal structure of the material can be determined.

An XRD instrument is called an *X – ray diffractometer*. This instrument uses a single wavelength X – ray beam to analyse a sample by continuously varying the beam incident angle (2θ) and measuring the diffracted beam. A plot of diffraction intensity versus the angle between the incident and diffracted beam gives the diffraction spectrum for the analysed material and by comparing this spectrum against a database the quality and crystal structure of said material can be identified.

A simple arrangement for a diffractometer is presented in Figure 2-10, consisting of an X – ray source, primary optics, sample mount, secondary optics and finally, a monochromator and detector.

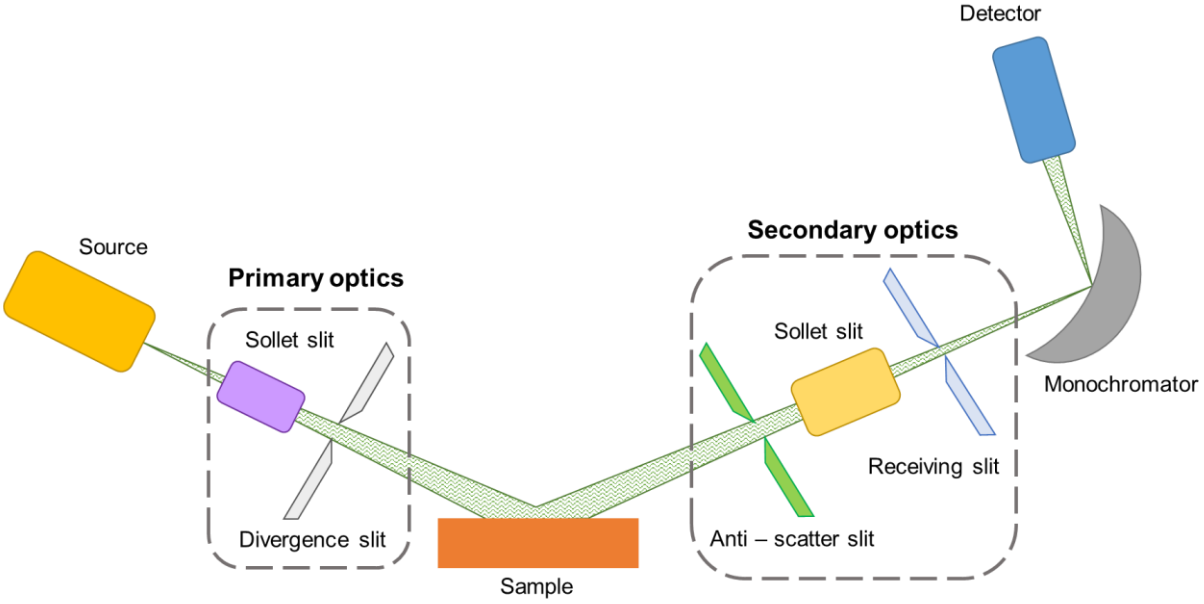

Figure 2-10 Simple arrangement for an X-ray diffractometer

The X- rays are produced in the source by an X – ray tube, the beam will pass through the *Soller* and divergence slits in the primary optics that help confine and direct its path to hit the surface of the sample. The diffracted X – ray from the sample will the pass through another set of anti-scatter, Soller and receiving slits that will converge the beam and reduce signal noise whilst the monochromator filters out any unwanted radiation before the beam reaches the detector [142].

Identification of substance and its crystalline phases is achieved by comparing the diffraction spectrum with spectra of known crystalline substances recorded as *powder* *diffraction files* (PDF) that usually obtained using Cu$K\alpha$ radiation and published by the ICDD (International Centre for Diffraction Data) [143].

Despite its inherent advantages, some of the more important limitations for XRD analysis include the requirement for tenths of gram per sample, access to data bases with standard reference files, for which licenses can be expensive, and a 2% detection limit when samples contain a mixture of materials [144].

2.7.3 Scanning electron microscopy (SEM)

Scanning electron microscopy is the most widely used type of electron microscopy. Images are formed by scanning the surface area of a sample with a focused beam of accelerated electrons to obtain microstructural and surface morphology information.

SEM equipment (Figure 2-11) consists of an electron gun and a series of electromagnetic lenses and apertures that help guide and condense the beam to a fine probe (10 nm in diameter usually) used for surface scanning. A deflection system moves the probe along the surface of the specimen surface and the electrons emitted from it are collected by the detector, amplified, and used to reconstruct a point-by-point image on the display screen. There are two types of electrons that are useful in SEM, *backscattered electrons* (BSEs) and *secondary electrons* (SEs) [145].

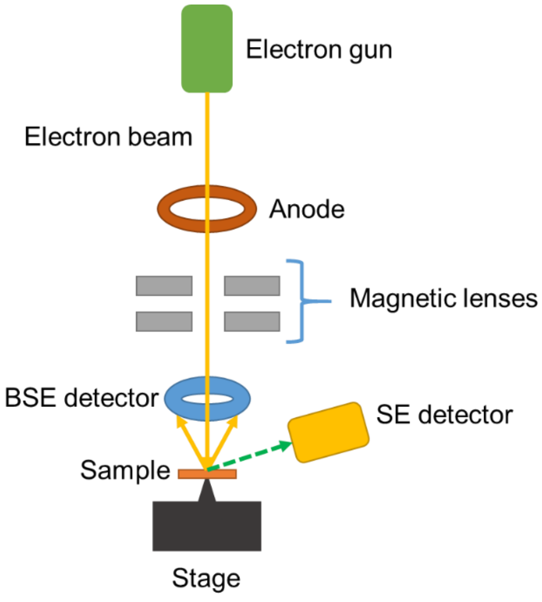

Figure 2-11 Simple arrangement for a Scanning Electron Microscope

As high energy electrons from the beam impact the sample surface, they can experience both elastic and inelastic scattering. Elastic scattering is a product of the electrostatic interaction of the beam with the atomic nuclei of the atoms in the sample where the electrons from the beam loose practically no energy. Due to their high energy, after interacting with the sample these electrons are backscattered and collected as the *backscattered electron signal* (BSE).

Oppositely, inelastic scattering is the product of the beam interaction with the atomic electrons from said sample, electrons from the beam will lose a considerable amount of energy transferring it to the sample electrons. The energy gained will allow for the sample electrons to be released from its particular atom and travel through the sample as a *secondary electron (SE)* that will also be inelastically scattered whilst gradually losing their kinetic energy.

The described electron/matter interactions occur in a specific interaction zone (Figure 2-12) usually depicted pear shaped. The size of this interaction zone will be dependent on the acceleration of the electron beam and the atomic number of atoms in the sample according to Figure 2-12

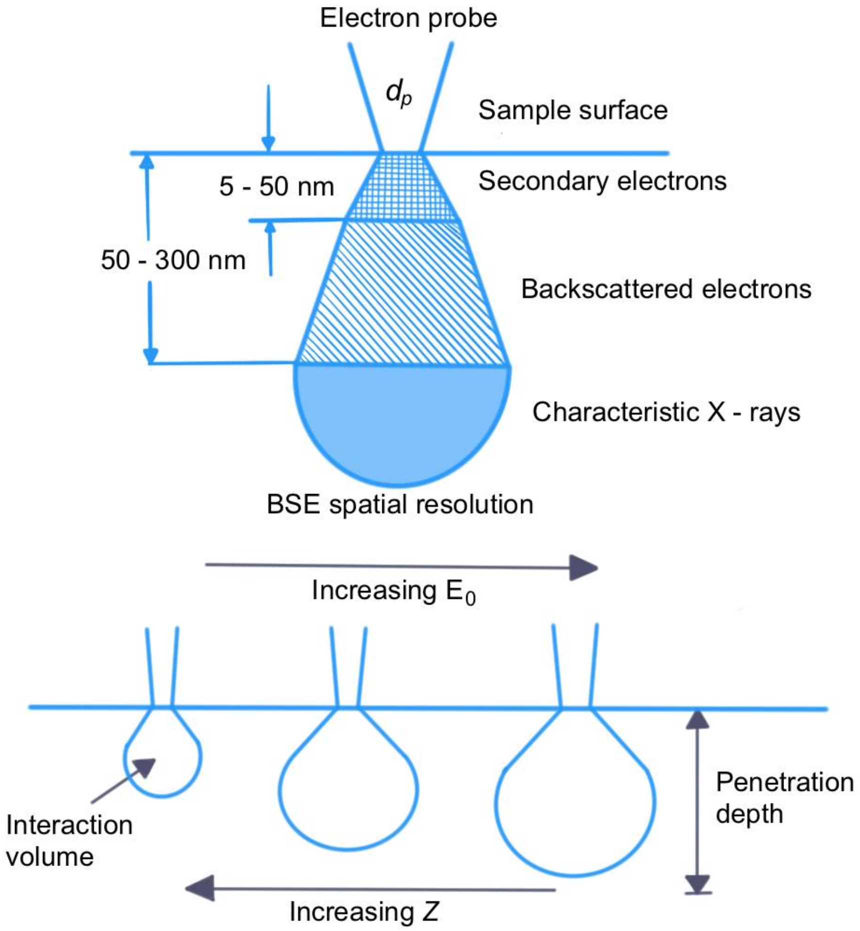

Figure 2-12 The different origin of SEs and BSEs within a spatial sample region and its dependence as a function of beam acceleration E_0 and atomic number Z

Since SE have lower energy than BSE and originate only a few nm below the sample surface they have very high spatial resolution and thus very useful to obtain topographic information. On the other hand, BSE interact strongly with the sample at a deeper level, so they have a lower spatial resolution. Nevertheless, because heavier elements (high atomic number, Z) backscatter electrons strongly than lighter ones (low Z) they appear brighter on image, hence offering elemental composition information [146].

3 Materials and methods

In this chapter the, all the different methodologies followed to produce all the different samples analysed in the course of this work will be detailed. Additionally, a brief overview on the characterisation techniques and instruments used will also be presented in this chapter.

3.1 Sample preparation

3.1.1 Symmetric LSCF/GDC/LSCF cells

3.1.1.1 Ceramic powder processing

Appropriate amounts of gadolinium doped ceria (10% Gd, GDC, Daiichi Kigenso Kagaku Kogyo Co., Ltd.) and lanthanum strontium iron and cobalt oxide (LSCF with molar composition 6/4/2/8, Fuel Cell Materials) were weighed and mixed with 0.1 wt% Triton X-114 (nonionic detergent, Sigma Aldrich) and isopropyl alcohol (Sigma Aldrich) to produce two powder suspensions. The suspensions were ball milled for 18 h at 1800 rpm and allowed to dry at 90 °C in a drying oven before further processing.

3.1.1.2 GDC electrolyte fabrication

Once the GDC powder was completely dry, ~0.5 g portions were uniaxially pressed at 430 MPa for 2 min (GS15011, Specac manual hydraulic press) using a stainless-steel die to produce disk electrolytes. The green electrolytes (Figure 3-1) were later sintered in a box furnace (BRF15/5, Thermal Systems) at 1400 °C for 5 h (heating and cooling ramps were 5 °C/min) to obtain dense electrolytes with the following characteristics: 94.513% ±3.456% relative density, 0.73 mm ±0.04 mm thickness and 10.85 mm ±.0.09 mm in diameter.

Sintering @1400°C x 5 h to obtain dense pellets (94.51 ± 3.46% dense, 0.73 ± 0.04 mm thick, 10.85 ± 0.09 mm Ø)

Figure 3-1 Simple schematic showing electrolyte production

Density of the electrolytes was measured using a density balance (Newclassic MS, Mettler Toledo) whilst diameter and thickness were measured using a digital calliper (RS Pro)

3.1.1.3 LSCF ink preparation

The electrode ink recipe consisted of the cathode powder, a dispersant agent, a binding agent, and solvent. To prepare this, appropriate amounts of LSCF powder (70 wt%), Triton X-114 (0.1 wt%). AqualonTM EC (3 wt%, ethyl cellulose grade N7, Ashland) and TexanolTM ester alcohol (30 wt%, Eastman) were mixed in a plastic tub using a SpeedMixedTM (DAC 800.1 FVZ, Figure 3-2) at 2500 rpm for 5 intervals of 2 min until a homogenous and glossy ink was obtained.

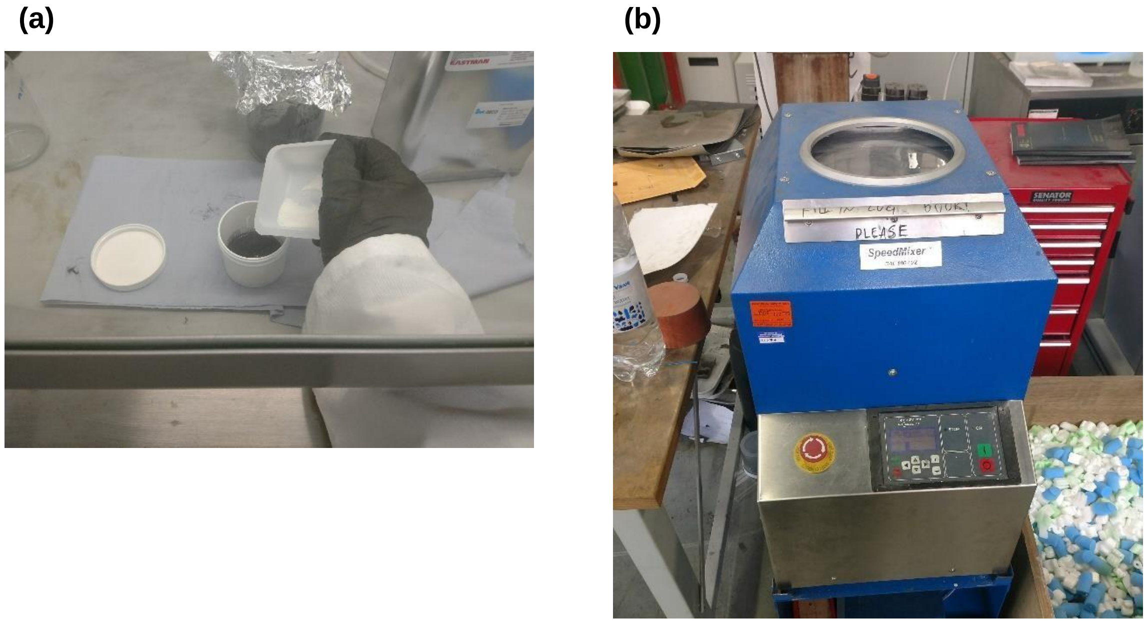

Figure 3-2 (a) LSCF ink ingredients and (b) speed – mixer equipment used.

3.1.1.4 LSCF electrode deposition onto GDC electrolytes

To deposit the LSCF electrodes onto the dense GDC electrolytes a Scotch® Magic^{TM} tape mas was created by adhering two stripes of tape one onto the other and cutting a circular perforation (6 mm in diameter) was made using a standard hole-punch. The mask was then secured to the electrolyte followed by a small dab of ink which was doctor bladed using a glass slide to remove the excess ink. The mask was then removed, and the ink was dried at 50 °C for 10 min in a drying oven before repeating this procedure on the opposite side of the electrolyte, thus producing the symmetric cells.

Once both electrodes were deposited, they were sintered at 1050 °C for 3 h (heating and cooling ramps of 5 °C/min) in a box furnace to obtain the porous electrode scaffolds (~30µm) ready to be infiltrated. A diagram depicting this process is presented in the following Figure 3-3.

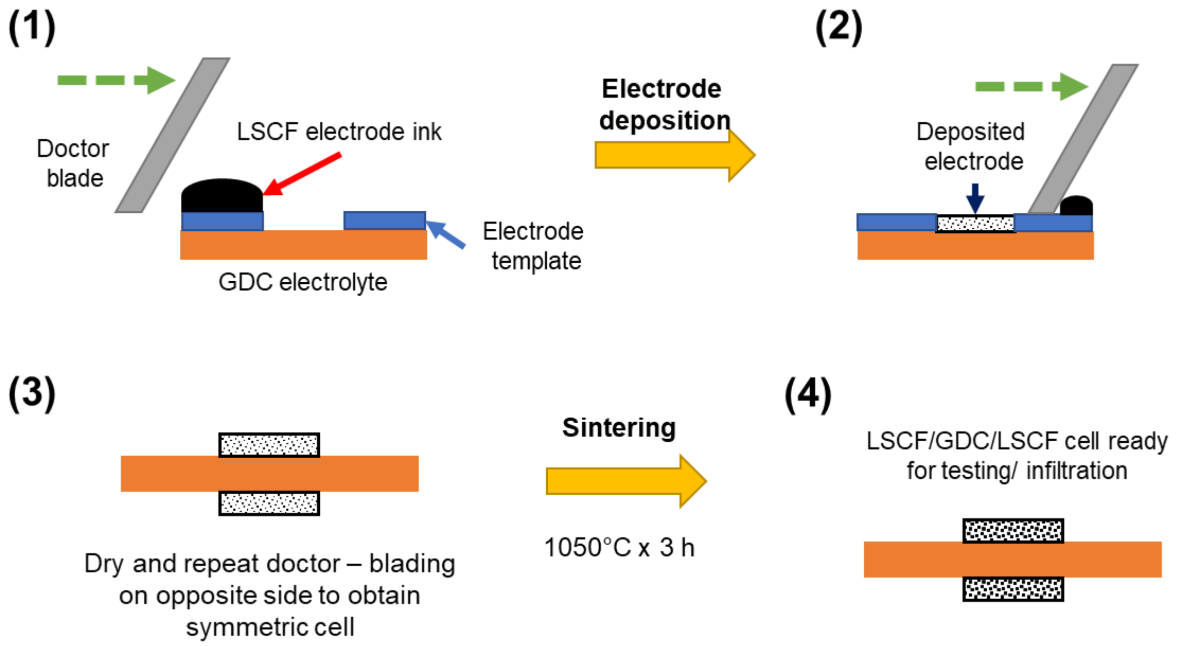

Figure 3-3 Steps for LSCF/GDC/LSCF cell production: (1) masking electrolyte to create an electrode template, (2) doctor – blading to create electrode, (3) let ink dry and repeat steps on opposite side, (4) sinter electrodes to produce symmetric cell ready for testing/infiltration

3.1.1.5 Precursor solution preparation

A 4 mol L^{-1} GDC ($Gd_{0.1}Ce_{0.9}O_{1.95}$) stock solution was prepared by mixing the proper amounts of $Gd(NO_3)_3{\cdot}6H_2O$ (99.99%, Sigma Aldrich), $Ce(NO_3)_3{\cdot}6H_2O$ (99.9%, Sigma Aldrich) and 3 wt% Triton X114 (Sigma Aldrich) in deionised water. Adequate amounts of the stock solution were diluted to produce 1.000, 0.500, 0.250, 0.125, 0.050 and 0.025 mol L^{-1} different precursor solution to use for infiltrations.

For the HfO_2 stock solution, 5 g of $HfCl_4$ (99.9%, Sigma Aldrich) were dissolved in 8 mL of deionised water producing a highly exothermic hydrolysis reaction according to the following Equation 6 and Equation 7 [147]:

$$HfCl_4 + H_2O \rightarrow Hf(OH)Cl_3 + HCl \qquad \text{Equation 6}$$

$$Hf(OH)Cl_3 \rightarrow HfOCl_3 + HCl \qquad \text{Equation 7}$$

The same dilution process was followed to obtain several HfO_2 precursors with different concentrations. However, after preliminary analysis it was found that the high acidity of these precursors caused chemical etching on the LSCF surface.

To prevent this phenomenon, the following alternative precursor route was followed [148]: 1 mol L^{-1} aqueous NH_3 solution (Sigma Aldrich) was added to the stock solution previously obtained forming a white gelatinous precipitate. The precipitate was allowed to settle before washing with deionised water to remove excess Cl^- ions, the washing procedure was repeated for a minimum of 5 times until the discarded liquid had pH close to neutral. The recovered solids where then treated with concentrated H_2O_2 (30 wt%, Sigma Aldrich) and 2 mol L^{-1} HNO_3 solution. The produced suspension was stirred overnight to produce the final HfO_2 stock suspension with a concentration of 420 mg mL^{-1}.

Finally, dilutions from the stock solutions were made to obtain 210.56, 105.28, 52.64, 26.32, 13.16, and 6.58 mg mL^{-1} in correspondence with the molar concentration for the GDC precursor solutions.

3.1.1.6 Cell infiltration using precursor solutions/suspensions

Symmetric cells were infiltrated by dripping 10 µL of precursor solutions onto the porous LSCF electrodes and allowed to absorb by capillarity and dry at room temperature. Once absorption and drying were completed the same process was repeated on the opposite side to complete the infiltration.

Whilst this concluded fabrication for the HfO_2–infiltrated cells, cells infiltrated with the GDC precursors required a calcination step for 1 h at 700 °C to obtain the desired GDC phase.

Mass change for samples was monitored by using a microbalance weighing scale (CPA2P, Sartorius). Weight gain for the different precursor and concentrations is presented on Table 3-1**.**

Table 3-1 Scaffold weight gain with different precursors at various concentrations

Concentration (mol L^{-1})	**GDC weight gain (mg)**	**Concentration (mg L^{-1})**	**HfO_2 weight gain (mg)**
0.025	0.038 ± 0.013	*6.58*	0.116 ± 0.035
0.050	0.127 ± 0.008	*13.16*	0.269 ± 0.041
0.125	0.314 ± 0.007	*26.32*	0.575 ± 0.013
0.250	0.557 ± 0.025	*52.64*	1.350 ± 0.107
0.500	1.031 ± 0.085	*105.28*	2.804 ± 0.155
1.000	1.906 ± 0.087		

3.1.2 Flat LSCF substrates

3.1.2.1 Ceramic powder processing

Lanthanum strontium iron and cobalt oxide (LSCF-with molar composition 6/4/2/8, Fuel Cell Materials) was weighed and mixed with 0.1 wt% Triton X-114 (Sigma Aldrich) and isopropyl alcohol (Sigma Aldrich) to produce a powder suspension. The suspension was ball milled for 18 h at 1800 rpm and allowed to dry at 90 °C in a drying oven before further processing.

3.1.2.2 Flat LSCF substrate production

Once the LSCF powder was completely dry, ~0.75 g portions were uniaxially pressed at 86.7 MPa for 30 s (GS15011, Specac manual hydraulic press) using a stainless-steel die to produce disk ceramic substrates. The green substrates were later sintered in a box furnace (BRF15/5, Thermal Systems) at 1300 °C for 5 h (heating and cooling ramps were 5 °C min^{-1}) to obtain dense pellet substrates with the following characteristics: 97.345% ±1.030% relative density, 0.70 ±0.05 mm thickness and 11.00 ±0.06 mm in diameter.

Density of the substrates was measured using a density balance (Newclassic MS, Mettler Toledo) whilst diameter and thickness were measured using a digital calliper (RS Pro)

3.1.2.3 Grinding and Polishing of LSCF substrates

The sintered LSCF substrates were mounted onto an aluminium stub with thermal resin for grinding and polishing until mirror finish. The equipment used was the EcoMet^{TM} 30 semi-automatic grinder polisher (Buehler). The grinding steps used P800, P1200 and P2500 SiC sandpapers (CarbiMet, Buehler); the polishing steps used monocrystalline diamond paste in the following sizes 6, 3, 1, 0.25 µm (MetaDi II, Buehler) and the mirror finish was achieved by polishing with 70 v/v% colloidal SiO_2 (0.06 µm, MasterMet, Buehler).

After polishing the substrates were removed from the aluminium stub and cleaned in 3 steps using an ultrasonic bath. During the first step the samples were sonicated while submerged in acetone (Sigma Aldrich) to remove any leftover resin, followed by sonication in isopropyl alcohol (Sigma Aldrich) and finishing with deionised water to ensure the removal of all colloidal SiO_2 from polishing. Substrates were then allowed to air dry before handling.

3.1.2.4 Spin-coating of substrates using precursor solutions/suspensions

LSCF substrates were coated using a personal spin–coater (Ossila). Selected programme spun the sample at 2500 rpm for 30 s and 50 µL of either HfO_2 or GDC solution precursor were pipetted onto the sample through the door aperture. Finally, coated samples were annealed at 120 °C for 5 min to ensure full solvent evaporation.

The annealing step concluded the fabrication steps for the HfO_2–coated substrates. For the GDC–coated substrates a calcination step for 1 h at 700 °C was required to obtain the desired ceramic phase.

3.2 Sample characterisation

All processed samples were analysed as described in the sections below, these were analysed in several batches due to university closure because of the COVID-19 pandemic, with some batches being analysed before and after lockdown. In most cases, repeat measurements were performed on more than one cell processed under the same conditions (either blank or infiltrated). A sample set of data will be presented for each batch/condition and the rest of the obtained data will be available to the reader on the relevant *Annex* section. Particularly for impedance measurements, the decision to measure repeats on different cells instead of re-testing the same cell was made because of two reasons. Firstly, cell integrity, since after monitoring the electrochemical performance of the cell for 50 h (100 h in some cases) in the compression jig, the Ag- paste used to establish appropriate electrical contact would sometimes peel off some of the LSCF electrode from the electrolyte. Lastly, since more Ag-paste would need to be added in order to assure good electrical contact, an excess of Ag (especially after 1 measurement), which is also catalytically active for ORR [149] would introduce undesirable variables into the analysed system and would difficult the identification of the contributions from electrode performance and Ag-paste towards ORR.

3.2.1 Electrochemical impedance spectroscopy (EIS) setup

For electrochemical evaluation all samples had a silver current collector (Ag – ink, C2010515D4, Gwent Group) screen printed (250 µm mesh, 12 µm thick, MCI Precision Screens Ltd.) onto both electrodes and cured at 100 °C for 10 min in a drying oven.

Due to budgetary considerations, a compression electrochemical testing jig was designed and built in house with the purpose of analysing fabricated cells at high temperatures and under synthetic air flow.

The produced samples were then placed in the testing jig (Figure 3-4). The sample was sandwiched between two gold meshes to ensure proper electrical contact and secured using the pyrophyllite stopper before being placed inside the atmospheric chamber.

The jig was then placed in the horizontal tube furnace (EST12150B, CarboliteGero Ltd.). Samples were heated to 700 °C at a 5 °C/min rate and held at that temperature for 50 h (unless stated otherwise) under a flowing 20 mL/min (Supelco rotameter) synthetic air atmosphere. Temperature was monitored using a K – type thermocouple and a PicoLog data logger (TC – 08, Pico Technology). For a majority of the samples, electrochemical impedance spectroscopy (EIS) measurements were collected during heating every 50 °C from 300 – 700 °C and every 30 min during the dwelling stage using the FRA/EIS analyser IviumStat.h standard (Ivium Technologies) in a frequency range between 100 kHz and 100 mHz with a signal amplitude of 20 mV using a two-electrode configuration.

The remaining fraction of the tested samples were analysed using a Solartron Modulab 1250 FRA and 1287 electrochemical interface in the range 65 kHz using – 100 mHz with a signal amplitude of 20 mV in a two-electrode configuration.

All data was collected using he proprietary software for Ivium and Scribner ZView, respectively; whilst data analysis and *electric circuit fitting* (ECF) was done using Scribner ZView software.

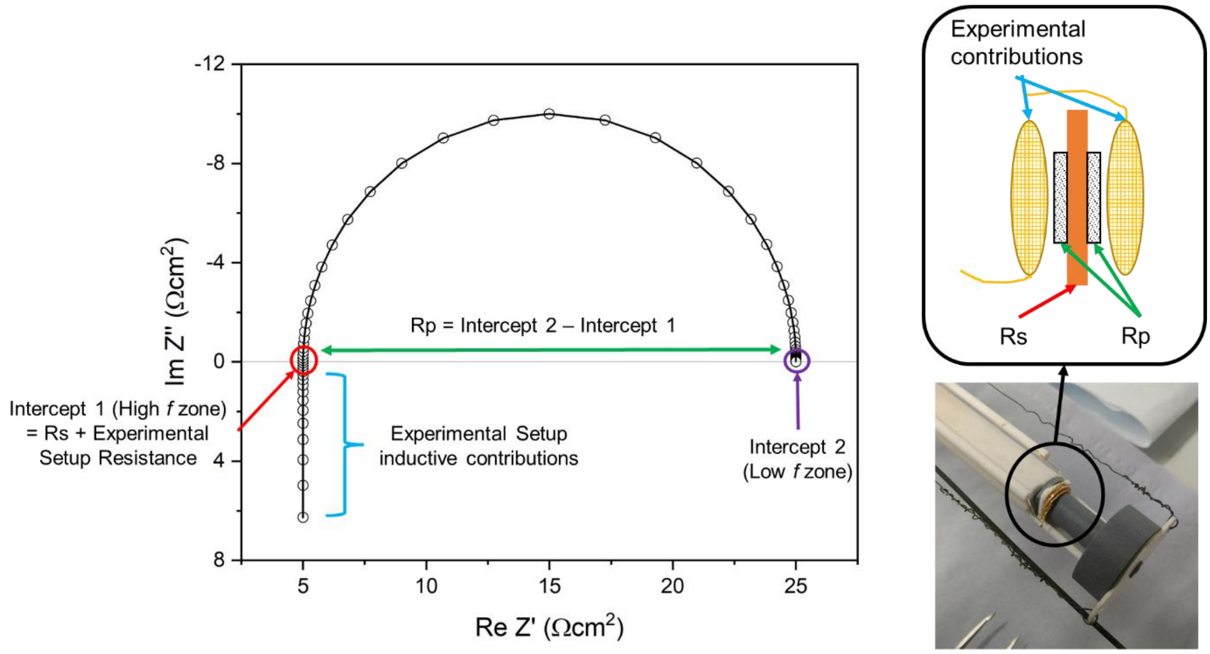

Figure 3-4 In house-built impedance jig and basic information that can be obtained from Nyquist plots

3.2.2 Ageing of LSCF substrates using box furnace

It has been described in literature that thermal treatment of LSCF for an extended period, known as *ageing*, induces Sr – segregation [10, 81, 103]. To study the effects of the different precursors on this phenomenon, coated and bare LSCF substrates were aged at 800 °C for a period of 50 and 100 h and compared against unaged samples.

This specific window for ageing treatment was decided since 100h would allow enough time to induce Sr segregation on analysed samples [10, 45, 150] and would allow to analyse the required surface modified samples.

3.2.3 X-ray diffraction (XRD) and phase analysis

Existing phases on different samples were studied using a D2 Phaser benchtop diffractometer (Bruker) and an Aeris benchtop diffractometer (Malvern Panalytical Ltd.).

Powdered samples were grounded using a mortar and pestle prior to measurement, whilst pellet samples were mounted onto a deep-dish plastic sample holder using Apiezon putty.

When using the D2 Phaser, samples were scanned for 26 min from 20 to 80 2θ degree, whilst samples analysed on the Aeris were scanned for 10 min in the 10 – 100 2θ degrees range.

Obtained data was not corrected for instrument broadening. Diffraction patterns were analysed indexed for phase identification using the ICDD PDF4+ 2016, Crystallography Open Data Base and Bruker Diffrac Eva software.

3.2.4 Scanning electron microscopy (SEM)

LSCF substrates to be analysed were mounted to an aluminium pin stub using carbon tape (Agar Scientific Ltd.), a small dab of Ag – paste was used to ensure electronic conductivity between the sample and the stub to aid in imaging. Infiltrated cells were sectioned and mounted using the same procedure previously described. No gold sputtering was required thanks to the mixed ionic and electronic conductive nature of the analysed materials.

Scanning electron microscopy (SEM) and Electron backscatter diffraction (EBSD) images were obtained using an InTouchScope^{TM} (JSM – 6010LA, JEOL) and Inspect^{TM} (F50, FEI Company).

4 Experimental study of strontium segregation on LSCF

4.1 Chapter overview

The present chapter will explore the potential signs of Sr segregation on the electrode material LSCF, with specific composition $La_{0.6}Sr_{0.4}Co_{0.2}Fe_{0.8}O_{3-\delta}$, under a variety of techniques to identify them and thus, set them as a benchmark for upcoming chapters where surface modifications will be made to prevent this phenomenon.

As already stated on the literature review portion of this work, lanthanum strontium cobalt and iron oxide, commonly known as LSCF, is a state-of-the-art material for Solid Oxide Fuel Cells (SOFCs) applications due to its intrinsic nature as a mixed ionic and electronic conductor, as well as a good mechanical compatibility with both: stabilised yttria zirconia (YSZ) and gadolinium doped ceria (GDC), two of the most used electrolyte materials for these types of devices [3, 151-155].

LSCF powder was processed to produce the following different types of samples: flat pellet substrates of pure LSCF and LSCF/GDC/LSCF test cells. Two different tubs of LSCF powder (FuelCellMaterials) were used for sample fabrication according to the methods previously described in Chapter 3 of this work.

Since several batches of samples were produced, these have been separated and labelled as follow for easier identification:

- **Batch A:** LSCF powder was purchased in 2018 and processed in 2020 for sample and ink production. The time gap between production and processing for this batch is derived from the university having to shut down due to the COVID-19 pandemic.
- **Batch B:** LSCF powder was purchased and processed in 2018 for sample and ink production.
- **Batch C:** LSCF purchased and processed in 2021 for sample and ink production.

Furthermore, and due to equipment availability, a small portion of Batch B samples were analysed using a Solartron Modulab 1250 FRA and a 1287 electrochemical interface; the rest of Batch B and the entirety of Batches A and C were analysed using the FRA/EIS analysed IviumStat.h standard. Regardless of recording equipment, all EIS data was analysed and fitted using ZView ® software in accordance with the protocols described in Chapter 3.

4.2 Results and discussion

4.2.1 Electrochemical analysis via EIS and ECM fitting

Batch B samples were the first ones to be fabricated and analysed. After experimental jig reached the desired operating temperature (700 °C), EIS data was recorded hourly for 50h under synthetic air flow set at 20 mL/min using the Solartron Modulab.

Plots for two of these samples can be observed in Figure 4-1 (remaining Nyquist plot for these set of samples can be found on Annex A). Nyquist plots were obtained by plotting the real part (Z1) vs the imaginary part (Z2) of impedance. Only the data at every 10h interval is shown to observe the evolution of impedance spectra over testing time. Additionally, impedance data has been normalised to electrode area and electrolyte resistance (Rs) was subtracted from all when plotting to ease comparison between the electrodes [122].

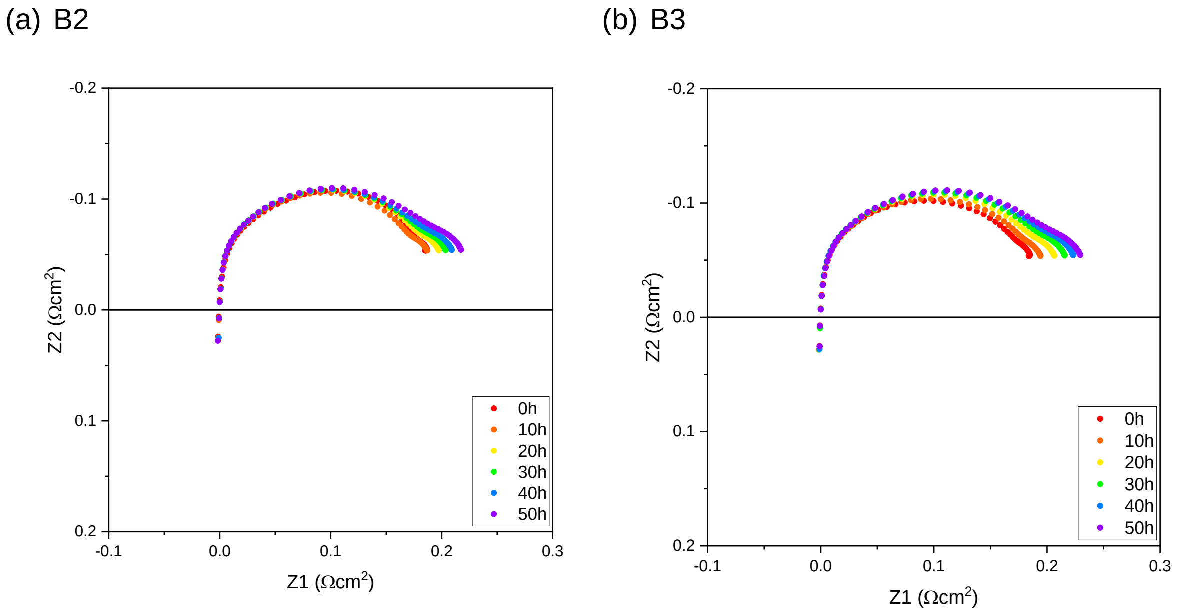
(a) B2

(b) B3

Figure 4-1 EIS spectra for set 1, Batch B LSCF/GDC/LSCF cells recorded on Solartron Modulab

As can be observed from these plots, some key landmarks can be identified. Firstly, the tail at high frequencies and into the positive Z2 axis is commonly associated to inductive contributions from the experimental setup [156], which was corroborated experimentally by conducting the same experiment without placing a sample in the jig. Next, two semi-arcs of different size can be observed; the larger one at the high frequency (HF) and the smaller one at the low frequency (LF) range, which is what to be expected from typical impedance data for the ORR in LSCF electrodes [157].

Identifying these landmarks is useful for further analysis using an equivalent circuit model (ECM) for data fitting, which in turn will help in gaining a better understanding on the processes occurring on the electrode. As the first approach, a literature search was performed to find the mechanisms that had already been proposed for cells using LSCF as the cathode [156-162]. Next, a preliminary fitting was performed with all models using experimental data and after comparing these results, it was ultimately decided that the model that gave the best fitting corresponded to the one presented in Figure 4-2(a). An example of fitted data is presented in Figure 4-2(b), where the dotted plots correspond to experimental data and the overlayed solid lines correspond to the fitted data using the proposed ECM.

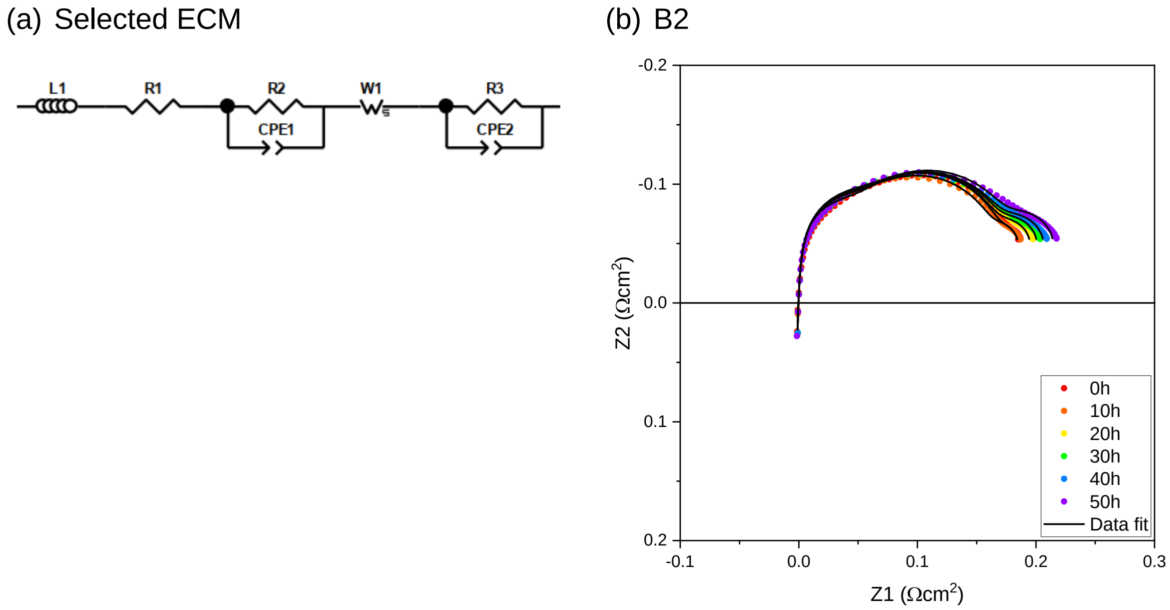
(a) Selected ECM

(b) B2

Figure 4-2 Fitted EIS spectra for se1, Batch B LSCF/GDC/LSCF cells recorded on Solartron Modulab

ECMs are formed of electrical elements that are associated to the different contributions and phenomena occurring on the electrode at any given moment. For the proposed model, L1 accounts for the inductive contributions from the experimental jig, whilst R1 represents the electrolyte resistance also known as Rs. Regarding the following two semi-arcs, each of these can be represented by a resistor and a constant phase element connected in parallel. The first arc at high frequencies (HF), formed by R2 and CPE1, correspond to the charge transfer at the electrode/electrolyte surface and oxygen ion diffusion in the bulk of the electrode. The second arc at low frequency (LF), R3 and CPE2, account for the adsorption/desorption process of oxygen at the electrode surface and the gas diffusion in the pore structure of the electrode [124, 156].

Additionally, there are two other main features about both semi-arcs that provide useful information about the electrode. Firstly, the remarkable difference in size with respect to each other shows that the predominant phenomenon for the analysed electrodes is the charge transfer process at the electrode/electrolyte interface. Lastly, it can be observed that the arches in experimental data are depressed, suggesting non-ideal electrode behaviour, which is often modelled using a Warburg element. This particular element is known as a finite-length Warburg and it usually describes the one-dimensional diffusion of a particle [151].

Experimental data was fitted using the ZView® software. During fitting procedures, the following parameters were kept fixed at the stated values for the following reasons:

- The inductive contribution was first modelled using the *Instant Fit* tool available in ZView to approximate its value. Once this was done, the obtained value was fixed for all subsequent measures for that sample since the same experimental setup was used in all cases.
- The CPE-P parameter was fixed to a 0.9 value to account for the rough and porous electrode surface.
- The Ws-P parameter was fixed to 0.5 to account for the non-ideal behaviour exhibited by the depressed semi-arcs present in some of the samples. At its core, the Warburg element is a modification of a CPE, only made possible when Ws-P = 0.5.

A summary of the fitting results for each of the 10h intervals of sample B2 is presented on Table 4-1. Fixed parameters are not included in the table and the data presented corresponds to the fitting of the raw data (not normalised to electrode area). Result tables for raw data fittings for these samples can be found on Annex A.

As previously discussed on Chapter 3 of this work, the polarisation resistance, Rp, is obtained by calculating the difference between the intercepts at the x-axis from the corresponding Nyquist plot. For the fitted parameter results in Table 4-1, this corresponds to the addition of all the resistive elements R2, R3 and the Ws-R, but omitting the resistive element associated to the electrolyte, Rs (represented as R1 on the ECM) [139].

Calculations for Rs and Rp values obtained from the fitted data for sample B2 and normalised to the electrode area are presented on Table 4-2. Since chi-squared value for each fit are very small and associated error for the fitted data in all cases is below 5% it is safe to assume that the proposed model is appropriate to use for data fitting [163]

Traditionally, literature has shown that a conventional way to monitor the electrode performance is to monitor the electrode polarisation resistance (Rp) and track how it changes over time [44, 45]. The change in Rp was calculated as a percentage (dRp%) according to the following equation:

$$dRp\ (\%) = \frac{Rp_f - Rp_i}{Rp_i}\ x\ 100 \qquad \text{Equation 8}$$

Where Rp_f corresponds to the Rp value after 50h of testing and Rp_i corresponds to the Rp value after the *cathode activation period*. The *cathode activation period* refers to the processes that occur during the first hours of operation and are associated with drastic changes in electrode resistance derived from changes to the initial electrode microstructure and connectivity with other cell components, *i.g* electrolyte, current collector, etc. [150, 164].

According to Equation 8, a positive dRp value means that Rp increased over the testing period, which has been commonly associated to electrode degradation [12, 44, 45]; whilst a negative value would indicate a decrease in Rp over time, consistent with a better performance for the electrode and ultimately, a more desirable outcome [124]. For the first 10h, Rs and Rp were measured every half an hour and hourly after that, values for this set of samples can be observed on Figure 4-3, the Rs should be read on the left y-axis whilst the Rp should be read on the right side of the plot.

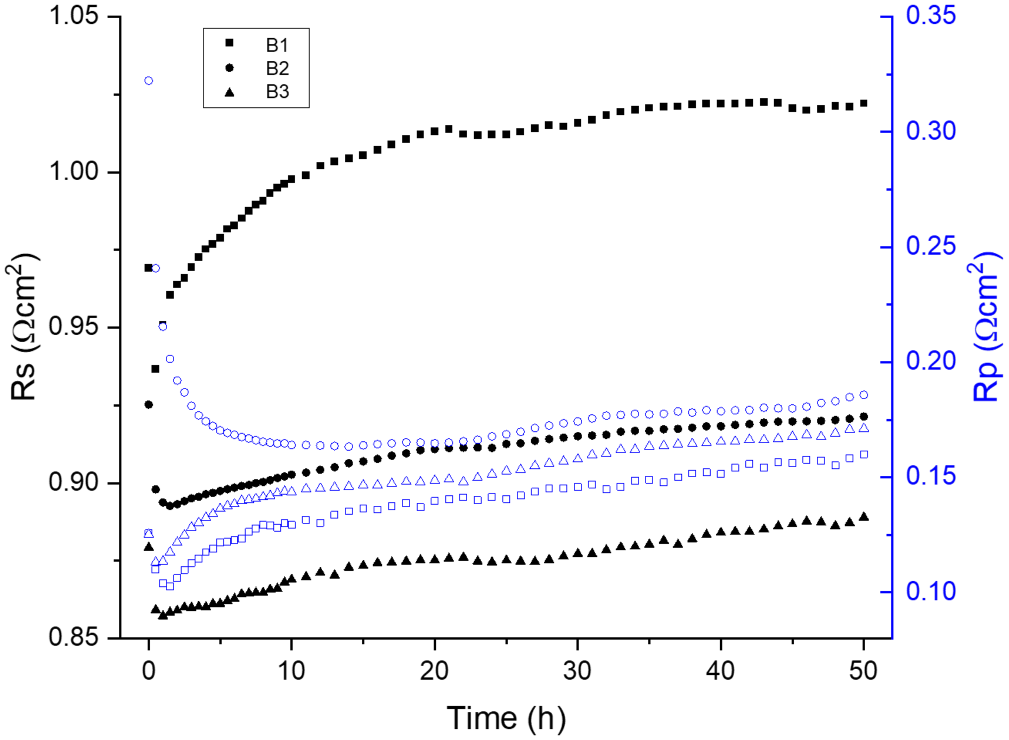

Figure 4-3 Rs and Rp for set 1, Batch B LSCF/GDC/LSCF cells measured using Solartron Modulab

Table 4-1 EIS data fitting summary report for sample B2, set 1, Batch B. Fitting was performed in ZView on raw impedance data

B2	Chi-Sqr	Sum-Sqr	R1	%error	R2	%error	CPE1-T	%error	W-R	%error	W-T	%error	R3	%error	CPE2-T	%error
0h	1.59E-04	2.02E-04	0.04563	0.04563	0.9605	0.00197	0.00197	2.6394	0.34967	2.637	1.81E-04	4.5829	0.10849	5.521	0.31845	14.82
10h	1.65E-04	2.33E-04	0.0462	0.0462	1.3643	0.0023	0.0023	3.6766	0.36674	3.4376	2.53E-04	5.2358	0.14928	4.1867	0.26169	11.252
20h	1.40E-04	2.10E-04	0.04358	0.04358	0.82909	0.00229	0.00229	3.4923	0.3797	3.2721	2.67E-04	4.9197	0.18135	3.3988	0.213	9.0995
30h	1.40E-04	2.22E-04	0.04449	0.04449	0.83134	0.00236	0.00236	3.6258	0.38785	3.3353	2.77E-04	4.9924	0.21309	3.0676	0.1785	8.1748
40h	1.46E-04	2.44E-04	0.04613	0.04613	0.8276	0.00249	0.00249	3.8641	0.40043	3.4291	2.95E-04	5.1106	0.24228	2.8959	0.16043	7.6906
50h	1.65E-04	2.90E-04	0.04973	0.04973	0.83888	0.00262	0.00262	4.2027	0.41444	3.6483	3.17E-04	5.4225	0.2741	2.8931	0.14439	7.6418

Table 4-2 Rs and Rp values for sample B2, set 1 Batch B, obtained from EIS data fitting using ZView. Data has been normalised to the electrode area

B2	Rs (Ωcm^2)	%error	Rp (Ωcm^2)	%error
0h	0.0065	0.0456	0.1509	2.7200
10h	0.0066	0.0462	0.2171	2.5422
20h	0.0062	0.0436	0.1468	2.2244
30h	0.0064	0.0445	0.1528	2.1351
40h	0.0066	0.0461	0.1583	2.1092
50h	0.0071	0.0497	0.1665	2.1813

Table 4-3 Experimental values for Rp, Rp$_i$, Rp$_f$, and calculated dRp for set 1, Batch B, LSCF/GDC/LSCF cells

Sample	Rp (Ωcm^2, 0h)	Rp$_i$ (Ωcm^2, 10h)	Rp$_f$ (Ωcm^2,50h)	dRp (%)
B1	0.3223	0.1640	0.1858	13.2855
B2	0.1257	0.1293	0.15999	23.7629
B3	0.1253	0.1436	0.17119	19.1812

After analysing Figure 4-3, it was clear that after reaching operation temperature, samples usually underwent a stabilisation period, better known as the *cathode activation period* [150, 164]. For this set of samples, this activation period was determined to be the first 10h of operation, after Rs and Rp roughly stabilised, thus for the corresponding dRp calculations, Rp_i was the Rp value at 10h for each sample.

From data for this set, it can be observed that Rp values at the beginning of testing, particularly for samples B2 and B3 are very similar to values reported for symmetric cells tested under similar conditions by Ascolani-Yael *et al.* [122] and Wang *et al.* [12], who also monitored Rp for LSCF electrodes for 500h. Upon reviewing obtained Rp data and calculated dRp values (Table 4-3), a clear increase in Rp of roughly ~20% was observed. Such increase is also in line with the findings for these two studies, which attributed the increase in Rp mainly because of Sr-surface segregation rather than microstructural changes (*i.g.* porosity) of the material.

It is also worth mentioning that from plotted impedance and fitted impedance data, the resistance for the arc at high frequency (R2 in Table 4-1) remains fairly constant throughout testing, whilst resistance for the arc at lower frequencies increases to almost double of its initial value (R3 in Table 4-1). This means that, as testing progressed, the limiting steps for the ORR on this batch of samples remained the bulk O^{2-} ion diffusion and the charge transfer at the electrode/electrolyte interface with an increase in resistance for oxygen exchange at the gas/electrode interface [36, 122].

Due to the Solartron Modulab becoming unavailable, a second set of batch B samples was analysed now using the IviumStat FRA analyser, a portion of plotted and fitted experimental data is presented on Figure 4-4 (samples B8 – B10). Only spectra at 10h intervals are presented, electrolyte resistance has been removed to ease comparison [122] and the proposed ECM used for fitting remains the same as for set 1 of batch B. The complete fitting results for raw data corresponding to each sample can be found on the appropriate section on Annex A.

Rp values normalised to electrode area for all samples on this set are presented in Table 4-4. Initial Rp values are listed for comparison against set 1, Rpi and Rpf were used to calculate dRp(%) according to Equation 8, and the full monitoring of Rp through time for samples B8 – B10 is presented in Figure 4-5. Appropriate graphs for the rest of samples in this set can be found in section 10.2.3 of Annex A.

(a) B8 (b) B9

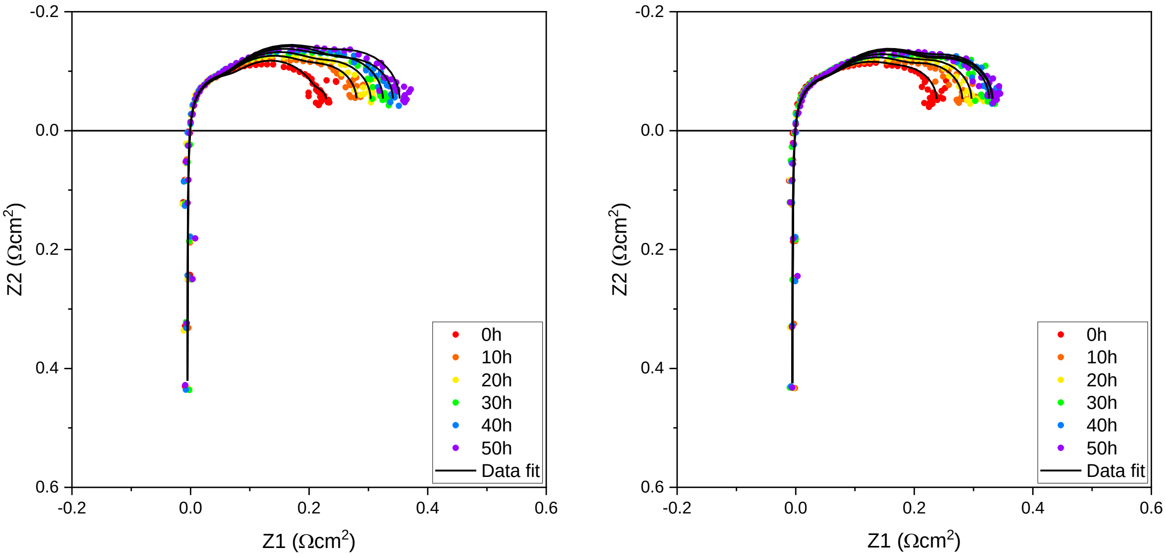

(c) B10 (d) ECM

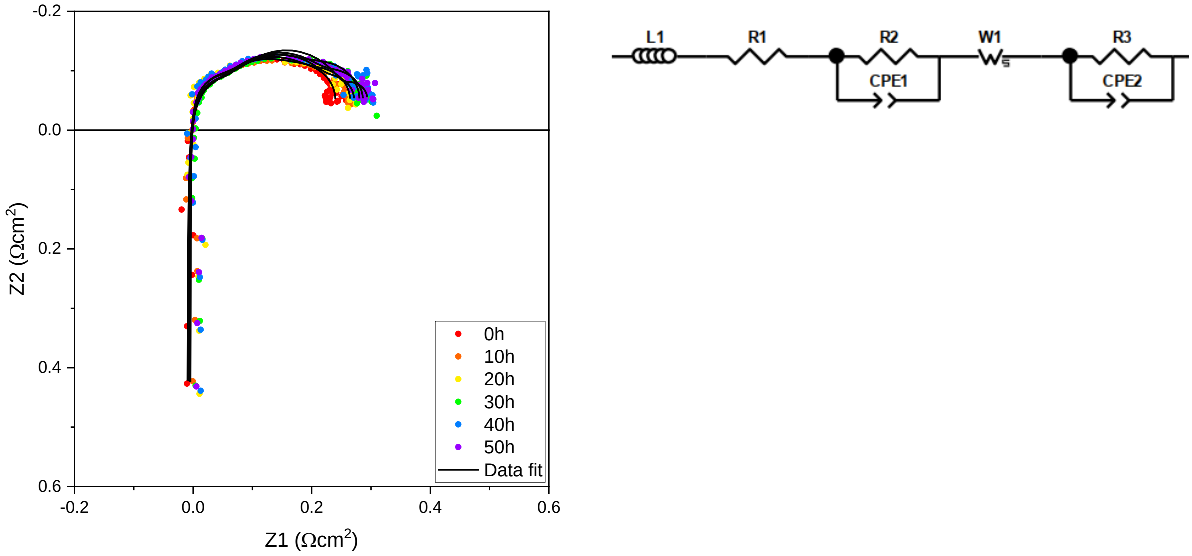

Figure 4-4 Fitted EIS spectra for set 2, Batch B LSCF/GDC/LSCF cells recorded on IviumStat FRA analyser

Table 4-4 Experimental values for Rp, Rp_i, Rp_f and dRp of set 2, Batch B, LSCF/GDC/LSCF cells

Sample	Rp (Ωcm^2, 0h)	Rp_i (Ωcm^2, 10h)	Rp_f (Ωcm^2, 50h)	dRp (%)
B4	0.2503	0.3433	0.4951	44.2192
B5	0.3902	0.3641	0.5166	41.8917
B6	0.2821	0.3334	0.3344	0.3095
B7	0.2663	0.2832	0.2681	-5.3646
B8	0.1709	0.2262	0.3035	34.1596
B9	0.1884	0.2272	0.2765	21.7047
B10	0.1842	0.2110	0.2443	15.7624
B11	0.1916	0.0998	0.1270	27.3023

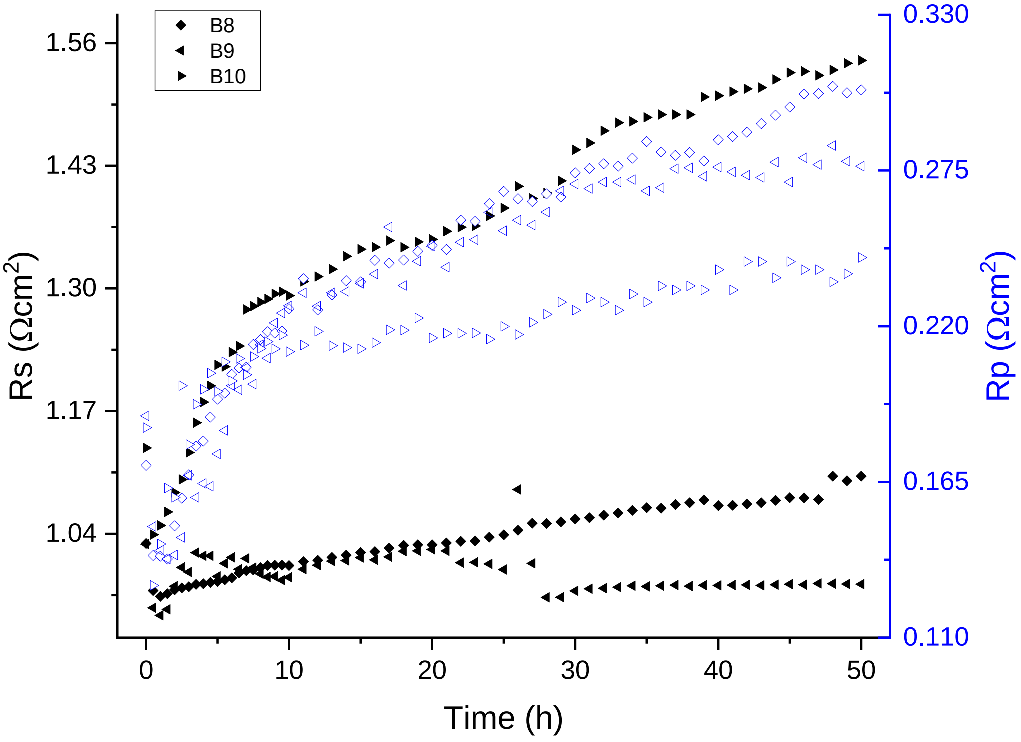

Figure 4-5 Rs and Rp for set 2, Batch B, LSCF/GDC/LSCF cells measured using IviumStat FRA analyser

From the Nyquist for samples in this set (Figure 4-4) the same data features from experimental jig and the two characteristic semi-arcs for the ORR on MIEC electrodes can be observed [36]. For this set of samples, all initial Rp values are higher than the recorded values for set 1 (Table 4-3) and values from literature [12, 122] by at least 36%.

With testing time, an increase in total Rp was observed as shown in Figure 4-5 and quantified in Table 4-4 where dRp(%) values are presented. Majority of calculated dRp(%) values were positive, meaning that Rp kept rising with testing time; moreover, dRp for set 1 tended to be greater than dRp for set 1. Hourly monitoring of Rp value showed that, all samples steadily increased their value over time which again could be associated with Sr-segregation from the LSCF electrode material [45, 165, 166].

Cells form this sets 1 and 2 were both fabricated during the same period, and the only difference between them is that set 1 was tested prior to the lockdown period whilst set 2 sat in storage during this time before being tested under the same conditions. The differences between the initial Rp values and estimated degradation values (dRp) suggests that some sort of degradation, or *calendar ageing effect* could have occurred during storing, which to the authors knowledge has yet to be reported in literature. Similar increases in measured Rp have been reported for similar cell assemblies by Baqué *et al.* [45] but only after thermal ageing at high temperatures (800°C) that resulted in Sr-surface segregation leading to poor electrode performance.

When studying the increments on R2 and R3 from raw data fitting, both of these values increased over the testing period, but the high frequency semi-arc remained the larger source of resistance.

The only outlier samples from this set are samples B6 and B7, where 0.3% dRp and -5.36% dRp were calculated respectively. This could be attributed to the possibility that for these samples the cathode activation period extended further than 10h [150, 164] which interfered with the systematic dRp calculations.

Lastly, to test if Rp could still increase with longer testing times after samples were left in storage, a third set of batch B samples was analysed on the IviumStat, this time for an extended period of 100h under the same testing conditions. EIS experimental and fitted data for two of the samples and the ECM used for data fitting are presented in Figure 4-6. Even though testing was performed for 100h, only the first 50h of testing are presented. Hourly monitoring of samples for the entirety of the test is presented in Figure 4-7. Results for EIS data fitting of raw data can be found in section 10.1.4 and 10.3.4 of Annex A.

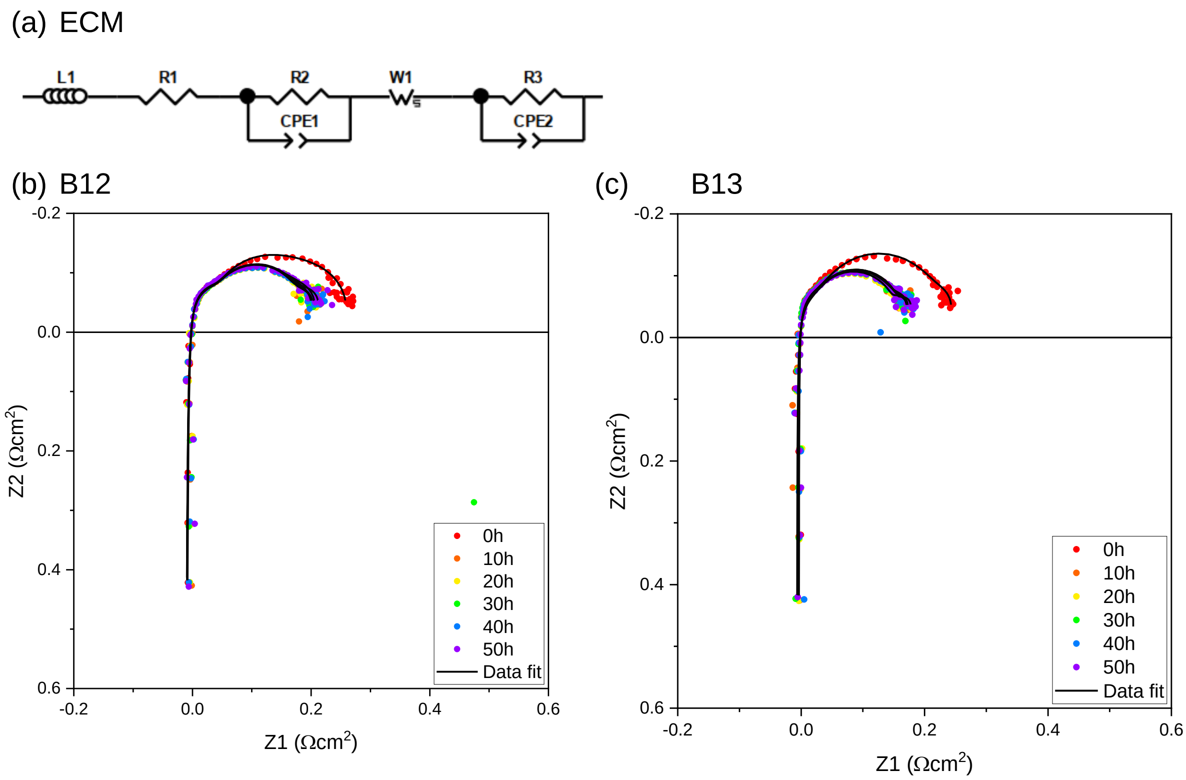

Figure 4-6 Fitted EIS spectra for set 3, Batch B, LSCF/GDC/LSCF cells recorded on IviumStat FRA analyser

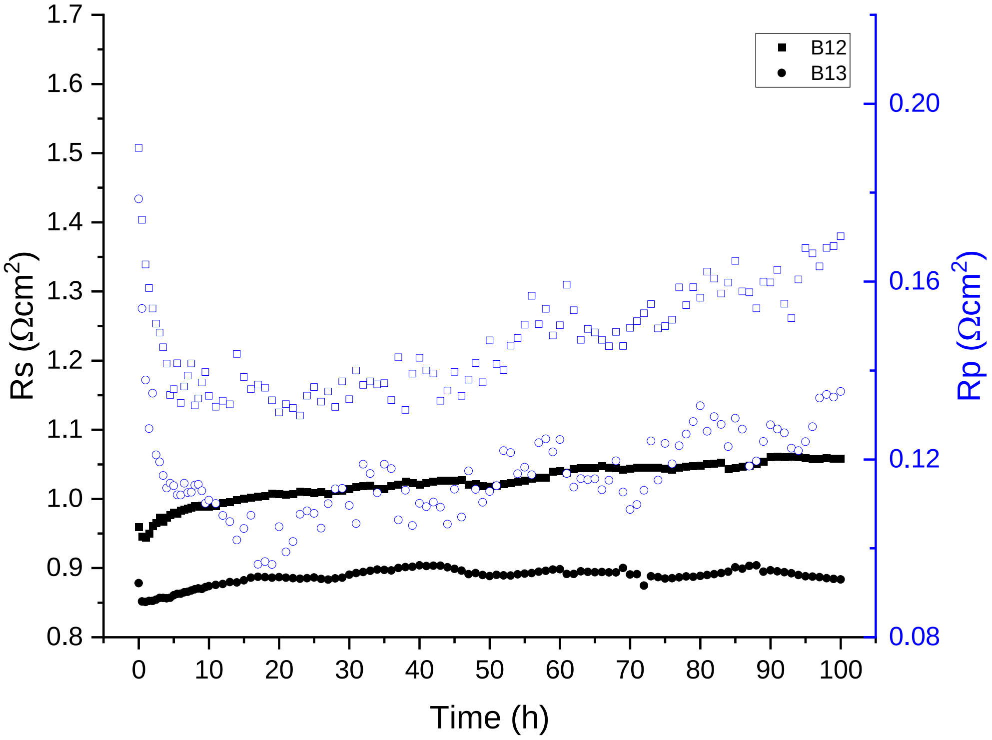

Figure 4-7 Rs and Rp for set 3, Batch B, LSCF/GDC/LSCF cells measured using IviumStat FRA analyser

A look at the first 50h of testing for set 3 samples of batch B (Figure 4-6 and Figure 4-7) would suggest that for this set, cathode activation period occurred during the first 20h of testing [150, 164]. After this, electrode resistance increased along with testing time. Rp values and calculated dRp at 50 and 100h for this set are presented in Table 4-5

Table 4-5 Experimental values for Rp, Rp_i, Rp_f and dRp_{50} and dRp_{100} of set 3, Batch B, LSCF/GDC/LSCF cells

Sample	Rp (Ωcm^2, 0h)	Rp_i (Ωcm^2, 20h)	Rp_f (Ωcm^2, 50h)	Rp_f (Ωcm^2, 100h)	dRp_{50} (%)	dRp_{100} (%)
B12	0.1901	0.13430	0.1468	0.1702	12.4063	30.3355
B13	0.1786	0.11081	0.1128	0.1353	7.5596	29.0092
B14	0.1988	0.14622	0.1488	0.1557	2.7407	7.4613

Initial Rp values for set 3 of samples are at least 40% higher than the ones initially recorded for set 1 and reported values from Ascolani-Yael *et al.* [122] and Wang *et al*. [12] for LSCF/GDC/LSCF cells tested under similar conditions, further reinforcing the possibility of the *calendar ageing effect* being the cause of this initial increase.

The calculated dRp(%) for the first 50h revealed a minor increase during this initial period, whilst further testing revealed that electrode performance degraded even more after 100h of testing. Finally, the dRp of all the sets were compared against their date of testing (Figure 4-8)

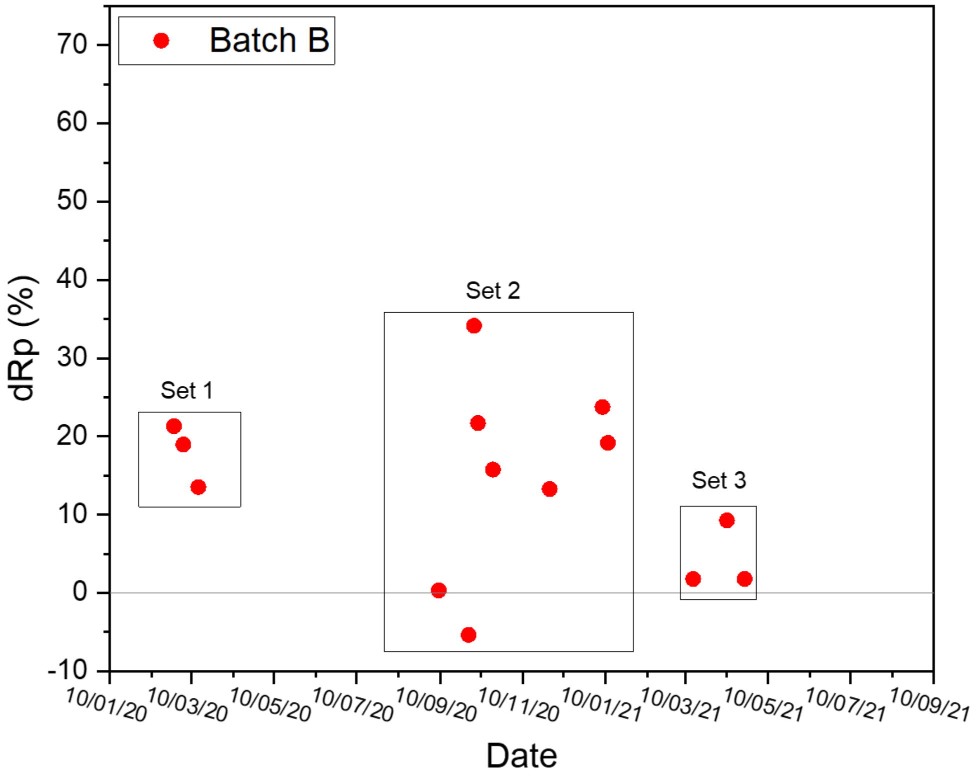

Figure 4-8 dRp(%) for all sets from Batch B, LSCF/GDC/LSCF cells, against date of testing

From the comparison of all dRp(%) values from the different sets in Batch B it can be observed that, samples that sat in storage the longest tended to degrade less, possibly due to the degradation suffered because of the calendar ageing. This was also supported by the fact that each set of samples had initial Rp values higher than set 1, ~36% and ~40% for sets 2 and 3, respectively.

Regardless of initial Rp values, majority of samples exhibited an increase in Rp after 50h of testing, consistent with findings reported in the literature for the same type of cells [12]. This increase in Rp for all sets of samples can be attributed to SSS rather than changes in the electrode microstructure [108, 167]. When samples were tested for an extended period of time, further degradation was observed (set 3, batch B), which was also in line with observations previously reported in literature [45, 78]

To rule out possible interferences or sources of error associated with the ink used to fabricate samples in batch B, a new ink was prepared using the LSCF powder that was already in stock. Thus, a new portion of LSCF powder that was bought in 2018 was processed to produce a new batch (Batch A) of LSCF/GDC/LSCF test cells and flat LSCF substrate samples. The new batch of samples was processed and analysed using the same protocol followed for Batch B. However, during the time that samples were being prepared, the experimental jig suffered a fall with damage to its sample-holding section. The state of the experimental jig was evaluated, and it was determined that despite the damages, measurements were still viable without needing major repairs.

For EIS measurements, a set of three samples were analysed and obtained data was fitted to the same ECM used for Batch B. In the case of sample A2 (Nyquist plot can be found in section 10.1.1, Annex A, some of the intermediate measurements were lost, the sample was still subjected to 50h of operation conditions and relevant Rp values were still analysed and compared.

Since data had been collected in a continuous manner and without any other issues prior to the jig being broken, and after the integrity of the other individual components of the experimental setup was carefully evaluated: IviumStat FRA analyser, connection cables from IviumStat to the jig, and contact gold cables for electrical connection, it was determined that the loss of some of the experimental data was directly associated to the slightly damaged sample-holding port on the jig.

Nyquist plots for Batch A samples without missing data are presented in Figure 4-9, in the same figure, the ECM, which is the same one used for data fitting on Batch B, is also present (fitted data is represented by the superposed solid lines). Batch A of samples was also tested for 100h, the appropriate Rp monitoring for samples in this batch is presented in Figure 4-10 whilst the normalised Rp values for dRp calculations are presented in Table 4-6. Full fitting results for raw EIS data can be found in section 10.3.1 of Annex A.

Table 4-6 Experimental values for Rp, Rp_i, Rp_f and dRp_{50} and dRp_{100} for Batch A, LSCF/GDC/LSCF cells

Sample	**Rp (Ωcm^2, 0h)**	**Rp_i (Ωcm^2, 10h)**	**Rp_f (Ωcm^2, 50h)**	**Rp_f (Ωcm^2, 100h)**	**dRp_{50} (%)**	**dRp_{100} (%)**
A1	0.3933	0.3575	0.3618	0.3933	1.2031	10.0246
A2	0.3518	0.3991	0.4206	0.4722	5.3880	18.3195
A3	0.3783	0.3845	0.4068	0.4200 (*)	5.8166	9.2472

(*) *This value corresponds to 77h*

The calculated dRp values at 50h for this batch were also compared to the corresponding Rp values for the sets in Batch B and this is shown in Figure 4-11.

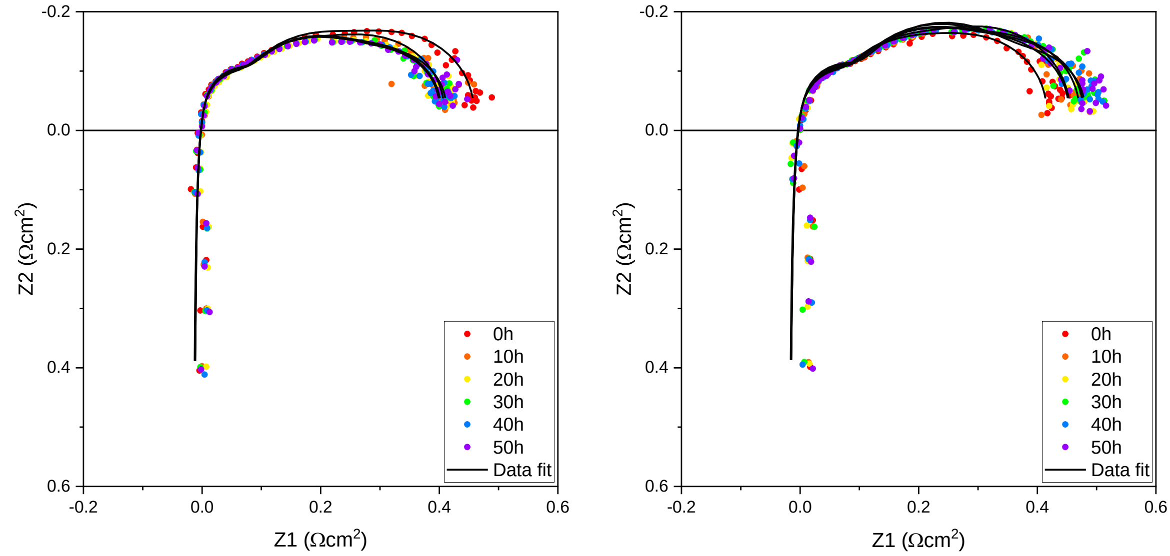

(a) A1

(b) A2

(c) ECM

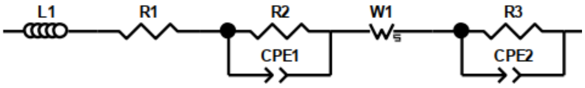

Figure 4-9 Fitted EIS spectra for Batch A LSCF/GDC/LSCF cells recorded on IviumStat FRA analyser

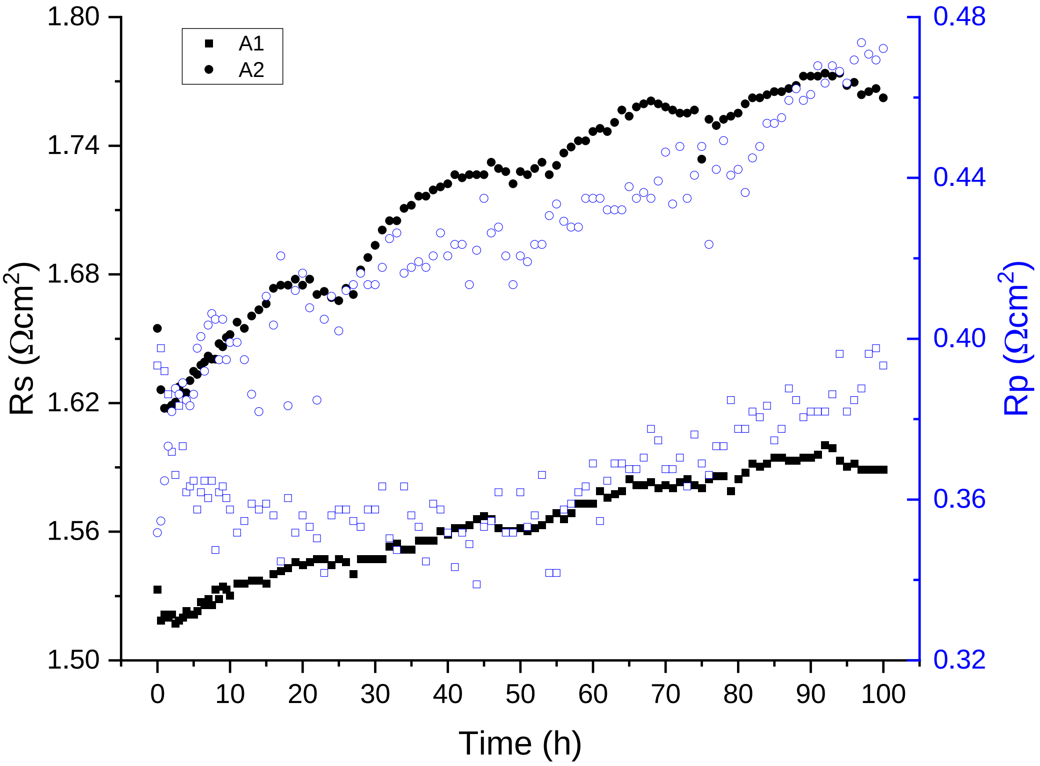

Figure 4-10 Rs and Rp for Batch A LSCF/GDC/LSCF cells measured using IviumStat FRA analyser

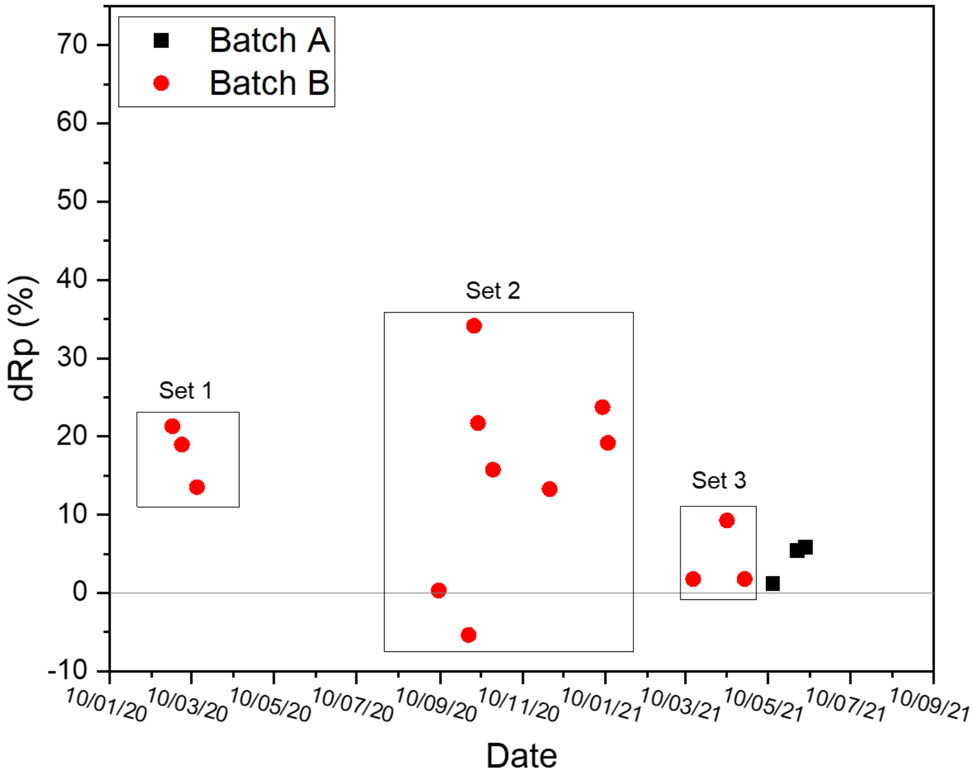

Figure 4-11 dRp(%) for Batch A and B, LSCF/GDC/LSCF cells against date of testing

Initial Rp values for al samples in Batch A were ~2.8 times bigger than the ones recorded for set 1, *i.e.* also ~3 times larger than usual values reported in literature [122]. Regardless of this, Batch A samples still showed an increase in Rp after testing associated to SSS degradation [45, 166]; however, the calculated values for dRp were smaller than the calculated values for most of the sets in Batch B. This was attributed once again to the *calenda ageing effect* of the samples and the ink being stored for a significant amount of time without testing, causing the higher initial Rp values and thus, leaving room for less degradation that samples could have shown if they were tested at a time closer to their production date.

In order to corroborate if the *calendar ageing effect* was a factor on the previously discussed results, it was determined that a new tub of LSCF-6428 powder would be purchased and processed to obtain a new ink and new batch of LSCF/GDC/LSCF test cells and flat substrates that would be analysed immediately after production. It is worth mentioning that, although some sets/batches were tested for an extended period of time, *i.e.* 100h, in order to accommodate all necessary measurements, testing protocols would only be carried out for a maximum of 50h.

Samples produced using the new ink conformed Batch C. Experimental and fitted EIS data normalised to electrode area are presented in Figure 4-12, data was fitted using the proposed ECM [159], full results for raw data can be found in section 10.3.5 in Annex A and the hourly Rp monitoring is shown in Figure 4-13. The corresponding Rp values normalised to electrode area and calculated dRp values are presented in Table 4-7.

(a) C1 (b) C2

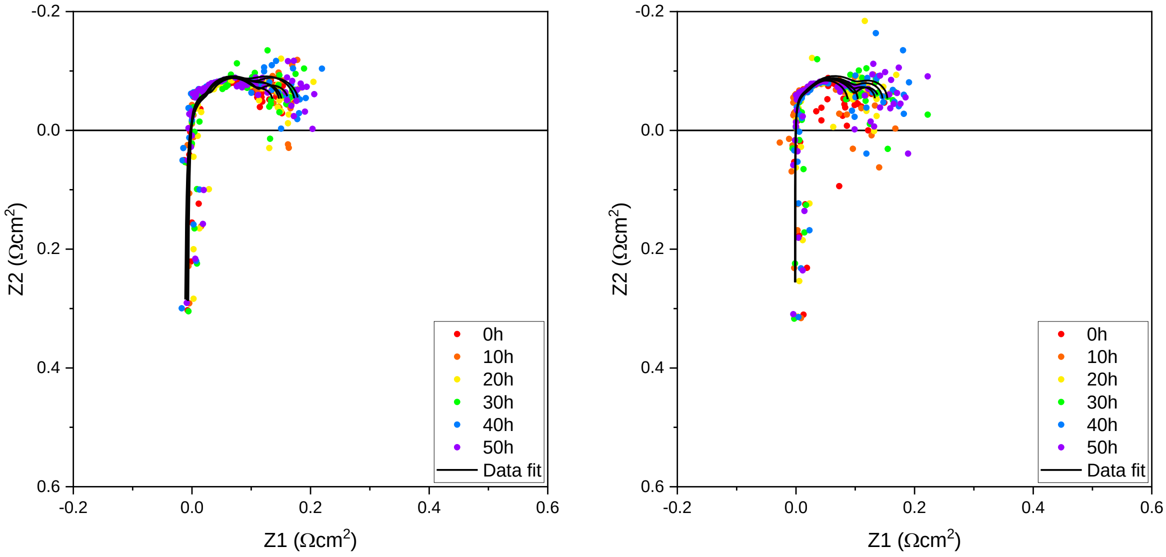

(c) ECM

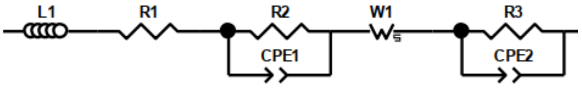

Figure 4-12 Fitted EIS spectra for Batch C, LSCF/GDC/LSCF cells recorded on IviumStat FRA analyser

Table 4-7 Experimental values for Rp, Rp_i, Rp_f and dRp for Batch C, LSCF/GDC/LSCF cells

Sample	**Rp (Ωcm², 0h)**	**Rp_i (Ωcm², 10h)**	**Rp_f (Ωcm², 50h)**	**dRp(%)**
C1	0.0812	0.0962	0.1465	52.3182
C2	0.0324	0.0415	0.0713	71.5723

Nyquist plots for this set showed the same features that had been previously observed, *i.e.* induction element from the jig wires, and the two characteristic semi-arcs for ORR in MIEC cathodes [36, 44, 45, 122]. For this set of samples, it was clearly observed that recorded data presented some noise, particularly at the low-frequency region, associated with the deteriorated sample-holder of the experimental jig. This was experimentally corroborated after individually evaluating the other experimental jig components and confirming that everything was working as usual.

Although initial Rp values for Batch C samples were smaller than values recorded for set 1 of Batch B, similar values for this type of electrode have been reported by [12, 122]. During Rp monitoring it was determined that the cathode activation period for this batch was 10h, and dRp% values were calculated accordingly. As time passes, Rp increased significantly, when analysing the behaviour of R2 and R3 in the raw data results, it was clear that both of these values increased as time passed but R2 remained the larger contributor to total resistance, which meant that the bulk ion O^{2-} diffusion and electrode/electrolyte charge transfer remained the limiting steps in the ORR for these electrodes [122].

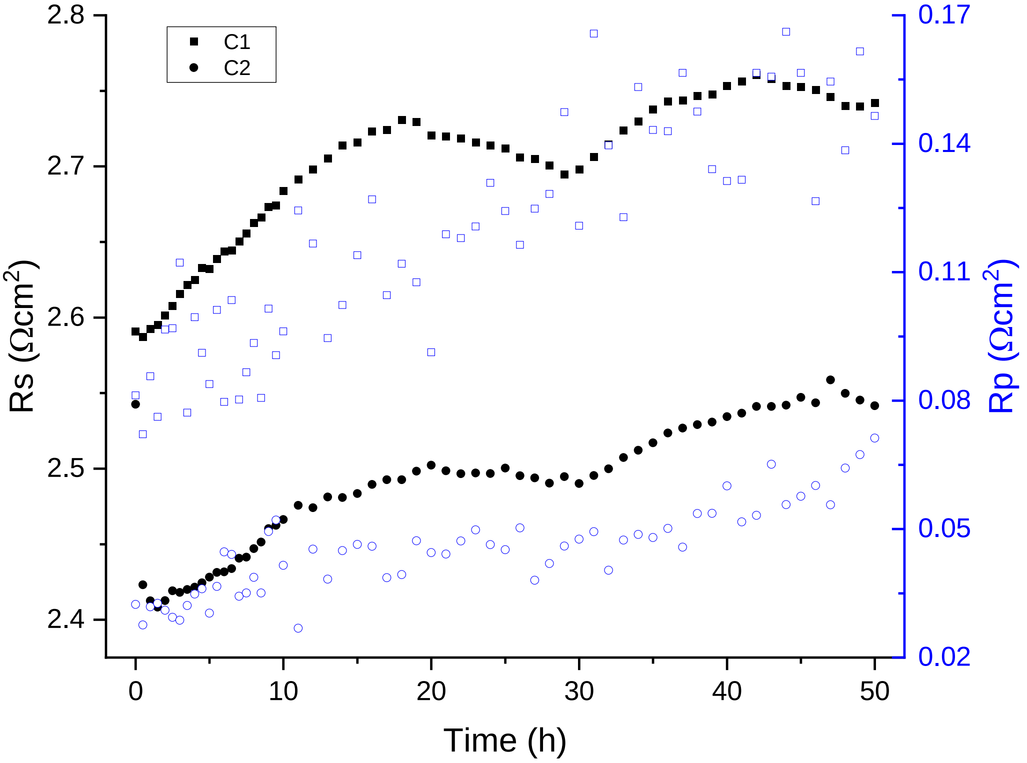

Figure 4-13 Rs and Rp for Batch C, LSCF/GDC/LSCF cells measured using IviumStat FRA analyser

Finally, the calculated dRp(%) values for this batch were compared to the previous batches (Figure 4-14). From this comparison, it was clear that with the new ink produced electrodes that showed more degradation than the electrodes that were fabricated and were left in storing before testing. These findings further supported the theory of the proposed *calendar ageing effect* that was observed on the results from previous produced batches.

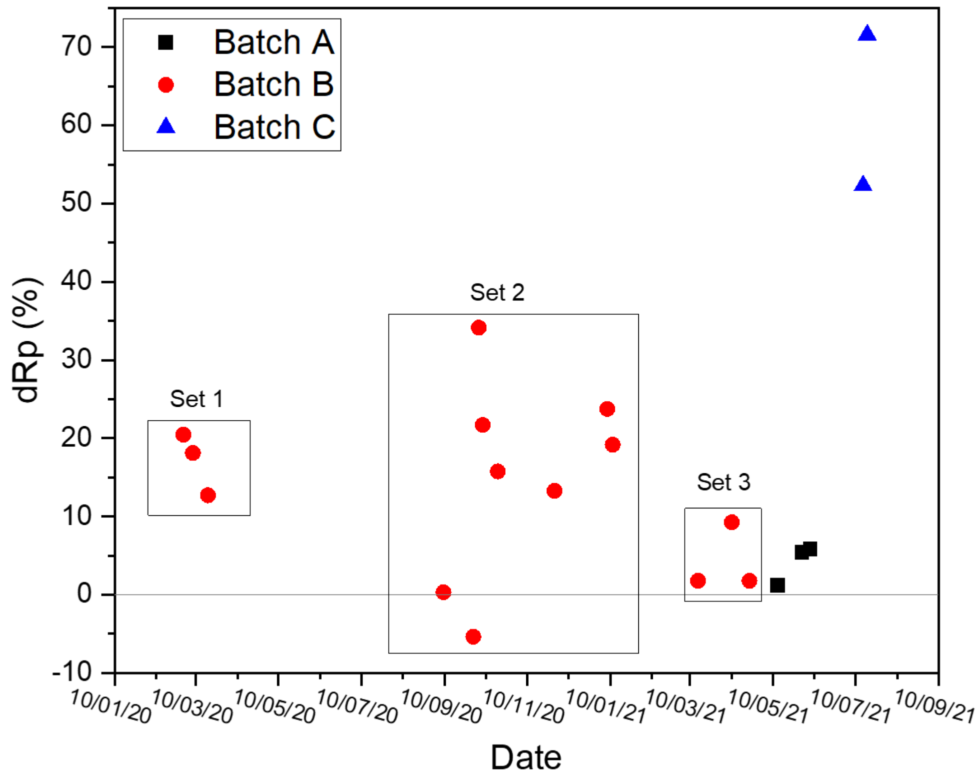

Figure 4-14 dRp(%) for Batch A, B and C, LSCF/GDC/LSCF cells against their date of testing

4.2.2 Physical analysis *via* XRD

After grinding and polishing to mirror finish, flat and dense LSCF substrates for three different batches (A, B, and C) were subjected to a thermal ageing treatment consisting of heating the substrates at 800°C for periods of 50 and 100h. Exposing LSCF materials at elevated temperatures has been previously used as a way to promote Sr-surface segregation [10, 81, 103].

Unaged and aged substrates where then and analysed using X-ray diffraction (XRD) to evaluate any structural changes and possible formation of secondary Sr-containing phases on the surface in accordance with the protocols described in section 3.2.3 in Chapter 3. The presence of these Sr-containing phases has been linked to poor electrode performance for SOFC applications [12, 78, 108].

It is well known that an ideal perovskite (ABO_3) structure is cubic with A-site cations occupying the corners of the cube and B-site cations occupying the centre of the body; however, slight deviations can cause a distortion resulting in a rhombohedral structure [168].

Batch B of flat substrates is comprised of two different sets. Obtained patterns for set 1 of Batch B samples at different ageing times are showed in Figure 4-15. It was clear from collected data that LSCF substrates were polycrystalline. Thus, reference patterns for the most common LSCF phases reported in literature, *i.e.* cubic (PDF 04-018-5108) [151] and rhombohedral (PDF 04-017-2448) [169] were also plotted for comparison. For the samples where the analysis was possible, Rietveld refinement was used to calculate sample composition. For the cases where Rietveld analysis was nor possible due to non-convergence, sample composition was calculated using the Reference Intensity Ratio (RIR) analysis [141, 144]. All analysis were performed using *Match!© Phase Analysis using Powder Diffraction* software. Additional graphic reports for XRD analysis for samples on this chapter can be found on Annex A.

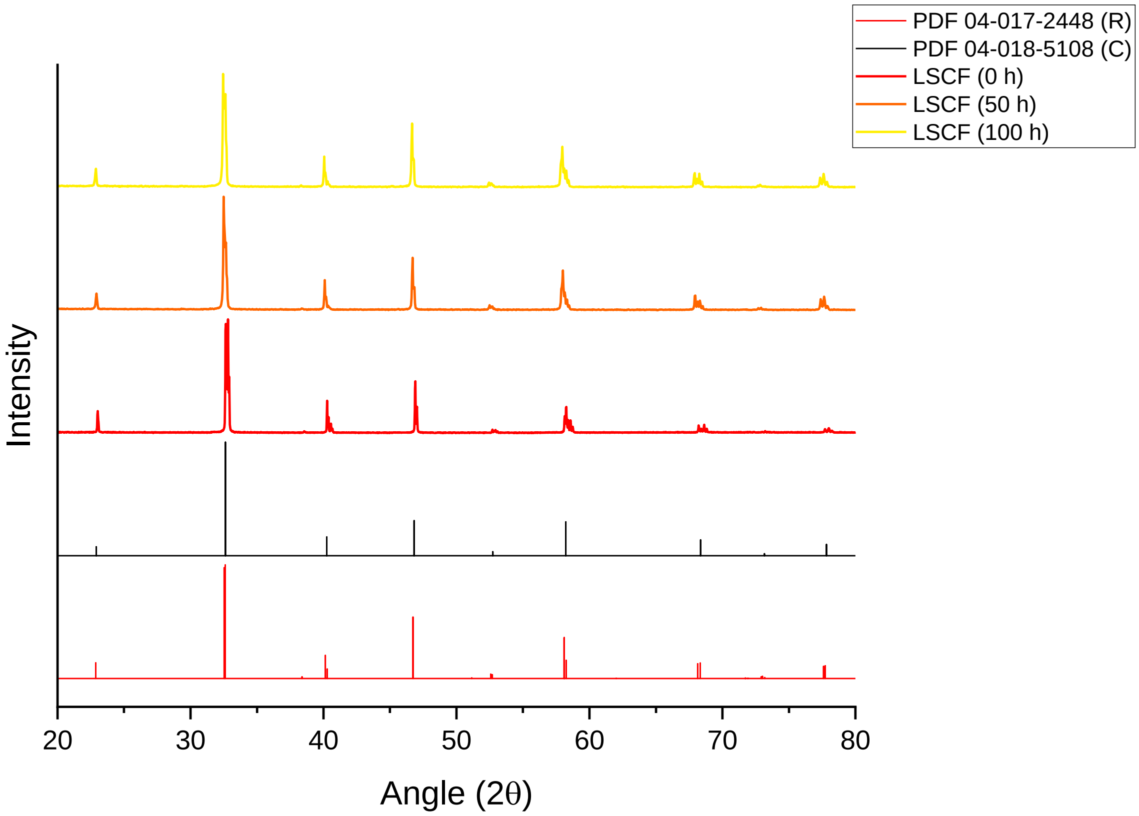

Figure 4-15 XRD patterns for set 1, Batch B, flat LSCF substrates at different stages of ageing (samples were aged in a box furnace at 800°C in ambient air. Reference patterns for cubic and rhombohedral LSCF have also been plotted for comparison.

As observed from the figure above, XRD data showed the presence of both cubic and rhombohedral LSCF phases regardless of ageing time. XRD data analysis suggests that phase composition went from 100% rhombohedral composition at 0h, to a combination of 78.1% rhombohedral phase and 21.9% cubic phase after 50h of ageing and finally 89.8% rhombohedral and 10.2% cubic phases, after the same sample was thermally aged for another 50h for a total of 100h. These findings coincide with what has been reported in literature for

LSCF. Huang *et.al.* [170] reported that at low temperatures, LSCF presents a rhombohedral structure. Moreover, LSCF undergoes a rhombohedral – cubic phase transition at high temperatures (~750°C) when heated in air [10] which then is susceptible to be reversed when the material cools down. The final phase composition when LSCF has cooled depend greatly on the conditions, mainly cooling ramp and atmosphere [168], for example, when cooling at 5°C min^{-1} a 15% cubic phase composition was reported [170].

After 100h of ageing, no new phases were detected by the XRD equipment. Nevertheless, this is not enough reason to rule out the presence of Sr-containing segregated phases on the surface of the material. This can be explained by the fact that if these secondary phases are not present in a high enough proportion (higher than 2%), or they are not crystalline, their signal will not be picked up by the used instruments [141, 144] .

A second set of Batch B polished substrates were subjected to the same thermal ageing treatment as set 1 and collected data is presented in Figure 4-16. Cubic and rhombohedral reference patterns are present for relevant comparison.

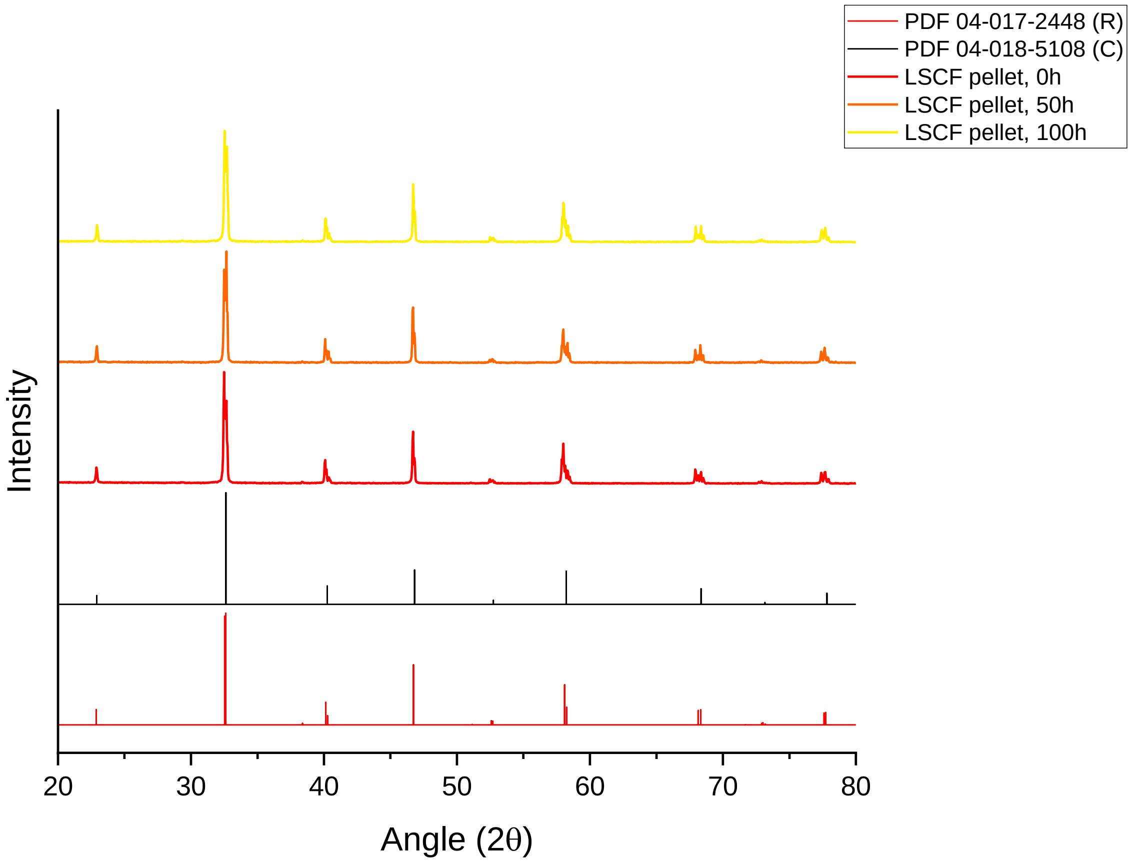

Figure 4-16 XRD patterns for set 2, Batch B, flat LSCF substrates at different stages of ageing (samples were aged in a box furnace at 800°C in ambient air. Reference patterns for cubic and rhombohedral LSCF have also been plotted for comparison.

The only difference between these sets 1 and 2 is that after polishing, substrates from set 2 were stored in sealed bags until their thermal ageing treatment took place, a similar situation to what occurred to LSCF/GDC/LSCF cells from Batch B set 2. Retvield and RIR analysis for this set can be found in section 10.4.3 of Annex A.

For this set of samples, a combination of rhombohedral and cubic phases was detected in all ageing stages. Compositions were as follows, 62.9% rhombohedral and 37.1% cubic at 0h, 50.8% rhombohedral and 49.2% cubic at 50h; and finally, 73.5% rhombohedral and 26.5% cubic phases at 100h. In contrast with set 1 for this same batch, set 2 displayed a more balanced coexistence between the rhombohedral and cubic phases. The coexistence of both phases is not abnormal [168]. However, purely cubic phases or compositions with a higher percentage of cubic phase have only been observed when LSCF is cooled at high rates in air or under an oxygen-deficient atmosphere [170].

After ageing for 50h, composition was almost 50/50 and after 100h of ageing, the rhombohedral phase became the dominant phase again. The fact that initial composition of samples changed after only being stored under regular laboratory conditions became a subject of interest as this strongly suggested that *calendar ageing* could be responsible for the change in behaviour on the analysed cells and flat substrates. To the author’s knowledge, *calendar ageing* for LSCF is not a reported phenomenon, and this only became apparent due to the extraordinary circumstances caused by the Covid-19 pandemic, which forced university facilities to completely shut down during quarantine period. Additionally, for this set, no new phases that could be correlated to SSS were detected. However, its presence cannot be discarded, especially if they were not crystalline or sufficient in amount to be properly detected by the equipment used [141, 144].

A new batch of substrates (Batch A) were fabricated and polished for thermal ageing. XRD data for this new batch and appropriate cubic and rhombohedral standard patterns are presented in Figure 4-17.

XRD analysis for this batch showed the following compositions, 70.2% rhombohedral and 29.8% cubic phases at 0h; 74.3% rhombohedral and 25.7% cubic at 50h; and lastly, 87.9% rhombohedral and 12.1% cubic phases at 100h. Batch A showed a mixed composition for all ageing stages that were in agreement with the literature [10, 168, 170-172]. However, changes in composition with ageing were not as drastic as observed for set 2 of Batch B. Once again, no new Sr-containing phases were detected, but their presence cannot be entirely ruled out [141, 144].

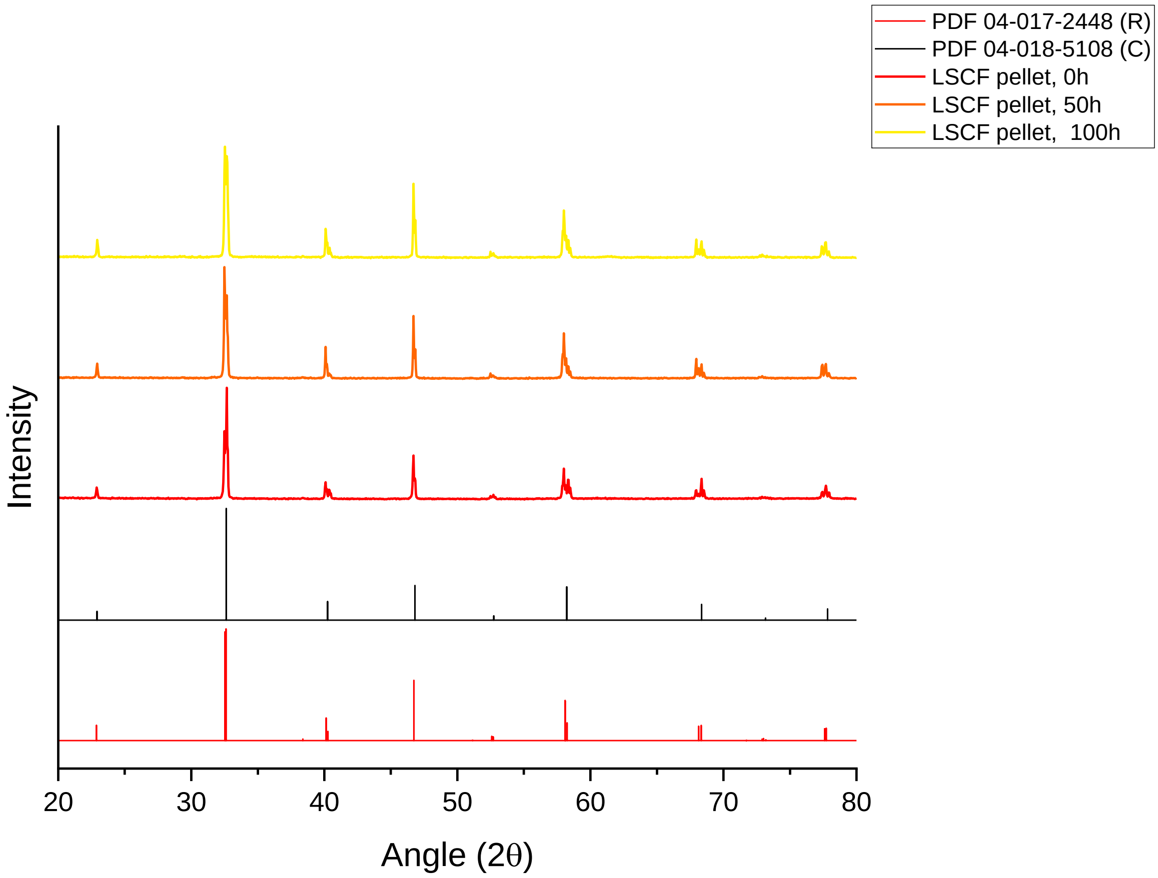

Figure 4-17 XRD patterns for Batch A, flat LSCF substrates at different stages of ageing (samples were aged in a box furnace at 800°C in ambient air. Reference patterns for cubic and rhombohedral LSCF have also been plotted for comparison.

Lastly, a new tub of LSCF-6428 powder was purchased and processed to fabricate new LSCF flat substrates. These were polished and subjected to the same thermal ageing regime. XRD data was collected and analysed to determine phase composition, appropriate data and reference patterns are presented in Figure 4-18.

Phase composition for this batch, as determined by Retvield and RIR analysis showed that at 0h sample contained 56.7% rhombohedral and 43.3% cubic phases; at 50h, 55.6% rhombohedral and 44.1% cubic phases; and finally, for 100h, 50% and 50% rhombohedral and cubic phase, respectively. For this batch, no new phases that could be associated to Sr-containing phases appeared.

These compositions differ greatly from what is reported in literature, since LSCF phases depend greatly on the cooling rate and atmosphere used during thermal ageing, an approximate 85% rhombohedral and 15% cubic phase composition is what would be expected when LSCF is cooled from 800°C at a cooling rate of 5°C min^{-1}. [10, 168, 170-172].

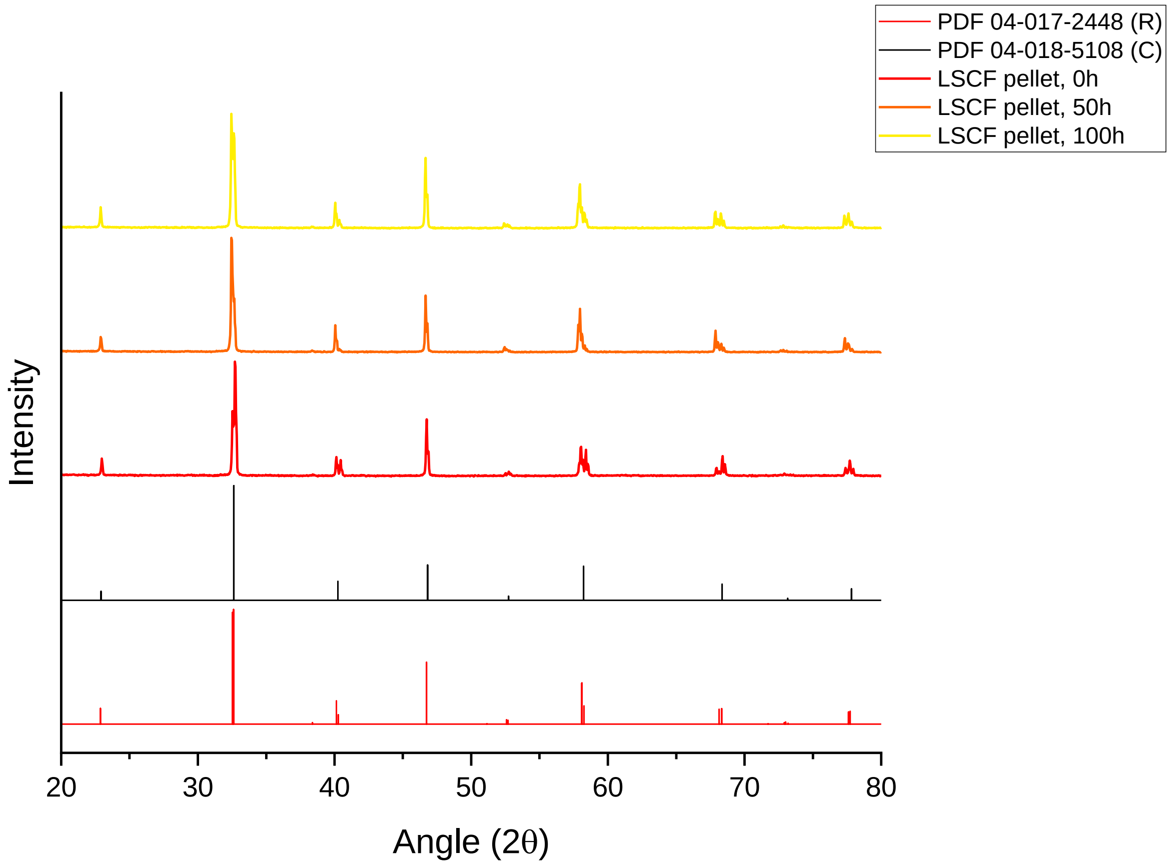

Figure 4-18 XRD patterns for Batch C, flat LSCF substrates at different stages of ageing (samples were aged in a box furnace at 800°C in ambient air. Reference patterns for cubic and rhombohedral LSCF have also been plotted for comparison.

Overall, when analysing thermally aged on mirror polished, flat and dense LSCF substrates via XRD, it was found that in most cases LSCF was polycrystalline presenting a mixture of cubic and rhombohedral phases in various ratios. No apparent trend in composition ratio derived from ageing was observed. However, this is to be expected since pure LSCF phase composition has been proved to be heavily dependent on cooling conditions, *i.e.* atmosphere and cooling ramp. LSCF that would normally have a rhombohedral structure at room temperature undergoes a rhombohedral – cubic phase transition at ~750°C. Upon cooling, the transition can be completely reversed if cooling rate is sufficiently low in air (0.5°C min^{-1}) [170]. For the conditions used in this study, LSCF substrates should have suffered a complete rhombohedral – cubic transition at 750°C, posterior to ageing, samples were cooled down at a 5°C min^{-1} rate, which should give a final LSCF composition of 85% rhombohedral and 15% cubic when LSCF is cooled in air.

Additionally, no new Sr-containing phases were detected after ageing treatment for any of the analysed batches. Regardless of this, the presence of said phases cannot be entirely ruled out since the possibility exists that they were not present in a sufficient amount (at least 2%) or a crystalline state to be detected by the equipment used [141, 144].

4.2.3 Surface analysis *via* SEM-EBSD

Three different batches (A, B, and C) of flat and dense LSCF substrates were fabricated, ground and polishes until mirror-finish, and finally subjected to a thermal ageing treatment consisting of heating the substrates at 800°C for periods of 50 and 100h. Exposing LSCF materials at elevated temperatures has been previously used as a way to promote Sr-surface segregation [10, 81, 103].

Sr-surface segregation (SSS) has been identified as one of the main degradation mechanisms for LSCF under SOFC operation conditions [12, 78, 108]. Furthermore, it has been reported that the occurrence of SSS significantly hinders the oxygen reduction reaction (ORR) on LSCF cathodes by blocking active sites [44, 45]. Thus, understanding why SSS occurs and more importantly, how to prevent it have become an important research topic for the development of Sr-based cathode materials [104, 165].

Batch B consisted of two sets of ground and polished substrates, the main difference between these sets being that set 1 was processed, aged and analysed prior to the COVID-19 lockdown, whilst set 2 of samples were fabricated prior to lockdown, but their grinding, polishing, ageing, and SEM analysis all occurred after lockdown.

SEM images for Batch B, set 1are presented in Figure 4-19. The images for the unaged substrates (Figure 4-19a, a1) revealed that the grinding and polished protocol described in section 3.1.2.3 in Chapter 3 of this thesis achieved a scratch-free surface that will enable to easily identify any changes to the sample surface after ageing.

After 50h of ageing, samples were imaged again (Figure 4-19b, b1), where the presence of angular particles of about 1 µm, that concentrated at the grain boundaries, was observed. Following an extra period of ageing (50h more), the new images (Figure 4-19c, c1) revealed that the previously observed particles grew significantly in size (~ 5 µm) and were well dispersed on the sample surface instead of just localised along the grain boundary.

The formation of particles along the grain boundary and the subsequent particle growth observed after prolonged ageing has been reported previously on studies by Araki *et.al.* [10]. Araki *et.al* positively identified the surface particles to be Sr–containing phases using energy dispersive X-ray analysis (EDX), produced when Sr atoms from the bulk of the material migrate to the surface and form new phases, which are not conductive and block ORR active sites, in addition to changing the composition of the surrounding material and modifying its inherent conductive properties [10, 12, 45].

For the purposes of this work, it was assumed that the observed segregated particles were Sr-rich segregated phases from the LSCF bulk. However, since no other complimentary elemental analysis to SEM, like EDX was conducted on any of the analysed substrates, this cannot be said with a total certainty.

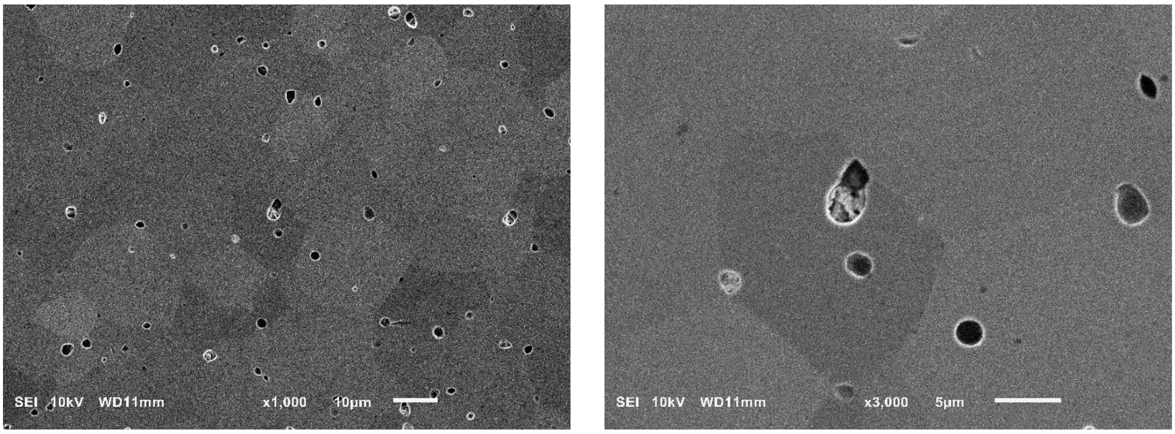

(a) Batch B, set 1, 0h

(a1) Batch B, set 1, 0h

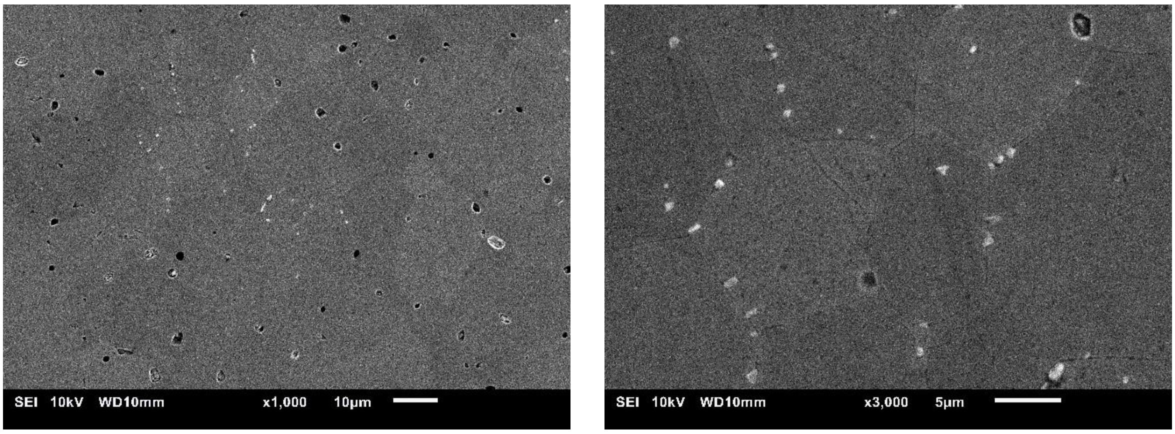

(b) Batch B, set 1, 50h

(b1) Batch B, set 1, 50h

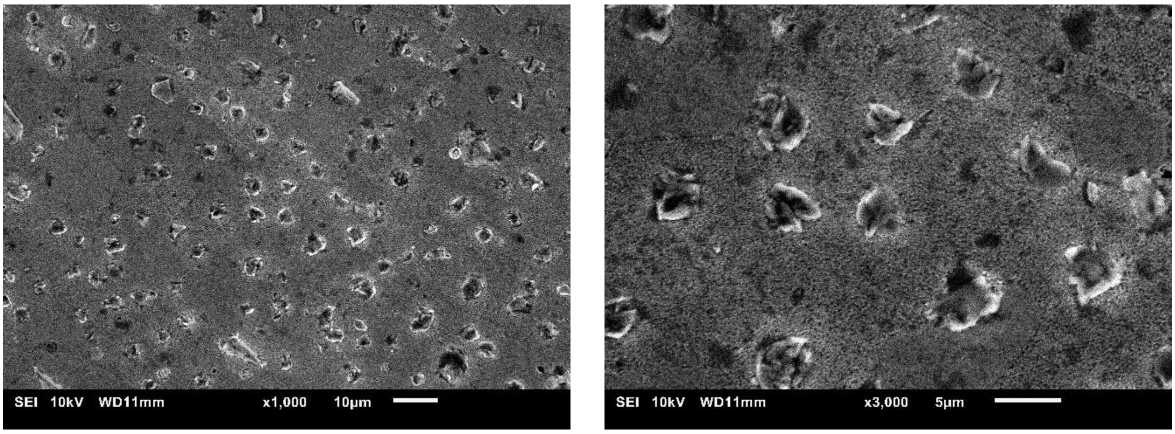

(c) Batch B, set 1, 100h

(c1) Batch B, set 1, 100h

Figure 4-19 SEM images for set 1, Batch B, flat LSCF substrates at different ageing times (a) 0h, (b) 50h, (c) 100h. Samples were aged at 800 °C in ambient air

As previously discussed, set 2 of Batch B substrates sat in storage after production due to the COVID-19 closure of university facilities. Afterwards, substrates were ground and polished until mirror finish as per the described protocol in Chapter 3 of this work. The followed ageing protocol was the same as followed for set 1. Substrates were imaged at 0, 50 and 100h of ageing with corresponding SEM micrographs presented in Figure 4-20, relevant back-scattered electron images (EBSD) can be found in section 10.5.2 of Annex A.

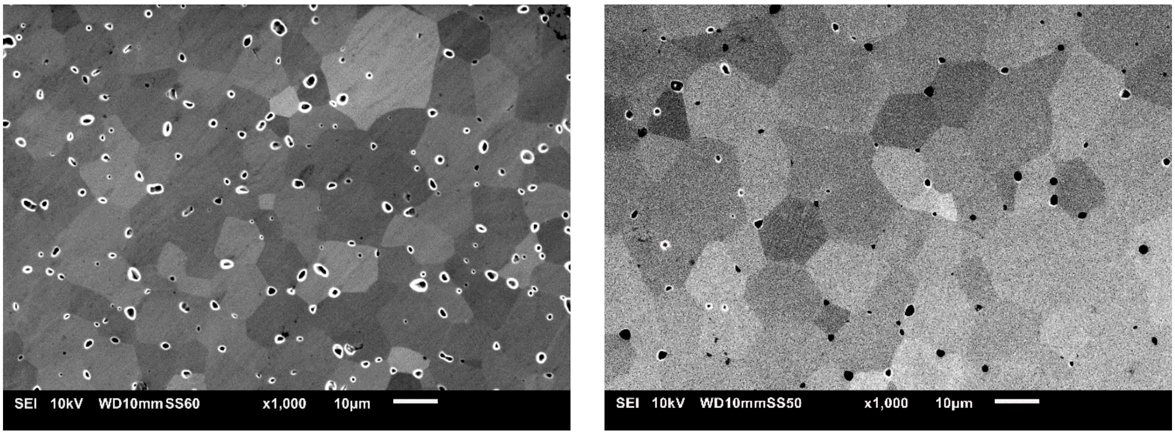

(a) Batch B, set 2, 0h

(b) Batch B, set 2, 50h

(c) Batch B, set 2, 100h

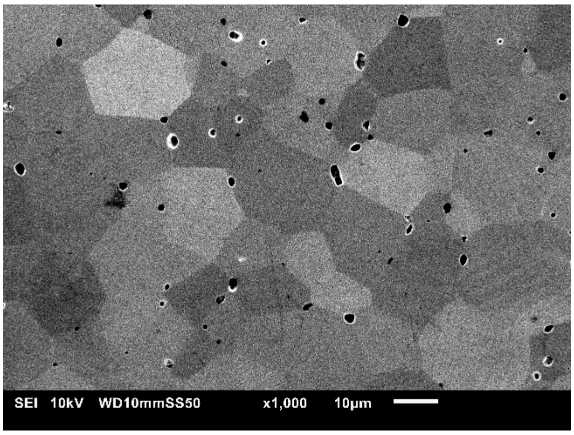

Figure 4-20 SEM images for set 2, Batch B, flat LSCF substrates at different ageing times (a) 0h, (b) 50h, (c) 100h. Samples were aged at 800 °C in ambient air

Once again, images at 0h of ageing showed that substrates had a flat surface where grains were clearly visible. However, after thermal ageing, samples did not show any signs of segregated particles, not even after prolonged ageing (100h).

Since this contradicted previous observations and reports from literature [10], a new batch of samples (Batch A) was processed for thermal ageing. However, the ageing protocol was modified for this batch (ageing at 1000°C, heating, and cooling rates of 5°C min^{-1}) and substrates were imaged at shorter interval to identify Sr-surface precipitates.

SEM images for Batch A at different ageing times are presented in Figure 4-21, with corresponding EBSD images in section 10.5.1 of Annex A.

(a) Batch A, 0h

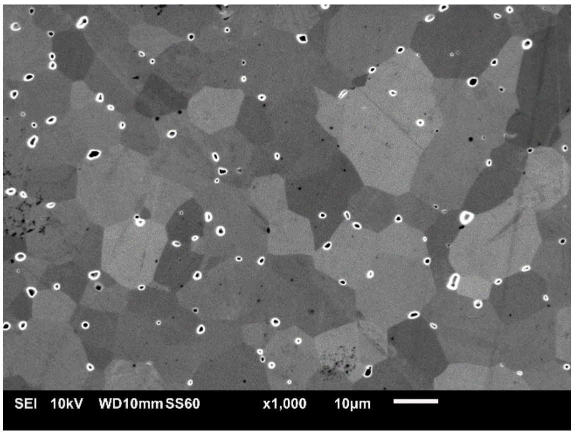

(b) Batch A, 12h

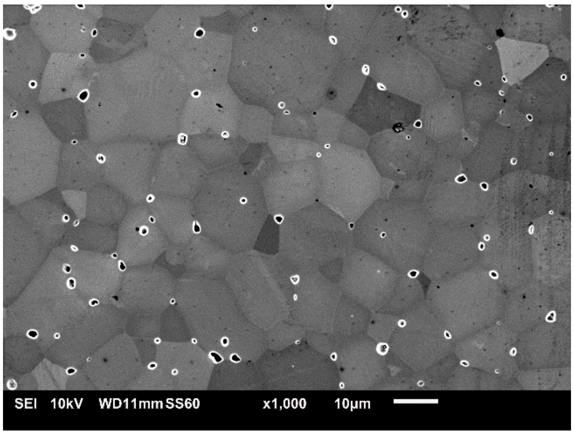

(c) Batch A, 24h

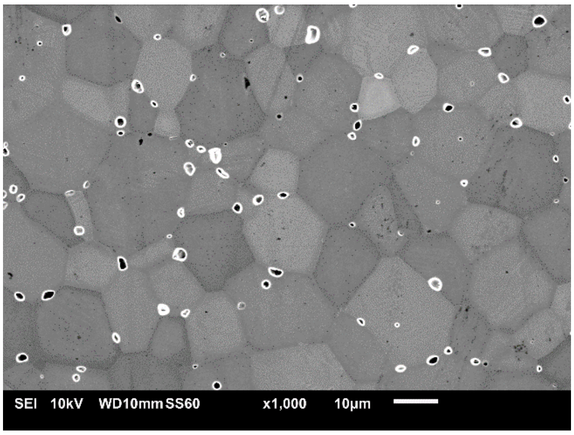

(d) Batch A, 36h

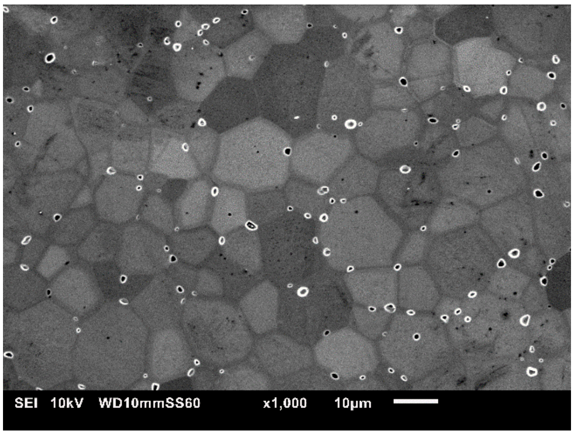

(e) Batch A, 48h

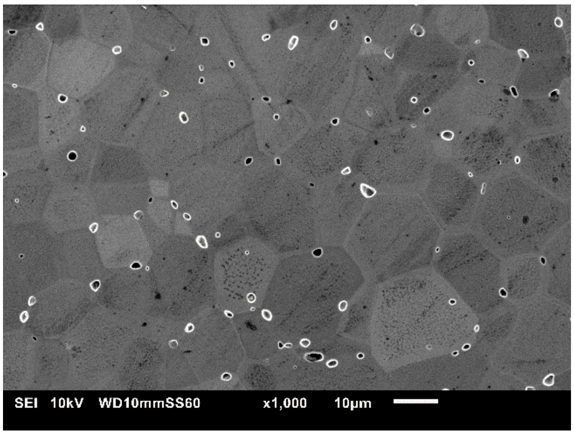

Figure 4-21 SEM images for Batch A, flat LSCF substrates at different ageing times (a) 0h, (b) 12h, (c) 24h, (d) 36h and (e) 48h. Samples were aged at 1000 °C in ambient air

Like for the previously discussed, unaged substrates showed a clean surface. However, even after the substrates were subjected to higher ageing temperatures, no changes were detected. This was completely against what would be expected, since signs of SSS have been detected as early as 1h after heating LSCF at 900°C [10]. The lack of segregated particles in addition to the atypical behaviour observed for LSCF porous electrodes after 50h of operation and the fact that XRD analysis confirmed that substrates for all batches were LSCF-6428 supported the initial theory of a *calendar ageing effect*, in which after samples sat in storage for a prolonged period of time after processing caused some sort of material stabilisation, which prevented further degradation of the analysed material.

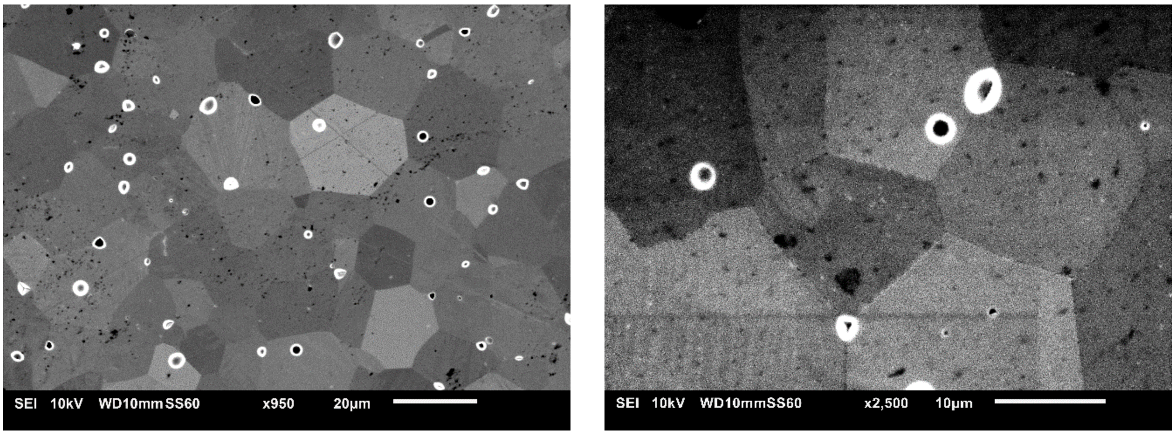
(a) Batch C, 0h

(b) Batch C, 12h

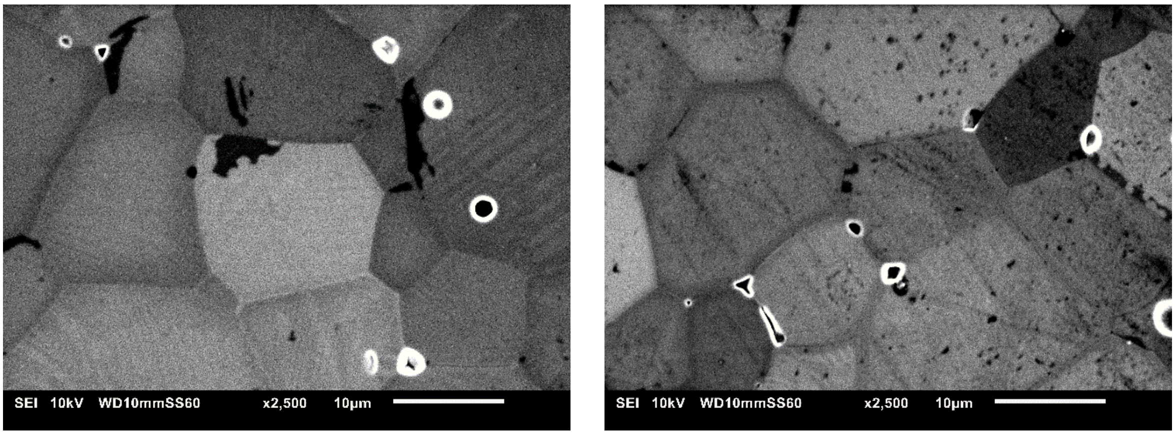
(c) Batch C, 24h

(d) Batch C, 36h

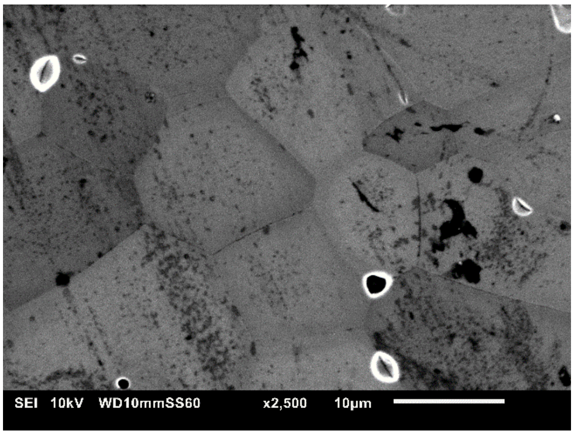
(e) Batch C, 48h

Figure 4-22 SEM images for Batch C, flat LSCF substrates at different ageing times (a) 0h, (b) 12h, (c) 24h, (d) 36h and (e) 48h. Samples were aged at 1000 °C in ambient air

Finally, a new tub of LSCF-6428 powder was purchased to fabricate a new batch (Batch C) of substrates to conduct the same modified ageing treatment. Micrographs at different ageing times are presented in Figure 4-22, appropriate EBSD images can be found in section 10.5.3 in Annex A.

At 0h, SEM images show that the grinding and polishing procedure produced a smooth surface that would facilitate the observation of any surface changes. However, after ageing at 1000°C for 12, 24, 36, and 48h, no surface segregated particles that could be associated to SSS were observed. These findings, although consistent with had been previously observed for Batch A and set 2 of Batch B, were completely contradictory to what is reported in literature. No apparent causes for this strange occurrence could be identified. Additionally, due to time constraints, it was not possible to repeat the ageing treatment to corroborate these results.

Three different batches (A, B, and C) of mirror polished LSCF-6428 substrates were subjected to high temperature ageing treatment to promote Sr-surface segregation (SSS) and then imaged using scanning electron microscopy (SEM). Signs of SSS in the form of segregated particles were observed in Batch B, set 1. The observed particles (~1 µm) were angular and appeared at the grain boundaries after 50h of ageing. After 100h of high temperature ageing, segregated particles grew to ~5µm, which was in complete agreement to what Araki *et.al.* [10] had previously reported and positively identified as Sr-rich particles by using EDX. For the purpose of this work, the observed particles on set 1 of Batch B were considered as Sr-rich segregated particles.

However, when imaging a second set for Batch B, aged under the same conditions, no segregated particles were observed. To corroborate these results, Batch A was aged under a modified regime (1000°C for 12, 24, 36 and 48h), but once again, no segregated particles were observed. These findings, in addition to the atypical behaviours of different batches for porous LSCF electrodes supported the author's theory of a *calendar ageing effect*, in which samples that sat in storage somehow stabilised during this time, which in turn prevented further measurable and observable signs of degradation.

Finally, a new batch (Batch C) of substrates were fabricated with a newly purchased LSCF-6428 tub. This last batch was aged under the modified ageing regime, but once again no segregated particles that could be associated to SSS could be observed. No apparent causes for this strange occurrence could be identified. Due to time constraints, it was not possible to repeat the ageing treatment to corroborate these results. Moreover, additional elemental analysis techniques coupled with SEM would be required for a positive identification of Sr-rich segregated particles.

4.3 Summary and conclusions

Impedance data for three different batches of samples (A, B and C) were obtained and fitted to an appropriate ECM model. The electrical elements included in this ECM described the key features observed on the impedance data; this is, the induction contribution from the jig wires/connections, the two characteristic semi-arcs for the ORR on MIEC electrodes and the finite Warburg element accounting for the non-ideal behaviour of the electrode.

Batches B and A were fabricated using the same ink (LSCF powder was bought and processed in 2018). Batch B was comprised of three different sets, set 1 was tested prior to COVID-19 lockdown while sets 2 and 3 were tested after this. Rp values for cells in set 1 of Batch B were similar to values reported in literature and the shown increase after 50h of testing at 700°C under synthetic gas flow was attributed to the Sr-surface segregation that occurs on this type of electrodes, as supported by several studies. Sets 2 and 3 of Batch B showed two key findings, firstly that initial Rp for both sets was higher than values from set 1, and lastly, that the electrodes that were stored for longer *degraded less* (dRp for set 2 was ~36% and for set 3 was ~30%) the longer they were stored, which suggested that these sets had suffered some kind of degradation during storage, named as *calendar ageing effect* by the author. As a way of corroborating this, the same ink was used to produce a new batch of samples (Batch A), once again initial Rp values for this set where higher than those for set 1 and the change in Rp, although still positive, was lower that for sets in Batch B (~5%, for Batch A), supporting the theory of the *calendar ageing effect.*

Lastly, a new tub of LSCF-6428 powder was purchased and processed to produce a new batch of cells (Batch C). This time, initial Rp values were slightly lower than those obtained for set 1 of Batch B, but this set showed and even greater degradation than any other set analysed (~60%).

Regarding the mechanism for electrode degradation, in all cases it was attributed to Sr-surface segregation as supported by numerous reports in literature, The rate limiting step for the bare electrodes remained the charge transfer at the electrode/electrolyte interface and the O^{2-} ion bulk diffusion.

XRD analysis of three different batches (A, B and C) of mirror polished, flat and dense LSCF substrates showed that for most cases, LSCF presented a polycrystalline mixed composition of rhombohedral and cubic phases in various ratios. No apparent trend in composition ratio derived from ageing was observed. However, this was expected due to the fact that LSCF phase composition has been proved to be dependent on cooling conditions, *i.e.* atmosphere and cooling ramp.

Additionally, no new Sr-containing phases were detected after ageing treatment for any of the analysed batches. Regardless of this, the presence of said phases cannot be entirely ruled out since the possibility exists that they were not present in a sufficient amount (at least 2%) or a crystalline state to be detected by the equipment used.

Finally, batches A, B, and C of mirror polished LSCF-6428 substrates were subjected to high temperature ageing treatment to promote Sr-surface segregation (SSS) and then imaged using SEM to observe the appearance of segregated particles at the surface that can be associated to SSS. Such particles were observed in Batch B, set 1 after 50h (~1 µm) and after 100h particles (~5µm). However, when imaging a set 2 of Batch B, aged under the same conditions, no segregated particles were observed. Additional batches (A and C) were aged under a modified regime (1000°C for 12, 24, 36 and 48h), but once again no segregated particles were observed. This and the atypical behaviour for equivalent batches for porous LSCF electrodes supported the author’s theory of a *calendar ageing effect*, in which samples that sat in storage somehow stabilised during this time, which in turn prevented further measurable and observable signs of degradation.

Due to time constraints, it was not possible to repeat the ageing treatment on more Batch C substrates to corroborate these results. Moreover, it would be highly beneficial that in addition to SEM, some elemental analysis technique was used for positive identification of Sr-rich segregated particles.

5 LSCF stabilisation using GDC as surface modification

5.1 Chapter overview

On this chapter, LSCF/GDC/LSCF cells were infiltrated with ($Gd_{0.1}Ce_{0.9}O_{1.95}$) GDC precursor solutions at different concentrations (0.025, 0.050, 0.125, 0.250, 0.500 and 1.000 mol L^{-1}) in a one-step infiltration protocol as described in Chapter 3. Infiltrated cells were then calcined to obtain the desired GDC phase. It has already been reported that GDC infiltration effectively prevented Sr-surface segregation (SSS) in addition to enhancing cathode performance and making it more stable, therefore, less prone to degradation [44, 78, 122]. However, due to time constraints resulting from the COVID-19 pandemic, for some sets of analysed samples only selected concentrations were tested in an effort to try to cover the initially designed range of concentrations.

GDC precursors at different concentrations were used to obtain different levels of surface covering on LSCF/GDC/LSCF cells and flat LSCF substrates to identify the which of these would provide the best results when using a one-step infiltration protocol.

Fabricated samples were then analysed using a variety of techniques in an effort to identify the coating's effect on SSS when samples were tested at operating conditions (700 °C, 20 mL/min under synthetic airflow). Flat LSCF substrates were spin-coated using the same GDC precursors at various concentrations and subjected to thermal ageing treatment at 800°C for periods of 50 and 100h. This thermal treatment has been identified to promote SSS on LSCF materials [10]. After thermal ageing, flat substrates were analysed to observe potential signs of SSS or its prevention.

For easy identification, the different samples have been separated and labelled as:

- **Batch A:** LSCF powder was purchased in 2018 and processed in 2020 for sample and ink production. The time gap between production and processing for this batch is derived from the university having to shut down due to the COVID-19 pandemic.
- **Batch B:** LSCF powder was purchased and processed in 2018 for sample and ink production.
- **Batch C:** LSCF purchased and processed in 2021 for sample and ink production.

Similarly to non-infiltrated samples, due to equipment availability, a small portion of Batch B samples were analysed using a Solartron Modulab 1250 FRA and a 1287 electrochemical interface; the rest of Batch B and the entirety of Batches A and C were analysed using the FRA/EIS analysed IviumStat.h standard. Regardless of recording equipment, all EIS data was analysed and fitted using ZView ® software in accordance with the protocols described in Chapter 3.

5.2 Results and discussion

5.2.1 Electrochemical analysis via EIS and ECM fitting

The first batch of fabricated and analysed samples was Batch B, comprised of two different sets. Set 1 of samples was tested using the Solartron Modular while set 2 was tested using the IviumStat.

Set 1 of samples were infiltrated with precursor concentrations of 0.050, 0.125 and 1.000 M (mol L^{-1}). Collected impedance data, presented in Figure 5-1, has been normalised to electrode area and electrolyte contributions (Rs) have been subtracted to aid in comparison between the different infiltrated electrodes. Dotted plots represent experimental EIS data, and the solid lines correspond to the fitted data using the same ECM [122] as in Chapter 4 of this thesis. A preliminary data fitting with the proposed electrical circuit model (ECM) used to fit EIS data for the non-infiltrated electrodes revealed that this same model could be used for data fitting for the GDC-infiltrated electrodes since both the chi-squared and %error values were in the same range as the ones obtained for the fits of the non-infiltrated samples [163]. EIS data was collected hourly for 50h, however, only data at every 10h intervals are presented.

The same key landmarks as for non-infiltrated electrodes were identified, *i.e.* a tail at high frequencies and in the positive Z2 axis that corresponded to the inductive contributions from the experimental setup [156], two semi-arcs of different sizes located each at the high and low frequency zones, which are both typical for impedance data for the ORR reaction in LSCF electrodes [36, 122, 157].

The proposed ECM (Figure 5-1a) is comprised of an inductor (L1) accounting for the inductive contributions from the experimental jig, R1 represents the electrolyte resistance also known as Rs. The two semi-arcs are represented by a resistor and a constant phase element connected in parallel. The first arc at high frequencies (HF), formed by R2 and CPE1, correspond to the charge transfer at the electrode/electrolyte surface and O^{2-} ion diffusion in the bulk of the electrode. The second arc at low frequency (LF), R3 and CPE2, account for the adsorption/desorption process of oxygen at the electrode surface and the gas diffusion in the pore structure of the electrode [124, 156].

Additionally, a remarkable difference in size between the two semi-arcs shows that the predominant phenomenon for the analysed electrodes is the charge transfer process at the electrode/electrolyte interface (semi-arc at HF). Lastly, it can be observed that the arches in experimental data are depressed, suggesting non-ideal electrode behaviour, which is often modelled using a finite-length Warburg element, which usually describes the one-dimensional diffusion of a particle [151].

An example of full fitting results for raw data at every 10h interval for the 0.050 M sample is presented in Table 5-1, full fitting results for the rest of the samples can be found in section 11.3.2 of Annex B.

(a) ECM

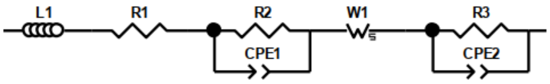

(b) 0.050 M

(c) 0.125 M (R2)

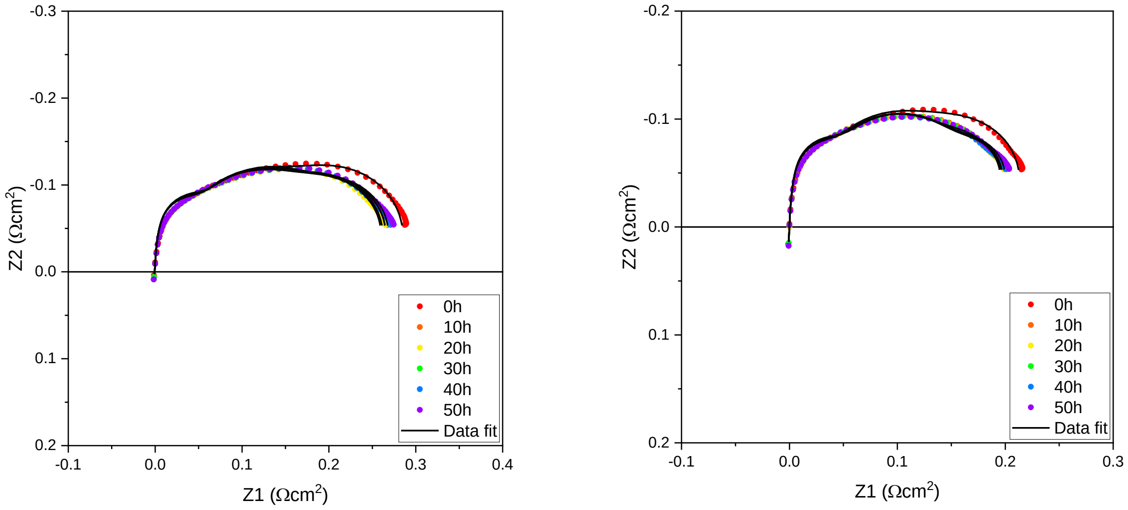

(d) 1.000 M

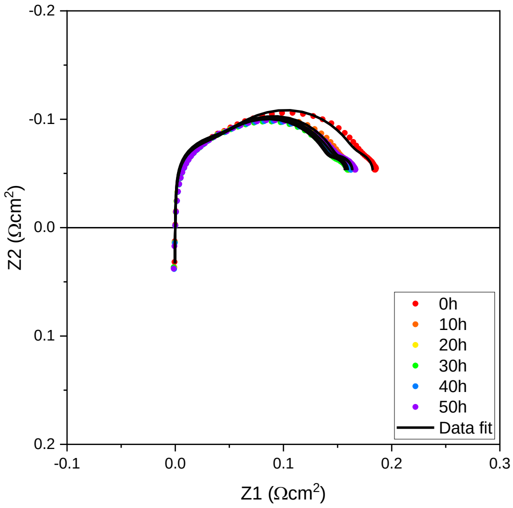

Figure 5-1 Fitted EIS spectra for set 1, Batch B, GDC-infiltrated cells at various concentrations, measurements recorded on Solartron Modulab

Table 5-1 EIS data fitting summary report for 0.050 M GDC-infiltrated sample for set 1, Batch B. Fitting was performed in ZView on raw impedance data

0.050 M	Chi-Sqr	Sum-Sqr	R1	%error	R2	%error	CPE1-T	%error	W-R	%error	W-T	%error	R3	%error	CPE2-T	%error
0h	1.89E-04	3.36E-04	7.269	0.06473	0.87922	2.2967	1.16E-02	5.0144	0.3906	2.9816	1.15E-04	5.4658	0.75965	2.3224	1.81E-03	3.8834
10h	2.48E-04	4.17E-04	7.231	0.06937	0.69826	3.5484	1.60E-02	7.5442	0.38932	3.3173	1.37E-04	6.0643	0.77587	2.7749	2.09E-03	4.2014
20h	2.82E-04	4.37E-04	7.333	0.07028	0.65566	3.8636	1.80E-02	8.2412	0.39751	3.3549	1.44E-04	6.1461	0.79681	2.7664	2.13E-03	4.2354
30h	3.02E-04	4.66E-04	7.386	0.07172	0.65447	3.9417	1.95E-02	8.46	0.41129	3.3453	1.53E-04	6.1525	0.82242	2.7362	2.20E-03	4.2518
40h	3.11E-04	5.12E-04	7.459	0.0743	0.62804	4.3051	2.17E-02	9.2627	0.41458	3.4891	1.62E-04	6.4343	0.84369	2.7997	2.27E-03	4.3685
50h	2.74E-04	5.32E-04	7.528	0.07485	0.6103	4.4924	2.39E-02	9.7068	0.42942	3.4651	1.72E-04	6.3893	0.86973	2.7574	2.32E-03	4.3695

Table 5-2 Rs and Rp values for 0.050 M GDC-infiltrated sample, set 1, Batch B, obtained from EIS data fitting using ZView. Data has been normalised to the electrode area

0.050 M	Rs (Ωcm^2)	%error	Rp (Ωcm^2)	%error
0h	0.9895	0.0647	0.2384	2.5336
10h	0.9841	0.0694	0.2146	3.2135
20h	0.9987	0.0703	0.2127	3.3283
30h	1.0063	0.0717	0.2182	3.3411
40h	1.0168	0.0743	0.2179	3.5313
50h	1.0267	0.0749	0.2212	3.5716

Table 5-3 Experimental values for Rp, Rp_i , Rp_f , and calculated dRp for set 1, Batch B, GDC-infiltrated electrodes

Sample [M]	Rp (Ωcm^2, 0h)	Rp_i (Ωcm^2, 10h)	Rp_f (Ωcm^2,50h)	dRp (%)
0.050	0.2277	0.2083	0.2138	2.5947
0.125 (R1)	0.2660	0.1288	0.1332	3.3937
0.125 (R2)	0.1550	0.1400	0.1446	3.2854
1.000	0.1324	0.1061	0.1055	-0.5552

Rp monitoring for set 1, Batch B samples is presented in Figure 5-2 (solid markers correspond to Rs and hollow markers correspond to Rp values), after analysing the evoluution of Rp against time, it was determined that for this set of samples, cathode activation period extended for the first 10h of operation [150, 164]. Changes in Rp (dRp%) were calculated using Equation 8 and corresponding data is presented in Table 5-3.

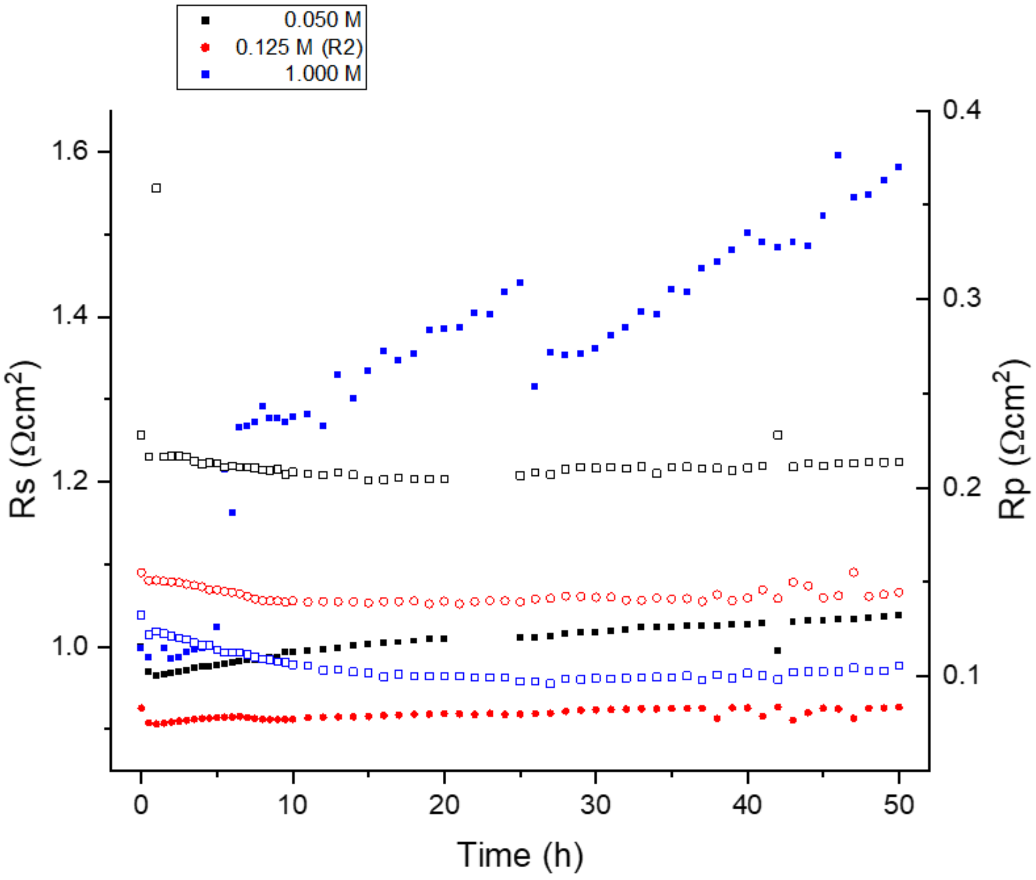

Figure 5-2 Rs and Rp for set 1, GDC-infiltrated, Batch B cells at various concentrations recorded using Solartron Modulab. Solid data markers correspond to Rs, hollow data markers correspond to Rp

The baseline Rp values for non-infiltrated samples in set 1 was ~0.125 Ωcm2 (Table 4-3). After infiltration with GDC precursors at various concentrations, all samples in this set presented initial values higher than non-infiltrated cells, except for the 1.000M GDC-infiltrated one which showed the closest values to the non-infiltrated ones. However, after the cathode activation period (10h) only the 0.050M infiltrated cell showed an Rp_i higher than its non-infiltrated counterpart; furthermore, after 50h of testing, all samples in this set exhibited lower Rp values than non-infiltrated cells, which means an improvement in electrode performance after infiltration [78, 122]. When calculating the change in resistance (dRp%) for infiltrated electrodes in this set, it was observed that Rp did increase, but the increase was less than the increase calculated for the non-infiltrated cells. Particularly for the case of the sample that was infiltrated with the highest concentration (1.000M), a decrease minor decrease in resistance was even observed (–0.55%). Which means GDC infiltration stabilised and enhanced electrode performance for ORR, which is in agreement with reports by dos Santos-Gomez *et.al.* [44]. There is still some debate on the exact enhancement mechanism for infiltrated electrodes [122]; however, this has been generally attributed to the increase in triple phase boundary (3PB) sites, this increasing the possible number of sites where the ORR can take place on the electrode surface [167].

A second set of samples for Batch B was analysed, this time using the IviumStat, a selection of fitted EIS data, along with the appropriate ECM is presented in Figure 5-3, the rest of collected and fitted data can be found in section 11.1.3 of Annex B.

(a) 0.025 M (R1) (b) 0.250 M (R1)

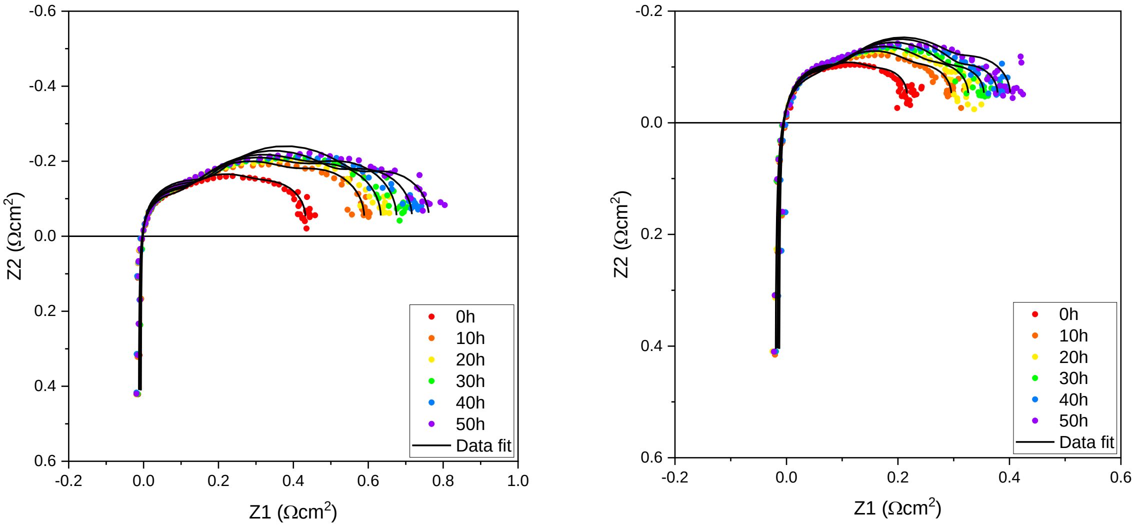

1.000 M (R1)

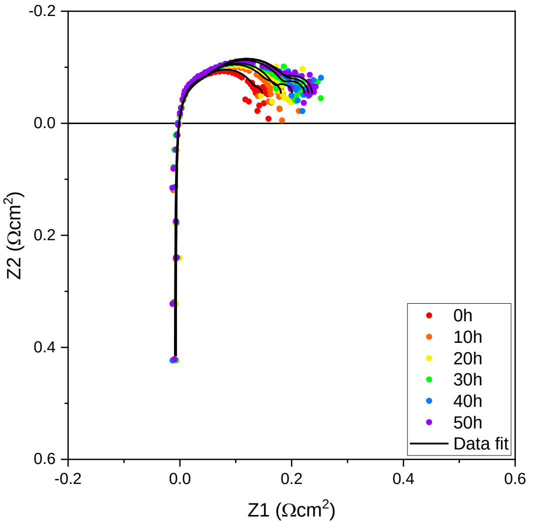

(d) ECM

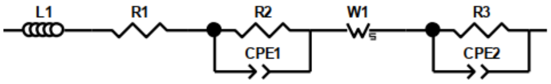

Figure 5-3 Fitted EIS spectra for set 2, Batch B GDC-infiltrated cells at various concentrations, measurements recorded on IviumStat FRA analyser

Normalised values to electrode area for Rp, Rp_i and Rp_f are presented in Table 5-4. Cathode activation period for this set was determined to be 10h, and changes in Rp were calculated for comparison. The hourly Rp monitoring for a selection of infiltrated samples for each concentration is presented in Figure 5-5, hollow data markers correspond to Rp values. Since this set was heavily populated by samples, the appropriate Rp *vs* time plots for the rest of samples in this set is presented in section 11.2.3 in Annex B. The samples presented in Figure 5-5 are in bold lettering in the following table for easy identification.

Table 5-4 Experimental values for Rp, Rp_i, Rp_f and dRp of set 2, Batch B GDC-infiltrated electrodes

Sample [M]	Rp (Ωcm^2, 0h)	Rp_i (Ωcm^2, 10h)	Rp_f (Ωcm^2, 50h)	dRp (%)
0.025 (R1)	***0.3809***	***0.5264***	***0.7301***	***38.7001***
0.025 (R2)	0.2232	0.2279	0.2778 (*)	21.8892
0.025 (R3)	0.3846	0.4738	0.5629	18.8204
0.025 (R4)	0.2941	0.2830	0.2706	-4.3545
0.025 (R5)	0.3261	0.3185	0.3535	10.9827
0.050 (R1)	***0.3211***	***0.4528***	***0.6656***	***46.9785***
0.050 (R2)	0.1588	0.1548	0.1949	25.9278
0.050 (R3)	0.2695	0.3260	0.3661	12.3134
0.050 (R4)	0.2683	0.2454	0.2850	16.1247
0.125 (R1)	***0.2057***	***0.3257***	***0.4199***	***28.9195***
0.125 (R2)	0.1740	0.1554	0.1981	27.4963
0.125 (R3)	0.2391	0.2203	0.2328	5.6628
0.250 (R1)	***0.1522***	***0.2259***	***0.3351***	***48.3544***
0.250 (R2)	0.0826	0.1468	0.2500	70.3208
0.250 (R3)	0.1464	0.1820	0.2387	31.1031
0.250 (R4)	0.3648	0.1676	0.1353	-19.2473
0.500 (R1)	***0.2503***	***0.3433***	***0.5138***	***49.6470***
0.500 (R2)	0.0755	0.1267	0.2185	72.4056
0.500 (R3)	0.2266	0.2670	0.3374	26.3565
0.500 (R4)	0.1393	0.1445	0.1345	-6.9434
1.000 (R1)	***0.0784***	***0.1016***	***0.1667***	***64.0425***
1.000 (R2)	0.3661	0.4048	0.3962	-2.1235
1.000 (R3)	0.2953	0.2983	0.2937	-1.5377

(*) Final Rp value measured at 48h

Initial Rp values for set 1 of GDC-infiltrated samples ranged from 0.1324 – 0.2660 Ωcm^2, whilst for this set ranged from 0.0755 – 0.3846 Ωcm^2. Although some values were significantly smaller, majority of them were similar or higher than the values recorded for set 1, and naturally, values after 50h at operation conditions were higher than the ones recorded for set 1 and consequently so were dRp values. A similar trend was observed for the sets 1 and 2 of non-infiltrated cells, as discussed in Chapter 4 of this thesis; in that case it was attributed to a *calendar ageing effect* on samples during storing.

Interestingly, when looking at a single concentration, for example 0.125M, initial Rp tended to increase with latter concentrations, but they suffered less change in electrode resistance after 50h under operation conditions. This is, samples tested at later dates, had higher initial values but they also degraded the less. This can be easily visualised in Figure 5-4, where the change in Rp (dRp%) clearly decreased the longer samples sat in storage prior to being tested. The 0.125M concentration was selected to make this comparison because this same concentration was systematically tested in other samples batches as well.

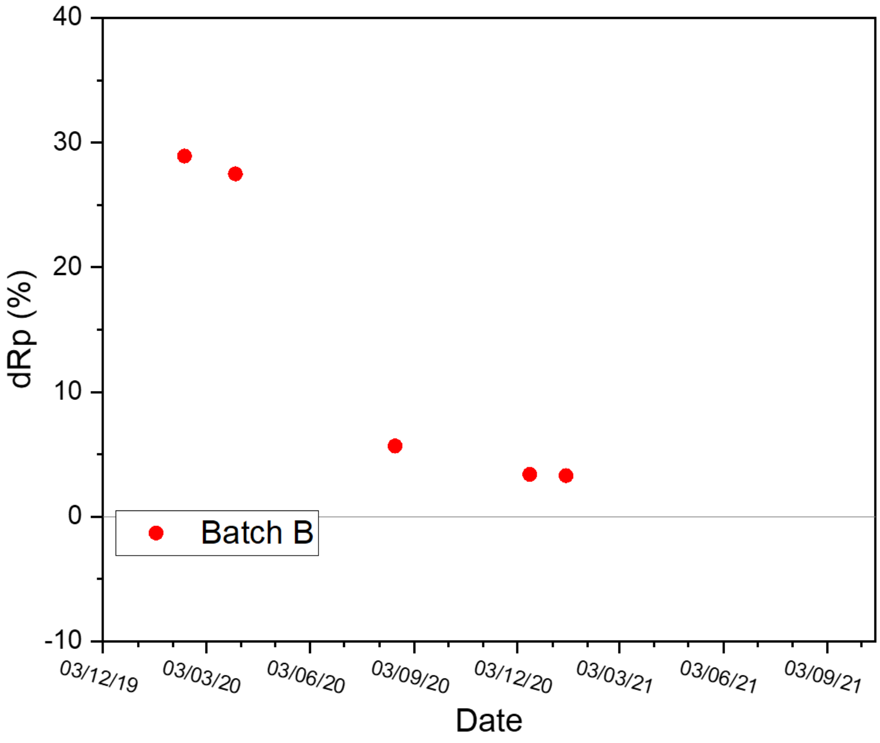

Figure 5-4 dRp(%) for 0.125M GDC-infiltrated samples from Batch B against their date of testing.

After 50h of testing at operating conditions, Batch B, set 2 of non-infiltrated samples showed final Rp values ranging from 0.1270 – 0.5166 Ωcm^2 (Table 4-4), while majority of the final Rp values for this set of infiltrated samples fell within that same range or were slightly higher, showing that for the case of set 2 samples, infiltration did not have any significant effect in lowering electrode polarisation resistance (Rp) nor stabilising its performance.

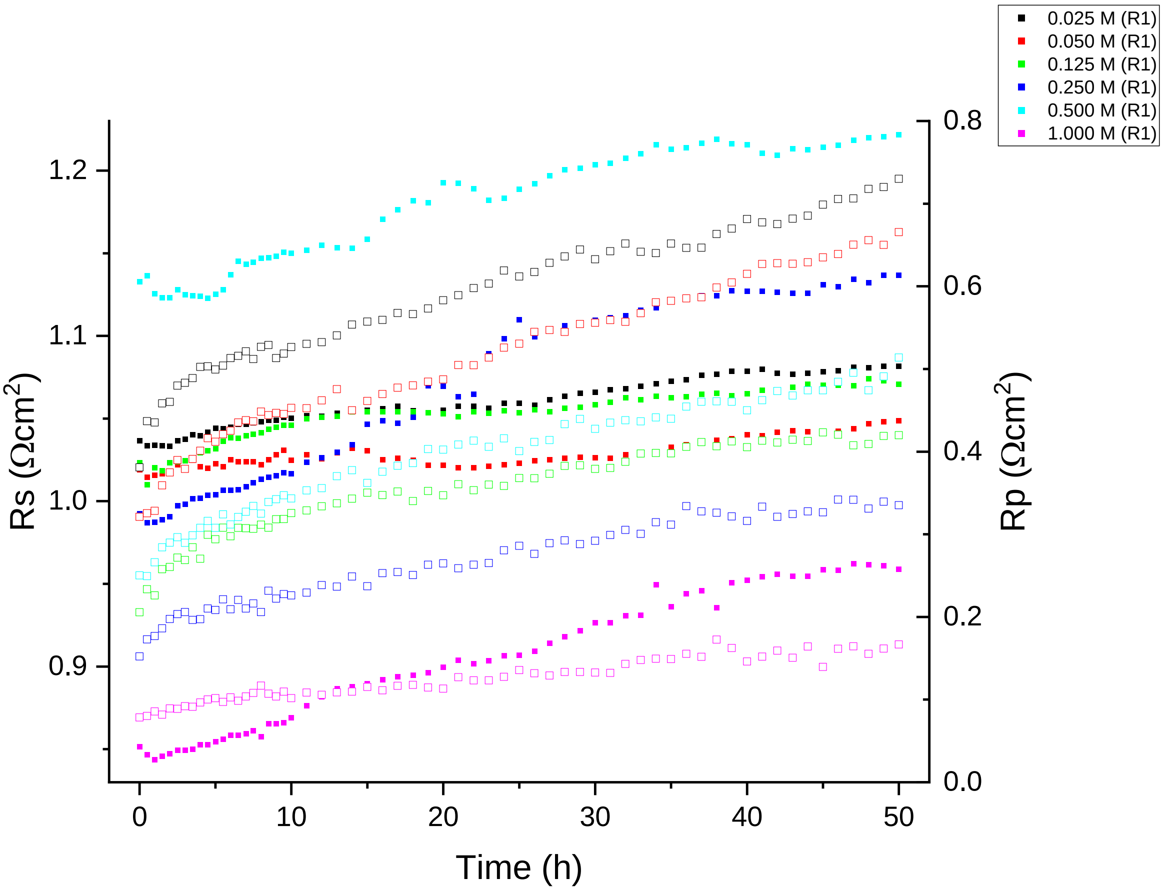

Figure 5-5 Rs and Rp for set 2, GDC-infiltrated, Batch B cells at various concentrations recorded using IviumStat FRA analyser. Solid data markers correspond to Rs, hollow data markers correspond to Rp

Following the same protocol as in Chapter 4, a new set of LSCF/GDC/LSCF cells was fabricated for infiltration, thus producing Batch A of GDC-infiltrated samples. Batches A and B were fabricated using the same ink, mixed from LSCF powder that was bought and processed in 2018. Due to time constraints, samples were only infiltrated with 0.025, 0.125, 0.250 and 1.000M GDC precursors, and only one repeat of each concentration was analysed. Fitted EIS data for a selection of concentrations and the corresponding ECM are presented in Figure 5-6, rest of EIS fitted plots can be found in section 11.1.1 of Annex B.

Nyquist plots at 10h intervals are shown, and the solid line corresponds to the data fitting using the appropriate ECM. Full ECM fitting results for raw data can be found in section 11.3.1 of Annex B. The corresponding hourly Rp monitoring for all samples in this batch is presented in Figure 5-6. Once again, cathode activation period was 10h and the appropriate values were used to calculate the changes in Rp (dRp%), this information is presented in Table 5-5.

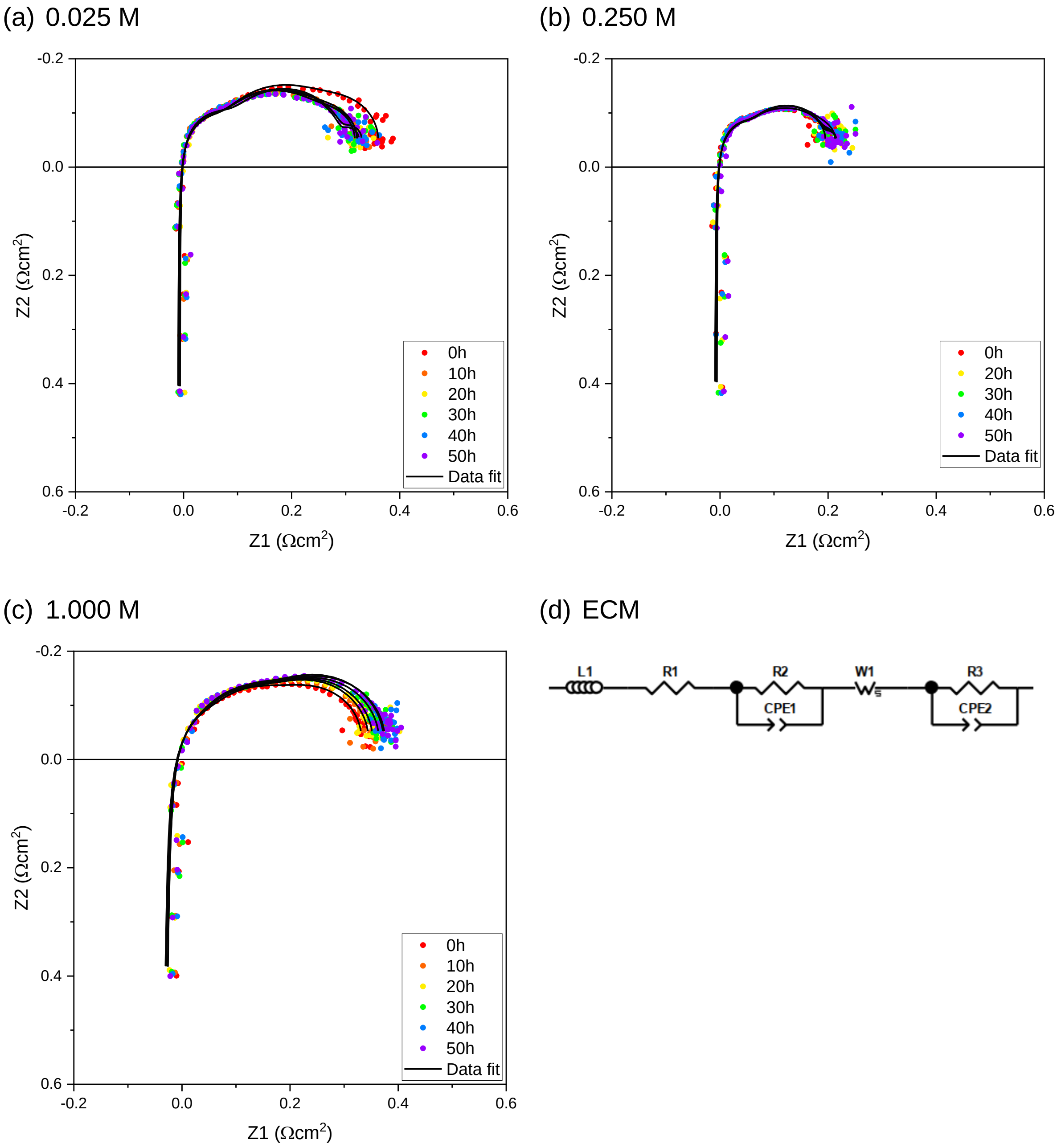

Figure 5-6 Fitted EIS spectra for Batch A, GDC-infiltrated cells at various, measurements recorded on IviumStat FRA analyser

When compared to non-infiltrated Batch A cells, all initial Rp values for this batch were lower, with the 0.250M GDC-infiltrated cell exhibiting the lowest Rp value (0.1439 Ωcm^2), and after 50h at operation conditions, all Rp$_f$ values were still lower than the ones recorded for the non-infiltrated cells. After evaluating the dRp% between these two sets of samples, it is also clear that GDC infiltration produced more stable electrodes, *i.e.* their degradation rate, or change in Rp was lower than for non-infiltrated samples. These findings are clearly supported by the literature [53, 167, 173], where it has been thoroughly discussed that GDC infiltration produces electrodes with a better performance and stability.

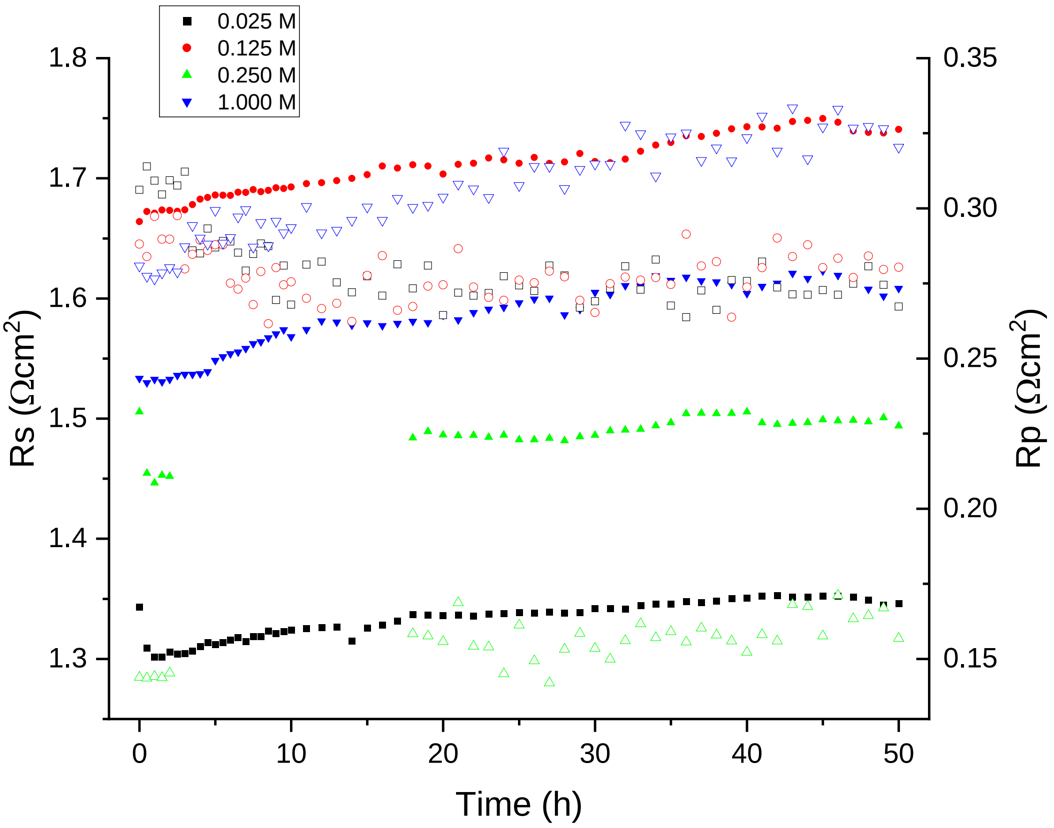

Figure 5-7 Rs and Rp for GDC-infiltrated, Batch A cells at various concentrations, measurements recorded using Solartron Modulab. Solid data markers correspond to Rs, hollow data markers correspond to Rp

Table 5-5 Experimental values for Rp, Rp$_i$, Rp$_f$ and dRp for Batch A, GDC-infiltrated electrodes

Sample [M]	Rp (Ωcm², 0h)	Rp$_i$ (Ωcm², 10h)	Rp$_f$ (Ωcm², 50h)	dRp (%)
0.025	0.3062	0.2679	0.2673	-0.2150
0.125	0.2881	0.2755	0.2804	1.7698
0.250	0.1439	0.1453	0.1568	7.8904
1.000	0.2808	0.2936	0.3204	9.1305

Finally, a Batch C of GDC-infiltrated cells was produced after a new tub of LSCF-6428 powder was purchased and processed. This set was in infiltrated with 0.025, 0.050, 0.125, 0.250, 0.500 and 1.000M GDC precursor solutions. No measurements could be repeated due to time constraints. A selection of EIS experimental data is presented in Figure 5-8, rest of data obtained can be found in section 11.1.4 of Annex B. Impedance data has been corrected to electrode area and electrolyte resistance (Rs) has been subtracted in the following plots

[122]. The dotted plot corresponds to experimentally obtained data while the solid black lines correspond to ECM fitted data.

(a) 0.025 M (b) 0.250 M

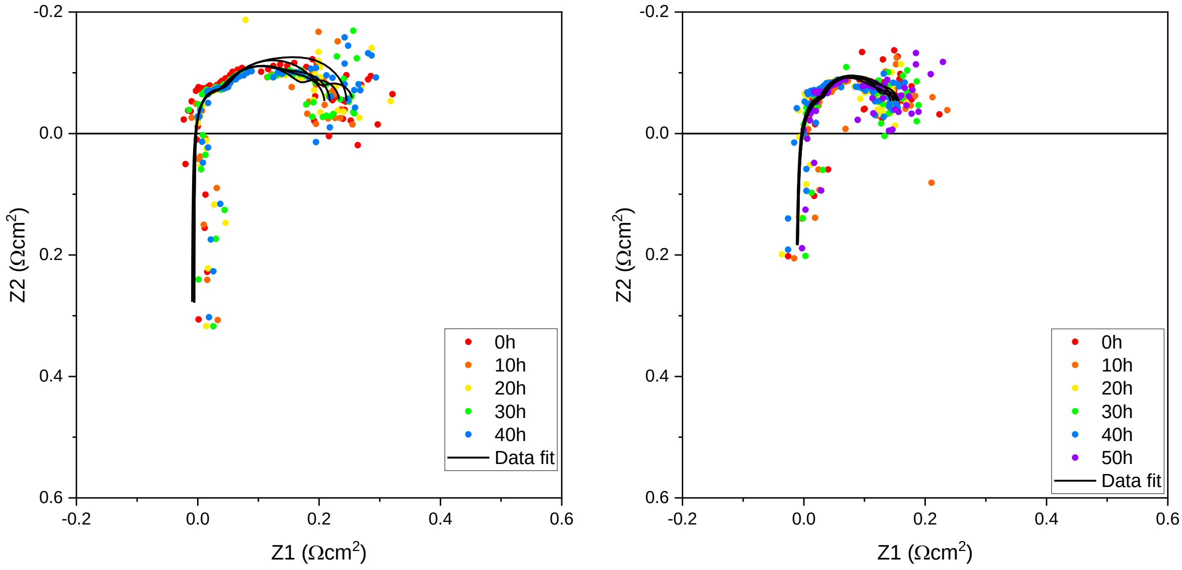

(c) 1.000 M (d) ECM

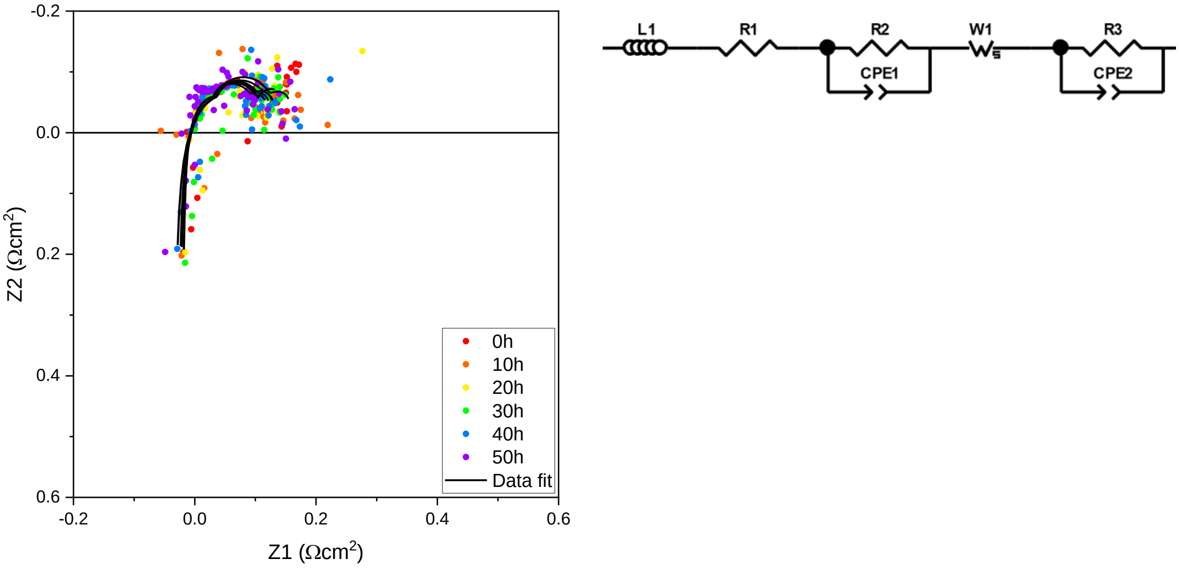

Figure 5-8 Fitted EIS spectra for Batch C, GDC-infiltrated cells at various concentrations, measurements recorded on IviumStat FRA analyser

As previously observed in other batches, the inductive contributions from the experimental setup can be observed [12]. However, when performing the data fitting with the proposed ECM, it was evident that for this case, chi-squared and error values were significantly higher than for previous fittings. Since the noise was present in all collected data, another performance check was performed in all experimental components. The IviumStat and proprietary software proved to be working correctly and since the experimental rig had been heavily used, the noise was attributed to the deterioration of the rig. This was the case for all Batch C samples, since these batches were the last to be measured after the jig broke.

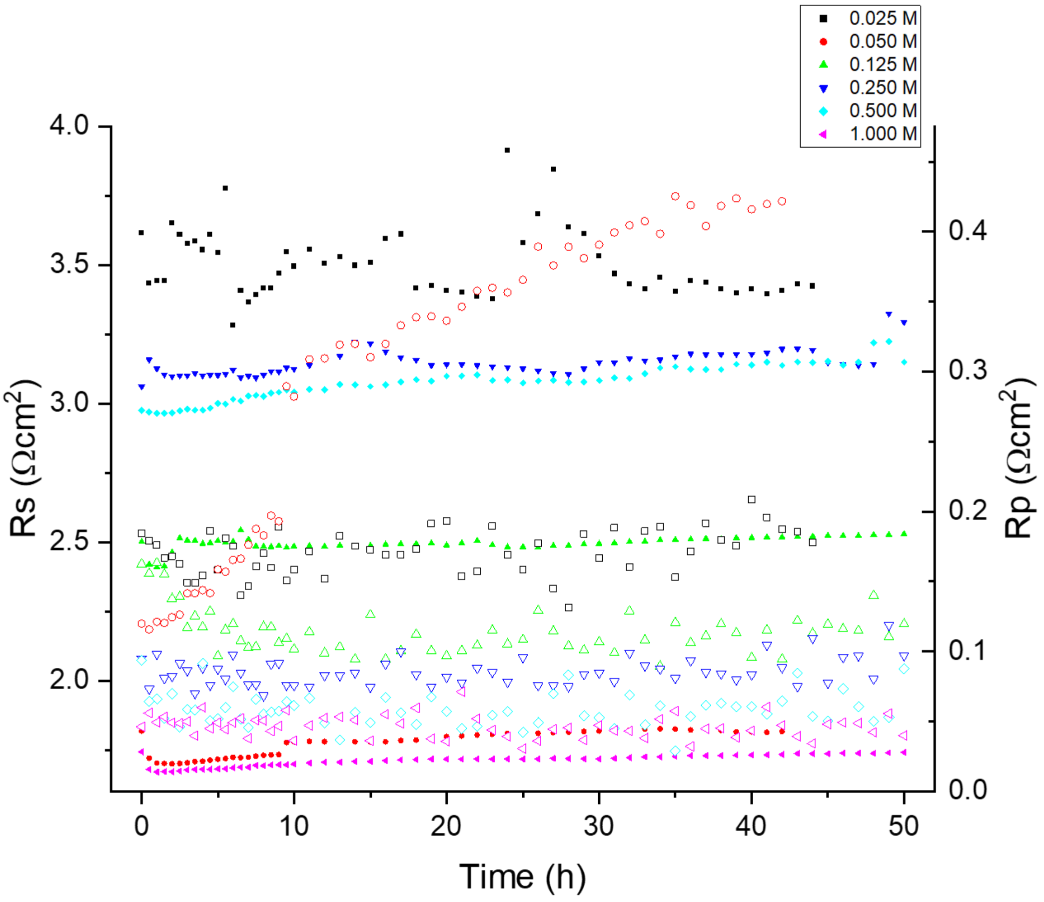

Figure 5-9 Rs and Rp for GDC-infiltrated, Batch C cells at various concentrations, measurements recorded using IviumStat FRA analyser. Solid data markers correspond to Rs, hollow data markers correspond to Rp

Table 5-6 Experimental values for Rp, Rp_i, Rp_f and dRp for Batch C, GDC-infiltrated electrodes

Sample [M]	Rp (Ωcm², 0h)	Rp_i (Ωcm², 10h)	Rp_f (Ωcm², 50h)	dRp (%)
0.025	0.1843	0.1587	0.1779	12.1041
0.050	0.1200	0.2822	0.4217	49.4184
0.125	0.1625	0.1018	0.1197	17.6054
0.250	0.0949	0.0757	0.0972	28.4566
0.500	0.0937	0.0615	0.0877	42.4879
1.000	0.0500	0.0365	0.0400	9.6071

Initial Rp values for Batch C non-infiltrated samples were 0.0812 Ωcm² and 0.0324 Ωcm², respectively. When comparing the initial values for this batch, electrodes infiltrated with the higher concentrations (0.250 – 1.000 M) showed comparable values. However, after being tested for 50h at operation conditions, 0.125 – 1.000 M infiltrated samples exhibited lower Rp values than non-infiltrated electrodes. For this batch of samples, infiltrating with higher concentrations produced electrodes with better performance for ORR. Moreover, after monitoring the change in Rp through time, even though all infiltrated samples showed an Rp increase with testing time, the calculated dRp% values for infiltrated cells were lower than for non-infiltrated ones. This corroborated that GDC infiltration improves electrode stability on top of performance [78, 122, 167].

Finally, the calculated dRp% values for all 0.125 M GDC-infiltrated samples across batches were compared (Figure 5-10).

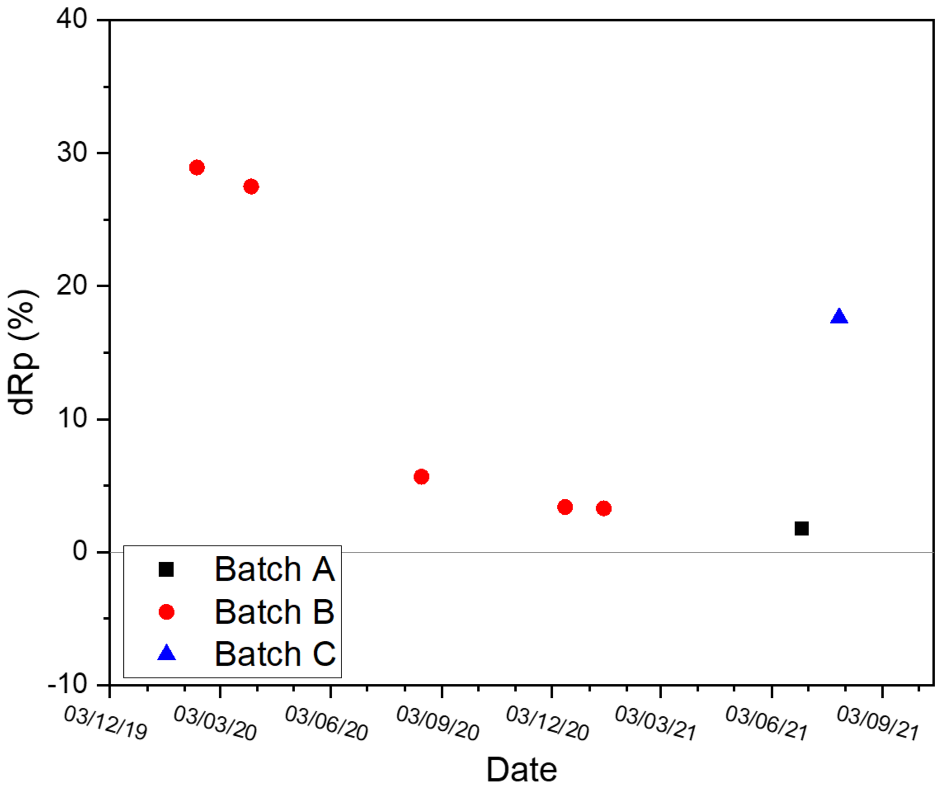

Figure 5-10 dRp(%) for Batch A, B and C of GDC-infiltrated cells at various concentrations against their date of testing

As it can be observed, from the figure above, for Batch B infiltrated cells, change in Rp decreased at later testing dates. When taking into account the fact that all samples on this batch were fabricated at the same time and sat in storage until testing, it can be deduced that the longer the samples sat in storage, the Rp changed less, this is, samples degraded less. For set 1, all samples showed a better performance and stability when compared to non-infiltrated cells than set 2. Regarding set 2 of infiltrated samples, both initial and final Rp values were higher than for non-infiltrated samples, showing also similar dRp values, meaning that in this case, infiltration did not improve stability nor performance as it would be expected [167]. For batch B, generally 0.125, 0.250 and 0.500 M precursor produced the electrodes with the best performance.

However, when looking at single concentrations, a clear trend was observed in which the dRp value decreased with increasing storage time, further supporting the idea of the *calendar ageing effect* that was previously observed on non-infiltrated cells.

Batch A was fabricated using the same ink used to fabricate Batch B. For this new batch, infiltration proved to be an effective performance and stability enhancer [53, 167, 173], with 0.250 M GDC-infiltrated electrodes showing the best performance. Regarding Batch C, although initial Rp values were higher than their non-filtrated counterpart, after 50h under operation conditions, GDC infiltration proved to be an effective way to improve performance and prevent degradation on the electrode. For this last batch, 0.250 – 1.000 M precursor produced the better performing electrodes.

5.2.2 Physical analysis *via* XRD

After grinding and polishing to mirror finish, flat and dense LSCF substrates for three different batches (A, B, and C) were spin-coated with 50 µL gadolinium doped ceria (GDC) precursor solutions at different concentrations (0.025, 0.125, 0.250, and 1.000 M) following the described protocol in section 3.1.2.4 in Chapter 3 of this thesis. Only a selection of concentrations were selected for spin-coating under time constraints considerations.

Finally, only samples with the lowest and highest concentrations were subjected to a thermal ageing treatment consisting of heating the substrates at 800°C for periods of 50 and 100h, which has been proven to promote Sr-surface segregation [10, 81, 103]. Furthermore, GDC has been reported to be an effective suppressor for Sr-surface segregation (SSS) [167, 173], so it is expected that spin-coating with GDC precursor will prevent SSS from occurring on the analysed samples.

Unaged and aged spin-coated (0.025 and 1.000 M) substrates where then analysed using X-ray diffraction (XRD) to evaluate any structural changes and possible formation of secondary Sr-containing phases on the surface. The presence of these Sr-containing phases has been linked to poor electrode performance for SOFC applications [45, 78, 165].

Ideally, perovskite (ABO_3) materials present a cubic crystalline structure with A-site cations occupying the corners of the cube and B-site cations occupying the centre of the body; however, slight deviations can cause a distortion resulting in a rhombohedral structure [168].

Similarly, GDC, which is a fluorite type material (AO_2) also presents a cubic crystalline structure [151].

X-ray diffraction data (XRD) patterns were obtained according to the protocols described in section 3.2.3 in Chapter 3. Patterns for Batch B of spin-coated substrates at different ageing stages are showed in Figure 5-11. Phase analysis reports for this set can be found in section 11.4.2 of Annex B.

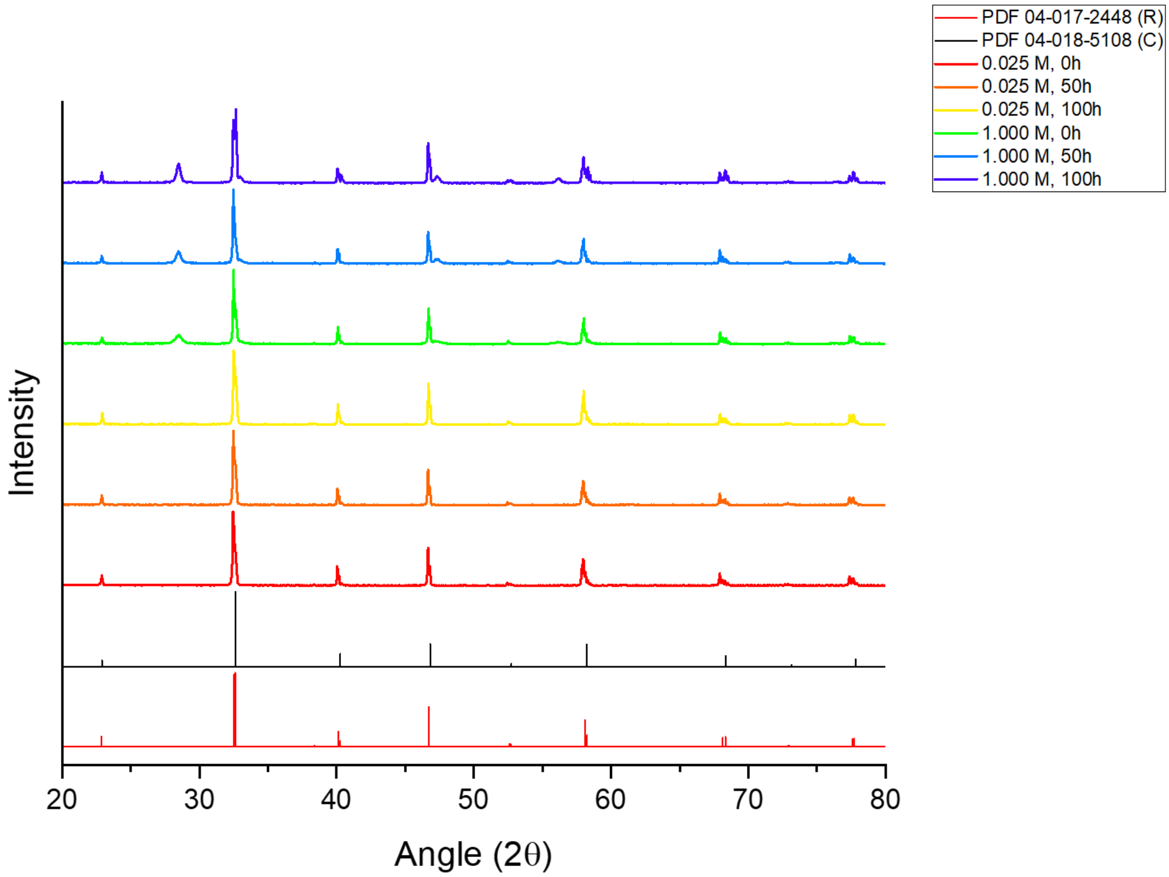

Figure 5-11 XRD patterns for Batch B, LSCF pellets spin coated with GDC at various concentrations and stages of ageing (samples were aged in a box furnace at 800°C in ambient air). Reference patterns for cubic and rhombohedral LSCF have also been plotted for comparison.

It was clear from collected data that LSCF substrates presented a mixture of phases, especially after ageing. Therefore, reference patterns for the most common LSCF phases reported in literature, *i.e.* cubic (PDF 04-018-5108) [151] and rhombohedral (PDF 04-017-2448) [169] were also plotted for comparison. Additionally, the GDC cubic structure (PDF 01-086-9063) was only detectable by XRD when the precursors used were at least 0.250M. For the samples where the analysis was possible, Rietveld refinement was used to calculate sample composition. For the cases where Rietveld analysis was nor possible due to non-convergence, sample composition was calculated using the Reference Intensity Ratio (RIR) analysis [141, 144]. All analysis were performed using *Match!© Phase Analysis using Powder Diffraction* software.

Phase analysis for Batch B samples revealed that for the lowest concentration (0.025M) no GDC phase was detectable and all LSCF substrates exhibited a 100% rhombohedral composition. For 1.000M spin-coated substrates, the characteristic cubic phase for GDC was detected [151] with the (111) peak at ~27 2θ degrees, whilst the LSCF substrates presented a mixed phase composition of 84% rhombohedral and 16% cubic, which is to be expected when substrates are cooled down from 800°C at a 5°C min^{-1} rate [170]. Furthermore, with increasing ageing time, the (111) peak for GDC became narrower, which is associated to the enlarging or particles, consistent with particle coarsening with ageing time. [141, 143, 144, 174].

No new Sr-containing phases were detected in any of the measurements for this batch of samples, but their possible presence cannot be ruled out. Similarly to what was observed with GDC at lower concentrations, the amount present is not enough for these phases to be detected using this XRD technique [141, 144].

A new batch of substrates (Batch A) was fabricated, polished and spin-coated with the same concentrations as for Batch B, then subjected to the same thermal ageing protocol. XRD data for this new batch and appropriate cubic and rhombohedral LSCF standard patterns are presented in Figure 5-12, reports for phase analysis for this batch can be found in section 11.4.1 of Annex B.

Similarly to what was observed with Batch B, the cubic GDC phase was only detected when precursor concentration for spin-coating was 0.250M or higher, and the (111) peak became narrower with increasing ageing time, suggesting the coarsening and particle growth of the spin-coated GDC phase [141, 143, 144, 174]

The LSCF substrates presented a 100% rhombohedral phase before ageing and a mixture of approximately 85% rhombohedral and 15% cubic phases after the ageing treatment, consistent with reports from literature [170]. No Sr-containing phases were detected on this batch either.

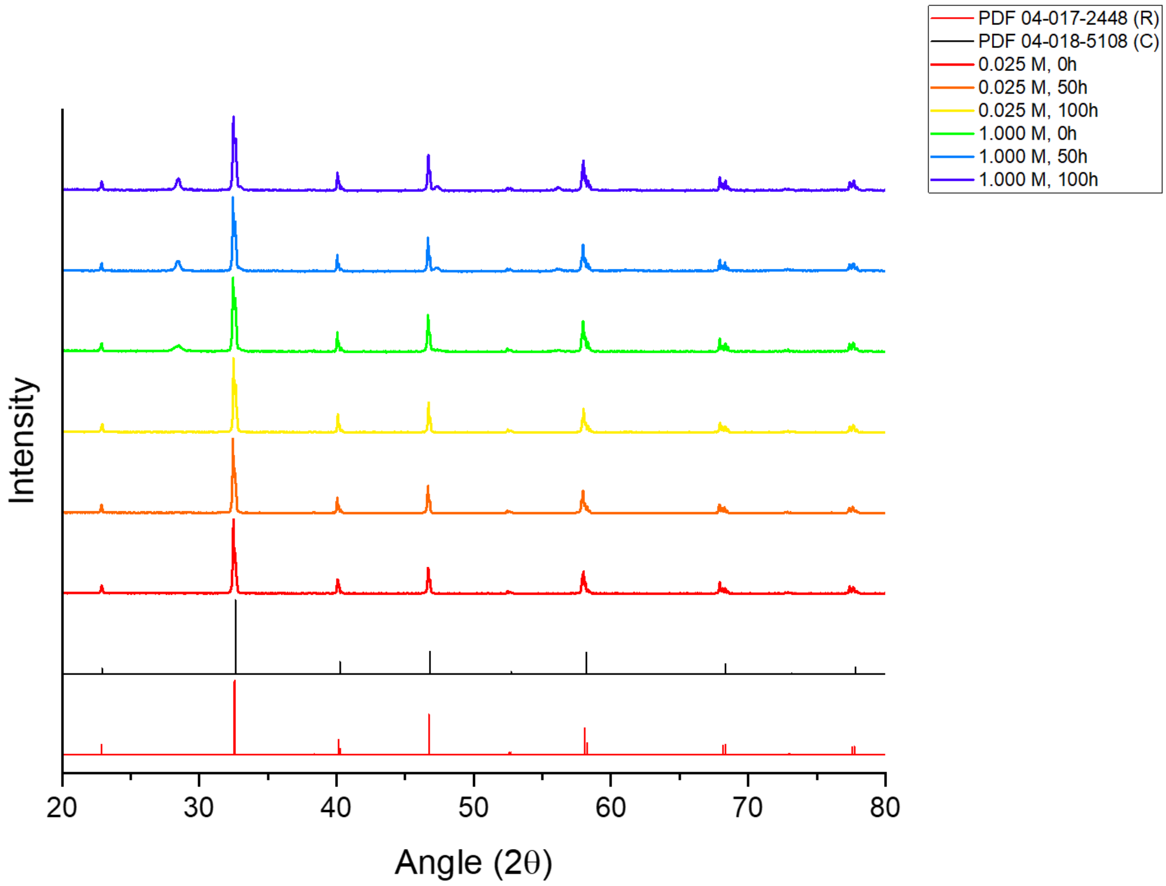

Figure 5-12 XRD patterns for Batch A, LSCF pellets spin coated with GDC at various concentrations and stages of ageing (samples were aged in a box furnace at 800°C in ambient air). Reference patterns for cubic and rhombohedral LSCF have also been plotted for comparison.

Lastly, a new tub of LSCF-6428 powder was purchased and processed to fabricate new LSCF flat substrates that were spin-coated and aged as the previously analysed batches. The new samples conformed Batch C. Collected XRD data for this batch with corresponding cubic and rhombohedral LSCF standard patterns are presented in Figure 5-13; additional XRD phase analysis can be found in section 11.4.3 of Annex B.

This time, all LSCF patterns exhibited a rhombohedral and cubic phase mixture of approximately 80% and 20%, respectively, and regardless of ageing time. This composition deviates from what would be expected [170], but values are still similar. The cubic GDC phase was only detected when the precursor used for spin-coating had a concentration of 0.250M or higher. Also, it was clearly observed that the (111) peak became shaper and narrower with increasing ageing time, suggesting the coarsening and particle growth of the spin-coated GDC phase [141, 143, 144, 174]

GDC phases were not detectable by XRD when using precursors with concentrations below 0.250M, however, this does not mean that GDC is not present in those samples, but that the amount is not enough for it to be detected using this method. Similarly, the fact that no Sr-containing phases were detected either does not mean that their presence can be entirely ruled out, since they might not be present at a high enough concentration or crystalline state to be detected [141, 143, 144]

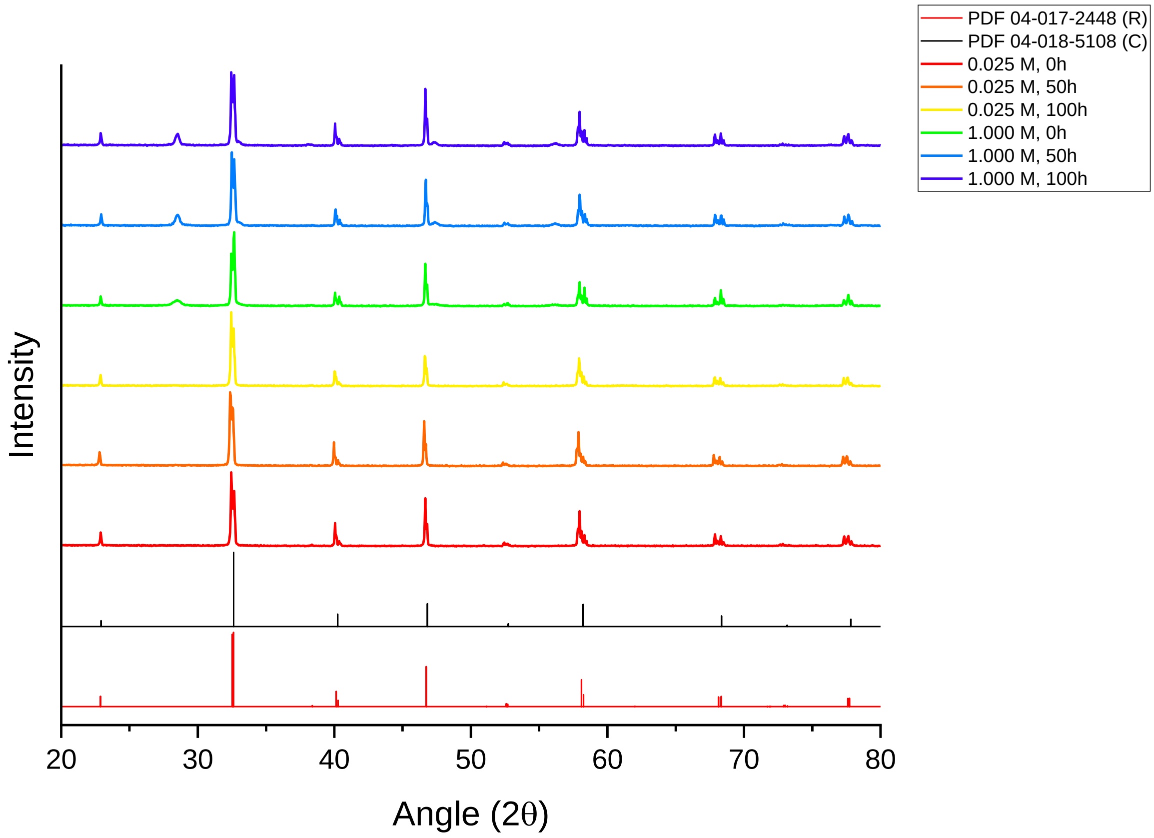

Figure 5-13 XRD patterns for Batch C, LSCF pellets spin coated with GDC at various concentrations and stages of ageing (samples were aged in a box furnace at 800°C in ambient air). Reference patterns for cubic and rhombohedral LSCF have also been plotted for comparison.

After analysing three different batches (A, B and C) of mirror-polished, GDC spin-coated and aged samples at different stages, it was found that in most cases LSCF was polycrystalline presenting a mixture of cubic and rhombohedral phases of approximately 15% and 85%, respectively. For the cases where sample presented a single phase, it was rhombohedral. All this is in agreement with the literature regarding the expected phases for LSCF at room temperature before and after being subjected to high temperatures and being cooled down at 5°C min^{-1} in air atmosphere [10, 168, 170].

Furthermore, it was found that GDC was not detectable when the precursor used for spin-coating had a concentration lower than 0.250M. Above this concentration, the respective cubic phase for GDC (PDF 01-086-9063) was clearly detected with the (111) peak at ~27 2θ degrees being clearly visible. As ageing time progressed, this peak became sharper and narrower, indicating that the GDC phase coarsened or enlarged in size [81, 141, 143, 144, 174].

As it was previously observed for bare LSCF mirror-polished substrates (section 4.2.2 in Chapter 4), no new Sr-containing phases were detected after ageing treatment for any of the analysed batches, which makes difficult to assess whether GDC prevented this from occurring as it has been previously reported in literature [44, 173]. Regardless of this, the presence of said segregated Sr-containing phases cannot be entirely ruled out since the possibility exists that they were not present in a sufficient amount (at least 2%) or a crystalline state to be detected by the equipment used [141, 144].

5.2.3 Surface analysis *via* SEM-EBSD

After grinding and polishing to mirror finish, flat and dense LSCF substrates for three different batches (A, B, and C) were spin-coated with 50 µL gadolinium doped ceria (GDC) precursor solutions at different concentrations (0.025, 0.125, 0.250, and 1.000 M) following the described protocol in section 3.1.2.4 in Chapter 3 of this thesis. Only a selection of concentrations were selected for spin-coating because of time constraints, and out of these only the lowest and highest concentration were thermally aged at 800°C for 50 and 100h to promote Sr-surface segregation (SSS) [10, 81, 103, 108].

Scanning electron microscopy (SEM) was used to evaluate the different morphologies when spin-coating the substrates at different concentrations. Additionally, substrates were re-imaged after every ageing stage to evaluate possible changes in the coating microstructure.

SEM images for Batch B are presented in Figure 5-14, with corresponding electron backscattered images (EBSD) in section 11.5.2 of Annex B. Images (a), (c), (d), and (e) show unaged GDC spin-coated substrates. It was observed that 0.025 M produced dispersed particle clusters, 0.125M produced a more uniform coating whilst 0.250M and 1.000M spin-coated samples exhibited a thicker but uneven covering with cracks and ridges that left some LSCF surface exposed. Different morphologies with varying concentration have been reported before [123, 131], as reflected from this, the thickness and covering increased when increasing the precursor concentration.

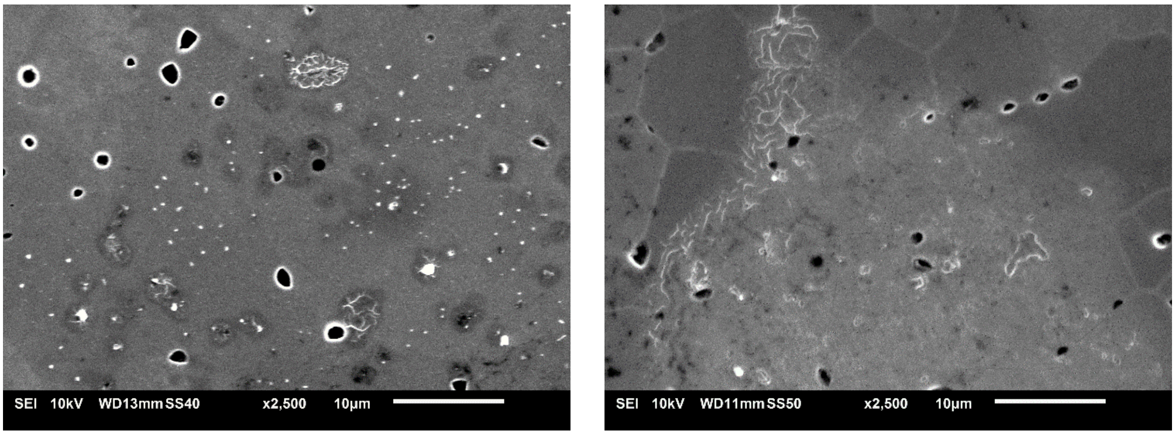

(a) Batch B, 0.025M, 0h

(b) Batch B, 0.025M, 100h

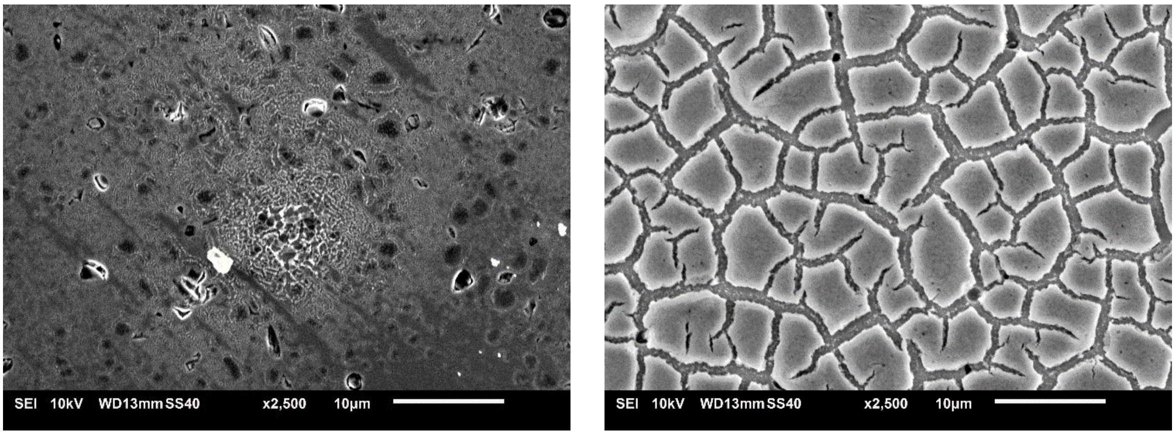

(c) Batch B, 0.125M, 0h

(d) Batch B, 0.250M, 0h

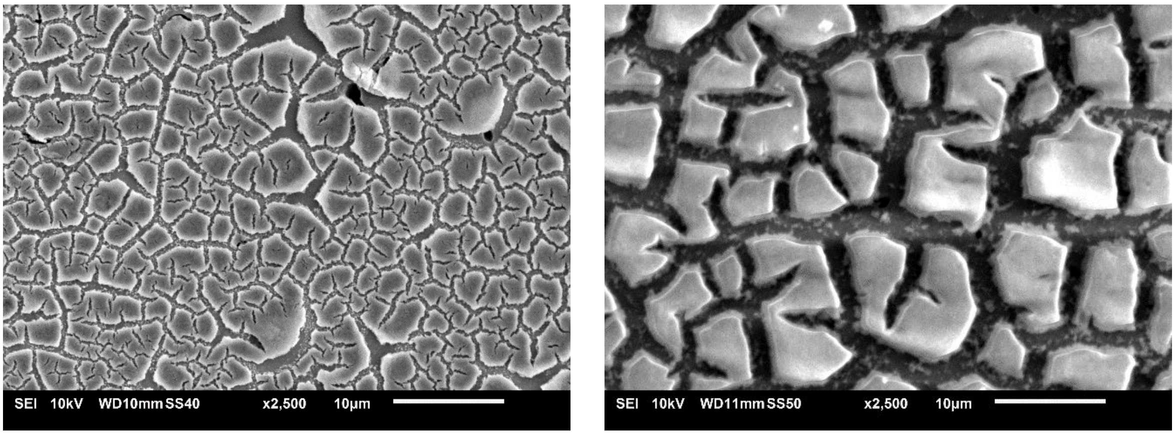

(e) Batch B, 1.000M, 0h

(f) Batch B, 1.000M, 100h

Figure 5-14 SEM images Batch B, GDC spin-coated flat LSCF substrates at various concentrations and ageing stages. Samples were aged at 800 °C in ambient air using a box furnace

Due to time constraints, only the lowest and highest spin-coated substrates were subjected to thermal ageing at 800°C, images after 100h for both concentrations showed that at high concentrations the microstructure of the GDC coating did not change drastically which was to be expected as the surface coating was already bulky and thick [123]. Oppositely, at low concentrations, the dispersed clusters coarsened and presented as an uneven surface covering. Particle coarsening at high temperatures has always been a cause of concern [175], especially for SOFC electrodes that operate under severe conditions.

Regardless of any observed microstructural changes, no segregated particles that could be associated to Sr-surface segregation (SSS) appeared on either of the surface-modified substrates on Batch B. In contrast, for bare and aged LSCF substrates, particles of ~5 µm appeared on the surface after ageing at 800°C for 100h. Although for our particular study, no elemental analysis was performed to corroborate that these segregated particles were Sr-rich phases, these were assumed to be so based on numerous reports in literature [10, 170, 172].

A new batch of substrates (Batch A) was processed, spin-coated and aged following the same protocol as for Batch B. Appropriate images are presented in Figure 5-15 with corresponding EBSD images in section 11.5.1 of Annex B.

Similar to observation from the previous batch, 0.025M GDC precursor produced well dispersed clusters of particles on top of the LSCF surface, 0.125M precursor produced a more even surface covering since no visible grains from the LSCF surface were visible under SEM. Additionally, some areas where the precursor pooled produced a large (~10 µm) cluster of GDC. The 0.250M and 1.000M precursors produced even thicker but uneven surface coatings with large cracks and ridges were bare LSCF surface was left exposed.

Only the highest and lowest concentration spin-coated substrates were aged at 800°C for 50 and 100h to evaluate changes in the coating's microstructure and the possible appearance of any segregated Sr-containing phases. Images after 100h of ageing showed that for the lowest concentration, particles began to agglomerate but they remained well dispersed onto the substrate surface, this was in agreement with reports from literature [167].

Like it was observed for Batch B, the highest concentration on Batch A did not suffer any significant changes to its microstructure. Regardless of any observed microstructural changes after ageing, no segregated particles that could be associated to Sr-surface segregation (SSS) appeared on either of the surface-modified substrates on Batch A.

(a) Batch A, 0.025M, 0h (b) Batch A, 0.025M, 100h

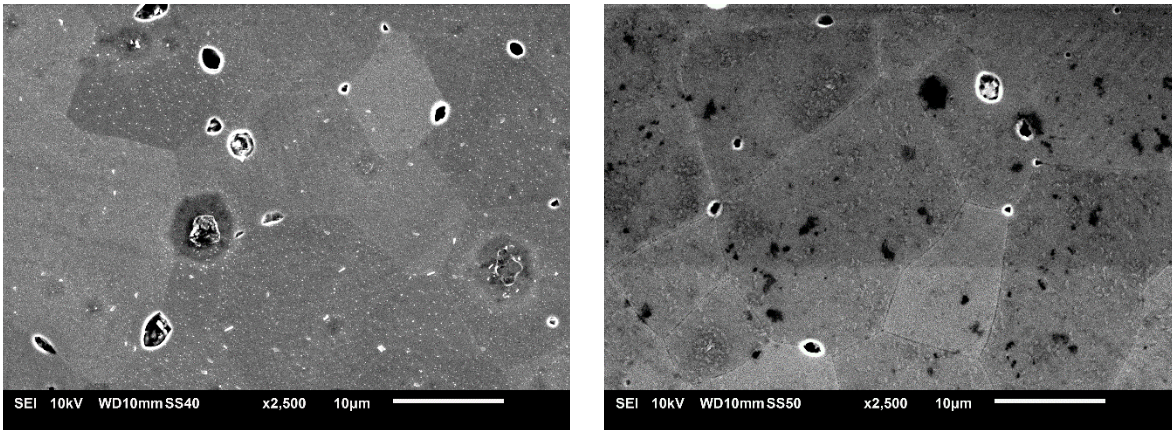

(c) Batch A, 0.125M, 0h (d) Batch A, 0.250M, 0h

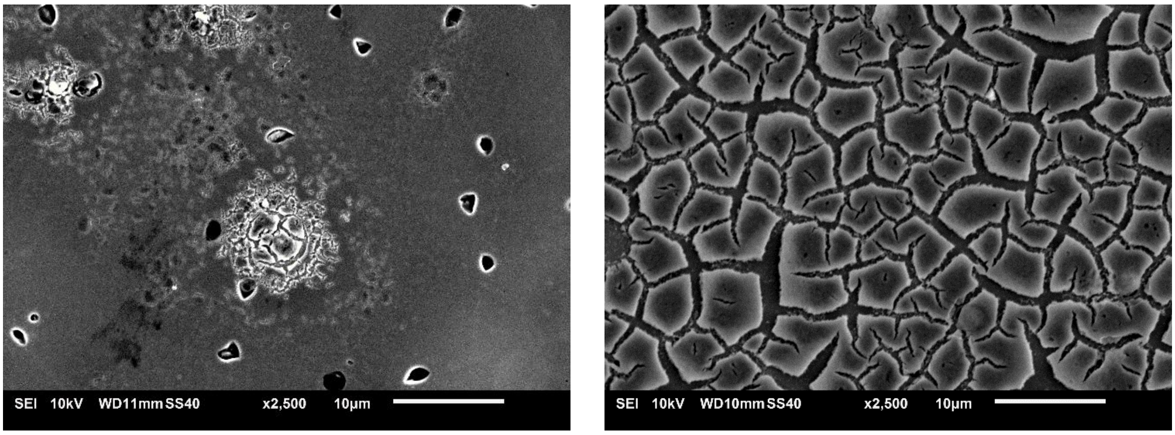

(e) Batch A, 1.000M, 0h (f) Batch A, 1.000M, 100h

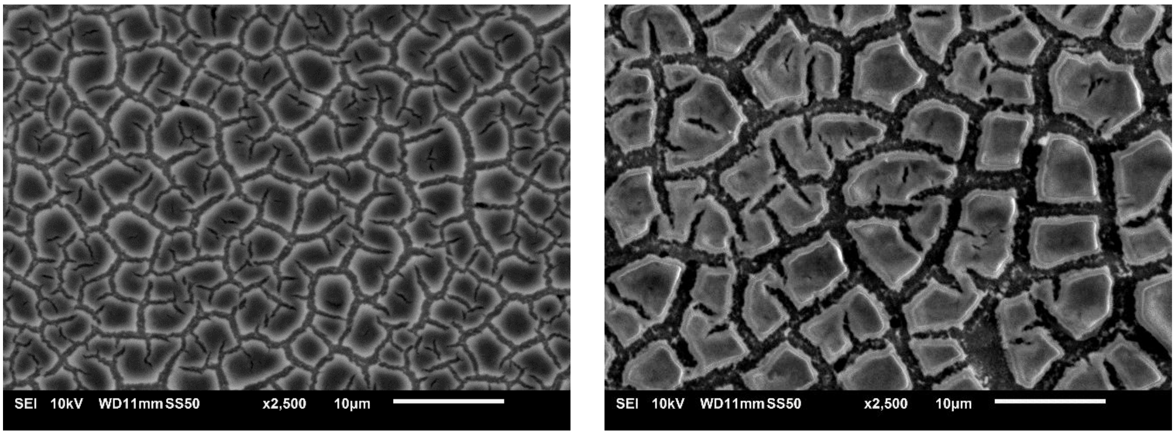

Figure 5-15 SEM images for Batch A, GDC spin coated flat LSCF substrates at different concentrations and ageing stages. Samples were aged at 800 °C in ambient air

Finally, a new tub of LSCF-6428 powder was purchased to fabricate a new batch (Batch C) of substrates to conduct the same ageing treatment. Micrographs at different ageing times are presented in Figure 5-16, appropriate EBSD images can be found in section 11.5.3 in Annex B.

(a) Batch C, 0.025M, 0h (b) Batch C, 0.025M, 100h

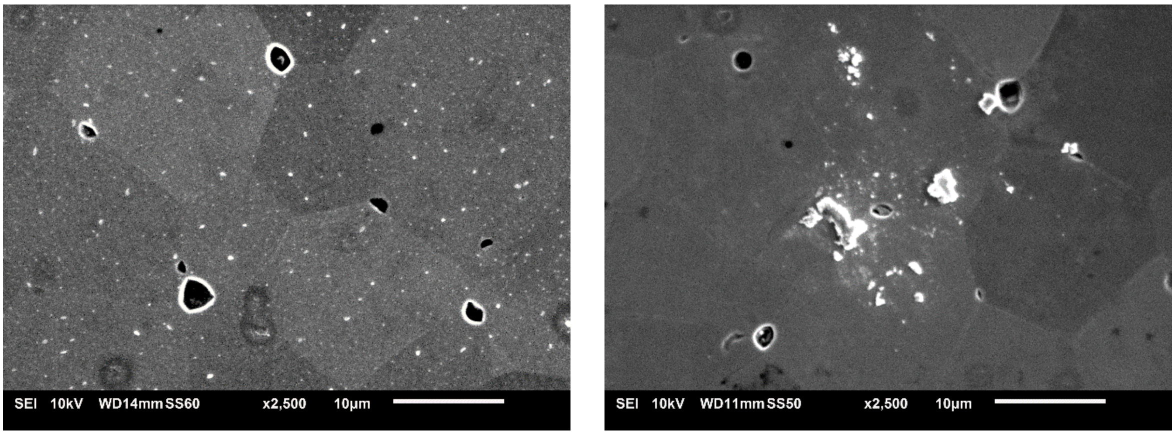

(c) Batch C, 0.125M, 0h (d) Batch C, 0.250M, 0h

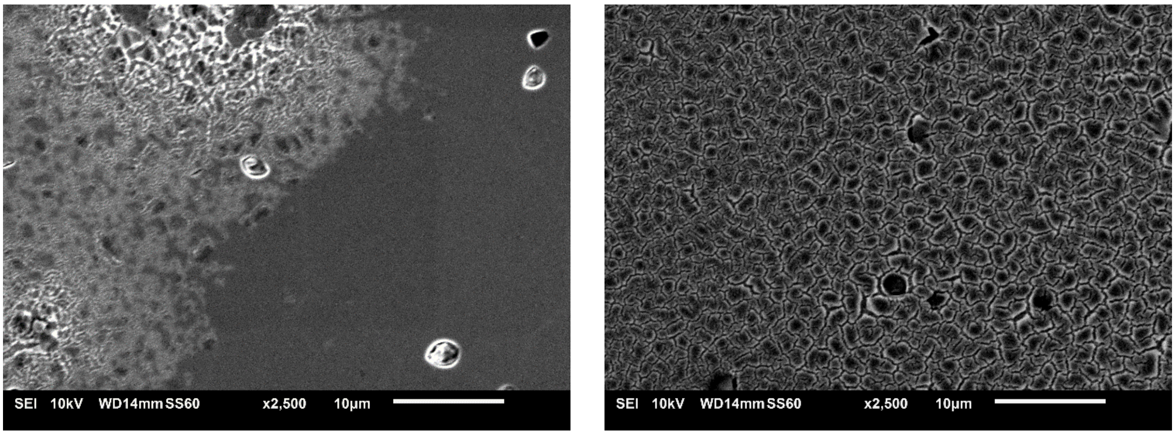

(e) Batch C, 1.000M, 0h (f) Batch C, 1.000M, 100h

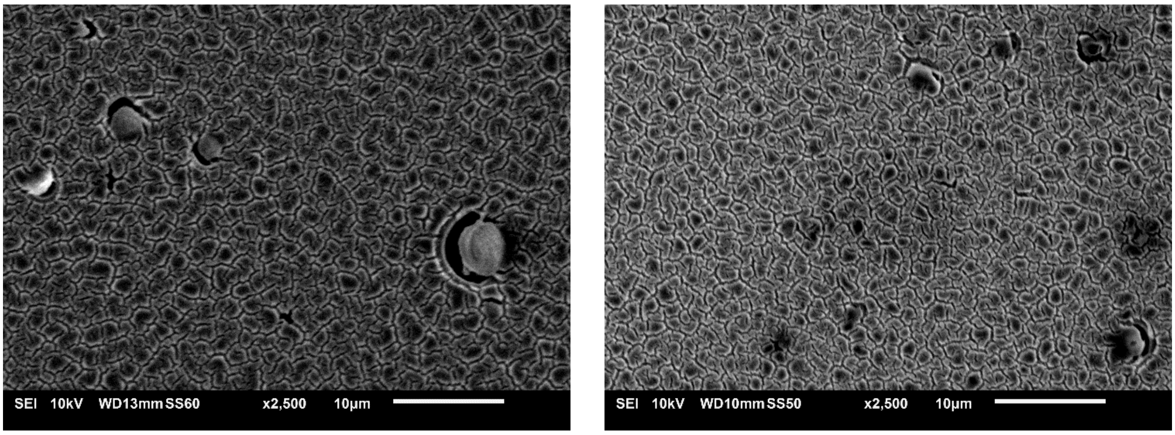

Figure 5-16 SEM images for Batch C, flat LSCF substrates at different concentrations and ageing stages. Samples were aged at 800 °C in ambient air

When observing the different surface coatings achieved by using GDC at different concentrations for Batch C substrates, it was clear that the 0.025M GDC precursor produced well dispersed clusters of particles on top of the LSCF surface, the 0.125M precursor produced a more even surface covering. However, for this case, some precursor solution pooling was observed since a fraction of the LSCF surface was left clear. When using precursors with 0.250M concentration and upwards, a clear thick surface coating with ridges and cracks was observed.

Only the highest and lowest concentration spin-coated substrates were aged at 800°C for 50 and 100h to evaluate changes in the coating's microstructure and the possible appearance of any segregated Sr-containing phases.

Images after 100h of ageing showed that for the lowest concentration, particles thermally agglomerated to give even larger GDC particles (~2 µm), Additionally, some areas of the LSCF surface became exposed after the ageing treatment. Oppositely, the highest concentration spin-coated substrates showed no significant changes to the microstructure. Regardless of any observed microstructural changes after ageing, no segregated particles that could be associated to Sr-surface segregation (SSS) appeared on either of the surface-modified substrates on Batch A.

After modifying the surface of mirror-polished LSCF substrates with GDC precursors at different concentrations (0.025, 0.125, 0.250, and 1.000M) a variety of coatings microstructures were obtained. When using 0.025M precursor, well dispersed particles on top of the LSCF substrates were observed. The 0.125M precursor produced a film-like surface modification, whilst the higher concentration precursors produced a very thick and uneven coating with cracks and ridges where produced.

Only the substrates that were spin-coated with the highest and lowest concentration precursors were aged at 800°C for 50 and100h, they were also imaged at every step. When comparing the SEM images, only microstructural changes were observed for the 0.025M concentration. This is, the initially well dispersed particles on the LSCF surface demonstrated signs of coarsening after being exposed to high temperatures. Particle coarsening has always been a cause for concern in SOFC systems since the high temperatures is one of the main coarsening drivers [78, 81]. The 1.000M spin-coated substrates presented thick surface coating with cracks and ridges that left a bit of surface LSCF exposed, however no signs of microstructural change were observed after 100h of ageing [130].

Additionally, when bare LSCF substrates were analysed in Chapter 4, angular particles (~1 µm) appeared along the grain boundaries after 50h of ageing, and after 100h of high temperature ageing, segregated particles grew to ~5µm, which was in complete agreement to what Araki *et.al.* [10] had previously reported and positively identified as Sr-rich particles by using EDX. For the purpose of this work, the observed particles were considered as Sr-rich segregated particles.

After modifying LSCF substrates with GDC precursor solutions, no segregated particles that could be associated with SSS were observed, meaning that Sr-segregation was prevented by spin-coating dense LSCF substrates with GDC precursors. The absence of Sr-particles at the material surface due to GDC has been thoroughly reported before [44, 167, 173]. The inhibition effect is believed to be caused thanks to GDC's fluorite structure abilities to reduce the concentration of oxygen vacancies at the LSCF surface [167], thus degreasing the electrostatic interactions between charged defects that ultimately have been proven to drive Sr-segregation [19, 121, 165].

Although it has been recognised that Sr segregation induced by high temperature is more likely to occur on dense samples than porous ones [45], there is still not a clear consensus on how much observed results on dense samples can be extrapolated into porous materials.

5.3 Summary and conclusions

GDC precursors at different concentrations (0.025, 0.050, 0.125, 0.250, 0.500, and 1.000 M) were used to either infiltrate porous electrodes or coat flat LSCF-6428 substrates.

Impedance and ECM data fitting of three different batches (A, B and C) showed that generally, GDC infiltration proved to be an effective way to produce better performing and more stable electrodes. The best performing electrodes were those infiltrated with 0.125 and 0.250 M precursors. Although the mechanism through which GDC enhances electrode performance is still highly debated, it has been generally agreed that because of its superior ionic conductive properties, GDC infiltration significantly increase the triple phase boundary (3PB), hence increasing the number of sites for the ORR to take place. Additionally, because GDC has demonstrated to suppress Sr-surface strontium segregation (SSS) on LSCF, the infiltrated electrodes become more stable, and their lifetime can be extended.

More importantly, the *calendar ageing effect* previously observed on non-infiltrated cells, was also recognised on measurements for infiltrated electrodes. However, more research on this subject is needed to properly identify why the behaviour of electrodes that sit in storage without use for prolonged time differs from electrodes that are fabricated and used immediately afterwards.

Three different batches (A, B and C) of mirror-polished, flat, and dense LSCF substrates were spin coated with GDC precursors at various concentrations (0.025, 0.125, 0.250, and 1.000M) and then aged for 50 and 100h at 800°C before being cooled down to room temperature for XRD analysis. Phase composition analysis showed that in most cases, LSCF presented as polycrystalline mix composed of approximately 85% rhombohedral and

15% cubic phases, which agreed with reports in literature for samples processed under similar conditions. For the rest of the cases, LSCF substrates presented a 100% rhombohedral composition.

Additionally, the characteristic cubic gadolinium doped ceria phase (PDF 01-086-9063) for surface modifications could only be identified when precursors with high concentrations (0.250, and 1.000M) were used, namely by the (111) peak at ~27 2θ degrees. For the rest of the precursors, no GDC phases could be identified due to the amount not being high enough for the detection threshold. Moreover, the (111) peak for the cubic GDC sharpened and became narrower with increasing ageing time, meaning that surface modifications coarsened and grew in particle size. Similarly to what was observed for bare LSCF substrates, no new Sr-containing phases were detected after ageing treatment for any of the analysed batches, nevertheless, this could be because like the case of low concentration GDC, the amount is not enough to be identified using XRD. Because of this, it was determined that, by itself, XRD is not enough to confirm if GDC spin-coating of LSCF substrates prevented Sr-surface segregation.

SEM images of flat and dense LSCF substrates that have been spin-coated with GDC precursor solutions at various concentrations showed that by varying the precursor concentration, different coatings morphologies can be obtained, ranging from well dispersed particle clusters (0.025M) to thin even coatings (0.125) and finally thick, uneven coatings (0.250 and 1.000M). Only the 0.025M and 1.000M spin-coated substrates could be subjected to thermal ageing, because of time constraints. After 100h of ageing, no segregated particles that could be associated with SSS were observed on any of the samples, meaning that Sr-segregation was prevented by spin-coating dense LSCF substrates with GDC precursors. GDC is a well-known inhibitor of SSS due its ability to reduce the concentration of oxygen vacancies at the LSCF surface, thus degreasing the electrostatic interactions that drive Sr-segregation.

Finally, although it known that SSS at high temperatures is more likely to occur on dense samples than porous ones, there is still not a clear consensus on how much observed results on dense samples can be extrapolated into porous electrodes. Therefore, more research on this subject is needed.

6 LSCF stabilisation using HfO_2 surface modification

6.1 Chapter overview

On this chapter, sample LSCF/GDC/LSCF cells were infiltrated with HfO_2 suspension suspensions at different concentrations (6.58, 13.16, 26.32, 52.64, and 105.28 mg mL^{-1}) in a one-step infiltration protocol as described in Chapter 3. Infiltrated cells were then analysed using a variety of techniques to identify possible signs of Sr-segregation when electrodes have been modified and tested at operating conditions (700 °C, 20 mL/min synthetic airflow), It has been reported that HfO_2 effectively prevents Sr-surface segregation (SSS) [19, 176], particularly for the case of LSCF, HfO_2 surface modifications have proved to significantly enhance cathode performance while effectively preventing SSS [176]. However, for this study, LSCF powder particles were covered with a HfO_2 using atomic layer deposition (ALD) prior to the powder processing to fabricate the electrode; hence a one-step infiltration approach has yet to be documented for this material. However, due to time constraints resulting from the COVID-19 pandemic, for some sets of analysed samples only selected concentrations were tested in an effort to try to cover the initially designed range of concentrations.

HfO_2 suspensions at different concentrations were used to obtain different levels of surface covering on LSCF/GDC/LSCF cells and flat LSCF substrates to identify the which of these would provide the best results when using a one-step infiltration protocol.

Additionally, flat LSCF substrates will be spin-coated using the same HfO_2 precursor suspension at various concentrations and subjected to thermal ageing treatment at 800°C for periods of 50 and 100h to assess possible changes on the electrode surface according to the methods previously described in Chapter 3. Thermal treatment has been identified to promote SSS on LSCF materials [10, 108, 165]. After thermal ageing, flat substrates were analysed to observe potential signs of SSS or its prevention.

Similarly, to the Chapter 4 and 5, the different sample batches have been separated and labelled as:

- **Batch A:** cells and substrates made with LSCF powder purchased in 2018 and processed in 2020 for sample and ink production.
- **Batch B:** cells and substrates made with LSCF powder purchased and processed in 2018 for sample and ink production.
- **Batch C:** cells and substrates made with LSCF purchased and processed in 2021 for sample and ink production.

Furthermore, and due to equipment availability, a portion of the samples were analysed using a Solartron Modulab 1250 FRA and a 1287 electrochemical interface; while the rest were analysed using the FRA/EIS analysed IviumStat.h standard. Regardless of recording equipment, all EIS data was analysed and fitted using ZView ® software in accordance with the protocols described in Chapter 3.

6.2 Results and discussion

6.2.1 Electrochemical analysis via EIS and ECM fitting

Batch B infiltrated cells were the first ones to be fabricated and tested. This batch is comprised of two different sets; the first set was analysed using the Solartron Modulab whilst the second set was analysed using the IviumStat FRA/EIS analyser.

After experimental jig reached the desired operating temperature (700 °C), EIS data was recorded hourly for 50h under synthetic air flow set at 20 mL/min using the Solartron Modulab. Nyquist plots for a selection of infiltrated electrodes are presented in Figure 6-1. Data has been normalised to electrode area and electrolyte contributions (Rs) have been subtracted to ease comparison between the different infiltrated electrodes. Dotted plots represent experimental EIS data, and the solid lines correspond to the fitted data using the same ECM [122] as in Chapter 4 of this thesis. A preliminary data fitting with the proposed electrical circuit model (ECM) used to fit EIS data for the non-infiltrated electrodes revealed that this same model could be used for data fitting for the GDC-infiltrated electrodes since both the chi-squared and %error values were in the same range as the ones obtained for the fits of the non-infiltrated samples [163]. EIS data was collected hourly for 50h, however, only data at every 10h intervals are presented.

Some key landmarks were identified on the EIS data for this set of samples. Firstly, a tail at high frequencies and in the positive Z2 axis, which corresponds to the inductive contributions from the experimental setup [156], two semi-arcs of different sizes located each at the high and low frequency zones, which are both typical for impedance data for the ORR reaction in LSCF electrodes [36, 122, 157].

The proposed ECM (Figure 6-1d) is comprised of an inductor (L1) accounting for the inductive contributions from the experimental jig, R1 represents the electrolyte resistance also known as Rs. The two semi-arcs are represented by a resistor and a constant phase element connected in parallel. The first arc at high frequencies (HF), formed by R2 and CPE1, correspond to the charge transfer at the electrode/electrolyte surface and O^{2-} ion diffusion in the bulk of the electrode. The second arc at low frequency (LF), R3 and CPE2, account for the adsorption/desorption process of oxygen at the electrode surface and the gas diffusion in the pore structure of the electrode [124, 156].

(a) 6.58 mg mL^{-1} (b) 26.32 mg mL^{-1} (R1)

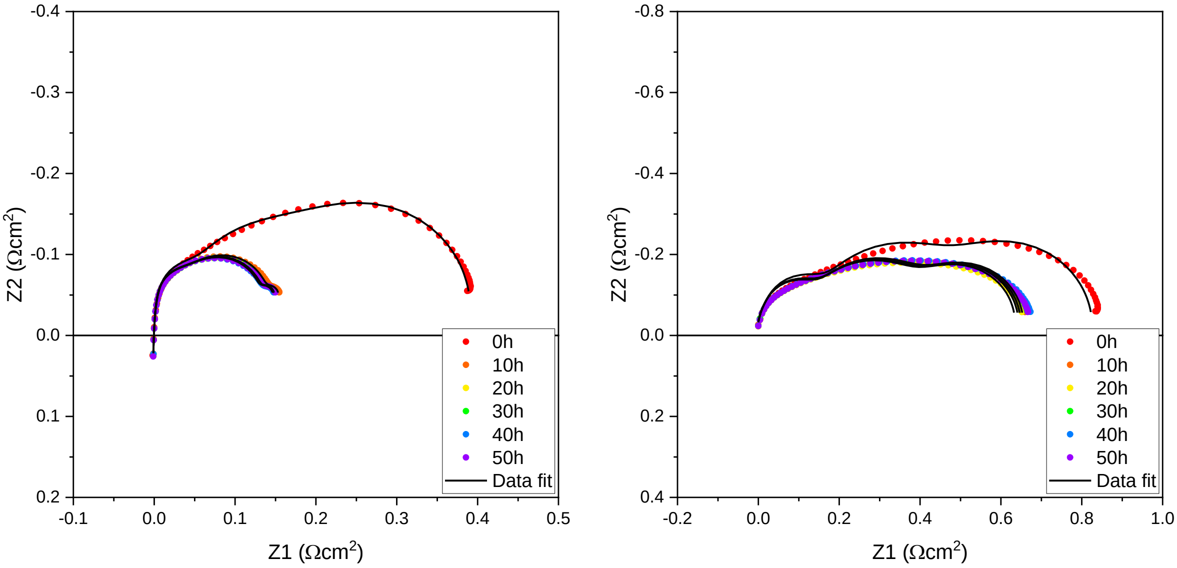

(c) 105.28 mg mL^{-1} (R1) (d) ECM

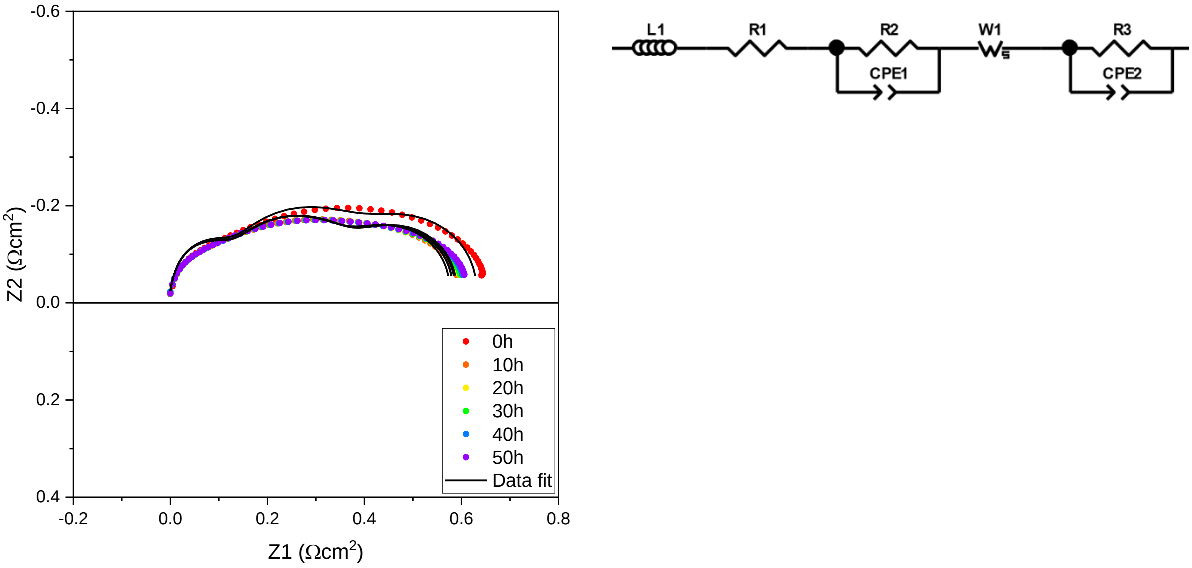

Figure 6-1 Fitted EIS spectra for set 1, Batch B HfO$_2$-infiltrated cells at various, measurements recorded on Solartron Modulab

An example of full fitting results for raw data at every 10h interval for the sample infiltrated with the 6.58 mg mL^{-1} suspension Table 6-1, full fitting results for the rest of the samples can be found in section 12.3.2 of Annex C.

Table 6-1 EIS data fitting summary report for 6.58 mg mL^{-1} HfO$_2$-infiltrated sample for set 1, Batch B. Fitting was performed in ZView on raw impedance data

6.58 mg mL^{-1}	Chi-Sqr	Sum-Sqr	R1	%error	R2	%error	CPE1-T	%error	W-R	%error	W-T	%error	R3	%error	CPE2-T	%error
0h	1.19E-04	3.31E-04	6.6100	0.0577	1.4980	1.4968	0.0089	3.1787	0.3846	3.1084	0.0002	5.3222	0.8716	2.1987	0.0023	3.4032
10h	1.03E-04	1.23E-04	6.4450	0.0363	0.0989	3.4852	0.5122	9.5988	0.3099	2.6268	0.0002	4.1921	0.6945	1.0481	0.0019	2.7351
20h	1.07E-04	1.25E-04	6.4730	0.0368	0.1030	3.3028	0.4914	9.1031	0.2977	2.9262	0.0002	4.5408	0.6621	1.1777	0.0018	3.0232
30h	9.32E-05	1.09E-04	6.5530	0.0343	0.1074	2.9844	0.4606	8.2323	0.2996	2.8629	0.0002	4.3489	0.6599	1.1622	0.0018	2.9569
40h	9.06E-05	1.04E-04	6.6200	0.0337	0.1099	2.8533	0.4426	7.8768	0.2944	2.9632	0.0002	4.4382	0.6498	1.2010	0.0017	3.0309
50h	1.09E-04	1.27E-04	6.6480	0.0371	0.1143	3.0754	0.4129	8.4949	0.2998	3.2612	0.0002	4.8567	0.6529	1.3373	0.0018	3.3767

Table 6-2 Rs and Rp values for 6.58 mg mL^{-1} HfO$_2$-infiltrated sample, set 1, Batch B, obtained from EIS data fitting using ZView. Data is normalised to the electrode area

6.58 mg mL^{-1}	Rs (Ωcm^2)	%error	Rp (Ωcm^2)	%error
0h	0.8951	0.0577	0.3423	2.2680
10h	0.8714	0.0363	0.1057	2.3867
20h	0.8754	0.0368	0.0999	2.4689
30h	0.8869	0.0343	0.1005	2.3365
40h	0.8965	0.0337	0.0986	2.3392
50h	0.9005	0.0371	0.1005	2.5580

Table 6-3 Experimental values for Rp, Rp$_i$, Rp$_f$, and calculated dRp for set 1, Batch B, HfO$_2$-infiltrated electrodes

Sample [mg mL^{-1}]	Rp (Ωcm^2, 0h)	Rp$_i$ (Ωcm^2, 5h)	Rp$_f$ (Ωcm^2,50h)	dRp (%)
6.58	0.3282	0.1050	0.0917	-12.6715
13.16	0.3019	0.2729	0.2932	7.4296
26.32 (R1)	0.7719	0.6044	0.6051	0.1084
26.32 (R2)	0.4412	0.3593	0.3797	5.6689
52.64 (R1)	0.5118	0.4339	0.4709	8.5331
52.64 (R2)	0.2558	0.1604	0.1485	-7.4094
105.28 (R1)	0.5799	0.5257	0.5445	3.5710
105.28 (R2)	0.3812	0.2882	0.3041	5.5068

Rp monitoring for set 1, Batch B samples is presented in Figure 6-2 (solid markers correspond to Rs and hollow markers correspond to Rp values), after analysing the evoluution of Rp against time, it was determined that for this set of samples, cathode activation period extended for the first 5h of operation [150, 164]. Changes in Rp (dRp%) were calculated using Equation 8 and corresponding data is presented in Table 6-3.

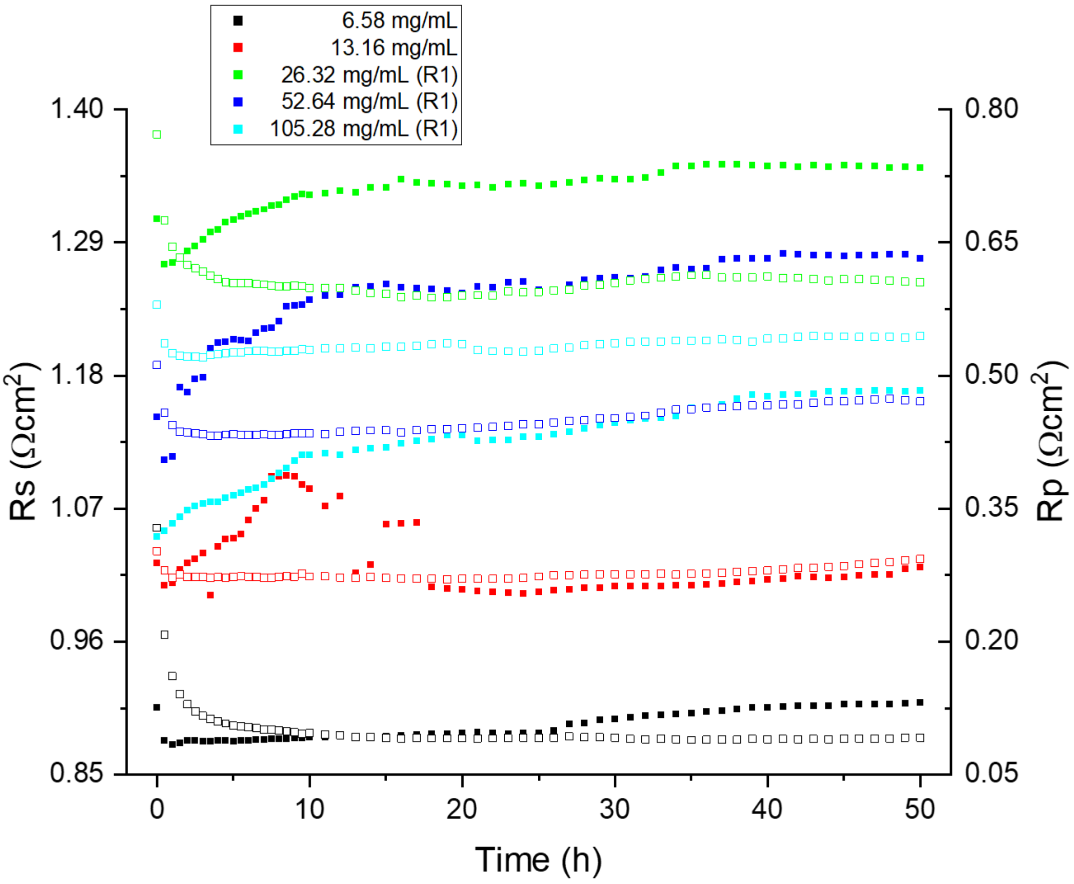

Figure 6-2 Rs and Rp or set 1, HfO_2-infiltrated, Batch B cells at various concentrations, recorded using Solarton Modulab. Solid data markers correspond to Rs, hollow data markers correspond to Rp

Base initial Rp values for non-infiltrated cells ranged from 0.1253 – 0.3223 Ωcm^2 (Table 4-3) when comparing this to what was observed for HfO_2 –infiltrated electrodes, recorded values were generally higher than those for non-infiltrated samples. After being tested for 50h at 700°C under synthetic air flow, only 6.58 and 52.64 mg mL^{-1} resulted in electrodes with a lower final Rp value than non-infiltrated samples. However, when comparing the changes in Rp (dRp%) for infiltrated samples, it was clear resistance tended to change less or even decreased from the initial recorded value. This means that for all cases, HfO_2 infiltration made the electrodes more stable, and in specific cases, enhanced the ORR performance when compared to non-infiltrated electrodes. These findings coincide with studies by Roeder *et al.* [176], who reported that atomic layer deposition (ALD) HfO_2 surface modifications tended to have similar or higher initial electrode resistance values than non-modified electrodes. However, after a significant testing period, over 600h, the degradation rate (dRp%) was less than for bare samples. Furthermore, the improvement for electrode degradation rate was attributed to the mitigation of Sr-surface segregation (SSS) by HfO_2, which is has been observed on other Sr-containing materials [19, 176].

A second set of HfO_2-infiltrated for Batch was tested, this time using the FRA/EIS IviumStat. For this set only three different concentrations (6.58, 13.16, and 26.32 mg mL^{-1}) with respective repeats could be assessed due to time constraints. Only a selection of samples is presented in Figure 6-3 with the appropriate fitted data and ECM used. The rest of the collected and fitted data can be found in Annex C.

6.58 mg mL^{-1} (R1) (b) 13.16 mg mL^{-1} (R1)

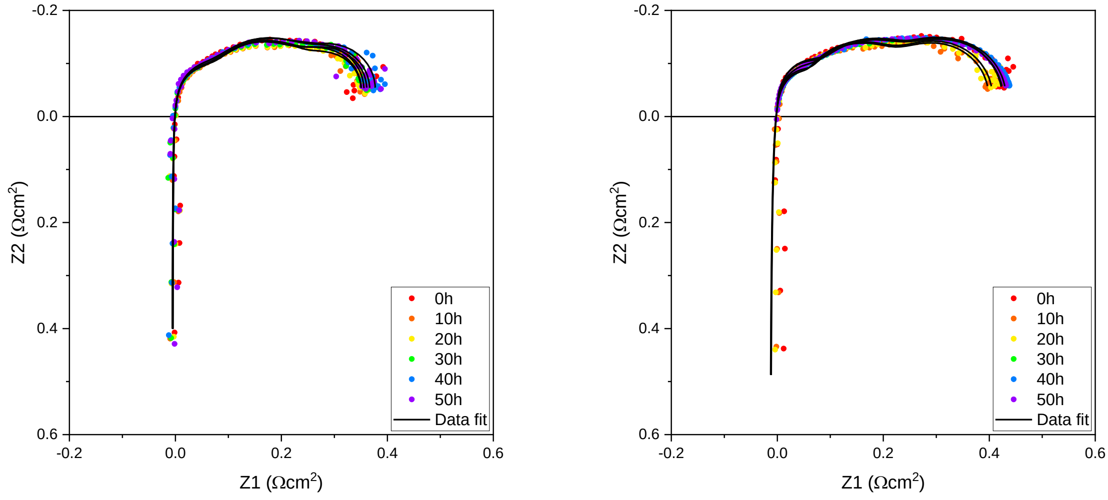

(c) 26.32 mg mL^{-1} (R2) (d) ECM

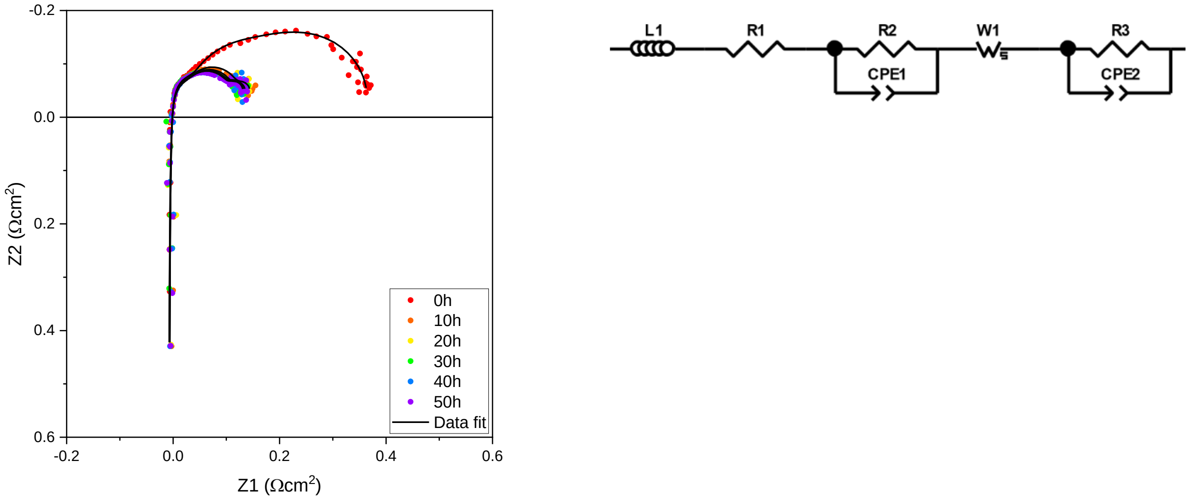

Figure 6-3 Fitted EIS spectra for set 2, Batch B, HfO_2-infiltrated cells at various, measurements recorded on IviumStat FRA analyser

Additionally, hourly monitoring for the same selection of samples is presented in Figure 6-4. Cathode activation time was determined to be 5h and the corresponding Rp values were used to calculate the change in Rp (Table 6-4).

Table 6-4 Experimental values for Rp, Rp$_i$, Rp$_f$, and calculated dRp for set 2, Batch B, HfO$_2$-infiltrated electrodes

Sample [mg mL^{-1}]	**Rp (Ωcm^2, 0h)**	**Rp$_i$ (Ωcm^2, 5h)**	**Rp$_f$ (Ωcm^2,50h)**	**dRp (%)**
6.58 (R1)	0.3144	0.2959	0.3296	11.3871
6.58 (R2)	0.3726	0.1400	0.1261	-9.9316
6.58 (R3)	0.1479	0.0671	0.0608	-9.3972
13.16 (R1)	0.3995	0.3629	0.4028	10.9804
13.16 (R2)	0.2395	0.1168	0.1065	-8.8388
13.16 (R3)	0.2375	0.0704	0.0626	-10.9990
26.32 (R1)	0.3439	0.1023	0.0943	-7.8437
26.32 (R2)	0.3058	0.0962	0.0634	-34.1291

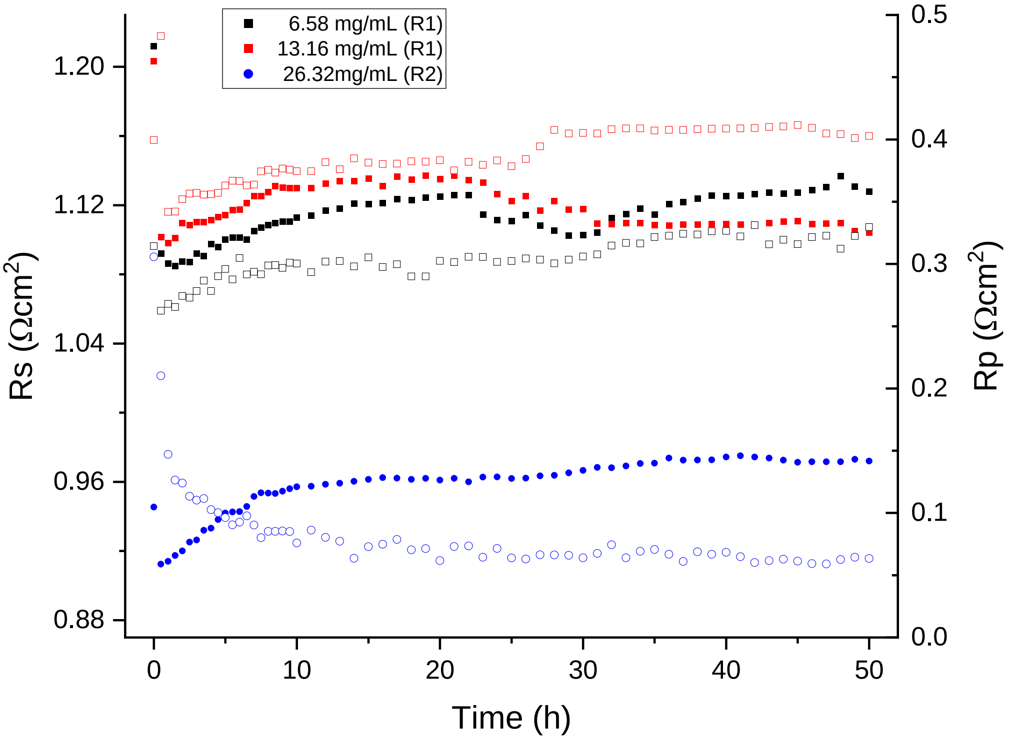

Figure 6-4 Rs and Rp or set 2, HfO$_2$-infiltrated, Batch B cells at various concentrations, recorded using IviumStat FRA analyser

When comparing the initial Rp values from this set to the non-infiltrated values from Batch B set 2 (Table 4-4), once again it was noticeable how the infiltrated electrodes exhibited initial Rp values that were comparable or slightly higher than the ones recorded for non-infiltrated cells. Similarly to what occurred during set 1 measurements, after 50h under operation conditions, infiltrated electrodes presented lower electrode resistance than their non-infiltrated counterparts. Furthermore, changes in Rp proved that the infiltrated electrodes showed a decrease in Rp, *i.e.* a negative dRp value was calculated for some of the cases. Which also aligned with the results from set 1 and were supported by the literature [176]. However, for this set, electrode polarisation decreased in value instead of remaining constant and infiltration with 26.32 mg mL^{-1} suspension produced the better performing electrodes.

A new batch of cells were fabricated for infiltration (Batch A), after identifying a *calendar ageing effect* on non-infiltrated cells. The ink used to fabricate samples in Batch B was used in production of this new batch. However, due to time constraints, only three concentrations were tested without repeats (6.58, 26.32, and 105.28 mg mL^{-1}).

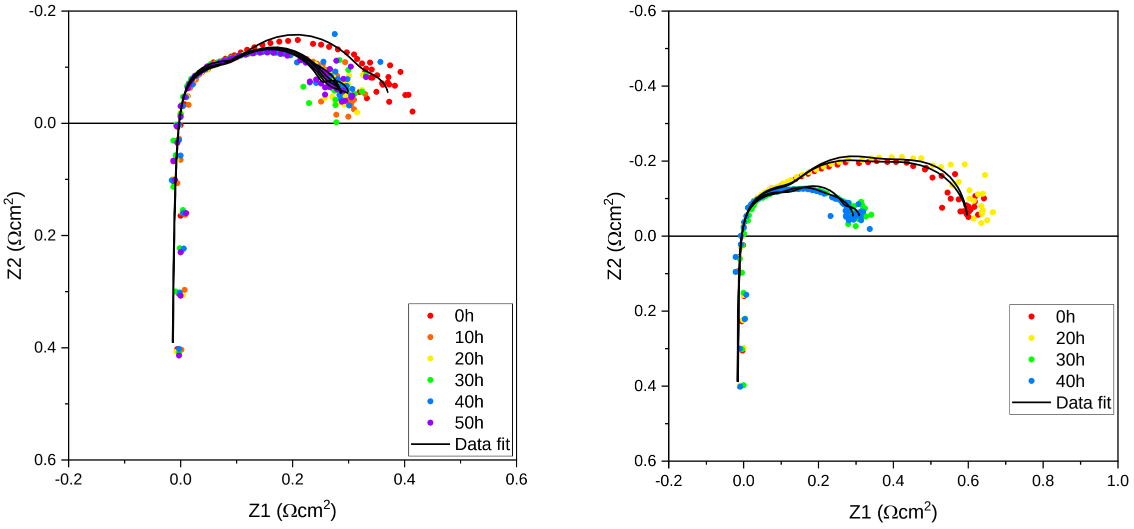

(a) 6.58 mg mL^{-1}

(b) 26.32 mg mL^{-1}

(c) 105.28 mg mL^{-1}

(d) ECM

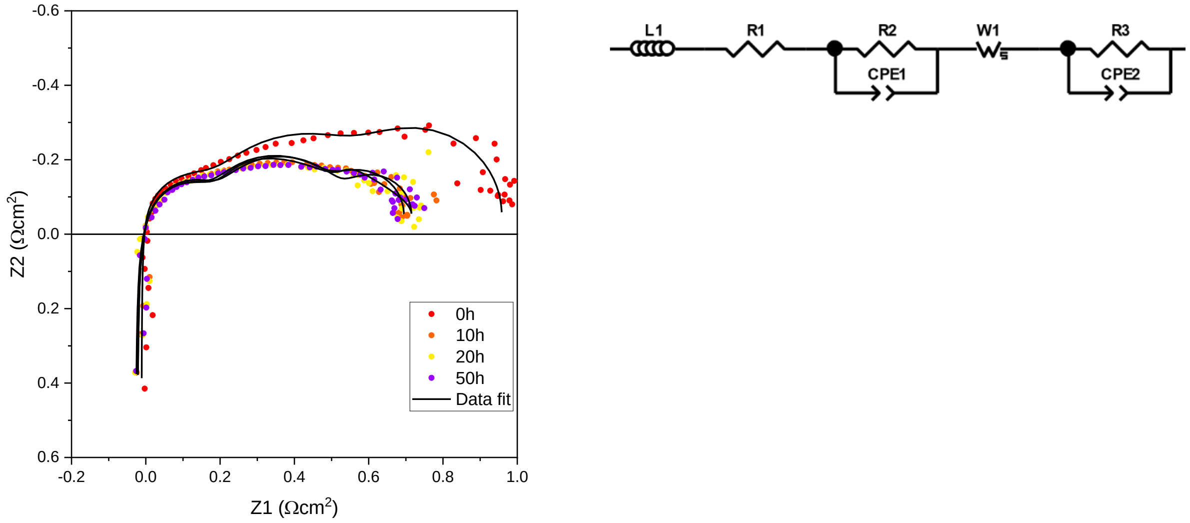

Figure 6-5 Fitted EIS spectra for Batch A, HfO_2-infiltrated cells at various, measurements recorded on IviumStat FRA analyser

Fitted EIS data for samples in Batch A is presented in Figure 6-5. Data has been normalised to electrode area and electrolyte contributions have been removed. Dotted plots represent experimental data, and the solid line represents fitted data using the appropriate ECM. Additionally, the hourly Rp monitoring for this samples are presented in Figure 6-6. Cathode activation period was determined to be 5h and the appropriate values were used to calculate the change in Rp (dRp%) for this batch (Table 6-5).

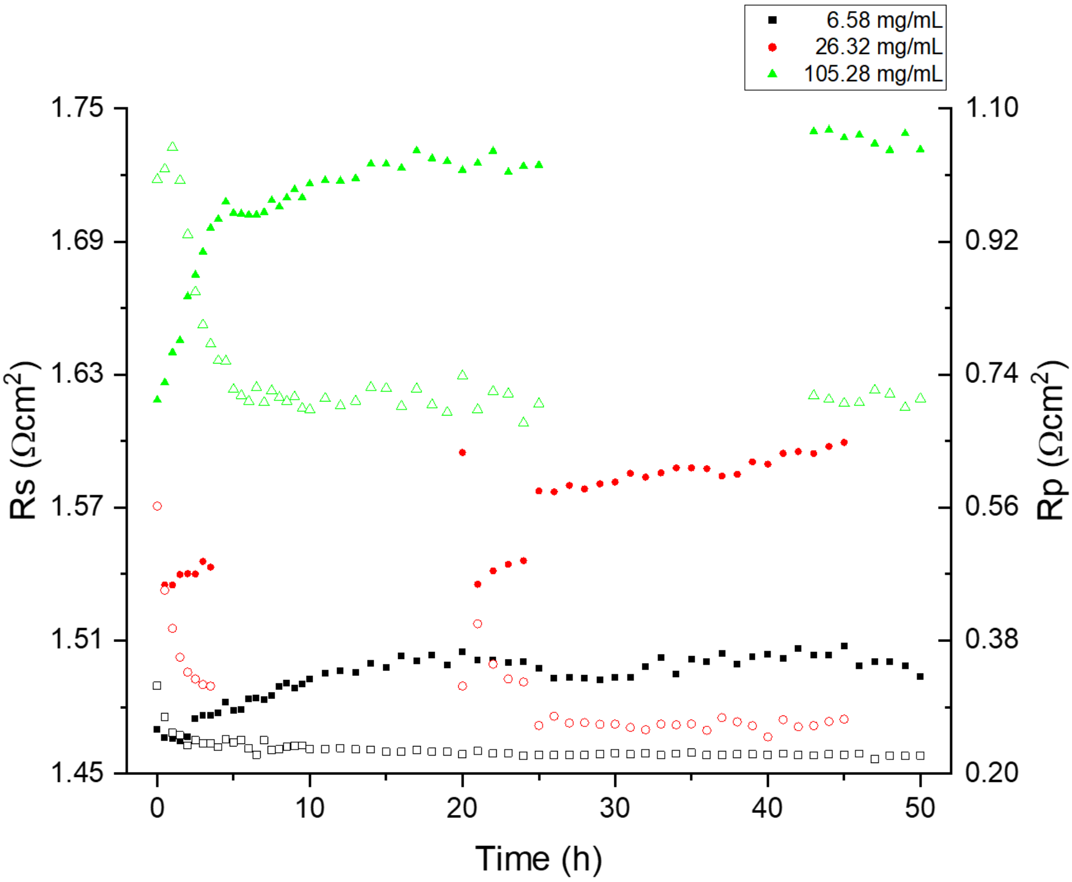

Figure 6-6 Rs and Rp for Batch A, HfO₂-infiltrated cells at various concentrations, recorded using IviumStat FRA analyser. Solid data markers correspond to Rs, hollow data markers correspond to Rp

Table 6-5 Experimental values for Rp, Rp_i , Rp_f , and calculated dRp for Batch A, HfO_2-infiltrated electrodes

Sample [mg mL^{-1}]	Rp (Ωcm², 0h)	Rp_i (Ωcm², 5h)	Rp_f (Ωcm²,50h)	dRp (%)
6.58	0.3189	0.2425	0.2245	-7.4476
26.32	0.5621	0.3185 (*)	0.2735	-14.1312
105.28	1.0039	0.7200	0.7074 (**)	-1.7516

(*) Rp value corresponds to 3.5h
(**)Rp value correspond to 45h

Similar to the observations for Batch B, initial Rp for infiltrated Batch A samples were significantly higher than the values recorded for Batch A of non-infiltrated cells. A slight increase to the baseline value is to be expected from HfO_2 infiltration; however, the recorded increase for this samples was more severe than what had been previously observed. Since the non-infiltrated samples consistently showed an increase in initial Rp values due to what was deemed a *calendar ageing effect*, it was considered that this was also the case for these samples.

Regardless form this initially high Rp, after 50h under testing conditions, final electrode polarisation values were lower than the non-infiltrated samples. Moreover, dRp values showed a decrease with testing time, meaning that not only electrode performance towards ORR was enhanced, but that the electrode did not degrade during the test. Additionally, the best performing electrode was obtained when infiltrating with the 26.32 mg mL^{-1} suspension.

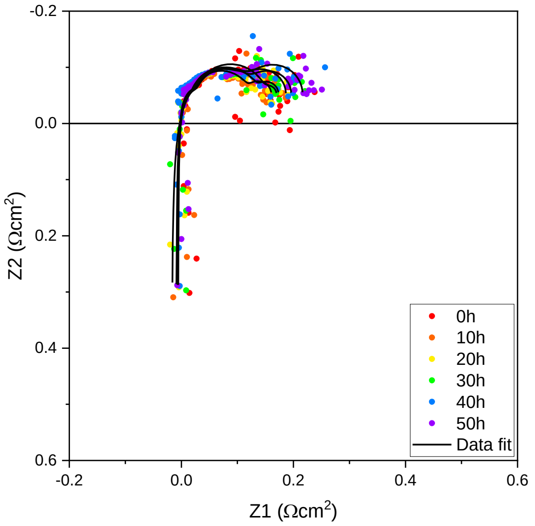
(a) 6.58 mg mL^{-1}

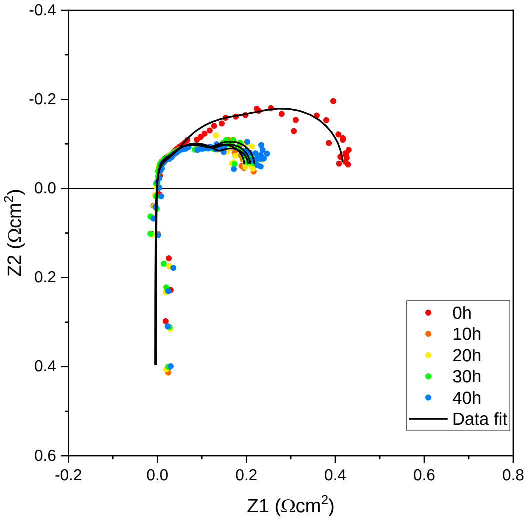
(b) 26.32 mg mL^{-1}

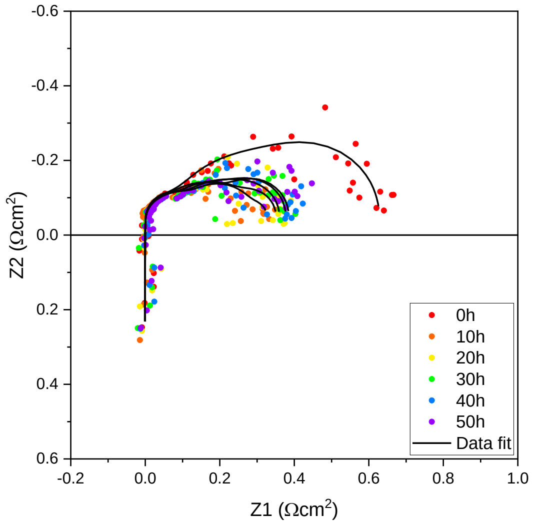
(c) 105.28 mg mL^{-1}

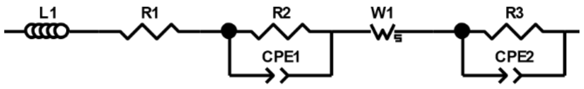
(d) ECM

Figure 6-7 Fitted EIS spectra for Batch C, HfO_2- infiltrated cells at various concentrations, measurements recorded on IviumStat FRA analyser

Lastly, a new tub of LSCF-6428 powder was purchased and processed to fabricate a new batch for HfO_2 infiltration (Batch C). The full range of concentrations (6.58 – 105.28 mg mL^{-1}) was tested for this batch, but due to time constraints, no repeats were performed. A selection of fitted EIS data is presented in Figure 6-7. Data was normalised to electrode area and Rs was eliminated to aid in comparison. Full fitting results for raw data can be found in section 12.3.4 in Annex C. Hourly monitoring for electrode resistance (Rp) for the entire batch is presented in Figure 6-8. Cathode activation time was determined as 5h and the appropriate values were used to calculate the change in Rp, values presented in Table 6-6.

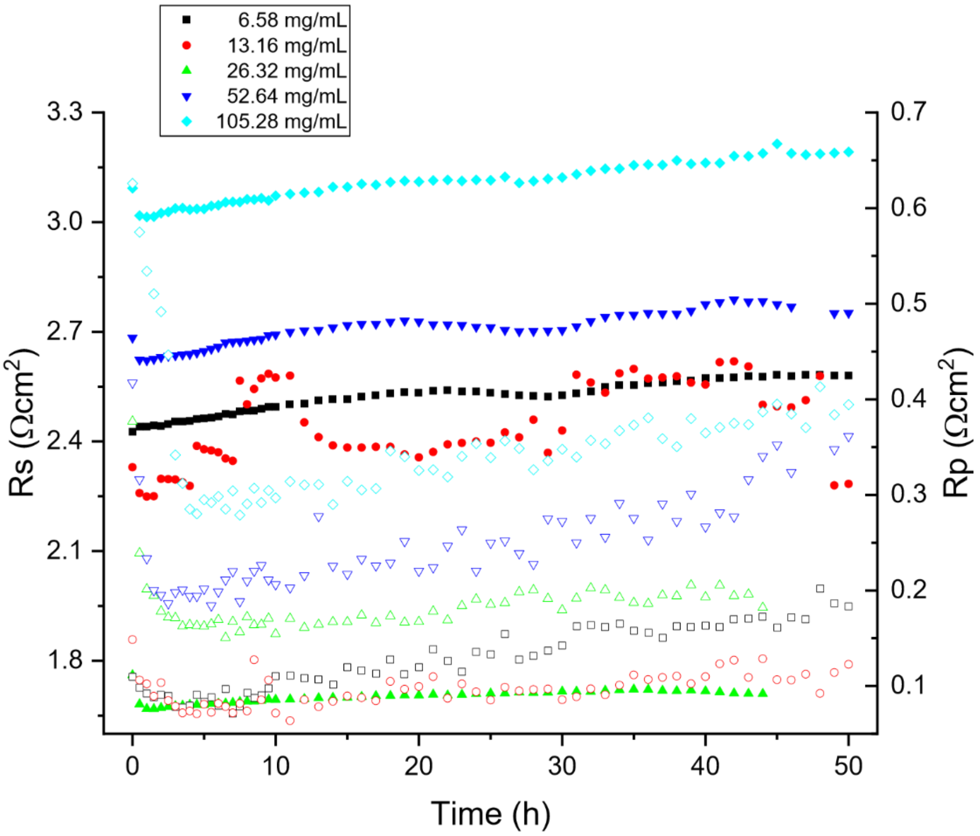

Figure 6-8 Rs and Rp for HfO_2 –infiltrated Batch C cells at various concentrations, recorded using IviumStat FRA analyser. Solid data markers correspond to Rs, hollow data markers correspond to Rp

Table 6-6 Experimental values for Rp, Rp_i , Rp_f , and calculated dRp for Batch C, HfO_2-infiltrated electrodes

Sample [mg mL^{-1}]	Rp (Ωcm², 0h)	Rp_i (Ωcm², 5h)	Rp_f (Ωcm²,50h)	dRp (%)
6.58	0.1094	0.0837	0.1830	118.7799
13.16	0.1486	0.0809	0.1227	51.5889
26.32	0.3770	0.1625	0.1820	11.9943
52.64	0.4173	0.2015	0.3612 (*)	79.2393
105.28	0.6259	0.2949	0.3943	33.7399

(*) Rp value corresponds to 44h

Initial Rp values for the infiltrated electrodes were higher than the values measured for non-infiltrated ones (Table 4-7), but oppositely to what was observed in Batch A, in this case the increment in initial Rp was minimal in comparison to the baseline values, which was expected in line with measurements for Batch B set 1 and reports from literature [176]. When infiltrating electrodes at high concentrations (26.32, 52.64, and 105.25 mg mL^{-1}) initial Rp was significantly higher. After 50h under operation conditions, all the samples exhibited an increment in electrode resistance, *i.e.* all dRp% calculated values were positive. Regardless of this, 13.16 and 26.32 mg mL^{-1} suspensions produced electrodes with final Rp similar or lower than non-infiltrated cells and the degradation rate for these electrodes was lower as well.

Finally, dRp% values for samples infiltrated using the 26.32 mg mL^{-1} precursor suspension across all batches were plotted in Figure 6-9.

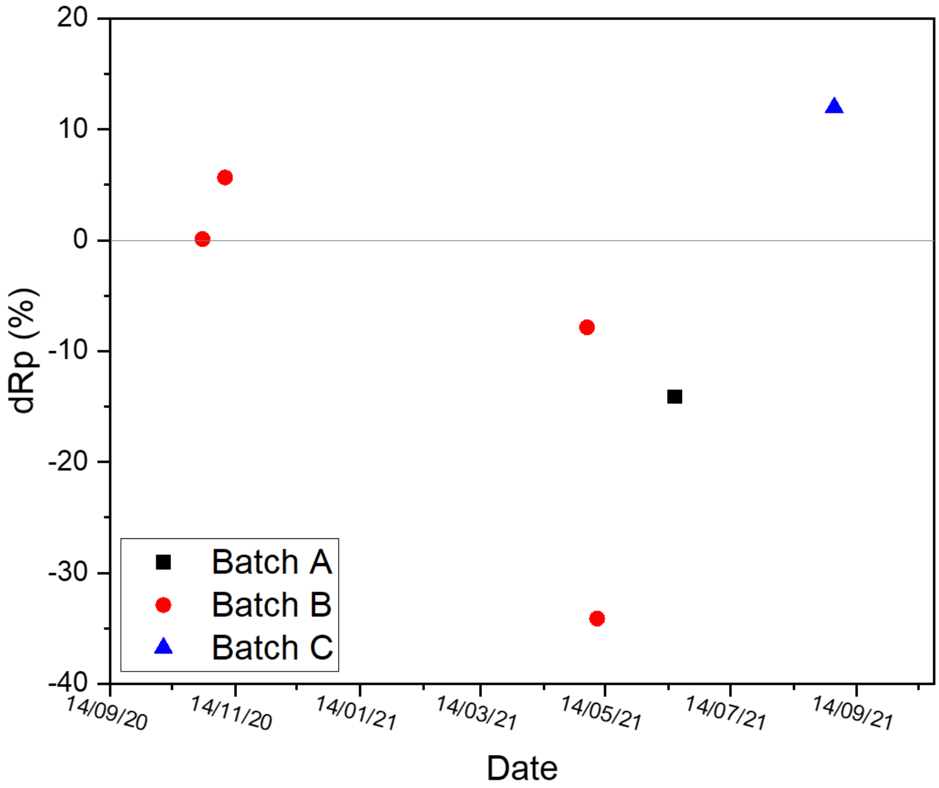

Figure 6-9 dRp(%) for Batch A, B and C of 26.32 mg mL^{-1} HfO$_2$ –infiltrated cells against their date of testing

As it can be observed, samples degraded less the longer they sat in storage before testing. Only set 1 of Batch B and Batch C samples, which were fabricated and tested shortly after showed an increase in Rp after infiltrated electrodes were tested for 50h under operation conditions. This was believed to be caused by the *calendar ageing effect* observed when testing non-infiltrated electrodes and discussed in Chapter 4 of this thesis.

Regardless of the infiltrated batch, initial electrode polarisation (Rp) values tended to be higher than non-infiltrated ones. However, after testing, electrodes exhibited a lower degradation rate and, in some cases, a lower final Rp than bare electrodes. Meaning that HfO_2 infiltration was an effective way of produce more stable and active ORR cathodes. The improvement in degradation and performance has been correlated to the ability of HfO_2 to prevent Sr-surface segregation (SSS), in addition to its great oxygen surface exchange properties [19, 176]. Additionally, the beneficial effects of HfO_2 infiltration were obtained after one-step infiltration with suspensions of low concentrations 6.58, 13.16, and 26.32 mg mL^{-1}.

6.2.2 Physical analysis *via* XRD

Three different batches (A, B, and C) of flat and dense LSCF substrates were ground and polished until mirror finish. Afterwards, the substrates were spin-coated with 50 µL hafnium oxide (HfO_2) suspension solutions at different concentrations (6.58, 26.32, and 105.28 mg mL^{-1}) following the described protocol in section 3.1.2.4 in Chapter 3 of this thesis. Only a selection of concentrations were selected for spin-coating under time constraints considerations.

Finally, only samples with the lowest and highest concentrations were subjected to a thermal ageing treatment consisting of heating the substrates at 800°C for periods of 50 and 100h, which has been proven to promote Sr-surface segregation [10, 81, 103]. Furthermore, HfO_2 has been reported to be an effective suppressor for Sr-surface segregation (SSS) [19, 176], so it is expected that spin-coating with HfO_2 suspensions will prevent SSS from occurring on the analysed samples.

Unaged and aged spin-coated (6.58 and 105.28 mg mL^{-1}) substrates where then analysed using X-ray diffraction (XRD) to evaluate any structural changes and possible formation of secondary Sr-containing phases on the surface. The presence of these Sr-containing phases has been linked to poor electrode performance for SOFC applications [45, 78, 165].

Ideally, perovskite (ABO_3) materials present a cubic crystalline structure with A-site cations occupying the corners of the cube and B-site cations occupying the centre of the body; however, slight deviations can cause a distortion resulting in a rhombohedral structure [168]. Alternatively, HfO_2, which is a fluorite type material (AO_2) presents a monoclinic crystalline after being annealed at temperatures higher than 450°C [148].

X-ray diffraction data (XRD) patterns were obtained according to the protocols described in section 3.2.3 in Chapter 3. Patterns for Batch B of spin-coated substrates at different ageing stages are showed in Figure 6-10. Phase analysis reports for this set can be found in section 12.4.2 of Annex C.

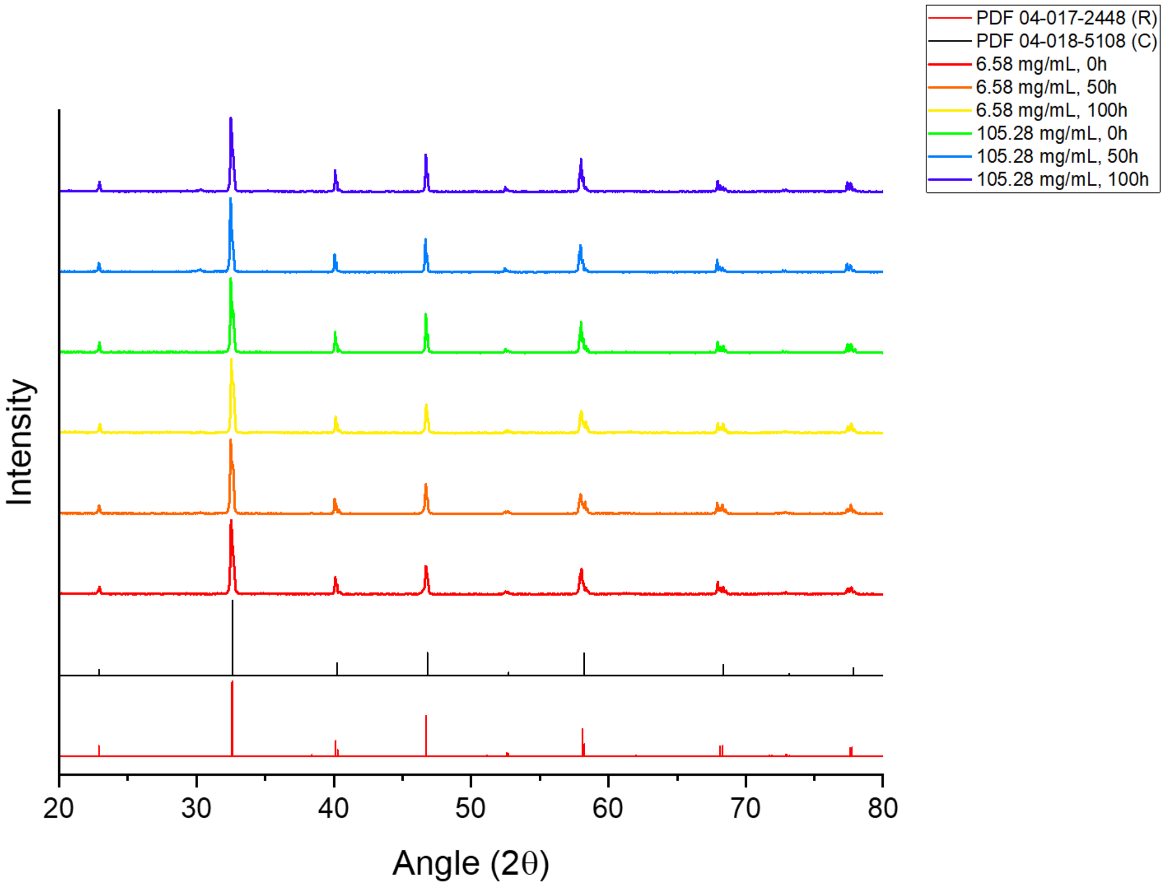

Figure 6-10 XRD patterns for Batch B, for LSCF pellets spin coated with HfO_2 at various concentrations and stages of ageing (samples were aged in a box furnace at 800°C in ambient air). Reference patterns for cubic and rhombohedral LSCF have also been plotted for comparison.

From collected patterns data it was observed that in all cases LSCF substrates presented a mixture of phases. This being the case, reference patterns for the most common LSCF phases reported in literature, *i.e.* cubic (PDF 04-018-5108) [151] and rhombohedral (PDF 04-017-2448) [169] were also plotted for comparison. For the samples where the analysis was possible, Rietveld refinement was used to calculate sample composition. For the cases where Rietveld analysis was nor possible due to non-convergence, sample composition was calculated using the Reference Intensity Ratio (RIR) analysis [141, 144]. All analysis were performed using *Match!© Phase Analysis using Powder Diffraction* software.

Phase analysis for Batch B samples revealed that in all cases LSCF presented as a mixture of phases, approximately 82% rhombohedral and 18% cubic phases. This composition is very similar to the reported in literature for LSCF materials subjected to thermal treatments like the ones used for ageing in this work [170].

Additionally, it was observed that for 0h of ageing, no HfO_2 phase peaks could be identified, which was to be expected since HfO_2 has been reported to stay amorphous when annealed at temperatures below 450°C, and to appear in its monoclinic from when annealing at higher temperatures remaining stable at 800°C [148]. However, only the aged 105.28 mg mL^{-1} spin-coated substrates presented evidence of a small peak for the (111) at ~28 2θ degrees for monoclinic phase of HfO_2 (PDF 00-034-0104).

No new Sr-containing phases were detected in any of the measurements for this batch of samples, but their possible presence cannot be ruled out. Similarly to what was observed with HfO_2 at lower concentrations, the amount present is not enough for this phase to be detected using this XRD technique [141, 144].

A new batch of substrates (Batch A) was fabricated, polished and spin-coated with the same concentrations as for Batch B, then subjected to the same thermal ageing protocol. XRD data for this new batch and appropriate cubic and rhombohedral LSCF standard patterns are presented in Figure 6-11, reports for phase analysis for this batch can be found in section 12.4.1 of Annex C.

For Batch A, low concentration spin-coated LSCF substrates presented a 100% rhombohedral phase regardless of ageing time. Alternatively, the high concentration spin-coated substrates presented a mixture of 87% rhombohedral and 13% cubic phases, which was expected from phase conversion when cooling down from ageing treatment [170]. For the 6.58 mg mL^{-1} spin-coated substrates no HfO_2 phases were identified even after ageing, this was because the amount present was so small that was impossible for the XRD equipment used to detect [144]. Similarly to what was observed with Batch B, the monoclinic HfO_2 phase was only detected when using a high concentration suspension and after ageing at 800°C [148].

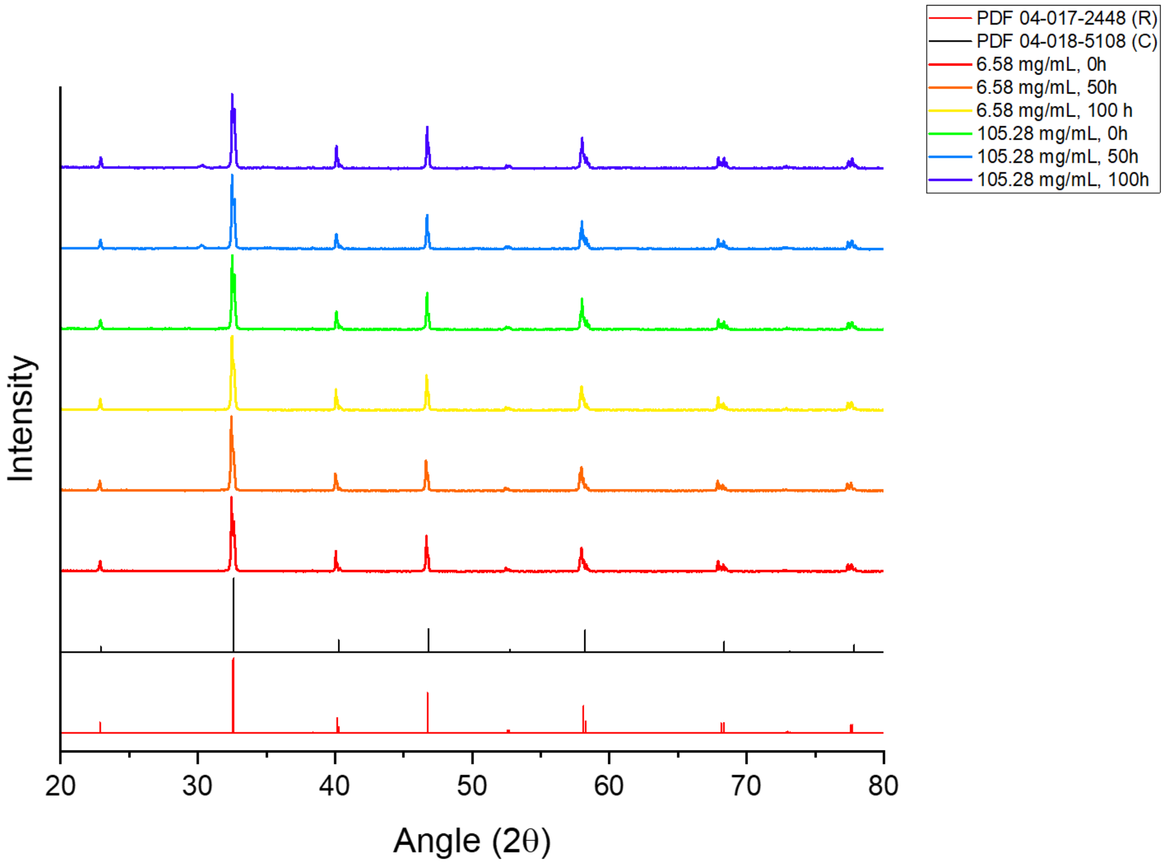

Figure 6-11 XRD patterns for Batch A, LSCF pellets spin coated with HfO_2 at various concentrations and stages of ageing (samples were aged in a box furnace at 800°C in ambient air). Reference patterns for cubic and rhombohedral LSCF have also been plotted for comparison.

Lastly, a new tub of LSCF-6428 powder was purchased and processed to fabricate new LSCF flat substrates that were spin-coated and aged as the previously analysed batches. These new samples conformed Batch C. Collected XRD data for this batch with corresponding cubic and rhombohedral LSCF standard patterns are presented in Figure 6-12; additional XRD phase analysis can be found in section 12.4.3 of Annex C.

This time, all LSCF patterns exhibited a rhombohedral and cubic phase mixture of approximately 80% and 20%, respectively, and regardless of ageing time. This composition deviates from what would be expected [170], but values were still close. The monoclinic HfO_2 phase was only detected by the presence of the (111) peak at 28 2θ degrees when the suspension used for spin-coating had the highest concentration (105.28 mg mL^{-1}) and after ageing treatment at 800°C [148]. Like the previous batches, no Sr-containing phases were identified on the substrates, even after 100h of ageing.

HfO_2 phases were not detectable by XRD when using suspensions at lower concentrations, however, this does not mean that HfO_2 is not present, but that the amount is not enough for it to be detected using this method. Similarly, the fact that no Sr-containing phases were detected either does not mean that their presence can be entirely ruled out, since they might not be present at a high enough concentration or crystalline state to be detected [141, 143, 144]

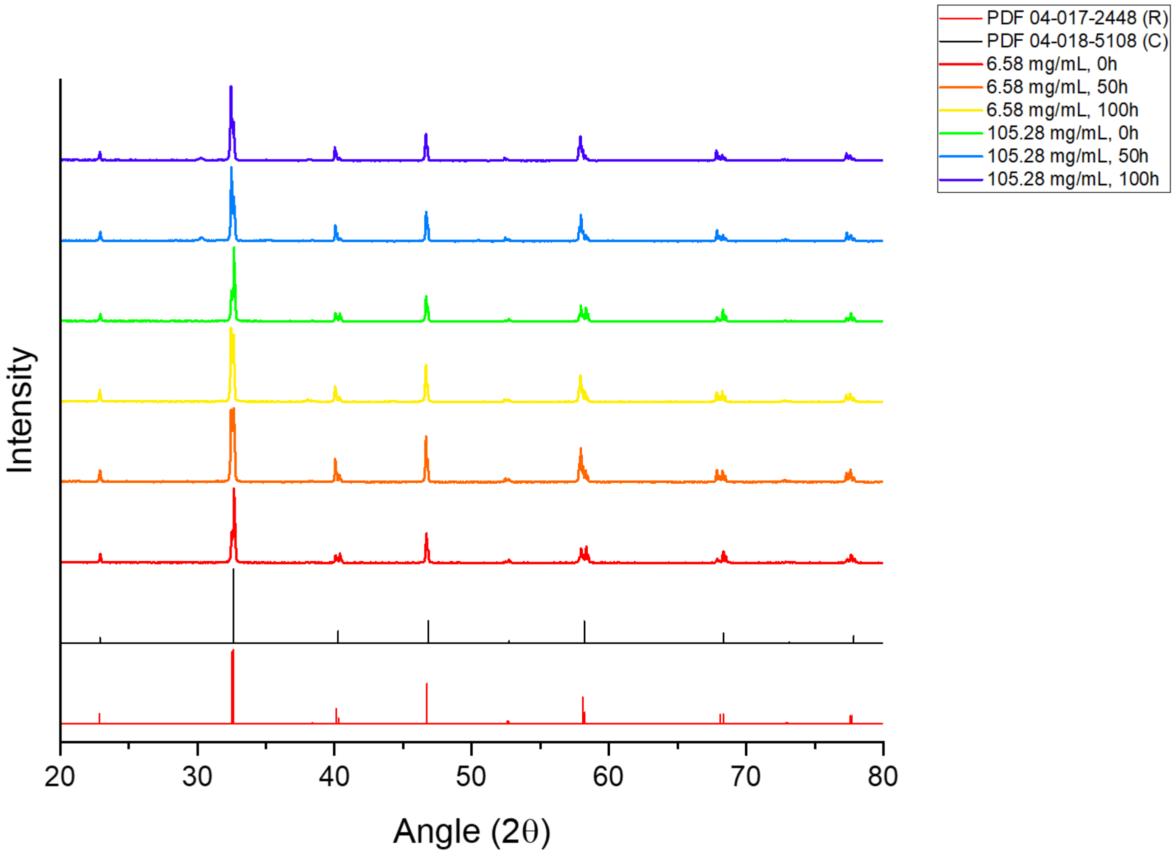

Figure 6-12 XRD patterns for Batch C, LSCF pellets spin coated with HfO_2 at various concentrations and stages of ageing (samples were aged in a box furnace at 800°C in ambient air). Reference patterns for cubic and rhombohedral LSCF have also been plotted for comparison.

After analysing three different batches (A, B and C) of mirror-polished, HfO_2 spin-coated and aged samples at different stages, it was found that for the cases were LSCF presented as polycrystalline, it presented an~85% rhombohedral and ~15% cubic phases, in agreement with previously published reports. For the cases where sample presented a single phase, it was rhombohedral. All this is in agreement with the literature regarding the expected phases for LSCF at room temperature before and after being subjected to high temperatures and being cooled down at 5°C min^{-1} in air atmosphere [10, 168, 170].

Furthermore, it was found that the presence of the monoclinic HfO_2 phase (PDF 00-034-0104) could only be detected when the 105.28 mg mL^{-1} suspension solution was used for spin-coating and after substrates were subjected to high temperatures, like after ageing at 800°C for at least 50h. At lower suspension concentrations, no XRD peaks for HfO_2 were visible.

As it was previously observed for bare LSCF mirror-polished substrates (section 4.2.2 in Chapter 4), no new Sr-containing phases were detected after ageing treatment for any of the analysed batches, which makes difficult to assess whether HfO_2 prevented this from occurring as it has been previously reported in literature [19, 176]. Regardless of this, the presence of said segregated Sr-containing phases cannot be entirely ruled out since the possibility exists that they were not present in a sufficient amount (at least 2%) or a crystalline state to be detected by the equipment used [141, 144].

6.2.3 Surface analysis *via* SEM-EBSD

After grinding and polishing to mirror finish, flat and dense LSCF substrates for three different batches (A, B, and C) were spin-coated with 50 µL HfO_2 suspension solutions at different concentrations (6.58, 26.32, and 105.28 mg mL^{-1}) following the described protocol in section 3.1.2.4 in Chapter 3 of this thesis. Only a selection of concentrations were selected for spin-coating because of time constraints, and out of these only the lowest and highest concentration were thermally aged at 800°C for 50 and 100h to promote Sr-surface segregation (SSS) [10, 81, 103, 108].

Scanning electron microscopy (SEM) was used to evaluate the different morphologies when spin-coating the substrates using different concentrations. Additionally, substrates were re-imaged after every ageing stage to evaluate possible changes in the coating microstructure.

SEM images for Batch B are presented in Figure 6-13. The corresponding electron backscattered images (EBSD) can be found in section 12.5.2 of Annex C. Images (a) and (c) show unaged HfO_2 spin-coated substrates. It was observed that the 6.58 mg mL^{-1} suspension produced dispersed particles of various sizes and shapes, whilst the only difference with the 105.28 mg mL^{-1} suspension was the number of observable particles. This was of course a natural observation since the followed protocol for the HfO_2 produced a suspension (section 3.1.1.5 in Chapter 3) [148], rather than a precursor that could adopt different morphologies.

After 100h of ageing at 800°C, SEM images showed that particle morphology changed as observed particles seemed to shrink in size and sharpen around the edges, similar observations have been made by Aguirre *et.al* [177] when studying HfO_2 thin films annealed at different temperatures. Moreover, it is also known that HfO_2 is amorphous unless annealed at temperatures higher than 450°C [148] which only occurred after the ageing treatment as also corroborated by XRD analysis conducted in this study.

(a) Batch B, 6.58 mg mL^{-1}, 0h (b) Batch B, 6.58 mg mL^{-1}, 100h

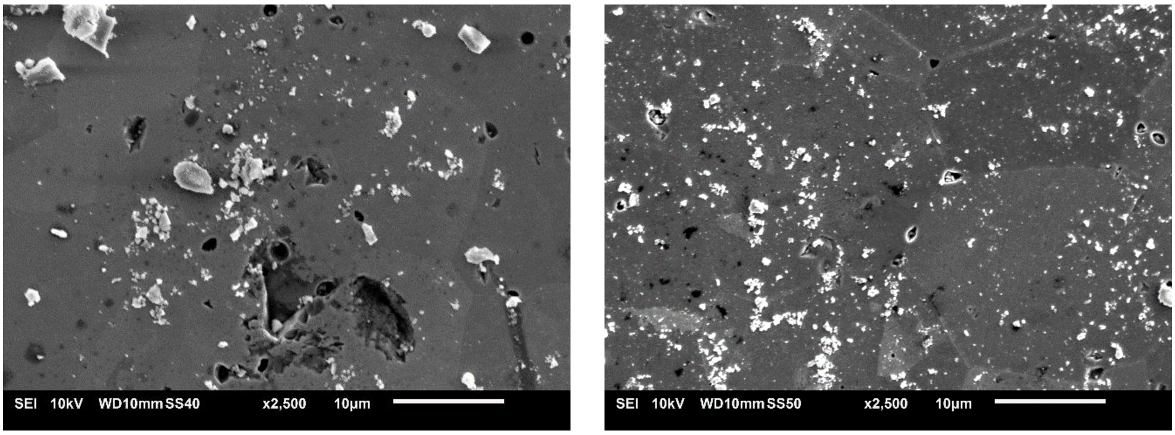

(c) Batch B, 105.28 mg mL^{-1}, 0h (d) Batch B, 105.28 mg mL^{-1}, 100h

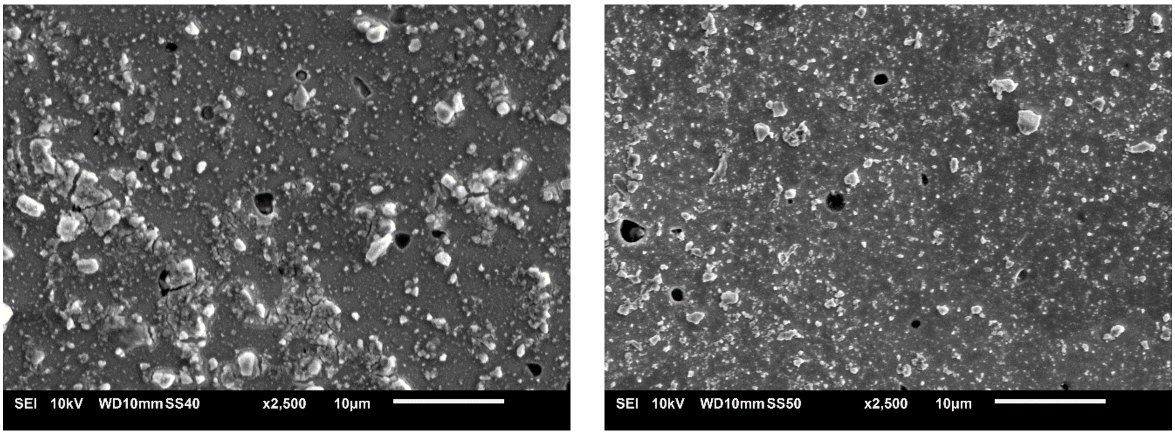

Figure 6-13 SEM images for Batch B, HfO_2 spin coated LSCF flat substrates at different concentration and ageing stages. Samples were aged at 800 °C in ambient air

SEM images at 100h of ageing also showed that no segregated particles that could be associated to Sr-surface segregation (SSS) appeared on the surface-modified substrates on Batch B. On the other hand, bare LSCF substrates exhibited the appearance and growth of particles of ~5 µm on the grain boundaries after ageing at 800°C for 100h. Although for this study, no elemental analysis was performed to corroborate that these segregated particles were Sr-rich phases, these were assumed to be so based on numerous reports in literature [10, 170, 172].

A new batch of substrates, Batch A, was processed, spin-coated and aged following the same protocol as for Batch B. Appropriate images are presented in Figure 6-14, with corresponding EBSD images in section 12.5.1 of Annex C. Like it was observed for the previous batch, unaged spin-coated substrates (Figure 6-14a, c) showed dispersed particles of various sizes and shapes, with the only difference being the number of particles present, *i.e.* the most concentrated suspension presented more particles [148].

(a) Batch A, 6.58 mg mL^{-1}, 0h (b) Batch A, 6.58 mg mL^{-1}, 100h

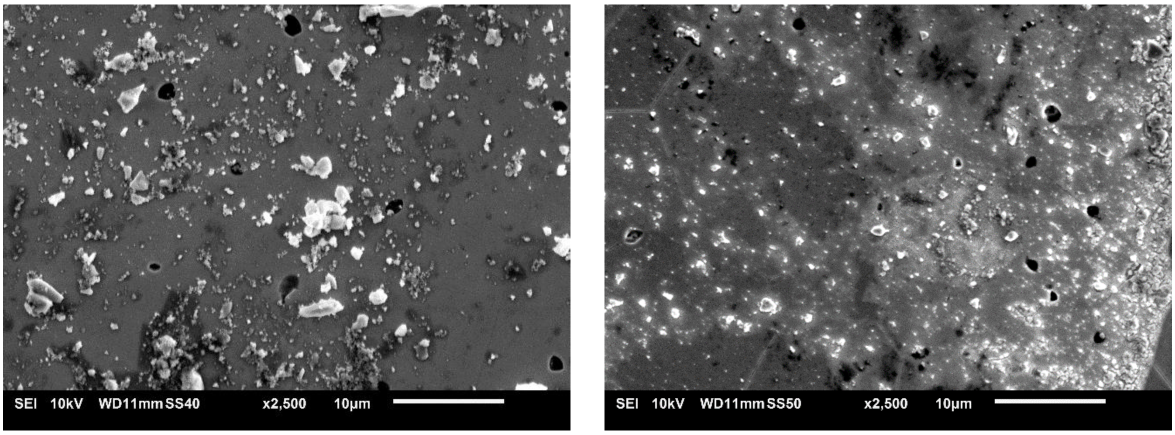

(c) Batch A, 105.28 mg mL^{-1}, 0h (d) Batch A, 105.28 mg mL^{-1}, 100h

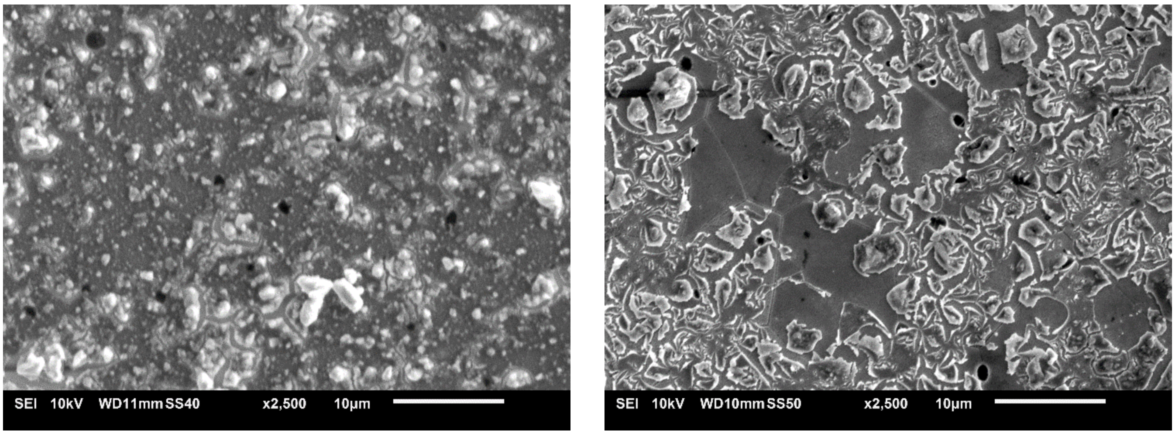

Figure 6-14 SEM images for Batch A, HfO_2 spin coated LSCF flat substrates at different concentration and ageing stages. Samples were aged at 800 °C in ambient air

After 100h of ageing, SEM images also showed that the deposited particles again sharpened around the edges, same as it was observed in the previous batch. Additionally, for the 105.28 mg mL-1 spin-coated substrate, images showed that the particles coarsened [81, 175] and its microstructure resembled an uneven film that cracked leaving small areas of LSCF material exposed. However, there was no visual trace of segregated particles that could be associated to Sr-surface segregation (SSS).

Finally, Batch C was fabricated after a new tub of LSCF-6428 powder was purchased. The new substrates were processed to conduct the same ageing treatment. Micrographs at different ageing times are presented in Figure 6-15Figure 5-16, appropriate EBSD images can be found in section 12.5.3 in Annex C.

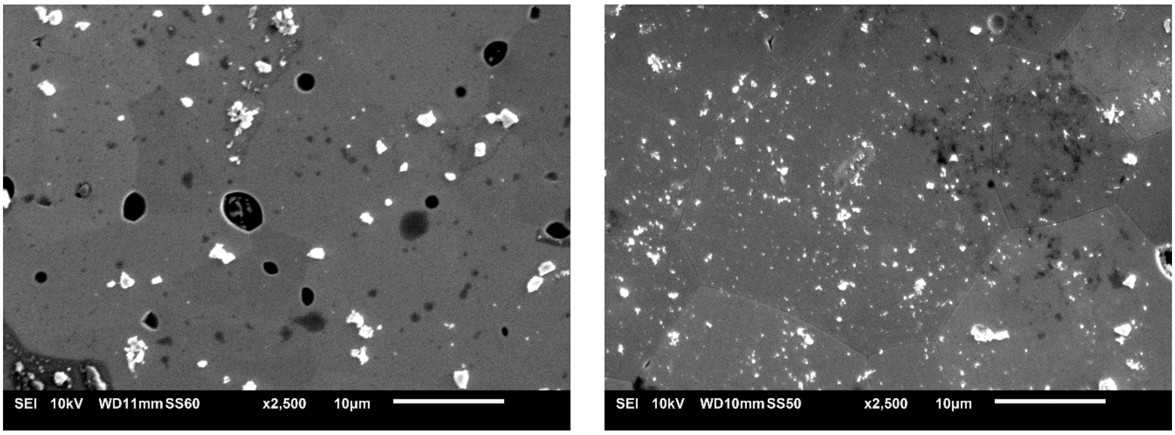

(a) Batch C, 6.58 mg mL^{-1}, 0h

(b) Batch C, 6.58 mg mL^{-1}, 100h

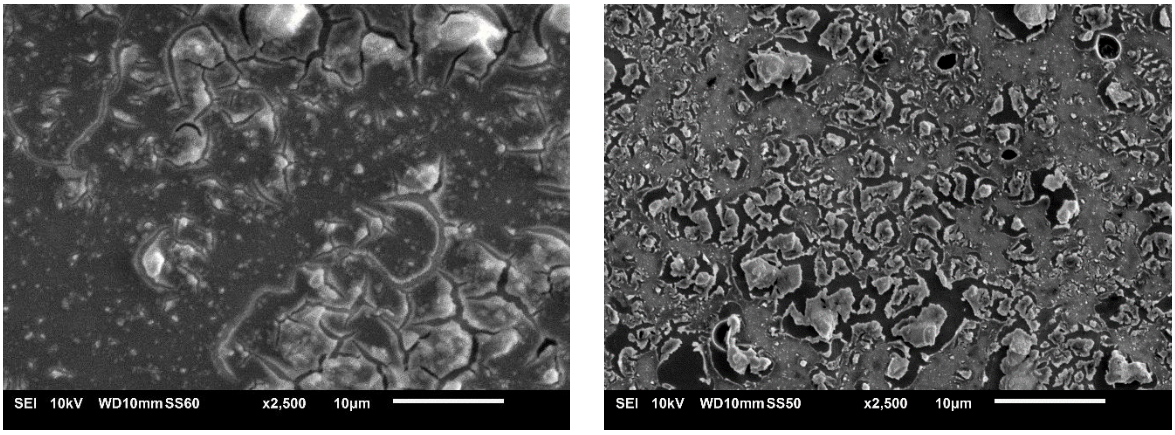

(c) Batch C, 105.28 mg mL^{-1}, 0h

(d) Batch C, 105.28 mg mL^{-1}, 100h

Figure 6-15 SEM images for Batch C, HfO_2 spin coated *LSCF flat substrates at different concentration and ageing stages. Samples were aged at 800 °C in ambient air*

The unaged spin-coated substrates (Figure 6-15Figure 6-14a, c) showed that the 6.58 mg mL^{-1} produced dispersed particles of various sizes and shapes, whilst the highest105.28 mg mL^{-1} presented as an uneven coating conformed by particles of various sizes.

After 100h of ageing, obtained SEM images showed that deposited particles for the 6.58 mg mL^{-1} suspension sharpened around the edges and shrunk in size, same as it was observed on Batch B. Furthermore, for the 105.28 mg mL^{-1} spin-coated substrate, the deposited film coarsened [81, 175] and left small areas of LSCF material exposed. Nevertheless, as it was observed before, there was no visual trace of segregated particles that could be associated to Sr-surface segregation (SSS).

After modifying the surface of mirror-polished LSCF substrates with HfO_2 suspension solutions at different concentrations (6.58, 26.32, and 105.28 mg mL^{-1}) two main different coating morphologies were observed. The 6.58 and 26.32 mg mL^{-1} suspension solutions produced well dispersed particles of various sizes, with the more concentrated exhibiting a higher number of particles. Alternatively, the 105.28 mg mL^{-1} suspension produced a film-like surface modification. After ageing, SEM images showed that particles shrunk in size and sharpened around the edges, whilst the film coarsened [78] and left small areas of LSCF exposed. This was associated to the fact that HfO_2 is amorphous if not annealed at temperatures above 450°C.

For the bare LSCF substrates analysed in Chapter 4, angular particles (~1 µm) appeared along the grain boundaries after 50h of ageing, and after 100h of high temperature ageing, segregated particles grew to ~5µm, which was in complete agreement to what Araki *et.al.* [10] had previously reported and positively identified as Sr-rich particles by using EDX. For the purpose of this work, the observed particles were considered as Sr-rich segregated particles.

After modifying LSCF substrates with HfO_2 suspension solutions, no segregated particles that could be associated with SSS were observed, meaning that Sr-segregation was prevented by spin-coating dense LSCF substrates with HfO_2 [19, 176]. The absence of SSS has been explained by the ability of HfO_2 to fine-tune the number oxygen vacancies at the LSCF surface [167], thus degreasing the electrostatic interactions between charged defects that ultimately have been proven to drive Sr-segregation [19, 121, 165].

Although it has been recognised that Sr segregation induced by high temperature is more likely to occur on dense samples than porous ones [45], there is still not a clear consensus on how much observed results on dense samples can be extrapolated into porous materials.

6.3 Summary and conclusions

HfO_2 precursor suspensions at different concentrations (6.58, 13.16, 26.32, 52.64, and 105.28 mg mL^{-1}) were used to either infiltrate porous electrodes or coat flat LSCF-6428 substrates.

Impedance and corresponding ECM data fitting for three different batches (A, B, and C) showed that HfO_2 infiltration produced electrodes that were more stable, *i.e.* tended to degrade less that non-infiltrated electrodes and in some cases performed better as well, especially after prolonged testing. The benefits of HfO_2 infiltration were achieved when using suspension with concentrations as low as 13.16 and 26.32 mg mL^{-1}, producing the electrodes with the best performance and lower degradation rate. The stabilising effect of HfO_2 coatings has been demonstrated before on Sr-containing materials and on LSCF. And this has been explained thanks to the HfO_2 superior oxygen exchange kinetics facilitating ORR kinetics but still preventing SSS by tunning the amount of oxygen vacancies formed at LSCF surfaces.

More importantly, although HfO_2 surface modifications on LSCF have been previously reported, a one-step infiltration protocol, like the one presented in this thesis is yet to be reported.

Three different batches (A, B and C) of mirror-polished, flat, and dense LSCF substrates were spin-coated with HfO_2 suspensions at various concentrations (6.58, 26.32, and 105.28 mg mL^{-1}) and then aged for 50 and 100h at 800°C before being cooled down to room temperature for XRD analysis. Phase composition analysis showed that in most cases, LSCF presented as polycrystalline ~ 85% rhombohedral and ~15% cubic phase mixture, which agreed with reports in literature for samples processed under similar conditions. For the rest of the cases, LSCF substrates presented a 100% rhombohedral composition.

Additionally, the characteristic monoclinic HfO_2 phase (PDF 00-034-0104) for surface modifications could only be identified when the substrates were treated at high temperatures and the highest suspension concentration (105.28 mg mL^{-1}) was used. Identification was possible namely by the (111) peak at ~28 2θ degrees. For the low concentration suspension and substrates that were not thermally treated, no HfO_2 phases could be identified due to the amount not being high enough for the detection threshold and because HfO_2 is amorphous unless treated at temperatures above 450°C.

Lastly, like it was also observed for bare LSCF substrates, no new Sr-containing phases were detected after ageing treatment for any of the analysed batches, nevertheless, this could be because like the case of low concentration HfO_2, the amount is not enough to be identified using XRD. Because of this, it was determined that, by itself, XRD is not enough to confirm if HfO_2 spin-coating of LSCF substrates prevented Sr-surface segregation.

SEM images of flat and dense LSCF substrates that have been spin-coated with HfO_2 suspension solutions at various concentrations showed two main different coating morphologies, well dispersed particles of various sizes for lower concentrations and film-like surface modification for the highest concentration. After 100h of ageing at high temperature, the morphology of the coatings tended to sharpen around the edges, caused by the amorphous – crystalline transition of the material at temperatures above 450°C. Additionally, the film-like coatings tended to coarse and left small areas of LSCF exposed. Regardless of this, no segregated particles that could be associated with SSS were observed, meaning that Sr-segregation was prevented by spin-coating dense LSCF substrates with HfO_2 suspensions. The absence of SSS has been explained by the ability of HfO_2 to reduce the concentration of oxygen vacancies at the LSCF surface, thus degreasing the electrostatic interactions that drive Sr-segregation.

Ultimately, even though thermally induced Sr segregation is more likely to occur on dense than porous samples there is still not a clear consensus on how much observed results on dense samples can be extrapolated into porous electrodes. Therefore, more research on this subject is needed.

7 Summary and conclusions

As discussed in the abstract of this thesis, the objective of this work was to evaluate two different surface modifications, HfO_2 and $Gd_{0.1}Ce_{0.9}O_{1.95}$ (GDC) on the state-of-the-art $La_{0.6}Sr_{0.4}Co_{0.2}Fe_{0.8}O_{3-\delta}$, (LSCF-6458) material, to assess their effect on electrode performance and as inhibitors of Sr-surface segregation (SSS), which has been recognised as the main degradation mechanism for LSCF electrodes in operating SOFCs.

This was achieved by first studying modified and surface-modified LSCF porous electrodes and flat substrates using electrochemical impedance spectroscopy (EIS), and X-ray diffraction (XRD) and scanning electron microscopy (SEM), respectively. Obtained data for unmodified materials served as benchmark for comparison for surface-modified materials. Particularly for the HfO_2 surface modifications, a gap in the literature has been addressed, since to the authors knowledge, this would constitute the first in corporation onto LSCF surfaces using a single-step infiltration protocol. Additionally, and due to extraordinary circumstances, a *calendar ageing effect* was identified, which has not been addressed in literature.

Finally, as the efforts to make SOFC technology tend to lower operation temperatures the requirement for electrodes with enhanced performance for oxygen reduction reaction (ORR) and resistance to SSS becomes imperative. Thus, research like the one presented in this work become part of the building blocks for finding more simple and economic ways of producing these electrodes.

7.1 Experimental study of strontium segregation on LSCF

Impedance data of porous LSCF-6428 electrodes for three different batches of samples (A, B and C) were obtained and fitted to an appropriate ECM model. The electrical elements included in this ECM described the key features observed on the impedance data; this is, the induction contribution from the jig wires/connections, the two characteristic semi-arcs for the ORR on MIEC electrodes and the finite Warburg element accounting for the non-ideal behaviour of the electrode.

Three different batched of electrodes (A, B, and C) were tested after observing that for the three sets of samples conforming batch B, initial Rp values were increasingly higher and the degradation or change in Rp (dRp%), was lower for samples that had been stored for longer (Figure 4-14). It was ultimately identified that, when samples were tested shortly after being fabricated, they exhibited a tendency for higher degradation rate, which was labelled as a *calendar ageing effect* by the author. Ageing, particularly thermal ageing, is a common method of exposing samples to temperatures higher than the operation ones to promote material degradation and study its effects. However, the observations made during this experimental work could not be compared to anything reported in literature since, to the authors knowledge, this is the first time something like this has been discussed. Moreover, these conditions for these observations were made possible only due to the COVID-19 lockdown, that closed access to research facilities for several months.

Regarding the mechanism for electrode degradation, in all cases it was attributed to Sr-surface segregation as supported by numerous reports in literature, The rate limiting step for the bare electrodes remained the charge transfer at the electrode/electrolyte interface and the O^{2-} ion bulk diffusion.

XRD and SEM analysis of three different batches (A, B and C) of mirror polished, flat and dense LSCF substrates showed that for most cases, LSCF presented a polycrystalline mixed composition of rhombohedral and cubic phases in various ratios, which is consistent due to the phase transitions susceptible from occurring during our thermal ageing regime. The appearance of segregated particles (~1 µm) along the grain boundaries after 50h of ageing and their growth (~5µm) after 100h of ageing could only be confirmed *via* SEM on Batch B substrates. These segregated particles were assumed to be Sr-containing segregated phases based on several reports from literature. SEM for substrates for other batches showed only clean surfaces, even after more severe ageing treatments. This occurrence was thought to be caused by the previously discussed *calendar ageing effect*.

XRD failed to show any other information other than the polycrystalline composition of LSCF, this is, no Sr-containing phases were identified, even for samples where segregated particles were clearly observed (Batch B). However, this was explained by the possibility of the segregated phase being under the detection threshold for the technique. This being the case, it would be highly beneficial that in addition to SEM and XRD, another elemental analysis technique was used for positive identification of Sr-rich segregated particles.

7.2 LSCF stabilisation using GDC as surface modification

GDC precursors at different concentrations (0.025, 0.050, 0.125, 0.250, 0.500, and 1.000 M) were used to infiltrate porous electrodes. Impedance and ECM data fitting of three different batches (A, B and C) showed that generally, GDC infiltration proved to be an effective way to produce better performing and more stable electrodes. The best performing electrodes were those infiltrated with 0.125 and 0.250 M precursors, which showed Rp values lower than those measured for non-infiltrated electrodes, as well as lower degradation rates. Although the mechanism through which GDC enhances electrode performance is still highly debated, it has been generally agreed that because of its superior ionic conductive properties, GDC infiltration significantly increase the triple phase boundary (3PB), hence increasing the number of sites for the oxygen reduction reaction (ORR) to take place. Additionally, because GDC has demonstrated to suppress Sr-surface strontium segregation (SSS) on LSCF, the infiltrated electrodes become more stable, and their lifetime can be extended.

Interestingly, the *calendar ageing effect* previously observed on non-infiltrated cells, was also recognised on measurements for this chapter, as samples that were tested closer to their fabrication date degraded more than those that were stored prior to their testing. However, more research on this subject is needed to properly identify why this happens.

Three different batches (A, B and C) of mirror-polished, flat, and dense LSCF substrates were spin coated with GDC precursors at various concentrations (0.025, 0.125, 0.250, and 1.000M) and then aged for 50 and 100h at 800°C. Phase composition analysis showed that in most cases, LSCF presented as polycrystalline mix (85% rhombohedral and 15% cubic phases), which is in agreement with literature for our thermal ageing protocol. Additionally, the characteristic cubic GDC phase (PDF 01-086-9063) for surface modifications could only be identified when using precursors with high concentrations (0.250, and 1.000M). Moreover, the (111) peak for the cubic GDC sharpened and became narrower with increasing ageing time, meaning that surface modifications coarsened with ageing. SEM images for GDC spin-coated LSCF substrates showed that different coatings morphologies can be obtained, ranging from well dispersed particle clusters (0.025M) to thin even coatings (0.125) and finally thick, uneven coatings (0.250 and 1.000M). Only the 0.025M and 1.000M spin-coated substrates were thermally aged. After 100h of ageing, no segregated particles that could be associated with SSS were observed on any of the samples, meaning that Sr-segregation was prevented by spin-coating dense LSCF substrates with GDC precursors. GDC is a well-known inhibitor of SSS due its ability to reduce the concentration of oxygen vacancies at the LSCF surface, thus degreasing the electrostatic interactions that drive Sr-segregation.

Finally, although it known that SSS at high temperatures is more likely to occur on dense samples than porous ones, there is still not a clear consensus on how much observed results on dense samples can be extrapolated into porous electrodes. Therefore, more research on this subject is needed.

7.3 LSCF stabilisation using HfO_2 surface modification

HfO_2 suspensions at different concentrations (6.58, 13.16, 26.32, 52.64, and 105.28 mg mL^{-1}) were used to infiltrate porous electrodes. Impedance and corresponding ECM data fitting for three different batches (A, B, and C) showed that HfO_2 infiltration with suspensions at low concentrations, *i.e.* 13.16 and 26.32 mg mL^{-1}, produced electrodes that were more stable, *i.e.* tended to degrade less that non-infiltrated electrodes and performed better that non-infiltrated electrodes especially after prolonged testing. The stabilising effect of HfO_2 coatings has been demonstrated before on Sr-containing materials and it has been attributed to the HfO_2 superior oxygen exchange kinetics facilitating ORR kinetics but still preventing Sr-surface segregation (SSS) by reducing the amount of oxygen vacancies formed at LSCF surfaces hence diminishing the electrostatic interactions that drive SSS.

Interestingly, the *calendar ageing effect* previously observed on non-infiltrated cells, was also observed on measurements for this chapter, as samples that were tested closer to their fabrication date degraded more than those that were stored prior to their testing. However, more research on this subject is needed to properly identify why this happens.

More importantly, although HfO_2 surface modifications on LSCF have been previously reported, to the authors knowledge, a one-step infiltration protocol, like the one presented in this thesis is reported for the first time.

Three different batches (A, B and C) of mirror-polished, flat, and dense LSCF substrates were spin-coated with HfO_2 precursors at various concentrations (6.58, 26.32, and 105.28 mg mL^{-1}) and then aged for 50 and 100h at 800°C. before being cooled down to room temperature for XRD analysis. Phase composition analysis showed that, generally, LSCF presented polycrystalline phase mixture (~ 85% rhombohedral and ~15% cubic), which agrees with literature for our thermal ageing protocol. Furthermore, the characteristic monoclinic HfO_2 phase (PDF 00-034-0104) for surface modifications could only be identified when spin-coating with the highest suspension concentration (105.28 mg mL^{-1}), and after substrates were thermally treated at temperatures higher than 450°C; below this temperature HfO_2 phase is amorphous and thus indetectable by XRD. SEM images of flat and dense LSCF substrates that were spin-coated with HfO_2 suspension solutions at various concentrations showed two main different coating morphologies, well dispersed particles of various sizes for lower concentrations (6.58 and 26.32 mg mL^{-1}), and film-like surface modification for the highest concentration (105.28 mg mL^{-1}). After 100h of ageing at high temperature, the morphology of the coatings tended to sharpen around the edges (amorphous–crystalline transition at 450°C). Additionally, the film-like coatings tended to coarse and left small areas of LSCF exposed. Regardless of this, no segregated particles that could be associated with SSS were observed, meaning that Sr-segregation was prevented by spin-coating dense LSCF substrates with HfO_2 suspensions. The absence of SSS has been explained by the ability of HfO_2 to reduce the concentration of oxygen vacancies at the LSCF surface, thus degreasing the electrostatic interactions that drive Sr-segregation.

Ultimately, even though thermally induced Sr segregation is more likely to occur on dense than porous samples there is still not a clear consensus on how much observed results on dense samples can be extrapolated into porous electrodes. Therefore, more research on this subject is needed.

8 Future work

Despite the time, technical and personal constraints in finishing this work, this study revealed several interesting findings, for which further work would significantly complement and improve on the information obtained from the performed experiments.

In this work, Sr-surface segregation was assumed to have been observed due to the electrode polarisation resistance increase after 50h of operation and SEM imaging on flat substrates showing growing particles at the material's surface after ageing. However, other elemental and quantifying analysis would be recommended for a positive corroboration on Sr-surface segregation. For this purpose, energy-dispersive X-ray spectroscopy (EDS) coupled with SEM analysis would be a good option, as well as microscopy technologies with better resolution like transmission electron microscopy (TEM).

For the case of spin-coated flat LSCF substrates, this work centred only in ageing the lowest and highest concentration for both GDC and HfO_2. However, a more detailed insight could be obtained from analysing flat substrates spin-coated with either the full range of concentrations used for electrode infiltration, or at least with some intermediate concentrations to assess any changes in coating morphology due to ageing. Alternatively, this type of analyses could also be performed on infiltrated electrodes. However, unless *in-operando* analysis is available, X-ray would most likely be the case for this scenario, any other analysis would have to be post-mortem, for example for SEM or TEM, since sample preparation, although usually non-destructive, could render the cell as non-recoverable for further electrochemical assessment.

Regarding data analysis, a more detailed and comprehensive Rietveld analysis for quantitative phase analysis of all samples would be required; also, pertinent data corrections (like for instrumental peak broadening) can be applied. Additionally, for equivalent circuit fitting (ECF) a single equivalent circuit model (ECM) was used to fit all collected data, and whilst the herein proposed model fitted the non-infiltrated and GDC infiltrated EIS data with a good margin, data fitting for HfO_2-infiltrated could be refined, *e.g.* a different model would need to be proposed to fit this data.

As mentioned previously, the experimental jig used for electrochemical data collection suffered a breakage to the sample-holding compartment, thus yielding particularly noisy EIS data for all Batch C measurements and for some Batch A measurements as well. Appropriate repairs or even complete replacement of the experimental jig could effectively eliminate noisy data and prevent gaps and missing data on samples recorded over extended periods of time.

A commercial SOCF cell testing jig over an in-house designed one would provide extra technical support if needed.

Finally, regarding the interesting experimental observations during this work, mainly the *calendar ageing effect,* a more systematic and comprehensive approach would be necessary to assess if storing electrodes for prolonged periods prior to their use has any effects on their performance, and if so, whether this would constitute a beneficial or detrimental quality, since per our observations, electrodes that were stored for longer tended to degrade less but their starting performance was worse. Additionally, when including infiltration as another factor contributing to electrode performance, the possible interactions between *calendar ageing* and benefits of infiltration would need to further be investigated. It would also be interesting to investigate if infiltration time has any effect on electrode performance, since for the purposes of this work, electrodes were fabricated/infiltrated and then stored prior to testing; therefore, it would be interesting to see if infiltrating *calendar aged* electrodes produces any interesting observations.

9 References

[1] M. H. Syed and M. M. Khan, *Encyclopaedia of Global Warming : Volumes 1- 5*. Mumbai, INDIA: Himalaya Publishing House, 2008.

[2] R. Lindsey and L. Dahlman. (2023, 20/01/2023). *Climate Change: Global Temperature*. Available: https://www.climate.gov/news-features/understanding-climate/climate-change-global-temperature#:~:text=January%2018%2C%202023-,Highlights,0.18%C2%B0%20C)%20per%20decade.

[3] N. Meng and T. S. Zhao, Eds. *Solid Oxide Fuel Cells: From Materials to System Modeling* (Energy and Environment). Cambridge: RSC Publishing, 2013.

[4] L. Carrette, K. A. Friedrich, and U. Stimming, "Fuel Cells: Principles, Types, Fuels, and Applications," *European Journal of Chemical Physics and Physical Chemistry,* vol. 1, no. 4, pp. 162-193, 2000.

[5] V. S. Bagotsky, *Fuel cells: problems and solutions* (The Electrochemical Society Series). John Wiley & Sons, 2012.

[6] S. P. Jiang, Y. Yan, and M. Lu, *Materials for High-Temperature Fuel Cells*. Weinheim, GERMANY: John Wiley & Sons, Incorporated, 2013.

[7] K. Kendall and S. C. Singhal, *High temperature Solid Oxide Fuel Cells: Fundamentals, Design, and Applications*. Elsevier Advanced Technology, 2003.

[8] D. Stolten and B. Emonts, *Fuel Cell Science and Engineering : Materials, Processes, Systems and Technology*. Weinheim, GERMANY: John Wiley & Sons, Incorporated, 2012.

[9] K. Huang and J. B. Goodenough, *Solid oxide fuel cell technology: principles, performance and operations* (Series in Energy). Cambridge, UK: Woodhead Publishing Limited, 2009.

[10] W. Araki, T. Yamaguchi, Y. Arai, and J. Malzbender, "Strontium surface segregation in $La_{0.58}Sr_{0.4}Co_{0.2}Fe_{0.8}O_{3-\delta}$ annealed under compression," *Solid State Ionics,* vol. 268, pp. 1-6, 2014/12/15/ 2014.

[11] K. Chen, N. Li, N. Ai, Y. Cheng, W. D. A. Rickard, and S. P. Jiang, "Polarization-induced interface and Sr segregation of in situ assembled $La_{0.6}Sr_{0.4}Co_{0.2}Fe_{0.8}O_{3-\delta}$ electrodes on Y_2O_3-ZrO_2 electrolyte of solid oxide fuel cells," *ACS Applied Materials and Interfaces,* vol. 8, no. 46, pp. 31729-31737, 2016.

[12] H. Wang *et al.*, "Mechanisms of Performance Degradation of (La,Sr)(Co,Fe)O3-δ Solid Oxide Fuel Cell Cathodes," *J. Electrochem. Soc,* vol. 163, no. 6, pp. F581-F585, 2016.

[13] J. Y. Koo *et al.*, "Suppression of Cation Segregation in (La,Sr)$CoO_{3-\delta}$, by Elastic Energy Minimization," *Acs Applied Materials & Interfaces,* vol. 10, no. 9, pp. 8057-8065, Mar 7 2018.

[14] B. Koo, H. Kwon, Y. Kim, H. G. Seo, J. W. Han, and W. Jung, "Enhanced oxygen exchange of perovskite oxide surfaces through strain-driven chemical stabilization," *Energy & Environmental Science,* vol. 11, no. 1, pp. 71-77, Jan 2018.

[15] Y. Yu *et al.*, "Effect of Sr Content and Strain on Sr Surface Segregation of $La_{1-x}Sr_xCo_{0.2}Fe_{0.8}O_{3-\delta}$ as Cathode Material for Solid Oxide Fuel Cells," *Acs Applied Materials & Interfaces,* Article vol. 8, no. 40, pp. 26704-26711, Oct 2016.

[16] Y. Li *et al.*, "Controlling cation segregation in perovskite-based electrodes for high electro-catalytic activity and durability," *Chemical Society Reviews,* vol. 46, no. 20, pp. 6345-6378, Oct 21 2017.

[17] W. Lee, J. W. Han, Y. Chen, Z. Cai, and B. Yildiz, "Cation size mismatch and charge interactions drive dopant segregation at the surfaces of manganite perovskites," *Journal of the American Chemical Society,* vol. 135, no. 21, pp. 7909-7925, 2013/05/29 2013.

[18] Y. Chen *et al.*, "A robust and active hybrid catalyst for facile oxygen reduction in solid oxide fuel cells," *Energy & Environmental Science,* vol. 10, no. 4, pp. 964-971, Apr 1 2017.

[19] N. Tsvetkov, Q. Lu, L. Sun, E. J. Crumlin, and B. Yildiz, "Improved chemical and electrochemical stability of perovskite oxides with less reducible cations at the surface," *Nature Materials,* vol. 15, no. 9, pp. 1010-1016, 2016.

[20] N. Tsvetkov, Q. Lu, and B. Yildiz, "Improved electrochemical stability at the surface of $La_{0.8}Sr_{0.2}CoO_3$ achieved by surface chemical modification," *Faraday Discussions,* vol. 182, pp. 257-269, 2015.

[21] S. Saher *et al.*, "Tailoring the surface of perovskite oxide for enhanced oxygen exchange kinetics," in *International Conference on Emerging Technologies (ICET)*, Islamabad, Pakistan, 2016, pp. 1-4: IEEE.

[22] R. Kiebach, C. Knöfel, F. Bozza, T. Klemensø, and C. Chatzichristodoulou, "Infiltration of ionic-, electronic- and mixed-conducting nano particles into $La_{0.75}Sr_{0.25}MnO_3$-$Y_{0.16}Zr_{0.84}O_2$ cathodes-A comparative study of performance enhancement and stability at different temperatures," *Journal of Power Sources,* vol. 228, pp. 170-177, 2013.

[23] L. Carrette, K. A. Friedrich, and U. Stimming, "Fuel Cells – Fundamentals and Applications," *Fuel Cells,* vol. 1, no. 1, pp. 5-39, 2001.

[24] M. Tang, S. Zhang, and S. Chen, "Pt utilization in proton exchange membrane fuel cells: structure impacting factors and mechanistic insights," *Chemical Society Reviews,* 10.1039/D1CS00981H vol. 51, no. 4, pp. 1529-1546, 2022.

[25] E. H. Majlan, D. Rohendi, W. R. W. Daud, T. Husaini, and M. A. Haque, "Electrode for proton exchange membrane fuel cells: A review," *Renewable and Sustainable Energy Reviews,* vol. 89, pp. 117-134, 2018.

[26] J. M. Vohs and R. J. Gorte, "High-Performance SOFC Cathodes Prepared by Infiltration," *Advanced Materials,* Review vol. 21, no. 9, pp. 943-956, Mar 2009.

[27] S. Jiang *et al.*, "Solid oxide fuel cells: materials properties and performance," *Fergus, JW,* pp. 131-137, 2009.

[28] N. M. Beekmans and L. Heyne, "Correlation between impedance, microstructure and composition of calcia-stabilized zirconia," *Electrochimica Acta,* vol. 21, no. 4, pp. 303-310, 1976/04/01/ 1976.

[29] M. J. Verkerk, B. J. Middelhuis, and A. J. Burggraaf, "Effect of grain boundaries on the conductivity of high-purity ZrO2 · Y2O3 ceramics," *Solid State Ionics,* vol. 6, no. 2, pp. 159-170, 1982/03/01/ 1982.

[30] R. M. Ormerod, "Solid oxide fuel cells," *Chemical Society Reviews,* vol. 32, no. 1, pp. 17-28, 2003.

[31] A. Jacobson, "Materials for Solid Oxide Fuel Cells," *Chemistry of Materials,* vol. 22, no. 3, pp. 660-674, 2010.

[32] E. D. Wachsman and K. T. Lee, "Lowering the Temperature of Solid Oxide Fuel Cells," *Science,* vol. 334, no. 6058, pp. 935-939, 2011.

[33] S. B. Adler, "Factors governing oxygen reduction in solid oxide fuel cell cathodes," *Chemical Reviews,* Review vol. 104, no. 10, pp. 4791-4843, Oct 2004.

[34] S. B. Adler, X. Y. Chen, and J. R. Wilson, "Mechanisms and rate laws for oxygen exchange on mixed-conducting oxide surfaces," *Journal of Catalysis,* vol. 245, no. 1, pp. 91-109, 2007/01/01/ 2007.

[35] S. P. Jiang, "Use of gaseous Cr species to diagnose surface and bulk process for O2 reduction in solid oxide fuel cells," *Journal of Applied Electrochemistry,* vol. 31, no. 2, pp. 181-192, 2001/02/01 2001.

[36] J. Ascolani-Yael *et al.*, "The oxygen reduction reaction in solid oxide fuel cells: from kinetic parameters measurements to electrode design," *Journal of Physics: Energy,* vol. 2, no. 4, p. 042004, 2020/10/07 2020.

[37] M. N. Rahaman, *Ceramic processing and sintering*, 2nd ed. ed. New York: New York : M. Dekker, c2003, 2003.

[38] E. V. Tsipis and V. V. Kharton, "Electrode materials and reaction mechanisms in solid oxide fuel cells: a brief review," *Journal of Solid State Electrochemistry,* vol. 12, no. 11, pp. 1367-1391, Nov 2008.

[39] S. Rousseau, S. Loridant, P. Delichere, A. Boreave, J. P. Deloume, and P. Vernoux, "$La_{(1-x)}Sr_xCo_{1-y}Fe_yO_3$ perovskites prepared by sol–gel method: Characterization and relationships with catalytic properties for total oxidation of toluene," *Applied Catalysis B: Environmental,* vol. 88, no. 3, pp. 438-447, 2009/05/20/ 2009.

[40] E. Suvaci and E. Özel, "Hydrothermal Synthesis," in *Encyclopedia of Materials: Technical Ceramics and Glasses*, M. Pomeroy, Ed. Oxford: Elsevier, 2021, pp. 59-68.

[41] O. Celikbilek, E. Siebert, D. Jauffres, C. L. Martin, and E. Djurado, "Influence of sintering temperature on morphology and electrochemical performance of LSCF/GDC composite films as efficient cathode for SOFC," *Electrochimica Acta,* Article vol. 246, pp. 1248-1258, Aug 2017.

[42] H. Yokokawa, K. Yamaji, M. E. Brito, H. Kishimoto, and T. Horita, "General considerations on degradation of Solid Oxide Fuel Cell anodes and cathodes due to impurities in gases," *Journal of Power Sources,* vol. 196, no. 17, pp. 7070-7075, 2011.

[43] Y. Liu, J. Chen, F. Wang, B. Chi, J. Pu, and L. Jian, "Performance stability of impregnated $La_{0.6}Sr_{0.4}Co_{0.2}Fe_{0.8}O_{3-\delta}$–$Y_2O_3$ stabilized ZrO_2 cathodes of intermediate temperature solid oxide fuel cells," *International Journal of Hydrogen Energy,* vol. 39, no. 7, pp. 3404-3411, 2014.

[44] L. dos Santos-Gomez, J. M. Porras-Vazquez, E. R. Losilla, F. Martin, J. R. Ramos-Barrado, and D. Marrero-Lopez, "Stability and performance of $La_{0.6}Sr_{0.4}Co_{0.2}Fe_{0.8}O_{3-\delta}$ nanostructured cathodes with $Ce_{0.8}Gd_{0.2}O_{1.9}$ surface coating," *Journal of Power Sources,* vol. 347, pp. 178-185, 2017.

[45] L. C. Baqué, A. L. Soldati, E. Teixeira-Neto, H. E. Troiani, A. Schreiber, and A. C. Serquis, "Degradation of oxygen reduction reaction kinetics in porous $La_{0.5}Sr_{0.4}Co_{0.2}Fe_{0.8}O_{3-\delta}$ cathodes due to aging-induced changes in surface chemistry," *Journal of Power Sources,* vol. 337, pp. 166-172, 2017.

[46] Z. Pan, Q. Liu, L. Zhang, X. Zhang, and S. Chan, "Effect of Sr Surface Segregation of $La_{0.6}Sr_{0.4}Co_{0.2}Fe_{0.8}O_{3-\delta}$ Electrode on Its Electrochemical Performance in SOC," *J. Electrochem. Soc.,* vol. 162, no. 12, pp. F1316-F1323, 2015.

[47] Y. Wen, T. Yang, D. Lee, L. Ho Nyung, E. J. Crumlin, and K. Huang, "Temporal and thermal evolutions of surface Srsegregation in pristine and atomic layer deposition modified $La_{0.6}Sr_{0.4}CoO_{3-\delta}$ epitaxial films," *Journal of Materials Chemistry A,* vol. 6, no. 47, pp. 24378-24388, Dec 21 2018.

[48] Z. Jiang, C. Xia, and F. Chen, "Nano-structured composite cathodes for intermediate-temperature solid oxide fuel cells via an infiltration/impregnation technique," *Electrochimica Acta,* vol. 55, no. 11, pp. 3595-3605, 2010.

[49] D. Ding, X. Li, S. Y. Lai, K. Gerdes, and M. Liu, "Enhancing SOFC cathode performance by surface modification through infiltration," *Energy and Environmental Science,* vol. 7, no. 2, pp. 552-575, 2014.

[50] A. J. Samson, M. Søgaard, and P. V. Hendriksen, "Model for solid oxide fuel cell cathodes prepared by infiltration," *Electrochimica Acta,* vol. 229, pp. 73-95, Mar 1 2017.

[51] I. Ismail, N. Osman, and A. M. Md Jani, "Tailoring the microstructure of $La_{0.6}Sr_{0.4}Co_{0.2}Fe_{0.8}O_{3-\alpha}$ cathode material: the role of dispersing agent," *Journal of Sol-Gel Science and Technology,* vol. 80, no. 2, pp. 259-266, 2016.

[52] B. Molero-Sánchez, E. Morán, and V. Birss, "Rapid and Low-Energy Fabrication of Symmetrical Solid Oxide Cells by Microwave Methods," *ACS Omega,* vol. 2, no. 7, pp. 3716-3723, 2017/07/31 2017.

[53] T. E. Burye and J. D. Nicholas, "Nano-ceria pre-infiltration improves $La_{0.6}Sr_{0.4}Co_{0.8}Fe_{0.2}O_{3-x}$ infiltrated Solid Oxide Fuel Cell cathode performance," *Journal of Power Sources,* vol. 300, pp. 402-412, 2015.

[54] T. E. Burye and J. D. Nicholas, "Precursor solution additives improve desiccated $La_{0.6}Sr_{0.4}Co_{0.8}Fe_{0.2}O_{3-x}$ infiltrated solid oxide fuel cell cathode performance," *Journal of Power Sources,* Article vol. 301, pp. 287-298, 2016.

[55] T. E. Burye, H. Tang, and J. D. Nicholas, "The effect of precursor solution desiccation or nano-ceria pre-infiltration on various $La_{0.6}Sr_{0.4}Fe_{y}Co_{1-y}O_{3-x}$ infiltrate compositions," *Journal of the Electrochemical Society,* vol. 163, no. 9, pp. F1017-F1022, 2016.

[56] S. V. Seyed-Vakili, C. R. Graves, A. Babaei, S. Heshmati-Manesh, and M. B. Mogensen, "Performance Improvement of an Inhomogeneous Cathode by Infiltration," *Fuel Cells,* vol. 17, no. 1, pp. 108-114, 2017.

[57] W. Zhu, D. Ding, and C. Xia, "Enhancement in three-phase boundary of SOFC electrodes by an ion impregnation method: A modeling comparison," *Electrochemical and Solid State Letters,* vol. 11, no. 6, pp. B83-B86, 2008 2008.

[58] N. Q. Zhang, J. Li, D. Ni, and K. N. Sun, "Preparation of honeycomb porous $La_{0.6}Sr_{0.4}Co_{0.2}Fe_{0.8}O_{3-\delta}$–$Gd_{0.2}Ce_{0.8}O_{2-\delta}$ composite cathodes by breath figures method for solid oxide fuel cells," *Applied Surface Science,* Article vol. 258, no. 1, pp. 50-57, Oct 2011.

[59] F. Zhao, Z. Wang, M. Liu, L. Zhang, C. Xia, and F. Chen, "Novel nano-network cathodes for solid oxide fuel cells," *Journal of Power Sources,* vol. 185, no. 1, pp. 13-18, Oct 15 2008.

[60] X. Zhu, D. Ding, Y. Li, Z. Lû, W. Su, and L. Zhen, "Development of $La_{0.6}Sr_{0.4}Co_{0.2}Fe_{0.8}O_{3-\delta}$ cathode with an improved stability via $La_{0.8}Sr_{0.2}MnO_3$-film impregnation," *International Journal of Hydrogen Energy,* vol. 38, no. 13, pp. 5375-5382, 2013.

[61] X. Zhu, Z. Lû, and L. Zhen, "Preparation of LSM-Nano-Film via a Water-Based Impregnation Process and Its Application onto Porous LSCF Cathode," *Journal of the Electrochemical Society,* vol. 160, no. 9, pp. F905-F909, 2013.

[62] S. P. Jiang, "Nanoscale and nano- structured electrodes of solid oxide fuel cells by infiltration: Advances and challenges," *International Journal of Hydrogen Energy,* vol. 37, no. 1, pp. 449-470, 2011.

[63] Z. Liu *et al.*, "Electrochemical behaviors of infiltrated (La, Sr)MnO_3 and Y_2O_3–ZrO_2 nanocomposite layer," *International Journal of Hydrogen Energy,* Article vol. 42, no. 8, pp. 5360-5365, 2017.

[64] H. Dai, S. He, H. Chen, S. Yu, and L. Guo, "Performance enhancement for solid oxide fuel cells using electrolyte surface modification," *Journal of Power Sources,* vol. 280, pp. 406-409, 2015.

[65] M. Shah, J. D. Nicholas, and S. A. Barnett, "Prediction of infiltrated solid oxide fuel cell cathode polarization resistance," *Electrochemistry Communications,* vol. 11, no. 1, pp. 2-5, 2009.

[66] C. W. Tanner, K. Z. Fung, and A. V. Virkar, "The Effect of Porous Composite Electrode Structure on Solid Oxide Fuel Cell Performance: I. Theoretical Analysis," *Journal of The Electrochemical Society,* vol. 144, no. 1, p. 21, 1997/01/01 1997.

[67] J. D. Nicholas, L. Wang, A. V. Call, and S. A. Barnett, "Use of the Simple Infiltrated Microstructure Polarization Loss Estimation (SIMPLE) model to describe the performance of nano-composite solid oxide fuel cell cathodes," *Physical Chemistry Chemical Physics,* Article vol. 14, no. 44, pp. 15379-15392, 2012.

[68] R. Küngas , F. Bidrawn, E. Mahmoud, J. M. Vohs, and R. J. Gorte, "Evidence of surface-reaction rate limitations in SOFC composite cathodes," *Solid State Ionics,* vol. 225, pp. 146-150, 2012.

[69] W. Wang, M. D. Gross, J. M. Vohs, and R. J. Gorte, "The stability of LSF-YSZ electrodes prepared by infiltration," *Journal of the Electrochemical Society,* vol. 154, no. 5, pp. B439-B445, 2007.

[70] Baijnath, P. Tiwari, and S. Basu, "Fabrication and electrochemical performance of $La_{0.5}Sr_{0.5}CoO_3$ impregnated porous YSZ cathode," *Ionics,* pp. 1-9, 2017.

[71] Y. Y. Huang, J. M. Vohs, and R. J. Gorte, "An examination of LSM-LSCo mixtures for use in SOFC cathodes," *Journal of the Electrochemical Society,* vol. 153, no. 6, pp. A951-A955, 2006.

[72] F. Bidrawn, S. Lee, J. M. Vohs, and R. J. Gorte, "The effect of Ca, Sr, and Ba doping on the ionic conductivity and cathode performance of $LaFeO_3$" *Journal of the Electrochemical Society,* vol. 155, no. 7, pp. B660-B665, 2008.

[73] J. Chen, Y. Liu, B. Chi, J. Pu, and J. Li, "Electrocatalytic performance enhancement of $La_{0.6}Sr_{0.4}Co_{0.2}Fe_{0.8}O_{3-\delta}$-$Y_2O_3$ stabilized ZrO_2 cathodes prepared by an impregnation technique," *Journal of Power Sources,* Article vol. 256, pp. 312-318, 2014.

[74] H. Fan, M. Keane, N. Li, D. Tang, P. Singh, and M. Han, "Electrochemical stability of $La_{0.6}Sr_{0.4}Co_{0.2}Fe_{0.8}O_{3-\delta}$-infiltrated YSZ oxygen electrode for reversible solid oxide fuel cells," *International Journal of Hydrogen Energy,* vol. 39, no. 26, pp. 14071-14078, 2014.

[75] J. Ju, Y. Xie, Z. Wang, Y. Zhang, and C. Xia, "Electrical Performance of Nano-Structured $La_{0.6}Sr_{0.4}Co_{0.2}Fe_{0.8}O_{3-\delta}$ Impregnated onto Yttria-Stabilized Zirconia Backbone," *Journal of the Electrochemical Society,* vol. 163, no. 5, pp. F393-F400, 2016.

[76] Y. Zhou *et al.*, "Performance and degradation of metal-supported solid oxide fuel cells with impregnated electrodes," *International Journal of Hydrogen Energy,* vol. 39, no. 5, pp. 2279-2285, 2014.

[77] G. Yang, W. Zhou, M. Liu, and Z. Shao, "Enhancing Electrode Performance by Exsolved Nanoparticles: A Superior Cobalt-Free Perovskite Electrocatalyst for Solid Oxide Fuel Cells," *ACS Applied Materials and Interfaces,* Article vol. 8, no. 51, pp. 35308-35314, Dec 28 2016.

[78] Y. Liu *et al.*, "Performance stability and degradation mechanism of $La_{0.6}Sr_{0.4}Co_{0.2}Fe_{0.8}O_{3-\delta}$ cathodes under solid oxide fuel cells operation conditions," *International Journal of Hydrogen Energy,* Article vol. 39, no. 28, pp. 15868-15876, 2014.

[79] T. E. Burye and J. D. Nicholas, "Improving $La_{0.6}Sr_{0.4}Co_{0.8}Fe_{0.2}O_{3-\delta}$ infiltrated solid oxide fuel cell cathode performance through precursor solution desiccation," *Journal of Power Sources,* vol. 276, pp. 54-61, 2015.

[80] Y. Liu, F. Wang, B. Chi, J. Pu, L. Jian, and S. P. Jiang, "A stability study of impregnated LSCF-GDC composite cathodes of solid oxide fuel cells," *Journal of Alloys and Compounds,* vol. 578, pp. 37-43, 2013.

[81] M. Shah, P. W. Voorhees, and S. A. Barnett, "Time-dependent performance changes in LSCF-infiltrated SOFC cathodes: The role of nano-particle coarsening," *Solid State Ionics,* vol. 187, no. 1, pp. 64-67, 2011.

[82] Y. Liu, J. Bi, B. Chi, J. Pu, and L. Jian, "Effects of impregnating palladium on catalytic performance of LSCF-GDC composite cathodes for intermediate temperature solid oxide fuel cells," *International Journal of Hydrogen Energy,* Article vol. 41, no. 15, pp. 6486-6492, 2016.

[83] Y. Liu *et al.*, "Effects of oxygen partial pressure on the performance stability of impregnated $La_{0.6}Sr_{0.4}Co_{0.2}Fe_{0.8}O_{3-\delta}$-$Sm_{0.2}Ce_{0.8}O_2$ cathodes of solid oxide fuel cells," *Fuel Processing Technology,* vol. 135, pp. 203-206, Jul 2015.

[84] M. Shah and S. A. Barnett, "Solid oxide fuel cell cathodes by infiltration of $La_{0.6}Sr_{0.4}Co_{0.2}Fe_{0.8}O_{3-\delta}$ into Gd-Doped Ceria," *Solid State Ionics,* vol. 179, no. 35, pp. 2059-2064, 2008.

[85] A. J. Samson *et al.*, "Durability and Performance of High Performance Infiltration Cathodes," *Fuel Cells,* Article vol. 13, no. 4, pp. 511-519, 2013.

[86] Y. Tan *et al.*, "High-performance oxygen electrode for reversible solid oxide cells with power generation and hydrogen production at intermediate temperature," *International Journal of Hydrogen Energy,* vol. 42, no. 7, pp. 4456-4464, 2017.

[87] C. Nicollet, A. Flura, V. Vibhu, A. Rougier, J.-M. Bassat, and J.-C. Grenier, "An innovative efficient oxygen electrode for SOFC: Pr_6O_{11} infiltrated into Gd-doped ceria backbone," *International Journal of Hydrogen Energy,* vol. 41, no. 34, pp. 15538-15544, 2016/09/14/ 2016.

[88] C. Nicollet *et al.*, "Preparation and characterization of $Pr_2NiO_{4+\delta}$ infiltrated into Gd-doped ceria as SOFC cathode," *Journal of Solid State Electrochemistry,* vol. 20, no. 7, pp. 2071-2078, 2016.

[89] P. Kim-Lohsoontorn, Y.-M. Kim, N. Laosiripojana, and J. Bae, "Gadolinium doped ceria-impregnated nickel-yttria stabilised zirconia cathode for solid oxide electrolysis cell," *International Journal of Hydrogen Energy,* vol. 36, no. 16, pp. 9420-9427, Aug 2011.

[90] S. A. Muhammed Ali, M. Anwar, N. Ashikin, A. Muchtar, and M. R. Somalu, "Influence of oxygen ion enrichment on optical, mechanical, and electrical properties of LSCF perovskite nanocomposite," *Ceramics International,* vol. 44, no. 9, pp. 10433-10442, 2018/06/15/ 2018.

[91] F. Zhou *et al.*, "Effects of cerium doping on the performance of LSCF cathodes for intermediate temperature solid oxide fuel cells," *International Journal of Hydrogen Energy,* Article vol. 43, no. 41, pp. 18946-18954, Oct 2018.

[92] X. Xu, Z. Jiang, X. Fan, and C. Xia, "LSM-SDC electrodes fabricated with an ion-impregnating process for SOFCs with doped ceria electrolytes," *Solid State Ionics,* vol. 177, no. 19-25, pp. 2113-2117, 2006.

[93] R. Tian, J. Fan, Y. Liu, and C. Xia, "Low-temperature solid oxide fuel cells with $La_{1-x}Sr_xMnO_3$ as the cathodes," *Journal of Power Sources,* vol. 185, no. 2, pp. 1247-1251, 2008.

[94] R. Chiba, F. Yoshimura, Y. Sakurai, Y. Tabata, and M. Arakawa, "A study of cathode materials for intermediate temperature SOFCs prepared by the sol-gel method," *Solid State Ionics,* vol. 175, no. 1-4, pp. 23-27, 2004.

[95] S. P. Yoon *et al.*, "Performance of anode-supported solid oxide fuel cell with $La_{0.85}Sr_{0.15}MnO_3$ cathode modified by sol-gel coating technique," *Journal of Power Sources,* vol. 106, no. 1-2, pp. 160-166, 2002.

[96] J. Li, J. Shi, H. Nie, Z. Zhan, and S. Wang, "Improvement of a GDC-based composite cathode for intermediate-temperature solid oxide fuel cells," *Journal of Electroceramics,* Article vol. 32, no. 4, pp. 339-343, 2014.

[97] R. Kiebach *et al.*, "Infiltration of SOFC Stacks: Evaluation of the Electrochemical Performance Enhancement and the Underlying Changes in the Microstructure," *Fuel Cells,* vol. 16, no. 1, pp. 80-88, 2016.

[98] S. U. Rehman, R. H. Song, J. W. Lee, T. H. Lim, S. J. Park, and S. B. Lee, "Effect of GDC addition method on the properties of LSM-YSZ composite cathode support for solid oxide fuel cells," *Ceramics International,* vol. 42, no. 10, pp. 11772-11779, 2016.

[99] A. Wang *et al.*, "Promoted electrochemical performance of intermediate temperature solid oxide fuel cells with $Pd_{0.95}Mn_{0.05}O$-infiltrated $(La_{0.8}Sr_{0.2})_{0.95}MnO_{3-\delta}$ -$Y_{0.16}Zr_{0.84}O_2$ composite cathodes," *Journal of Power Sources,* vol. 303, pp. 137-141, 2016.

[100] Y. Cheng, A. S. Yu, X. Li, T.-S. Oh, J. M. Vohs, and R. J. Gorte, "Preparation of SOFC Cathodes by Infiltration into LSF-YSZ Composite Scaffolds," *Journal of the Electrochemical Society,* vol. 163, no. 2, pp. F54-F58, 2016.

[101] S. L. Zhang, C. J. Li, C. X. Li, G. J. Yang, K. Huang, and M. L. Liu, "Liquid plasma sprayed nano-network $La_{0.4}Sr_{0.6}Co_{0.2}Fe_{0.8}O_3/Ce_{0.8}Gd_{0.2}O_2$ composite as a high-performance cathode for intermediate-temperature solid oxide fuel cells," *Journal of Power Sources,* Article vol. 327, pp. 622-628, Sep 2016.

[102] H. Gregor, *Fuel Cell Technology Handbook* (Handbook Series for Mechanical Engineering). Boca Raton, Fla: CRC Press, 2003.

[103] H. Y. Tu and U. Stimming, "Advances, aging mechanisms and lifetime in solid-oxide fuel cells," *Journal of Power Sources,* Article; Proceedings Paper vol. 127, no. 1-2, pp. 284-293, Mar 2004.

[104] S. P. Jiang, "Development of lanthanum strontium cobalt ferrite perovskite electrodes of solid oxide fuel cells - A review," *International Journal of Hydrogen Energy,* vol. 44, no. 14, pp. 7448-7493, Mar 15 2019.

[105] A. Mineshige *et al.*, "Introduction of A-site deficiency into La0.6Sr0.4Co0.2Fe0.8O3–δ and its effect on structure and conductivity," *Solid state ionics,* vol. 176, no. 11-12, pp. 1145-1149, 2005.

[106] Z.-P. Li, M. Toshiyuki, G. J. Auchterlonie, J. Zou, and D. John, "Mutual Diffusion Occurring at the Interface between La 0.6 Sr 0.4 Co 0.8 Fe 0.2 O 3 Cathode and Gd-doped Ceria Electrolyte during IT-SOFC Cell Preparation," *ACS applied materials & interfaces,* vol. 3, no. 7, pp. 2772-2778, 2011.

[107] F. Wang *et al.*, "Evaluation of Sulfur Dioxide Poisoning for LSCF Cathodes," *Fuel Cells,* vol. 13, no. 4, pp. 520-525, 2013.

[108] D. Oh, D. Gostovic, and E. Wachsman, "Mechanism of $La_{0.6}Sr_{0.4}Co_{0.2}Fe_{0.8}O_3$ cathode degradation," *Journal of Materials Research,* vol. 27, no. 15, pp. 1992-1999, 2012.

[109] R. Kiebach *et al.*, "Stability of $La_{0.6}Sr_{0.4}Co_{0.2}Fe_{0.8}O_3/Ce_{0.9}Gd_{0.1}O_2$ cathodes during sintering and solid oxide fuel cell operation," *Journal of Power Sources,* vol. 283, pp. 151-161, 2015/06/01/ 2015.

[110] F. Paloukis *et al.*, "Insights into the Surface Reactivity of Cermet and Perovskite Electrodes in Oxidizing, Reducing, and Humid Environments," *ACS Applied Materials and Interfaces,* Article vol. 9, no. 30, pp. 25265-25277, 2017.

[111] H. Kwon, W. Lee, and J. W. Han, "Suppressing cation segregation on lanthanum-based perovskite oxides to enhance the stability of solid oxide fuel cell cathodes," *RSC Adv.,* vol. 6, no. 74, pp. 69782-69789, 2016 2016.

[112] L. Zhao, J. Drennan, C. Kong, S. Amarasinghe, and S. P. Jiang, "Insight into surface segregation and chromium deposition on La0.6Sr0.4Co0.2Fe0.8O3- delta cathodes of solid oxide fuel cells," *Journal of materials chemistry. A, Materials for energy and sustainability,* vol. 2, no. 29, pp. 11114-11123, 2014.

[113] S.-P. Jiang, J.-P. Zhang, L. Apateanu, and K. Foger, "Deposition of chromium species on Sr-doped LaMnO3 cathodes in solid oxide fuel cells," *Electrochemistry communications,* vol. 1, no. 9, pp. 394-397, 1999.

[114] T. Zhang, W. G. Fahrenholtz, S. T. Reis, and R. K. Brow, "Borate Volatility from SOFC Sealing Glasses," *Journal of the American Ceramic Society,* vol. 91, no. 8, pp. 2564-2569, 2008.

[115] C. C. Wang, K. Chen, and S. P. Jiang, "Sulfur Deposition and Poisoning of La0.6Sr0.4Co0.2Fe0.8O3-δ Cathode Materials of Solid Oxide Fuel Cells," *J. Electrochem. Soc,* vol. 161, no. 12, pp. F1133-F1139, 2014.

[116] C. C. Wang *et al.*, "Effect of SO2 Poisoning on the Electrochemical Activity of La0.6Sr0.4Co0.2Fe0.8O3-δ Cathodes of Solid Oxide Fuel Cells," *J. Electrochem. Soc,* vol. 164, no. 6, pp. F514-F524, 2017.

[117] Y. Chen *et al.*, "A highly active, CO_2-tolerant electrode for the oxygen reduction reaction," *Energy & Environmental Science,* vol. 11, no. 9, pp. 2458-2466, Sep 1 2018.

[118] Y. L. Huang, C. Pellegrinelli, and E. D. Wachsman, "Fundamental Impact of Humidity on SOFC Cathode ORR," *J. Electrochem. Soc,* vol. 163, no. 3, pp. F171-F182, 2016.

[119] H. Chen *et al.*, "Improving the Electrocatalytic Activity and Durability of the $La_{0.6}Sr_{0.4}Co_{0.2}Fe_{0.8}O_{3-\delta}$ Cathode by Surface Modification," *Acs Applied Materials & Interfaces,* vol. 10, no. 46, pp. 39785-39793, Nov 21 2018.

[120] K. Chen *et al.*, "Nb and Pd co-doped La0.57Sr0.38Co0.19Fe0.665Nb0.095Pd0.05O3-δ as a stable, high performance electrode for barrier-layer-free Y2O3-ZrO2 electrolyte of solid oxide fuel cells," *Journal of power sources,* vol. 378, pp. 433-442, 2018.

[121] H. Ding, A. V. Virkar, M. Liu, and F. Liu, "Suppression of Sr surface segregation in $La_{1-x}Sr_xCo_{1-y}Fe_y O_{3-\delta}$: a first principles study," *Phys. Chem. Chem. Phys.,* vol. 15, no. 2, pp. 489-496, 2012.

[122] J. Ascolani-Yael, A. Montenegro-Hernández, H. Troiani, L. Mogni, and A. Caneiro, "Study of the Rate Limiting Steps and Degradation of a GDC Impregnated $La_{0.6}Sr_{0.4}Co_{0.8}Fe_{0.2}O_{3-\delta}$ Cathode," *ECS Meeting Abstracts,* 2017.

[123] L. Nie, M. Liu, Y. Zhang, and M. Liu, "$La_{0.6}Sr_{0.4}Co_{0.2}Fe_{0.8}O_{3-\delta}$ cathodes infiltrated with samarium-doped cerium oxide for solid oxide fuel cells," *Journal of Power Sources,* vol. 195, no. 15, pp. 4704-4708, 2010.

[124] M. Liu, D. Ding, K. Blinn, X. Li, L. Nie, and M. Liu, "Enhanced performance of LSCF cathode through surface modification," *International Journal of Hydrogen Energy,* vol. 37, no. 10, pp. 8613-8620, May 2012.

[125] D. Ding *et al.*, "Efficient Electro-Catalysts for Enhancing Surface Activity and Stability of SOFC Cathodes," *Advanced Energy Materials,* vol. 3, no. 9, pp. 1149-1154, 2013.

[126] M. E. Lynch *et al.*, "Enhancement of $La_{0.6}Sr_{0.4}Co_{0.2}Fe_{0.8}O_{3-\delta}$ durability and surface electrocatalytic activity by $La_{0.85}Sr_{0.15}MnO_{3-\delta}$ investigated using a new test electrode platform," *Energy Environ. Sci.,* vol. 4, no. 6, pp. 2249-2258, 2011.

[127] Z. Liu, M. Liu, L. Yang, and M. Liu, "LSM-infiltrated LSCF cathodes for solid oxide fuel cells," *Journal of Energy Chemistry,* vol. 22, no. 4, pp. 555-559, 2013/07/01/ 2013.

[128] J. J. Choi, W. Qin, M. Liu, and M. Liu, "Preparation and Characterization of $(La_{0.8}Sr_{0.2})_{0.95}MnO_{3-\delta}$ (LSM) Thin Films and LSM/LSCF Interface for Solid Oxide Fuel Cells," *Journal of the American Ceramic Society,* vol. 94, no. 10, pp. 3340-3345, 2011.

[129] S.-i. Lee *et al.*, "High performance air electrode for solid oxide regenerative fuel cells fabricated by infiltration of nano-catalysts," *Journal of Power Sources,* vol. 250, pp. 15-20, 2014.

[130] X. Lou, Z. Liu, S. Wang, Y. Xiu, C. P. Wong, and M. Liu, "Controlling the morphology and uniformity of a catalyst-infiltrated cathode for solid oxide fuel cells by tuning wetting property," *Journal of Power Sources,* vol. 195, no. 2, pp. 419-424, 2010.

[131] X. Lou, S. Wang, Z. Liu, L. Yang, and M. Liu, "Improving $La_{0.6}Sr_{0.4}Co_{0.2}Fe_{0.8}O_{3-\delta}$ cathode performance by infiltration of a $Sm_{0.5}Sr_{0.5}CoO_{3-\delta}$ coating," *Solid State Ionics,* vol. 180, no. 23, pp. 1285-1289, 2009.

[132] F. Si, G. Zhang, and K. Huang, "Communication-Improving Intermediate-Temperature Performance of a Screen-Printed LSCF Cathode with Infiltrated LSCF Nanoparticles," *Journal of the Electrochemical Society,* vol. 163, no. 7, pp. F626-F628, 2016.

[133] B.-Y. Chang and S.-M. Park, "Electrochemical Impedance Spectroscopy," in *Annual Review of Analytical Chemistry, Vol 3*, vol. 3, E. S. Yeung and R. N. Zare, Eds. (Annual Review of Analytical Chemistry, 2010, pp. 207-229.

[134] S. Khan, S. M. A. Rizvi, and S. Urooj, "Equivalent circuit modelling using electrochemical impedance spectroscopy for different materials of SOFC," in *2016 3rd International Conference on Computing for Sustainable Global Development (INDIACom)*, 2016, pp. 1563-1567.

[135] M. P. Carpanese *et al.*, "Understanding the electrochemical behaviour of LSM-based SOFC cathodes. Part I — Experimental and electrochemical," (in English), *Solid State Ionics,* vol. 301, pp. 106-115, 2017.

[136] F. S. Baumann, J. Fleig, H.-U. Habermeier, and J. Maier, "Impedance spectroscopic study on well-defined (La,Sr)(Co,Fe)O3−δ model electrodes," *Solid State Ionics,* vol. 177, no. 11, pp. 1071-1081, 2006/04/01/ 2006.

[137] F. Bidrawn, R. Kûngas, J. M. Vohs, and R. J. Gorte, "Modeling Impedance Response of SOFC Cathodes Prepared by Infiltration," *Journal of the Electrochemical Society,* vol. 158, no. 5, pp. B514-B525, 2011 2011.

[138] A. Lasia, "Electrochemical impedance spectroscopy and its applications," in *Modern aspects of electrochemistry*: Springer, 2002, pp. 143-248.

[139] M. E. Orazem, *Electrochemical impedance spectroscopy*. Hoboken, N.J.: Hoboken, N.J. : Wiley, c2008, 2008.

[140] C. Endler-Schuck, J. Joos, C. Niedrig, A. Weber, and E. Ivers-Tiffee, "The chemical oxygen surface exchange and bulk diffusion coefficient determined by impedance spectroscopy of porous $La_{0.58}Sr_{0.4}Co_{0.2}Fe_{0.8}O_{3-\delta}$ (LSCF) cathodes," *Solid State Ionics,* Article vol. 269, pp. 67-79, Jan 2015.

[141] D. R. Askeland, *The science and engineering of materials*, Seventh edition / Donald R. Askeland, Wendelin J. Wright.

SI edition / SI edition prepared by D.K. Bhattacharya, Raj P. Chhabra. ed. Australia: Cengage Learning, 2016, 2016.

[142] Y. Leng, *Materials characterization [electronic resource] : introduction to microscopic and spectroscopic methods*, Second edition. ed. Weinheim, Germany

Weinheim: Weinheim, Germany : Wiley-VCH Verlag GmbH, 2013, 2013.

[143] M. Leoni, "Introduction to Diffraction Methods," in *Materials Characterization*, vol. 10: ASM International, 2019, p. 0.

[144] M. Leoni, "X-Ray Powder Diffraction[1]," in *Materials Characterization*, vol. 10: ASM International, 2019, p. 0.

[145] Y. N. Picard, "Scanning Electron Microscopy," in *Materials Characterization*, vol. 10: ASM International, 2019, p. 0.

[146] R. F. Egerton, *Physical principles of electron microscopy : an introduction to TEM, SEM, and AEM*. New York, NY: New York, NY : Springer, c2005, 2005.

[147] Y. B. Yoo *et al.*, "Solution-processed high-k HfO_2 gate dielectric processed under softening temperature of polymer substrates," *Journal of Materials Chemistry C,* vol. 1, no. 8, pp. 1651-1658, 2013 2013.

[148] K. Jiang, J. T. Anderson, K. Hoshino, D. Li, J. F. Wager, and D. A. Keszler, "Low-Energy Path to Dense HfO_2 Thin Films with Aqueous Precursor," *Chemistry of Materials,* vol. 23, no. 4, pp. 945-952, Feb 22 2011.

[149] Y. Sakitou, A. Hirano, K. Hanai, T. Matsumura, N. Imanishi, and Y. Takeda, "LSCF-Ag Composite Cathode for Reduced-temperature SOFCs," *ECS Transactions,* vol. 7, no. 1, p. 1305, 2007/05/25 2007.

[150] V. A. C. Haanappel, A. Mai, and J. Mertens, "Electrode activation of anode-supported SOFCs with LSM- or LSCF-type cathodes," *Solid state ionics,* vol. 177, no. 19, pp. 2033-2037, 2006.

[151] D. S. Gyan, R. Gupta, and P. K. Roy, "Comparison of GDC electrolyte-LSCF cathode IT-SOFC system with conventional power sources," in *2015 International Conference on Energy Economics and Environment (ICEEE)*, 2015, pp. 1-6.

[152] C. Xia, "Electrolytes," in *Solid Oxide Fuel Cells*(Green Chemistry and Chemical Engineering: CRC Press, 2008, pp. 1-71.

[153] C. R. Xia and M. L. Liu, "A simple and cost-effective approach to fabrication of dense ceramic membranes on porous substrates," *Journal of the American Ceramic Society,* Article vol. 84, no. 8, pp. 1903-1905, Aug 2001.

[154] L. Zhang, F. Liu, K. Brinkman, K. L. Reifsnider, and A. V. Virkar, "A study of gadolinia-doped ceria electrolyte by electrochemical impedance spectroscopy," *Journal of Power Sources,* vol. 247, pp. 947-960, 2014/02/01/ 2014.

[155] L. Zhang, F. Liu, and A. V. Virkar, "Investigation of Electrolyte and Electrode Effects on GDC Electrolyte by Electrochemical Impedance Spectroscopy," *ECS Meeting Abstracts,* 2012.

[156] C. Fu, K. Sun, N. Zhang, X. Chen, and D. Zhou, "Electrochemical characteristics of LSCF–SDC composite cathode for intermediate temperature SOFC," *Electrochimica Acta,* vol. 52, no. 13, pp. 4589-4594, 2007/03/20/ 2007.

[157] F. Qiang, K. Sun, N. Zhang, X. Zhu, S. Le, and D. Zhou, "Characterization of electrical properties of GDC doped A-site deficient LSCF based composite cathode using impedance spectroscopy," *Journal of Power Sources,* vol. 168, no. 2, pp. 338-345, 2007.

[158] L. Zhao, S. Amarasinghe, and S. P. Jiang, "Enhanced chromium tolerance of La0.6Sr0.4Co0.2Fe0.8O3−δ electrode of solid oxide fuel cells by Gd0.1Ce0.9O1.95 impregnation," *Electrochemistry Communications,* vol. 37, pp. 84-87, 2013/12/01/ 2013.

[159] D. Marinha, L. Dessemond, J. S. Cronin, J. R. Wilson, S. A. Barnett, and E. Djurado, "Microstructural 3D Reconstruction and Performance Evaluation of LSCF Cathodes Obtained by Electrostatic Spray Deposition," *Chem. Mater,* vol. 23, no. 24, pp. 5340-5348, 2011.

[160] J.-W. Lee *et al.*, "Preparation of dense and uniform $La_{0.6}Sr_{0.4}Co_{0.2}Fe_{0.8}O_{3-\delta}$ (LSCF) films for fundamental studies of SOFC cathodes," *Journal of Power Sources,* vol. 190, no. 2, pp. 307-310, 2009/05/15/ 2009.

[161] N. Grunbaum, L. Dessemond, J. Fouletier, F. Prado, L. Mogni, and A. Caneiro, "Rate limiting steps of the porous La0.6Sr0.4Co0.8Fe0.2O3−δ electrode material," *Solid State Ionics,* vol. 180, no. 28, pp. 1448-1452, 2009/11/12/ 2009.

[162] H. Zhao, L. Huo, L. Sun, L. Yu, S. Gao, and J. Zhao, "Preparation, chemical stability and electrochemical properties of LSCF–CBO composite cathodes," *Materials Chemistry and Physics,* vol. 88, no. 1, pp. 160-166, 2004/11/15/ 2004.

[163] I. Gamry Instruments. (2019, 10/01/2023). *Quality of Your Fit in EIS* [Online aplication note]. Available: https://www.gamry.com/application-notes/EIS/fit-in-eis/

[164] A. Arregui, L. M. Rodriguez-Martinez, S. Modena, M. Bertoldi, J. van Herle, and V. M. Sglavo, "Stability of ferritic perovskite cathodes in anode-supported solid oxide fuel cells under different processing and operation parameters," *Electrochimica acta,* vol. 58, no. 1, pp. 312-321, 2011.

[165] B. Koo, K. Kim, J. K. Kim, H. Kwon, J. W. Han, and W. Jung, "Sr Segregation in Perovskite Oxides: Why It Happens and How It Exists," *Joule,* vol. 2, no. 8, pp. 1476-1499, Aug 15 2018.

[166] M. Finsterbusch, A. Lussier, J. A. Schaefer, and Y. U. Idzerda, "Electrochemically driven cation segregation in the mixed conductor $La_{0.6}Sr_{0.4}Co_{0.2}Fe_{0.8}O_{3-\delta}$," *Solid State Ionics,* Article vol. 212, pp. 77-80, Mar 2012.

[167] S. Hwang *et al.*, "Infiltrated thin film structure with hydrogel-mediated precursor ink for durable SOFCs," *Scientific Reports,* vol. 11, no. 1, p. 7109, 2021/03/29 2021.

[168] M. A. S. A, M. Anwar, N. F. Raduwan, A. Muchtar, and M. R. Somalu, "Optical, mechanical and electrical properties of LSCF–SDC composite cathode prepared by sol–gel assisted rotary evaporation technique," *Journal of Sol-Gel Science and Technology,* vol. 86, no. 2, pp. 493-504, 2018/05/01 2018.

[169] A. P. Jamale, C. H. Bhosale, and L. D. Jadhav, "Electrochemical behavior of LSCF/GDC interface in symmetric cell: An application in solid oxide fuel cells," *Journal of Alloys and Compounds,* vol. 623, pp. 136-139, 2015/02/25/ 2015.

[170] B. X. Huang, J. Malzbender, R. W. Steinbrech, E. Wessel, H. J. Penkalla, and L. Singheiser, "Mechanical aspects of ferro-elastic behavior and phase composition of $La_{0.58}Sr_{0.4}Co_{0.2}Fe_{0.8}O_{3-\delta}$," *Journal of Membrane Science,* vol. 349, no. 1-2, pp. 183-188, Mar 1 2010.

[171] B. X. Huang, R. W. Steinbrech, and J. Malzbender, "Direct observation of ferroelastic domain effects in LSCF perovskites," *Solid State Ionics,* vol. 228, pp. 32-36, Nov 30 2012.

[172] W. Araki and J. Malzbender, "Ferroelastic deformation of $La_{0.58}Sr_{0.4}Co_{0.2}Fe_{0.8}O_{3-\delta}$ under uniaxial compressive loading," *Journal of the European Ceramic Society,* vol. 33, no. 4, pp. 805-812, Apr 2013.

[173] R. I. Tomov *et al.*, "The synergistic effect of cobalt oxide and Gd-CeO_2 dual infiltration in LSCF/CGO cathodes," *Journal of Materials Chemistry A,* vol. 6, no. 12, pp. 5071-5081, Mar 28 2018.

[174] J. I. Langford and A. J. C. Wilson, "SCHERRER AFTER 60 YEARS - SURVEY AND SOME NEW RESULTS IN DETERMINATION OF CRYSTALLITE SIZE," *Journal of Applied Crystallography,* Article vol. 11, no. APR, pp. 102-113, 1978.

[175] A. V. Call, J. G. Railsback, H. Wang, and S. A. Barnett, "Degradation of nano-scale cathodes: a new paradigm for selecting low-temperature solid oxide cell materials," *Physical Chemistry Chemical Physics,* vol. 18, no. 19, pp. 13216-13222, May 21 2016.

[176] J. F. Roeder *et al.*, "Group IVA Oxide Surface Modification of LSCF Cathode Powders by Atomic Layer Deposition," in *Solid Oxide Fuel Cells 15*, vol. 78, S. C. Singhal and T. Kawada, Eds. (ECS Transactions, no. 1), 2017, pp. 935-942.

[177] B. Aguirre *et al.*, "Growth, microstructure and electrical properties of sputter-deposited hafnium oxide (HfO2) thin films grown using a HfO2 ceramic target," *Applied Surface Science,* vol. 257, no. 6, pp. 2197-2202, 2011/01/01/ 2011.

10 Annex A – LSCF/GDC/LSCF cells

10.1 EIS data plots

10.1.1 Batch A

(a) ECM

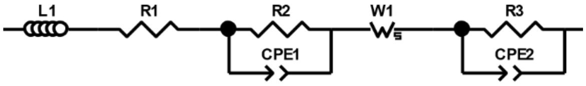

(b) A1

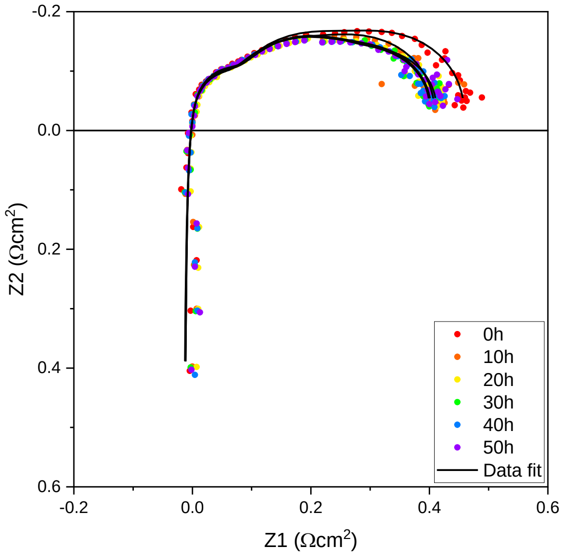

(c) A2

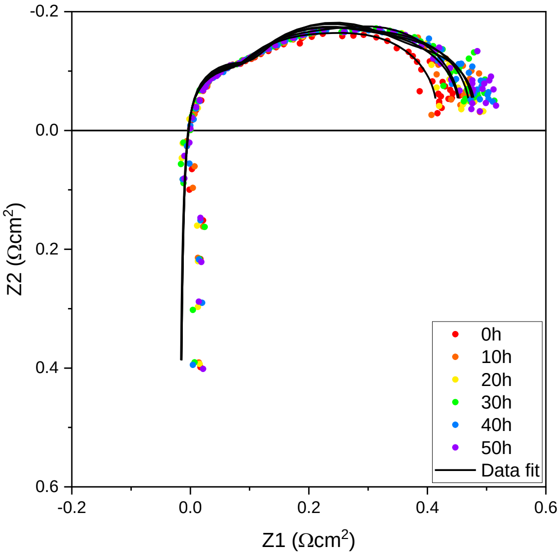

(d) A3

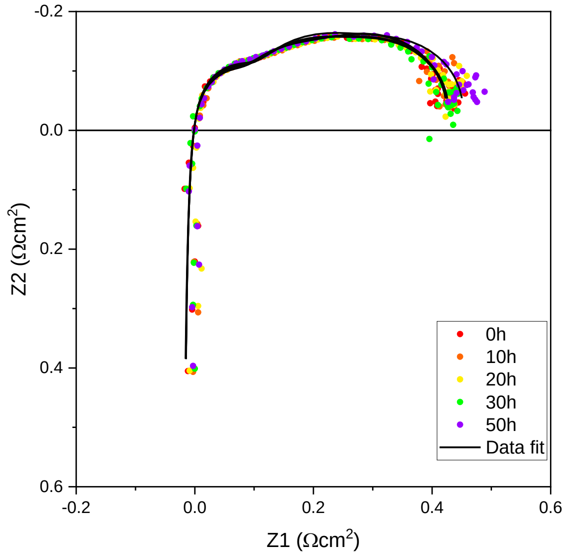

10.1.2 Batch B, set 1

(a) Electrical circuit model

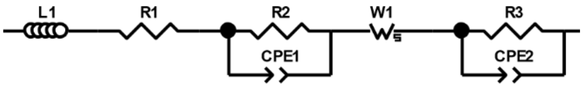

(b) B1

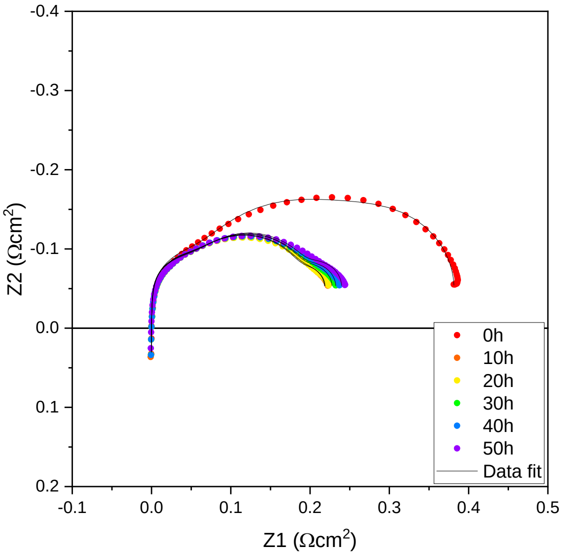

(c) B2

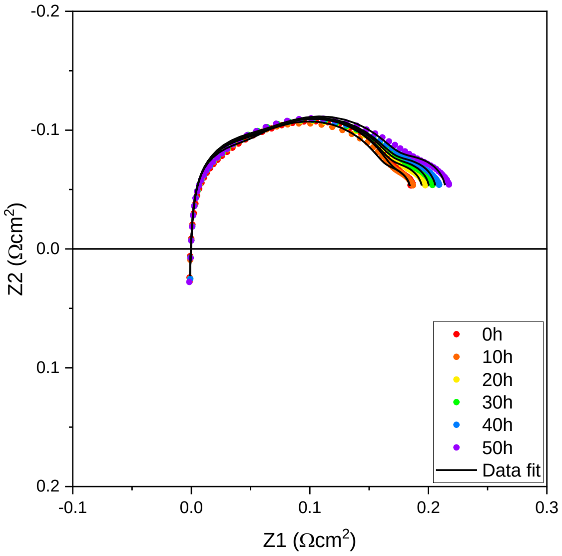

(d) B3

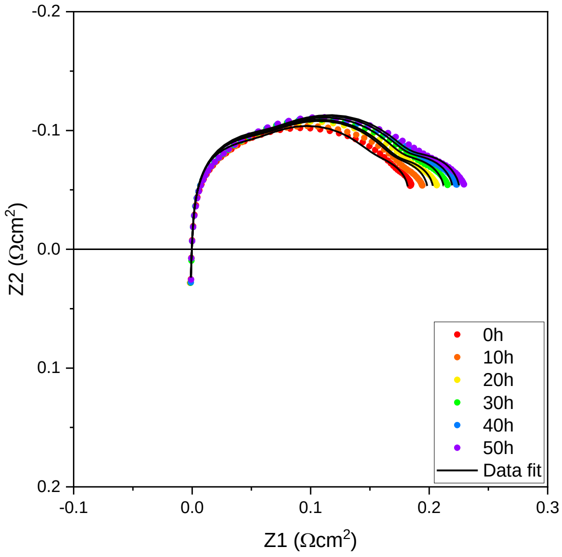

10.1.3 Batch B, set 2

(a) Electrical circuit model

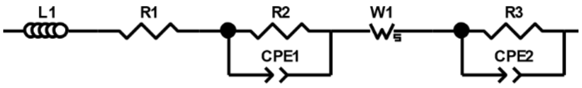

(b) B4

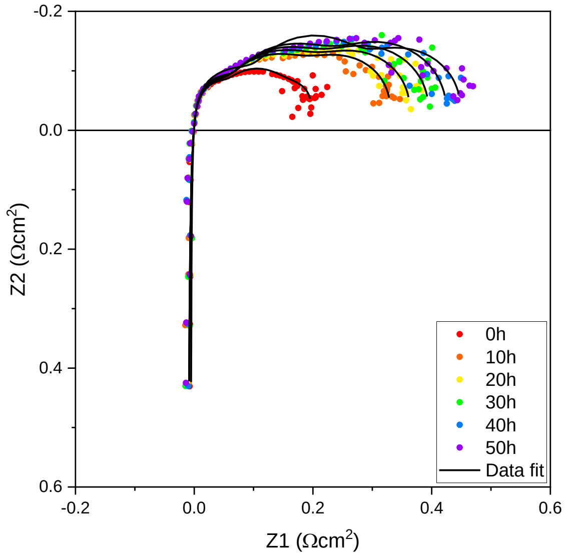

(c) B5

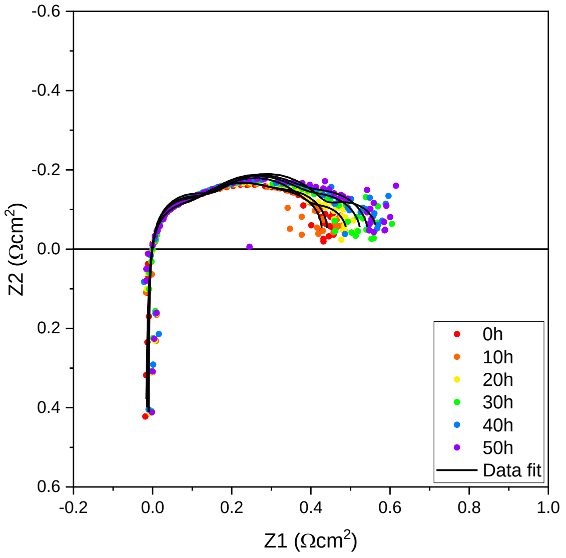

(d) B6

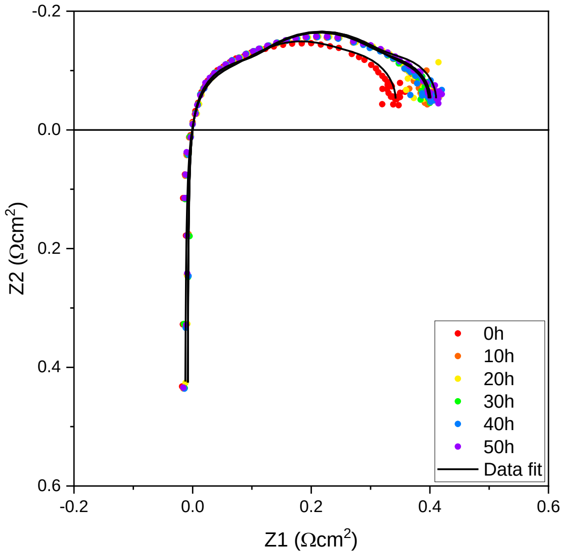

(e) B7

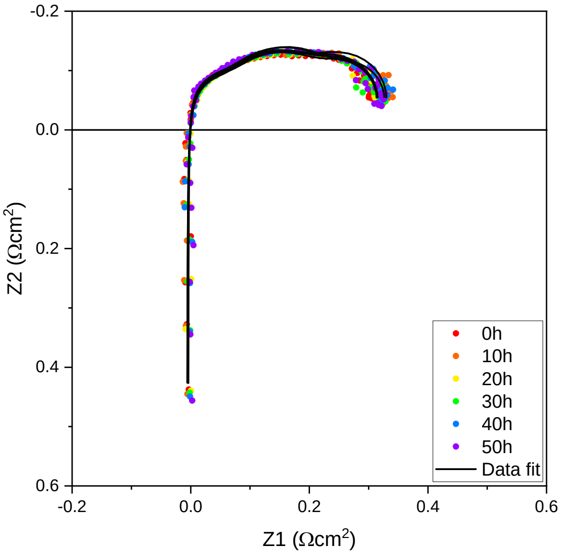

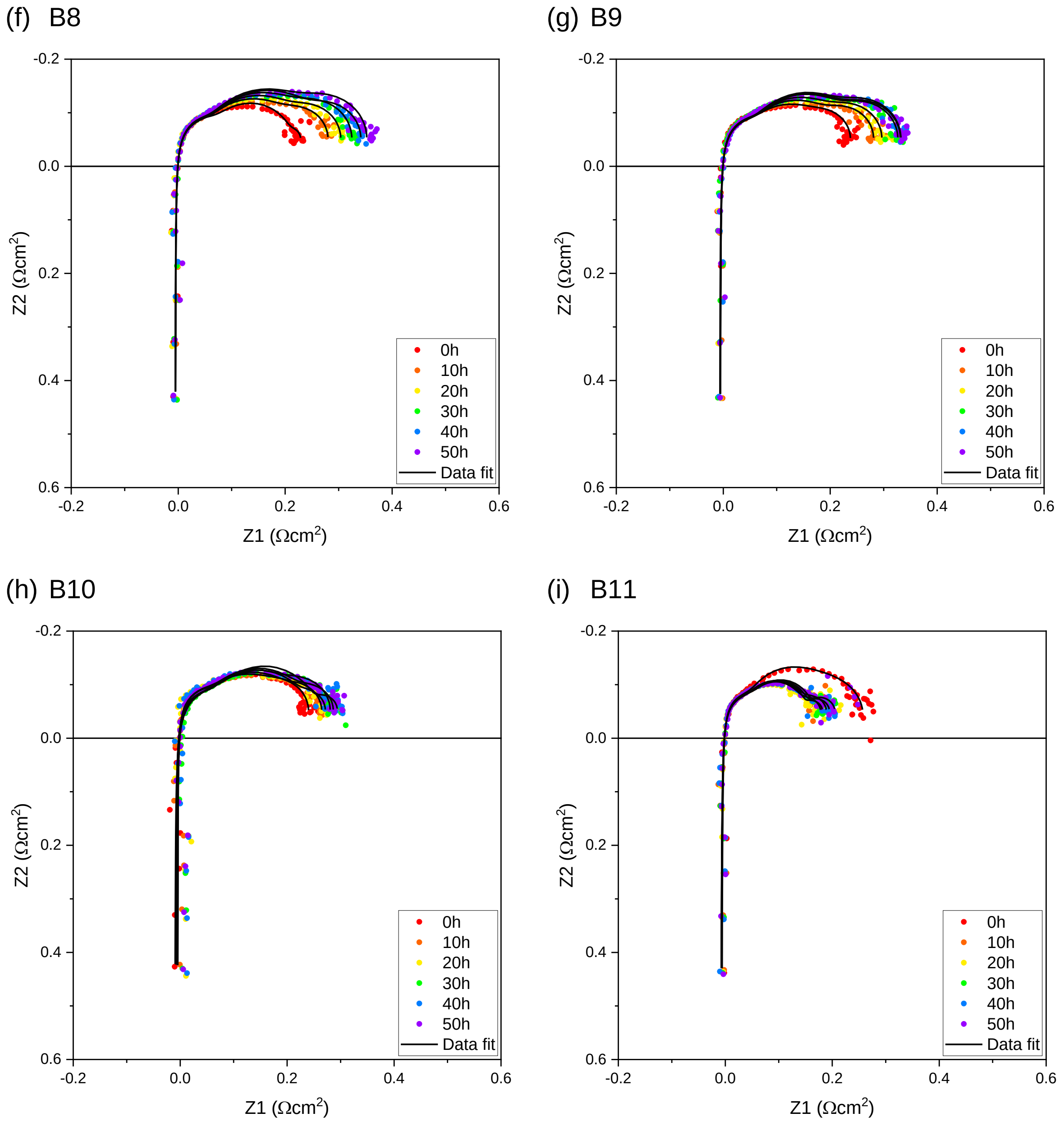
(f) B8

(g) B9

(h) B10

(i) B11

10.1.4 Batch B, set 3

(a) ECM

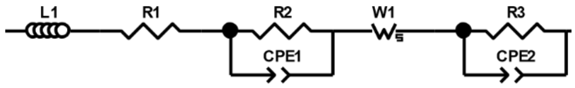

(b) B12

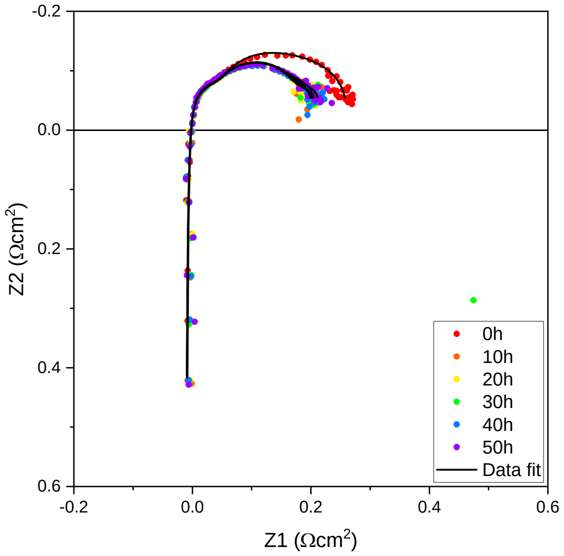

(c) B13

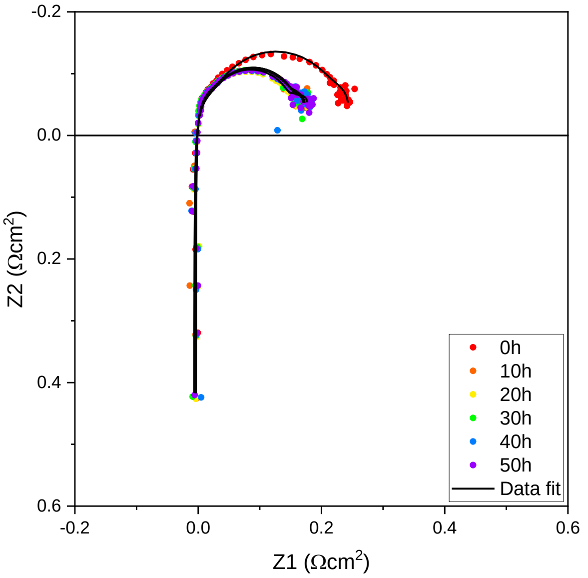

(d) B14

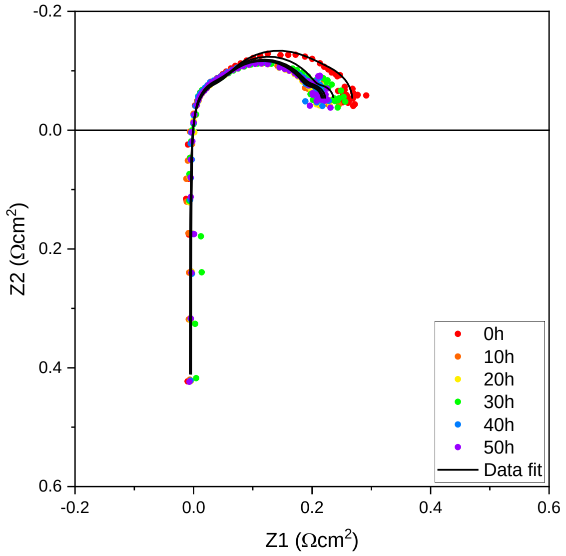

10.1.5 Batch C

(a) ECM

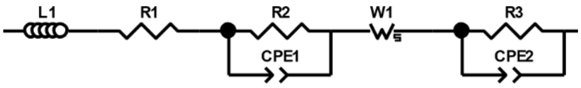

(b) C1

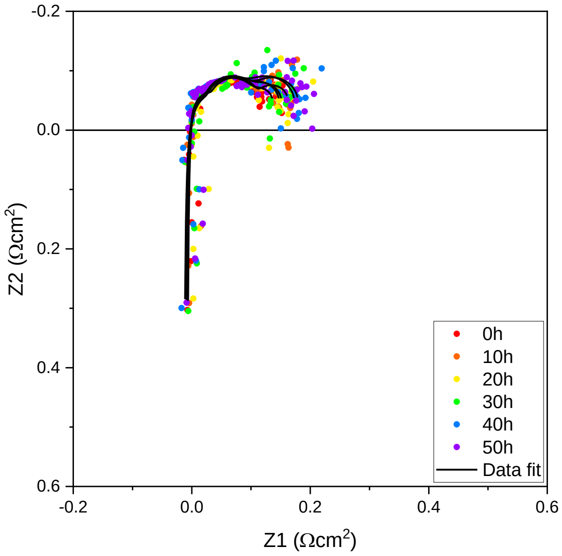

(c) C2

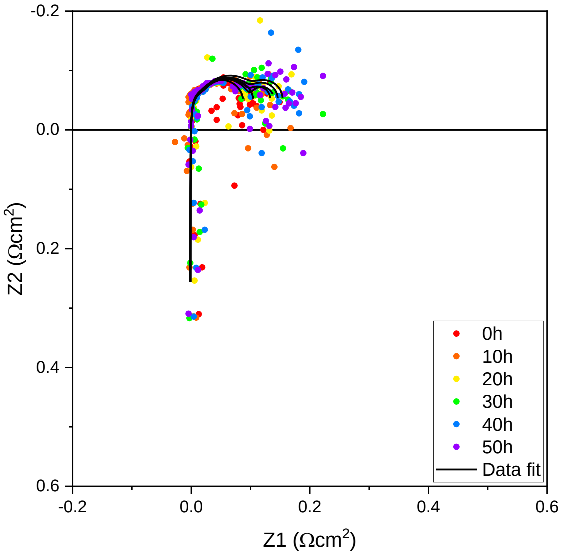

10.2 Rp and Rs monitoring against time

10.2.1 Batch A

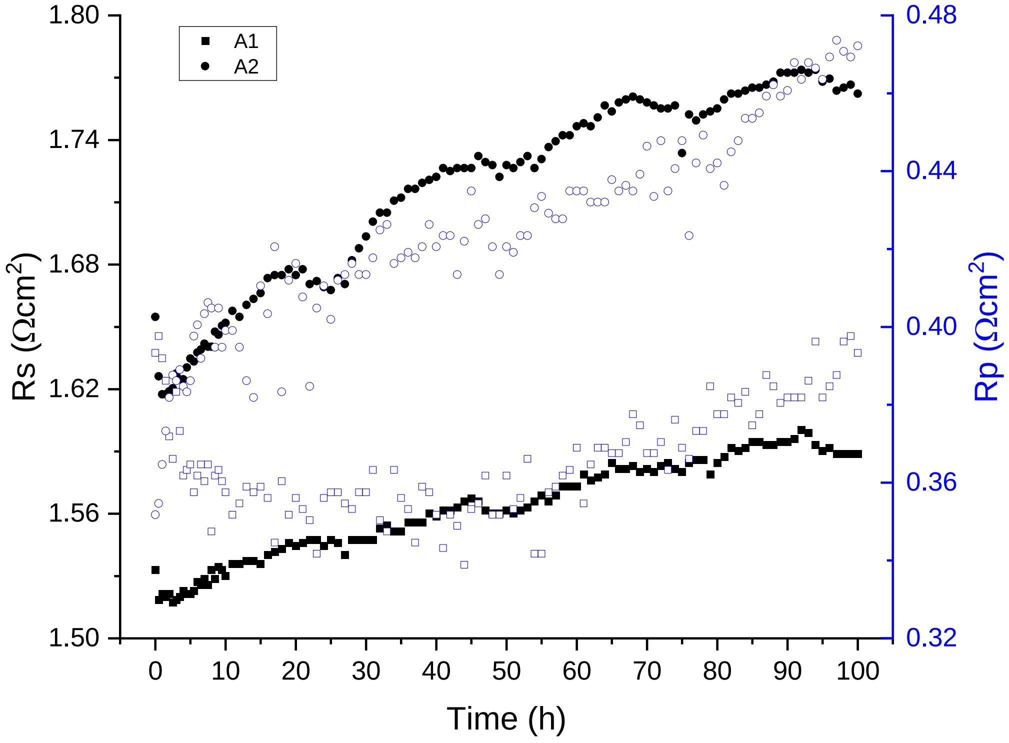

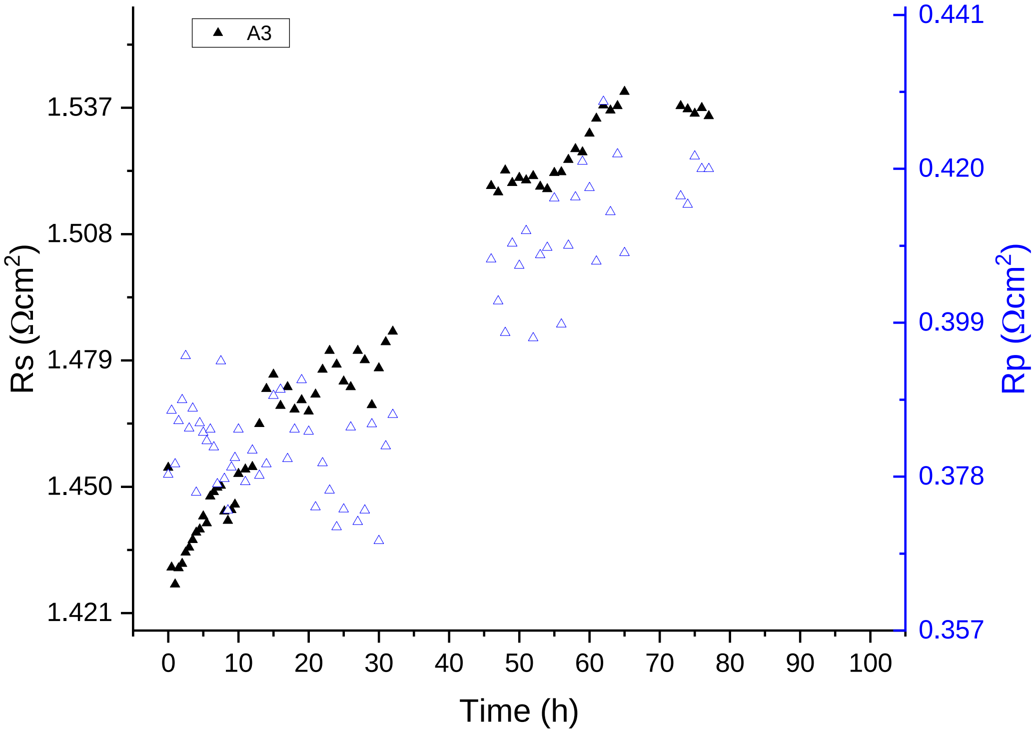

10.2.2 Batch B, set 1

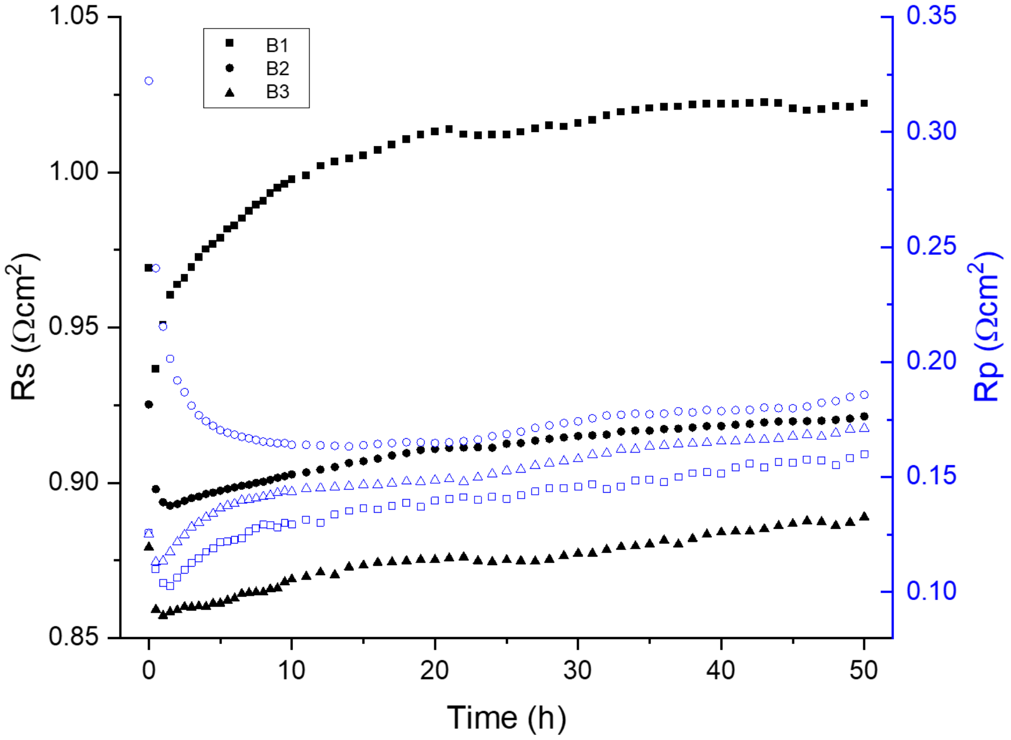

10.2.3 Batch B, set 2

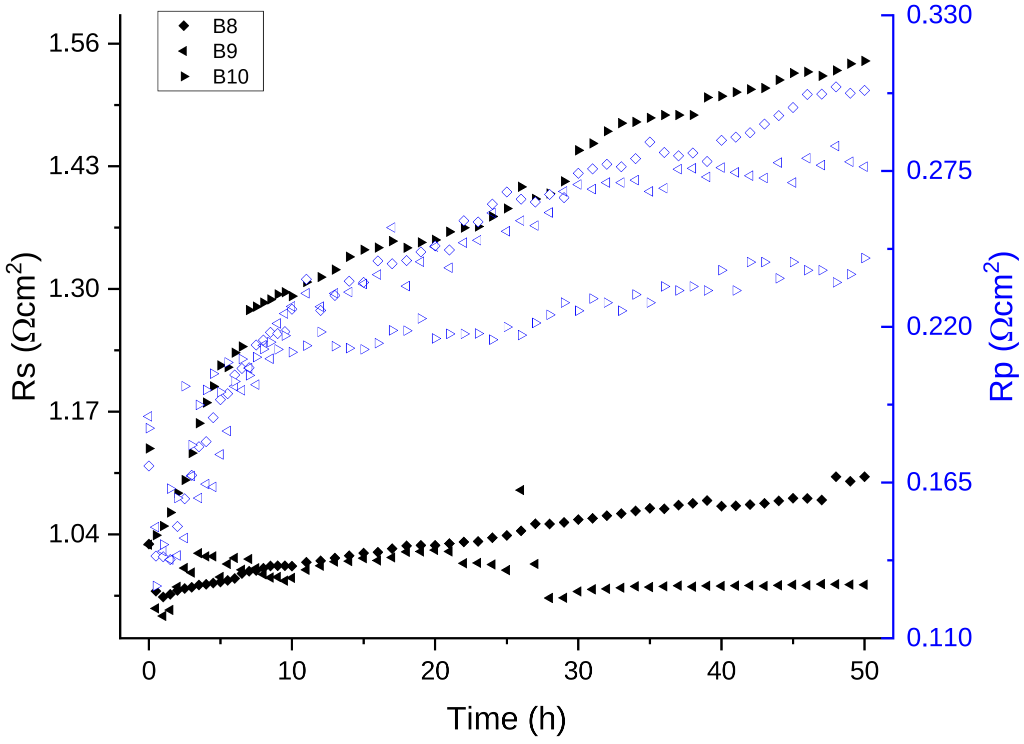

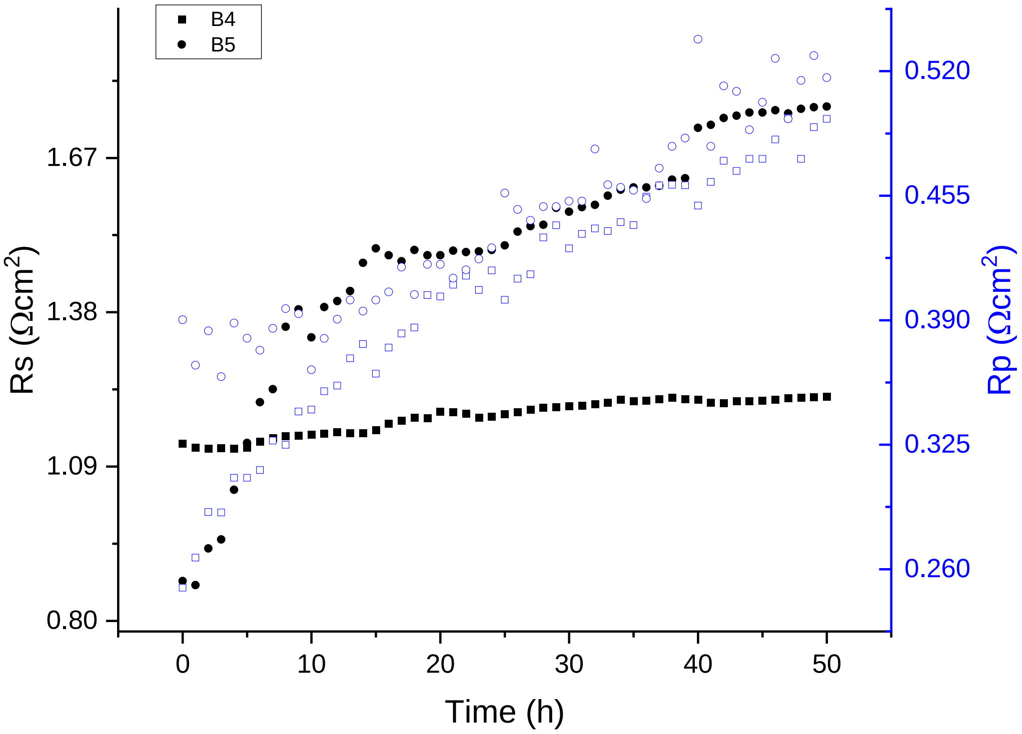
B4
B5
Rs (Ωcm²)
1.67
1.38
1.09
0.80
Rp (Ωcm²)
0.520
0.455
0.390
0.325
0.260
0
10
20
30
40
50
Time (h)

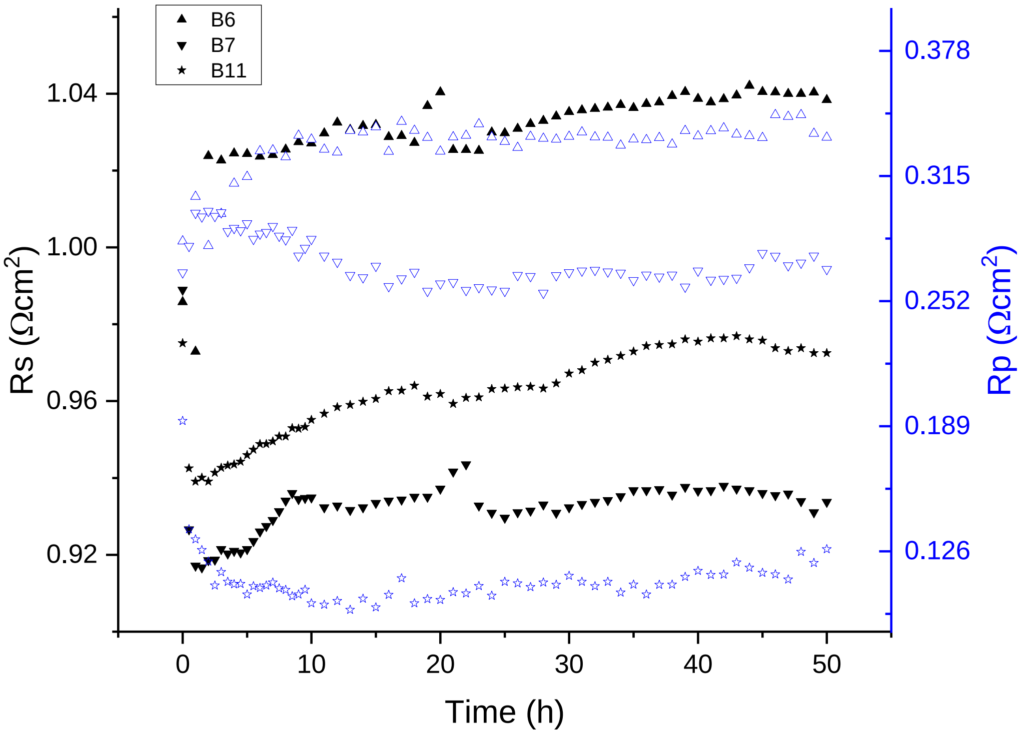
B6
B7
B11
Rs (Ωcm²)
1.04
1.00
0.96
0.92
Rp (Ωcm²)
0.378
0.315
0.252
0.189
0.126
0
10
20
30
40
50
Time (h)

10.2.4 Batch B, set 3

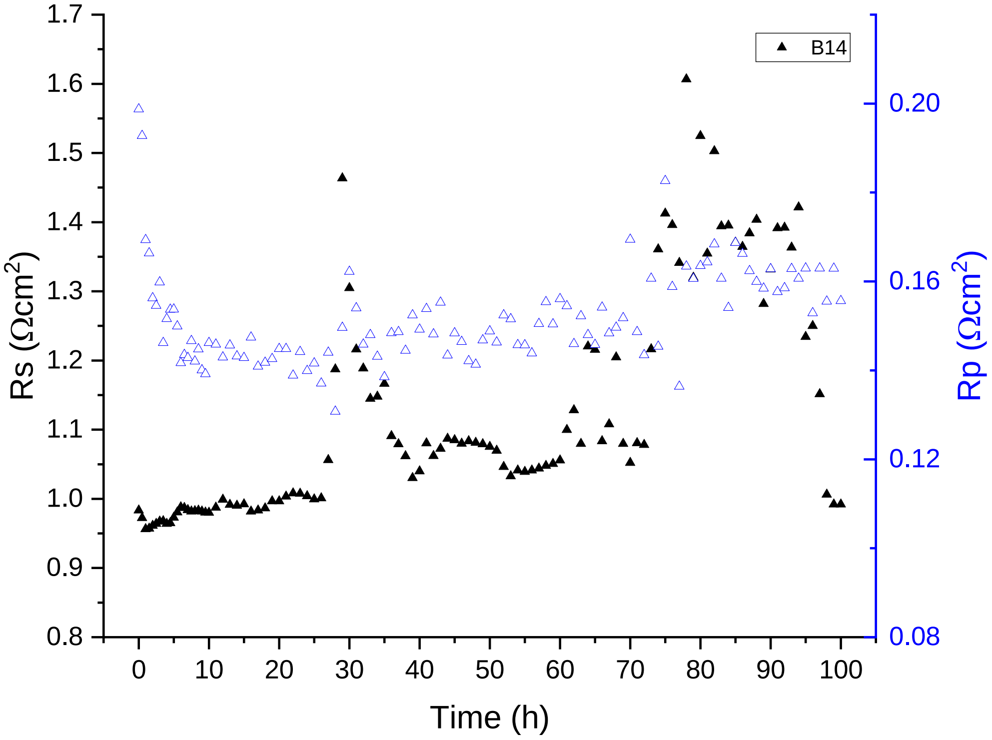

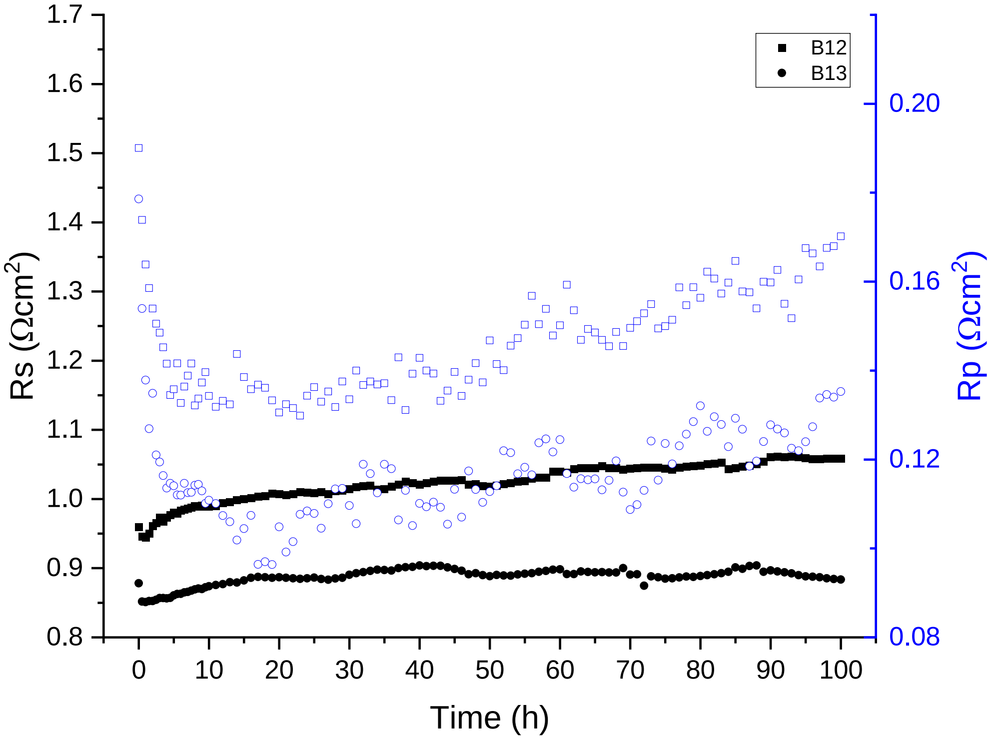

10.2.5 Batch C

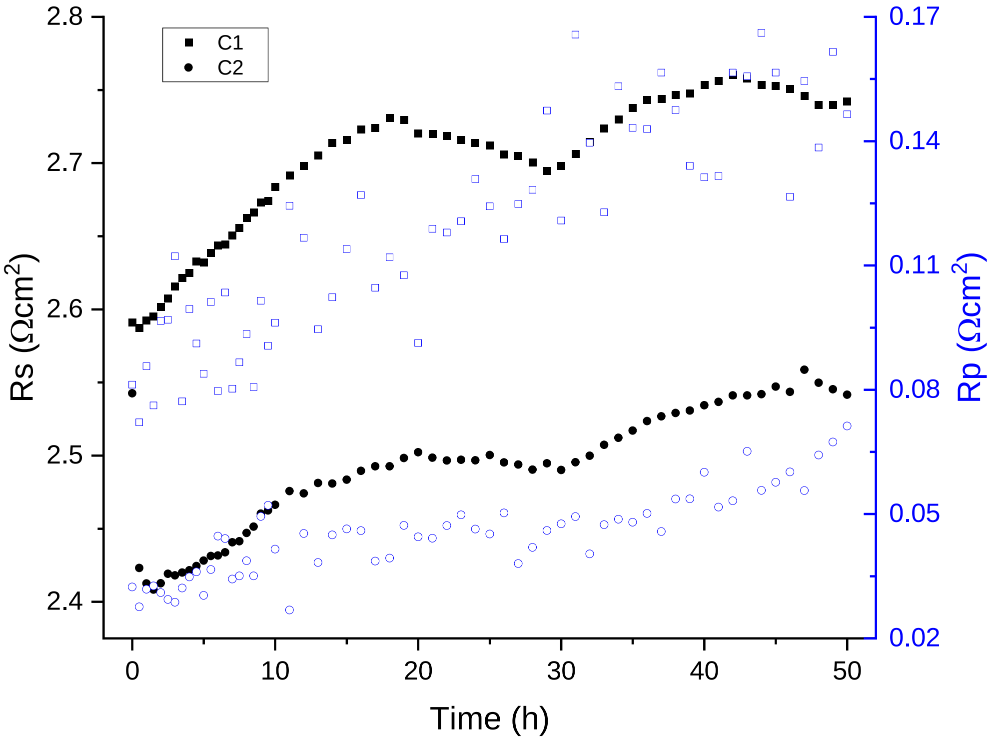
Rs (Ωcm^2)
2.8
2.7
2.6
2.5
2.4
Rp (Ωcm^2)
0.17
0.14
0.11
0.08
0.05
0.02
Time (h)
0
10
20
30
40
50
■ C1
● C2

10.3 ECM fitting results

10.3.1 Batch A

Sample	Date	14/05/2021																			
PC1	Chi-Sqr	Sum-Sqr	**L**	R1	%error	R2	%error	CPE1-T	%error	W-R	%error	W-T	%error	R3	%error	CPE2-T	%error	**Rs**	**%error**	**Rp**	**%error**
0h	1.25E-03	0.00352	4.97E-06	10.9	0.18172	1.298	7.3725	1.74E-03	9.2206	0.64206	7.071	1.51E-04	14.296	1.379	7.7078	1.13E-02	16.608	1.510035	0.18172	0.423307	7.383767
10h	2.38E-03	0.00568	4.97E-06	10.91	0.23437	1.074	14.021	1.63E-03	15.83	0.58636	11.577	1.38E-04	21.605	1.305	13.141	7.88E-03	26.603	1.511468	0.23437	0.372604	12.913
20h	1.28E-03	0.00313	4.97E-06	11	0.16762	1.343	7.374	1.79E-03	8.7258	0.64368	6.9911	1.70E-04	13.844	0.93825	11.797	1.65E-02	24.762	1.52437	0.16762	0.366808	8.7207
30h	1.06E-03	0.00262	4.97E-06	11.02	0.15347	1.39	6.0638	1.82E-03	7.4809	0.65503	6.0115	1.70E-04	12.181	0.87081	10.741	1.98E-02	22.993	1.527237	0.15347	0.365505	7.605433
40h	1.07E-03	0.00258	4.97E-06	11.12	0.1517	1.305	6.742	1.77E-03	8.5644	0.63261	6.8159	1.73E-04	13.212	0.97022	10.217	1.57E-02	21.547	1.541572	0.1517	0.364357	7.924967
50h	1.48E-03	0.00383	4.97E-06	11.13	0.18132	1.426	6.0395	1.90E-03	9.1875	0.67111	7.3156	1.94E-04	14.663	0.88889	10.742	2.39E-02	24.062	1.543005	0.18132	0.375563	8.032367
60h	0.00102	0.00254	4.97E-06	11.23	0.14856	1.319	6.2594	0.0018	8.7403	0.64309	6.9079	1.87E-04	13.201	1.025	9.114	0.01593	19.511	1.55734	0.14856	0.375719	7.4271
70h	0.00113	0.00291	4.97E-06	11.26	0.16012	1.359	5.8461	0.0018	8.6625	0.65398	6.8111	1.79E-04	13.464	1.029	8.62	0.0179	19.041	1.561641	0.16012	0.383587	7.0924
80h	0.00155	0.00401	4.97E-06	11.26	0.19392	1.241	8.5979	0.00168	11.554	0.63526	8.7064	1.58E-04	16.823	1.19	10.106	0.01194	21.602	1.561641	0.19392	0.387068	9.136767
90h	0.00166	0.00431	4.97E-06	11.34	0.19694	1.309	8.0932	0.0017	11.355	0.66531	8.5704	1.69E-04	16.593	1.183	10.089	0.01325	21.793	1.573109	0.19694	0.40012	8.917533
100h	0.00181	0.00476	4.97E-06	11.31	0.20338	1.326	8.6508	0.00182	11.841	0.66503	9.0808	1.87E-04	17.482	1.165	11.111	0.01424	23.813	1.568808	0.20338	0.399936	9.6142

Sample	Date	01/06/2021																			
PC2	Chi-Sqr	Sum-Sqr	**L**	R1	%error	R2	%error	CPE1-T	%error	W-R	%error	W-T	%error	R3	%error	CPE2-T	%error	**Rs**	**%error**	**Rp**	**%error**
0h	1.90E-03	0.00446	4.97E-06	10.25	0.22632	0.93256	11.28	1.20E-03	16.521	0.74947	8.1994	9.22E-05	14.804	1.453	8.3723	5.12E-03	17.637	1.416857	0.22632	0.396926	9.2839
10h	1.92E-03	0.00468	4.97E-06	10.23	0.22154	1.134	11.332	1.39E-03	12.562	0.82651	6.8038	1.16E-04	12.968	1.168	12.431	8.07E-03	25.31	1.41399	0.22154	0.395991	10.18893
20h	1.78E-03	0.0042	4.97E-06	10.38	0.21015	1.12	11.204	1.30E-03	12.923	0.82532	7.0233	1.15E-04	12.93	1.199	11.965	7.16E-03	24.205	1.435493	0.21015	0.398258	10.0641
30h	2.74E-03	0.00632	4.97E-06	10.43	0.26549	0.96751	13.795	1.18E-03	19.994	0.74981	10.404	9.88E-05	18.334	1.404	11.081	5.23E-03	23.038	1.44266	0.26549	0.394961	11.76
50h	1.66E-03	0.00426	4.97E-06	10.74	0.20695	1.297	9.1889	1.46E-03	10.37	0.85971	6.0372	1.28E-04	11.964	1.157	11.496	1.03E-02	23.958	1.487099	0.20695	0.42254	8.907367
60h	0.00185	0.0049	4.97E-06	10.83	0.21786	1.494	7.7851	0.00158	9.0581	0.90321	5.6175	1.42E-04	11.692	0.94178	13.563	0.01713	29.121	1.5	0.21786	0.426164	8.988533

PC3	Chi-Sqr	Sum-Sqr	**L**	R1	%error	R2	%error	CPE1-T	%error	W-R	%error	W-T	%error	R3	%error	CPE2-T	%error	**Rs**	**%error**	**Rp**	**%error**
0h	1.46E-03	0.00307	4.97E-06	11.71	0.17705	1.106	12.851	1.43E-03	11.814	0.6831	7.804	1.20E-04	14.636	1.258	12.745	6.66E-03	24.804	1.626148	0.17705	0.384321	11.13333
10h	2.32E-03	0.00549	4.97E-06	11.71	0.22777	1.472	11.359	1.65E-03	10.329	0.76518	7.6615	1.48E-04	15.815	1.073	17.074	1.31E-02	34.63	1.626148	0.22777	0.422034	12.0315
20h	1.97E-03	0.00456	4.97E-06	11.85	0.22074	1.113	12.451	1.32E-03	14.227	0.67493	9.2636	1.07E-04	17.817	1.543	10.15	5.82E-03	20.842	1.646217	0.22074	0.425008	10.62153
30h	1.76E-03	0.00443	4.97E-06	11.98	0.20792	1.505	8.4352	1.59E-03	8.9704	0.75379	6.7507	1.35E-04	14.313	1.179	11.753	1.33E-02	24.934	1.664853	0.20792	0.440327	8.979633
40h	1.59E-03	0.00417	4.97E-06	12.18	0.19447	1.85	4.5705	1.72E-03	6.9143	0.8425	5.4883	1.66E-04	12.1	0.8092	11.18	3.58E-02	26.392	1.693523	0.19447	0.449488	7.0796
50h	2.40E-03	0.0059	4.97E-06	12.23	0.23397	1.691	7.7765	1.65E-03	9.3034	0.78491	7.4174	1.55E-04	15.942	1.001	14.278	2.00E-02	31.332	1.70069	0.23397	0.445935	9.823967
60h	0.00247	0.00666	4.97E-06	12.35	0.24671	1.768	6.6408	0.00168	9.4768	0.82527	7.3969	1.62E-04	16.079	1.051	12.05	0.02382	27.829	1.717892	0.24671	0.469926	8.6959
70h	0.0026	0.00698	4.97E-06	12.42	0.25334	1.795	6.7588	0.00165	9.5478	0.83382	7.4878	1.60E-04	16.332	1.005	13.015	0.02484	30.021	1.727927	0.25334	0.468428	9.0872
80h	0.00231	0.00615	4.97E-06	12.39	0.24102	1.643	8.4626	0.0016	9.9956	0.79542	7.671	1.48E-04	16.392	1.248	12.136	0.01496	26.515	1.723626	0.24102	0.475968	9.4232
90h	0.00162	0.00459	4.97E-06	12.52	0.19956	2.035	3.1672	0.00182	6.5541	0.90484	5.2682	1.89E-04	11.864	0.87413	7.5425	0.06106	19.642	1.742262	0.19956	0.494252	5.325967
100h	0.00202	0.00573	4.97E-06	12.47	0.23188	1.697	6.4655	0.0016	9.3175	0.80235	7.2147	1.51E-04	15.591	1.329	8.927	0.01724	20.632	1.735094	0.23188	0.496314	7.535733

10.3.2 Batch B, set 1

Sample	Date	30/11/2020																			
126	Chi-Sqr	Sum-Sqr	**L**	R1	%error	R2	%error	CPE1-T	%error	W-R	%error	W-T	%error	R3	%error	CPE2-T	%error	**Rs**	**%error**	**Rp**	**%error**
0h	1.68E-04	4.23E-04	1.44E-06	7.09	0.05518	1.229	2.4937	0.00356	2.6261	1.061	3.6938	3.38E-02	3.2503	0.3827	3.9778	9.38E-04	3.822	0.963871	0.05518	0.330651	3.388433
10h	2.08E-04	3.24E-04	1.44E-06	7.298	0.04792	0.91863	1.4548	0.00321	3.5817	0.22566	5.3266	6.25E-02	8.6878	0.38349	3.5698	8.16E-04	3.3286	0.993688	0.04792	0.166527	3.4504
20h	1.85E-04	2.92E-04	1.44E-06	7.406	0.04555	0.90933	1.4136	0.00314	3.5248	0.2397	4.373	7.13E-02	7.6116	0.38394	3.4789	8.11E-04	3.2043	1.00917	0.04555	0.167271	3.0885
30h	1.92E-04	3.21E-04	1.44E-06	7.425	0.04739	0.92678	1.4358	0.00329	3.5725	0.27392	4.0607	7.57E-02	7.0577	0.39314	3.4901	8.26E-04	3.2813	1.011893	0.04739	0.175997	2.995533
40h	2.01E-04	3.48E-04	1.44E-06	7.469	0.04914	0.92232	1.5085	0.00335	3.7573	0.3045	3.7767	7.88E-02	6.6261	0.40009	3.5894	8.25E-04	3.3697	1.018201	0.04914	0.180737	2.9582
50h	3.27E-04	5.93E-04	1.44E-06	7.463	0.06552	0.94456	1.7742	0.00327	4.3567	0.35162	4.2685	7.77E-02	7.5092	0.38233	4.3295	7.63E-04	4.6482	1.017341	0.06552	0.188134	3.4574

Sample	Date	08/01/2021																			
125	Chi-Sqr	Sum-Sqr	**L**	R1	%error	R2	%error	CPE1-T	%error	W-R	%error	W-T	%error	R3	%error	CPE2-T	%error	**Rs**	**%error**	**Rp**	**%error**
0h	1.59E-04	2.02E-04	1.35E-06	0.04563	0.04563	0.9605	0.00197	0.00197	2.6394	0.34967	2.637	1.81E-04	4.5829	0.10849	5.521	0.31845	14.82	0.006541	0.04563	0.150884	2.71999
10h	1.65E-04	2.33E-04	1.35E-06	0.0462	0.0462	1.3643	0.0023	0.0023	3.6766	0.36674	3.4376	2.53E-04	5.2358	0.14928	4.1867	0.26169	11.252	0.006623	0.0462	0.217063	2.5422
20h	1.40E-04	2.10E-04	1.35E-06	0.04358	0.04358	0.82909	0.00229	0.00229	3.4923	0.3797	3.2721	2.67E-04	4.9197	0.18135	3.3988	0.213	9.0995	0.006247	0.04358	0.146796	2.224397
30h	1.40E-04	2.22E-04	1.35E-06	0.04449	0.04449	0.83134	0.00236	0.00236	3.6258	0.38785	3.3353	2.77E-04	4.9924	0.21309	3.0676	0.1785	8.1748	0.006378	0.04449	0.152837	2.135087
40h	1.46E-04	2.44E-04	1.35E-06	0.04613	0.04613	0.8276	0.00249	0.00249	3.8641	0.40043	3.4291	2.95E-04	5.1106	0.24228	2.8959	0.16043	7.6906	0.006613	0.04613	0.158289	2.109163
50h	1.65E-04	2.90E-04	1.35E-06	0.04973	0.04973	0.83888	0.00262	0.00262	4.2027	0.41444	3.6483	3.17E-04	5.4225	0.2741	2.8931	0.14439	7.6418	0.007129	0.04973	0.166475	2.18134

Sample	Date	12/01/2021																			
127	Chi-Sqr	Sum-Sqr	**L**	R1	%error	R2	%error	CPE1-T	%error	W-R	%error	W-T	%error	R3	%error	CPE2-T	%error	**Rs**	**%error**	**Rp**	**%error**
0h	2.10E-04	2.70E-04	1.36E-06	6.435	0.05089	0.72361	1.6058	0.0024	4.3856	0.37908	3.5164	2.26E-04	5.3472	0.20246	5.0785	9.77E-02	12.3	0.869977	0.05089	0.134613	3.400233
10h	2.06E-04	3.34E-04	1.36E-06	6.369	0.0536	0.79038	1.5577	0.00291	4.2972	0.42917	3.3136	3.07E-04	5.1163	0.19999	4.5187	1.73E-01	11.631	0.860516	0.0536	0.151011	3.13
20h	1.84E-04	3.12E-04	1.36E-06	6.413	0.05188	0.8095	1.4829	0.00279	4.0732	0.42477	3.2651	3.04E-04	5.0347	0.21812	3.7098	1.76E-01	9.7336	0.866823	0.05188	0.15572	2.819267
30h	1.89E-04	3.42E-04	1.36E-06	6.428	0.05363	0.83261	1.5063	0.00292	4.14	0.43622	3.3146	3.28E-04	5.1288	0.24638	3.4657	1.68E-01	9.0957	0.868973	0.05363	0.164725	2.7622
40h	1.83E-04	3.44E-04	1.36E-06	6.476	0.05373	0.85089	1.4788	0.0029	4.0636	0.44411	3.2584	3.32E-04	5.0676	0.27241	3.1435	1.57E-01	8.2714	0.875854	0.05373	0.172208	2.6269
50h	1.83E-04	3.55E-04	1.36E-06	6.509	0.05424	0.85572	1.5173	0.00297	4.1675	0.45691	3.2735	3.46E-04	5.0621	0.29487	2.979	1.49E-01	7.8366	0.880585	0.05424	0.177955	2.589933

10.3.3 Batch B, set 2

Sample	Date	27/02/2020																	
114	Chi-Sqr	Sum-Sqr	**L**	R1	%error	R2	%error	CPE1-T	%error	W-R	%error	W-T	%error	R3	%error	CPE2-T	%error	**Rs**	**%error**	**Rp**	**%error**
0h	3.90E-03	0.00829	5.32E-06	6.594	0.27978	0.72142	9.2989	2.75E-03	17.546	0.45024	10.774	1.63E-04	20.373	0.27778	26.817	6.15E-02	61.147	0.892769	0.27978	0.155297	15.62997
10h	1.50E-03	0.00568	5.32E-06	6.604	0.23128	0.96016	5.3026	2.49E-03	9.7683	0.46429	7.4798	1.64E-04	15.206	0.9603	5.7365	2.44E-02	13.789	0.894203	0.23128	0.289373	6.172967
20h	1.99E-03	0.0084	5.32E-06	6.607	0.27537	1.057	5.6114	2.68E-03	10.447	0.48559	8.3128	1.86E-04	17.278	1.07	5.9352	FALSE	14.551	0.894633	0.27537	0.322034	6.6198
30h	2.02E-03	0.00929	5.32E-06	6.624	0.28333	1.124	5.3574	2.92E-03	10.179	0.49915	8.3071	2.10E-04	17.477	1.208	5.2976	3.34E-02	13.206	0.89707	0.28333	0.353365	6.3207
40h	2.54E-03	0.01249	5.32E-06	6.667	0.32395	1.206	5.6616	3.12E-03	10.758	0.52752	8.8232	2.29E-04	18.919	1.308	5.5158	7.82E-04	13.963	0.903234	0.32395	0.383521	6.666867
50h	2.25E-03	0.01181	5.32E-06	6.805	0.26538	1.184	5.2218	6.44E-02	14.122	1.478	4.8603	9.47E-03	9.6016	0.50845	9.1297	CPE2-T(+)	13.25	0.923016	0.26538	0.402004	6.403933

Sample	Date	05/03/2020																			
72	Chi-Sqr	Sum-Sqr	**L**	R1	%error	R2	%error	CPE1-T	%error	W-R	%error	W-T	%error	R3	%error	CPE2-T	%error	**Rs**	**%error**	**Rp**	**%error**
0h	3.01E-03	0.01037	5.23E-06	6.275	0.31031	0.75873	7.4219	1.67E-04	8.8324	1.023	11.347	1.72E-02	13.28	1.382	6.8035	1.25E-03	9.9302	0.847041	0.31031	0.40104	8.524133
10h	0.00558	0.01306	5.23E-06	9.506	0.33688	0.74132	13.007	1.83E-04	14.95	0.89662	22.903	1.59E-02	24.283	1.422	11.509	1.25E-03	15.905	1.310205	0.33688	0.386162	15.80633
20h	1.65E-03	0.0053	5.12E-06	10.52	0.21155	0.63965	8.4338	8.21E-02	22.482	1.047	5.186	2.14E-04	10.503	1.886	3.0679	FALSE	7.7994	1.455562	0.21155	0.459659	5.562567
30h	0.00334	0.01052	5.12E-06	11.09	0.3035	0.94702	11.501	3.15E-02	28.671	0.99478	8.3297	1.89E-04	16.631	1.878	5.5527	1.12E-01	11.948	1.537271	0.3035	0.495088	8.461133
40h	0.0021	0.0074	4.91E-06	12.17	0.24438	2.059	3.3658	1.75E-03	8.8978	1.185	5.663	2.41E-04	12.034	0.87244	7.1987	2.42E-02	19.25	1.692089	0.24438	0.537611	5.409167
50h	0.0107	0.03073	4.91E-06	12.41	0.536	1.9	10.603	1.23E-03	21.272	1.008	14.743	1.55E-04	30.347	1.065	19.992	CPE2-T(+)	49.362	1.726493	0.536	0.517049	15.11267

Sample	Date	09/09/2020																			
74	Chi-Sqr	Sum-Sqr	**L**	R1	%error	R2	%error	CPE1-T	%error	W-R	%error	W-T	%error	R3	%error	CPE2-T	%error	**Rs**	**%error**	**Rp**	**%error**
0h	1.47E-03	0.00305	5.37E-06	7.046	0.17968	1.202	5.6411	8.99E-04	8.0259	0.66008	13.425	8.21E-03	12.795	0.62692	6.9349	1.60E-04	6.6831	0.957564	0.17968	0.304318	8.667
10h	0.00121	0.00347	5.37E-06	7.343	0.17146	1.535	3.2769	1.31E-03	5.8276	0.55729	10.69	2.59E-02	14.358	0.75107	4.6988	1.95E-04	5.88	1.000139	0.17146	0.355115	6.2219
20h	1.53E-03	0.00435	5.37E-06	7.436	0.19169	1.572	3.4767	1.28E-03	6.4031	0.52354	12.2	2.78E-02	16.985	0.75429	5.2197	1.94E-04	6.634	1.01347	0.19169	0.356043	6.965467
30h	9.25E-04	0.00266	5.37E-06	7.408	0.14943	1.536	2.834	1.27E-03	5.2489	0.58976	8.6847	2.60E-02	11.849	0.73867	4.3176	2.01E-04	5.2656	1.009456	0.14943	0.358136	5.278767
40h	0.00121	0.00343	5.37E-06	7.431	0.17078	1.506	3.333	1.26E-03	6.1394	0.62227	9.5322	2.46E-02	12.857	0.72682	5.0575	2.00E-04	6.1157	1.012753	0.17078	0.356797	5.974233
50h	9.04E-04	0.0027	5.37E-06	7.421	0.15184	1.528	2.8226	1.28E-03	5.2066	0.67852	7.4425	2.66E-02	10.347	0.72577	4.3	1.97E-04	5.4323	1.01132	0.15184	0.367863	4.855033

Sample	Date	01/10/2020																			
110	Chi-Sqr	Sum-Sqr	**L**	R1	%error	R2	%error	CPE1-T	%error	W-R	%error	W-T	%error	R3	%error	CPE2-T	%error	**Rs**	**%error**	**Rp**	**%error**
0h	8.63E-04	0.00257	5.36E-06	7.146	0.13953	0.9425	4.2856	2.60E-03	7.9171	0.79248	6.0419	3.18E-02	8.0324	0.50101	6.0017	3.78E-04	7.1392	0.971899	0.13953	0.268049	5.443067
10h	0.00104	0.00348	5.36E-06	6.772	0.16401	0.91624	5.0368	2.80E-03	8.4844	0.99942	5.5303	3.18E-02	7.2273	0.43459	7.1548	4.17E-04	9.0983	0.918286	0.16401	0.284428	5.9073
20h	8.71E-04	0.00278	5.36E-06	6.791	0.14413	0.98107	4.3204	2.77E-03	7.2568	0.82055	6.2223	3.30E-02	7.9493	0.44079	6.521	4.50E-04	7.9828	0.921009	0.14413	0.268969	5.6879
30h	1.26E-03	0.00389	5.36E-06	6.757	0.17338	0.96078	5.6785	2.62E-03	8.7115	0.86396	7.745	2.71E-02	9.2074	0.41248	8.3483	4.44E-04	10.101	0.916136	0.17338	0.268225	7.257267
40h	9.73E-04	0.00331	5.36E-06	6.803	0.15134	1.124	3.7846	2.90E-03	6.9877	0.71291	6.9901	4.63E-02	9.6991	0.47471	6.5632	5.07E-04	7.9823	0.92273	0.15134	0.27889	5.7793
50h	1.66E-03	0.0053	5.36E-06	6.817	0.18672	1.08	6.0452	3.06E-03	10.398	0.69694	11.604	3.68E-02	13.662	0.45215	10.54	6.37E-04	10.542	0.924737	0.18672	0.26706	9.3964

Sample	Date	02/10/2020																			
111	Chi-Sqr	Sum-Sqr	**L**	R1	%error	R2	%error	CPE1-T	%error	W-R	%error	W-T	%error	R3	%error	CPE2-T	%error	**Rs**	**%error**	**Rp**	**%error**
0h	1.82E-03	0.00386	5.28E-06	7.422	0.16939	0.95481	3.7869	2.76E-03	9.0867	0.14987	22.654	7.99E-02	42.907	0.53045	6.2	3.57E-04	8.5436	1.011463	0.16939	0.181915	10.8803
10h	7.83E-04	0.00243	5.28E-06	7.28	0.14194	0.91121	4.814	2.73E-03	7.909	0.65651	8.0489	2.92E-02	10.206	0.42934	6.7932	4.14E-04	8.5443	0.991108	0.14194	0.233798	6.552033
20h	1.14E-03	0.00328	5.28E-06	7.43	0.15637	0.99424	4.8356	2.82E-03	8.0492	0.73279	7.829	3.53E-02	10.184	0.43473	7.3305	4.40E-04	9.5754	1.01261	0.15637	0.257408	6.665033
30h	1.14E-03	0.00339	5.28E-06	7.62	0.1585	1.037	5.1628	2.81E-03	8.0043	0.83072	7.7754	3.40E-02	9.6896	0.43957	7.5936	4.44E-04	9.8644	1.039847	0.1585	0.27827	6.843933
40h	7.23E-04	0.00232	5.28E-06	7.718	0.12931	1.152	3.3149	2.87E-03	5.7681	0.79063	5.6098	4.91E-02	8.0162	0.48027	5.3291	4.28E-04	7.5227	1.053895	0.12931	0.294842	4.751267
50h	1.03E-03	0.00318	5.28E-06	7.942	0.15351	1.087	4.9495	2.75E-03	7.4985	0.98916	6.5404	3.52E-02	8.2163	0.42885	7.5975	4.48E-04	10.188	1.086005	0.15351	0.306613	6.362467

Sample	Date	08/10/2020																			
112	Chi-Sqr	Sum-Sqr	**L**	R1	%error	R2	%error	CPE1-T	%error	W-R	%error	W-T	%error	R3	%error	CPE2-T	%error	**Rs**	**%error**	**Rp**	**%error**
0h	1.61E-03	0.00313	5.33E-06	7.417	0.16106	0.7308	9.3696	2.48E-03	12.907	0.55537	16.004	1.44E-02	15.076	0.42321	10.119	3.81E-04	9.8742	1.010747	0.16106	0.192559	11.83087
10h	1.65E-03	0.00455	5.33E-06	7.195	0.18869	0.86033	6.0464	2.81E-03	10.848	0.72397	8.4736	3.19E-02	11.408	0.42218	8.7799	4.06E-04	11.381	0.978923	0.18869	0.235148	7.766633
20h	1.24E-03	0.00349	5.33E-06	7.394	0.16319	0.91859	5.4783	2.80E-03	9.1484	0.77071	7.8446	3.11E-02	9.9984	0.42343	7.9843	4.30E-04	10.15	1.007449	0.16319	0.250379	7.1024
30h	1.49E-03	0.00501	5.33E-06	7.088	0.19307	1.018	4.9808	2.94E-03	8.9562	0.85164	6.8841	4.53E-02	9.9881	0.44987	7.8207	4.27E-04	10.922	0.963584	0.19307	0.280021	6.561867
40h	8.86E-04	0.00295	5.33E-06	7.124	0.14928	1.037	3.8552	2.81E-03	6.766	0.86675	5.3656	4.25E-02	7.6546	0.4522	5.9973	4.09E-04	8.4084	0.968745	0.14928	0.285245	5.0727
50h	1.01E-03	0.00328	5.33E-06	7.125	0.15992	1.032	4.4113	2.68E-03	7.0767	0.90672	5.9454	3.58E-02	7.9645	0.42681	6.6866	4.02E-04	9.4448	0.968888	0.15992	0.286618	5.6811

Sample	Date	19/10/2020																			
109	Chi-Sqr	Sum-Sqr	**L**	R1	%error	R2	%error	CPE1-T	%error	W-R	%error	W-T	%error	R3	%error	CPE2-T	%error	**Rs**	**%error**	**Rp**	**%error**
0h	1.67E-03	0.00261	5.31E-06	8.104	0.15982	0.3889	10.499	2.85E-04	11.092	0.57315	16.899	9.45E-03	14.901	0.78775	9.5152	1.70E-03	11.26	1.109228	0.15982	0.198353	12.3044
10h	0.00126	0.00254	5.31E-06	9.302	0.14032	0.43032	7.9378	3.86E-04	10.707	0.54221	11.1	3.07E-02	14.317	0.9185	5.5109	2.68E-03	9.3293	1.280961	0.14032	0.218599	8.1829
20h	1.87E-03	0.00397	5.31E-06	9.792	0.15974	0.51661	9.3256	5.22E-04	11.308	0.38252	15.542	6.46E-02	24.304	1.03	5.4057	3.35E-03	11.865	1.351203	0.15974	0.22406	10.0911
30h	1.58E-03	0.00304	5.31E-06	10.35	0.15377	0.41153	10.224	3.96E-04	13.6	0.68709	12.023	2.66E-02	14.281	0.92099	7.3889	2.66E-03	11.215	1.431192	0.15377	0.237031	9.878633
40h	0.00176	0.00355	5.31E-06	10.85	0.15294	0.46951	11.139	5.32E-04	13.076	0.51989	12.685	5.20E-02	18.936	1.045	5.7847	2.94E-03	12.514	1.502867	0.15294	0.239151	9.869567
50h	1.25E-03	0.00292	5.31E-06	11.06	0.13684	0.52789	6.9454	4.89E-04	10.681	0.34562	10.494	2.18E-01	22.604	1.211	3.2976	3.45E-03	8.1887	1.532971	0.13684	0.246334	6.912333

Sample	Date	16/03/2021																			
2	Chi-Sqr	Sum-Sqr	**L**	R1	%error	R2	%error	CPE1-T	%error	W-R	%error	W-T	%error	R3	%error	CPE2-T	%error	**Rs**	**%error**	**Rp**	**%error**
0h	0.00287	0.00725	5.38E-06	7.051	0.23424	0.23129	18.399	9.09E-04	25.461	0.98191	17.314	0.00342	19.498	0.6429	24.548	0.01813	50.374	0.95828	0.23424	0.213592	20.087
10h	0.00288	0.00594	5.38E-06	6.916	0.21881	0.22972	18.159	8.09E-04	21.871	0.80857	6.2693	0.00249	12.154	0.27103	13.553	0.09079	36.468	0.938928	0.21881	0.135211	12.66043
20h	0.00468	0.01104	5.38E-06	6.97	0.28418	0.27792	22.044	8.92E-04	24.313	0.81037	8.2264	0.00309	14.771	0.23707	15.631	0.24238	43.259	0.946669	0.28418	0.13751	15.30047
30h	0.00173	0.00386	5.38E-06	6.999	0.17495	0.23613	14.116	8.11E-04	17.326	0.82592	4.919	0.00266	9.5895	0.32305	9.1497	0.08299	24.695	0.950826	0.17495	0.146074	9.3949
40h	0.00247	0.00635	5.38E-06	7.065	0.21616	0.27583	15.824	8.47E-04	18.907	0.84904	5.6504	0.00324	10.482	0.29364	9.5872	0.21787	26.435	0.960287	0.21616	0.150863	10.35387
50h	0.00444	0.01239	5.38E-06	7.047	0.29356	0.29639	21.281	9.39E-04	24.237	0.85426	8.0525	0.00373	14.665	0.33352	11.84	0.22301	32.428	0.957707	0.29356	0.160275	13.7245

10.3.4 Batch B, set 3

Sample	Date	10/04/2021																					
44	Chi-Sqr	Sum-Sqr	**L**	R1	%error	R2	%error	CPE1-T	%error	W-R	%error	W-T	%error	R3	%error	CPE2-T	%error	**Rs**	**%error**	**Rp**	**%error**
0h	1.11E-03	0.00277	5.22E-06	6.898	0.16705	0.95917	11.772	2.59E-03	6.1608	0.37784	6.2018	1.34E-04	13.069	0.55556	21.661	0.01979	39.881	0.936348	0.16705	0.218819	13.2116
10h	0.00224	0.00423	5.27E-06	7.112	0.20808	0.91528	6.4408	2.23E-03	8.975	0.35021	8.8216	1.27E-04	18.266	0.21742	29.893	0.0709	65.967	0.967025	0.20808	0.160095	15.0518
20h	1.67E-03	0.00347	5.27E-06	7.234	0.18727	0.94503	3.2643	2.28E-03	7.612	0.36475	7.3141	1.31E-04	15.612	0.18548	16.366	0.17806	42.713	0.984513	0.18727	0.161865	8.981467
30h	0.00121	0.00249	5.27E-06	7.291	0.15903	0.95075	3.1268	2.31E-03	6.6537	0.36141	6.4744	1.36E-04	13.702	0.18682	16.364	0.14652	41.258	0.992684	0.15903	0.162398	8.655067
40h	0.00165	0.00321	5.27E-06	7.342	0.18067	0.90092	5.3923	2.16E-03	8.4654	0.3482	8.2433	1.29E-04	16.8	0.27303	19.638	0.05783	44.24	0.999995	0.18067	0.16572	11.0912
50h	0.0013	0.00301	5.27E-06	7.336	0.16847	0.95604	2.9434	2.45E-03	7.3381	0.35614	7.3409	1.57E-04	15.377	0.24606	10.754	0.16731	28.577	0.999135	0.16847	0.170893	7.012767
60h	0.00165	0.00376	5.27E-06	7.475	0.18633	1.029	2.835	2.59E-03	7.3697	0.39599	7.1123	1.66E-04	15.306	0.18145	14.493	0.34902	39.204	1.019061	0.18633	0.177803	8.146767
70h	0.00156	0.00349	5.27E-06	7.501	0.18308	0.97734	3.2088	2.41E-03	7.7011	0.3666	7.6105	1.48E-04	16.184	0.25597	11.858	0.15077	31.248	1.022788	0.18308	0.176867	7.5591
80h	0.0014	0.00366	5.27E-06	7.549	0.18017	1.046	2.8226	2.71E-03	7.3459	0.38813	7.3504	1.85E-04	15.68	0.25931	10.258	0.25314	27.679	1.029669	0.18017	0.190274	6.810333
90h	1.05E-03	0.00251	5.27E-06	7.63	0.15229	0.99201	2.9507	2.42E-03	6.8877	0.36724	6.9118	1.64E-04	14.32	0.32565	8.9222	0.10423	23.024	1.04128	0.15229	0.18905	6.261567
100h	0.001	0.00246	5.27E-06	7.616	0.15264	0.98351	3.0384	2.42E-03	6.7016	0.35395	6.888	1.54E-04	14.473	0.38019	7.9999	0.08174	20.372	1.039273	0.15264	0.193745	5.975433

Sample	Date	16/03/2021																			
25	Chi-Sqr	Sum-Sqr	**L**	R1	%error	R2	%error	CPE1-T	%error	W-R	%error	W-T	%error	R3	%error	CPE2-T	%error	**Rs**	**%error**	**Rp**	**%error**
0h	9.35E-04	0.0024	5.23E-06	6.417	0.13302	0.24538	8.8275	8.03E-04	12.437	0.20476	16.844	0.04943	25.04	1.271	2.3806	0.0024	4.4535	0.867397	0.13302	0.194245	9.3507
10h	0.00188	0.00359	5.23E-06	6.363	0.18545	0.20659	11.024	5.13E-04	19.016	0.13527	18.501	0.06491	37.088	0.89781	2.9104	0.00205	6.8791	0.859656	0.18545	0.125226	10.8118
20h	9.33E-04	0.002	5.23E-06	6.479	0.12778	0.20341	10.915	7.53E-04	14.179	0.18587	8.8304	0.10355	19.545	0.83156	2.7037	0.00218	6.8755	0.876284	0.12778	0.122527	7.483033
30h	0.00186	0.00367	5.23E-06	6.499	0.17506	0.20715	13.166	6.94E-04	18.999	0.14701	17.455	0.07253	35.152	0.88363	3.2996	0.00224	8.1432	0.879151	0.17506	0.124957	11.30687
40h	0.00311	0.00574	5.23E-06	6.599	0.21611	0.20795	19.087	7.47E-04	23.886	0.17753	22.91	0.04242	39.447	0.84408	5.027	0.00221	11.988	0.893486	0.21611	0.123777	15.67467
50h	0.00142	0.00329	5.23E-06	6.481	0.16656	0.21757	10.942	6.39E-04	17.115	0.16308	12.143	0.17275	28.346	0.89166	2.7801	0.00232	7.1554	0.876571	0.16656	0.129905	8.6217
60h	0.00108	0.00264	5.23E-06	6.56	0.14211	0.2278	11.084	7.80E-04	14.52	0.20849	8.9246	0.15265	20.338	0.89095	2.8746	0.00242	7.3392	0.887896	0.14211	0.137779	7.627733
70h	0.00207	0.00424	5.23E-06	6.512	0.17869	0.22216	16.831	8.56E-04	18.645	0.22073	14.718	0.05314	26.559	0.83937	4.4884	0.00241	11.106	0.881015	0.17869	0.131332	12.01247
80h	0.00222	0.0044	5.23E-06	6.497	0.18609	0.19919	17.982	8.55E-04	21.317	0.27998	15.596	0.03355	23.473	0.85578	4.736	0.00236	10.478	0.878865	0.18609	0.138885	12.77133
90h	9.92E-04	0.00249	5.23E-06	6.545	0.13677	0.24752	9.9503	7.56E-04	12.91	0.22043	8.4467	0.14222	18.898	0.89332	2.802	0.00254	7.1388	0.885745	0.13677	0.142658	7.066333
100h	0.00269	0.00634	5.23E-06	6.456	0.22134	0.22078	17.109	7.91E-04	22.89	0.26519	13.456	0.07414	26.2	0.89072	4.4985	0.00253	11.05	0.872987	0.22134	0.144868	11.68783

Sample	Date	23/04/2021																			
45	Chi-Sqr	Sum-Sqr	**L**	R1	%error	R2	%error	CPE1-T	%error	W-R	%error	W-T	%error	R3	%error	CPE2-T	%error	**Rs**	**%error**	**Rp**	**%error**
0h	1.36E-03	0.00338	5.18E-06	7.093	0.16738	1.141	5.2795	2.78E-03	5.5371	0.39695	17.953	3.06E-02	19.835	0.37682	6.743	3.87E-04	10.852	0.964301	0.16738	0.222002	9.991833
10h	0.00161	0.00368	5.18E-06	7.066	0.17825	0.99696	3.1083	2.48E-03	6.8037	0.2342	13.612	7.02E-02	25.62	0.3678	6.7398	3.52E-04	11.727	0.960431	0.17825	0.17673	7.820033
20h	1.30E-03	0.00294	5.18E-06	7.191	0.158	0.9681	2.7563	2.43E-03	6.5661	0.21768	11.695	9.04E-02	23.868	0.36746	6.3452	3.65E-04	10.654	0.978349	0.158	0.170177	6.932167
30h	0.00188	0.00405	5.18E-06	9.391	0.17813	1.07	4.0985	2.49E-03	10	0.22947	17.663	1.00E-01	35.825	0.37967	10.586	4.70E-04	15.742	1.293719	0.17813	0.188224	10.7825
40h	0.00128	0.00271	5.18E-06	7.516	0.14622	0.98683	2.968	2.49E-03	6.9427	0.20858	13.671	7.24E-02	25.804	0.36623	7.0005	4.37E-04	10.565	1.024938	0.14622	0.171381	7.879833
50h	0.00151	0.00331	5.18E-06	7.744	0.1659	0.99231	2.9662	2.47E-03	7.2129	0.21136	12.966	1.12E-01	27.484	0.36855	7.1127	3.76E-04	12.066	1.057622	0.1659	0.172897	7.681633
60h	0.00111	0.00318	5.18E-06	7.614	0.15708	1.042	2.5311	2.70E-03	6.6082	0.28346	8.186	3.76E-01	19.476	0.39829	6.3117	4.09E-04	10.61	1.038986	0.15708	0.194619	5.676267
70h	0.00325	0.00622	5.18E-06	7.594	0.23313	0.8588	10.916	2.66E-03	13.133	0.45973	25.282	1.97E-02	25.551	0.38362	12.776	3.78E-04	16.838	1.036119	0.23313	0.191523	16.32467
80h	0.00233	0.00428	5.18E-06	10.95	0.1743	0.98464	5.562	2.81E-03	13.556	0.32739	15.209	8.69E-02	29.071	0.34403	14.933	6.05E-04	20.139	1.517202	0.1743	0.184916	11.90133
90h	2.28E-03	0.00413	5.18E-06	9.585	0.17379	0.95806	5.3167	2.75E-03	11.749	0.31804	16.745	5.42E-02	27.557	0.34008	12.759	5.50E-04	17.546	1.321529	0.17379	0.179199	11.6069
100h	0.0011	0.00287	5.18E-06	7.17	0.14848	1.044	2.3766	2.88E-03	5.9232	0.20125	11.302	1.82E-01	25.111	0.40127	5.6005	4.21E-04	9.3982	0.975339	0.14848	0.183548	6.426367

10.3.5 Batch C

Sample	Date	16/07/2021																			
314	Chi-Sqr	Sum-Sqr	**L**	R1	%error	R2	%error	CPE1-T	%error	W-R	%error	W-T	%error	R3	%error	CPE2-T	%error	**Rs**	**%error**	**Rp**	**%error**
0h	4.11E-03	0.00251	3.81E-06	18.31	0.19054	0.55097	9.8463	3.33E-03	20	0.27248	16.544	5.03E-05	38.373	0.21767	24.862	1.39E-01	65.677	2.572258	0.19054	0.096764	17.0841
10h	7.73E-03	0.00515	3.81E-06	18.93	0.2699	0.54068	18.308	4.29E-03	29.059	0.2733	23.592	5.26E-05	55.266	0.33023	30.642	8.36E-02	76.83	2.661135	0.2699	0.111542	24.18067
20h	6.70E-03	0.00389	3.81E-06	19.18	0.25063	0.50116	20.907	4.34E-03	26.73	0.29291	19.657	4.07E-05	45.253	0.35069	30.68	5.99E-02	73.377	2.696973	0.25063	0.111621	23.748
30h	5.98E-03	0.00534	3.81E-06	19.05	0.24689	0.56177	10.683	6.18E-03	27.474	0.28971	21.538	8.44E-05	52.179	0.35065	17.863	4.53E-01	44.878	2.678337	0.24689	0.119845	16.69467
40h	5.77E-03	0.00425	3.81E-06	19.42	0.24659	0.49834	17.192	4.65E-03	29.109	0.26395	22.714	5.13E-05	53.168	0.53297	16.353	5.70E-02	41.797	2.731377	0.24659	0.133195	18.753
50h	4.55E-03	0.00409	3.81E-06	19.38	0.22084	0.56638	11.76	5.12E-03	25.421	0.22976	24.931	7.61E-05	59.642	0.52277	12.665	1.12E-01	33.982	2.725643	0.22084	0.136585	16.452

Sample	Date	19/07/2021																			
315	Chi-Sqr	Sum-Sqr	**L**	R1	%error	R2	%error	CPE1-T	%error	W-R	%error	W-T	%error	R3	%error	CPE2-T	%error	**Rs**	**%error**	**Rp**	**%error**
0h	3.24E-02	0.00882	3.43E-06	18.06	0.31272	0.42615	308.15	3.75E-03	378.4	0.07379	1936.4	2.47E-03	1352.7	0.12174	215.57	1.29E-03	233.84	2.536421	0.31272	0.036637	820.04
10h	3.17E-02	0.01278	3.43E-06	17.56	0.32518	0.42782	163.29	5.53E-03	87.467	0.16719	514.76	1.09E-02	275.84	0.1457	143.65	1.16E-03	138.63	2.464746	0.32518	0.0537	273.9
20h	9.49E-03	0.00857	3.43E-06	17.77	0.24089	0.49212	20.641	6.23E-03	53.718	0.3227	25.993	8.00E-01	60.025	0.16266	62.062	1.29E-03	95.515	2.494849	0.24089	0.087641	36.232
30h	1.01E-02	0.00806	3.43E-06	17.71	0.24037	0.50081	19.498	6.02E-03	48.751	0.29725	28.514	1.56E-01	61.264	0.14061	65.143	1.27E-03	107.8	2.486248	0.24037	0.082078	37.71833
40h	1.03E-02	0.00807	3.43E-06	18.02	0.24931	0.4896	20.719	5.78E-03	48.434	0.38824	25.194	9.81E-02	49.565	0.1544	57.234	9.62E-04	101.31	2.530687	0.24931	0.095491	34.38233
50h	9.95E-03	0.00824	3.43E-06	18.08	0.23735	0.51534	22.962	6.12E-03	52.624	0.43073	27.314	7.85E-02	48.047	0.13916	74.626	1.48E-03	111.42	2.539288	0.23735	0.103087	41.634

10.4 XRD pattern analysis for flat LSCF substrates

10.4.1 Batch A

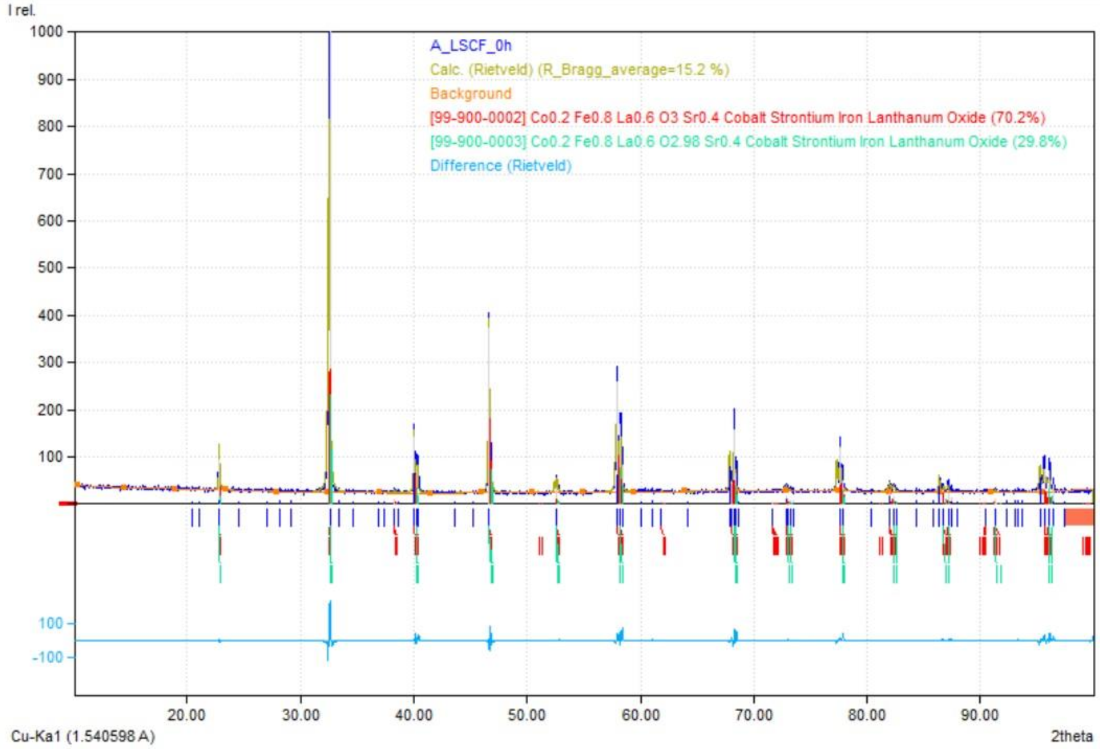

Match! Copyright © 2003-2021 CRYSTAL IMPACT, Bonn, Germany

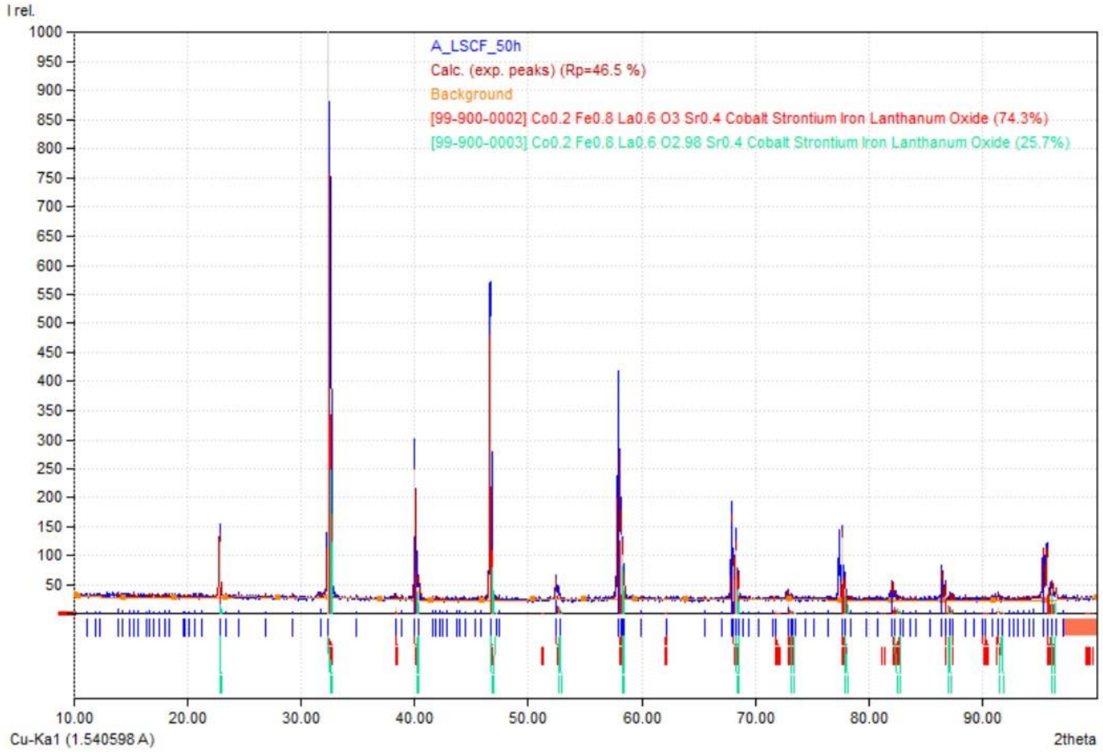

Match! Copyright © 2003-2021 CRYSTAL IMPACT, Bonn, Germany

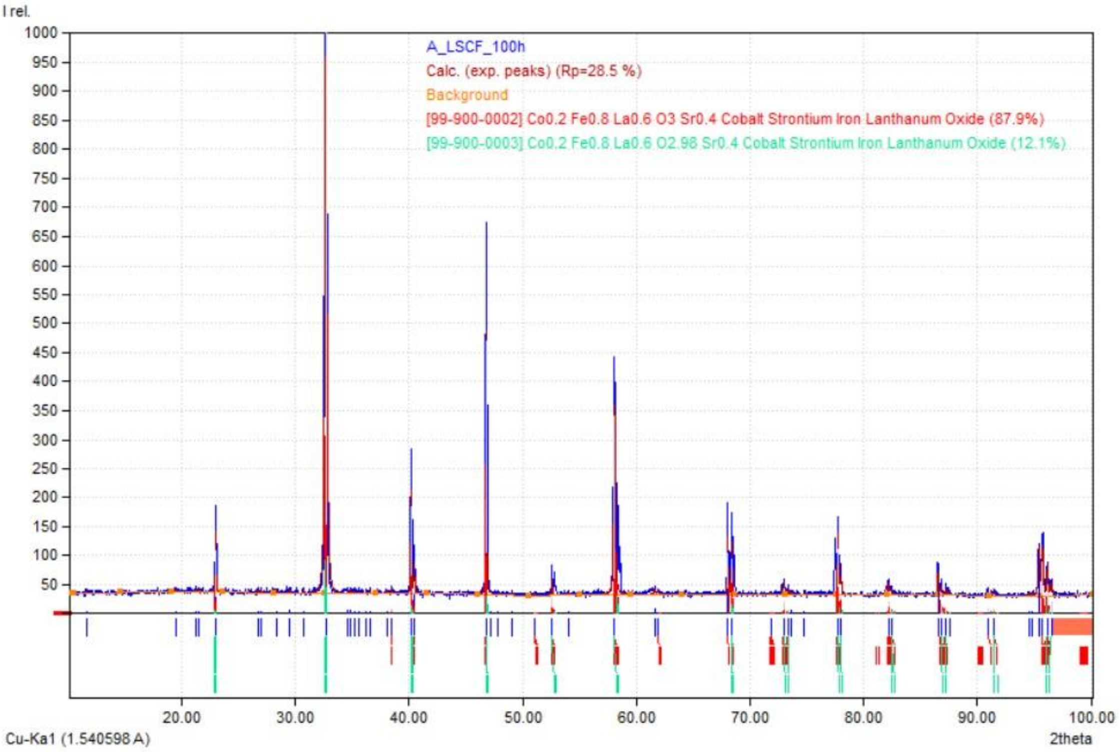

10.4.2 Batch B, set 1

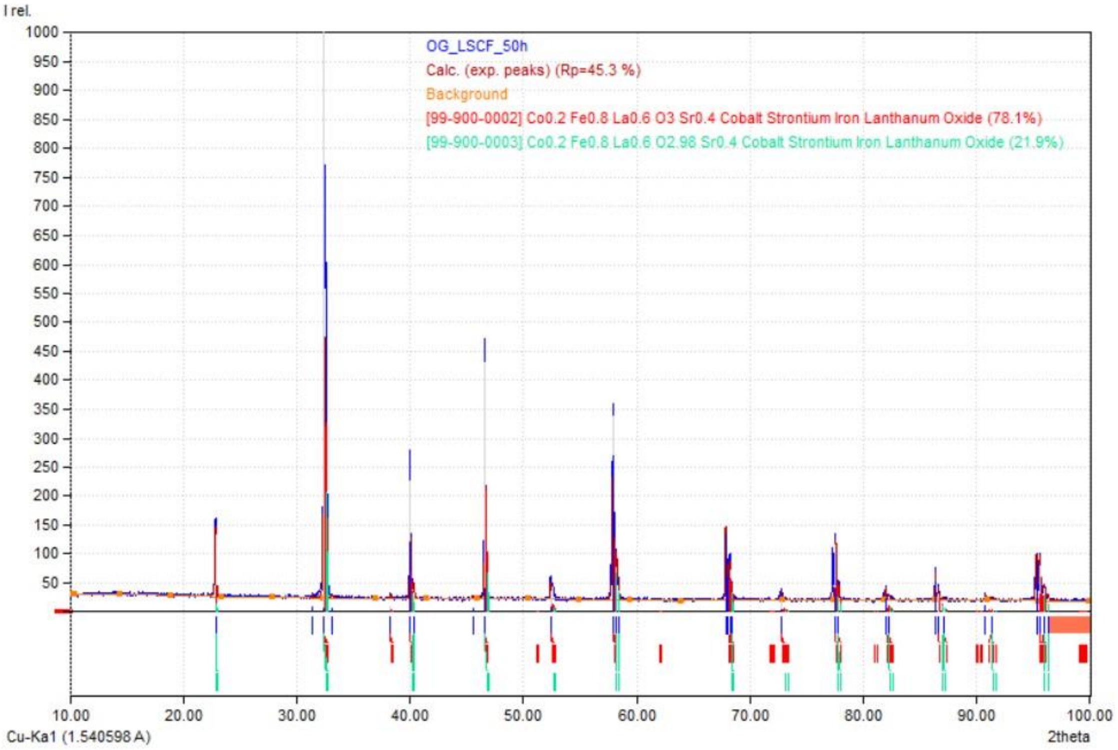

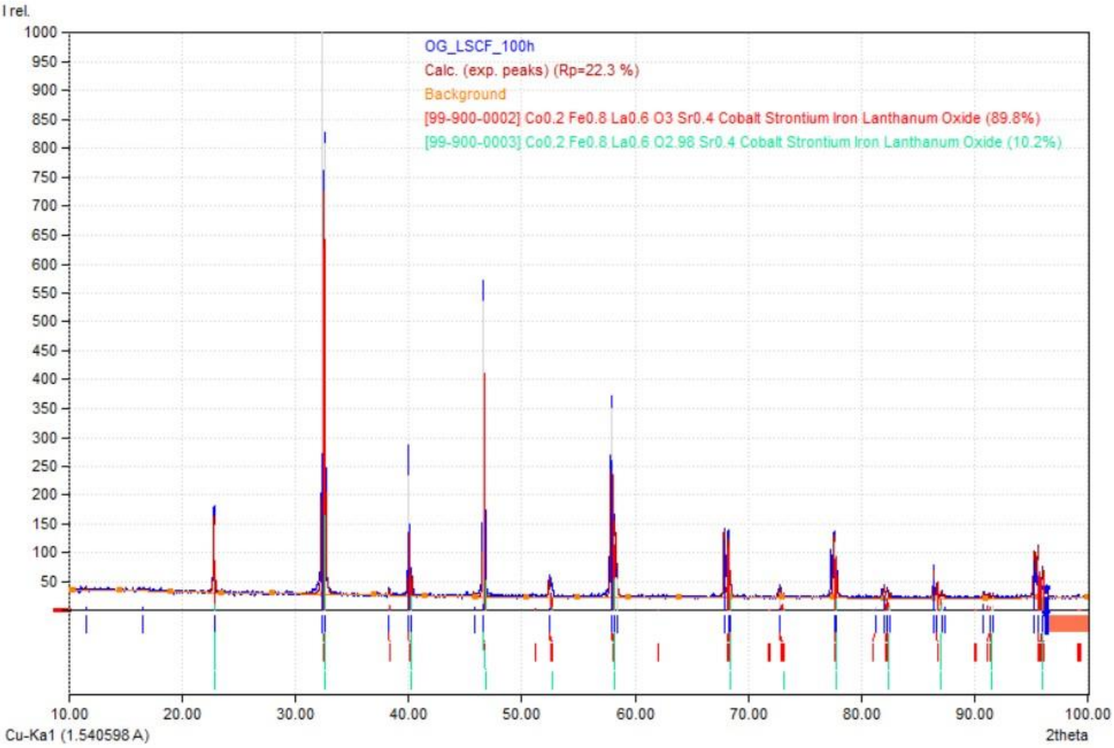

10.4.3 Batch B, set 2

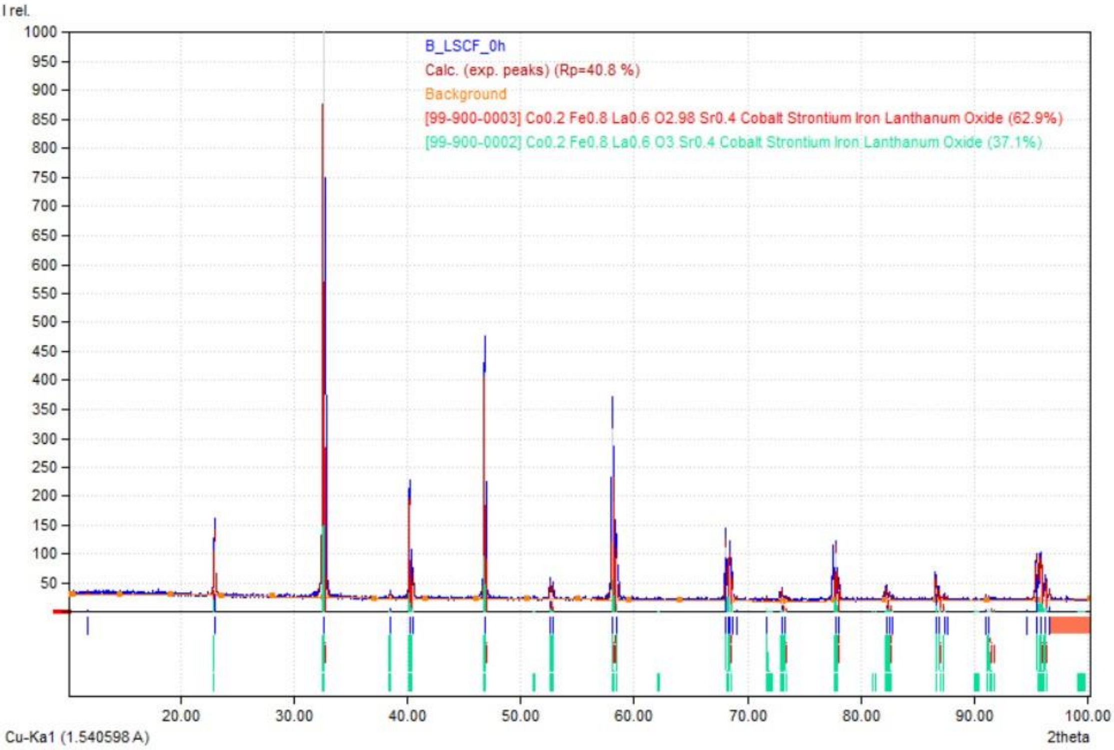

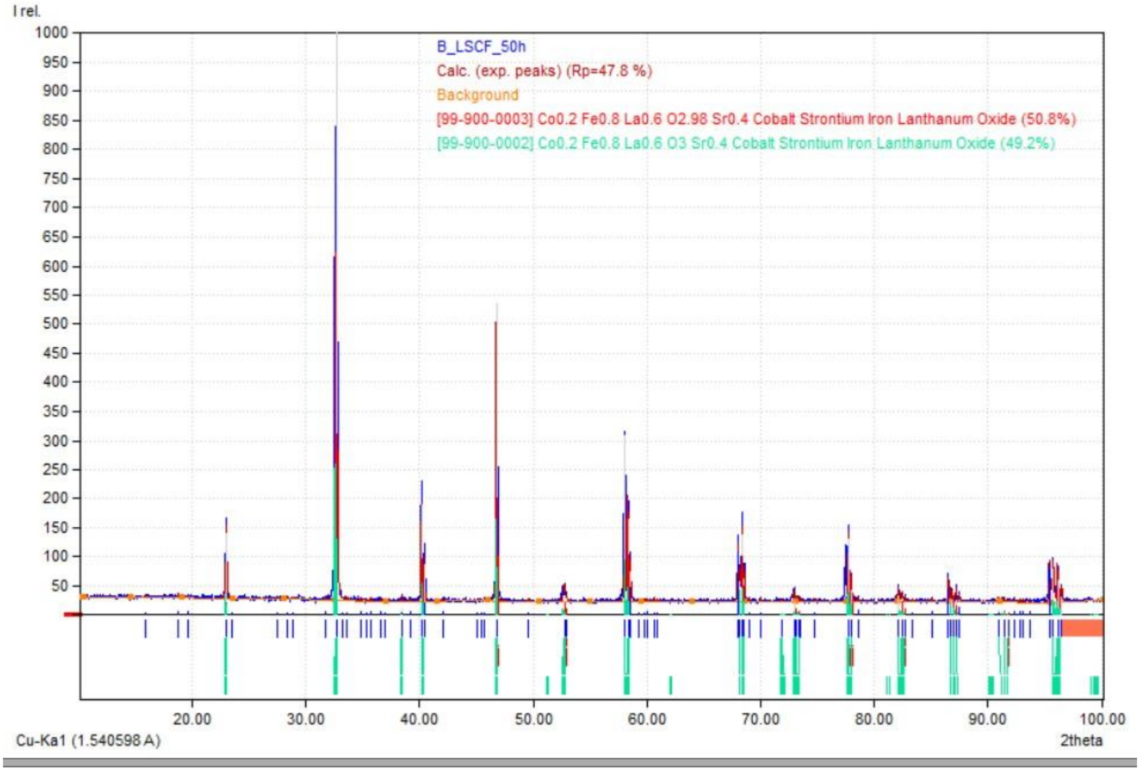
I rel.
1000
950
900
850
800
750
700
650
600
550
500
450
400
350
300
250
200
150
100
50
B_LSCF_50h
Calc. (exp. peaks) (Rp=47.8 %)
Background
[99-900-0003] Co0.2 Fe0.8 La0.6 O2.98 Sr0.4 Cobalt Strontium Iron Lanthanum Oxide (50.8%)
[99-900-0002] Co0.2 Fe0.8 La0.6 O3 Sr0.4 Cobalt Strontium Iron Lanthanum Oxide (49.2%)
20.00
30.00
40.00
50.00
60.00
70.00
80.00
90.00
100.00
Cu-Ka1 (1.540598 A)
2theta

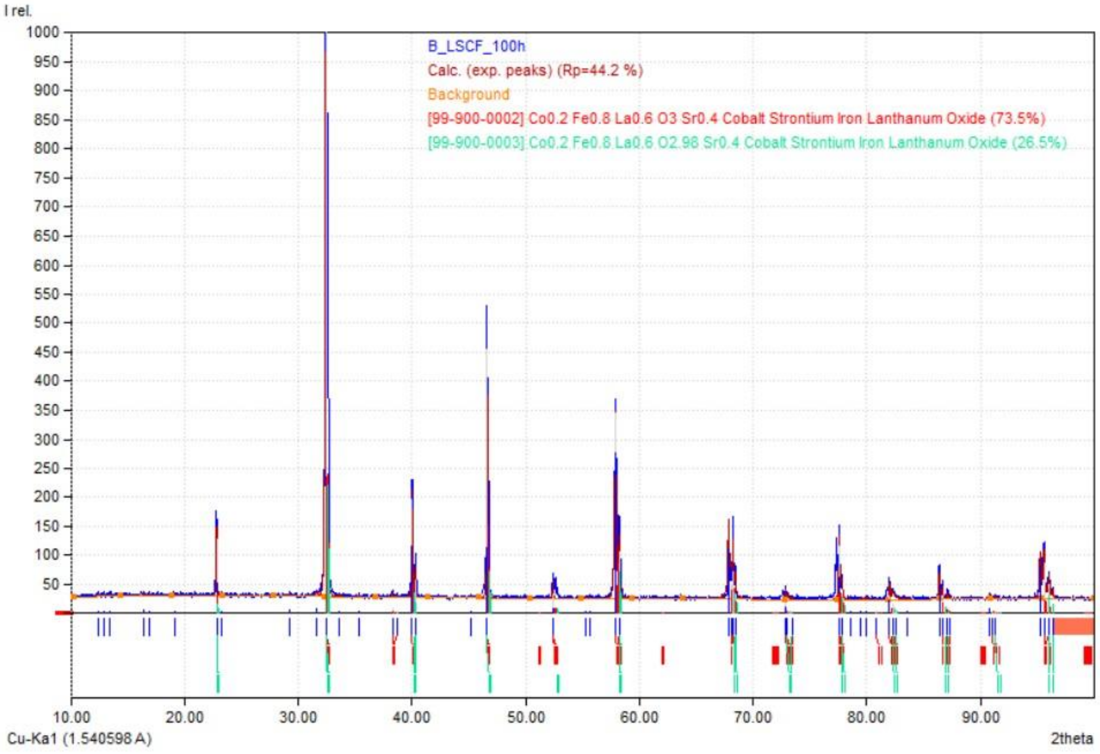
I rel.
1000
950
900
850
800
750
700
650
600
550
500
450
400
350
300
250
200
150
100
50
B_LSCF_100h
Calc. (exp. peaks) (Rp=44.2 %)
Background
[99-900-0002] Co0.2 Fe0.8 La0.6 O3 Sr0.4 Cobalt Strontium Iron Lanthanum Oxide (73.5%)
[99-900-0003] Co0.2 Fe0.8 La0.6 O2.98 Sr0.4 Cobalt Strontium Iron Lanthanum Oxide (26.5%)
10.00
20.00
30.00
40.00
50.00
60.00
70.00
80.00
90.00
Cu-Ka1 (1.540598 A)
2theta

10.4.4 Batch C

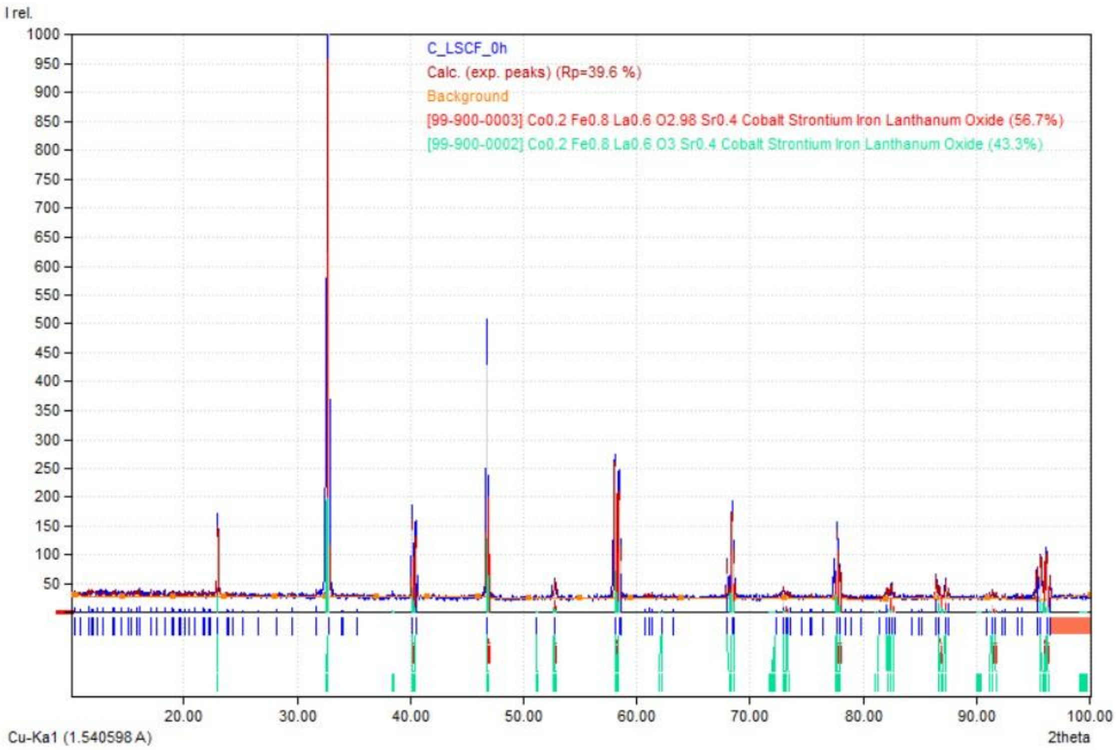
I rel.
1000
950
900
850
800
750
700
650
600
550
500
450
400
350
300
250
200
150
100
50
C_LSCF_0h
Calc. (exp. peaks) (Rp=39.6 %)
Background
[99-900-0003] Co0.2 Fe0.8 La0.6 O2.98 Sr0.4 Cobalt Strontium Iron Lanthanum Oxide (56.7%)
[99-900-0002] Co0.2 Fe0.8 La0.6 O3 Sr0.4 Cobalt Strontium Iron Lanthanum Oxide (43.3%)
20.00
30.00
40.00
50.00
60.00
70.00
80.00
90.00
100.00
Cu-Ka1 (1.540598 A)
2theta

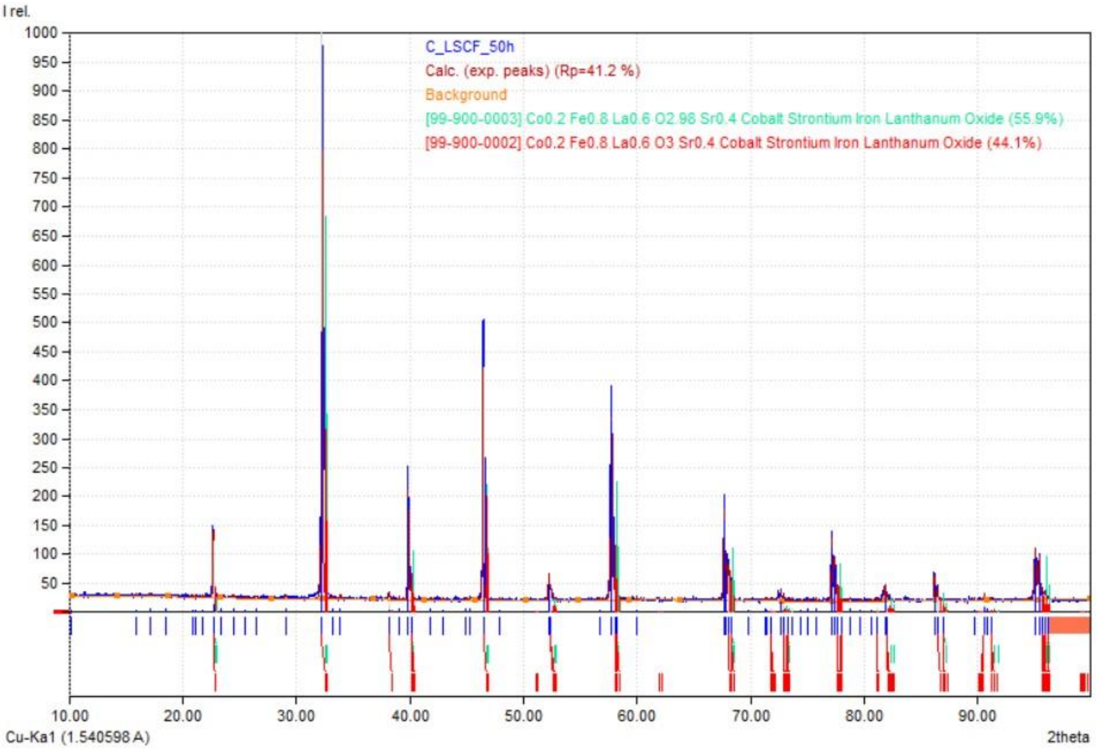
I rel.
1000
950
900
850
800
750
700
650
600
550
500
450
400
350
300
250
200
150
100
50
C_LSCF_50h
Calc. (exp. peaks) (Rp=41.2 %)
Background
[99-900-0003] Co0.2 Fe0.8 La0.6 O2.98 Sr0.4 Cobalt Strontium Iron Lanthanum Oxide (55.9%)
[99-900-0002] Co0.2 Fe0.8 La0.6 O3 Sr0.4 Cobalt Strontium Iron Lanthanum Oxide (44.1%)
10.00
20.00
30.00
40.00
50.00
60.00
70.00
80.00
90.00
Cu-Ka1 (1.540598 A)
2theta

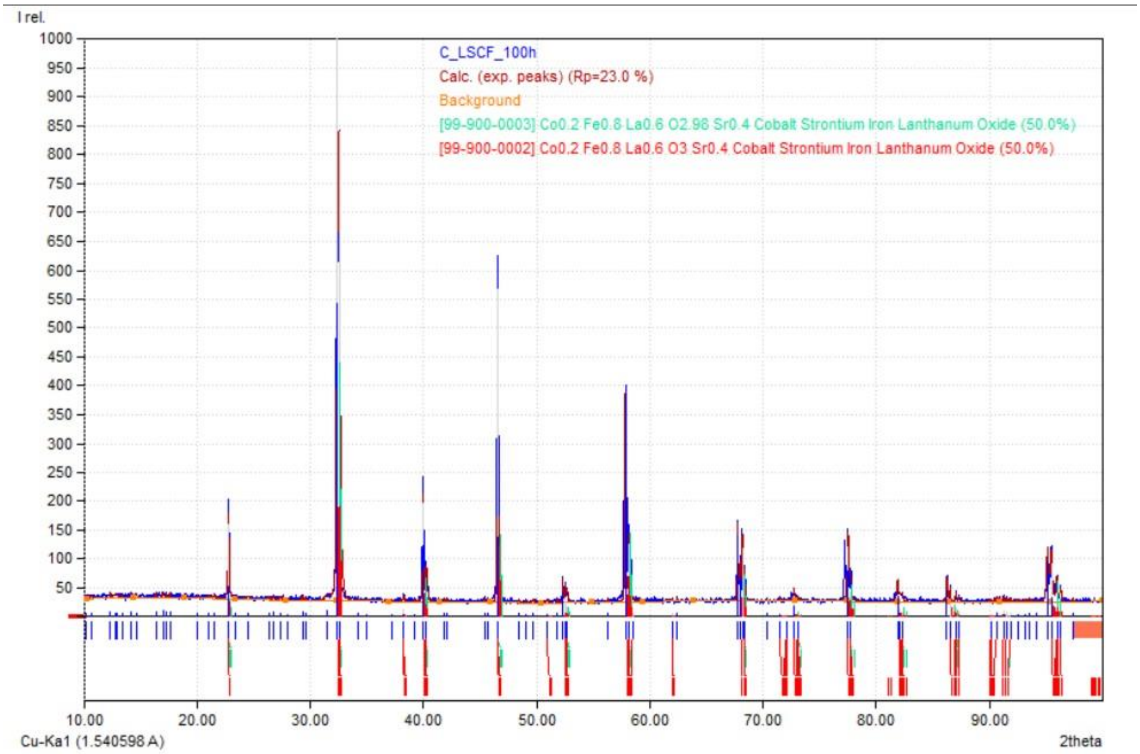
I rel.
1000
950
900
850
800
750
700
650
600
550
500
450
400
350
300
250
200
150
100
50
C_LSCF_100h
Calc. (exp. peaks) (Rp=23.0 %)
Background
[99-900-0003] Co0.2 Fe0.8 La0.6 O2.98 Sr0.4 Cobalt Strontium Iron Lanthanum Oxide (50.0%)
[99-900-0002] Co0.2 Fe0.8 La0.6 O3 Sr0.4 Cobalt Strontium Iron Lanthanum Oxide (50.0%)
10.00
20.00
30.00
40.00
50.00
60.00
70.00
80.00
90.00
Cu-Ka1 (1.540598 A)
2theta

10.5 BSE supplementary images

10.5.1 BSE images, Batch A

(a) BSE, Batch A, 0h

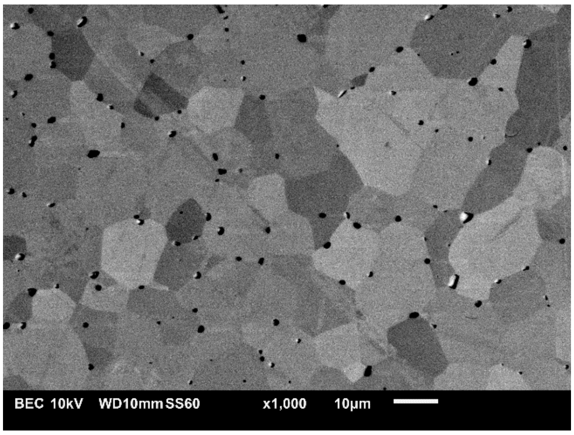

(b) BSE, Batch A, 12h

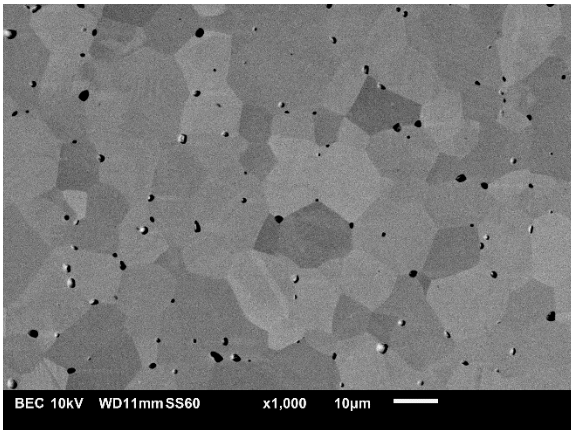

(c) BSE, Batch A, 24h

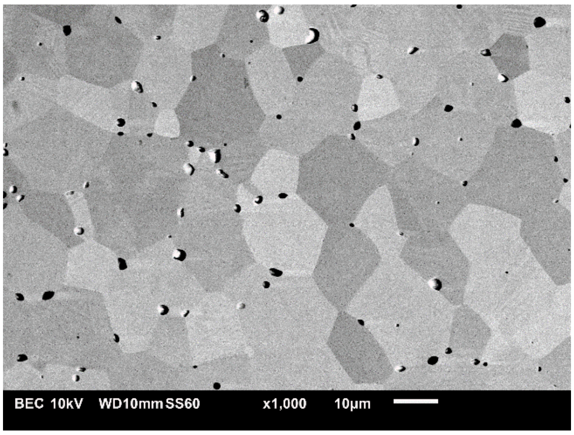

(d) BSE, Batch A, 36h

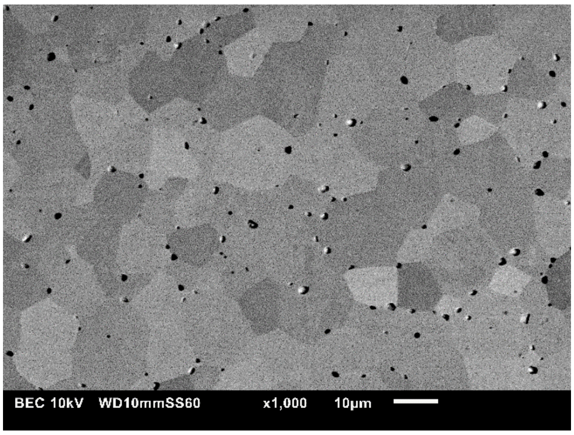

(e) BSE, Batch A, 48h

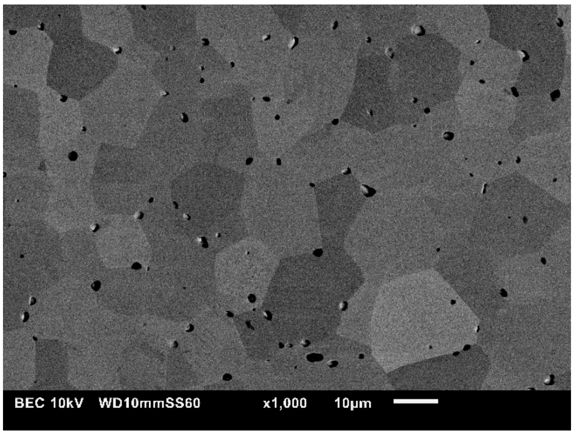

10.5.2 BSE images, Batch B, set 2

(a) BSE, Batch B, set 2, 0h

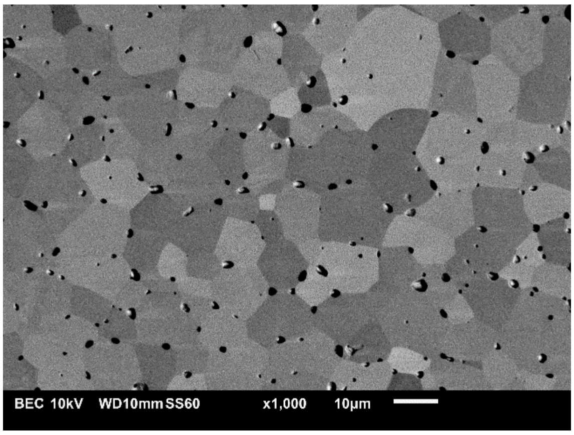

(b) BSE, Batch B, set 2, 50h

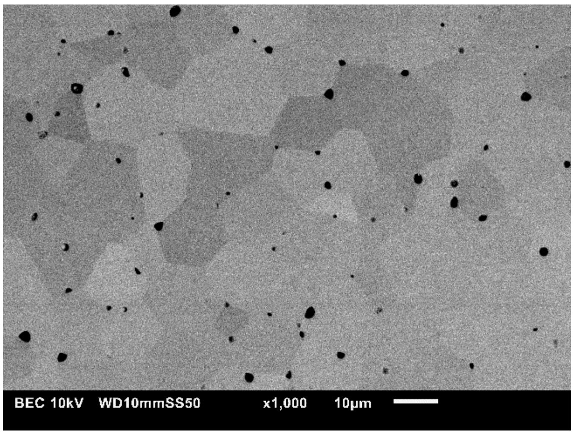

(c) BSE, Batch B, set 2, 100h

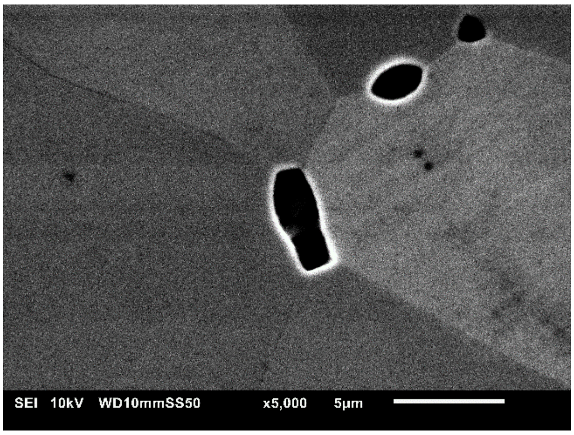

(d)

10.5.3 BSE images, Batch C

(a) BSE, Batch C, 0h

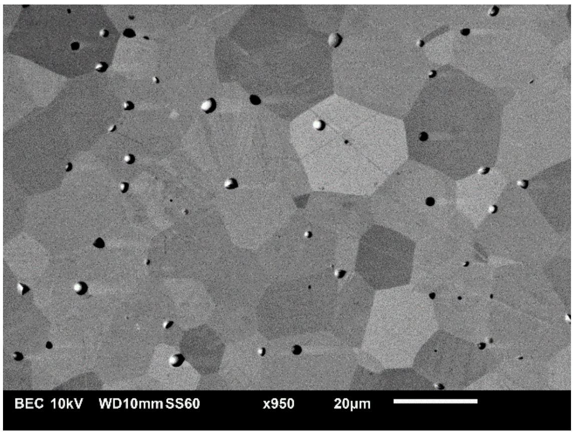

(b) BSE, Batch C, 12h

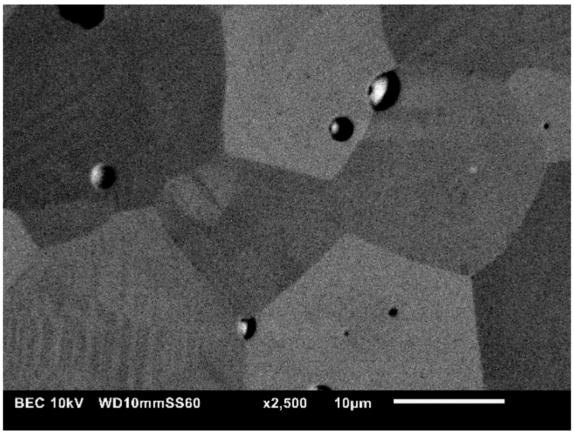

(c) BSE, Batch C, 24h

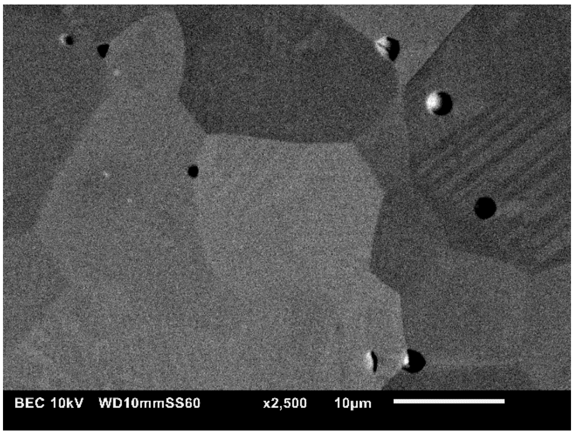

(d) BSE, Batch C, 36h

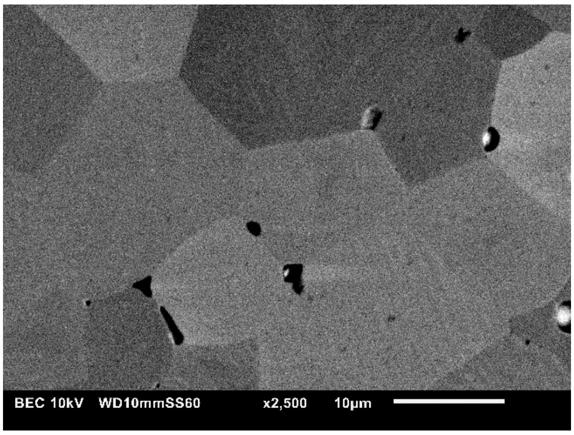

(e) BSE, Batch C, 48h

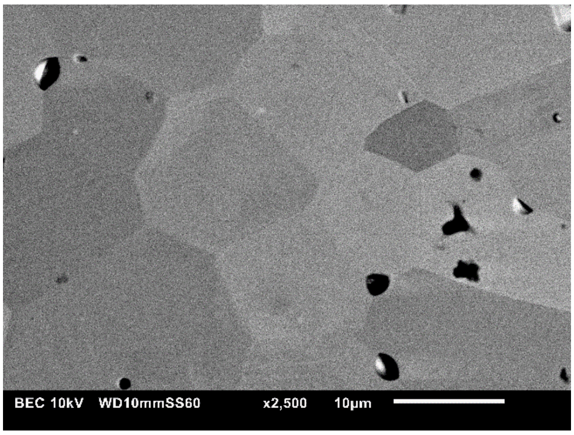

11 Annex B – GDC infiltrated cells

11.1 EIS data plots

11.1.1 Batch A

(a) ECM

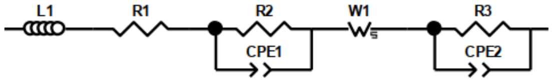

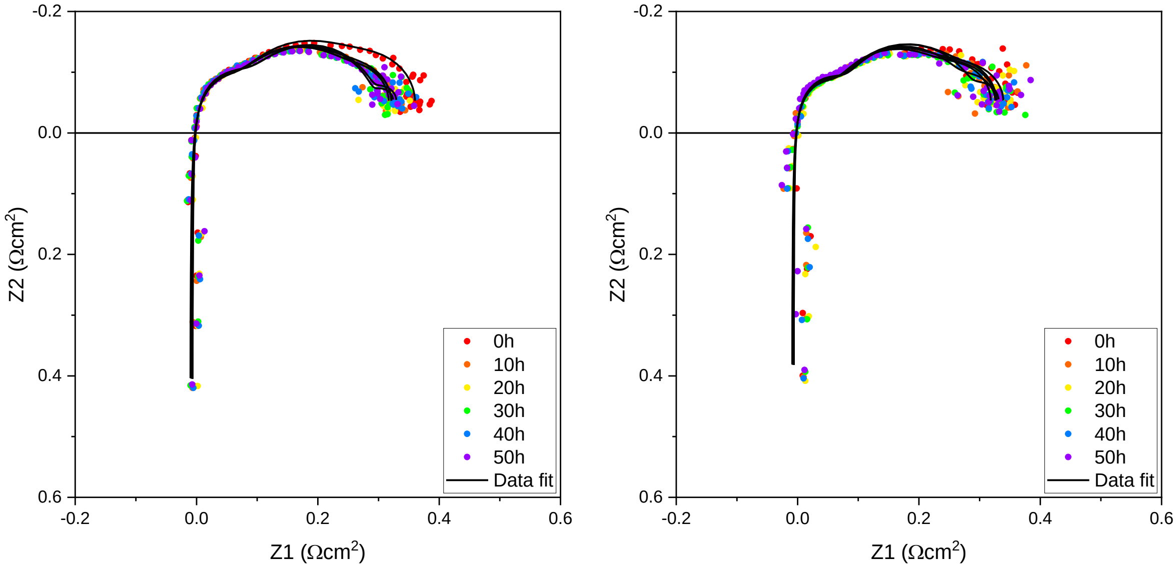

(b) 0.025 M (c) 0.125 M

(d) 0.250 M (e) 1.000 M

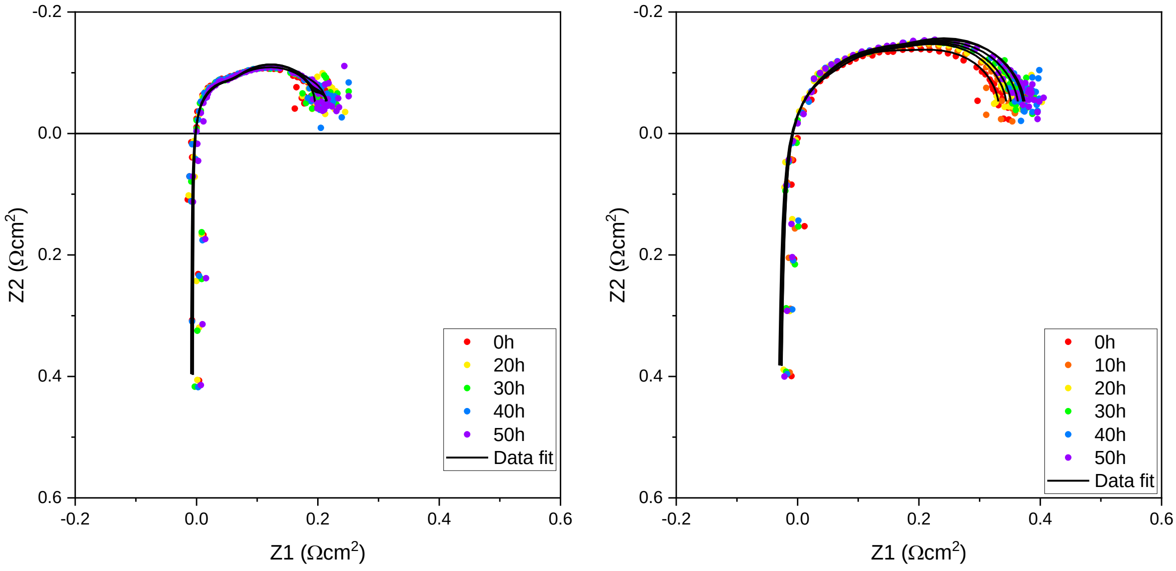

11.1.2 Batch B, set 1

(a) ECM

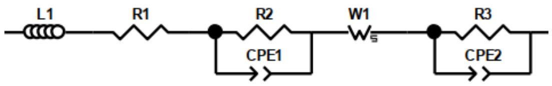

(b) 0.050 M

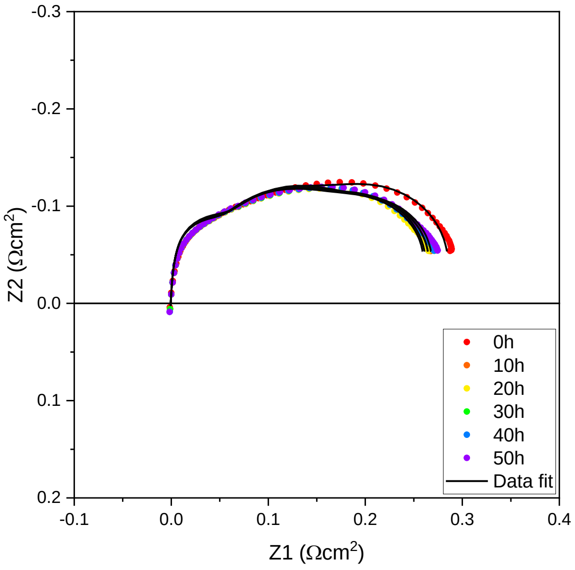

(c) 0.125 M (R1)

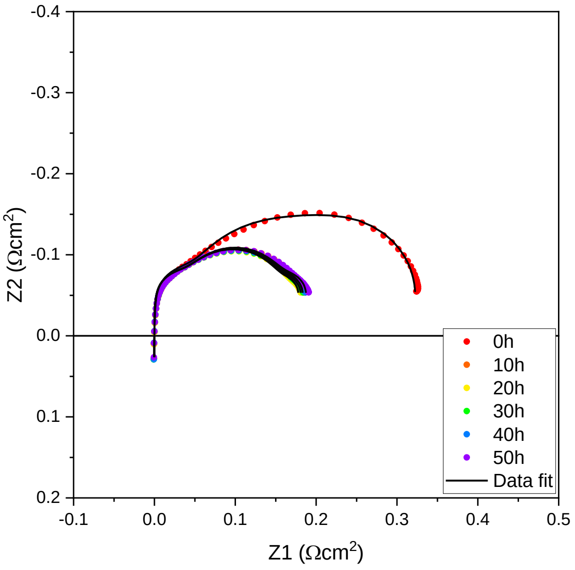

(d) 0. .125 M (R2)

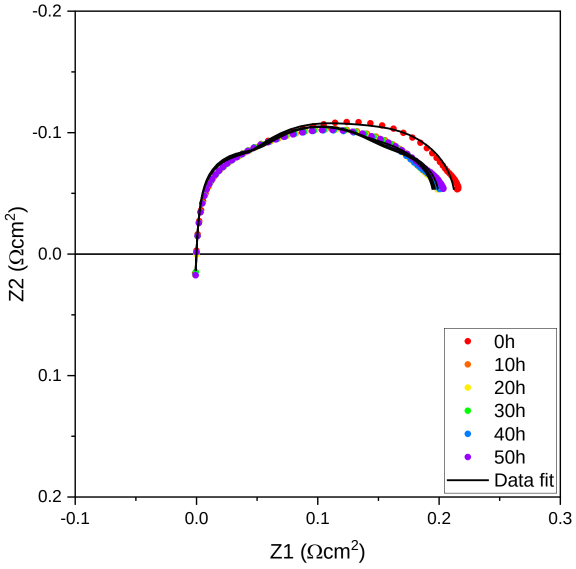

(e) 1.000 M

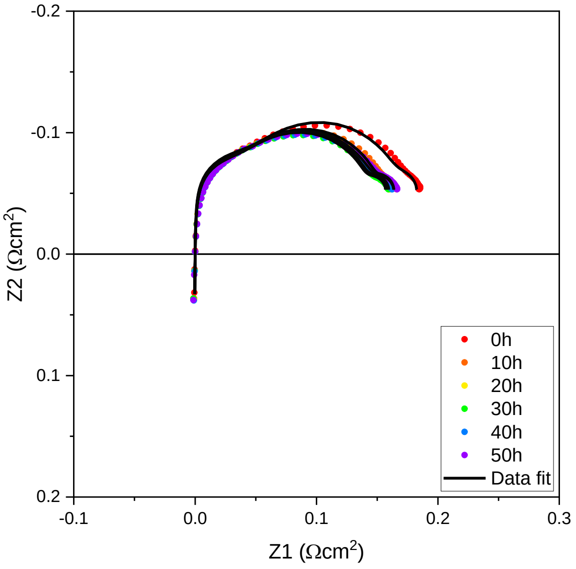

11.1.3 Batch B, set 2

(a) ECM

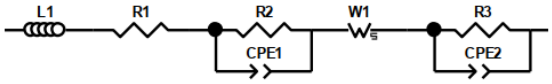

(b) 0.025 M (R1)

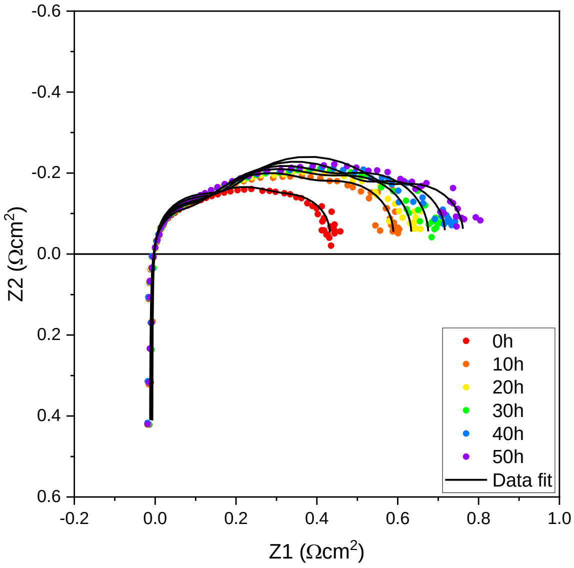

(c) 0.025 M (R2)

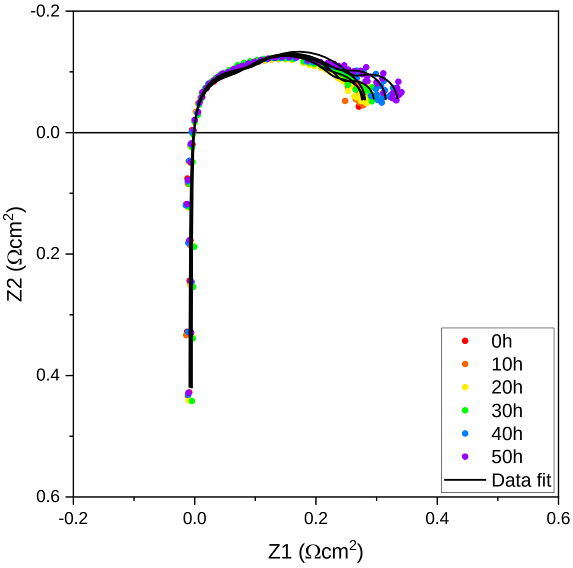

(d) 0.025 M (R3)

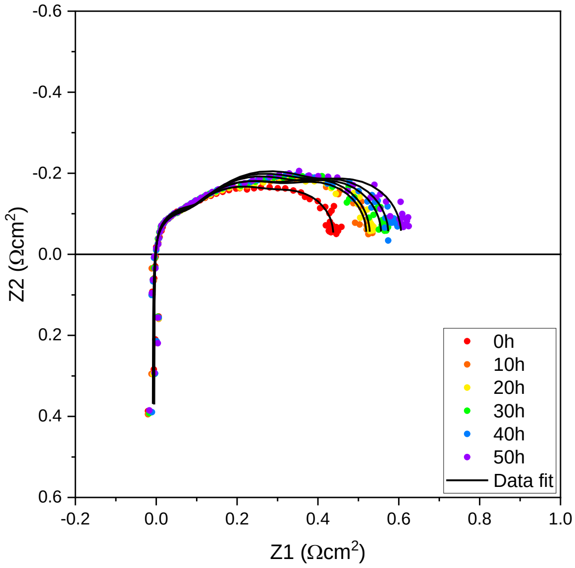

(e) 0.025 M (R4)

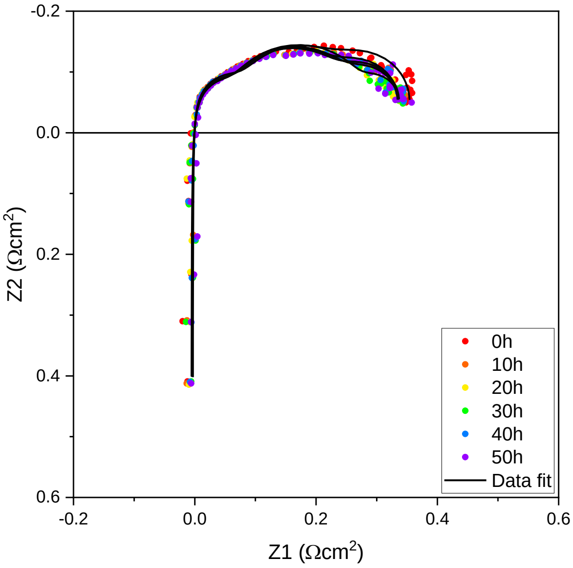

(f) 0.025 M (R5)

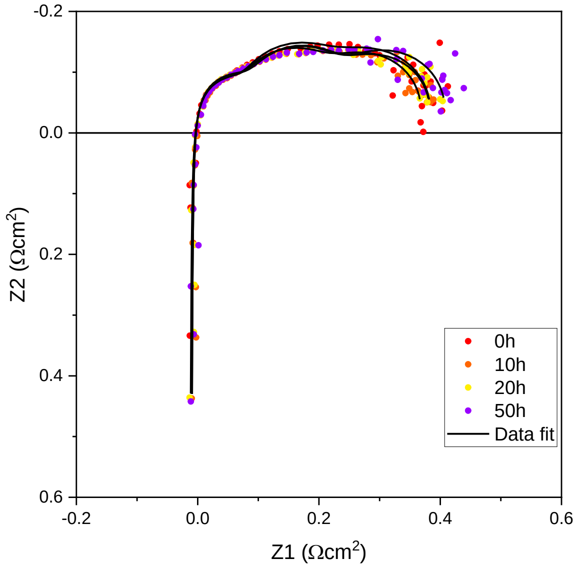

(g) 0.050 M (R1)

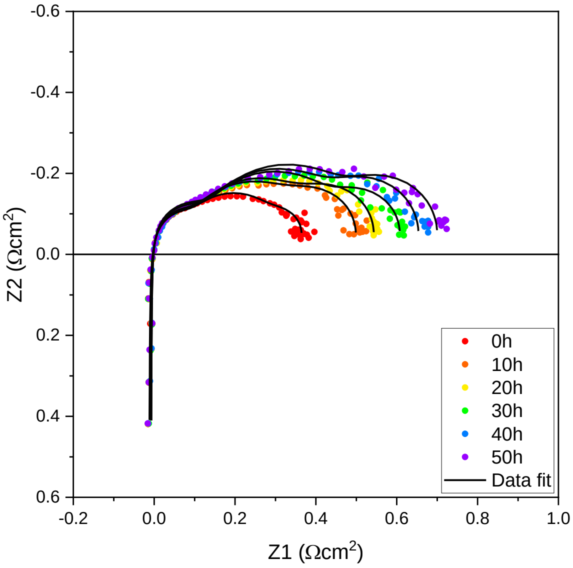

(h) 0.050 M (R2)

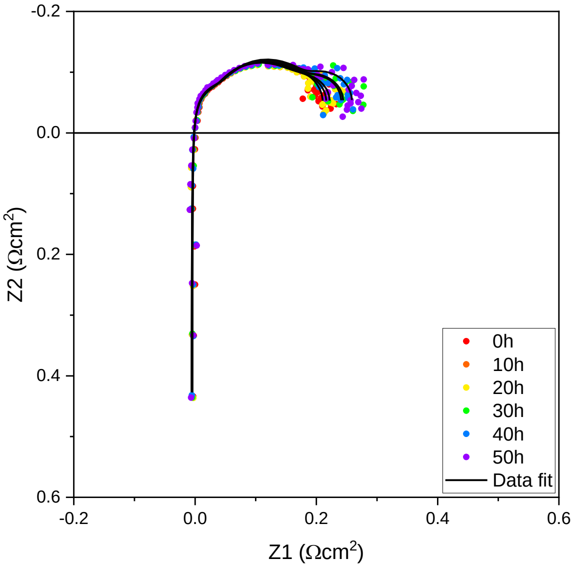

(i) 0.050 M (R3)

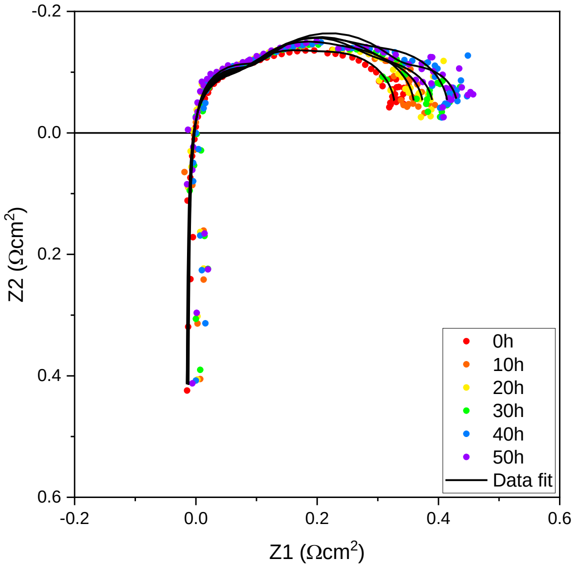

(j) 0.050 M (R4)

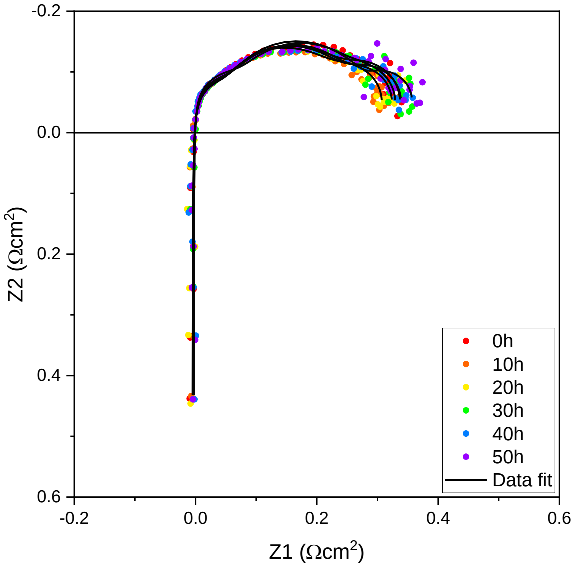

(k) 0.125 M (R1)

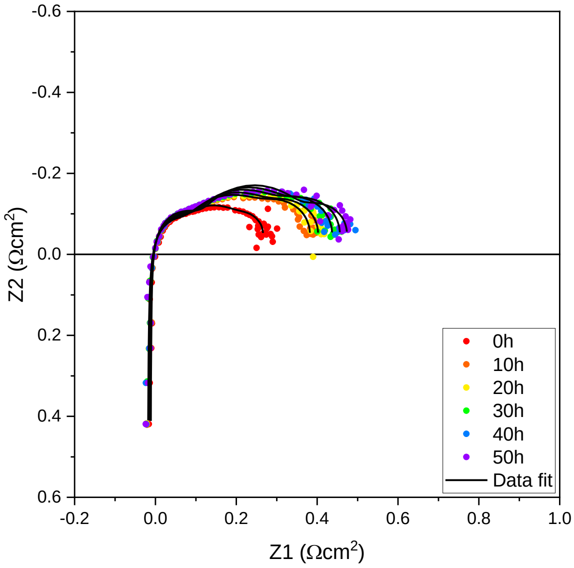

(l) 0.125 M (R2)

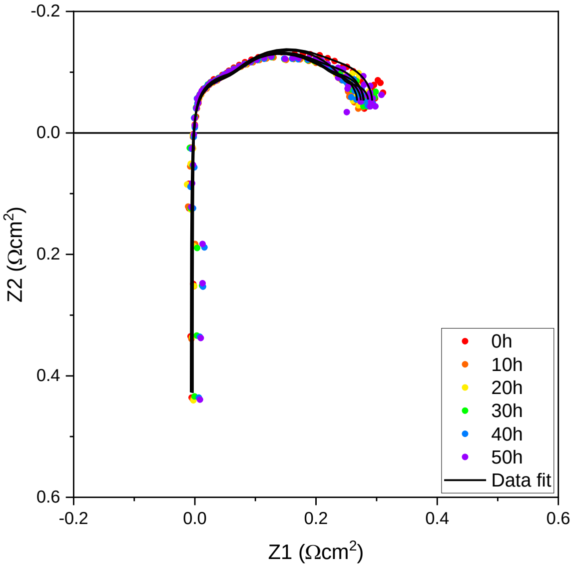

(m) 0.125 M (R3)

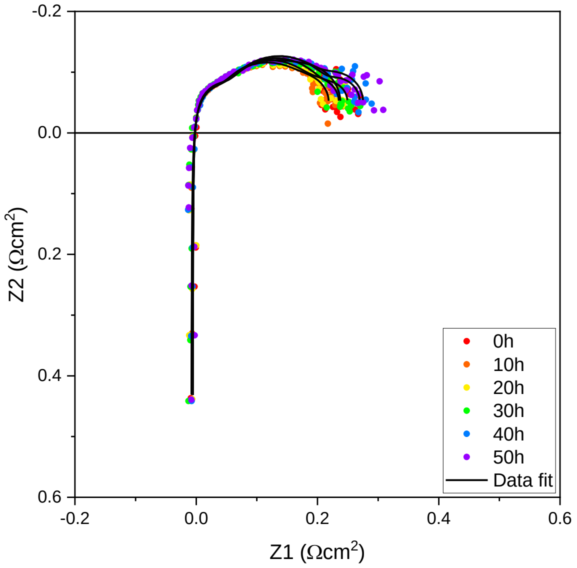

(n) 0.250 M (R1)

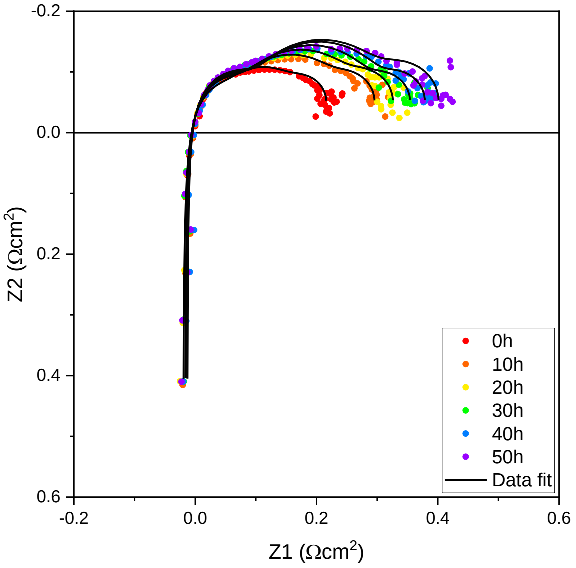

(o) 0.250 M (R2)

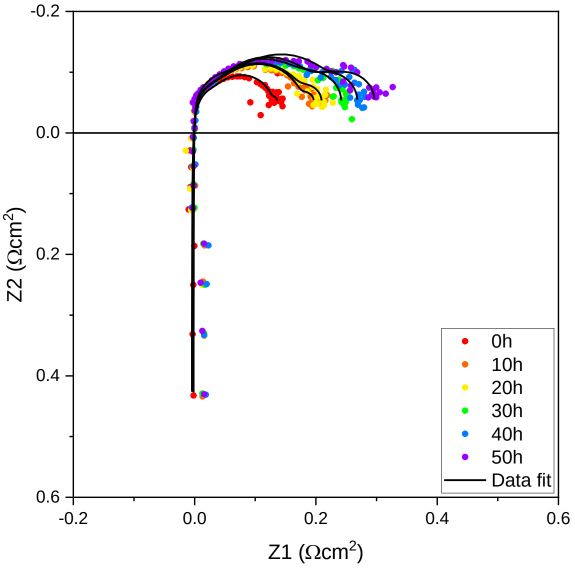

(p) 0.250 M (R3)

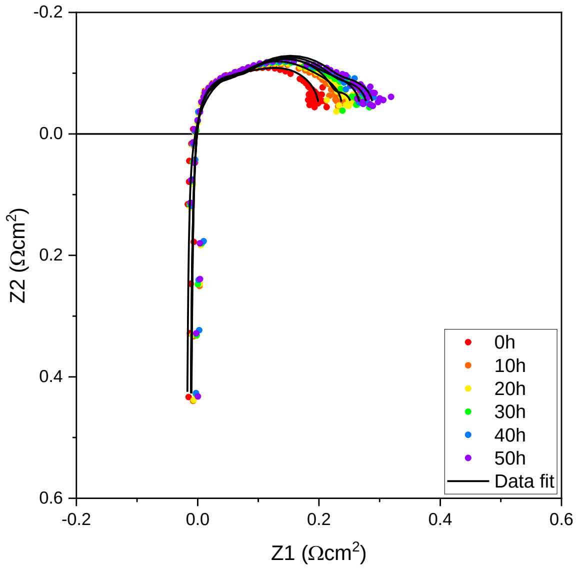

(q) 0.250 M (R4)

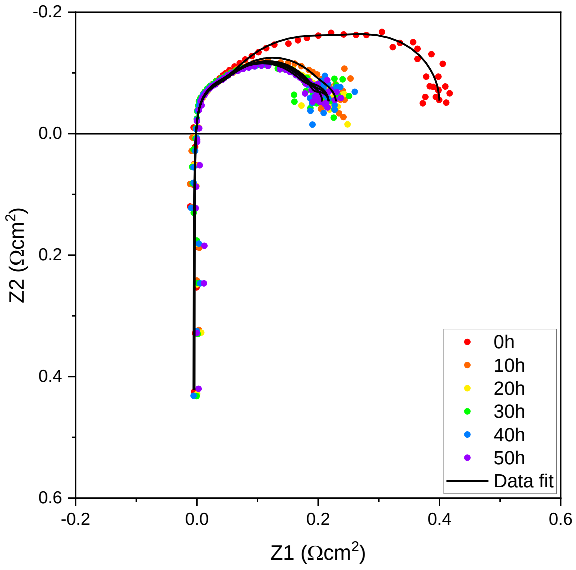

(r) 0.500 M (R1)

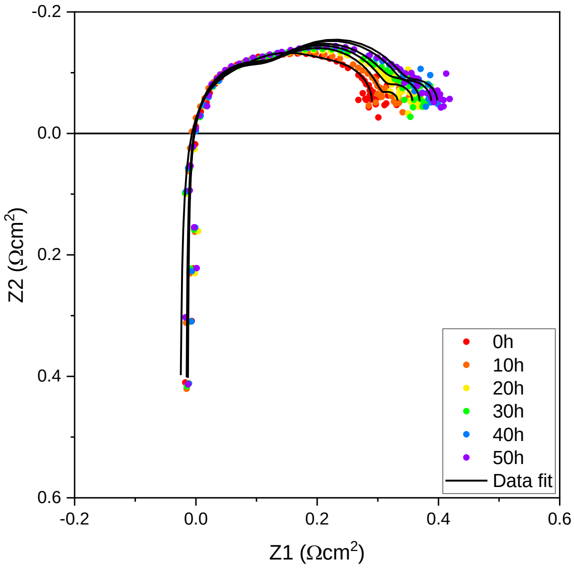

(s) 0.500 M (R2)

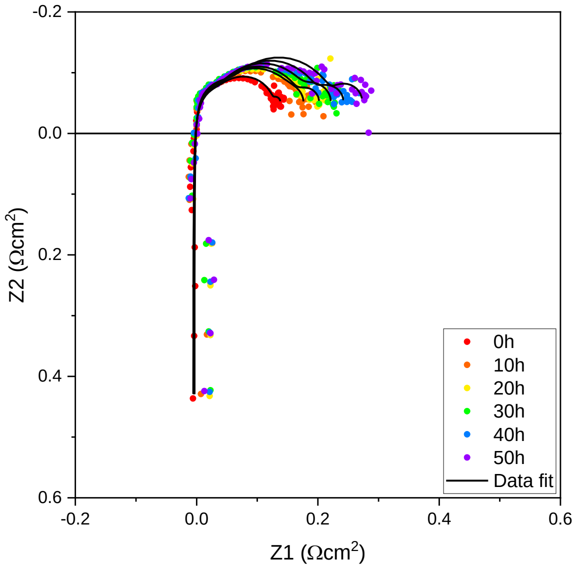

(t) 0.500 M (R3)

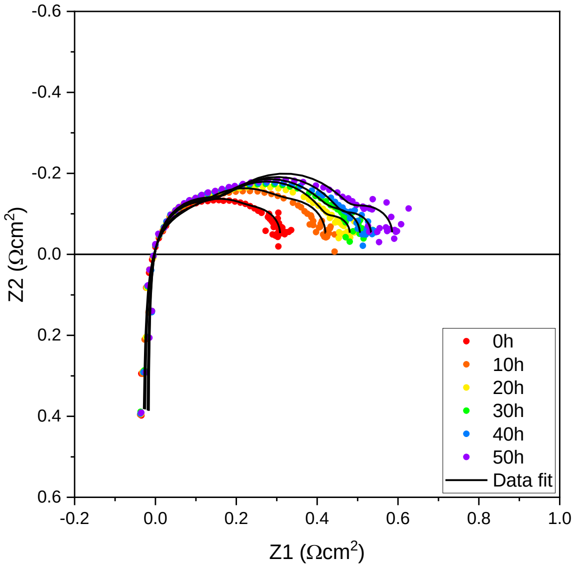

(u) 0.500 M (R4)

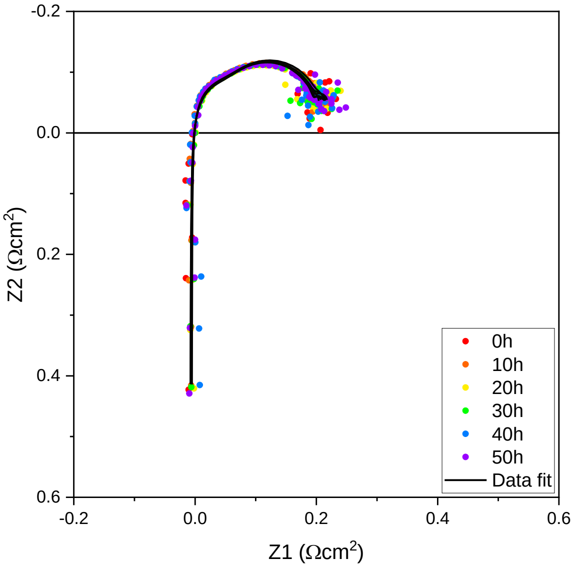

(v) 1.000 M (R1)

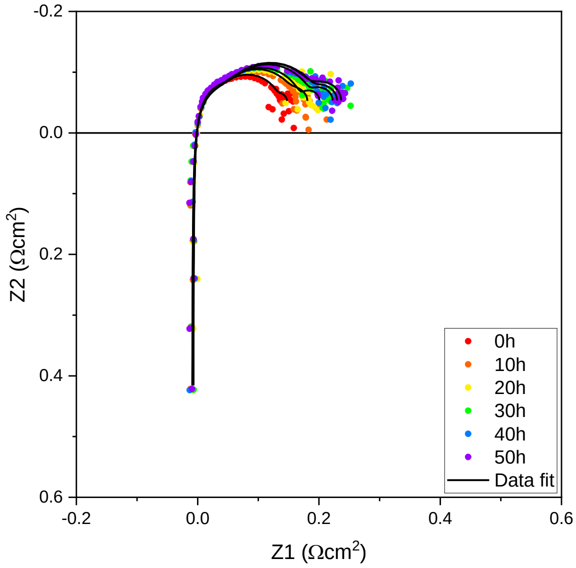

(w) 1.000 M (R2)

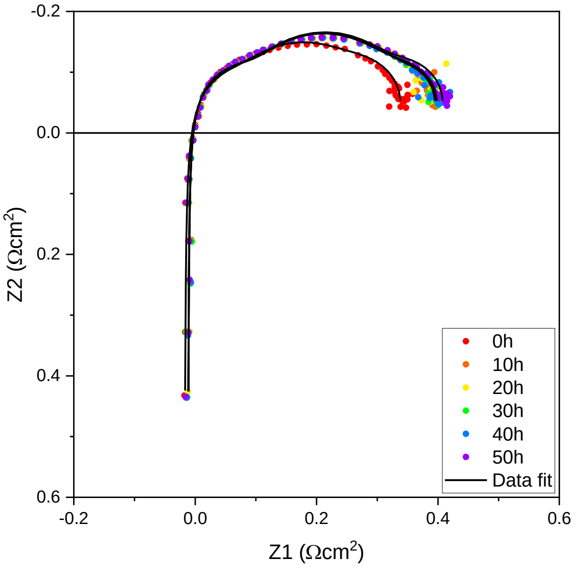

(x) 1.000 M (R3) 90

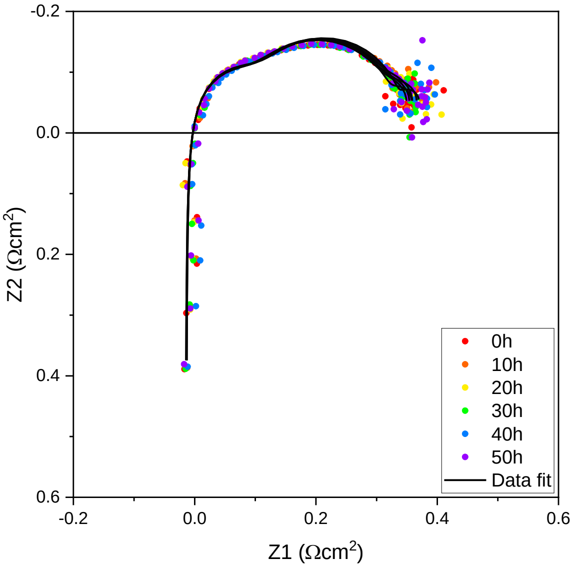

11.1.4 Batch C

(a) ECM

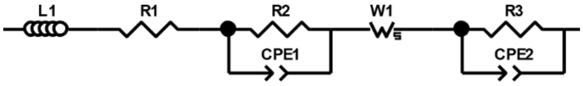

(b) 0.025 M

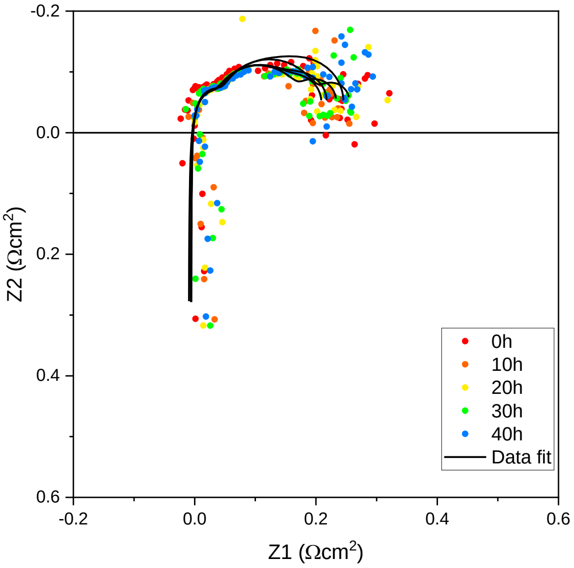

(c) 0.050 M

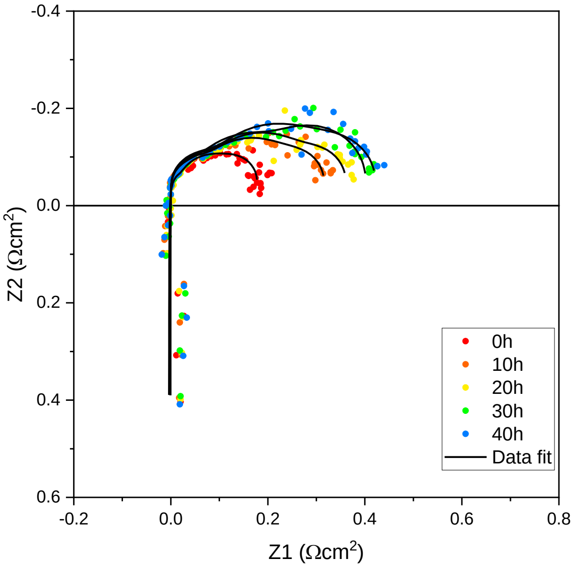

(d) 0.125 M

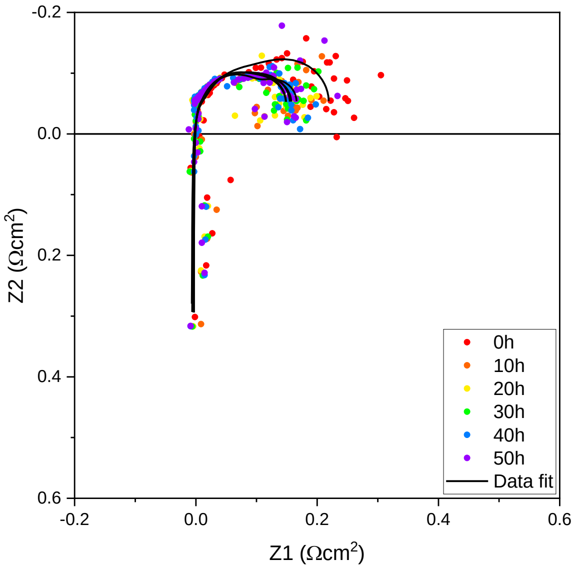

(e) 0.250 M

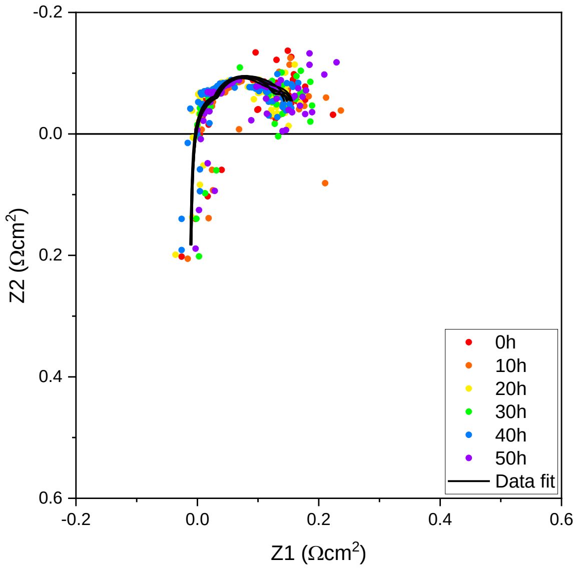

(f) 0.500 M

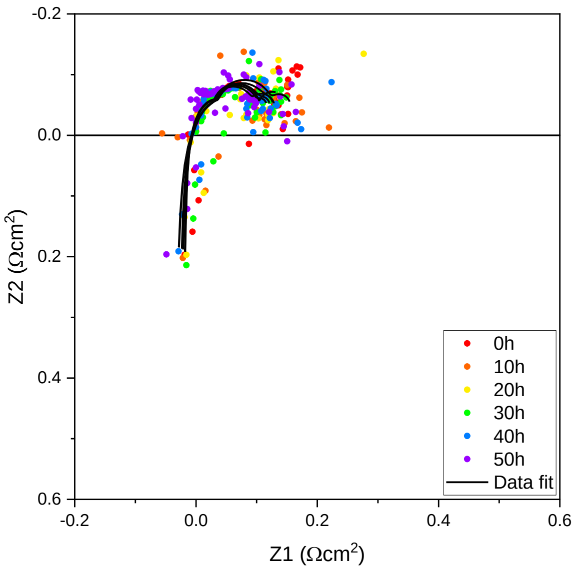

(g) 1.000 M

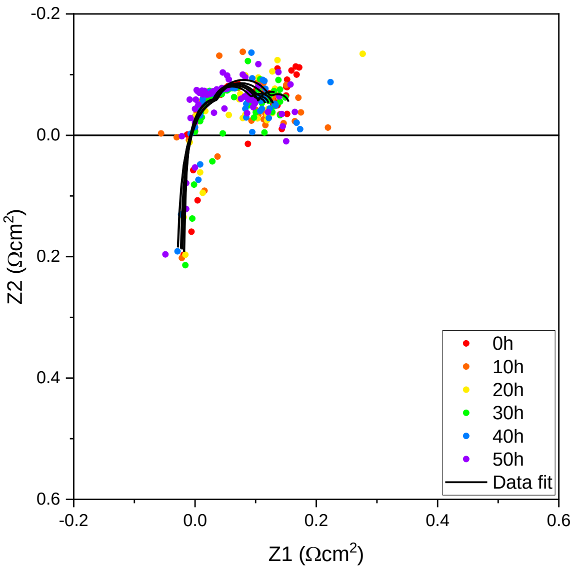

11.2 Rp and Rs monitoring against time

11.2.1 Batch A

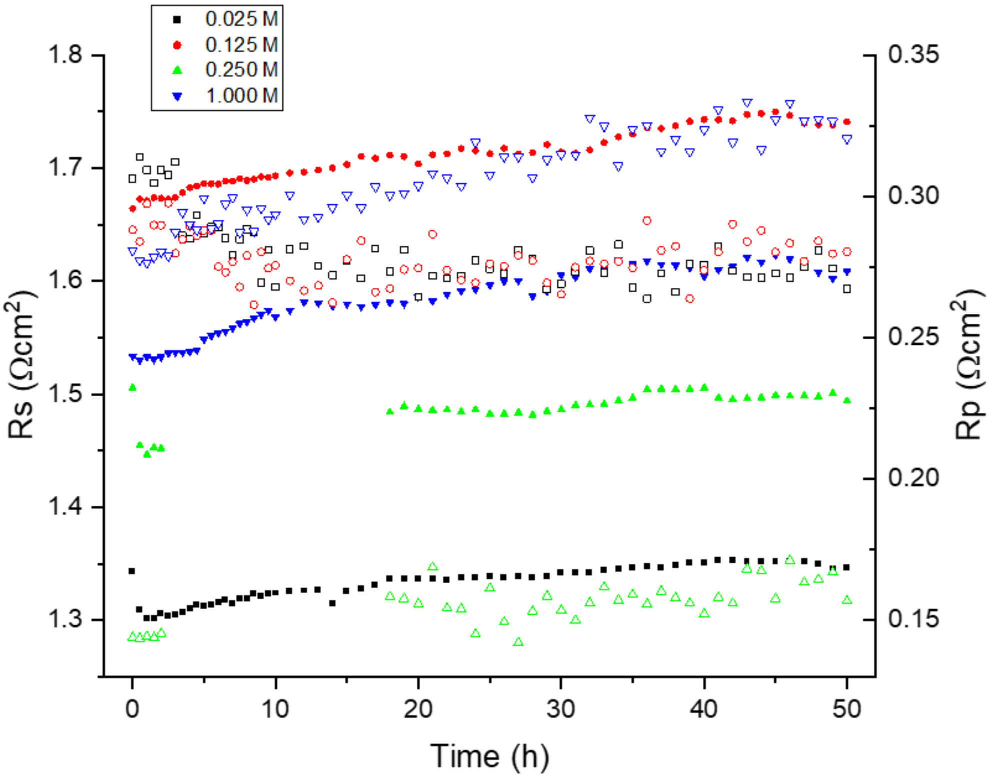

11.2.2 Batch B, set 1

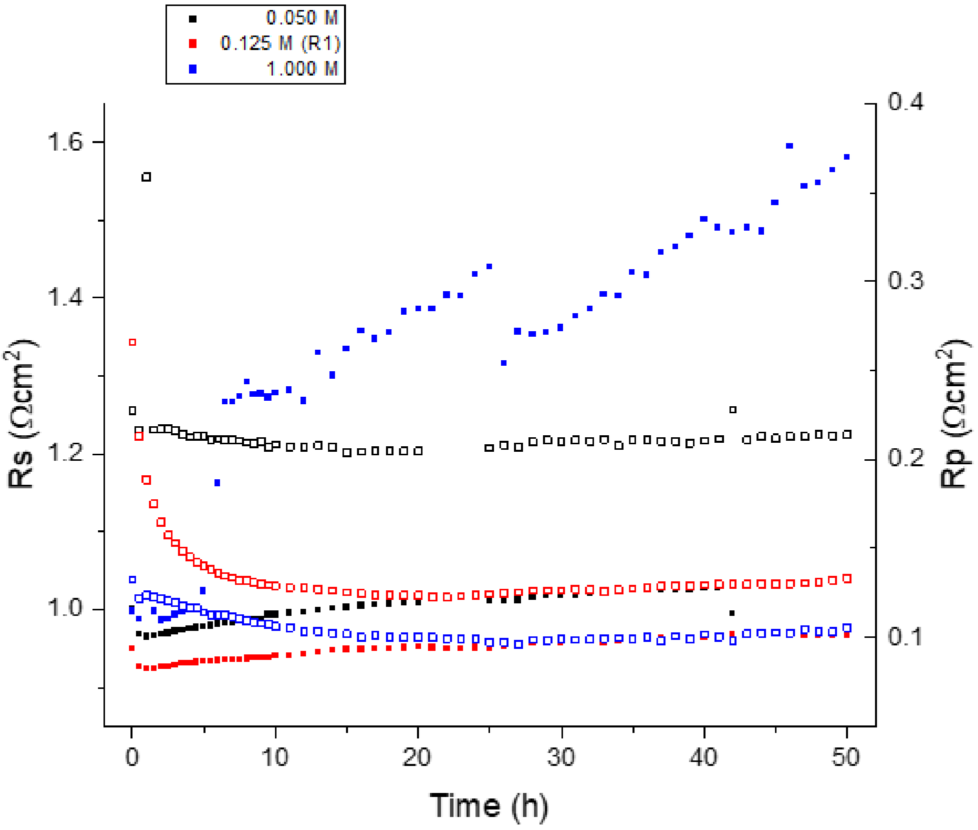

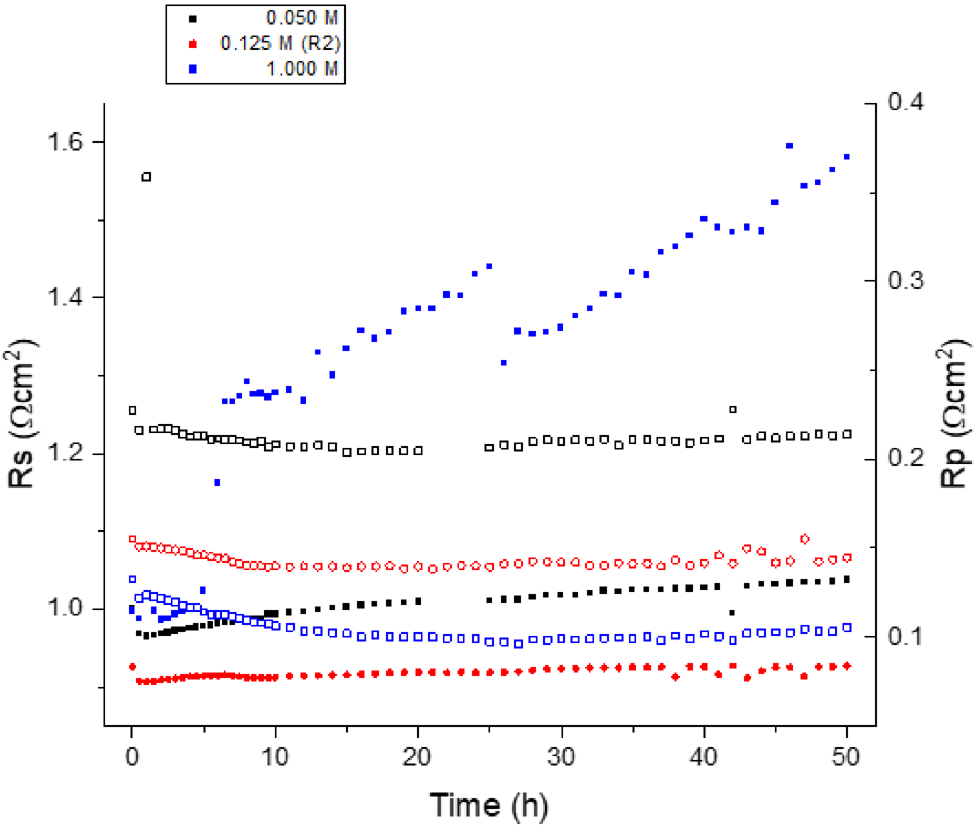

11.2.3 Batch B, set 2

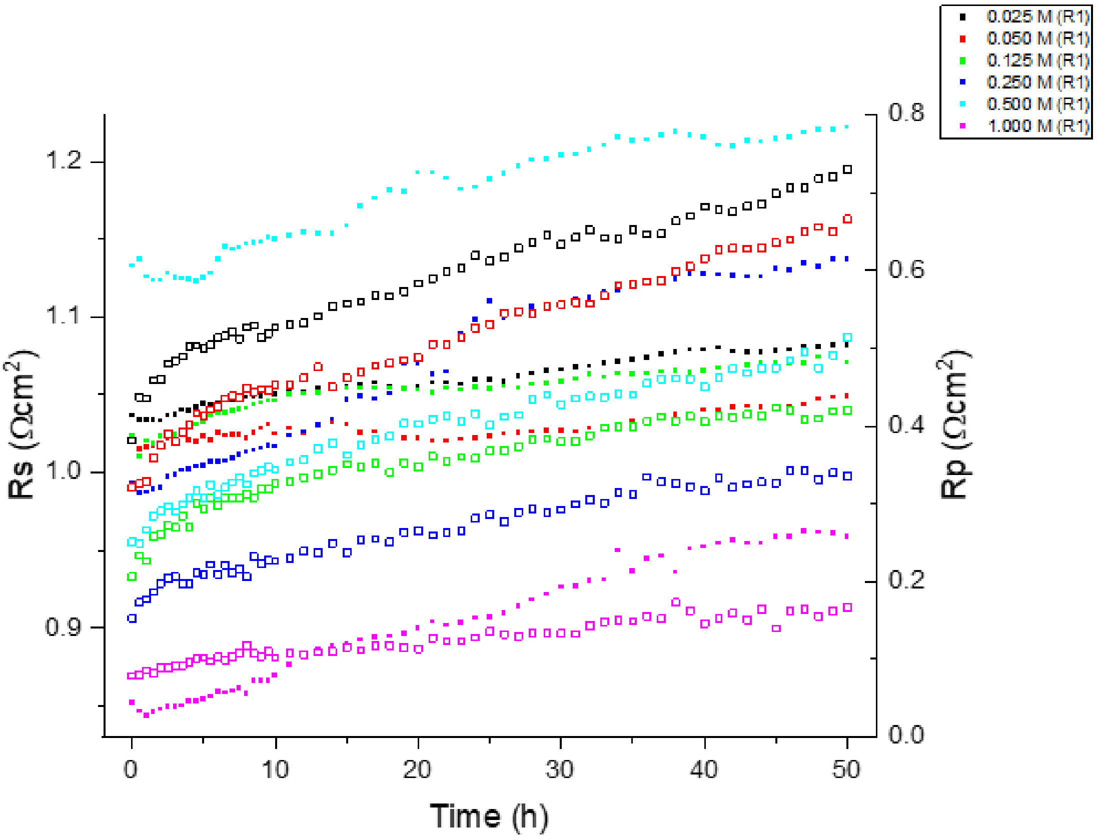

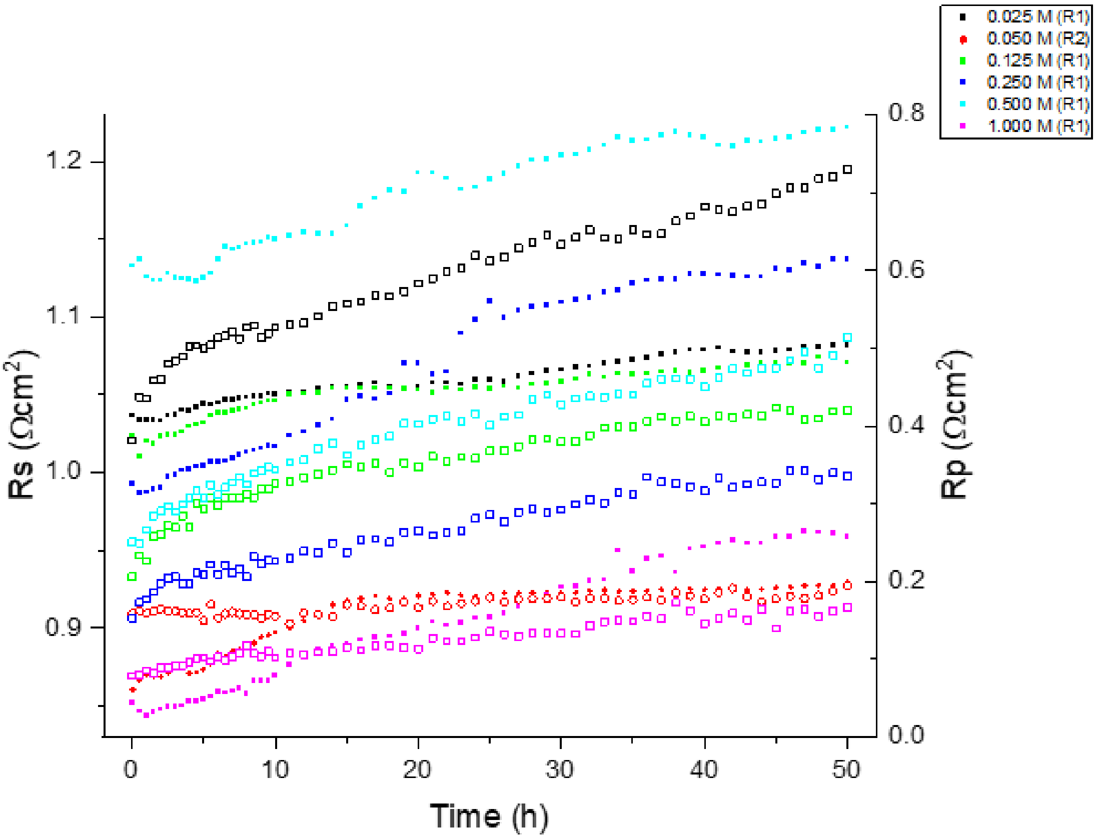

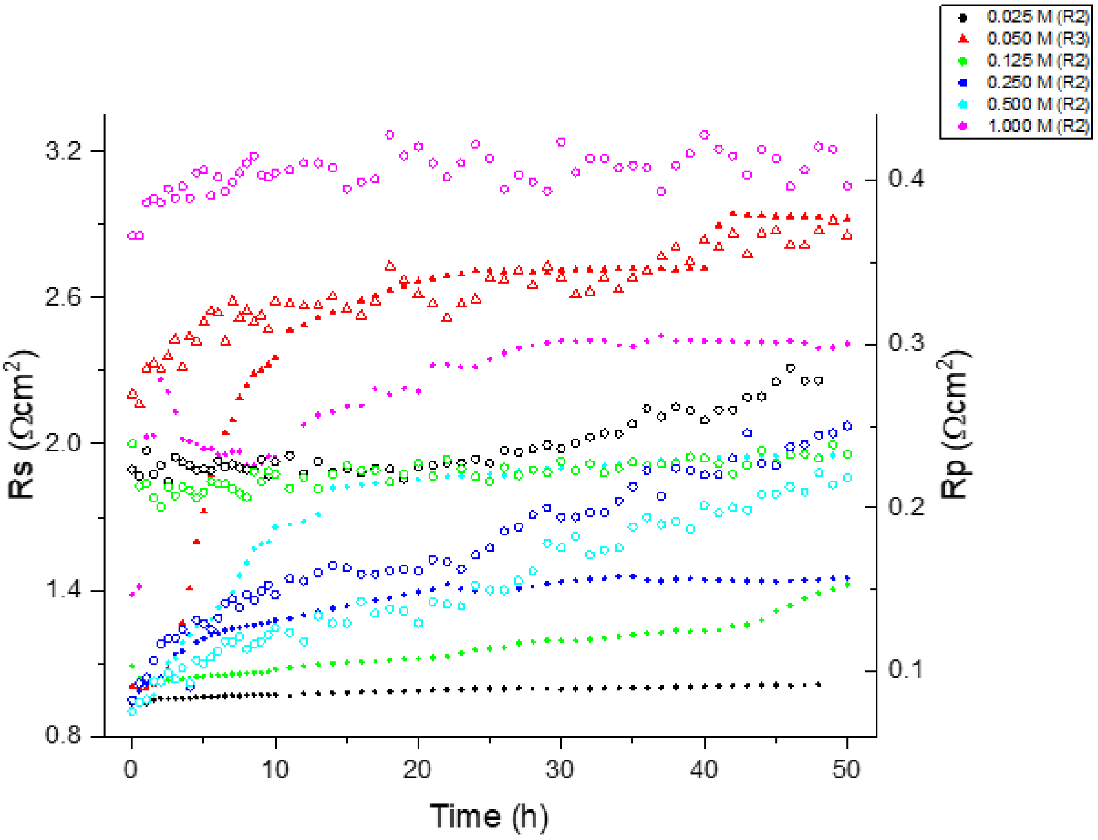

● 0.025 M (R2)
▲ 0.050 M (R3)
● 0.125 M (R2)
● 0.250 M (R2)
● 0.500 M (R2)
● 1.000 M (R2)
Rs (Ωcm²)
3.2
2.6
2.0
1.4
0.8
Rp (Ωcm²)
0.4
0.3
0.2
0.1
0
10
20
30
40
50
Time (h)

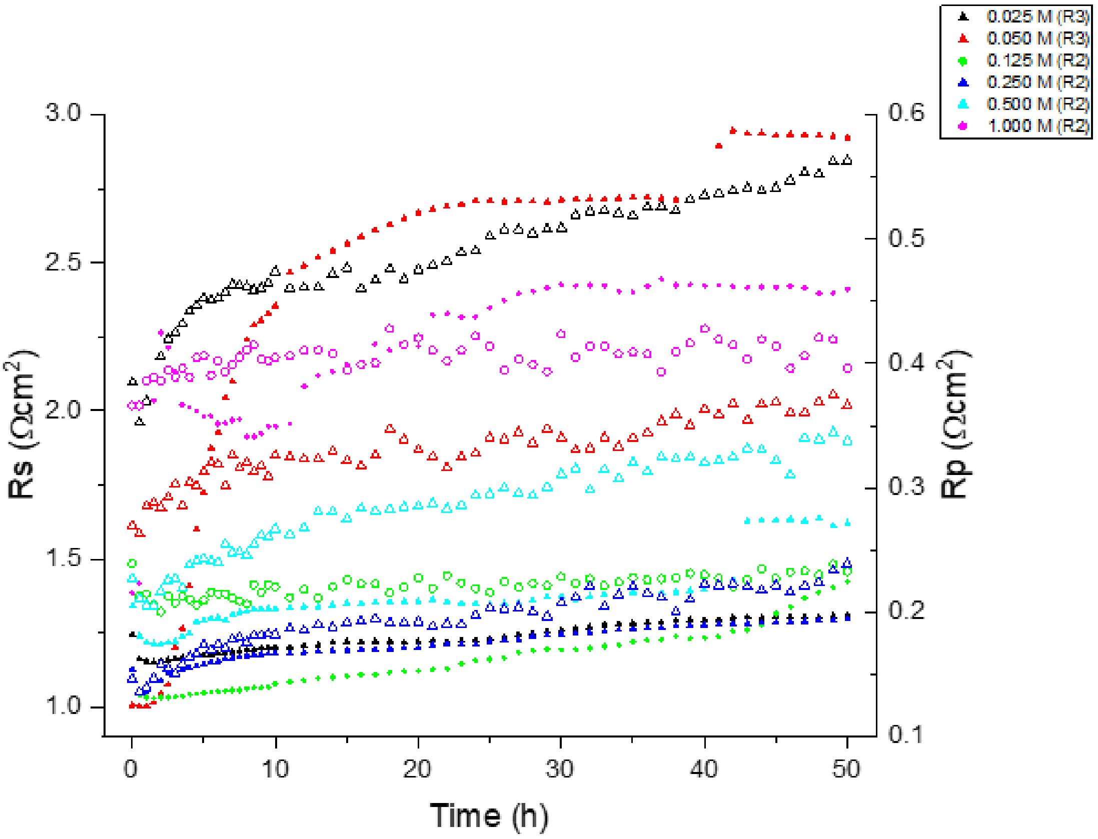

▲ 0.025 M (R3)
▲ 0.050 M (R3)
● 0.125 M (R2)
▲ 0.250 M (R2)
▲ 0.500 M (R2)
● 1.000 M (R2)
Rs (Ωcm²)
3.0
2.5
2.0
1.5
1.0
Rp (Ωcm²)
0.6
0.5
0.4
0.3
0.2
0.1
0
10
20
30
40
50
Time (h)

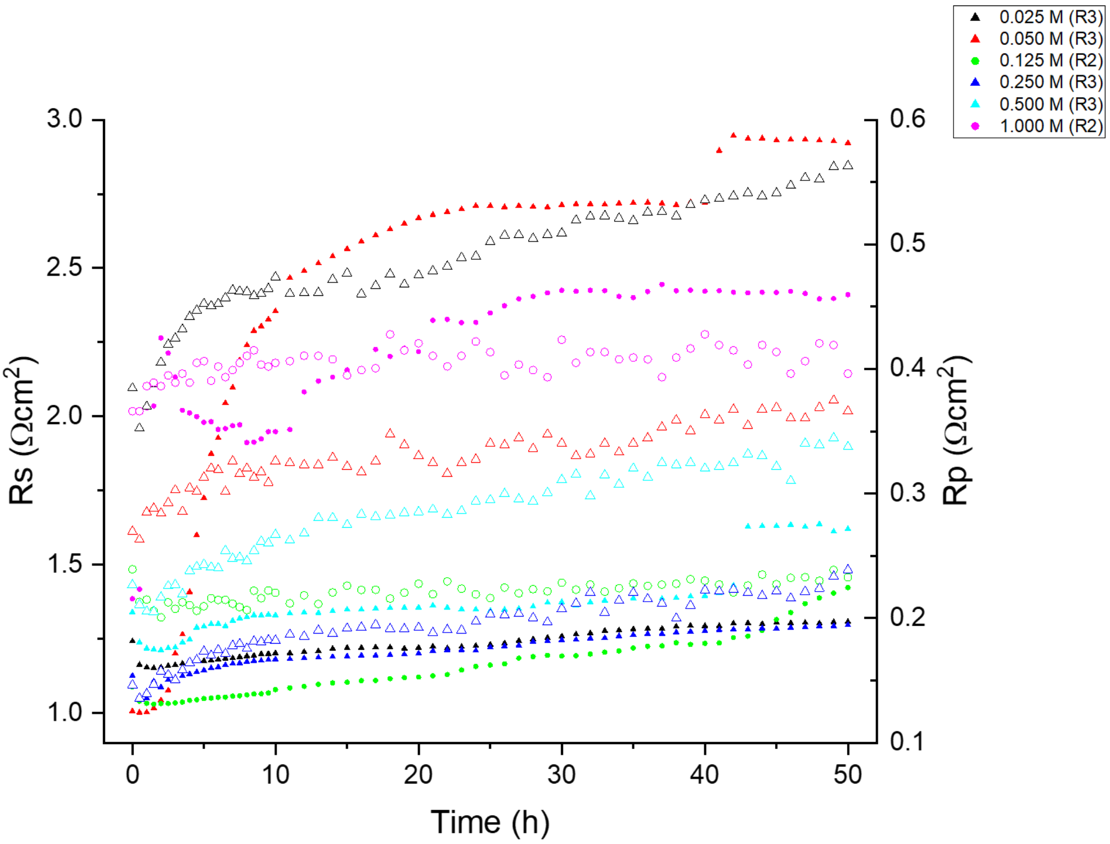

0.025 M (R3)
0.050 M (R3)
0.125 M (R2)
0.250 M (R3)
0.500 M (R3)
1.000 M (R2)
Rs (Ωcm^2)
Rp (Ωcm^2)
Time (h)
3.0
2.5
2.0
1.5
1.0
0.6
0.5
0.4
0.3
0.2
0.1
0
10
20
30
40
50

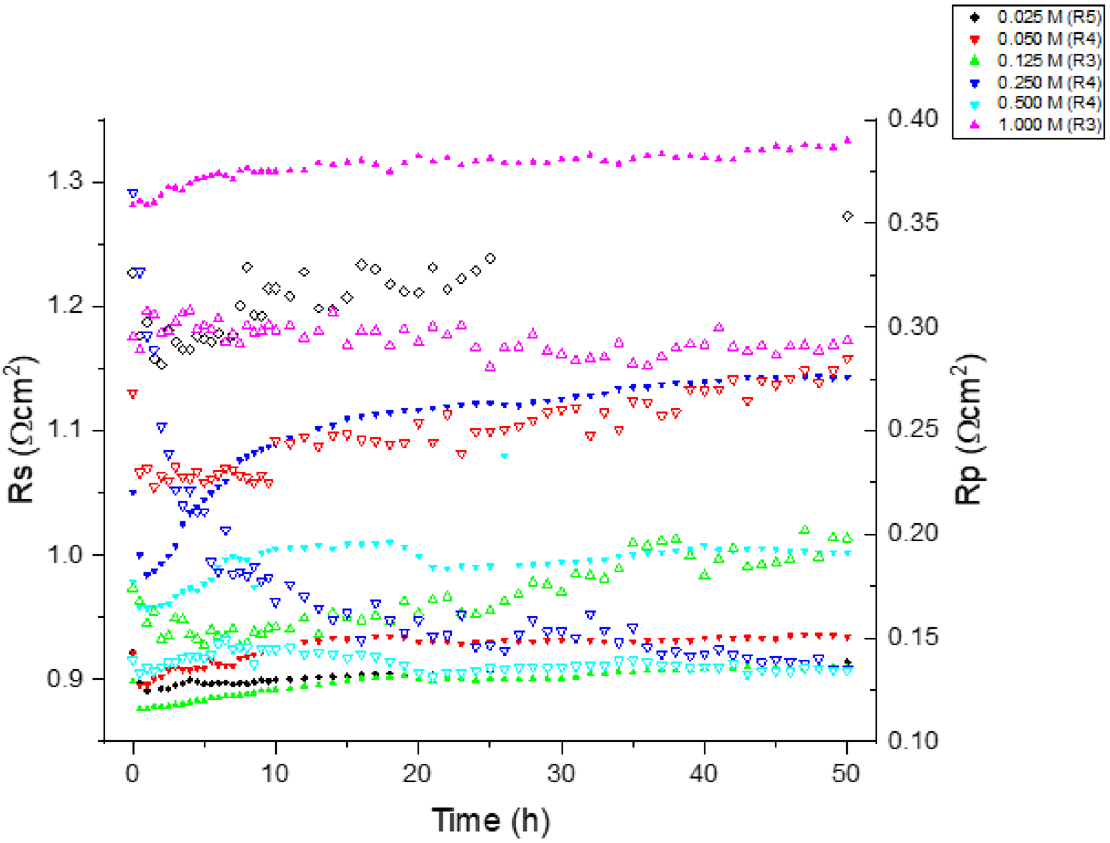

0.025 M (R5)
0.050 M (R4)
0.125 M (R3)
0.250 M (R4)
0.500 M (R4)
1.000 M (R3)
Rs (Ωcm^2)
Rp (Ωcm^2)
Time (h)
1.3
1.2
1.1
1.0
0.9
0.40
0.35
0.30
0.25
0.20
0.15
0.10
0
10
20
30
40
50

11.2.4 Batch C

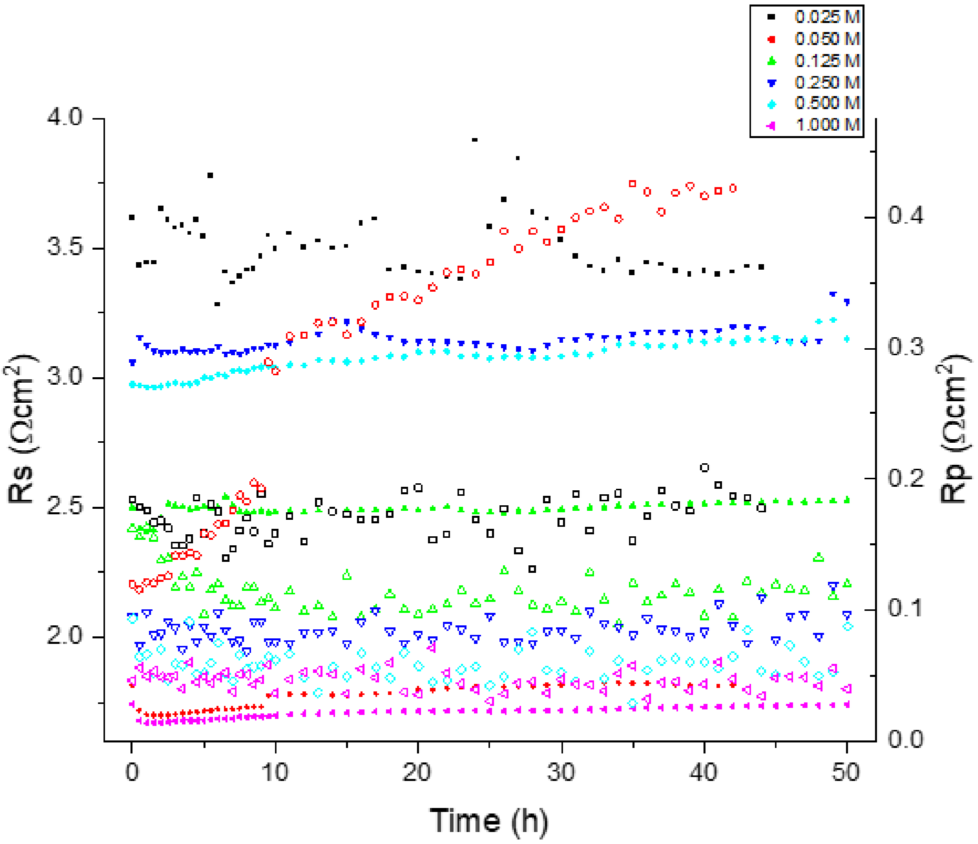
0.025 M
0.050 M
0.125 M
0.250 M
0.500 M
1.000 M
Rs (Ωcm²)
Rp (Ωcm²)
Time (h)
4.0
3.5
3.0
2.5
2.0
0.4
0.3
0.2
0.1
0.0
0
10
20
30
40
50

11.3 EIS data fitting results

11.3.1 Batch A

Sample	Date	24/06/2021		0.025	mol/L																
200	Chi-Sqr	Sum-Sqr	**L**	R1	%error	R2	%error	CPE1-T	%error	W-R	%error	W-T	%error	R3	%error	CPE2-T	%error	**Rs**	**%error**	**Rp**	**%error**
0h	1.70E-03	0.00371	5.12E-06	9.587	0.17804	0.56995	7.7266	2.38E-04	10.306	0.79872	14.238	1.88E-02	14.497	1.225	7.567	1.80E-03	8.4691	1.321816	0.17804	0.319322	9.843867
10h	2.09E-03	0.00422	5.12E-06	9.48	0.1853	0.55211	8.8589	2.76E-04	11.113	0.56734	19.805	2.04E-02	20.824	1.184	7.6665	1.90E-03	9.7677	1.306478	0.1853	0.277719	12.11013
20h	2.54E-03	0.00505	5.12E-06	9.555	0.20424	0.55393	9.4353	2.62E-04	12.252	0.54699	20.064	2.15E-02	22.716	1.178	7.5991	1.83E-03	10.77	1.317229	0.20424	0.274203	12.36613
30h	2.37E-03	0.00487	5.12E-06	9.6	0.19893	0.56866	8.9532	2.63E-04	11.744	0.55234	17.238	2.49E-02	21.218	1.187	6.6471	1.84E-03	10.643	1.32368	0.19893	0.278371	10.9461
40h	2.28E-03	0.00588	5.12E-06	9.677	0.20663	0.68383	6.78	2.76E-04	10.585	0.29139	15.311	1.83E-01	33.985	1.374	3.659	2.23E-03	9.1916	1.334718	0.20663	0.28428	8.583333
50h	2.52E-03	0.00666	5.12E-06	9.644	0.21953	0.68392	7.1443	2.78E-04	11.22	0.26394	16.784	2.86E-01	39.073	1.365	3.7832	2.25E-03	9.7537	1.329987	0.21953	0.279068	9.237167

Sample	Date	28/06/2021		0.125	mol/L																
202	Chi-Sqr	Sum-Sqr	**L**	R1	%error	R2	%error	CPE1-T	%error	W-R	%error	W-T	%error	R3	%error	CPE2-T	%error	**Rs**	**%error**	**Rp**	**%error**
0h	2.59E-03	0.00538	4.86E-06	11.85	0.20376	0.56017	8.1507	2.76E-04	15.051	0.56948	18.719	5.39E-02	25.088	1.295	7.1707	3.14E-03	9.3203	1.646217	0.20376	0.295093	11.3468
10h	3.20E-03	0.00723	4.86E-06	12.08	0.22861	0.60354	8.2969	2.97E-04	16.311	0.34768	18.569	2.16E-01	39.263	1.41	4.4296	3.30E-03	10.004	1.679188	0.22861	0.286	10.43183
20h	3.01E-03	0.00623	4.86E-06	12.16	0.21676	0.56536	8.7038	2.86E-04	16.414	0.45893	17.304	9.05E-02	29.933	1.305	5.5755	3.05E-03	10.385	1.690656	0.21676	0.281423	10.52777
30h	3.48E-03	0.00642	4.86E-06	12.2	0.23139	0.50662	10.567	2.56E-04	19.052	0.66062	19.324	3.79E-02	24.527	1.125	9.7787	2.82E-03	12.32	1.69639	0.23139	0.276112	13.22323
40h	2.14E-03	0.00399	4.86E-06	12.41	0.17729	0.53395	8.2086	2.78E-04	14.323	0.60795	16.995	4.16E-02	21.486	1.194	7.4341	2.90E-03	9.4946	1.726493	0.17729	0.282371	10.87923
50h	4.00E-03	0.00748	4.86E-06	12.39	0.24695	0.51812	11.54	2.64E-04	20.319	0.70126	21.056	3.70E-02	25.784	1.136	11.143	2.87E-03	13.499	1.723626	0.24695	0.285163	14.57967

Sample	Date	01/07/2021		0.25	mol/L																
203	Chi-Sqr	Sum-Sqr	**L**	R1	%error	R2	%error	CPE1-T	%error	W-R	%error	W-T	%error	R3	%error	CPE2-T	%error	**Rs**	**%error**	**Rp**	**%error**
0h	3.62E-03	0.00333	5.03E-06	10.73	0.1874	0.61054	43.797	2.36E-03	22.556	0.39443	84.588	5.85E-03	40.382	0.42762	18.944	2.80E-04	16.333	1.485665	0.1874	0.152881	49.10967
20h	3.55E-03	0.00493	5.03E-06	10.64	0.19845	0.89767	6.1025	2.62E-03	14.011	0.17271	31.39	6.32E-02	57.385	0.46866	10.077	3.13E-04	15.756	1.472764	0.19845	0.168141	15.8565
30h	2.92E-03	0.00457	5.03E-06	10.65	0.19	0.91045	5.1301	2.63E-03	13.007	0.16627	23.693	1.47E-01	52.779	0.46583	9.4605	3.20E-04	15.24	1.474197	0.19	0.168644	12.7612
40h	3.98E-03	0.00478	5.03E-06	10.77	0.19871	0.86492	10.735	2.52E-03	15.212	0.22241	50.919	2.19E-02	57.315	0.45208	11.959	3.10E-04	16.352	1.491399	0.19871	0.168194	24.53767
50h	2.84E-03	0.00427	5.03E-06	10.71	0.18113	0.90949	5.3571	2.66E-03	13.224	0.16922	25.44	9.74E-02	52.073	0.46396	9.7504	3.46E-04	14.789	1.482798	0.18113	0.168661	13.51583

Sample	Date	05/07/2021		1	mol/L																
205	Chi-Sqr	Sum-Sqr	**L**	R1	%error	R2	%error	CPE1-T	%error	W-R	%error	W-T	%error	R3	%error	CPE2-T	%error	**Rs**	**%error**	**Rp**	**%error**
0h	3.62E-03	0.00441	5.00E-06	10.67	0.27843	0.92631	11.47	3.84E-04	23.919	0.65945	14.567	3.84E-05	21.639	1.025	12.554	2.34E-03	25.952	1.477064	0.27843	0.321772	12.86367
10h	3.39E-03	0.00417	5.00E-06	10.97	0.28214	0.88645	11.232	3.22E-04	27.306	0.56347	18.966	3.32E-05	26.727	1.246	9.2849	1.68E-03	19.651	1.520069	0.28214	0.33398	13.16097
20h	3.95E-03	0.00496	5.00E-06	11.07	0.30754	0.91305	11.752	3.11E-04	29.177	0.55481	21.18	3.32E-05	29.839	1.279	9.5809	1.67E-03	20.467	1.534404	0.30754	0.341282	14.17097
30h	2.98E-03	0.00387	5.00E-06	11.21	0.25796	0.91418	11.409	3.52E-04	28.252	0.60393	19.261	4.06E-05	25.68	1.286	9.5257	1.76E-03	19.85	1.554473	0.25796	0.349489	13.39857
40h	3.01E-03	0.00407	5.00E-06	11.19	0.2629	0.9528	10.986	3.53E-04	26.673	0.61083	18.542	4.11E-05	25.347	1.317	9.3561	1.81E-03	19.595	1.551606	0.2629	0.360458	12.96137
50h	0.00328	0.00426	5.00E-06	11.21	0.2892	0.93733	10.472	2.83E-04	27.238	0.54147	20.877	3.16E-05	29.064	1.416	7.5487	0.0015	16.434	1.554473	0.2892	0.362489	12.9659

11.3.2 Batch B, set 1

Sample	Date	21/01/2021		0.05	mol/L																
86	Chi-Sqr	Sum-Sqr	**L**	R1	%error	R2	%error	CPE1-T	%error	W-R	%error	W-T	%error	R3	%error	CPE2-T	%error	**Rs**	**%error**	**Rp**	**%error**
0h	1.89E-04	3.36E-04	1.03E-06	7.269	0.06473	0.87922	2.2967	1.16E-02	5.0144	0.3906	2.9816	1.15E-04	5.4658	0.75965	2.3224	1.81E-03	3.8834	0.989531	0.06473	0.238444	2.533567
10h	2.48E-04	4.17E-04	1.03E-06	7.231	0.06937	0.69826	3.5484	1.60E-02	7.5442	0.38932	3.3173	1.37E-04	6.0643	0.77587	2.7749	2.09E-03	4.2014	0.984083	0.06937	0.214645	3.213533
20h	FALSE	4.37E-04	1.03E-06	7.333	0.07028	0.65566	3.8636	1.80E-02	8.2412	0.39751	3.3549	1.44E-04	6.1461	0.79681	2.7664	2.13E-03	4.2354	0.998705	0.07028	0.212714	3.3283
30h	3.02E-04	4.66E-04	1.03E-06	7.386	0.07172	0.65447	3.9417	1.95E-02	8.46	0.41129	3.3453	1.53E-04	6.1525	0.82242	2.7362	2.20E-03	4.2518	1.006303	0.07172	0.21819	3.341067
40h	3.11E-04	5.12E-04	1.03E-06	7.459	0.0743	0.62804	4.3051	2.17E-02	9.2627	0.41458	3.4891	1.62E-04	6.4343	0.84369	2.7997	2.27E-03	4.3685	1.016767	0.0743	0.217922	3.5313
50h	2.74E-04	5.32E-04	1.03E-06	7.528	0.07485	0.6103	4.4924	2.39E-02	9.7068	0.42942	3.4651	1.72E-04	6.3893	0.86973	2.7574	2.32E-03	4.3695	1.026658	0.07485	0.221239	3.571633

Sample	Date	14/12/2020		0.125	mol/L																
61	Chi-Sqr	Sum-Sqr	**L**	R1	%error	R2	%error	CPE1-T	%error	W-R	%error	W-T	%error	R3	%error	CPE2-T	%error	**Rs**	**%error**	**Rp**	**%error**
0h	1.43E-04	3.24E-04	1.37E-06	6.961	0.04817	0.94648	3.2591	5.70E-03	2.3349	1.03	3.6407	3.72E-02	2.9053	0.28347	3.7274	1.15E-03	4.3077	0.945379	0.04817	0.271483	3.5424
10h	1.59E-04	2.24E-04	1.37E-06	6.897	0.04047	0.81558	1.2177	4.30E-03	2.5721	0.18474	5.9695	5.77E-02	8.7126	0.28202	2.9623	9.94E-04	3.5709	0.936205	0.04047	0.131343	3.383167
20h	1.50E-04	2.05E-04	1.37E-06	6.98	0.03888	0.7904	1.131	4.15E-03	2.6145	0.17244	5.2654	6.72E-02	8.5101	0.28195	2.9023	9.72E-04	3.467	0.948103	0.03888	0.12596	3.099567
30h	1.65E-04	2.30E-04	1.37E-06	7.023	0.04123	0.79736	1.1893	4.19E-03	2.7162	0.18654	5.2308	6.75E-02	8.4162	0.28093	3.0401	9.68E-04	3.7097	0.954267	0.04123	0.128833	3.1534
40h	1.66E-04	2.36E-04	1.37E-06	7.072	0.04159	0.80233	1.2122	4.25E-03	2.7542	0.1986	5.0735	6.77E-02	8.1023	0.28316	3.0804	9.79E-04	3.7466	0.961291	0.04159	0.131594	3.122033
50h	1.64E-04	2.39E-04	1.37E-06	7.089	0.04173	0.81018	1.2284	4.38E-03	2.7152	0.21685	4.8863	6.67E-02	7.6094	0.28431	3.0506	9.91E-04	3.7586	0.963728	0.04173	0.1355	3.0551

Sample	Date	15/01/2021		0.125	mol/L																
119	Chi-Sqr	Sum-Sqr	**L**	R1	%error	R2	%error	CPE1-T	%error	W-R	%error	W-T	%error	R3	%error	CPE2-T	%error	**Rs**	**%error**	**Rp**	**%error**
0h	2.18E-04	2.94E-04	1.21E-06	6.742	0.06316	0.55956	4.2269	1.22E-02	8.5256	0.32802	3.2214	9.51E-05	5.7864	0.63632	3.2015	1.79E-03	4.0603	0.913985	0.06316	0.165971	3.549933
10h	2.69E-04	3.57E-04	1.21E-06	6.661	0.06564	0.35287	5.4215	3.17E-02	11.717	0.33792	3.1061	1.23E-04	5.8178	0.70678	2.3746	2.17E-03	3.7854	0.902374	0.06564	0.147861	3.634067
20h	2.72E-04	3.75E-04	1.21E-06	6.71	0.06553	0.31547	5.3656	4.43E-02	12.052	0.35048	3.0744	1.39E-04	5.7668	0.73048	2.0654	2.32E-03	3.7971	0.909398	0.06553	0.147698	3.5018
30h	2.63E-04	3.74E-04	1.21E-06	6.742	0.06466	0.3124	5.032	5.07E-02	11.533	0.35891	2.9704	1.48E-04	5.6077	0.73882	1.9221	2.44E-03	3.7344	0.913985	0.06466	0.149662	3.308167
40h	2.71E-04	3.93E-04	1.21E-06	6.761	0.06568	0.29997	4.9062	5.97E-02	11.516	0.36436	2.9839	1.55E-04	5.6534	0.74135	1.83	2.53E-03	3.8079	0.916709	0.06568	0.149024	3.240033
50h	2.75E-04	4.12E-04	1.21E-06	6.766	0.06674	0.31365	4.719	6.08E-02	11.137	0.36823	2.9932	1.61E-04	5.699	0.74416	1.8417	2.63E-03	3.8562	0.917426	0.06674	0.151942	3.184633

Sample	Date	17/11/2020		1	mol/L																
73	Chi-Sqr	Sum-Sqr	**L**	R1	%error	R2	%error	CPE1-T	%error	W-R	%error	W-T	%error	R3	%error	CPE2-T	%error	**Rs**	**%error**	**Rp**	**%error**
0h	1.41E-04	1.86E-04	1.42E-06	7.344	0.03764	0.82197	1.0334	3.52E-03	2.5544	0.13154	5.6051	8.53E-02	10.4	0.32474	2.5491	7.77E-04	3.0434	1.000282	0.03764	0.130757	3.062533
10h	1.17E-04	1.15E-04	1.42E-06	9.242	0.03015	0.73967	1.1443	3.19E-03	2.8848	0.11504	5.1173	1.06E-01	10.633	0.29141	2.9408	7.76E-04	3.3664	1.27236	0.03015	0.111816	3.067467
20h	9.40E-05	8.41E-05	1.48E-06	9.985	0.02659	0.71234	1.0793	2.92E-03	2.7223	0.1193	4.3013	1.07E-01	9.2235	0.27603	2.8131	7.12E-04	3.3322	1.378869	0.02659	0.106304	2.731233
30h	9.04E-05	8.21E-05	1.48E-06	9.814	0.02644	0.70252	1.0696	2.85E-03	2.6962	0.12697	3.9316	1.02E-01	8.4192	0.27051	2.8075	7.07E-04	3.3117	1.354356	0.02644	0.105205	2.6029
40h	9.09E-05	7.69E-05	1.48E-06	10.79	0.02555	0.70652	1.1359	2.83E-03	2.8613	0.13675	3.919	9.62E-02	8.2949	0.27628	2.9414	6.95E-04	3.4453	1.494266	0.02555	0.108007	2.665433
50h	9.63E-05	7.98E-05	1.48E-06	11.34	0.02606	0.71625	1.1918	2.81E-03	3.004	0.14743	3.9335	9.31E-02	8.2552	0.28476	3.0326	6.72E-04	3.5816	1.573109	0.02606	0.112148	2.7193

11.3.3 Batch B, set 2

Sample	Date	10/02/2020		0.025	mol/L																
65	Chi-Sqr	Sum-Sqr	**L**	R1	%error	R2	%error	CPE1-T	%error	W-R	%error	W-T	%error	R3	%error	CPE2-T	%error	**Rs**	**%error**	**Rp**	**%error**
0h	0.00156	0.00492	5.20E-06	7.42	0.20752	1.374	5.1914	1.45E-03	7.5162	1.021	8.531	2.08E-02	10.182	0.72081	5.8036	1.88E-04	7.4091	1.011177	0.20752	0.394171	6.508667
10h	0.00125	0.0057	5.20E-06	7.53	0.21126	1.799	3.7553	1.65E-03	5.8388	1.548	5.1279	4.13E-02	7.2864	0.85292	4.6664	2.01E-04	6.695	1.026945	0.21126	0.549578	4.516533
20h	0.00132	0.00646	5.20E-06	7.558	0.22187	1.885	3.9746	1.74E-03	5.9009	1.737	5.0792	4.48E-02	7.1369	0.88416	4.7633	2.08E-04	6.8674	1.030959	0.22187	0.593478	4.6057
30h	0.0014	0.00733	5.20E-06	7.646	0.23421	1.993	3.7989	1.74E-03	5.9903	1.879	4.6967	5.27E-02	7.0138	0.92687	4.7925	2.06E-04	7.039	1.043574	0.23421	0.635438	4.429367
40h	0.00139	0.00818	5.20E-06	7.753	0.23637	2.331	2.8305	2.00E-03	5.3634	1.642	4.4948	1.11E-01	8.1093	1.096	4.046	2.19E-04	6.287	1.058912	0.23637	0.674161	3.790433
50h	0.00246	0.01463	5.20E-06	7.78	0.30549	2.578	3.2357	2.35E-03	6.3934	1.569	5.9184	1.80E-01	11.451	1.224	4.6641	2.37E-04	7.4721	1.062783	0.30549	0.717452	4.606067

Sample	Date	18/08/2020		0.025	mol/L																
59	Chi-Sqr	Sum-Sqr	**L**	R1	%error	R2	%error	CPE1-T	%error	W-R	%error	W-T	%error	R3	%error	CPE2-T	%error	**Rs**	**%error**	**Rp**	**%error**
0h	0.00118	0.00296	5.29E-06	6.76	0.15993	0.54078	5.1267	2.57E-04	6.9148	0.48725	11.074	0.02388	13.714	1.001	4.4736	0.0021	6.9392	0.916566	0.15993	0.238381	6.891433
10h	0.00123	0.00305	5.29E-06	7.032	0.15685	0.55108	5.5892	2.91E-04	7.0602	0.43218	10.383	0.03178	14.884	0.99843	3.9426	0.00214	7.8383	0.955557	0.15685	0.231595	6.638267
20h	0.00142	0.00376	5.29E-06	7.145	0.16896	0.58079	5.7689	3.16E-04	7.4735	0.38273	9.398	0.06142	16.936	1.024	3.616	0.00235	8.5257	0.971755	0.16896	0.232431	6.260967
30h	0.0011	0.00361	5.29E-06	7.227	0.1581	0.61443	5.4361	3.77E-04	6.8726	0.41959	6.8059	0.13596	14.465	1.064	3.2542	0.00272	8.1934	0.98351	0.1581	0.248271	5.1654
40h	0.00147	0.00459	5.29E-06	7.26	0.18961	0.58948	6.1061	2.86E-04	8.3225	0.62674	6.5905	0.0579	11.811	1.037	3.9714	0.00226	9.137	0.988241	0.18961	0.270519	5.556
50h	0.00101	0.00365	5.29E-06	7.313	0.16353	0.66544	4.43	2.97E-04	6.5396	0.59414	5.0579	0.13286	10.648	1.121	2.9052	0.0027	7.1209	0.995838	0.16353	0.288776	4.131033

Sample	Date	14/09/2020		0.025	mol/L																
94	Chi-Sqr	Sum-Sqr	**L**	R1	%error	R2	%error	CPE1-T	%error	W-R	%error	W-T	%error	R3	%error	CPE2-T	%error	**Rs**	**%error**	**Rp**	**%error**
0h	9.04E-04	0.0027	4.73E-06	8.904	0.14578	0.57771	5.7262	2.79E-04	7.9284	1.213	6.333	2.79E-02	7.3792	1.334	4.7617	2.03E-03	6.1287	1.223908	0.14578	0.395447	5.606967
10h	1.25E-03	0.00502	4.73E-06	8.631	0.18519	0.60381	6.6895	3.82E-04	9.741	1.62	5.2672	5.50E-02	7.1141	1.452	4.9781	2.88E-03	7.2138	1.184773	0.18519	0.474447	5.644933
20h	6.64E-04	0.00265	4.73E-06	8.764	0.13631	0.56541	5.2595	3.77E-04	7.7057	1.765	3.51	5.08E-02	4.7804	1.408	3.7285	2.73E-03	5.4745	1.203839	0.13631	0.483421	4.166
30h	1.09E-03	0.00451	4.73E-06	9.038	0.1719	0.63987	5.9867	3.99E-04	9.0354	1.631	5.0148	6.90E-02	6.9913	1.656	4.2184	2.98E-03	6.0924	1.243117	0.1719	0.510436	5.0733
40h	1.21E-03	0.00502	4.73E-06	9.287	0.17923	0.67038	6.3043	4.09E-04	9.3148	1.629	5.6538	7.08E-02	7.6942	1.75	4.4782	2.98E-03	6.3204	1.278811	0.17923	0.527998	5.478767
50h	1.16E-03	0.00513	4.73E-06	9.383	0.17942	0.71827	5.7451	4.00E-04	8.8501	1.672	5.0124	9.07E-02	7.4432	1.878	3.8528	3.05E-03	5.9092	1.292573	0.17942	0.559376	4.8701

Sample	Date	05/03/2021		0.025	mol/L																
85	Chi-Sqr	Sum-Sqr	**L**	R1	%error	R2	%error	CPE1-T	%error	W-R	%error	W-T	%error	R3	%error	CPE2-T	%error	**Rs**	**%error**	**Rp**	**%error**
0h	8.30E-04	0.00276	5.07E-06	7.564	0.14372	0.43627	5.7467	4.21E-04	8.8758	0.98273	5.764	4.31E-02	7.3808	1.097	4.3722	3.26E-03	5.8774	1.031819	0.14372	0.308188	5.2943
10h	7.31E-04	0.0025	5.07E-06	7.338	0.13397	0.43208	5.2257	4.69E-04	8.2042	0.82056	5.316	5.80E-02	7.6571	1.125	3.349	3.45E-03	5.3124	0.999422	0.13397	0.288354	4.630233
20h	8.20E-04	0.00289	5.07E-06	7.411	0.13972	0.4821	5.0073	4.94E-04	7.9036	0.67344	5.9434	8.66E-02	9.6115	1.211	2.9455	3.71E-03	5.3981	1.009886	0.13972	0.286763	4.632067
30h	9.77E-04	0.00356	5.07E-06	7.458	0.14914	0.55226	4.7836	5.39E-04	7.6107	0.50486	7.183	1.64E-01	13.544	1.317	2.5969	4.24E-03	5.5531	1.016624	0.14914	0.28785	4.8545
40h	8.26E-04	0.0029	5.07E-06	7.496	0.14054	0.45918	5.4863	5.06E-04	8.4222	0.77139	5.2195	7.98E-02	8.4441	1.151	3.1254	3.61E-03	5.8789	1.022071	0.14054	0.288918	4.6104
50h	0.00102	0.00355	5.07E-06	7.496	0.15479	0.45327	6.2287	5.27E-04	9.4207	0.76977	5.9439	7.76E-02	9.4314	1.141	3.5616	3.68E-03	6.6149	1.022071	0.15479	0.286405	5.244733

Sample	Date	22/03/2021		0.025	mol/L																
134	Chi-Sqr	Sum-Sqr	**L**	R1	%error	R2	%error	CPE1-T	%error	W-R	%error	W-T	%error	R3	%error	CPE2-T	%error	**Rs**	**%error**	**Rp**	**%error**
0h	3.17E-03	0.01293	5.40E-06	6.629	0.32215	1.141	7.7116	2.03E-02	19.2	1.205	8.0524	3.90E-03	13.74	0.4179	11	4.11E-04	17.405	0.897787	0.32215	0.343725	8.921333
10h	1.30E-03	0.00555	5.40E-06	6.479	0.20707	1.087	4.2758	2.58E-02	11.093	1.128	4.6916	3.96E-03	8.757	0.43269	7.2015	4.50E-04	10.651	0.876284	0.20707	0.327066	5.389633
20h	1.49E-03	0.0068	5.40E-06	6.532	0.22197	1.057	4.3989	3.69E-02	11.709	1.221	4.4185	4.92E-03	8.5842	0.46127	7.4219	4.95E-04	11.016	0.883882	0.22197	0.340194	5.4131
50h	1.84E-03	0.00908	5.40E-06	6.597	0.2554	1.203	3.9825	3.96E-02	10.866	1.242	4.6052	5.07E-03	9.2857	0.47156	8.4483	4.94E-04	12.547	0.8932	0.2554	0.365608	5.678667

Sample	Date	06/02/2020		0.05	mol/L																
66	Chi-Sqr	Sum-Sqr	**L**	R1	%error	R2	%error	CPE1-T	%error	W-R	%error	W-T	%error	R3	%error	CPE2-T	%error	**Rs**	**%error**	**Rp**	**%error**
0h	0.00195	0.00533	5.18E-06	7.317	0.21461	1.314	4.8795	1.52E-03	8.0653	0.60433	12.706	2.39E-02	16.391	0.71499	5.8757	1.93E-04	7.6408	0.996412	0.21461	0.325006	7.8204
10h	0.00147	0.00566	5.18E-06	7.373	0.21331	1.503	5.1057	1.82E-03	6.7985	1.328	6.9501	3.01E-02	8.5428	0.73175	5.5356	2.22E-04	7.6223	1.004439	0.21331	0.45824	5.8638
20h	0.00114	0.00498	5.18E-06	7.349	0.19548	1.622	3.8856	2.02E-03	5.6653	1.486	4.9933	4.37E-02	6.8984	0.75751	4.612	2.36E-04	6.8162	1.000999	0.19548	0.50164	4.496967
30h	0.00124	0.00675	5.18E-06	7.408	0.21459	2.006	3.0035	2.46E-03	5.167	1.387	4.9288	9.88E-02	8.2816	0.90377	4.1036	2.65E-04	6.563	1.009456	0.21459	0.563462	4.011967
40h	0.00135	0.00747	5.18E-06	7.488	0.22867	1.96	3.5719	2.36E-03	5.6266	1.796	4.489	7.96E-02	7.077	0.86983	4.5978	2.58E-04	7.2838	1.020924	0.22867	0.610632	4.219567
50h	0.0015	0.00909	5.18E-06	7.575	0.24504	2.131	3.5133	2.62E-03	5.7404	1.864	4.5957	1.08E-01	7.6247	0.94528	4.6157	2.77E-04	7.4047	1.033396	0.24504	0.655709	4.241567

Sample	Date	12/03/2020		0.05	mol/L																
27	Chi-Sqr	Sum-Sqr	**L**	R1	%error	R2	%error	CPE1-T	%error	W-R	%error	W-T	%error	R3	%error	CPE2-T	%error	**Rs**	**%error**	**Rp**	**%error**
0h	0.00308	0.00697	5.34E-06	6.283	0.24337	0.85096	12.299	3.31E-03	9.9125	0.39368	32.026	0.02038	28.187	0.2688	13.971	5.51E-04	19.447	0.848188	0.24337	0.164471	19.432
10h	0.00288	0.0073	5.34E-06	6.542	0.24084	0.88458	6.9358	3.33E-03	10.436	0.41501	17.419	0.03733	22.874	0.2906	12.342	5.61E-04	18.94	0.885315	0.24084	0.175473	12.23227
20h	0.00161	0.00375	5.34E-06	6.702	0.17419	0.84816	6.0015	3.23E-03	8.1511	0.42062	14.53	0.02973	17.293	0.28308	9.7806	5.58E-04	14.336	0.908251	0.17419	0.169979	10.10403
30h	0.00289	0.0085	5.34E-06	6.719	0.2533	0.93373	5.7126	3.56E-03	10.809	0.49443	12.009	0.06304	19.333	0.31336	12.005	5.79E-04	19.277	0.910688	0.2533	0.197166	9.908867
40h	0.00285	0.00832	5.34E-06	6.742	0.24694	0.91563	5.8428	3.70E-03	11.266	0.48748	12.208	0.06353	19.512	0.31211	12.417	6.30E-04	19.109	0.913985	0.24694	0.193396	10.15593
50h	0.00246	0.00785	5.34E-06	6.769	0.24074	0.92342	5.3384	3.62E-03	10.79	0.61293	8.7587	0.07102	14.836	0.30332	12.229	6.31E-04	19.2	0.917856	0.24074	0.211236	8.775367

Sample	Date	21/08/2020		0.05	mol/L																
60	Chi-Sqr	Sum-Sqr	**L**	R1	%error	R2	%error	CPE1-T	%error	W-R	%error	W-T	%error	R3	%error	CPE2-T	%error	**Rs**	**%error**	**Rp**	**%error**
0h	0.00138	0.00343	5.26E-06	7.193	0.18581	0.99847	6.9503	7.10E-03	15.717	0.9006	8.2863	0.00142	12.751	0.51452	6.7817	2.25E-04	8.3071	0.978636	0.18581	0.293508	7.339433
10h	0.00185	0.00259	5.26E-06	16.65	0.14692	0.94743	15.789	1.06E-02	34.366	1.14	14.072	0.00235	19.409	0.53071	10.852	2.74E-04	15.47	2.334297	0.14692	0.32283	13.571
20h	0.00262	0.00364	5.26E-06	18.83	0.16834	0.71315	17.504	2.58E-02	42.204	1.451	9.5114	0.00322	16.287	0.55327	12.682	2.95E-04	19.38	2.6468	0.16834	0.337062	13.23247
30h	0.00237	0.00358	5.26E-06	19.11	0.17927	1.538	6.7373	1.83E-03	12.067	0.77793	8.7864	1.62E-04	19.096	0.55701	19.764	0.05101	47.485	2.686938	0.17927	0.359356	11.76257
40h	0.00182	0.00279	5.26E-06	19.11	0.163	1.378	8.0835	1.60E-03	12.639	0.74668	8.7509	1.38E-04	18.326	0.92925	13.126	0.01957	29.752	2.686938	0.163	0.3853	9.9868
50h	0.00141	0.0024	5.26E-06	20.58	0.14195	1.671	4.0633	2.01E-03	9.5303	0.84292	6.9453	1.97E-04	15.3	0.63847	10.358	0.08607	27.263	2.897663	0.14195	0.399415	7.1222

Sample	Date	26/03/2021		0.05	mol/L																
135	Chi-Sqr	Sum-Sqr	**L**	R1	%error	R2	%error	CPE1-T	%error	W-R	%error	W-T	%error	R3	%error	CPE2-T	%error	**Rs**	**%error**	**Rp**	**%error**
0h	1.12E-03	0.004	5.40E-06	6.701	0.16439	0.39809	7.1187	6.29E-04	10.178	0.57345	10.281	5.74E-02	13.608	1.359	3.6707	3.23E-03	5.3806	0.908108	0.16439	0.281602	7.023467
10h	2.08E-03	0.00706	5.40E-06	6.708	0.22607	0.34751	10.43	5.94E-04	15.703	0.65561	10.694	5.28E-02	14.973	1.178	5.0986	3.15E-03	8.0615	0.909111	0.22607	0.260183	8.740867
20h	1.77E-03	0.0066	5.40E-06	6.768	0.21215	0.38396	9.2869	6.27E-04	13.731	0.65935	8.4689	7.79E-02	13.694	1.248	3.9974	3.25E-03	7.6414	0.917712	0.21215	0.275979	7.251067
30h	1.91E-03	0.00741	5.40E-06	6.775	0.22294	0.38104	10.302	6.65E-04	14.636	0.78567	7.9023	7.37E-02	12.446	1.218	4.5096	3.36E-03	8.5287	0.918716	0.22294	0.289368	7.5713
40h	1.07E-03	0.00458	5.40E-06	6.804	0.173	0.41163	7.875	7.33E-04	10.781	0.71028	6.0865	1.06E-01	10.733	1.269	3.1716	3.58E-03	6.796	0.922873	0.173	0.290257	5.711033
50h	2.36E-03	0.01072	5.40E-06	6.817	0.24581	0.5171	9.6003	8.29E-04	12.711	0.64368	8.2995	2.42E-01	16.968	1.35	4.0907	4.53E-03	9.8634	0.924737	0.24581	0.30744	7.330167

Sample	Date	13/02/2020		0.125	mol/L																
67	Chi-Sqr	Sum-Sqr	**L**	R1	%error	R2	%error	CPE1-T	%error	W-R	%error	W-T	%error	R3	%error	CPE2-T	%error	**Rs**	**%error**	**Rp**	**%error**
0h	0.00368	0.00705	5.21E-06	7.297	0.276	0.86267	9.3524	1.65E-03	12.811	0.5199	18.838	1.39E-02	21.701	0.61224	7.2818	1.42E-04	10.729	0.993545	0.276	0.233476	11.82407
10h	0.00139	0.00424	5.21E-06	7.471	0.20254	1.137	5.2118	1.96E-03	6.8652	0.98207	7.0792	2.61E-02	9.1588	0.66978	4.4701	1.56E-04	7.5638	1.018487	0.20254	0.347301	5.587033
20h	0.00194	0.0064	5.21E-06	7.506	0.24519	1.25	5.5703	2.07E-03	7.418	0.97393	8.2856	3.30E-02	11.262	0.70206	4.968	1.56E-04	8.8351	1.023505	0.24519	0.36696	6.274633
30h	0.00183	0.00673	5.21E-06	7.554	0.24677	1.339	5.0391	2.18E-03	7.0476	1.094	7.0831	4.16E-02	10.231	0.72933	4.7775	1.62E-04	8.6991	1.030385	0.24677	0.40084	5.633233
40h	0.00188	0.00735	5.21E-06	7.606	0.25202	1.465	4.5799	2.31E-03	6.6795	1.041	7.3352	5.41E-02	11.174	0.78051	4.5524	1.66E-04	8.4675	1.03784	0.25202	0.418641	5.489167
50h	0.00194	0.00842	5.21E-06	7.654	0.26015	1.644	3.5554	2.61E-03	6.2566	0.90315	7.173	1.05E-01	13.019	0.8447	4.2577	1.80E-04	8.2949	1.04472	0.26015	0.433741	4.995367

Sample	Date	17/09/2020		0.125	mol/L																
96	Chi-Sqr	Sum-Sqr	**L**	R1	%error	R2	%error	CPE1-T	%error	W-R	%error	W-T	%error	R3	%error	CPE2-T	%error	**Rs**	**%error**	**Rp**	**%error**
0h	1.16E-03	0.00286	5.35E-06	7.848	0.14693	0.4363	7.3587	4.31E-04	9.4212	0.5246	14.381	2.76E-02	15.473	1.133	5.4257	2.57E-03	6.7662	1.07253	0.14693	0.24768	9.055133
10h	9.67E-04	0.00235	5.35E-06	7.795	0.13131	0.42456	6.1772	4.62E-04	8.6546	0.41457	12.029	4.04E-02	15.661	1.075	3.9134	2.95E-03	6.2042	1.064933	0.13131	0.22191	7.3732
20h	1.14E-03	0.00294	5.35E-06	8.101	0.14343	0.44236	6.4111	4.89E-04	9.5592	0.41131	10.476	6.77E-02	16.586	1.133	3.4208	3.20E-03	6.6426	1.108798	0.14343	0.232309	6.7693
30h	1.02E-03	0.00238	5.35E-06	8.611	0.12807	0.41181	7.7669	5.60E-04	9.7826	0.49782	12.302	3.86E-02	14.906	1.069	4.7297	3.13E-03	7.3524	1.181906	0.12807	0.231156	8.2662
40h	1.08E-03	0.00266	5.35E-06	8.934	0.12957	0.44533	7.6891	6.44E-04	9.7539	0.36908	11.859	7.63E-02	18.974	1.126	3.6221	3.45E-03	7.8245	1.228208	0.12957	0.225677	7.7234
50h	1.49E-03	0.00365	5.35E-06	10.24	0.14869	0.49449	8.1033	6.31E-04	11.686	0.2925	13.787	2.04E-01	28.503	1.236	3.5428	3.83E-03	8.6876	1.415424	0.14869	0.237515	8.4777

Sample	Date	29/03/2021		0.125	mol/L																
136	Chi-Sqr	Sum-Sqr	**L**	R1	%error	R2	%error	CPE1-T	%error	W-R	%error	W-T	%error	R3	%error	CPE2-T	%error	**Rs**	**%error**	**Rp**	**%error**
0h	3.90E-03	0.00923	5.40E-06	6.51	0.28237	0.77917	16.559	3.35E-03	13.328	0.59611	26.22	1.84E-02	22.683	0.34417	13.613	4.18E-04	18.249	0.880728	0.28237	0.194003	18.79733
10h	2.89E-03	0.00632	5.40E-06	6.472	0.22838	0.8647	8.4413	3.30E-03	9.7372	0.35731	24.543	2.75E-02	27.008	0.35521	9.6636	4.30E-04	14.395	0.875281	0.22838	0.173614	14.21597
20h	2.70E-03	0.00697	5.40E-06	6.521	0.2355	0.94774	5.4896	3.42E-03	9.0819	0.36715	16.188	5.13E-02	23.997	0.37578	8.5736	4.29E-04	14.299	0.882305	0.2355	0.189877	10.08373
30h	3.13E-03	0.00932	5.40E-06	6.544	0.26232	1.031	4.7505	3.80E-03	9.5841	0.33528	15.737	9.77E-02	28.276	0.41571	8.6115	4.62E-04	14.779	0.885602	0.26232	0.202968	9.699667
40h	2.90E-03	0.00962	5.40E-06	6.593	0.26554	1.067	4.5582	3.88E-03	9.3116	0.44219	11.801	1.13E-01	21.804	0.41427	8.6231	4.70E-04	15.142	0.892626	0.26554	0.223248	8.327433
50h	2.87E-03	0.00944	5.40E-06	6.604	0.26449	1.017	5.5296	3.96E-03	9.774	0.54714	11.527	7.71E-02	18.652	0.3984	9.1448	4.78E-04	15.652	0.894203	0.26449	0.22885	8.7338

Sample	Date	16/02/2020		0.25	mol/L																
68	Chi-Sqr	Sum-Sqr	**L**	R1	%error	R2	%error	CPE1-T	%error	W-R	%error	W-T	%error	R3	%error	CPE2-T	%error	**Rs**	**%error**	**Rp**	**%error**
0h	0.00344	0.00505	5.16E-06	7.08	0.2488	0.68257	8.8269	1.31E-03	15.59	0.47042	15.667	9.09E-03	18.663	0.50337	8.659	1.42E-04	11.094	0.962438	0.2488	0.184959	11.05097
10h	0.00196	0.00461	5.14E-06	7.275	0.21337	1.009	4.9492	1.71E-03	8.649	0.53639	10.741	2.44E-02	15.38	0.63558	5.2296	1.59E-04	8.1657	0.990391	0.21337	0.260162	6.973267
20h	0.00239	0.00611	5.14E-06	7.627	0.24467	1.136	5.044	1.71E-03	8.7224	0.58085	11.226	3.04E-02	16.892	0.6838	5.4109	1.47E-04	9.1291	1.04085	0.24467	0.291653	7.226967
30h	0.00169	0.005	5.14E-06	7.91	0.2119	1.295	3.4595	1.95E-03	6.8201	0.54313	8.9249	5.92E-02	15.858	0.74079	4.3053	1.59E-04	7.7362	1.081418	0.2119	0.317208	5.563233
40h	0.00189	0.00605	5.14E-06	8.049	0.22759	1.381	3.5377	2.08E-03	7.0887	0.58199	9.0264	7.37E-02	16.523	0.77696	4.5171	1.68E-04	8.1662	1.101344	0.22759	0.340291	5.693733
50h	0.0023	0.00753	5.14E-06	8.105	0.25646	1.358	4.5803	2.06E-03	8.1097	0.78052	8.8896	5.41E-02	14.683	0.76664	5.2109	1.64E-04	9.3361	1.109371	0.25646	0.363974	6.226933

Sample	Date	10/08/2020		0.25	mol/L																
32	Chi-Sqr	Sum-Sqr	**L**	R1	%error	R2	%error	CPE1-T	%error	W-R	%error	W-T	%error	R3	%error	CPE2-T	%error	**Rs**	**%error**	**Rp**	**%error**
0h	0.0042	0.0062	5.33E-06	6.987	0.22064	0.26631	16.157	6.25E-04	20.402	0.07018	44.245	0.10121	95.85	0.64642	6.6912	0.00298	16.979	0.949106	0.22064	0.08842	22.3644
10h	0.00181	0.00355	5.33E-06	9.272	0.14577	0.31162	15.113	1.07E-03	16.478	0.16594	19.299	0.19985	41.823	0.90822	5.1116	0.00387	12.902	1.276661	0.14577	0.146171	13.17453
20h	0.00179	0.00333	5.33E-06	10.09	0.14296	0.28606	17.481	1.08E-03	18.98	0.28977	14.916	0.09191	27.018	0.90262	5.5546	0.00368	13.744	1.393921	0.14296	0.159455	12.65053
30h	0.00166	0.00324	5.33E-06	10.38	0.14344	0.25396	19.696	1.12E-03	21.842	0.53691	12.873	0.04776	17.407	0.91822	6.5276	0.00367	13.284	1.435493	0.14344	0.192518	13.0322
40h	0.0013	0.00309	5.33E-06	10.46	0.13556	0.2876	16.522	1.17E-03	18.74	0.6156	7.3036	0.10238	13.104	0.98796	4.9612	0.0039	12.077	1.446961	0.13556	0.218617	9.5956
50h	0.00133	0.00359	5.33E-06	10.51	0.13279	0.46884	13.335	1.43E-03	12.079	0.60909	8.3131	0.17794	14.954	1.005	6.0088	0.00637	14.955	1.454128	0.13279	0.246108	9.218967

Sample	Date	27/08/2020		0.25	mol/L																
62	Chi-Sqr	Sum-Sqr	**L**	R1	%error	R2	%error	CPE1-T	%error	W-R	%error	W-T	%error	R3	%error	CPE2-T	%error	**Rs**	**%error**	**Rp**	**%error**
0h	0.00205	0.00236	5.38E-06	8	0.20694	0.5456	10.424	5.39E-04	26.745	0.26446	25.071	3.79E-05	32.98	0.7346	8.8946	2.85E-03	18.538	1.09432	0.20694	0.168947	14.79653
10h	0.00154	0.0027	5.39E-06	8.447	0.16182	0.93286	7.9571	1.94E-03	9.8165	0.51335	7.057	1.44E-04	13.198	0.31754	26.684	3.51E-02	54.565	1.158397	0.16182	0.200353	13.89937
20h	0.00141	0.00333	5.39E-06	8.586	0.1706	1.088	2.8798	2.51E-03	7.8896	0.60392	5.3664	1.93E-04	11.243	0.17559	14.507	5.88E-01	38.401	1.178323	0.1706	0.215227	7.5844
30h	0.00178	0.00354	5.39E-06	8.885	0.18273	1.026	5.2135	2.03E-03	10.066	0.57148	6.7962	1.54E-04	13.455	0.3783	15.346	0.05226	36.109	1.221184	0.18273	0.230748	9.118567
40h	0.00121	0.0027	5.39E-06	9.108	0.15655	1.098	3.2588	2.21E-03	7.8761	0.61621	5.225	1.70E-04	10.737	0.34188	10.149	0.10693	26.404	1.253151	0.15655	0.24226	6.210933
50h	0.00148	0.00335	5.39E-06	9.243	0.17395	1.126	3.7511	2.22E-03	8.6952	0.62413	5.8203	1.74E-04	11.977	0.37841	11.139	0.09045	28.548	1.272504	0.17395	0.252646	6.903467

Sample	Date	01/04/2021		0.25	mol/L																
143	Chi-Sqr	Sum-Sqr	**L**	R1	%error	R2	%error	CPE1-T	%error	W-R	%error	W-T	%error	R3	%error	CPE2-T	%error	**Rs**	**%error**	**Rp**	**%error**
0h	1.41E-03	0.00513	5.29E-06	7.595	0.19231	1.157	7.5889	3.51E-03	7.8711	1.331	7.9226	3.79E-02	8.5399	0.35065	10.796	6.25E-04	15.05	1.036263	0.19231	0.35444	8.769167
10h	3.36E-03	0.00695	5.29E-06	7.89	0.2248	1.083	5.7211	2.87E-03	10.645	0.20286	34.784	4.94E-02	50.984	0.34905	12.703	5.61E-04	18.236	1.078551	0.2248	0.181884	17.73603
20h	3.23E-03	0.00673	5.29E-06	8.08	0.22202	1.007	4.9247	2.75E-03	11.76	0.20042	23.404	8.68E-02	44.885	0.34535	12.943	5.51E-04	18.645	1.105788	0.22202	0.170109	13.75723
30h	3.78E-03	0.0088	5.29E-06	8.152	0.24746	0.99609	5.478	2.92E-03	14.028	0.19676	21.631	2.13E-01	49.13	0.35187	15.085	6.16E-04	20.909	1.116109	0.24746	0.168955	14.06467
40h	3.37E-03	0.00683	5.29E-06	8.232	0.22611	0.93986	5.8876	2.62E-03	13.556	0.28912	19.184	5.66E-02	33.19	0.32486	15.093	5.57E-04	20.43	1.127577	0.22611	0.170263	13.3882
50h	2.50E-03	0.0047	5.29E-06	8.286	0.18391	0.92302	5.42	2.73E-03	12.255	0.24256	21.44	4.85E-02	34.142	0.30961	14.403	6.54E-04	17.746	1.135318	0.18391	0.158988	13.75433

Sample	Date	19/02/2020		0.5	mol/L																
69	Chi-Sqr	Sum-Sqr	**L**	R1	%error	R2	%error	CPE1-T	%error	W-R	%error	W-T	%error	R3	%error	CPE2-T	%error	**Rs**	**%error**	**Rp**	**%error**
0h	0.00572	0.00665	5.01E-06	7.944	0.34119	1.062	8.4268	4.03E-04	16.531	0.60766	18.599	3.65E-03	20.325	0.71836	10.466	6.12E-05	11.119	1.086292	0.34119	0.289842	12.49727
10h	0.00322	0.00619	5.01E-06	8.077	0.29442	1.407	5.6918	5.41E-04	9.7143	0.83311	11.688	7.88E-03	14.469	0.90506	6.0398	6.33E-05	8.1616	1.105358	0.29442	0.39838	7.806533
20h	0.00204	0.00585	5.01E-06	8.414	0.25157	1.853	2.6398	7.61E-04	6.3489	0.47707	9.6831	5.65E-02	20.35	1.174	3.6149	7.12E-05	5.9819	1.153666	0.25157	0.449828	5.3126
30h	0.00257	0.00719	5.01E-06	8.495	0.28124	1.888	3.276	7.33E-04	7.06	0.62478	10.377	3.27E-02	18.761	1.175	4.1303	6.93E-05	6.7132	1.165278	0.28124	0.476163	5.927767
40h	0.00232	0.0076	5.01E-06	8.593	0.2786	2.011	2.8155	8.26E-04	6.6665	0.5944	9.2475	6.72E-02	19.462	1.254	3.8185	7.39E-05	6.4278	1.179326	0.2786	0.500765	5.293833
50h	0.00275	0.01012	5.01E-06	8.663	0.31696	2.095	3.2316	8.73E-04	7.3637	0.83916	8.1487	6.44E-02	16.6	1.286	4.264	7.61E-05	7.2439	1.189361	0.31696	0.55248	5.214767

Sample	Date	13/08/2020		0.5	mol/L																
34	Chi-Sqr	Sum-Sqr	**L**	R1	%error	R2	%error	CPE1-T	%error	W-R	%error	W-T	%error	R3	%error	CPE2-T	%error	**Rs**	**%error**	**Rp**	**%error**
0h	0.00164	0.00267	5.37E-06	6.841	0.14855	0.29452	10.287	5.12E-04	12.014	0.0951	18.593	0.14457	43.928	0.61317	4.9135	0.00254	12.319	0.928177	0.14855	0.09127	11.2645
10h	0.00414	0.00429	5.37E-06	11.91	0.18138	0.28863	22.046	5.81E-04	26.363	0.18733	54.455	0.02444	66.159	0.79122	10.697	0.00268	19.474	1.654818	0.18138	0.12917	29.066
20h	0.00235	0.00328	5.37E-06	13.27	0.15421	0.29792	18.143	6.21E-04	24.622	0.29273	14.888	0.1087	31.32	0.85107	6.4936	0.00278	16.405	1.849774	0.15421	0.15419	13.17487
30h	0.00299	0.00428	5.37E-06	13.6	0.17632	0.30436	19.334	5.97E-04	28.169	0.36785	16.665	0.0761	30.99	0.90761	7.1375	0.00291	16.993	1.89708	0.17632	0.173987	14.37883
40h	0.00178	0.00299	5.37E-06	13.91	0.14139	0.36526	13.251	6.17E-04	19.729	0.36055	11.92	0.18013	25.793	0.99336	5.1226	0.00337	12.911	1.941518	0.14139	0.193963	10.09787
50h	0.00258	0.00512	5.37E-06	13.98	0.17857	0.43389	14.092	6.34E-04	21.532	0.42604	12.651	0.37174	28.934	1.071	5.9426	0.00399	15.28	1.951553	0.17857	0.224318	10.8952

Sample	Date	31/08/2020		0.5	mol/L																
63	Chi-Sqr	Sum-Sqr	**L**	R1	%error	R2	%error	CPE1-T	%error	W-R	%error	W-T	%error	R3	%error	CPE2-T	%error	**Rs**	**%error**	**Rp**	**%error**
0h	0.00451	0.00475	5.13E-06	9.433	0.25853	0.94173	11.105	5.51E-04	20.625	0.62318	22.528	3.73E-03	20.971	0.66191	13.523	9.10E-05	11.317	1.29974	0.25853	0.266734	15.71867
10h	0.00163	0.00365	5.13E-06	9.467	0.18245	1.293	2.9776	1.35E-03	7.7774	0.21203	14.253	2.30E-01	34.621	0.91873	4.0387	1.23E-04	6.4494	1.304614	0.18245	0.294966	7.089767
20h	0.00157	0.00367	5.13E-06	9.625	0.18468	1.336	3.061	1.26E-03	7.746	0.34947	9.9093	9.78E-02	22.159	0.91528	4.1691	1.18E-04	6.6226	1.327263	0.18468	0.320337	5.713133
30h	0.00183	0.00404	5.13E-06	9.755	0.19656	1.36	3.4371	1.24E-03	7.9982	0.41714	10.941	5.10E-02	21.08	0.91748	4.3703	1.11E-04	7.0658	1.345899	0.19656	0.333793	6.249467
40h	0.00133	0.00324	5.13E-06	9.896	0.17191	1.441	2.7505	1.33E-03	6.7025	0.4009	9.1404	8.41E-02	19.344	0.97748	3.6042	1.15E-04	5.9617	1.366111	0.17191	0.351678	5.165033
50h	0.00137	0.00302	5.13E-06	11.44	0.16374	1.47	2.9796	1.38E-03	7.1943	0.4184	9.7863	8.28E-02	20.38	0.99553	3.8851	1.17E-04	6.47	1.587444	0.16374	0.360931	5.550333

Sample	Date	06/04/2021		0.5	mol/L																
144	Chi-Sqr	Sum-Sqr	**L**	R1	%error	R2	%error	CPE1-T	%error	W-R	%error	W-T	%error	R3	%error	CPE2-T	%error	**Rs**	**%error**	**Rp**	**%error**
0h	4.56E-03	0.00903	5.21E-06	7.053	0.28277	0.97945	5.0578	1.72E-03	12.844	0.14975	26.34	9.00E-02	57.853	0.42495	11.193	2.96E-04	16.108	0.958567	0.28277	0.170307	14.19693
10h	2.28E-03	0.00373	5.21E-06	7.24	0.18151	1.013	3.5378	1.66E-03	8.4568	0.1052	32.213	4.40E-02	58.642	0.42267	7.7469	3.00E-04	10.671	0.985374	0.18151	0.168403	14.49923
20h	3.55E-03	0.008	5.21E-06	7.202	0.26004	0.9687	4.8687	1.80E-03	12.554	0.12186	27.573	4.85E-01	66.888	0.43347	10.732	3.19E-04	15.019	0.979926	0.26004	0.165989	14.39123
30h	3.54E-03	0.0077	5.21E-06	7.168	0.26136	1.004	4.2964	1.69E-03	11.211	0.101	33.433	6.11E-01	79.978	0.40073	10.591	3.08E-04	16.02	0.975052	0.26136	0.163366	16.1068
40h	5.47E-03	0.00914	5.21E-06	7.305	0.27057	0.94903	6.5369	1.87E-03	16.027	0.10731	51.757	4.35E-02	91.419	0.40634	14.877	3.95E-04	17.114	0.994691	0.27057	0.157195	24.3903
50h	3.23E-03	0.00787	5.21E-06	7.236	0.25546	0.97444	4.7813	1.91E-03	12.35	0.17464	18.838	3.13E-01	46.006	0.41461	11.062	3.48E-04	15.567	0.9848	0.25546	0.171675	11.56043

Sample	Date	02/03/2020		1	mol/L																
35	Chi-Sqr	Sum-Sqr	**L**	R1	%error	R2	%error	CPE1-T	%error	W-R	%error	W-T	%error	R3	%error	CPE2-T	%error	**Rs**	**%error**	**Rp**	**%error**
0h	0.00609	0.00874	5.23E-06	6.17	0.30319	0.32649	13.959	2.84E-04	18.822	0.12005	31.925	0.03537	62.498	0.64747	7.2439	0.0017	18.111	0.831989	0.30319	0.104346	17.7093
10h	0.007	0.01235	5.23E-06	6.283	0.35451	0.34901	14.435	2.80E-04	21.109	0.21322	27.539	0.02858	46.882	0.76758	7.5448	0.00177	17.177	0.848188	0.35451	0.138148	16.50627
20h	0.00394	0.01026	5.23E-06	6.506	0.3051	0.37952	11.727	3.17E-04	17.831	0.25379	13.469	0.17938	32.45	0.8217	5.5658	0.00206	14.408	0.880155	0.3051	0.156095	10.25393
30h	0.00269	0.00716	5.23E-06	6.693	0.25232	0.40827	8.8539	3.04E-04	14.159	0.30726	10.623	0.11782	23.926	0.89416	4.3094	0.00217	10.92	0.906961	0.25232	0.178269	7.928767
40h	0.00267	0.00662	5.23E-06	6.869	0.23814	0.43218	8.2958	3.12E-04	13.083	0.31422	12.404	0.0721	24.475	0.91173	4.4739	0.00237	10.609	0.932191	0.23814	0.185213	8.391233
50h	0.00152	0.00396	5.23E-06	6.918	0.18734	0.39795	6.9064	3.12E-04	11.133	0.40727	7.4319	0.06683	14.67	0.90229	3.4848	0.00225	8.2278	0.939215	0.18734	0.192291	5.941033

Sample	Date	25/09/2020		1	mol/L																
91	Chi-Sqr	Sum-Sqr	**L**	R1	%error	R2	%error	CPE1-T	%error	W-R	%error	W-T	%error	R3	%error	CPE2-T	%error	**Rs**	**%error**	**Rp**	**%error**
0h	1.47E-03	0.00305	5.37E-06	7.046	0.17968	0.62692	6.9349	1.60E-04	6.6831	0.66008	13.425	8.21E-03	12.795	1.202	5.6411	8.99E-04	8.0259	0.957564	0.17968	0.304318	8.667
10h	1.21E-03	0.00347	5.37E-06	7.343	0.17146	0.75107	4.6988	1.95E-04	5.88	0.55729	10.69	2.59E-02	14.358	1.535	3.2769	1.31E-03	5.8276	1.000139	0.17146	0.355115	6.2219
20h	1.53E-03	0.00435	5.37E-06	7.436	0.19169	0.75429	5.2197	1.94E-04	6.634	0.52354	12.2	2.78E-02	16.985	1.572	3.4767	1.28E-03	6.4031	1.01347	0.19169	0.356043	6.965467
30h	9.25E-04	0.00266	5.37E-06	7.408	0.14943	0.73867	4.3176	2.01E-04	5.2656	0.58976	8.6847	2.60E-02	11.849	1.536	2.834	1.27E-03	5.2489	1.009456	0.14943	0.358136	5.278767
40h	1.21E-03	0.00343	5.37E-06	7.431	0.17078	0.72682	5.0575	2.00E-04	6.1157	0.62227	9.5322	2.46E-02	12.857	1.506	3.333	1.26E-03	6.1394	1.012753	0.17078	0.356797	5.974233
50h	9.04E-04	0.0027	5.37E-06	7.421	0.15184	0.72577	4.3	1.97E-04	5.4323	0.67852	7.4425	2.66E-02	10.347	1.528	2.8226	1.28E-03	5.2066	1.01132	0.15184	0.367863	4.855033

Sample	Date	09/03/2021		1	mol/L																
90	Chi-Sqr	Sum-Sqr	**L**	R1	%error	R2	%error	CPE1-T	%error	W-R	%error	W-T	%error	R3	%error	CPE2-T	%error	**Rs**	**%error**	**Rp**	**%error**
0h	3.49E-03	0.00677	4.82E-06	9.152	0.25346	1.455	4.6214	1.15E-03	9.4131	0.31136	23.594	3.04E-02	37.78	0.80645	6.3853	1.30E-04	9.7276	1.259459	0.25346	0.316332	11.53357
10h	1.79E-03	0.00467	4.82E-06	9.321	0.20757	1.56	2.6217	1.18E-03	6.8783	0.2614	13.165	2.70E-01	32.081	0.85843	4.5447	1.27E-04	7.6876	1.283685	0.20757	0.331673	6.777133
20h	4.11E-03	0.00807	4.82E-06	9.38	0.28334	1.473	5.3254	1.06E-03	10.541	0.34227	25.461	2.63E-02	39.485	0.79969	7.3422	1.24E-04	11.151	1.292143	0.28334	0.322374	12.70953
30h	3.21E-03	0.00594	4.82E-06	9.359	0.2411	1.462	4.3516	1.08E-03	8.8911	0.29419	23.557	2.89E-02	37.925	0.79129	6.1661	1.24E-04	9.5607	1.289132	0.2411	0.312701	11.35823
40h	3.01E-03	0.00688	4.82E-06	9.386	0.25552	1.502	3.5364	1.13E-03	8.9453	0.28001	16.374	1.05E-01	37.035	0.82035	5.9874	1.25E-04	9.8939	1.293003	0.25552	0.320568	8.6326
50h	0.00431	0.00922	4.82E-06	9.469	0.29669	1.516	4.4891	1.11E-03	10.52	0.32777	20.117	5.33E-02	39.384	0.81733	7.1729	1.25E-04	11.611	1.304901	0.29669	0.328988	10.593

11.3.4 Batch C

Sample	Date	26/07/2021		0.025	mol/L																
301	Chi-Sqr	Sum-Sqr	**L**	R1	%error	R2	%error	CPE1-T	%error	W-R	%error	W-T	%error	R3	%error	CPE2-T	%error	**Rs**	**%error**	**Rp**	**%error**
0h	6.75E-03	0.00456	3.70E-06	25.55	0.21066	0.31179	29.011	2.88E-04	55.321	0.79508	56.528	2.26E-02	42.948	0.68009	58.411	5.43E-03	31.976	3.610112	0.21066	0.20368	47.98333
10h	5.76E-03	0.00381	3.70E-06	24.76	0.18248	0.28702	24.723	3.79E-04	52.236	0.42055	44.164	4.63E-02	55.028	0.79787	20.546	4.92E-03	22.705	3.496866	0.18248	0.163324	29.811
20h	6.45E-03	0.00594	3.70E-06	24.11	0.22336	0.30194	26.798	3.87E-04	59.911	0.52	19.312	2.12E-01	41.921	0.84933	11.469	4.72E-03	25.936	3.403688	0.22336	0.187096	19.193
30h	6.08E-03	0.00422	3.70E-06	25	0.18957	0.27913	27.844	4.14E-04	56.834	0.5258	36.704	4.48E-02	46.405	0.75964	22.297	4.88E-03	26.245	3.53127	0.18957	0.171801	28.94833
40h	4.84E-03	0.00483	3.70E-06	24.1	0.1946	0.3522	19.664	3.86E-04	45.417	0.4307	20.424	4.42E-01	46.179	1.038	7.7649	5.26E-03	18.344	3.402255	0.1946	0.208546	15.95097

Sample	Date	24/08/2021		0.05	mol/L																
302	Chi-Sqr	Sum-Sqr	**L**	R1	%error	R2	%error	CPE1-T	%error	W-R	%error	W-T	%error	R3	%error	CPE2-T	%error	**Rs**	**%error**	**Rp**	**%error**
0h	3.39E-03	0.00404	4.92E-06	13.02	0.17224	0.58112	30.772	8.21E-03	19.269	0.54541	38.202	3.22E-02	30.48	0.14098	35.415	1.29E-03	55.542	1.813937	0.17224	0.129217	34.79633
10h	1.79E-03	0.00425	4.92E-06	12.79	0.12511	1.075	11.463	2.62E-02	16.628	0.62267	24.751	3.29E-01	27.043	0.50863	15.808	4.77E-03	14.248	1.780966	0.12511	0.263793	17.34067
20h	1.78E-03	0.00464	4.92E-06	12.92	0.12793	1.232	8.8125	2.80E-02	14.919	0.71145	18.419	5.03E-01	23.947	0.576	13.627	4.98E-03	13.103	1.799602	0.12793	0.308683	13.6195
30h	1.29E-03	0.00337	4.92E-06	13.06	0.1158	0.93859	9.8856	1.96E-02	19.549	1.548	7.1906	2.58E-01	9.0812	0.32708	24.555	5.45E-03	20.449	1.819671	0.1158	0.350859	13.87707
40h	1.70E-03	0.0048	4.92E-06	13.05	0.12925	1.389	11.092	3.12E-02	12.628	0.95641	19.694	4.85E-01	21.037	0.60235	13.22	5.33E-03	12.96	1.818237	0.12925	0.370081	14.66867

Sample	Date	29/07/2021		0.125	mol/L																
303	Chi-Sqr	Sum-Sqr	**L**	R1	%error	R2	%error	CPE1-T	%error	W-R	%error	W-T	%error	R3	%error	CPE2-T	%error	**Rs**	**%error**	**Rp**	**%error**
0h	1.21E-02	0.01154	3.71E-06	17.75	0.36385	0.50877	59.015	9.17E-03	39.39	0.94096	35.114	3.89E-02	35.068	0.13245	62.932	4.77E-04	149.4	2.491982	0.36385	0.174325	52.35367
10h	7.92E-03	0.00573	3.86E-06	17.68	0.23937	0.53978	44.537	7.46E-03	28.162	0.47949	56.274	2.96E-02	50.415	0.08823	71.71	9.41E-04	152.41	2.481948	0.23937	0.10628	57.507
20h	7.14E-03	0.00482	3.86E-06	17.72	0.21605	0.61088	44.148	7.05E-03	24.433	0.35069	86.281	2.75E-02	67.764	0.09998	60.827	8.98E-04	122.48	2.487682	0.21605	0.099693	63.752
30h	6.06E-03	0.00453	3.86E-06	17.76	0.21422	0.63739	25.794	7.05E-03	20.053	0.38714	47.241	4.20E-02	50.738	0.10179	51.502	7.81E-04	118.3	2.493416	0.21422	0.108978	41.51233
40h	9.08E-03	0.006	3.86E-06	17.9	0.25965	0.52871	63.557	7.52E-03	33.328	0.45097	82.799	2.32E-02	60.656	0.09235	73.635	7.30E-04	154.71	2.513485	0.25965	0.101195	73.33033
50h	0.00848	0.00716	3.86E-06	17.97	0.29841	0.60132	18.468	6.91E-03	25.466	0.49014	24.556	8.24E-02	40.625	0.11376	55.706	4.78E-04	141.88	2.523519	0.29841	0.120288	32.91

Sample	Date	02/08/2021		0.25	mol/L																
304	Chi-Sqr	Sum-Sqr	**L**	R1	%error	R2	%error	CPE1-T	%error	W-R	%error	W-T	%error	R3	%error	CPE2-T	%error	**Rs**	**%error**	**Rp**	**%error**
0h	8.35E-03	0.00476	2.69E-06	21.6	0.25387	0.61245	12.308	5.00E-03	25.213	0.22994	34.74	1.45E-01	74.36	0.30783	20.718	1.55E-04	52.883	3.04388	0.25387	0.112404	22.58867
10h	1.56E-02	0.00629	2.70E-06	21.92	0.34353	0.59994	63.206	4.75E-03	30.055	0.35463	23.744	3.09E-05	53.02	0.19856	193.65	7.03E-02	373.96	3.089752	0.34353	0.112821	93.53333
20h	5.46E-03	0.00238	2.70E-06	22.05	0.23025	0.59475	13.855	4.41E-03	18.086	0.32058	16.979	2.36E-05	36.369	0.22416	37.104	1.30E-01	92.151	3.108387	0.23025	0.110865	22.646
30h	7.55E-03	0.00395	2.70E-06	22.11	0.28226	0.69509	8.1549	4.85E-03	19.056	0.31464	21.423	2.73E-05	46.726	0.16691	37.224	8.21E-01	95.622	3.116988	0.28226	0.116191	22.2673
40h	4.30E-03	0.00218	2.70E-06	22.34	0.20649	0.66989	6.5421	4.78E-03	15.018	0.33216	15.121	2.87E-05	33.269	0.16213	28.884	7.21E-01	75.711	3.149959	0.20649	0.114405	16.84903
50h	0.00922	0.00471	2.70E-06	22.13	0.29413	0.64157	17.666	4.65E-03	24.075	0.3127	23.165	3.20E-05	51.884	0.26607	43.053	1.29E-01	107.67	3.119855	0.29413	0.122455	27.96133

Sample	Date	09/08/2021		0.5	mol/L														
305	Chi-Sqr	Sum-Sqr	**L**	R1	%error	R2	%error	CPE1-T	%error	W-R	%error	W-T	%error	R3	%error	CPE2-T	%error	**Rs**	**%error**	**Rp**	**%error**
0h	6.16E-03	0.00374	2.83E-06	20.83	0.27255	0.62383	8.0911	4.45E-03	19.994	0.4416	14.063	2.83E-05	30.945	0.21703	25.626	6.49E-01	64.833	2.9335	0.27255	0.13136	15.9267
10h	2.32E-02	0.00782	2.83E-06	21.26	0.45225	0.52454	26.351	3.69E-03	36.709	0.51929	19.511	1.92E-05	40.637	0.11802	118.45	1.93E-01	296.67	2.995141	0.45225	0.114071	54.77067
20h	1.21E-02	0.00616	2.83E-06	21.68	0.35956	0.52331	10.832	4.27E-03	31.561	0.39618	21.418	2.60E-05	46.639	0.31182	60.894	3.79E+00	57.182	3.055348	0.35956	0.124028	31.048
30h	1.04E-02	0.00373	2.83E-06	21.56	0.31523	0.47578	11.47	4.11E-03	27.159	0.463	15.365	1.86E-05	31.708	0.11002	51.204	7.00E-01	137.3	3.038146	0.31523	0.097865	26.013
40h	1.37E-02	0.00473	2.83E-06	21.86	0.38784	0.51947	14.721	3.75E-03	28.448	0.52049	16.641	1.52E-05	32.943	0.12018	64.138	3.42E-01	173.56	3.081151	0.38784	0.113826	31.83333
50h	0.01278	0.00568	2.83E-06	21.91	0.42557	0.44371	14.629	3.60E-03	36.47	0.50946	18.74	1.52E-05	37.289	0.24104	28.074	3.41E-01	74.256	3.088318	0.42557	0.11871	20.481

Sample	Date	06/08/2021		1	mol/L																
306	Chi-Sqr	Sum-Sqr	**L**	R1	%error	R2	%error	CPE1-T	%error	W-R	%error	W-T	%error	R3	%error	CPE2-T	%error	**Rs**	**%error**	**Rp**	**%error**
0h	8.16E-03	0.00816	4.88E-06	12.48	0.22038	0.59794	50.786	5.58E-03	24.556	0.0328	1066.4	1.61E-02	622.92	0.15419	40.414	7.65E-04	58.61	1.736528	0.22038	0.060039	385.8667
10h	9.77E-03	0.00977	4.88E-06	12.21	0.21989	0.53321	16.671	5.77E-03	28.18	0.04181	244.79	4.39E-02	336.03	0.10645	54.733	1.56E-03	88.47	1.697823	0.21989	0.045208	105.398
20h	7.10E-03	n	4.88E-06	12.33	0.22171	0.52087	9.914	5.58E-03	26.088	0.08429	55.129	4.76E-01	130.82	0.11135	45.101	1.29E-03	84.981	1.715025	0.22171	0.050231	36.71467
30h	6.17E-03	0.00617	4.88E-06	12.34	0.19882	0.49322	12.123	5.82E-03	29.66	0.13329	40.291	1.10E-01	81.194	0.10126	54.586	1.79E-03	86.231	1.716459	0.19882	0.051845	35.66667
40h	5.60E-03	0.0056	4.88E-06	12.43	0.18654	0.49926	9.8502	5.89E-03	25.002	0.10355	41.016	2.05E-01	92.52	0.11305	41.047	1.43E-03	72.023	1.72936	0.18654	0.050138	30.63773
50h	0.00706	0.00706	4.88E-06	12.51	0.20578	0.46597	14.467	5.57E-03	33.411	0.14284	46.424	6.55E-02	82.429	0.08478	70.181	1.99E-03	107.15	1.740828	0.20578	0.046946	43.69067

11.4 XRD pattern analysis for GDC spin coated LSCF substrates

11.4.1 Batch A

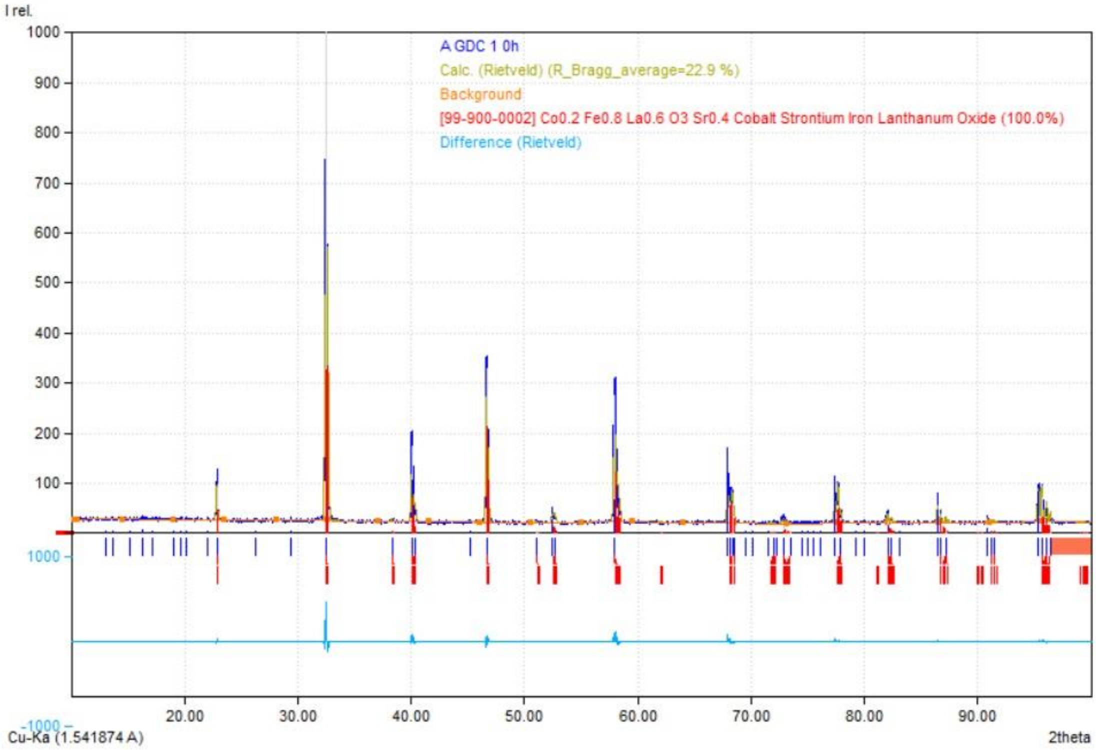

Match! Copyright © 2003-2021 CRYSTAL IMPACT, Bonn, Germany

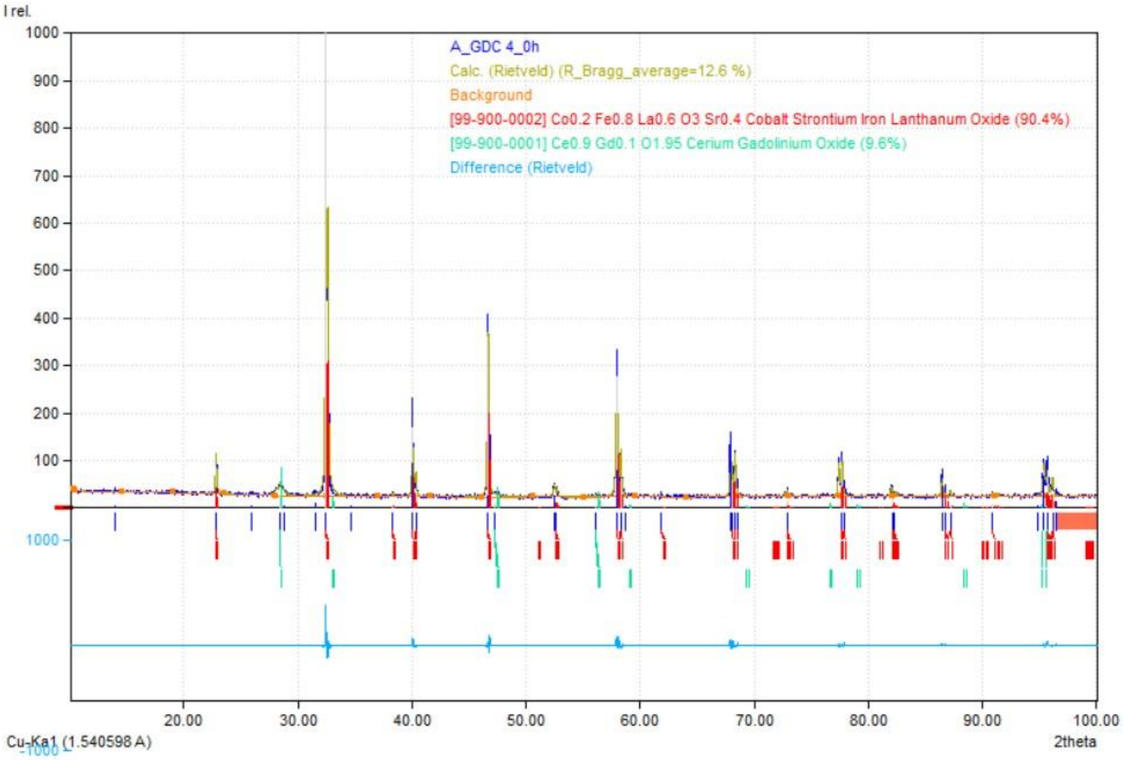

Match! Copyright © 2003-2021 CRYSTAL IMPACT, Bonn, Germany

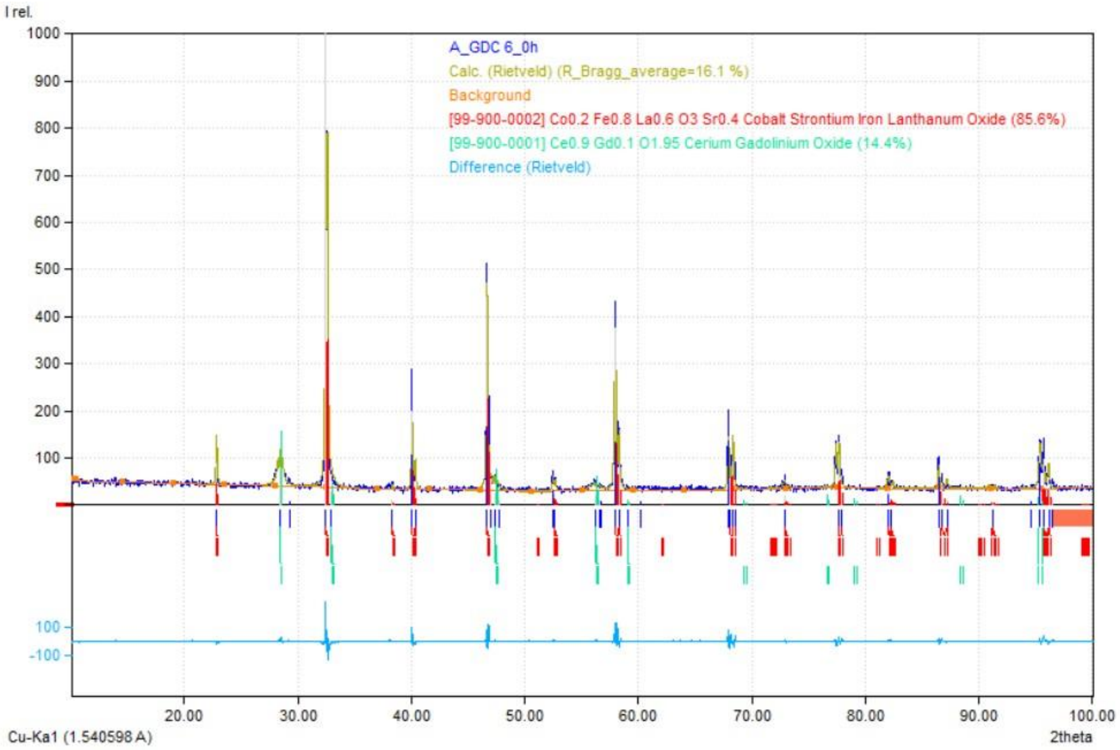
I rel.
1000
900
800
700
600
500
400
300
200
100
A_GDC 6_0h
Calc. (Rietveld) (R_Bragg_average=16.1 %)
Background
[99-900-0002] Co0.2 Fe0.8 La0.6 O3 Sr0.4 Cobalt Strontium Iron Lanthanum Oxide (85.6%)
[99-900-0001] Ce0.9 Gd0.1 O1.95 Cerium Gadolinium Oxide (14.4%)
Difference (Rietveld)
100
-100
20.00
30.00
40.00
50.00
60.00
70.00
80.00
90.00
100.00
Cu-Ka1 (1.540598 A)
2theta

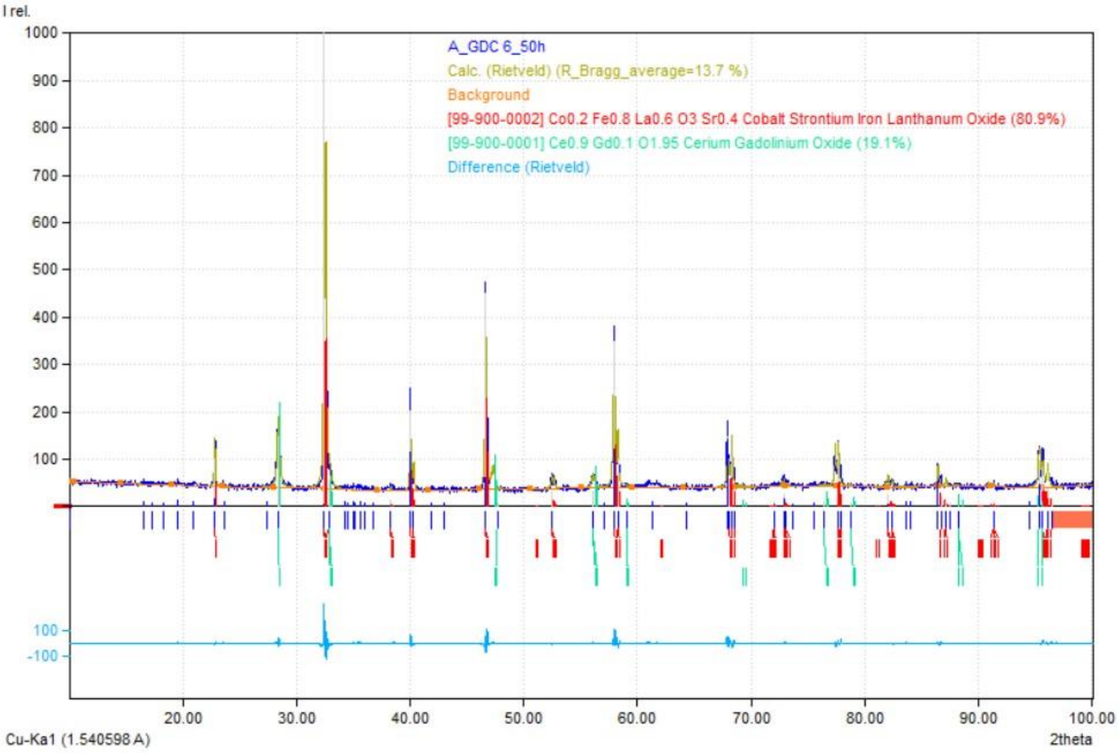
I rel.
1000
900
800
700
600
500
400
300
200
100
A_GDC 6_50h
Calc. (Rietveld) (R_Bragg_average=13.7 %)
Background
[99-900-0002] Co0.2 Fe0.8 La0.6 O3 Sr0.4 Cobalt Strontium Iron Lanthanum Oxide (80.9%)
[99-900-0001] Ce0.9 Gd0.1 O1.95 Cerium Gadolinium Oxide (19.1%)
Difference (Rietveld)
100
-100
20.00
30.00
40.00
50.00
60.00
70.00
80.00
90.00
100.00
Cu-Ka1 (1.540598 A)
2theta

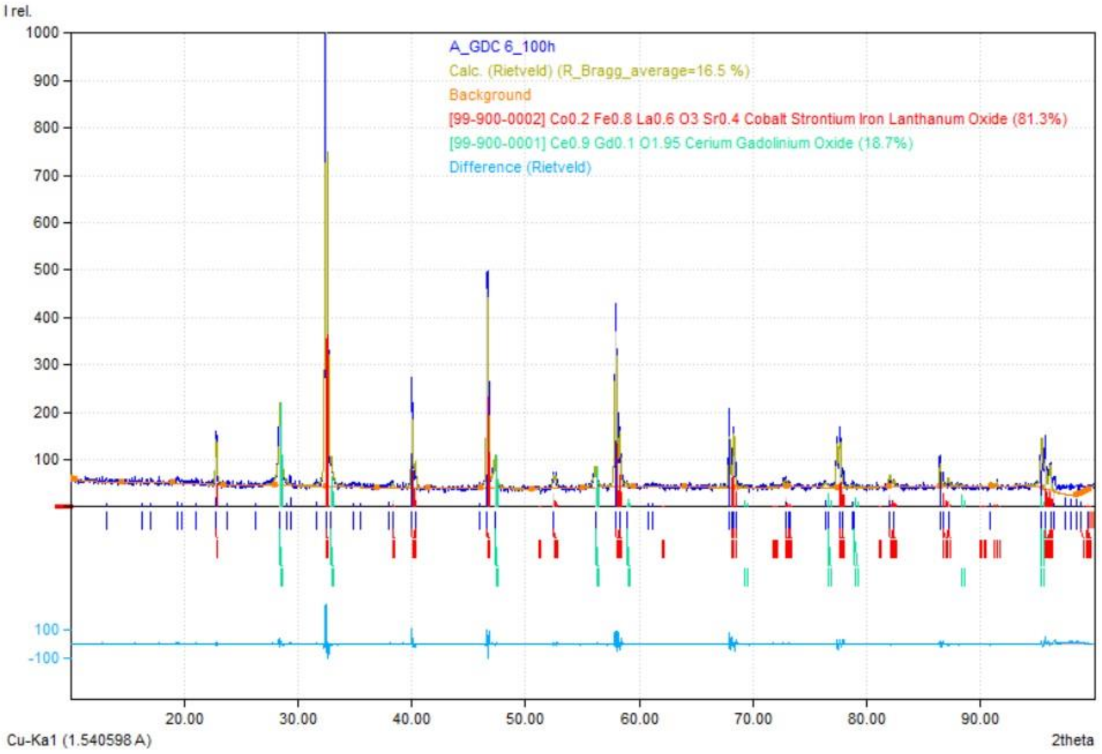
I rel.
1000
900
800
700
600
500
400
300
200
100
100
-100
A_GDC 6_100h
Calc. (Rietveld) (R_Bragg_average=16.5 %)
Background
[99-900-0002] Co0.2 Fe0.8 La0.6 O3 Sr0.4 Cobalt Strontium Iron Lanthanum Oxide (81.3%)
[99-900-0001] Ce0.9 Gd0.1 O1.95 Cerium Gadolinium Oxide (18.7%)
Difference (Rietveld)
20.00
30.00
40.00
50.00
60.00
70.00
80.00
90.00
Cu-Ka1 (1.540598 A)
2theta

11.4.2 Batch B

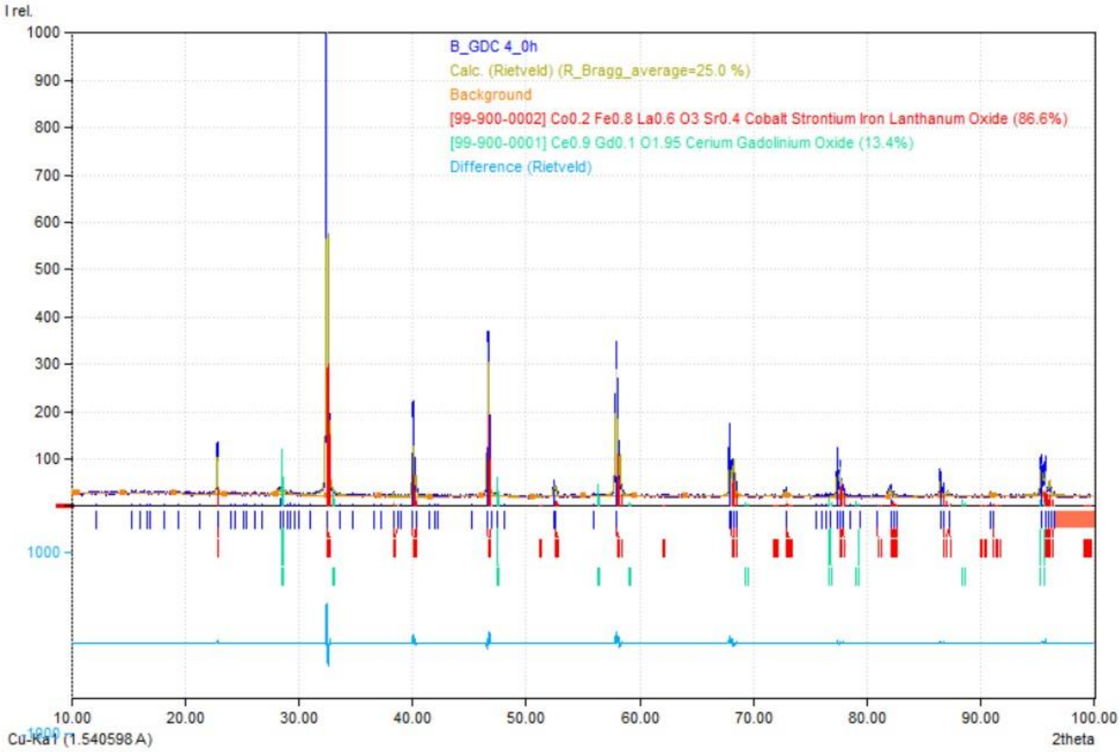
I rel.
1000
900
800
700
600
500
400
300
200
100
1000
B_GDC 4_0h
Calc. (Rietveld) (R_Bragg_average=25.0 %)
Background
[99-900-0002] Co0.2 Fe0.8 La0.6 O3 Sr0.4 Cobalt Strontium Iron Lanthanum Oxide (86.6%)
[99-900-0001] Ce0.9 Gd0.1 O1.95 Cerium Gadolinium Oxide (13.4%)
Difference (Rietveld)
10.00
20.00
30.00
40.00
50.00
60.00
70.00
80.00
90.00
100.00
Cu-Ka1 (1.540598 A)
2theta

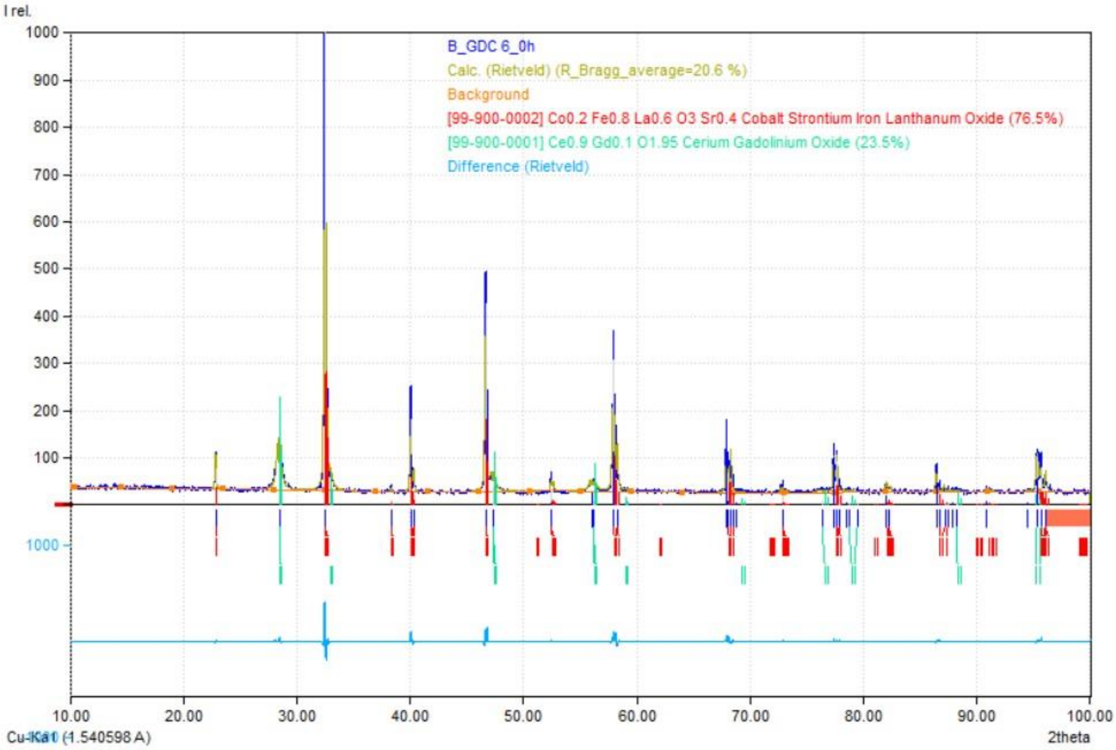
I rel.
1000
900
800
700
600
500
400
300
200
100
1000
B_GDC 6_0h
Calc. (Rietveld) (R_Bragg_average=20.6 %)
Background
[99-900-0002] Co0.2 Fe0.8 La0.6 O3 Sr0.4 Cobalt Strontium Iron Lanthanum Oxide (76.5%)
[99-900-0001] Ce0.9 Gd0.1 O1.95 Cerium Gadolinium Oxide (23.5%)
Difference (Rietveld)
10.00
20.00
30.00
40.00
50.00
60.00
70.00
80.00
90.00
100.00
2theta
Cu-Ka1 (1.540598 A)

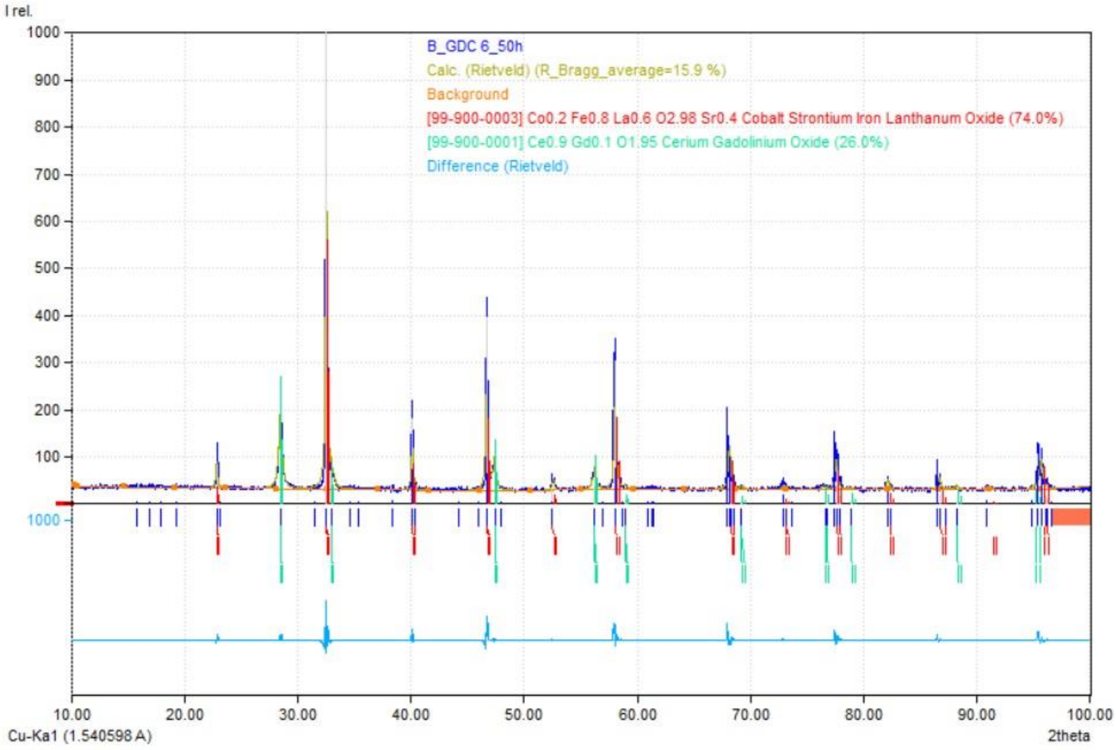
I rel.
1000
900
800
700
600
500
400
300
200
100
1000
B_GDC 6_50h
Calc. (Rietveld) (R_Bragg_average=15.9 %)
Background
[99-900-0003] Co0.2 Fe0.8 La0.6 O2.98 Sr0.4 Cobalt Strontium Iron Lanthanum Oxide (74.0%)
[99-900-0001] Ce0.9 Gd0.1 O1.95 Cerium Gadolinium Oxide (26.0%)
Difference (Rietveld)
10.00
20.00
30.00
40.00
50.00
60.00
70.00
80.00
90.00
100.00
2theta
Cu-Ka1 (1.540598 A)

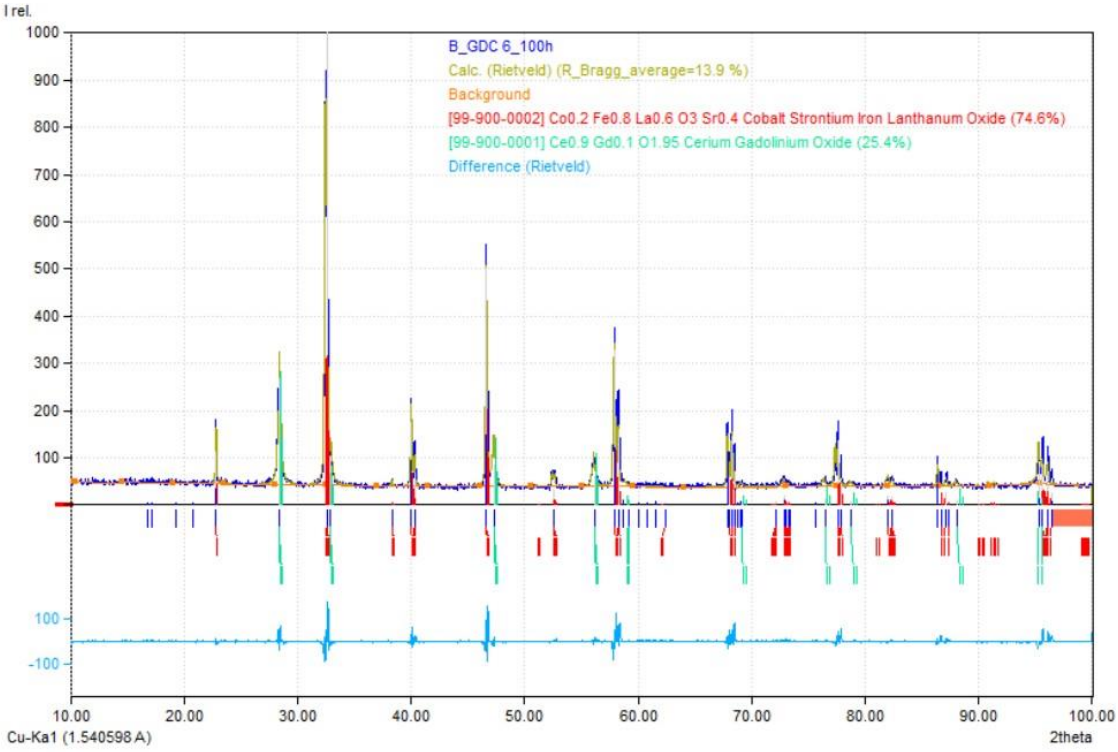
I rel.
1000
900
800
700
600
500
400
300
200
100
100
-100
10.00
20.00
30.00
40.00
50.00
60.00
70.00
80.00
90.00
100.00
Cu-Ka1 (1.540598 A)
2theta
B_GDC 6_100h
Calc. (Rietveld) (R_Bragg_average=13.9 %)
Background
[99-900-0002] Co0.2 Fe0.8 La0.6 O3 Sr0.4 Cobalt Strontium Iron Lanthanum Oxide (74.6%)
[99-900-0001] Ce0.9 Gd0.1 O1.95 Cerium Gadolinium Oxide (25.4%)
Difference (Rietveld)

11.4.3 Batch C

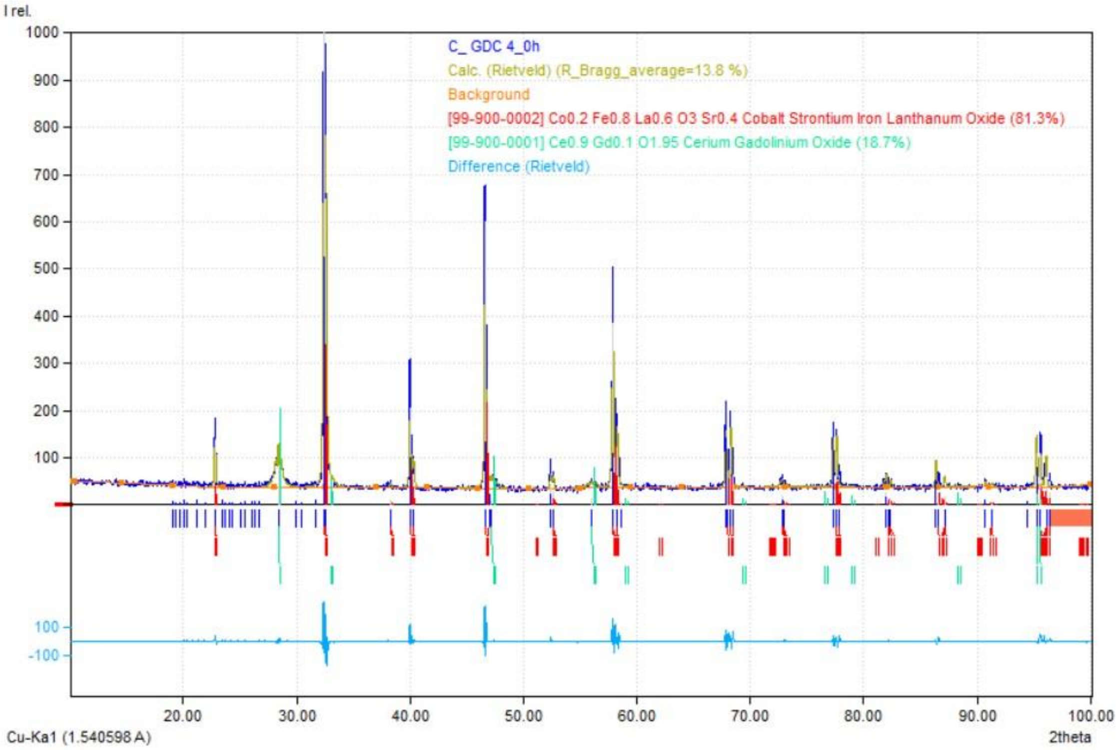
I rel.
1000
900
800
700
600
500
400
300
200
100
100
-100
20.00
30.00
40.00
50.00
60.00
70.00
80.00
90.00
100.00
Cu-Ka1 (1.540598 A)
2theta
C_ GDC 4_0h
Calc. (Rietveld) (R_Bragg_average=13.8 %)
Background
[99-900-0002] Co0.2 Fe0.8 La0.6 O3 Sr0.4 Cobalt Strontium Iron Lanthanum Oxide (81.3%)
[99-900-0001] Ce0.9 Gd0.1 O1.95 Cerium Gadolinium Oxide (18.7%)
Difference (Rietveld)

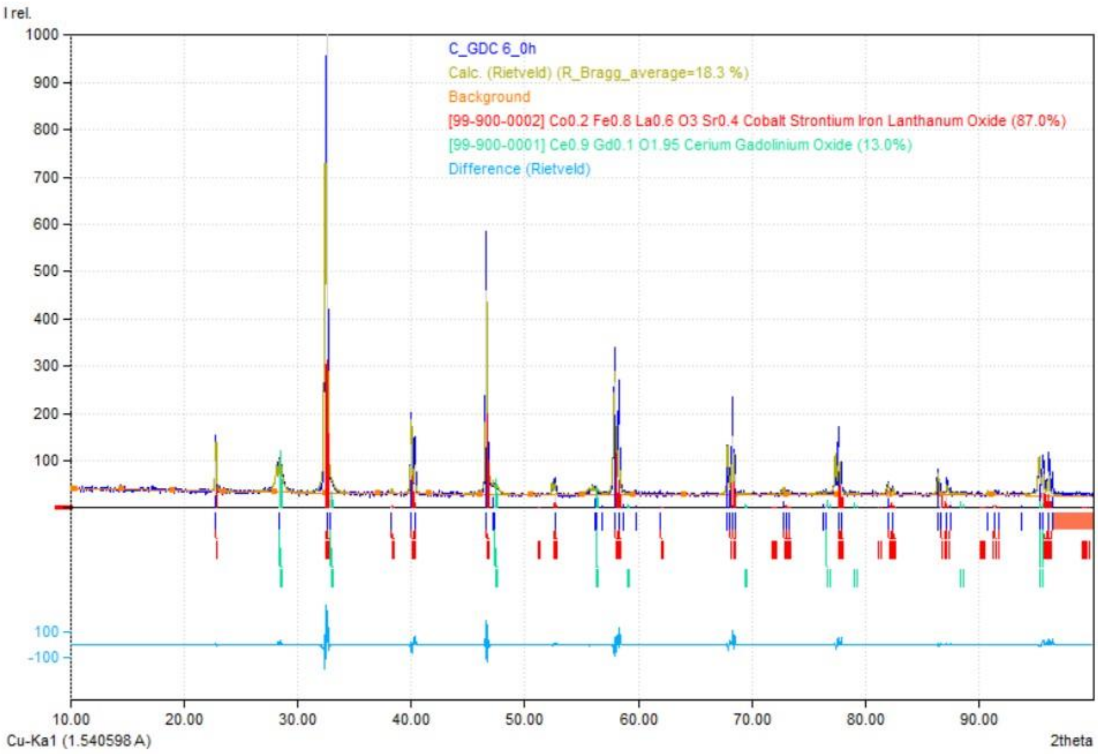

Match! Copyright © 2003-2021 CRYSTAL IMPACT, Bonn, Germany

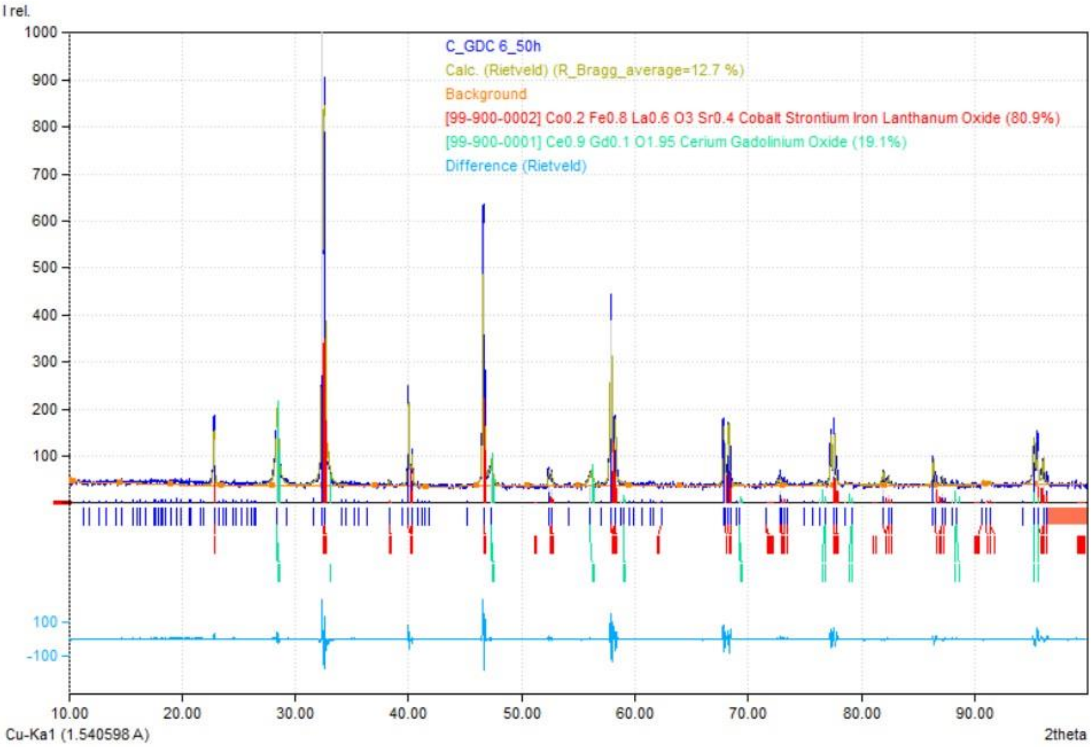

Match! Copyright © 2003-2021 CRYSTAL IMPACT, Bonn, Germany

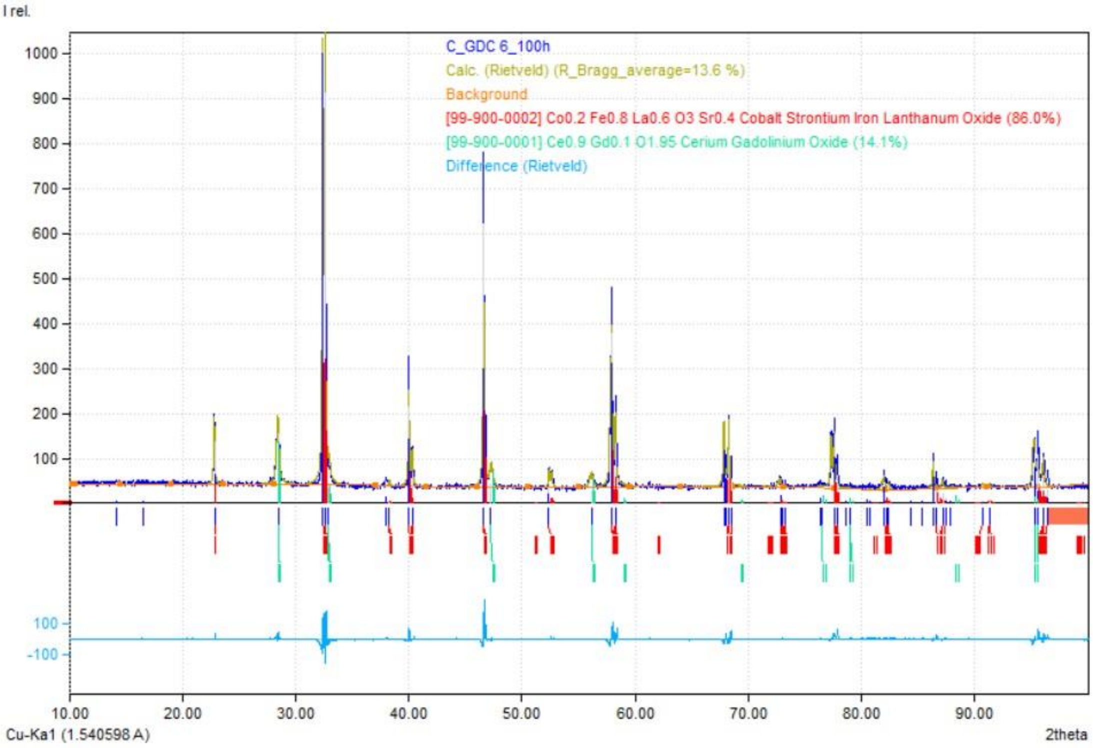
I rel.
1000
900
800
700
600
500
400
300
200
100
C_GDC 6_100h
Calc. (Rietveld) (R_Bragg_average=13.6 %)
Background
[99-900-0002] Co0.2 Fe0.8 La0.6 O3 Sr0.4 Cobalt Strontium Iron Lanthanum Oxide (86.0%)
[99-900-0001] Ce0.9 Gd0.1 O1.95 Cerium Gadolinium Oxide (14.1%)
Difference (Rietveld)
100
-100
10.00
20.00
30.00
40.00
50.00
60.00
70.00
80.00
90.00
Cu-Ka1 (1.540598 A)
2theta

11.5 SEM-BSE supplementary images

11.5.1 SEM-BSE images, Batch A

(a) BSE, Batch A, 0.025M, 0h

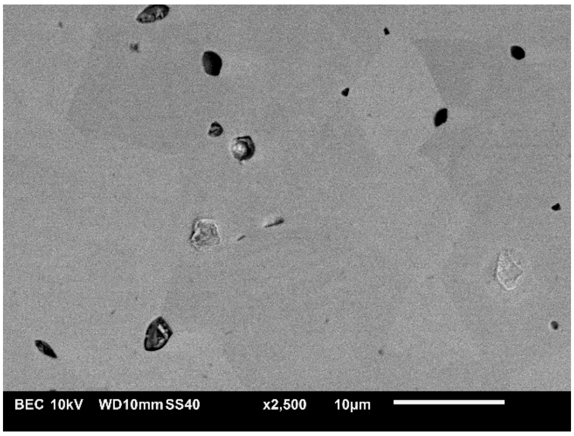

(b) BSE, Batch A, 0.025M, 100h

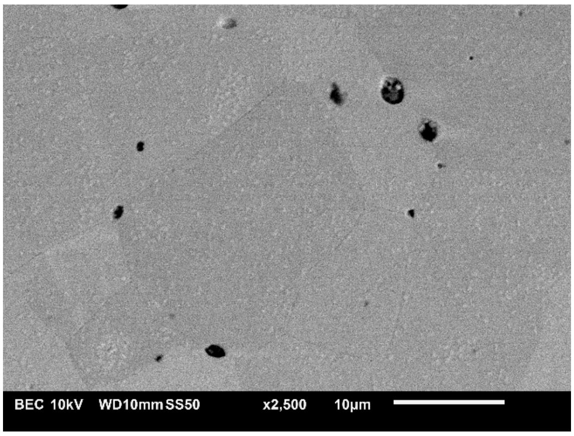

(c) SEM, Batch A, 0.025M, 50h

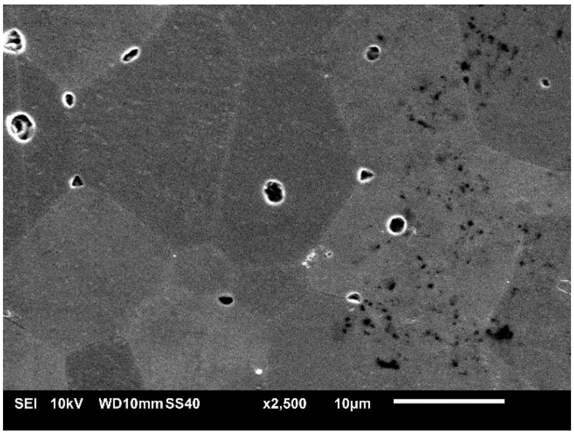

(d) BSE, Batch A, 0.025M, 50h

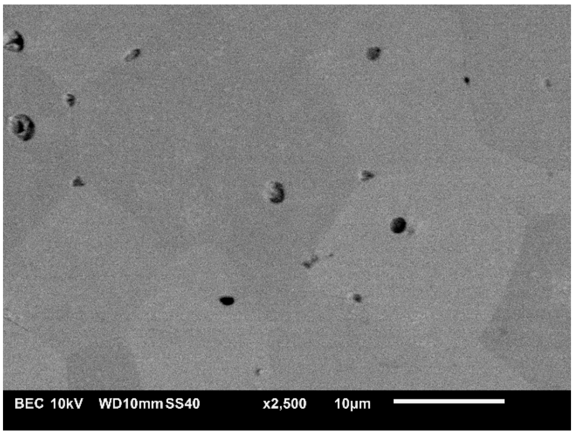

(e) BSE, Batch A, 0.125M, 0h

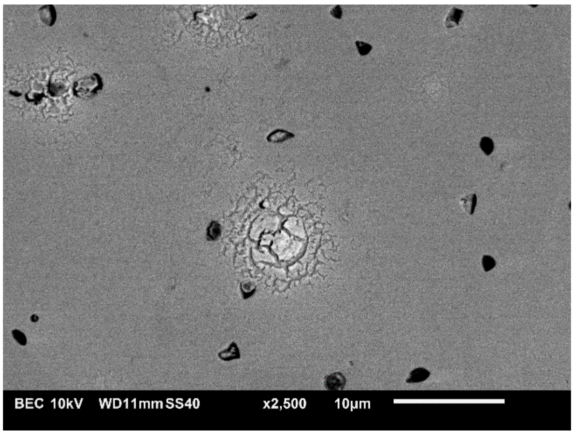

(f) BSE, Batch A, 0.250M, 0h

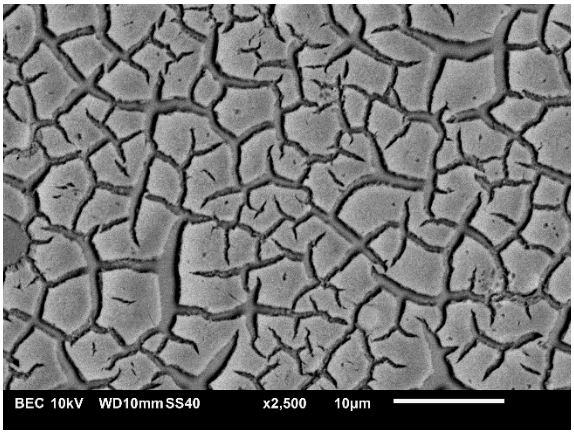

(g) BSE, Batch A, 1.000M, 0h

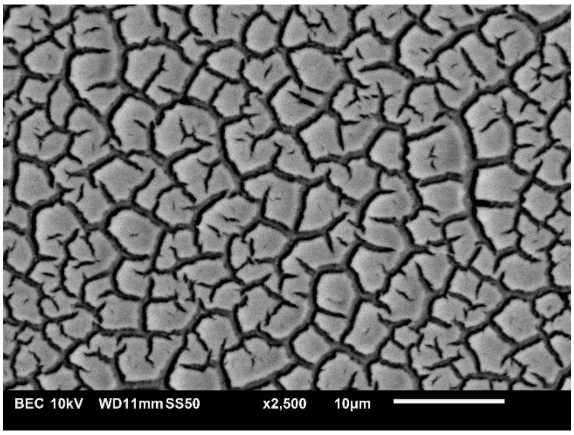

(h) BSE, Batch A, 1.000M, 100h

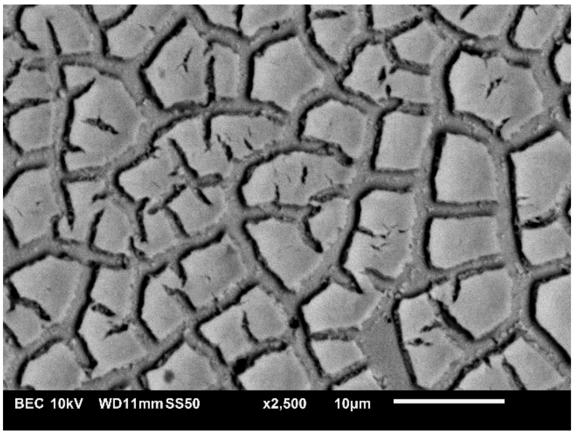

(i) SEM, Batch A, 1.000M, 50h

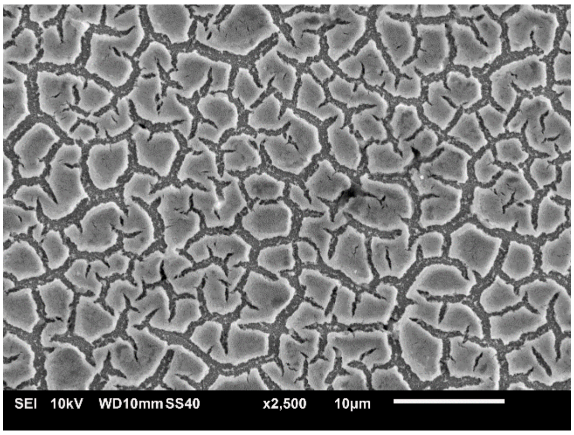

(j) BSE, Batch A, 1.000M, 50h

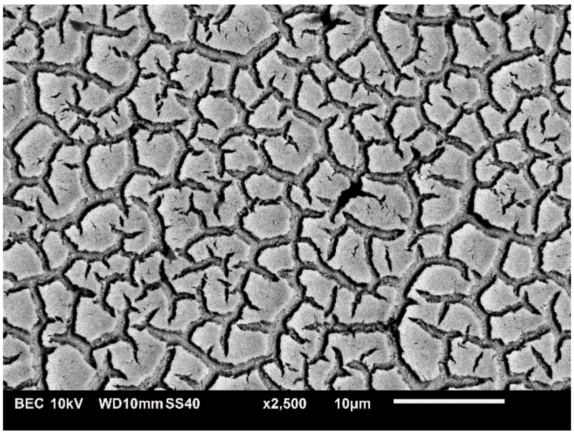

11.5.2 SEM-BSE images, Batch B

(a) BSE, Batch B, 0.025M, 0h

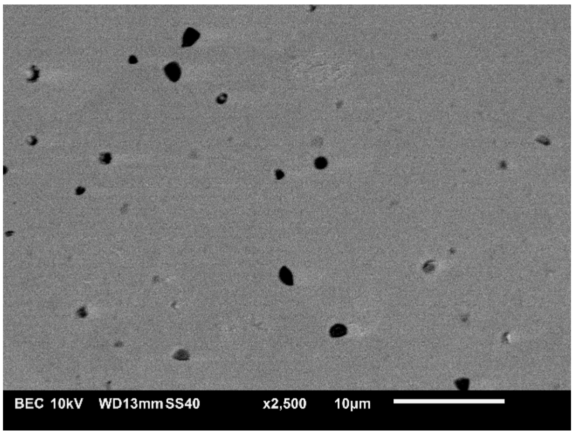

(b) BSE, Batch B, 0.025M, 100h

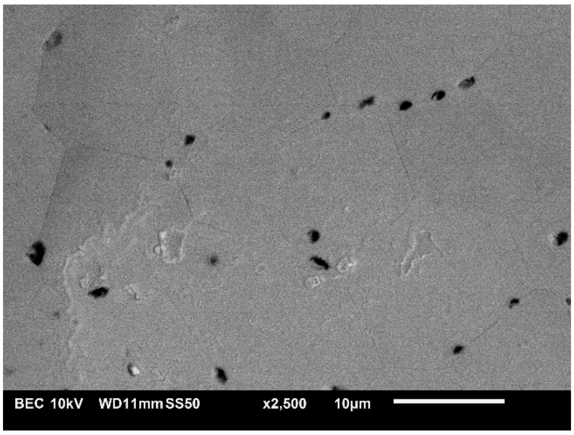

(c) SEM, Batch B, 0.025M, 50h

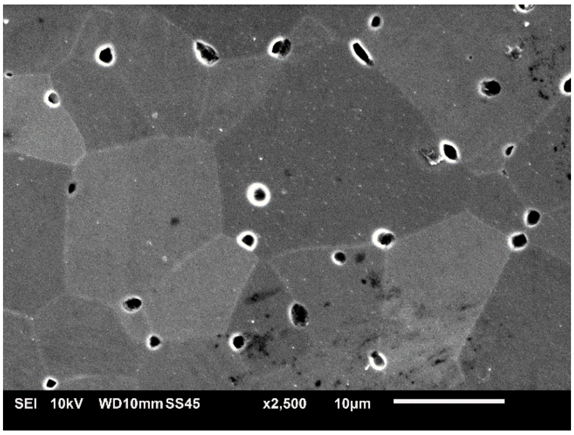

(d) BSE, Batch B, 0.025M, 50h

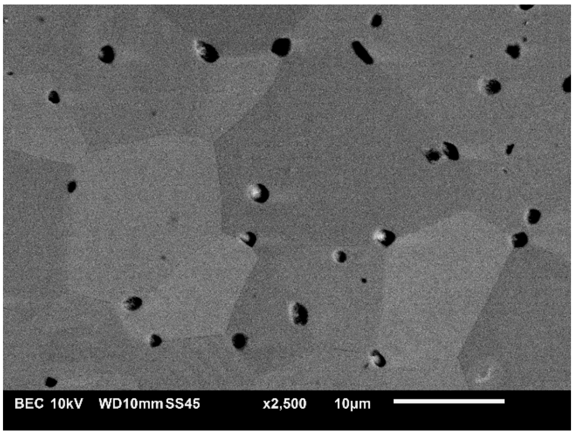

(e) BSE, Batch B, 0.125M, 0h

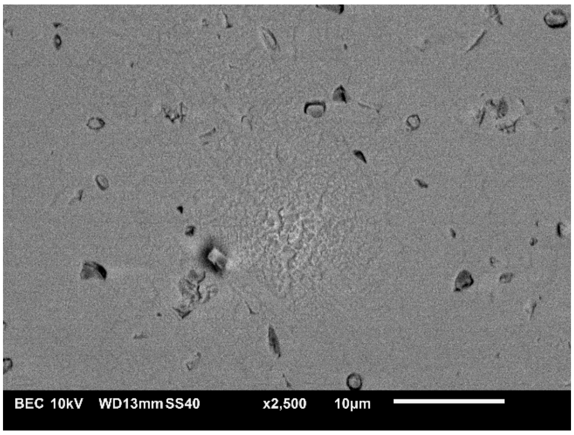

(f) BSE, Batch B, 0.250M, 0h

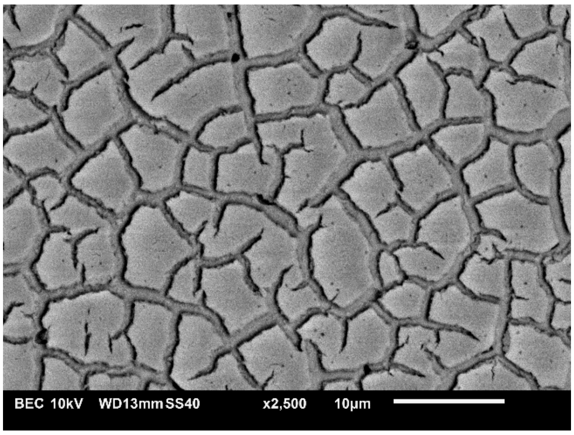

(g) BSE, Batch B, 1.000M, 0h

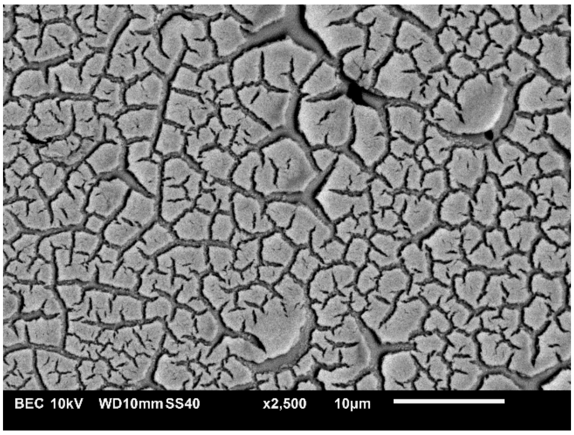

(h) BSE, Batch B, 1.000M, 100h

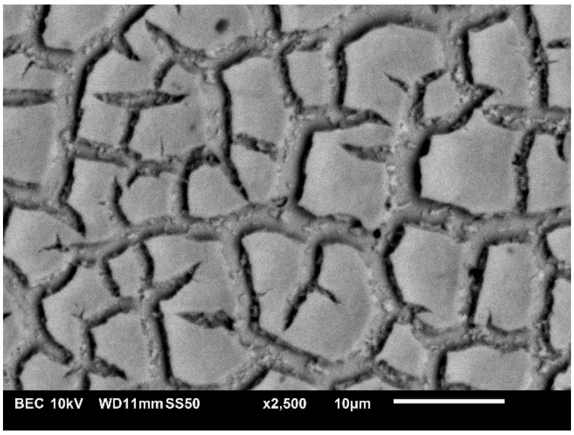

(i) SEM, Batch B, 1.000M, 50h

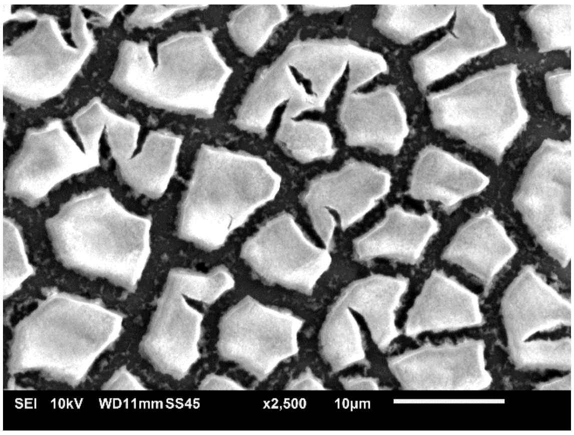

(j) BSE, Batch B, 1.000M, 50h

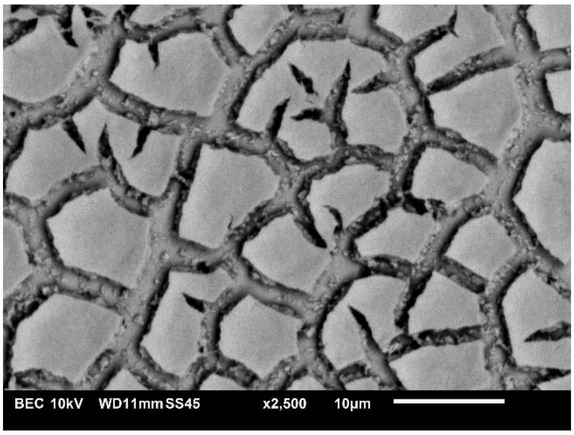

11.5.3 SEM-BSE images, Batch C

(a) BSE, Batch C, 0.025M, 0h

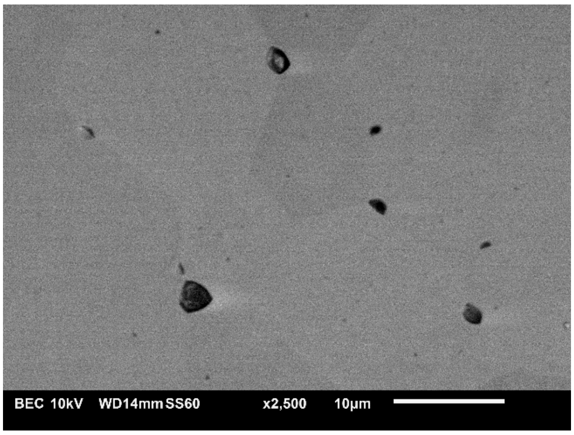

(b) BSE, Batch C, 0.025M, 100h

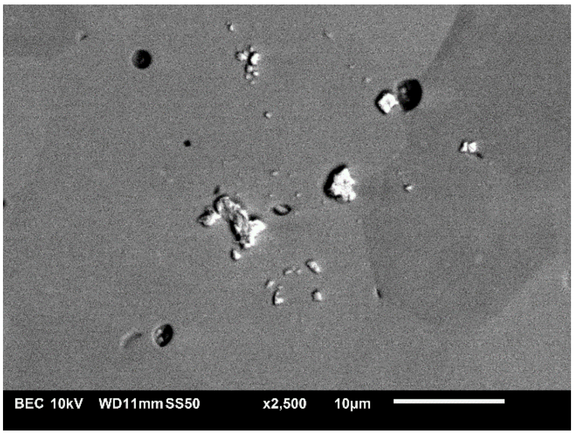

(c) SEM, Batch C, 0.025M, 50h

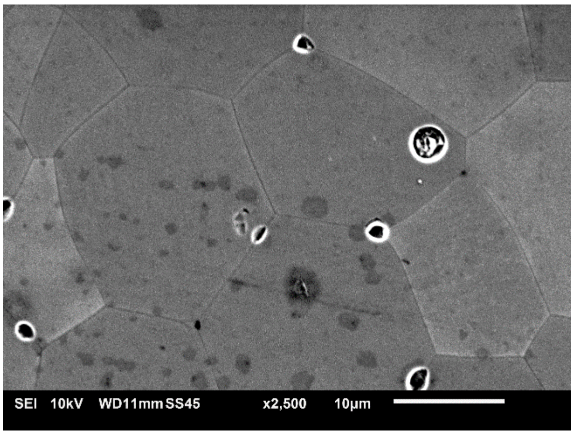

(d) BSE, Batch C, 0.025M, 50h

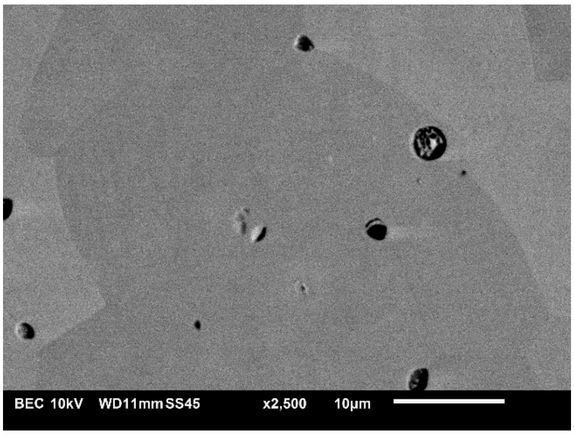

(e) BSE, Batch C, 0.125M, 0h

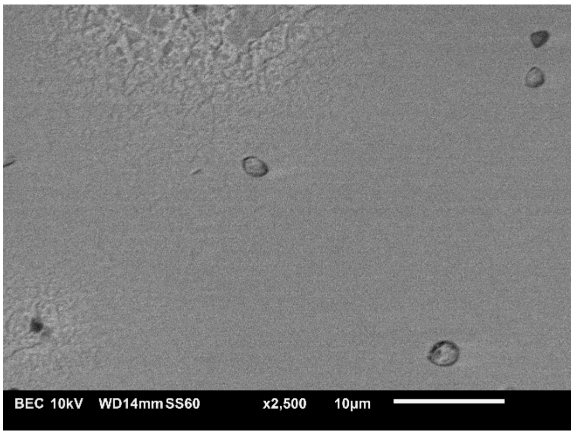

(f) BSE, Batch C, 0.250M, 0h

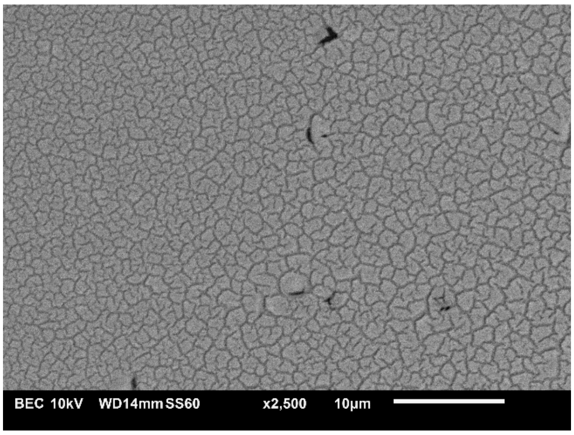

(g) BSE, Batch C, 1.000M, 0h

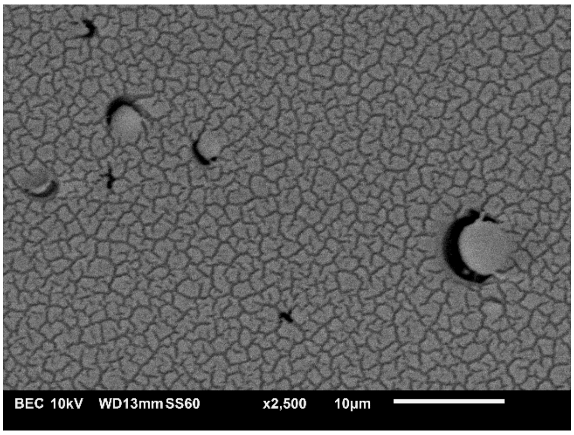

(h) BSE, Batch C, 1.000M, 100h

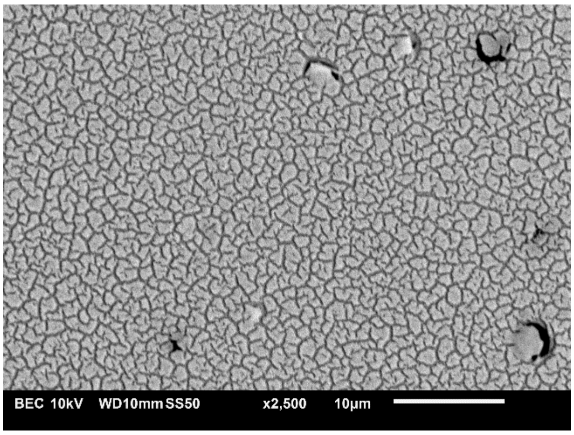

(i) SEM, Batch C, 1.000M, 50h

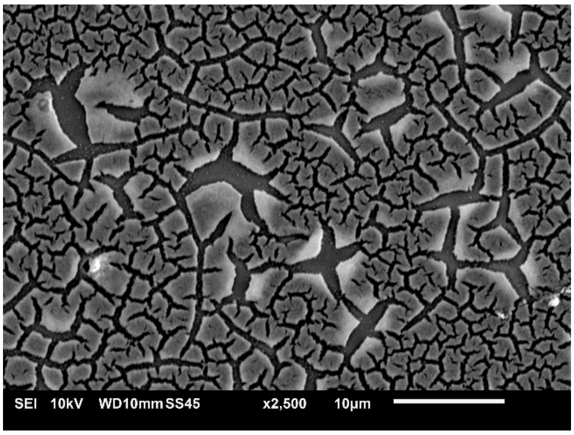

(j) BSE, Batch C, 1.000M, 50h

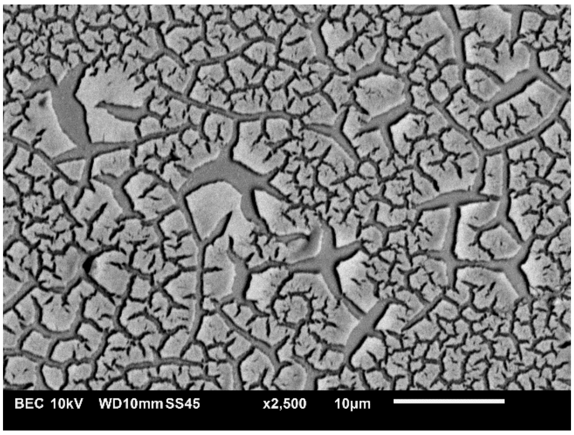

12 Annex C – HfO$_2$ infiltrated cells

12.1 EIS data plots

12.1.1 Batch A

(a) ECM

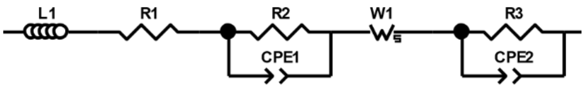

(b) 6.58 mg/mL

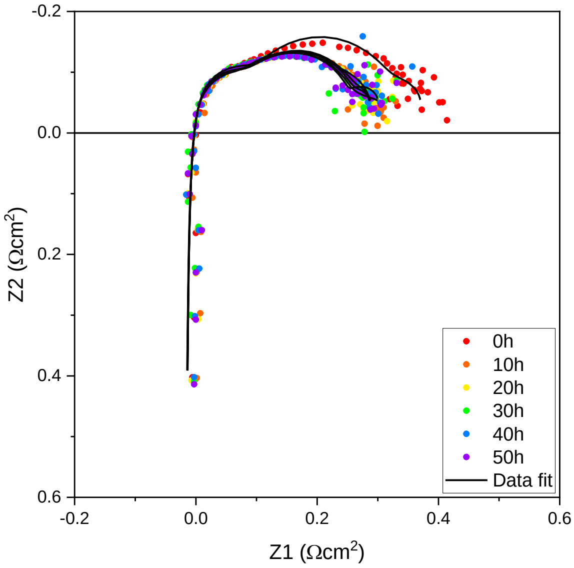

(c) 26.32 mg/mL

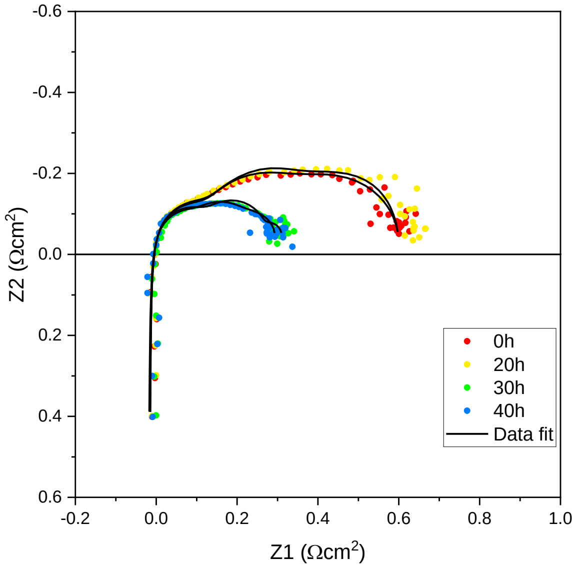

(d) 105.28 mg/mL

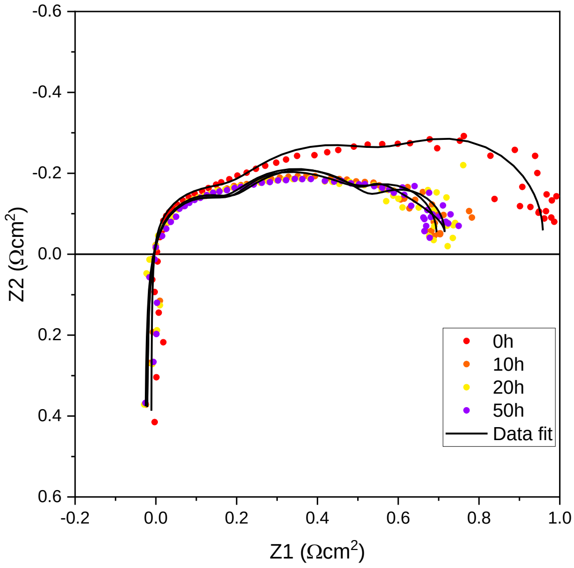

12.1.2 Batch B, set 1

(a) ECM

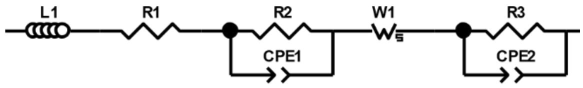

(b) 6.58 mg/mL

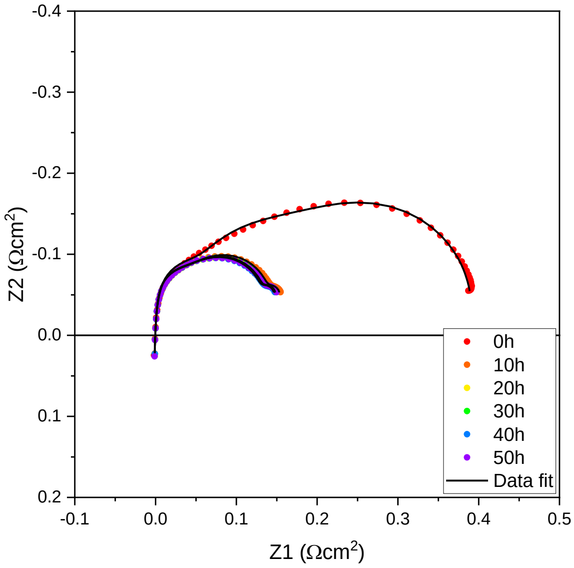

(c) 13.16 mg/mL

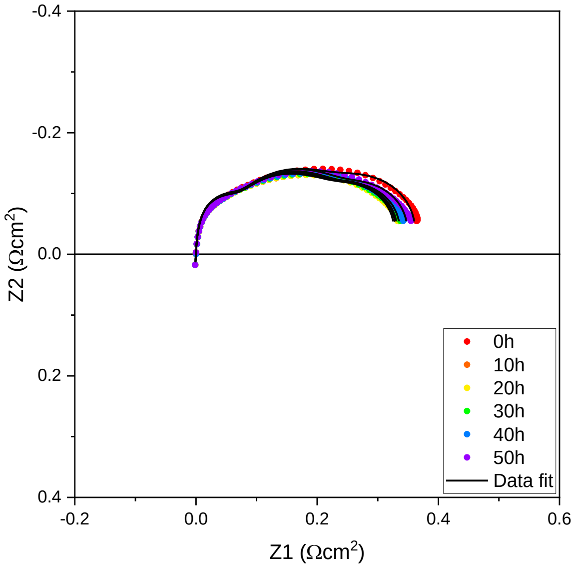

(d) 26.32 mg/mL (R1)

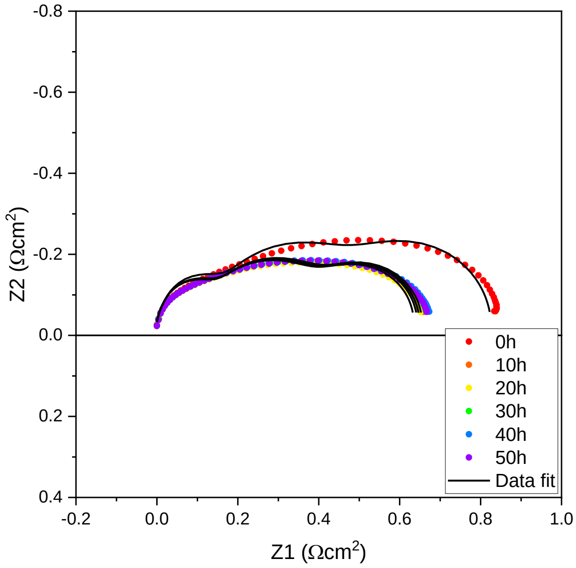

(e) 26.32 mg/mL (R2)

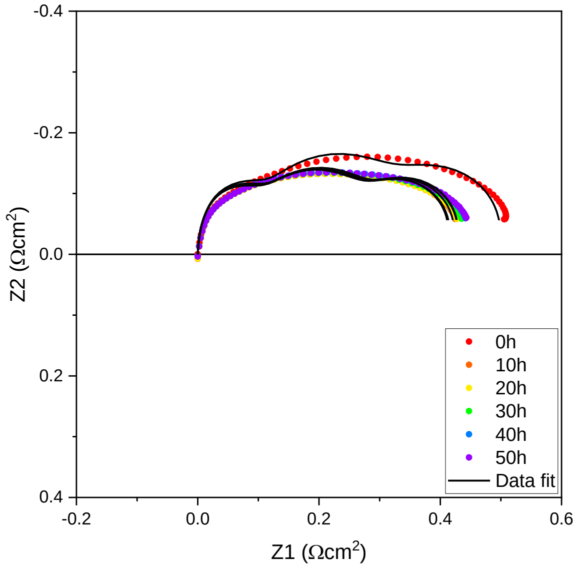

(f) 52.64 mg/mL (R1)

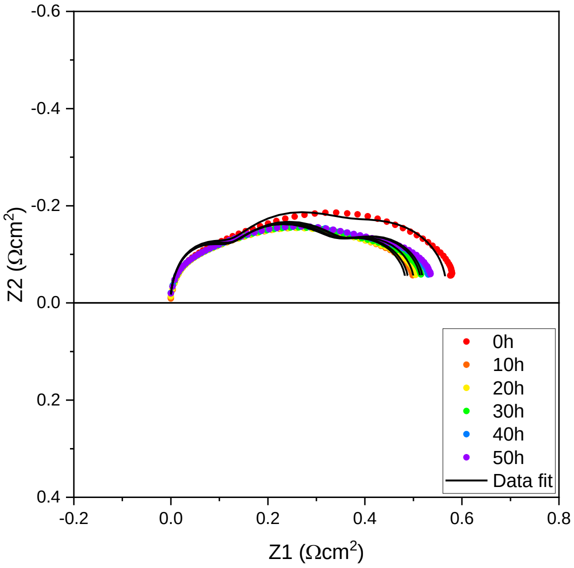

(g) 52.64 mg/mL (R2)

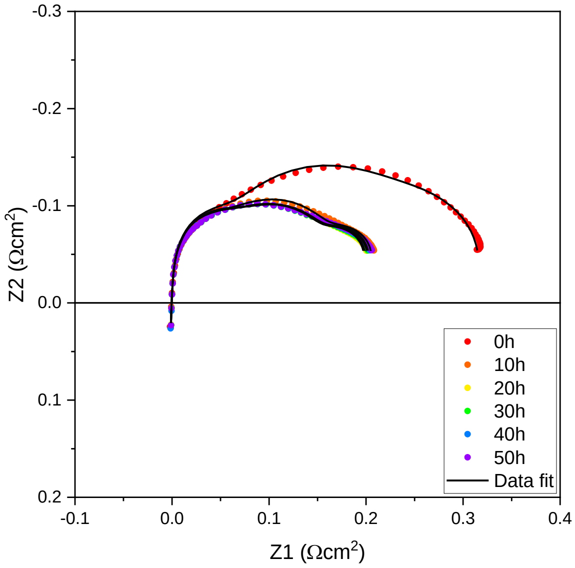

(h) 105.28 mg/mL (R1)

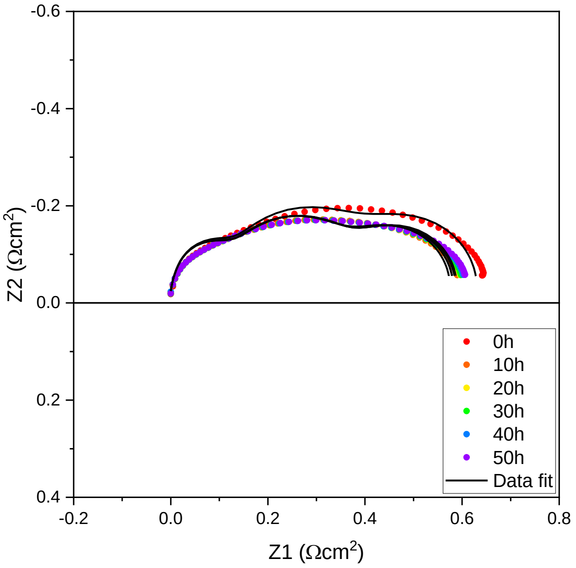

(i) 105.28 mg/mL (R2)

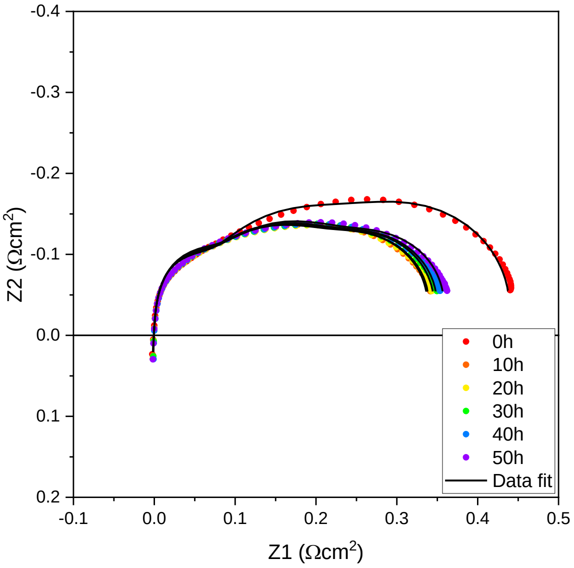

12.1.3 Batch B, set 2

(a) ECM

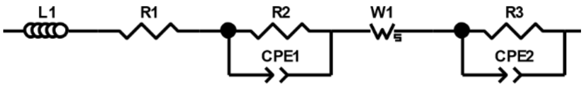

(b) 6.58 mg/mL (R1)

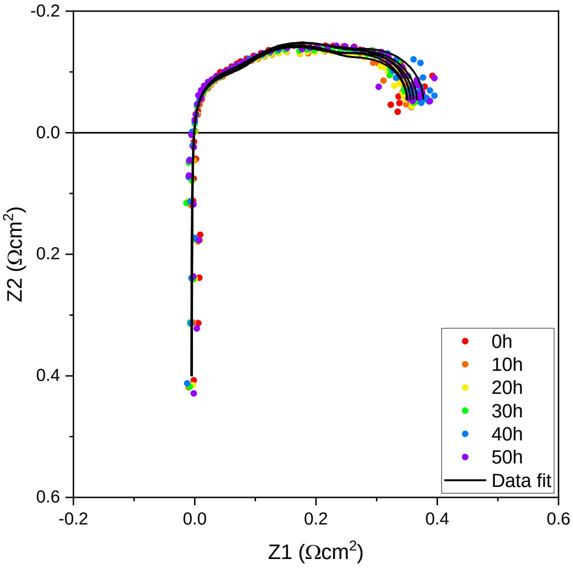

(c) 6.58 mg/mL (R2)

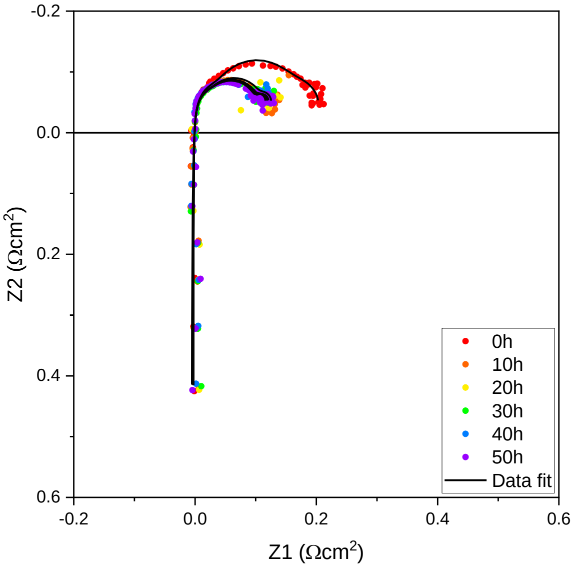

(d) 6.58 mg/mL (R3)

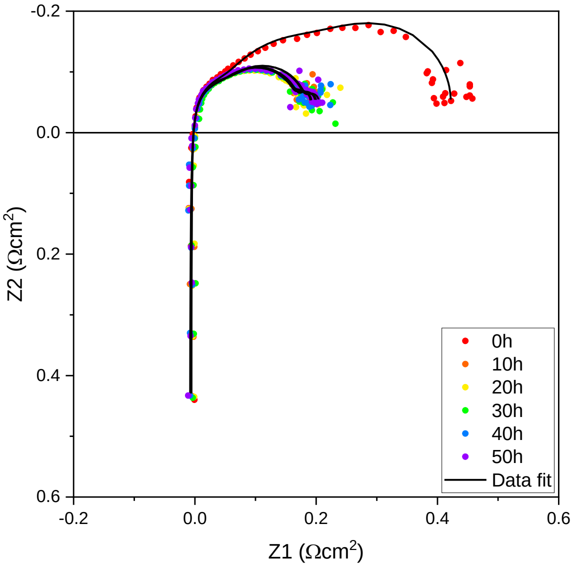

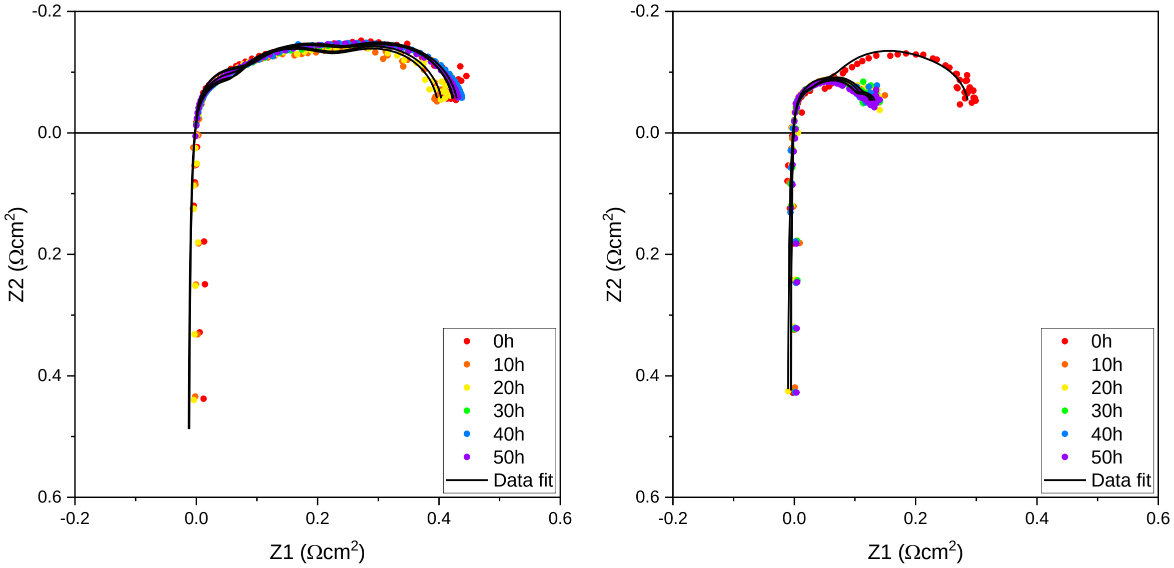

(e) 13.16 mg/mL (R1)

(f) 13.16 mg/mL (R2)

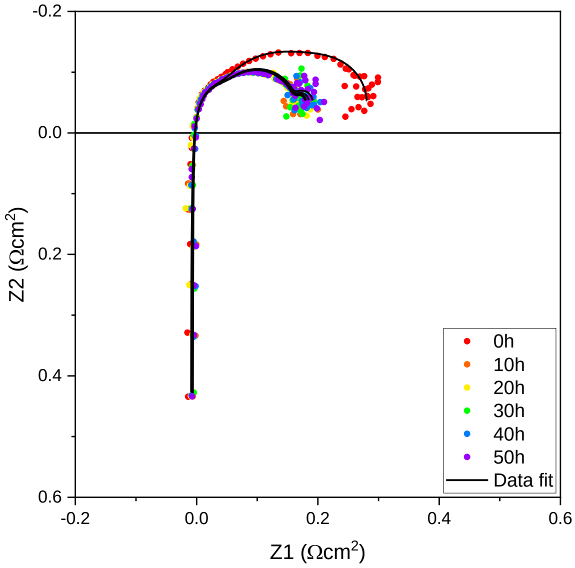

(g) 13.16 mg/mL (R3)

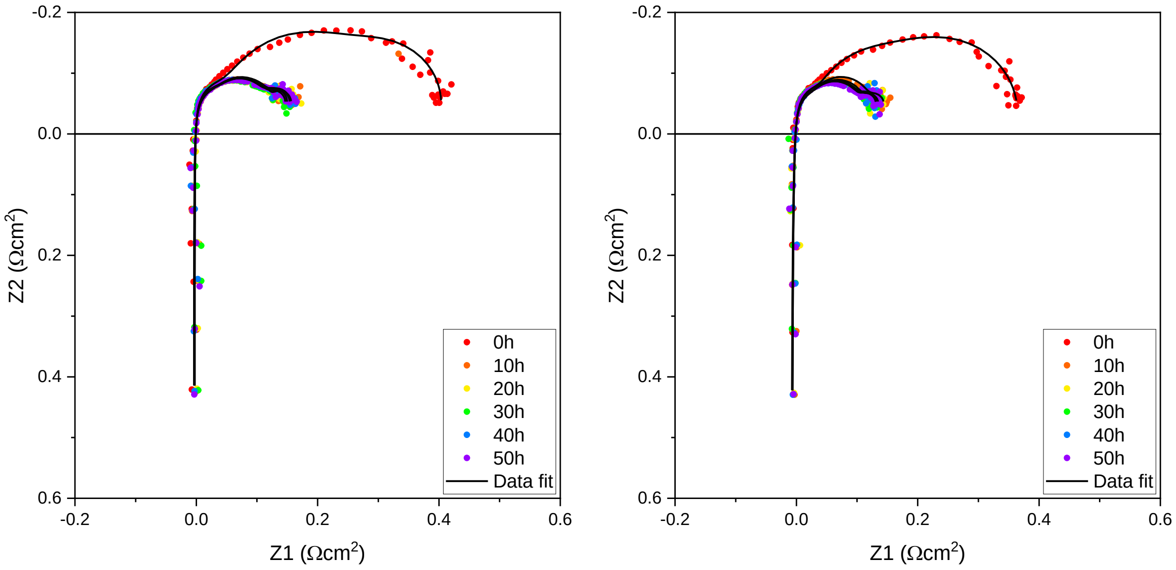
(h) 26.32 mg/mL (R1)

(i) 26.32 mg/mL (R2)

12.1.4 Batch C

(a) ECM

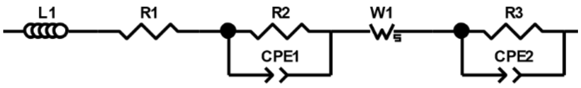

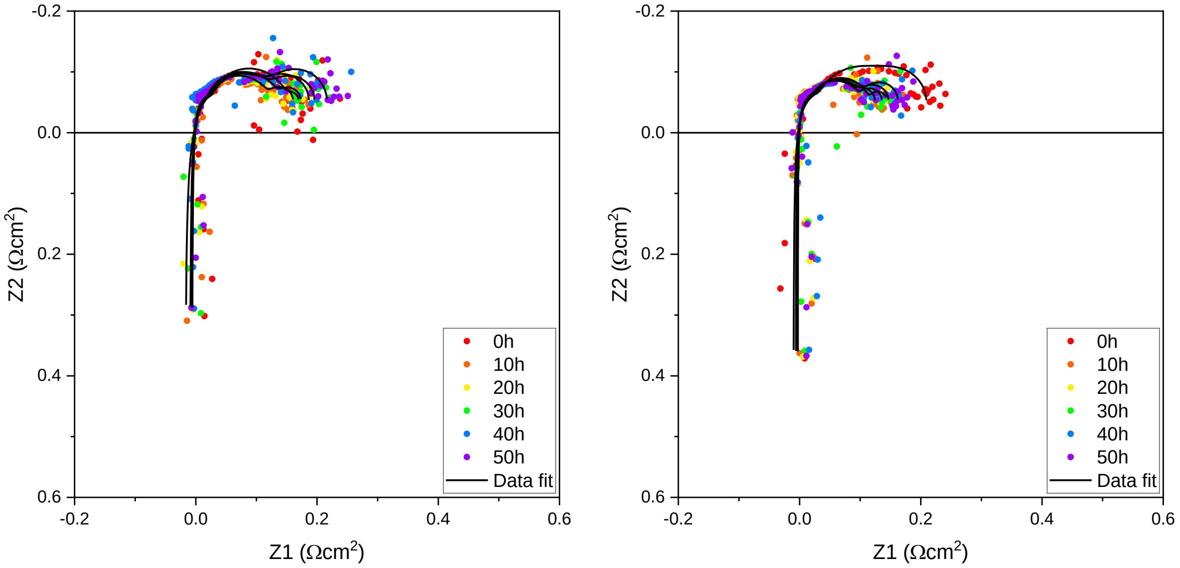
(b) 6.58 mg/mL

(c) 13.16 mg/mL

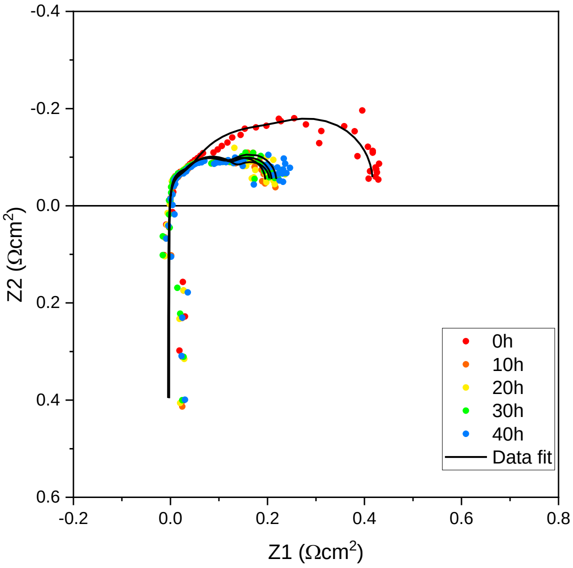
(d) 26.32 mg/mL

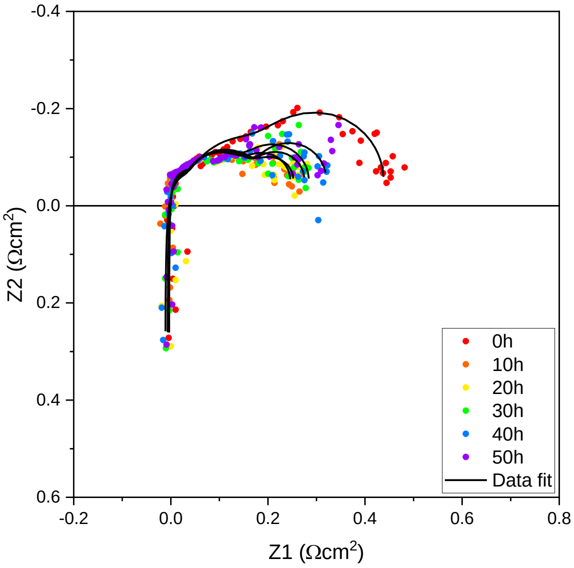
(e) 52.64 mg/mL

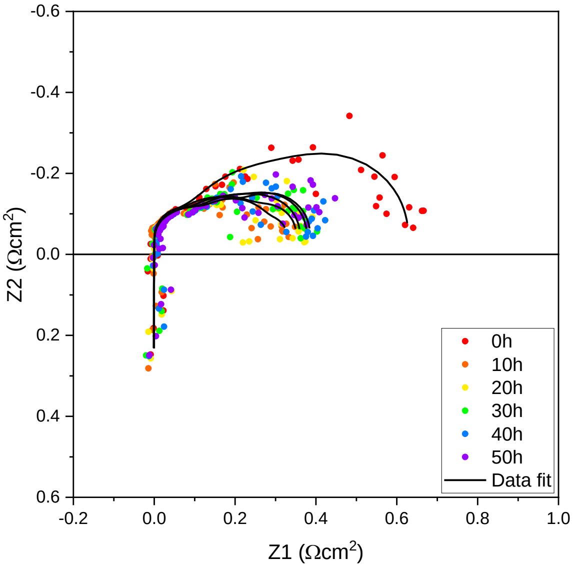
(f) 105.28 mg/mL

12.2 Rs and Rp monitoring over time

12.2.1 Batch A

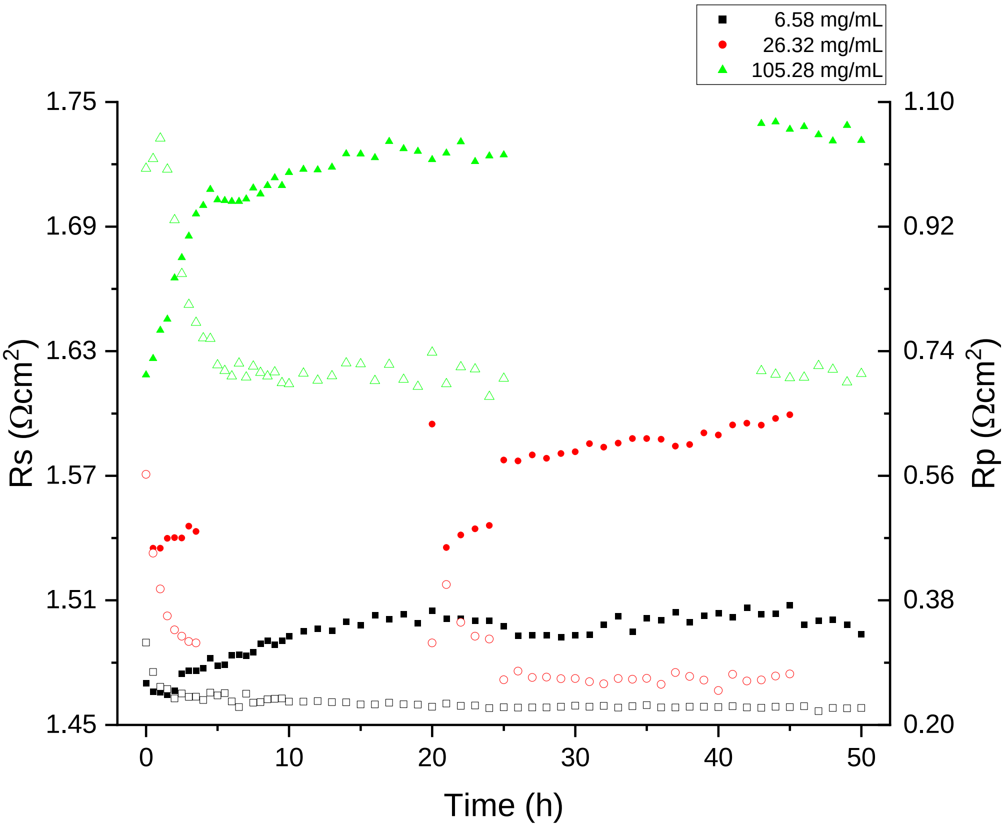

12.2.2 Batch B, set 1

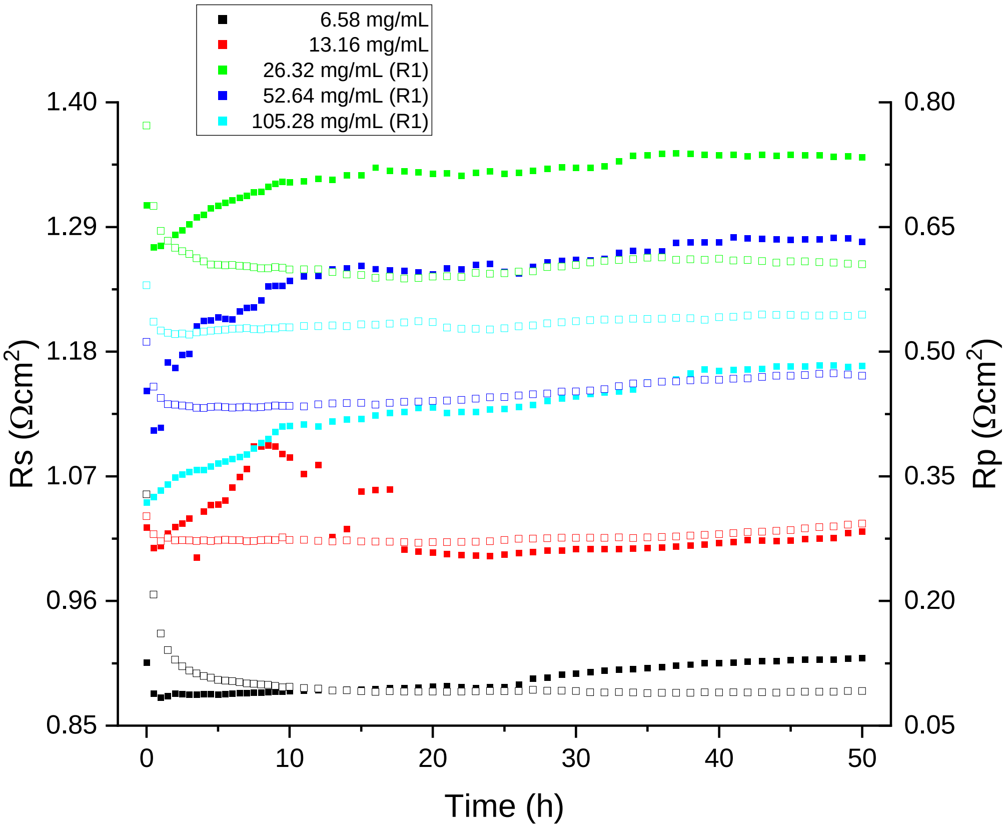

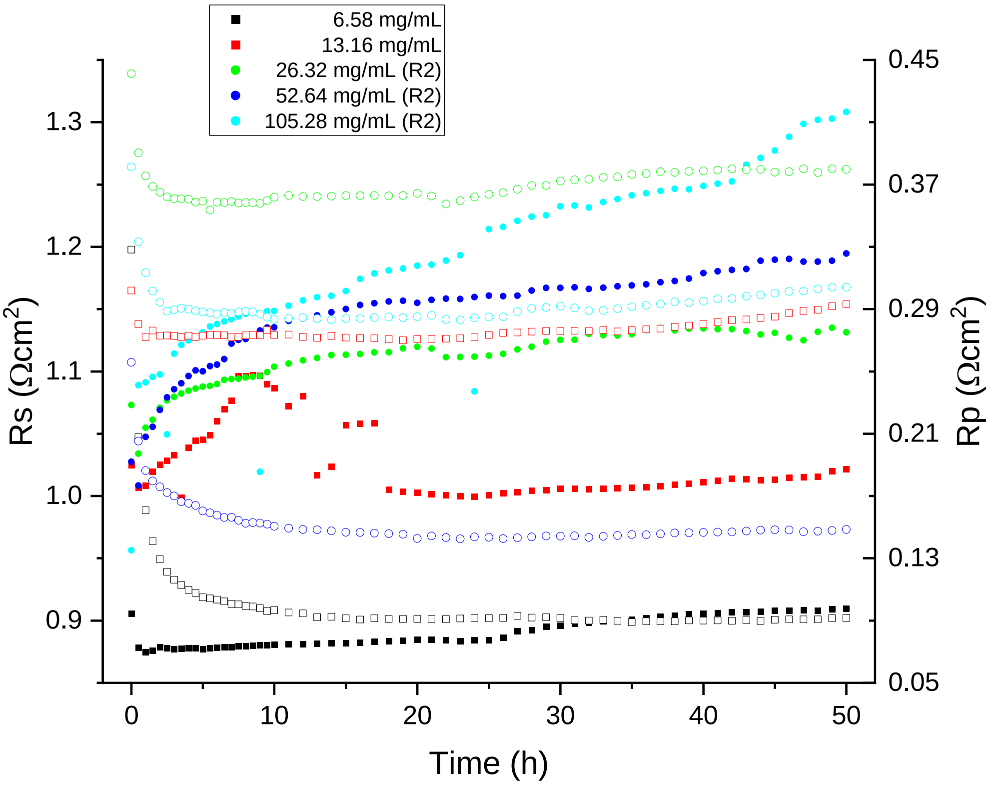

12.2.3 Batch B, set 2

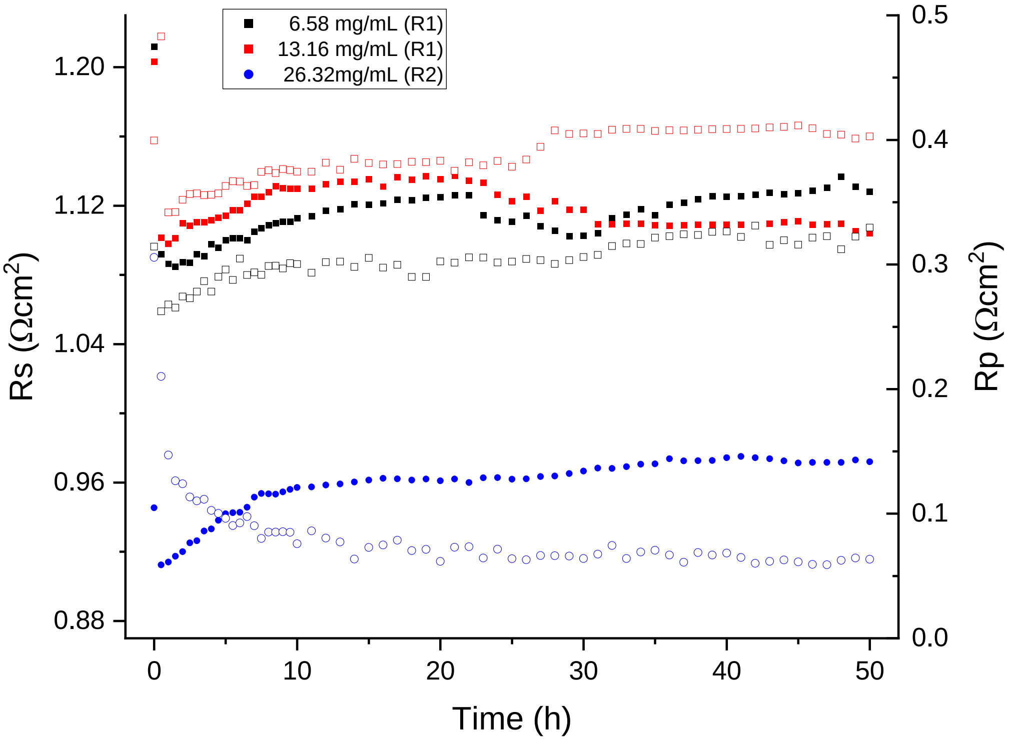

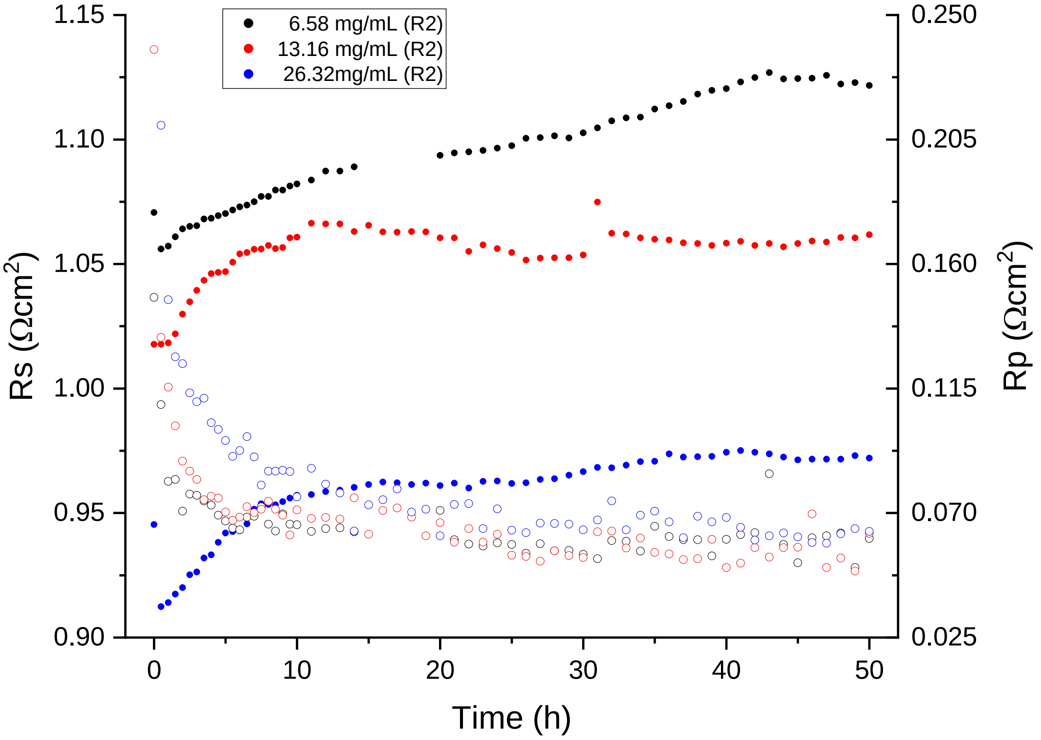

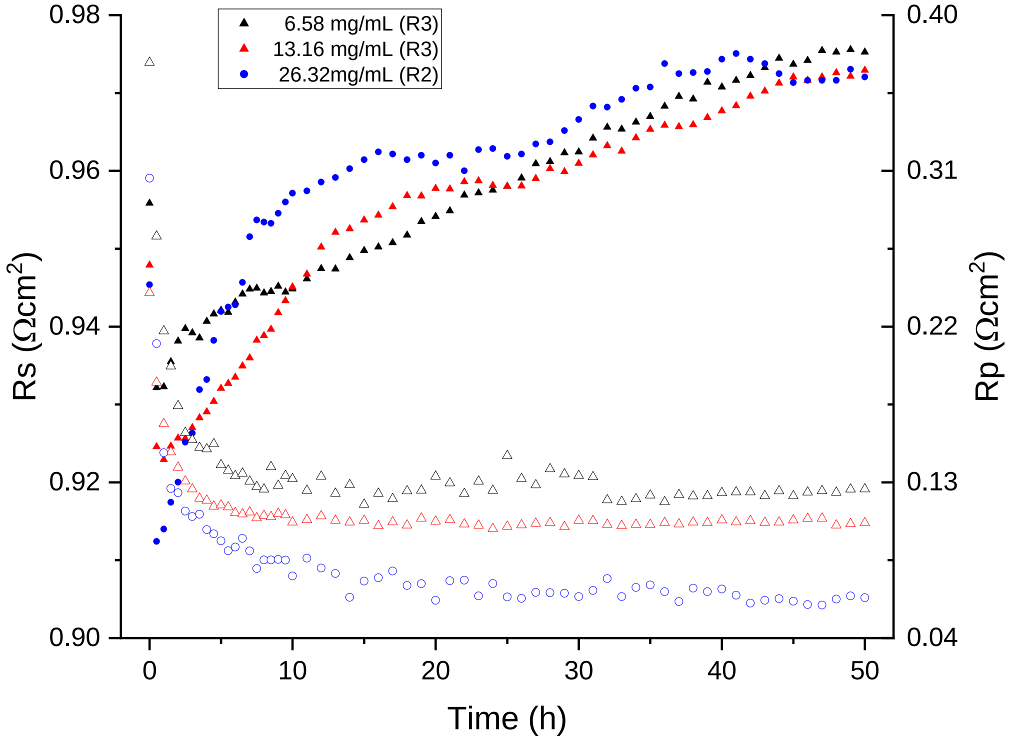

6.58 mg/mL (R3)
13.16 mg/mL (R3)
26.32mg/mL (R2)
Rs (Ωcm²)
Rp (Ωcm²)
Time (h)
0.98
0.96
0.94
0.92
0.90
0.40
0.31
0.22
0.13
0.04
0
10
20
30
40
50

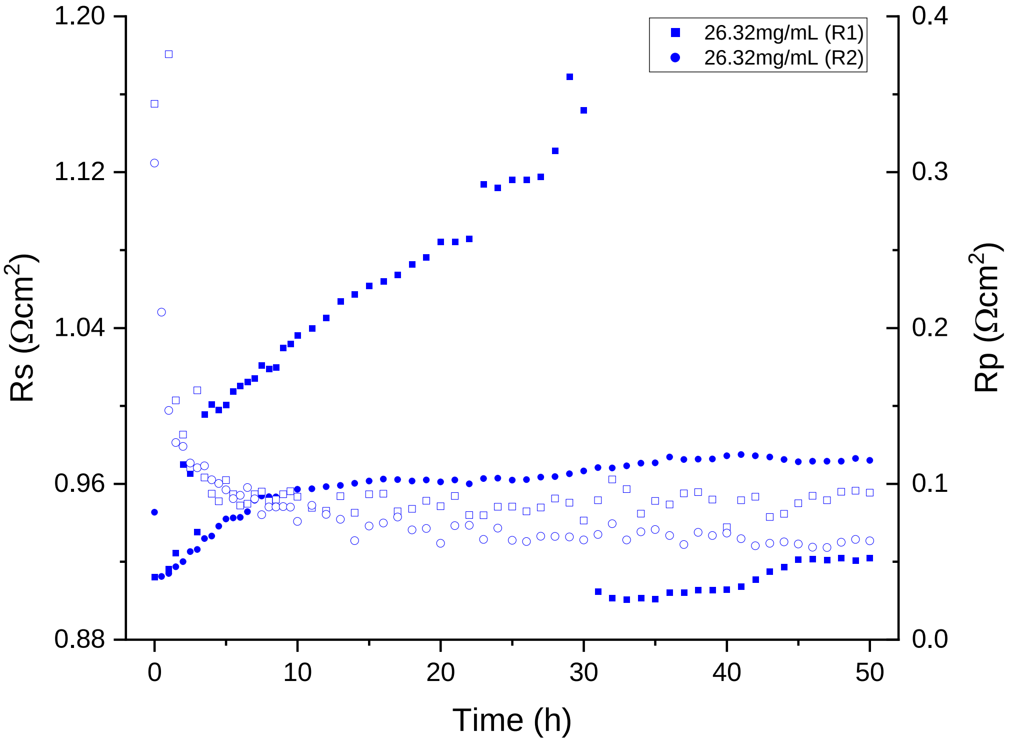

26.32mg/mL (R1)
26.32mg/mL (R2)
Rs (Ωcm²)
Rp (Ωcm²)
Time (h)
1.20
1.12
1.04
0.96
0.88
0.4
0.3
0.2
0.1
0.0
0
10
20
30
40
50

12.2.4 Batch C

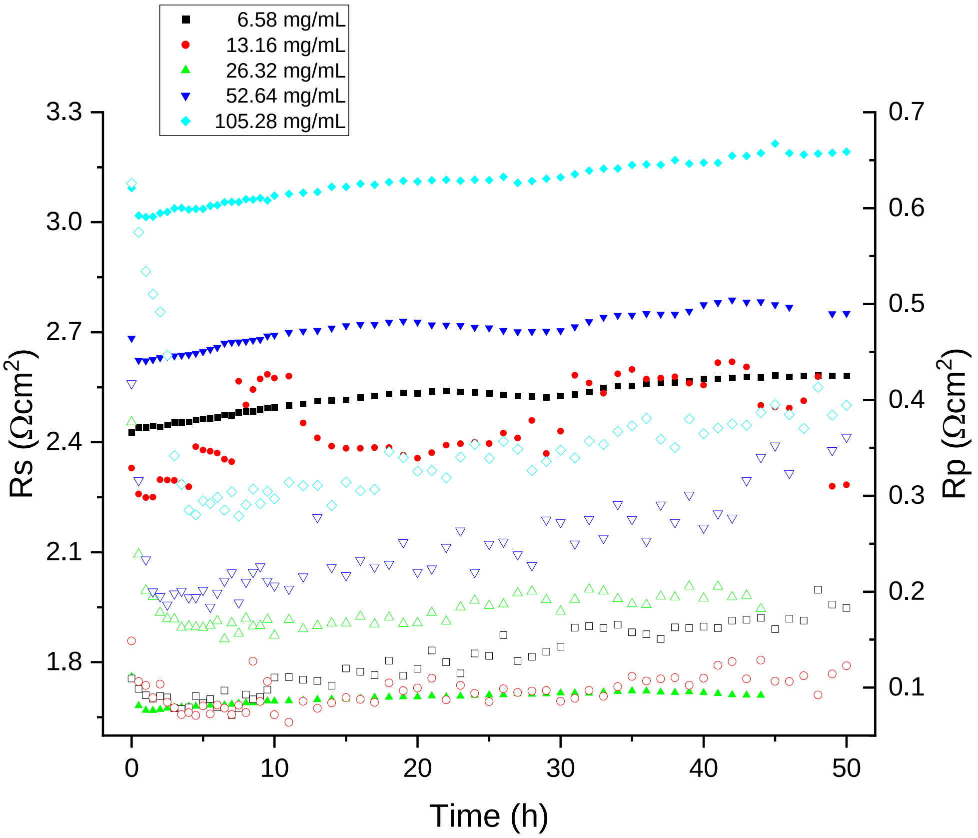
■ 6.58 mg/mL
● 13.16 mg/mL
▲ 26.32 mg/mL
▼ 52.64 mg/mL
◆ 105.28 mg/mL
Rs (Ωcm^2)
3.3
3.0
2.7
2.4
2.1
1.8
Rp (Ωcm^2)
0.7
0.6
0.5
0.4
0.3
0.2
0.1
0
10
20
30
40
50
Time (h)

12.3 EIS data fitting results

12.3.1 Batch A

Sample	Date	14/06/2021		6.58	mg/mL																
217	Chi-Sqr	Sum-Sqr	**L**	R1	%error	R2	%error	CPE1-T	%error	W-R	%error	W-T	%error	R3	%error	CPE2-T	%error	**Rs**	**%error**	**Rp**	**%error**
0h	2.85E-03	0.00704	5.01E-06	10.43	0.25115	0.3331	18.566	0.14379	49.026	0.78889	6.8982	1.76E-04	14.833	1.613	3.9212	1.79E-03	9.2535	1.44266	0.25115	0.33958	9.795133
10h	3.38E-03	0.00572	5.01E-06	10.59	0.23318	0.18571	30.675	0.16461	80.129	0.71403	8.1431	1.47E-04	16.224	1.256	4.8513	1.55E-03	12.254	1.465596	0.23318	0.256545	14.55647
20h	0.00323	0.00476	5.01E-06	10.65	0.22292	0.39794	31.872	0.02331	66.732	0.63695	9.9286	1.15E-04	18.205	1.117	9.863	1.25E-03	14.305	1.474197	0.22292	0.255993	17.2212
30h	5.10E-03	9.25E-03	5.01E-06	10.6	0.29773	0.18526	30.503	0.27315	82.841	0.71107	9.8861	1.44E-04	20.201	1.249	5.4912	1.59E-03	14.823	1.46703	0.29773	0.255053	15.29343
40h	4.39E-03	1.02E-02	5.01E-06	10.67	0.31153	0.33573	15.178	0.343	38.816	0.69575	10.895	1.45E-04	22.019	1.212	5.8368	1.54E-03	16.072	1.477064	0.31153	0.269122	10.6366
50h	3.88E-03	0.00669	5.01E-06	10.61	0.25206	0.24601	27.328	0.10395	69.872	0.68088	9.7427	1.47E-04	18.918	1.187	5.8983	1.55E-03	14.682	1.468463	0.25206	0.250546	14.323

Sample	Date	17/06/2021		26.32	mg/mL																
214	Chi-Sqr	Sum-Sqr	**L**	R1	%error	R2	%error	CPE1-T	%error	W-R	%error	W-T	%error	R3	%error	CPE2-T	%error	**Rs**	**%error**	**Rp**	**%error**
0h	1.61E-03	0.00524	4.98E-06	11.14	0.2043	1.862	6.0768	0.00779	14.408	1.695	7.2903	2.75E-03	11.772	0.75191	7.8084	2.31E-04	10.327	1.544439	0.2043	0.565202	7.0585
20h	0.00152	0.00528	4.98E-06	11.29	0.20189	1.919	5.8223	0.0089	13.942	1.887	6.4796	3.19E-03	10.544	0.78524	7.2964	2.35E-04	10.009	1.565941	0.20189	0.605674	6.532767
30h	2.11E-03	3.83E-03	4.98E-06	11.21	0.17754	0.30527	12.705	0.11277	35.35	1.156	5.2133	2.33E-03	10.103	0.82563	6.3897	1.98E-04	8.0469	1.554473	0.17754	0.275347	8.102667
40h	3.63E-03	4.81E-03	4.98E-06	11.26	0.21728	0.56899	20.969	0.01073	47.137	0.90697	14.39	1.17E-03	23.976	0.71518	11.593	1.83E-04	10.771	1.561641	0.21728	0.261619	15.65067

Sample	Date	21/06/2021		105.28	mg/mL																
216	Chi-Sqr	Sum-Sqr	**L**	R1	%error	R2	%error	CPE1-T	%error	W-R	%error	W-T	%error	R3	%error	CPE2-T	%error	**Rs**	**%error**	**Rp**	**%error**
0h	1.96E-03	0.00956	4.95E-06	11.5	0.25244	2.319	5.5692	0.00169	9.3244	3.21	4.724	5.88E-02	6.9317	1.251	6.6285	1.99E-04	8.7413	1.596045	0.25244	0.919433	5.640567
10h	3.52E-03	0.01033	4.95E-06	11.99	0.33729	2.064	4.875	8.39E-04	9.3793	1.605	6.833	3.88E-02	12.204	1.389	5.0253	5.51E-05	9.5101	1.666286	0.33729	0.672584	5.577767
20h	0.0036	0.01326	4.95E-06	12.09	0.36393	2.128	4.5615	0.00106	9.9605	1.535	6.5974	8.64E-02	13.779	1.5	4.9883	6.06E-05	9.8081	1.680621	0.36393	0.687636	5.3824
50h	2.88E-03	0.00896	4.95E-06	12.11	0.31277	1.937	4.7183	9.13E-04	9.3101	1.682	5.8701	4.25E-02	10.751	1.391	4.6687	5.57E-05	8.9036	1.683488	0.31277	0.665703	5.0857

12.3.2 Batch B, set 1

Sample	Date	03/12/2020		6.58	mg/mL																
128	Chi-Sqr	Sum-Sqr	**L**	R1	%error	R2	%error	CPE1-T	%error	W-R	%error	W-T	%error	R3	%error	CPE2-T	%error	**Rs**	**%error**	**Rp**	**%error**
0h	1.19E-04	3.31E-04	1.33E-06	6.61E+00	0.05767	1.498	1.4968	8.91E-03	3.1787	0.38463	3.1084	1.95E-04	5.32E+00	0.8716	2.1987	2.28E-03	3.4032	0.895063	0.05767	0.342338	2.267967
10h	1.03E-04	1.23E-04	1.33E-06	6.45E+00	0.03626	0.09887	3.4852	5.12E-01	9.5988	0.3099	2.6268	1.66E-04	4.19E+00	0.69453	1.0481	1.89E-03	2.7351	0.87141	0.03626	0.105678	2.3867
20h	1.07E-04	1.25E-04	1.33E-06	6.47E+00	0.0368	0.10303	3.3028	4.91E-01	9.1031	0.29773	2.9262	1.60E-04	4.54E+00	0.66207	1.1777	1.83E-03	3.0232	0.875424	0.0368	0.099876	2.4689
30h	9.32E-05	1.09E-04	1.33E-06	6.55E+00	0.03428	0.10738	2.9844	4.61E-01	8.2323	0.29958	2.8629	1.61E-04	4.35E+00	0.65993	1.1622	1.79E-03	2.9569	0.886892	0.03428	0.100458	2.3365
40h	9.06E-05	1.04E-04	1.33E-06	6.62E+00	0.03374	0.10994	2.8533	4.43E-01	7.8768	0.29439	2.9632	1.57E-04	4.44E+00	0.64984	1.201	1.74E-03	3.0309	0.896497	0.03374	0.098635	2.339167
50h	1.09E-04	1.27E-04	1.33E-06	6.65E+00	0.03706	0.11434	3.0754	4.13E-01	8.4949	0.2998	3.2612	1.61E-04	4.86E+00	0.65289	1.3373	1.76E-03	3.3767	0.90051	0.03706	0.100478	2.557967

Sample	Date	17/11/2020		13.16	mg/mL																
104	Chi-Sqr	Sum-Sqr	**L**	R1	%error	R2	%error	CPE1-T	%error	W-R	%error	W-T	%error	R3	%error	CPE2-T	%error	**Rs**	**%error**	**Rp**	**%error**
0h	2.85E-04	0.00066204	1.23E-06	7.422	0.08411	1.104	2.1546	0.0018	3.8415	0.53331	3.0686	1.69E-04	5.6786	0.92985	2.8827	1.74E-02	6.5096	1.011463	0.08411	0.315522	2.701967
10h	2.86E-04	0.00059659	1.23E-06	7.859	0.0792	1.036	2.0912	0.00199	4.0348	0.51725	3.1111	1.74E-04	5.8089	0.78834	3.0502	2.30E-02	7.0344	1.074107	0.0792	0.283186	2.750833
20h	3.21E-04	0.00071145	1.23E-06	7.276	0.08602	1.066	2.0545	0.00202	3.9507	0.52121	3.0917	1.80E-04	5.8064	0.73384	3.3029	2.62E-02	7.6567	0.990534	0.08602	0.280242	2.816367
30h	3.26E-04	7.30E-04	1.23E-06	7.296	0.08673	1.105	1.9966	0.00202	3.8535	0.53287	3.0493	1.85E-04	5.749	0.71916	3.3859	2.80E-02	7.8804	0.993401	0.08673	0.2854	2.8106
40h	3.33E-04	7.53E-04	1.23E-06	7.333	0.08762	1.132	1.9762	0.00203	3.8327	0.54323	3.0424	1.91E-04	5.7455	0.71231	3.4593	2.94E-02	8.0754	0.998705	0.08762	0.289773	2.825967
50h	3.35E-04	0.00077761	1.23E-06	7.404	0.08873	1.176	1.9537	0.00201	3.755	0.5555	3.0175	1.94E-04	5.7314	0.74277	3.4047	2.91E-02	7.9603	1.008883	0.08873	0.302206	2.791967

99	Chi-Sqr	Sum-Sqr	**L**	R1	%error	R2	%error	CPE1-T	%error	W-R	%error	W-T	%error	R3	%error	CPE2-T	%error	**Rs**	**%error**	**Rp**	**%error**
0h	6.61E-04	0.00238	6.26E-07	9.408	0.17168	2.42	2.1553	0.00892	5.3611	1.218	2.7273	1.27E-04	5.5726	2.226	2.3771	1.12E-03	3.9984	1.296156	0.17168	0.788124	2.4199
10h	6.55E-04	0.00197	6.26E-07	9.555	0.15867	1.707	2.2455	0.01354	5.7893	1.087	2.8469	1.16E-04	5.7772	1.793	1.9266	1.48E-03	4.3475	1.317229	0.15867	0.605066	2.339667
20h	6.73E-04	0.00199	6.26E-07	9.607	0.15905	1.668	2.3204	0.01375	5.9753	1.094	2.8822	1.17E-04	5.82	1.768	1.8726	1.47E-03	4.3858	1.324683	0.15905	0.596895	2.3584
30h	6.73E-04	2.01E-03	6.26E-07	9.643	0.15927	1.7	2.3474	0.01351	6.0217	1.107	2.8827	1.20E-04	5.8158	1.818	1.8916	1.43E-03	4.4897	1.329844	0.15927	0.610513	2.3739
40h	6.87E-04	2.06E-03	6.26E-07	9.72	0.16038	1.714	2.3824	0.01346	6.1045	1.117	2.9167	1.21E-04	5.8767	1.839	1.9165	1.40E-03	4.5948	1.340882	0.16038	0.616964	2.4052
50h	6.90E-04	0.00206	6.26E-07	9.712	0.16005	1.691	2.4195	0.01381	6.1966	1.113	2.9328	1.24E-04	5.9047	1.823	1.9101	1.41E-03	4.642	1.339735	0.16005	0.6108	2.4208

Sample	Date	09/11/2020		26.32	mg/mL																
105	Chi-Sqr	Sum-Sqr	**L**	R1	%error	R2	%error	CPE1-T	%error	W-R	%error	W-T	%error	R3	%error	CPE2-T	%error	**Rs**	**%error**	**Rp**	**%error**
0h	5.65E-04	0.00171	9.48E-07	7.76	0.13919	1.191	2.7283	0.02366	6.8421	0.83605	2.9227	1.77E-04	5.8569	1.514	2.0417	1.60E-03	4.3408	1.059916	0.13919	0.455129	2.564233
10h	5.80E-04	0.00158	1.06E-06	7.986	0.13201	0.9724	2.5839	0.03752	6.7677	0.77852	3.081	1.84E-04	6.1695	1.187	2.1845	2.03E-03	5.3665	1.092313	0.13201	0.36867	2.616467
20h	6.00E-04	0.00162	1.05E-06	8.098	0.13263	0.96248	2.6615	0.03983	6.9818	0.80404	3.072	1.92E-04	6.1448	1.185	2.2419	2.11E-03	5.5347	1.108368	0.13263	0.37062	2.658467
30h	6.02E-04	1.65E-03	1.03E-06	8.139	0.13263	0.98632	2.6246	0.04	6.8918	0.80394	3.1236	1.99E-04	6.2299	1.212	2.2206	2.11E-03	5.5014	1.114245	0.13263	0.377894	2.656267
40h	6.25E-04	1.72E-03	1.02E-06	8.204	0.13437	0.99191	2.6822	0.04183	7.0511	0.82356	3.1456	2.08E-04	6.2695	1.228	2.2577	2.17E-03	5.6074	1.123563	0.13437	0.383801	2.695167
50h	6.34E-04	0.00177	1.03E-06	8.183	0.13612	1.001	2.6582	0.04299	7.008	0.81886	3.1628	2.10E-04	6.3405	1.229	2.2591	2.22E-03	5.6132	1.120553	0.13612	0.384574	2.693367

Sample	Date	02/11/2020		52.64	mg/mL																
100	Chi-Sqr	Sum-Sqr	**L**	R1	%error	R2	%error	CPE1-T	%error	W-R	%error	W-T	%error	R3	%error	CPE2-T	%error	**Rs**	**%error**	**Rp**	**%error**
0h	6.03E-04	0.00175	8.06E-07	8.262	0.1453	1.391	3.2583	0.01267	7.666	0.90617	2.8486	1.31E-04	5.7027	1.738	2.3771	1.12E-03	3.9984	1.131877	0.1453	0.525961	2.828
10h	6.15E-04	0.00161	8.06E-07	8.954	0.13576	1.036	2.8981	0.03083	7.5151	0.87327	2.8342	1.48E-04	5.8772	1.54	1.9266	1.48E-03	4.3475	1.231075	0.13576	0.441972	2.552967
20h	6.24E-04	0.00168	8.06E-07	8.994	0.13849	1.052	2.7458	0.03344	7.2295	0.88377	2.8554	1.48E-04	5.937	1.555	1.8726	1.47E-03	4.3858	1.236809	0.13849	0.447921	2.491267
30h	6.77E-04	1.88E-03	8.06E-07	9.076	0.14744	1.083	2.7303	0.03454	7.2492	0.89917	2.9384	1.43E-04	6.1659	1.591	1.8916	1.43E-03	4.4897	1.248564	0.14744	0.459733	2.5201
40h	7.25E-04	2.06E-03	8.06E-07	9.179	0.15521	1.129	2.6989	0.03488	7.2147	0.91518	3.024	1.40E-04	6.3836	1.629	1.9165	1.40E-03	4.5948	1.263329	0.15521	0.47407	2.546467
50h	7.22E-04	0.00208	8.06E-07	9.182	0.15473	1.14	2.6573	0.03596	7.122	0.92847	3.0298	1.46E-04	6.3626	1.638	1.9101	1.41E-03	4.642	1.263759	0.15473	0.478842	2.5324

Sample	Date	07/12/2020		52.64	mg/mL																
130	Chi-Sqr	Sum-Sqr	**L**	R1	%error	R2	%error	CPE1-T	%error	W-R	%error	W-T	%error	R3	%error	CPE2-T	%error	**Rs**	**%error**	**Rp**	**%error**
0h	1.87E-04	3.78E-04	1.31E-06	7.47E+00	0.05721	0.60296	4.8496	3.42E-02	10.022	0.45349	3.0686	3.23E-04	5.36E+00	1.176	2.1406	2.79E-03	2.951	1.018631	0.05721	0.267541	3.352933
10h	1.40E-04	1.95E-04	1.31E-06	8.23E+00	0.04084	0.30157	2.8896	1.06E-01	7.4113	0.41561	3.7314	3.12E-04	5.47E+00	0.7461	1.7566	2.86E-03	4.8191	1.12729	0.04084	0.157281	2.792533
20h	1.33E-04	1.81E-04	1.31E-06	8.37E+00	0.03866	0.29841	2.8043	1.16E-01	7.216	0.45907	3.6308	3.56E-04	5.09E+00	0.65315	2.1386	3.45E-03	5.7895	1.146786	0.03866	0.149733	2.8579
30h	1.35E-04	1.85E-04	1.31E-06	8.45E+00	0.03905	0.3098	2.7529	1.14E-01	7.0873	0.46729	3.6335	3.60E-04	5.10E+00	0.64319	2.2132	3.54E-03	5.9919	1.158684	0.03905	0.151117	2.866533
40h	1.57E-04	2.17E-04	1.31E-06	8.53E+00	0.04181	0.31469	2.9698	1.18E-01	7.6431	0.48681	3.8296	3.85E-04	5.37E+00	0.63452	2.463	3.80E-03	6.6656	1.170725	0.04181	0.153373	3.087467
50h	1.42E-04	1.99E-04	1.31E-06	8.64E+00	0.03964	0.31682	2.8556	1.25E-01	7.3511	0.50195	3.541	4.06E-04	5.00E+00	0.62709	2.3802	4.08E-03	6.4551	1.18635	0.03964	0.154784	2.9256

Sample	Date	05/11/2020		105.28	mg/mL																
107	Chi-Sqr	Sum-Sqr	**L**	R1	%error	R2	%error	CPE1-T	%error	W-R	%error	W-T	%error	R3	%error	CPE2-T	%error	**Rs**	**%error**	**Rp**	**%error**
0h	6.67E-04	0.0022	7.47E-07	7.58E+00	0.17385	1.889	2.0942	8.22E-04	3.8412	0.9754	2.7531	1.01E-04	5.52E+00	1.63	2.6307	9.70E-03	6.4135	1.033826	0.17385	0.591792	2.492667
10h	7.29E-04	0.00226	7.47E-07	8.06E+00	0.1749	1.73	1.9513	9.22E-04	4.3372	0.94546	2.9488	1.03E-04	6.00E+00	1.428	2.4246	1.52E-02	6.2806	1.102204	0.1749	0.535751	2.441567
20h	7.40E-04	0.00233	7.47E-07	8.17E+00	0.17707	1.747	1.928	9.11E-04	4.4156	0.96601	2.9715	1.04E-04	6.05E+00	1.436	2.3723	1.60E-02	6.2045	1.118546	0.17707	0.54228	2.423933
30h	7.54E-04	2.36E-03	7.47E-07	8.24E+00	0.17782	1.747	1.9425	9.30E-04	4.4656	0.96304	3.0128	1.05E-04	6.14E+00	1.441	2.3759	1.65E-02	6.2277	1.12858	0.17782	0.542571	2.443733
40h	7.62E-04	2.40E-03	7.47E-07	8.39E+00	0.17918	1.755	1.9422	9.31E-04	4.5266	0.97502	3.0316	1.05E-04	6.20E+00	1.455	2.3438	1.70E-02	6.1808	1.150799	0.17918	0.547442	2.4392
50h	7.75E-04	0.00245	7.47E-07	8.43E+00	0.18043	1.76	1.9573	9.31E-04	4.5932	0.98096	3.0686	1.06E-04	6.27E+00	1.464	2.3459	1.72E-02	6.1955	1.155387	0.18043	0.550301	2.457267

Sample	Date	10/12/2020		105.28	mg/mL																
132	Chi-Sqr	Sum-Sqr	**L**	R1	%error	R2	%error	CPE1-T	%error	W-R	%error	W-T	%error	R3	%error	CPE2-T	%error	**Rs**	**%error**	**Rp**	**%error**
0h	2.29E-04	6.63E-04	1.33E-06	6.96E+00	0.07958	1.391	2.3334	1.30E-02	5.0292	0.54507	2.8701	2.27E-04	5.26E+00	1.169	2.4335	2.25E-03	3.4409	0.945666	0.07958	0.392631	2.545667
10h	1.73E-04	3.45E-04	1.33E-06	8.31E+00	0.05705	0.86745	2.8787	1.85E-02	6.223	0.49752	3.217	2.31E-04	5.39E+00	1.029	2.081	2.13E-03	3.8513	1.138901	0.05705	0.290695	2.725567
20h	1.86E-04	3.70E-04	1.33E-06	8.57E+00	0.05819	0.86877	2.9389	2.01E-02	6.4158	0.51793	3.3754	2.53E-04	5.59E+00	1.02	2.1576	2.27E-03	4.2361	1.175456	0.05819	0.29252	2.823967
30h	1.60E-04	3.19E-04	1.33E-06	8.90E+00	0.05244	0.86467	2.9377	2.22E-02	6.3648	0.5471	3.2336	2.99E-04	5.22E+00	1.037	2.0977	2.50E-03	4.1729	1.223621	0.05244	0.298551	2.756333
40h	1.89E-04	3.77E-04	1.33E-06	9.02E+00	0.05675	0.86546	3.173	2.31E-02	6.9067	0.55892	3.466	3.08E-04	5.61E+00	1.05	2.2483	2.54E-03	4.5239	1.239963	0.05675	0.302222	2.962433
50h	1.84E-04	3.63E-04	1.33E-06	9.43E+00	0.05522	0.87142	3.2103	2.43E-02	6.9981	0.58232	3.3942	3.25E-04	5.51E+00	1.081	2.2284	2.60E-03	4.4899	1.299453	0.05522	0.310875	2.9443

12.3.3 Batch B, set 2

Sample	Date	22/10/2020		6.58	mg/mL																
97	Chi-Sqr	Sum-Sqr	**L**	R1	%error	R2	%error	CPE1-T	%error	W-R	%error	W-T	%error	R3	%error	CPE2-T	%error	**Rs**	**%error**	**Rp**	**%error**
0h	1.63E-03	0.00409	5.06E-06	8.732	0.17266	1.099	7.2366	0.0022	11.314	0.92347	10.899	2.32E-02	11.777	0.50794	10.618	4.10E-04	10.759	1.199252	0.17266	0.310254	9.584533
10h	9.11E-04	0.00291	5.06E-06	8.017	0.1421	1.144	3.833	0.00304	6.8934	0.81975	6.1863	5.30E-02	8.9271	0.5184	5.8823	4.33E-04	8.0495	1.096757	0.1421	0.303336	5.300533
20h	0.00104	0.00319	5.06E-06	8.109	0.15117	1.064	4.6488	0.00281	8.197	0.94806	6.1525	4.06E-02	8.3672	0.47721	7.2325	4.36E-04	9.3203	1.109945	0.15117	0.304356	6.011267
30h	7.14E-04	0.00233	5.06E-06	7.945	0.12986	1.122	3.4635	0.0028	6.1872	0.97165	4.632	4.73E-02	6.6997	0.46688	5.7484	4.31E-04	7.9884	1.086435	0.12986	0.314572	4.614633
40h	0.0013	0.00424	5.06E-06	8.096	0.17673	1.158	4.8453	0.00268	8.0745	1.053	6.2483	4.32E-02	8.6961	0.46738	7.7528	4.08E-04	10.995	1.108081	0.17673	0.331465	6.282133
50h	0.00147	0.00467	5.06E-06	8.146	0.17971	1.169	5.5436	0.00287	9.0117	0.94502	8.2134	4.21E-02	10.614	0.48288	8.7249	4.75E-04	11.111	1.115249	0.17971	0.319785	7.493967

Sample	Date	20/04/2021		6.58	mg/mL																
4	Chi-Sqr	Sum-Sqr	**L**	R1	%error	R2	%error	CPE1-T	%error	W-R	%error	W-T	%error	R3	%error	CPE2-T	%error	**Rs**	**%error**	**Rp**	**%error**
0h	0.00123	0.00254	5.21E-06	7.753	0.12969	0.15247	23.698	2.22E-03	23.208	0.97278	5.7457	0.00385	9.92	0.34024	14.611	0.05907	34.396	1.058912	0.12969	0.157598	14.6849
10h	0.00217	0.00287	5.21E-06	7.859	0.14853	0.54411	7.2875	3.18E-03	18.234	0.1555	19.667	0.046	35.67	0.19886	20.654	9.18E-04	20.778	1.074107	0.14853	0.076315	15.8695
20h	0.0036	0.00488	5.21E-06	7.954	0.18588	0.49574	12.055	3.55E-03	29.41	0.14045	23.472	0.07321	47.967	0.2131	29.505	0.00103	24.92	1.087725	0.18588	0.069265	21.67733
30h	0.00111	0.00175	5.21E-06	8.006	0.11319	0.49083	6.8022	3.47E-03	16.415	0.16589	9.7727	0.16797	23.084	0.20921	16.28	9.47E-04	15.451	1.09518	0.11319	0.071651	10.95163
40h	0.00176	0.00224	5.21E-06	8.138	0.12728	0.47393	8.8838	3.46E-03	21.687	0.14631	16.153	0.06129	32.052	0.20985	21.218	9.85E-04	17.615	1.114102	0.12728	0.066513	15.41827
50h	0.00154	0.00225	5.21E-06	8.15	0.12663	0.47684	8.7564	3.56E-03	20.909	0.15778	12.37	0.12598	28.238	0.20399	21.111	0.00104	18.124	1.115822	0.12663	0.067734	14.07913

Sample	Date	12/03/2021		6.58	mg/mL																
146	Chi-Sqr	Sum-Sqr	**L**	R1	%error	R2	%error	CPE1-T	%error	W-R	%error	W-T	%error	R3	%error	CPE2-T	%error	**Rs**	**%error**	**Rp**	**%error**
0h	2.36E-03	0.0091	5.37E-06	6.913	0.27234	0.97213	11.942	0.00302	12.243	1.701	8.3427	2.53E-02	8.8125	0.33768	15.096	5.22E-04	19.651	0.938498	0.27234	0.379119	11.79357
10h	1.79E-03	0.00418	5.37E-06	6.848	0.18419	0.807	4.3473	0.00223	11.078	0.2172	10.884	1.46E-01	25.326	0.36444	9.5678	4.28E-04	12.146	0.92918	0.18419	0.146581	8.266367
20h	0.00353	0.00741	5.37E-06	6.912	0.24381	0.79333	6.1068	0.00234	15.428	0.20578	17.946	8.02E-02	37.493	0.379	12.631	4.24E-04	15.652	0.938355	0.24381	0.145072	12.22793
30h	3.51E-03	8.88E-03	5.37E-06	6.963	0.26605	0.8211	6.1953	0.00231	15.813	0.22007	15.188	2.76E-01	36.925	0.38908	12.976	4.16E-04	16.802	0.945666	0.26605	0.152546	11.4531
40h	2.04E-03	5.17E-03	5.37E-06	7.029	0.19509	0.84209	4.6438	0.00276	11.865	0.17194	15.427	3.83E-01	37.174	0.45128	8.5989	4.36E-04	10.981	0.955127	0.19509	0.157572	9.556567
50h	2.45E-03	0.00574	5.37E-06	7.062	0.20732	0.8503	4.9705	0.00256	12.672	0.15779	17.795	2.41E-01	42.334	0.42865	9.8057	4.39E-04	12.272	0.959857	0.20732	0.153476	10.85707

Sample	Date	26/10/2020		13.16	mg/mL																
98	Chi-Sqr	Sum-Sqr	**L**	R1	%error	R2	%error	CPE1-T	%error	W-R	%error	W-T	%error	R3	%error	CPE2-T	%error	**Rs**	**%error**	**Rp**	**%error**
0h	2.61E-03	0.01011	6.06E-06	8.593	0.29885	1.315	6.392	15.868	15.868	0.5866	10.549	1.90E-04	21.155	1.171	6.7962	2.20E-03	14.219	1.179326	0.29885	0.387977	7.9124
10h	2.34E-03	0.00958	6.06E-06	8.083	0.29753	1.197	5.3877	13.969	13.969	0.5385	8.7198	1.70E-04	19.15	1.155	5.4156	2.66E-03	11.212	1.106218	0.29753	0.361873	6.5077
20h	0.00217	0.00877	6.06E-06	8.098	0.29802	1.247	4.9188	12.768	12.768	0.50939	8.3906	1.33E-04	18.869	1.195	4.9593	2.30E-03	9.8432	1.108368	0.29802	0.370601	6.089567
30h	2.84E-04	7.73E-04	7.01E-07	8.042	0.08199	1.152	1.8777	4.1494	4.1494	0.58066	3.1121	2.93E-04	5.8994	1.263	1.8057	2.89E-02	4.4552	1.10034	0.08199	0.376947	2.265167
40h	2.67E-04	7.31E-04	7.01E-07	8.048	0.08	1.195	1.7743	3.8715	3.8715	0.57986	3.0111	2.88E-04	5.7302	1.263	1.7765	2.85E-02	4.3737	1.1012	0.08	0.382997	2.1873
50h	4.91E-04	0.00132	7.01E-07	8.029	0.10447	1.185	2.5211	5.6036	5.6036	0.59293	4.2868	3.44E-04	7.8304	1.219	2.6112	3.04E-02	6.3404	1.098477	0.10447	0.377129	3.1397

Sample	Date	29/04/2021		13.16	mg/mL																
18	Chi-Sqr	Sum-Sqr	**L**	R1	%error	R2	%error	CPE1-T	%error	W-R	%error	W-T	%error	R3	%error	CPE2-T	%error	**Rs**	**%error**	**Rp**	**%error**
0h	0.00151	0.00416	5.32E-06	7.328	0.19047	1.07	12.214	0.00312	7.4841	0.51128	6.1874	2.00E-04	12.834	0.51661	27.21	0.03065	51.405	0.997988	0.19047	0.248252	15.2038
10h	0.00158	0.00226	5.32E-06	7.686	0.14588	0.60022	4.7069	0.00267	12.896	0.24353	12.645	1.53E-04	23.212	0.1373	15.346	0.24048	41.23	1.049308	0.14588	0.088153	10.8993
20h	0.00176	0.00261	5.32E-06	7.683	0.15347	0.55834	5.684	0.00297	15.482	0.26113	13.46	1.73E-04	23.97	0.13441	14.659	0.35754	39.979	1.048878	0.15347	0.084258	11.26767
30h	0.00213	0.00318	5.32E-06	7.618	0.17379	0.53855	6.3634	0.00272	17.269	0.23789	15.94	1.50E-04	28.593	0.14979	13.738	0.31952	37.606	1.03956	0.17379	0.080295	12.0138
40h	0.0015	0.0022	5.32E-06	7.655	0.14543	0.53334	5.5216	0.00261	15.076	0.23096	14.209	1.45E-04	25.057	0.17003	10.957	0.21129	29.925	1.044864	0.14543	0.081456	10.2292
50h	0.00141	0.00221	5.32E-06	7.685	0.13858	0.50207	6.868	0.0031	18.502	0.25764	15.205	1.93E-04	24.59	0.1771	11.05	0.21027	29.961	1.049164	0.13858	0.081811	11.041

Sample	Date	19/03/2021		13.16	mg/mL																
148	Chi-Sqr	Sum-Sqr	**L**	R1	%error	R2	%error	CPE1-T	%error	W-R	%error	W-T	%error	R3	%error	CPE2-T	%error	**Rs**	**%error**	**Rp**	**%error**
0h	3.11E-03	0.00776	5.36E-06	6.831	0.26345	0.91927	13.887	0.00248	11.33	0.76133	20.479	1.56E-02	17.529	0.34809	13.664	3.85E-04	17.538	0.926743	0.26345	0.238332	16.01
10h	3.09E-03	0.00625	5.36E-06	6.835	0.22815	0.79517	4.8899	0.00243	12.564	0.12491	23.133	1.54E-01	53.595	0.38135	9.9483	3.81E-04	14.248	0.927317	0.22815	0.13408	12.65707
20h	0.00284	0.00618	5.36E-06	6.927	0.22366	0.77568	5.0821	0.00257	13.104	0.13111	21.056	2.90E-01	51.095	0.39656	9.8015	3.91E-04	13.727	0.940505	0.22366	0.134355	11.97987
30h	3.49E-03	7.87E-03	5.36E-06	6.953	0.25386	0.76087	6.0652	0.00243	15.553	0.1707	18.158	2.60E-01	44.016	0.37834	12.074	3.99E-04	16.333	0.944232	0.25386	0.135295	12.09907
40h	2.18E-03	4.98E-03	5.36E-06	7.013	0.19644	0.74789	5.3305	0.0026	13.522	0.18989	13.364	2.21E-01	31.99	0.39616	10.041	4.39E-04	12.365	0.952833	0.19644	0.13874	9.5785
50h	3.28E-03	0.00777	5.36E-06	7.03	0.24997	0.75343	6.3956	0.00247	16.319	0.24157	13.548	1.59E-01	31.714	0.38887	12.295	4.06E-04	15.898	0.95527	0.24997	0.145897	10.7462

Sample	Date	05/05/2021		26.32	mg/mL																
9	Chi-Sqr	Sum-Sqr	**L**	R1	%error	R2	%error	CPE1-T	%error	W-R	%error	W-T	%error	R3	%error	CPE2-T	%error	**Rs**	**%error**	**Rp**	**%error**
0h	0.00107	0.00461	5.20E-06	6.65	0.17095	1.38	5.2194	0.00457	5.1932	1.149	7.4092	0.0638	8.3142	0.31528	9.1826	9.58E-04	13.44	0.900797	0.17095	0.355247	7.2704
10h	0.0013	0.00256	5.20E-06	7.516	0.14391	0.57066	6.039	0.00332	15.15	0.29589	9.0287	0.06075	17.532	0.24266	14.42	7.59E-04	15.844	1.024938	0.14391	0.106525	9.829233
20h	0.00165	0.00274	5.20E-06	7.858	0.14462	0.53273	6.9763	0.00329	17.494	0.30888	8.9627	0.05387	17.011	0.23207	16.441	7.68E-04	17.325	1.073964	0.14462	0.101432	10.79333
30h	0.0014	0.00231	5.20E-06	8.354	0.12307	0.53092	7.7844	0.00425	19.344	0.24506	11.174	0.07057	21.008	0.26668	16.441	0.001	14.193	1.145065	0.12307	0.096985	11.7998
40h	0.00113	0.00263	5.20E-06	6.62	0.13481	0.56132	5.4511	0.0041	13.607	0.26357	7.0547	0.15424	15.853	0.28784	10.842	8.23E-04	11.321	0.896497	0.13481	0.107029	7.7826
50h	0.00124	0.00247	5.20E-06	6.719	0.13297	0.54688	5.5082	0.0039	13.832	0.2742	7.713	0.08262	15.555	0.27733	11.128	7.80E-04	11.641	0.910688	0.13297	0.104977	8.1164

Sample	Date	11/05/2021		26.32	mg/mL																
21	Chi-Sqr	Sum-Sqr	**L**	R1	%error	R2	%error	CPE1-T	%error	W-R	%error	W-T	%error	R3	%error	CPE2-T	%error	**Rs**	**%error**	**Rp**	**%error**
0h	7.22E-04	0.00277	5.31E-06	6.843	0.16038	0.89781	7.4031	0.00324	6.6637	0.32568	6.9838	1.66E-04	14.825	1.382	5.2148	0.01266	10.845	0.928464	0.16038	0.321017	6.5339
10h	0.00114	0.00212	5.31E-06	6.939	0.14506	0.16502	10.359	0.26999	28.17	0.25911	8.5956	1.36E-04	17.363	0.6436	3.3123	0.00279	8.9774	0.942225	0.14506	0.100579	7.4223
20h	0.00209	0.00375	TRUE	6.966	0.18932	0.17786	12.53	0.24722	34.149	0.26669	12.757	1.51E-04	24.114	0.5589	5.6074	0.00299	15.382	0.946096	0.18932	0.091364	10.29813
30h	0.00139	0.00232	5.31E-06	6.998	0.15736	0.19767	9.6914	0.15048	26.161	0.23984	10.471	1.13E-04	20.505	0.5468	4.3506	0.00258	11.768	0.950683	0.15736	0.08862	8.171
40h	0.00167	0.00293	5.31E-06	7.058	0.16985	0.19953	9.7404	0.20473	26.634	0.25407	12.394	1.38E-04	23.039	0.52229	5.4985	0.00283	15.074	0.959284	0.16985	0.087413	9.210967
50h	0.00181	0.00316	5.31E-06	7.043	0.18113	0.22584	9.4996	0.14456	25.831	0.24399	12.748	1.21E-04	24.304	0.5191	5.5423	0.00269	15.167	0.957134	0.18113	0.089283	9.2633

12.3.4 Batch C

Sample	Date	27/08/2021		6.58	mg/mL																
307	Chi-Sqr	Sum-Sqr	**L**	R1	%error	R2	%error	CPE1-T	%error	W-R	%error	W-T	%error	R3	%error	CPE2-T	%error	**Rs**	**%error**	**Rp**	**%error**
0h	9.57E-03	0.00824	3.80E-06	17.86	0.27828	0.83369	9.9519	0.00603	20.732	0.17137	52.304	2.59E-01	112.72	0.22475	29.023	4.03E-04	71.51	2.507751	0.27828	0.123813	30.4263
10h	2.98E-03	0.00267	3.80E-06	17.7	0.16941	0.62192	6.9367	0.00554	15.947	0.34069	13.43	2.52E-01	30.579	0.19911	19.223	3.54E-04	47.221	2.484815	0.16941	0.114052	13.19657
20h	0.00292	0.00265	3.80E-06	17.96	0.16896	0.71019	6.2021	0.00614	13.536	0.3111	15.458	2.87E-01	34.609	0.23928	15.685	2.91E-04	39.616	2.522086	0.16896	0.128222	12.44837
30h	4.74E-03	4.16E-03	3.80E-06	17.9	0.22128	0.54447	15.37	0.00589	22.882	0.62202	14.661	6.34E-02	24.256	0.18851	26.327	3.19E-04	64.439	2.513485	0.22128	0.141759	18.786
40h	6.11E-03	5.56E-03	3.80E-06	18.2	0.26974	0.62529	12.375	0.00581	22.129	0.60456	13.756	1.21E-01	27.2	0.20663	27.655	2.43E-04	70.868	2.55649	0.26974	0.153439	17.92867
50h	2.55E-03	0.00263	3.80E-06	18.23	0.22232	0.6051	8.6191	0.00575	14.875	0.79425	7.0824	1.21E-01	14.241	0.23942	17.863	1.28E-04	46.88	2.56079	0.22232	0.182437	11.18817

Sample	Date	31/08/2021		13.16	mg/mL																
308	Chi-Sqr	Sum-Sqr	**L**	R1	%error	R2	%error	CPE1-T	%error	W-R	%error	W-T	%error	R3	%error	CPE2-T	%error	**Rs**	**%error**	**Rp**	**%error**
0h	3.28E-03	0.00315	4.59E-06	16.49	0.18275	0.63257	22.595	0.00609	16.274	0.63569	25.155	3.24E-02	25.292	0.26683	15.946	2.80E-04	35.495	2.311361	0.18275	0.167575	21.232
10h	7.34E-03	0.00454	4.59E-06	18.27	0.21735	0.47874	17.595	0.00527	31.183	0.26056	34.986	5.42E-02	59.545	0.17403	32.661	4.40E-04	72.729	2.566524	0.21735	0.078445	28.414
20h	0.00256	0.00235	4.59E-06	16.78	0.13804	0.48449	9.1765	0.00569	23.205	0.31172	12.802	2.07E-01	29.205	0.1733	23.983	7.55E-04	45.847	2.352933	0.13804	0.086499	15.3205
30h	5.11E-03	4.75E-03	4.59E-06	17.26	0.20235	0.58525	9.0327	0.00632	23.922	0.23883	26.284	8.75E-01	60.188	0.21317	24.253	5.23E-04	54.732	2.421741	0.20235	0.096209	19.85657
40h	3.17E-03	2.76E-03	4.59E-06	18.18	0.14965	0.49098	11.298	0.00572	26.96	0.38797	13.583	1.25E-01	28.503	0.16828	29.098	7.78E-04	55.437	2.553623	0.14965	0.09764	17.993
50h	2.95E-03	0.00316	4.59E-06	16.27	0.15994	0.50797	10.311	0.00547	25.164	0.4615	10.558	1.44E-01	22.861	0.18818	25.093	7.02E-04	47.476	2.279824	0.15994	0.113469	15.32067

Sample	Date	03/09/2021		26.32	mg/mL																
309	Chi-Sqr	Sum-Sqr	**L**	R1	%error	R2	%error	CPE1-T	%error	W-R	%error	W-T	%error	R3	%error	CPE2-T	%error	**Rs**	**%error**	**Rp**	**%error**
0h	1.56E-03	0.00417	4.83E-06	12.61	0.16147	1.007	12.048	0.01087	9.611	1.687	8.0717	1.13E-01	9.0627	0.2398	15.659	1.11E-03	30.94	1.755163	0.16147	0.36808	11.92623
10h	2.09E-03	0.00325	4.99E-06	12.13	0.16277	0.55602	8.8659	0.00593	16.768	0.66183	8.0787	7.34E-02	13.889	0.18129	19.049	7.31E-04	37.217	1.686355	0.16277	0.148086	11.99787
20h	0.00298	0.00536	4.99E-06	12.24	0.19038	0.67291	8.0247	0.00707	18.509	0.54926	9.864	2.01E-01	20.415	0.22211	20.385	9.58E-04	37.887	1.702124	0.19038	0.154557	12.7579
30h	2.04E-03	3.45E-03	4.99E-06	12.28	0.16597	0.59602	7.6722	0.0061	15.902	0.68787	6.9865	1.11E-01	13.369	0.20709	16.754	6.67E-04	33.796	1.707858	0.16597	0.161252	10.4709
40h	2.51E-03	4.35E-03	4.99E-06	12.31	0.18303	0.55567	9.619	0.00596	21.161	0.80918	6.8089	1.04E-01	13.403	0.186	23.339	8.55E-04	42.42	1.712158	0.18303	0.169834	13.25563

Sample	Date	06/09/2021		52.64	mg/mL																
310	Chi-Sqr	Sum-Sqr	**L**	R1	%error	R2	%error	CPE1-T	%error	W-R	%error	W-T	%error	R3	%error	CPE2-T	%error	**Rs**	**%error**	**Rp**	**%error**
0h	1.26E-03	0.00222	3.50E-06	19.02	0.12896	0.69271	11.533	0.00931	14.877	2.147	4.1481	1.05E-01	6.2252	0.24931	15.422	6.17E-04	33.961	2.674037	0.12896	0.390331	10.3677
10h	3.31E-03	0.00349	3.50E-06	19.05	0.18798	0.70889	11.147	0.00523	17.709	0.79892	10.772	8.08E-02	18.46	0.25989	18.503	3.05E-04	43.919	2.678337	0.18798	0.200919	13.474
20h	0.00268	0.00316	3.50E-06	19.33	0.16062	0.86366	7.9383	0.00639	14.175	0.65538	11.325	1.59E-01	21.228	0.27173	16.582	4.57E-04	38.499	2.718475	0.16062	0.204226	11.94843
30h	3.62E-03	4.66E-03	3.50E-06	19.14	0.21137	0.81111	8.4857	0.00581	17.324	0.89322	8.3388	2.22E-01	17.756	0.25872	20.526	3.38E-04	50.376	2.691239	0.21137	0.228923	12.45017
40h	5.99E-03	6.36E-03	3.50E-06	19.57	0.28351	0.6745	14.891	0.00553	23.857	1.121	9.694	9.60E-02	17.767	0.27633	23.773	1.93E-04	60.426	2.752879	0.28351	0.244516	16.11933
50h	3.82E-03	0.00547	3.50E-06	19.44	0.23372	0.79887	8.4267	0.00679	18.488	1.231	6.2721	4.07E-01	14.204	0.25412	22.385	3.15E-04	56.804	2.734244	0.23372	0.27493	12.36127

Sample	Date	09/09/2021		105.28	mg/mL																
311	Chi-Sqr	Sum-Sqr	**L**	R1	%error	R2	%error	CPE1-T	%error	W-R	%error	W-T	%error	R3	%error	CPE2-T	%error	**Rs**	**%error**	**Rp**	**%error**
0h	2.45E-03	0.00469	3.16E-06	21.94	0.13351	1.477	22.63	0.02142	17.852	2.456	16.5	2.73E-01	14.111	0.46169	27.928	4.52E-03	28.423	3.092619	0.13351	0.577498	22.35267
10h	3.36E-03	0.00442	3.16E-06	21.81	0.12237	1.154	11.36	0.03617	24.073	0.3108	46.589	9.43E-01	80.327	0.81045	13.771	4.01E-03	15.089	3.073983	0.12237	0.273677	23.90667
20h	0.00499	0.00683	3.16E-06	22.08	0.15851	1.088	18.968	0.02097	38.937	0.78292	31.109	3.43E-01	40.276	0.57983	31.871	3.90E-03	26.995	3.112688	0.15851	0.298835	27.316
30h	4.30E-03	5.76E-03	3.16E-06	22.16	0.14626	0.93809	54.78	0.03794	36.122	0.90518	70.273	2.52E-01	46.562	0.67486	28.206	4.30E-03	23.378	3.124156	0.14626	0.308494	51.08633
40h	2.97E-03	4.15E-03	3.16E-06	22.43	0.12441	0.84557	27.406	0.02632	42.284	1.247	24.281	2.28E-01	23.394	0.54519	31.435	4.27E-03	23.449	3.16286	0.12441	0.325642	27.70733
50h	3.63E-03	0.00515	3.16E-06	22.6	0.14107	0.90031	21.936	0.01492	54.685	1.401	12.445	2.49E-01	18.078	0.39242	57.456	4.66E-03	35.873	3.18723	0.14107	0.333666	30.61233

12.4 XRD pattern analysis for HfO_2 spin coated LSCF substrates

12.4.1 Batch B

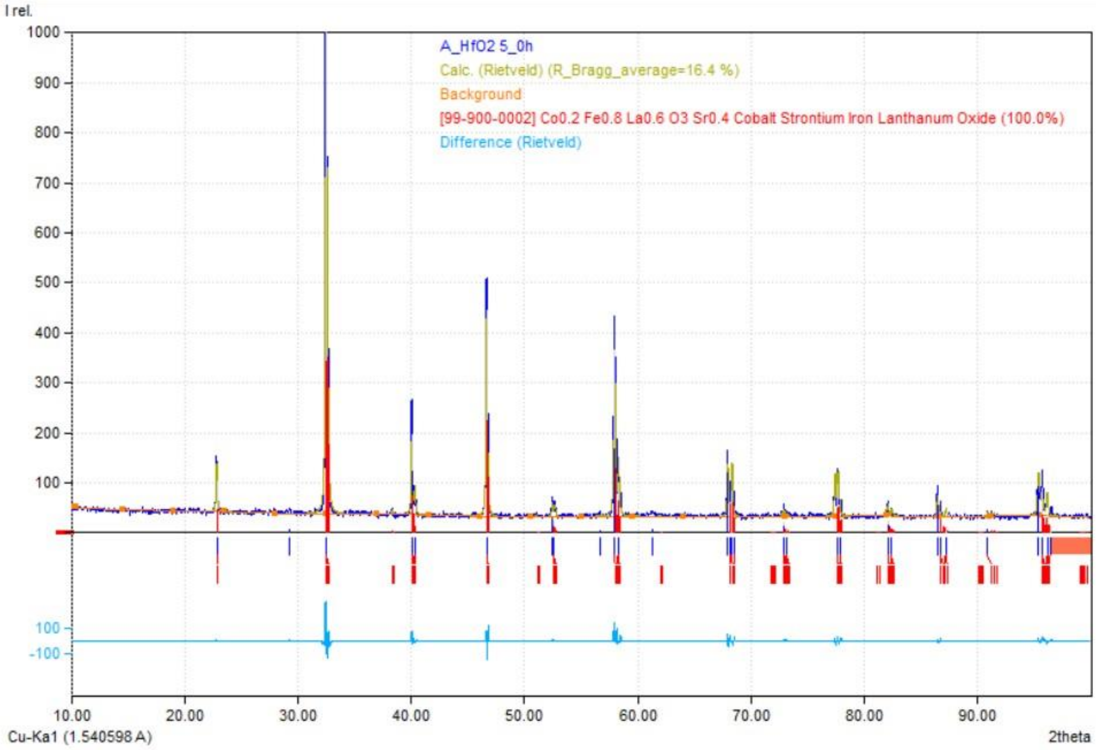

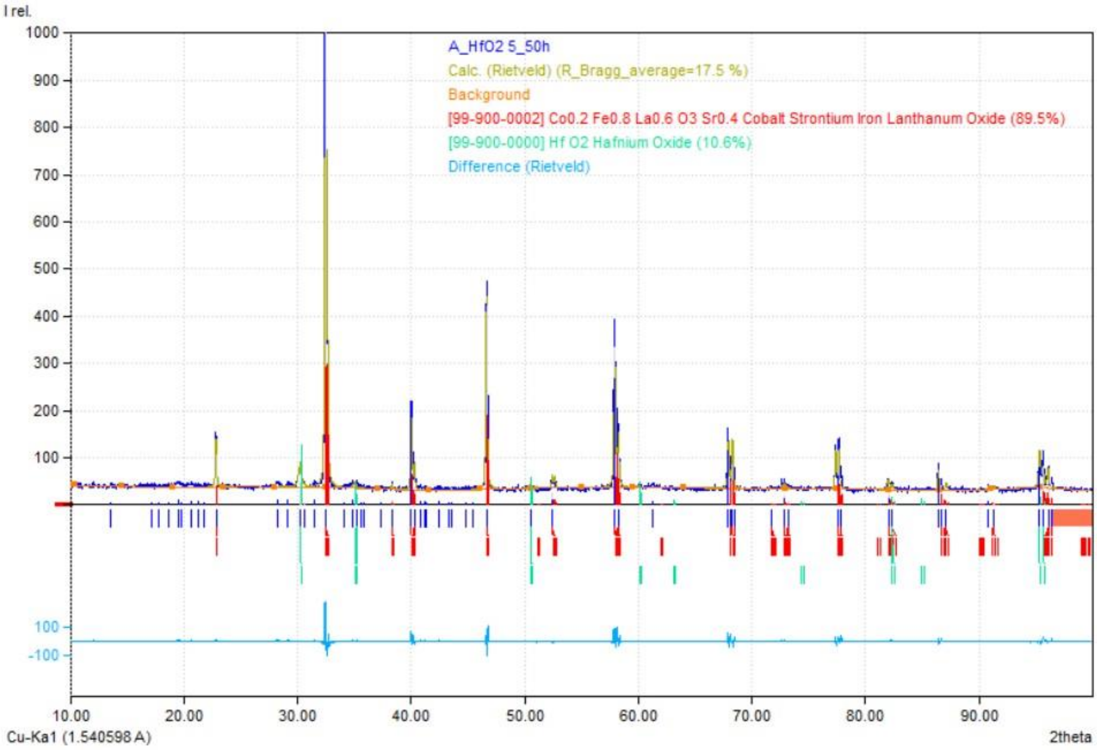

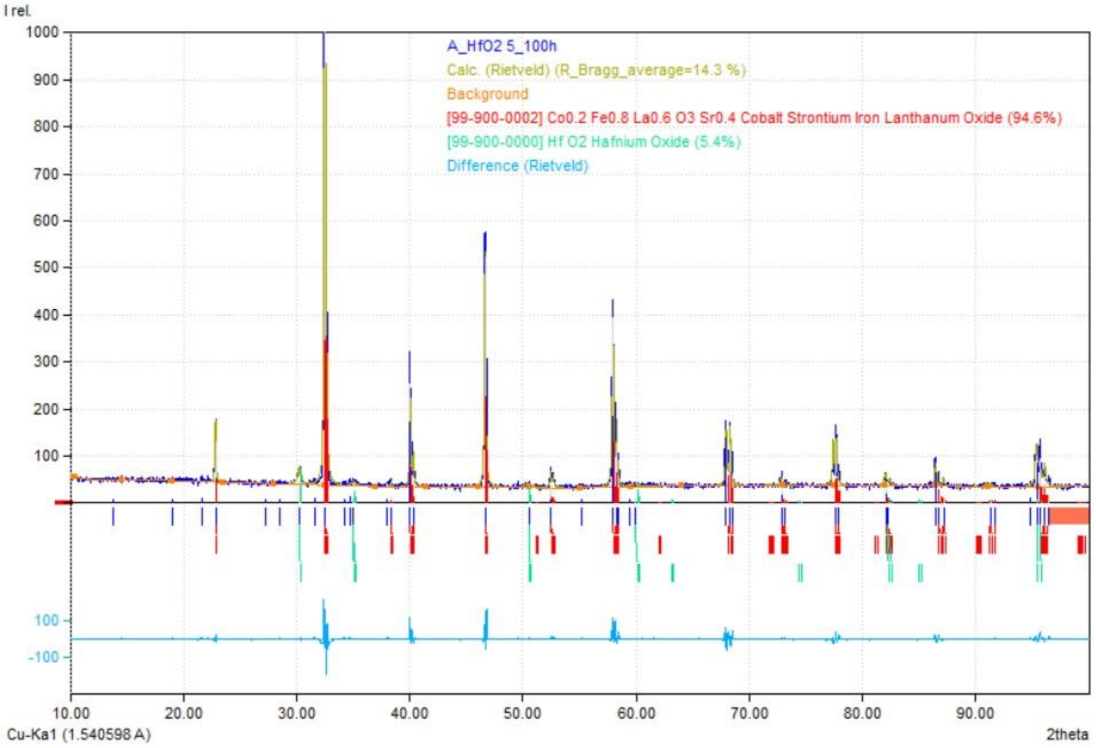
I rel.
1000
900
800
700
600
500
400
300
200
100
100
-100
10.00
20.00
30.00
40.00
50.00
60.00
70.00
80.00
90.00
Cu-Ka1 (1.540598 A)
2theta
A_HfO2 5_100h
Calc. (Rietveld) (R_Bragg_average=14.3 %)
Background
[99-900-0002] Co0.2 Fe0.8 La0.6 O3 Sr0.4 Cobalt Strontium Iron Lanthanum Oxide (94.6%)
[99-900-0000] Hf O2 Hafnium Oxide (5.4%)
Difference (Rietveld)

12.4.2 Batch B

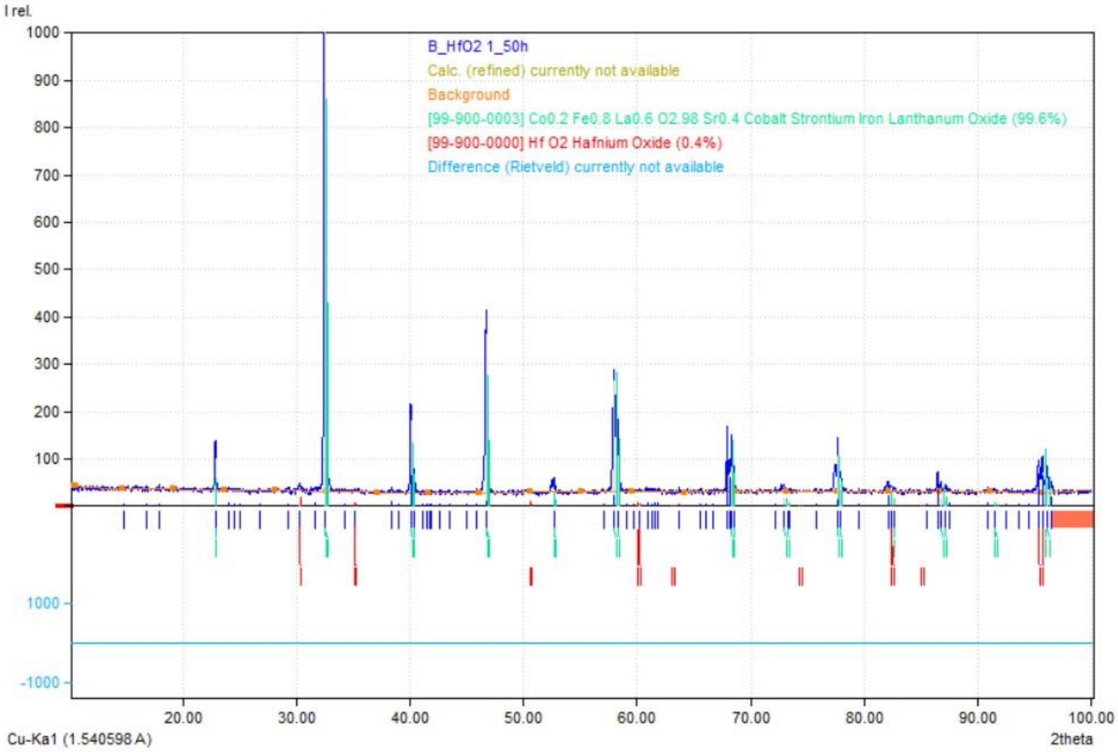
I rel.
1000
900
800
700
600
500
400
300
200
100
1000
-1000
20.00
30.00
40.00
50.00
60.00
70.00
80.00
90.00
100.00
Cu-Ka1 (1.540598 A)
2theta
B_HfO2 1_50h
Calc. (refined) currently not available
Background
[99-900-0003] Co0.2 Fe0.8 La0.6 O2.98 Sr0.4 Cobalt Strontium Iron Lanthanum Oxide (99.6%)
[99-900-0000] Hf O2 Hafnium Oxide (0.4%)
Difference (Rietveld) currently not available

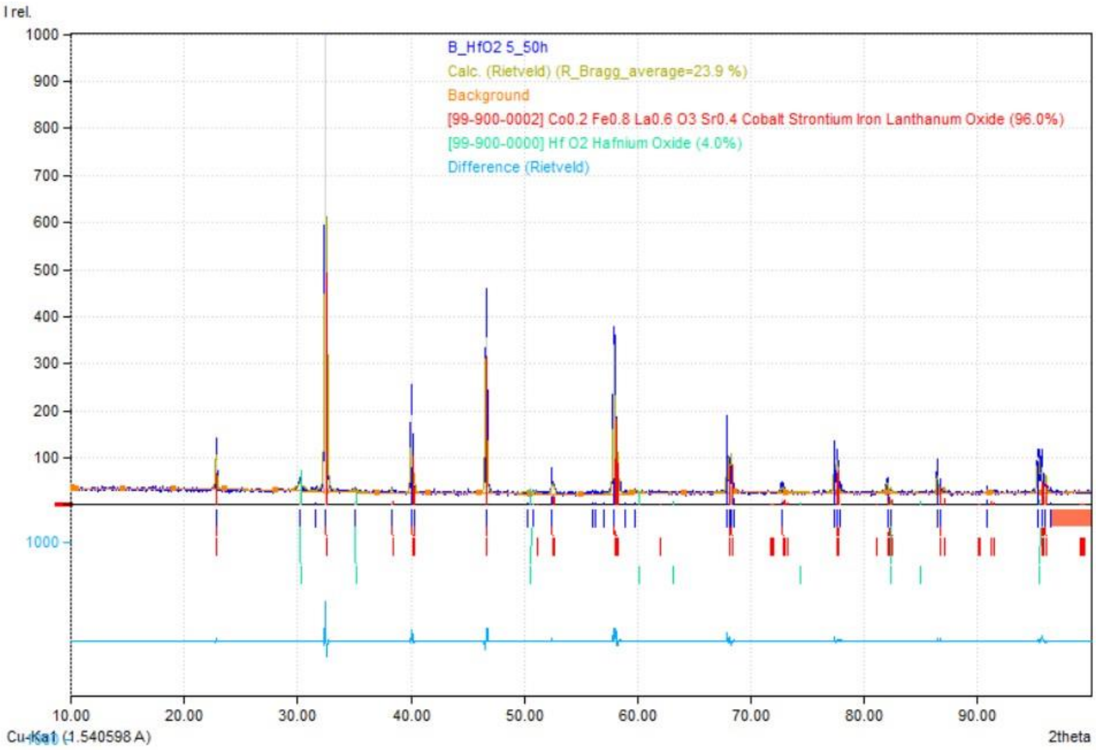
I rel.
1000
900
800
700
600
500
400
300
200
100
1000
B_HfO2 5_50h
Calc. (Rietveld) (R_Bragg_average=23.9 %)
Background
[99-900-0002] Co0.2 Fe0.8 La0.6 O3 Sr0.4 Cobalt Strontium Iron Lanthanum Oxide (96.0%)
[99-900-0000] Hf O2 Hafnium Oxide (4.0%)
Difference (Rietveld)
10.00
20.00
30.00
40.00
50.00
60.00
70.00
80.00
90.00
2theta
Cu-Ka1 (1.540598 A)

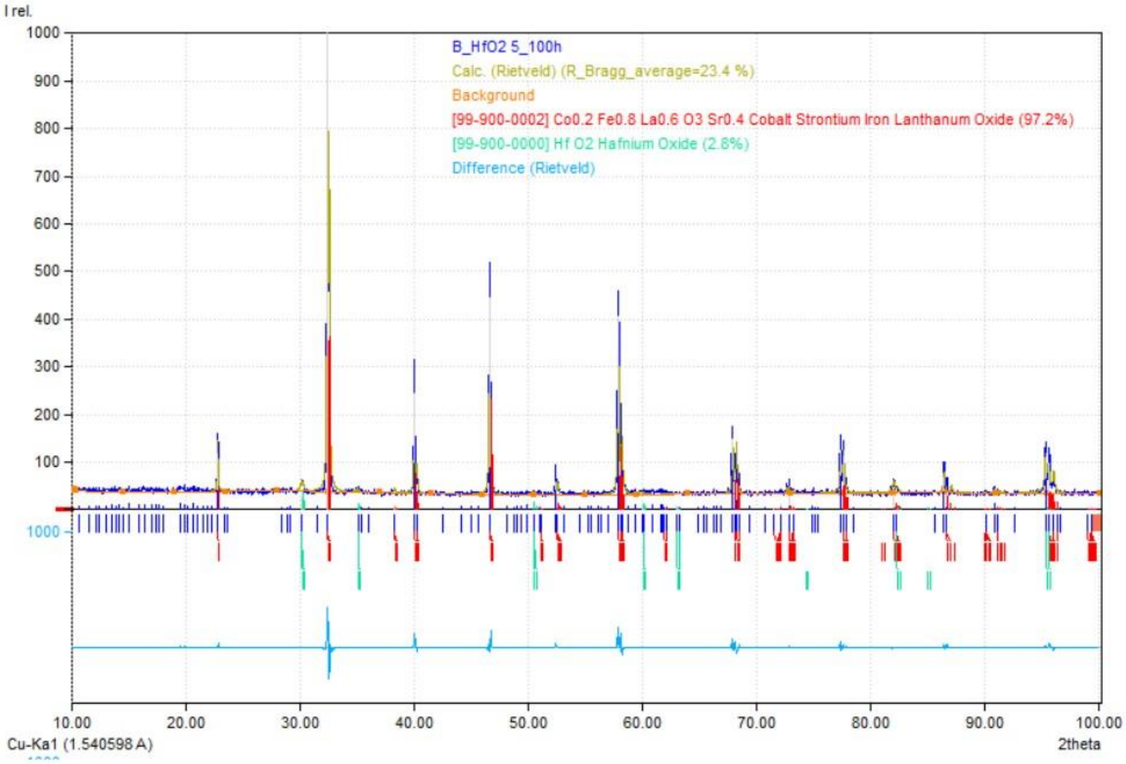
I rel.
1000
900
800
700
600
500
400
300
200
100
1000
B_HfO2 5_100h
Calc. (Rietveld) (R_Bragg_average=23.4 %)
Background
[99-900-0002] Co0.2 Fe0.8 La0.6 O3 Sr0.4 Cobalt Strontium Iron Lanthanum Oxide (97.2%)
[99-900-0000] Hf O2 Hafnium Oxide (2.8%)
Difference (Rietveld)
10.00
20.00
30.00
40.00
50.00
60.00
70.00
80.00
90.00
100.00
2theta
Cu-Ka1 (1.540598 A)

12.4.3 Batch C

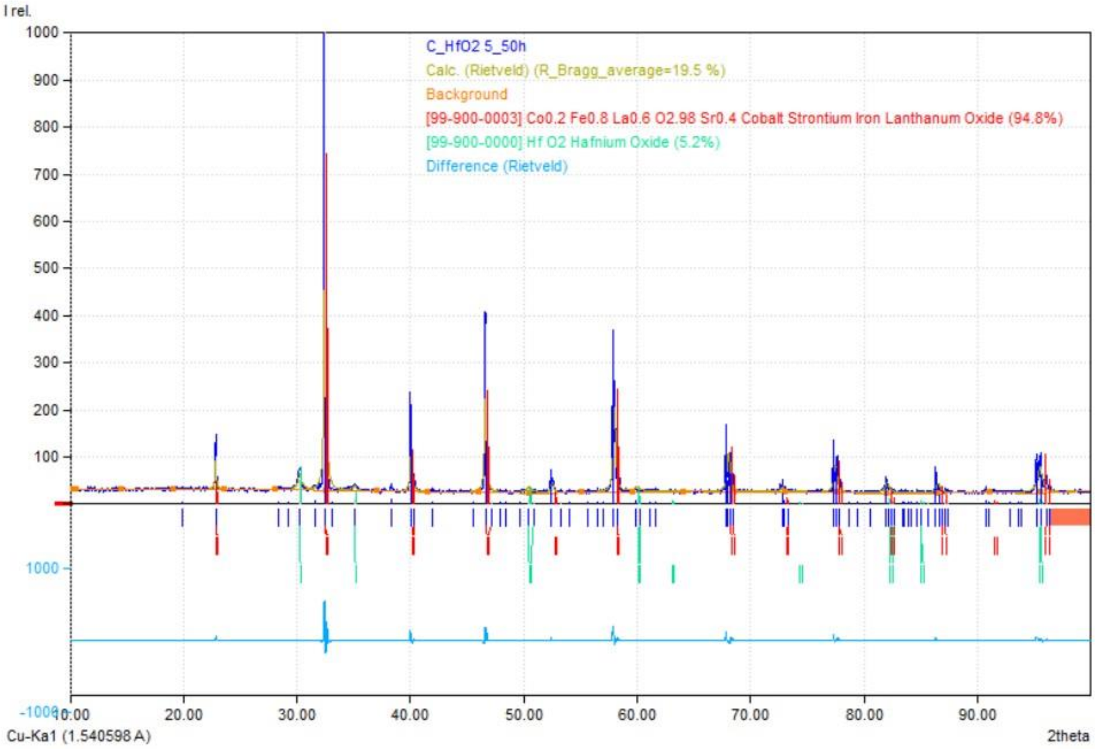
I rel.
1000
900
800
700
600
500
400
300
200
100
1000
-1000
10.00
20.00
30.00
40.00
50.00
60.00
70.00
80.00
90.00
Cu-Ka1 (1.540598 A)
2theta
C_HfO2 5_50h
Calc. (Rietveld) (R_Bragg_average=19.5 %)
Background
[99-900-0003] Co0.2 Fe0.8 La0.6 O2.98 Sr0.4 Cobalt Strontium Iron Lanthanum Oxide (94.8%)
[99-900-0000] Hf O2 Hafnium Oxide (5.2%)
Difference (Rietveld)

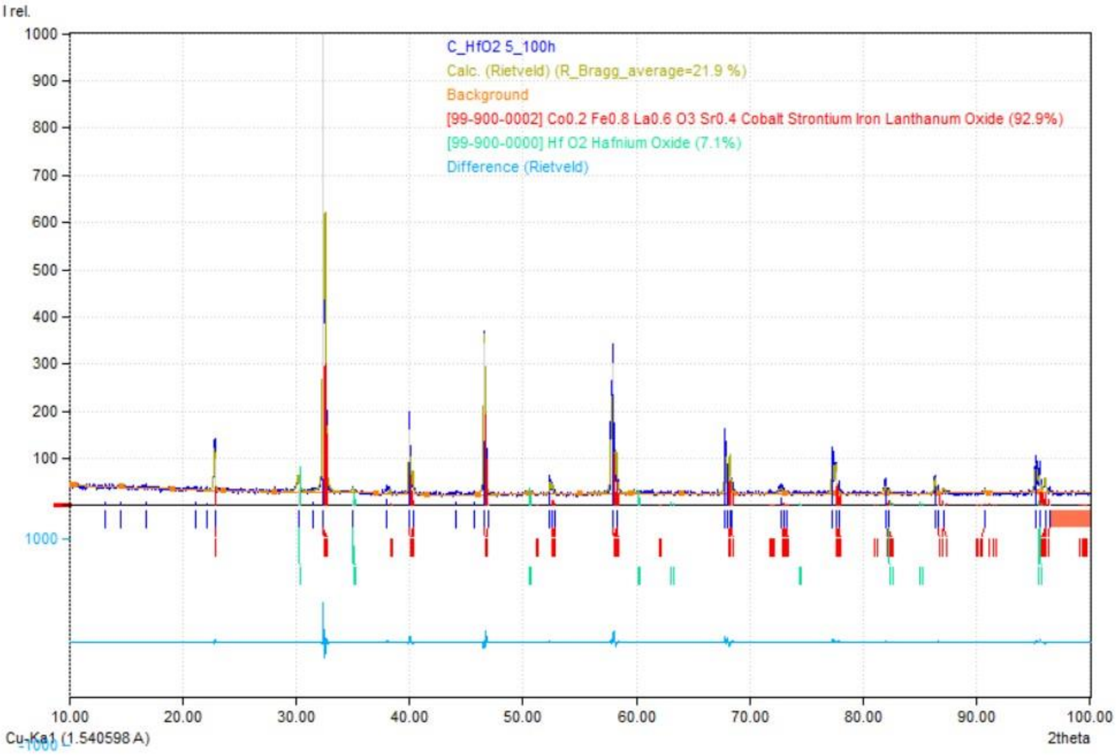
I rel.
1000
900
800
700
600
500
400
300
200
100
1000
-1000
10.00
20.00
30.00
40.00
50.00
60.00
70.00
80.00
90.00
100.00
Cu-Ka1 (1.540598 A)
2theta
C_HfO2 5_100h
Calc. (Rietveld) (R_Bragg_average=21.9 %)
Background
[99-900-0002] Co0.2 Fe0.8 La0.6 O3 Sr0.4 Cobalt Strontium Iron Lanthanum Oxide (92.9%)
[99-900-0000] Hf O2 Hafnium Oxide (7.1%)
Difference (Rietveld)

12.5 SEM-BSE supplementary images

12.5.1 SEM-BSE Batch A

(a) BSE, Batch A, 6.58 mg mL^{-1}, 0h

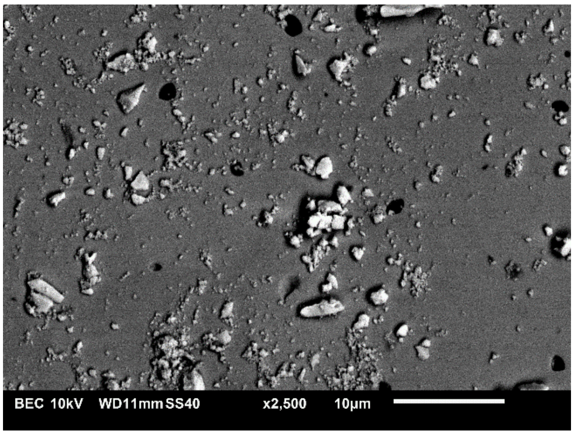

(b) BSE, Batch A, 6.58 mg mL^{-1}, 100h

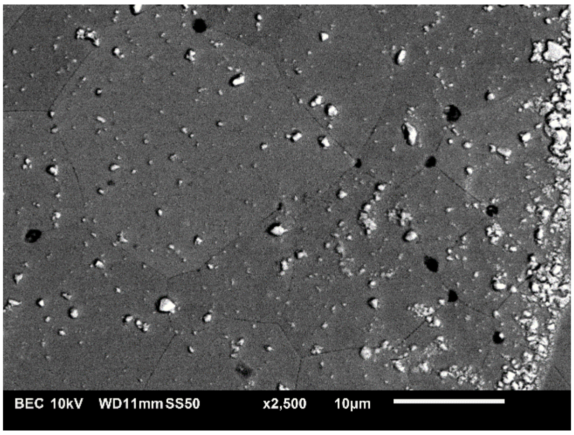

(c) SEM, Batch A, 6.58 mg mL^{-1}, 50h

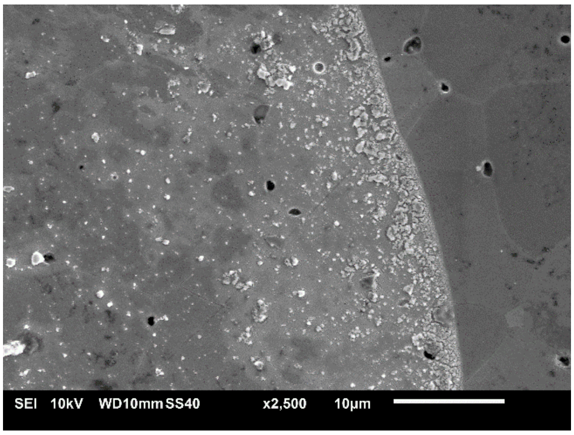

(d) BSE, Batch A, 6.58 mg mL^{-1}, 50h

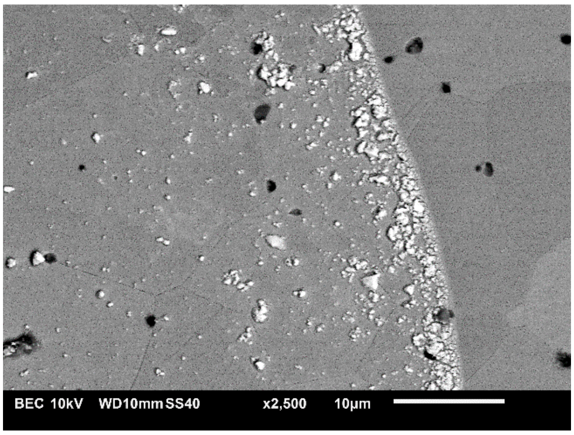

(e) BSE, Batch A, 26.32 mg mL^{-1}, 0h

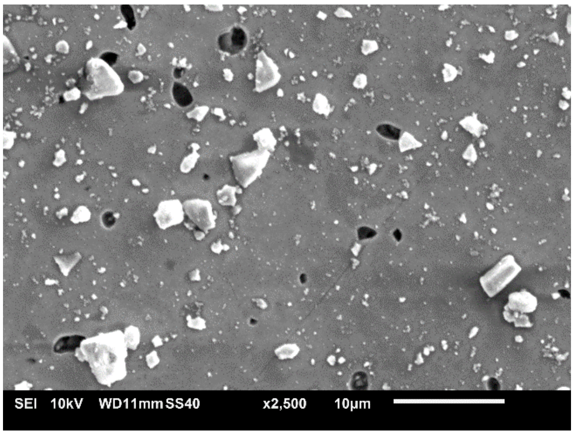

(f) BSE, Batch A, 26.32 mg mL^{-1}, 0h

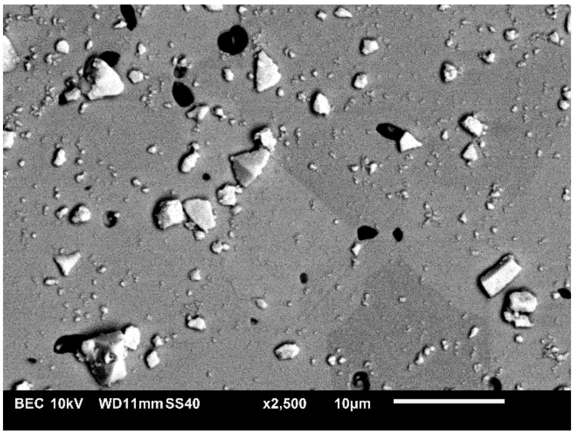

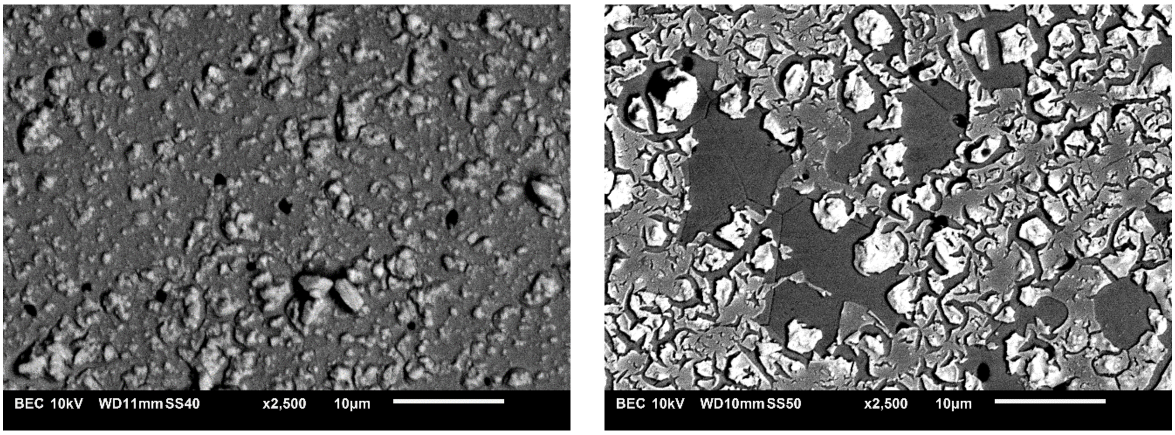
(g) BSE, Batch A, 105.28 mg mL^{-1}, 0h

(h) BSE, Batch A, 105.28 mg mL^{-1}, 100h

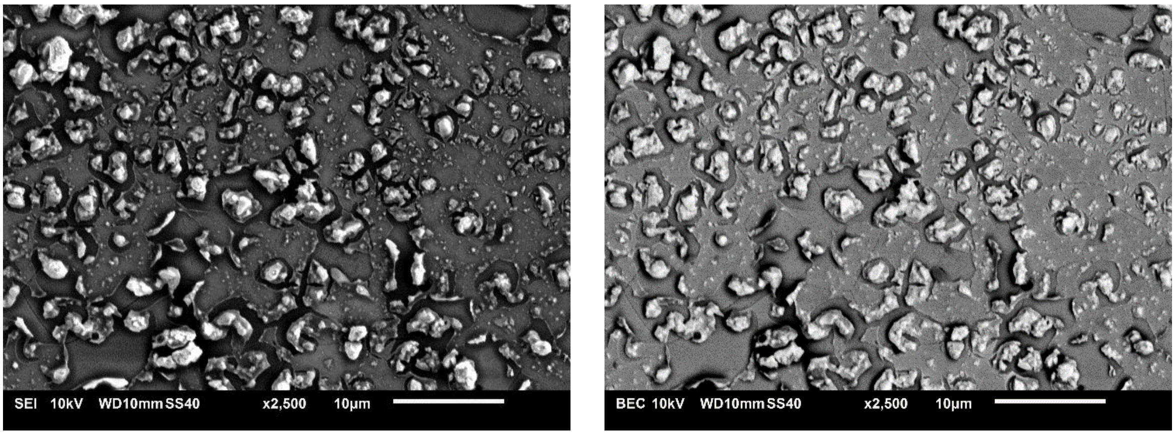
(i) SEM, Batch A, 105.28 mg mL^{-1}, 50h

(j) BSE, Batch A, 105.28 mg mL^{-1}, 50h

12.5.2 SEM-BSE, Batch B

(a) BSE, Batch B, 6.58 mg mL^{-1}, 0h

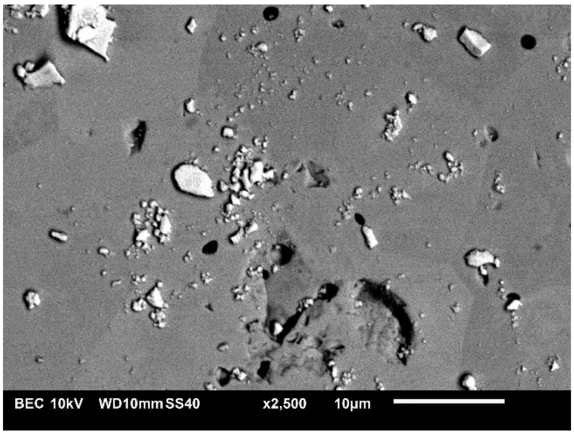

(b) BSE, Batch B, 6.58 mg mL^{-1}, 100h

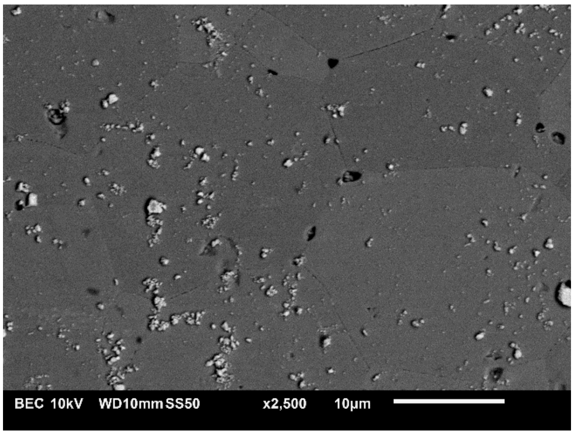

(c) SEM, Batch B, 6.58 mg mL^{-1}, 50h

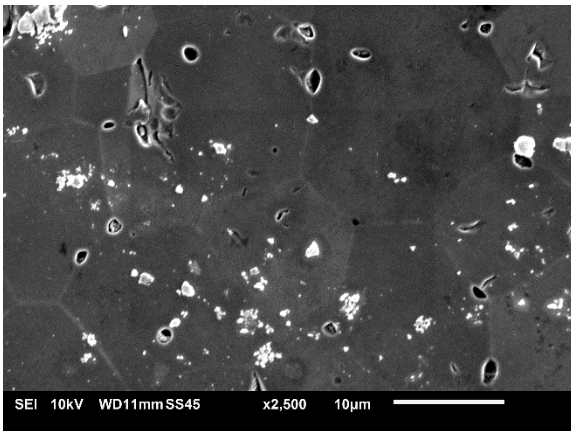

(d) BSE, Batch B, 6.58 mg mL^{-1}, 50h

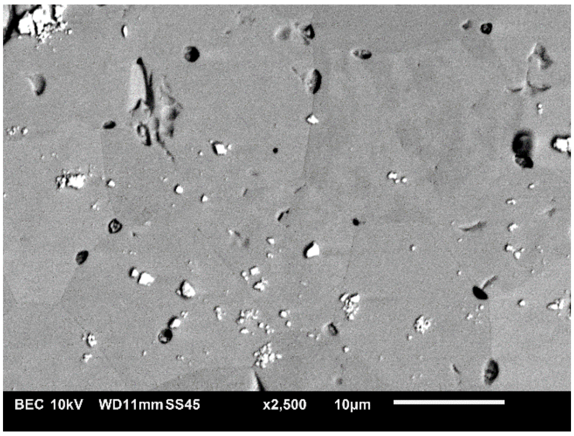

(e) BSE, Batch B, 26.32 mg mL^{-1}, 0h

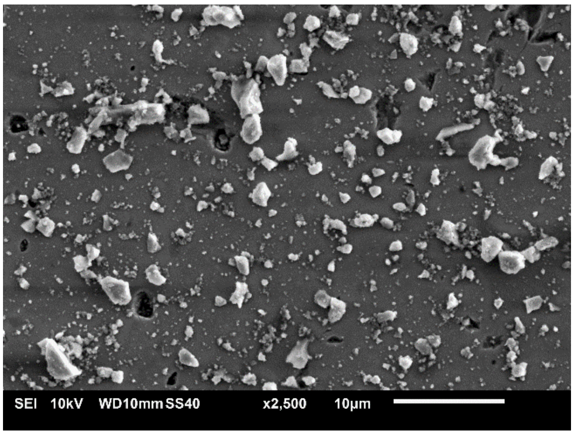

(f) BSE, Batch B, 26.32 mg mL^{-1}, 0h

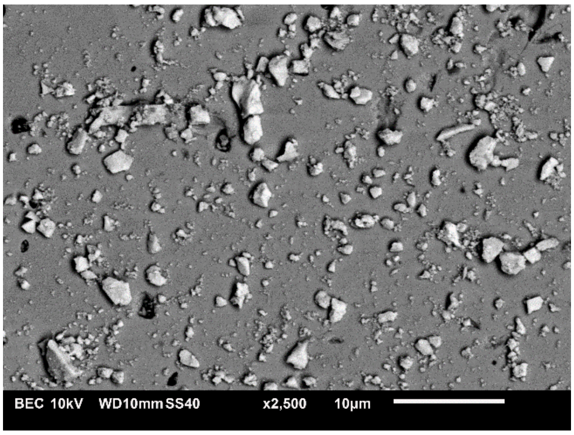

(g) BSE, Batch B, 105.28 mg mL^{-1}, 0h

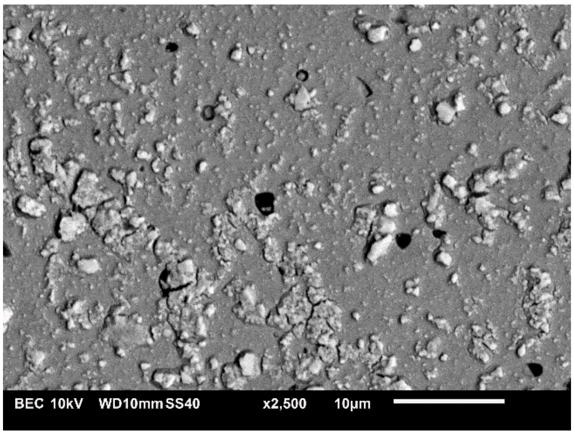

(h) BSE, Batch B, 105.28 mg mL^{-1}, 100h

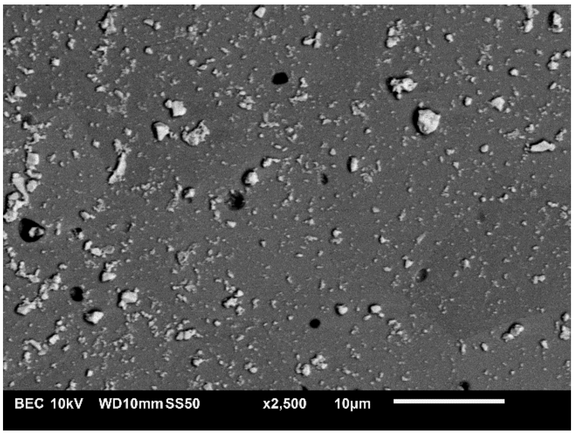

(i) SEM, Batch B, 105.28 mg mL^{-1}, 50h

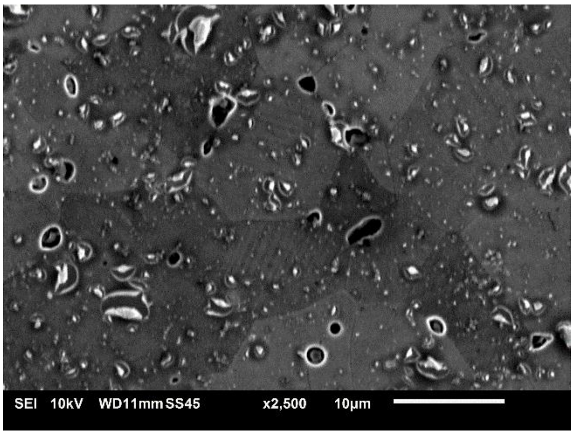

(j) BSE, Batch B, 105.28 mg mL^{-1}, 50h

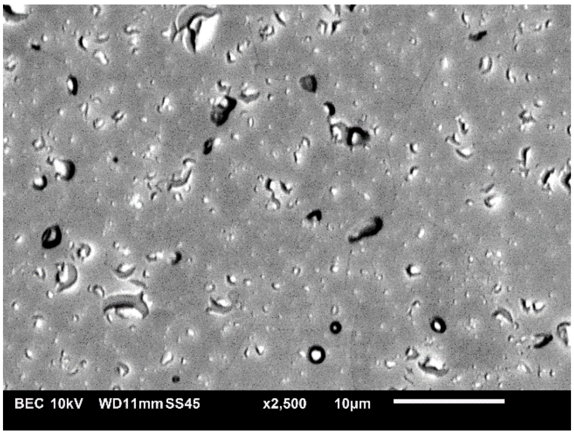

12.5.3 SEM-BSE, Batch C

(a) BSE, Batch C, 6.58 mg mL^{-1}, 0h

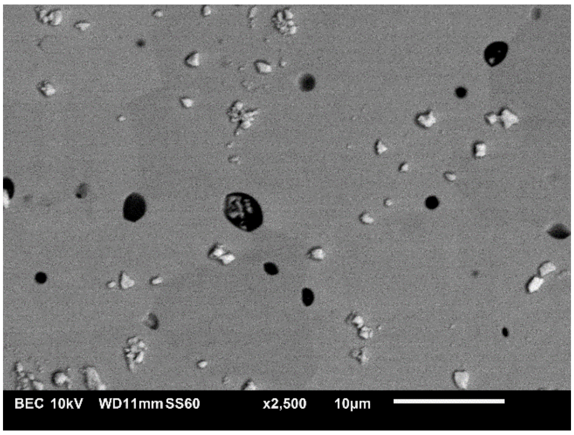

(b) BSE, Batch C, 6.58 mg mL^{-1}, 100h

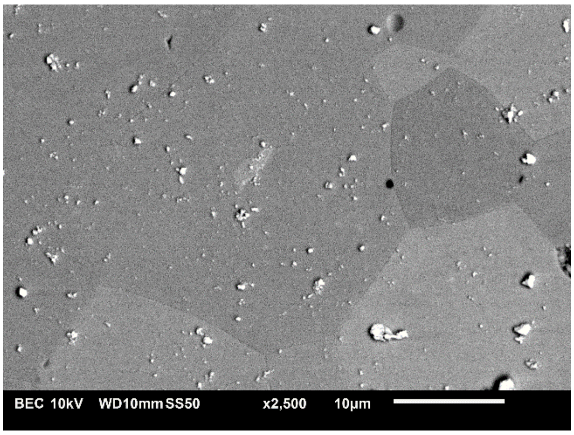

(c) SEM, Batch C, 6.58 mg mL^{-1}, 50h

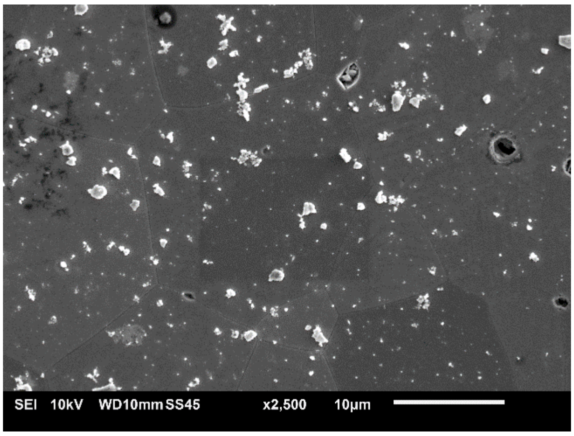

(d) BSE, Batch C, 6.58 mg mL^{-1}, 50h

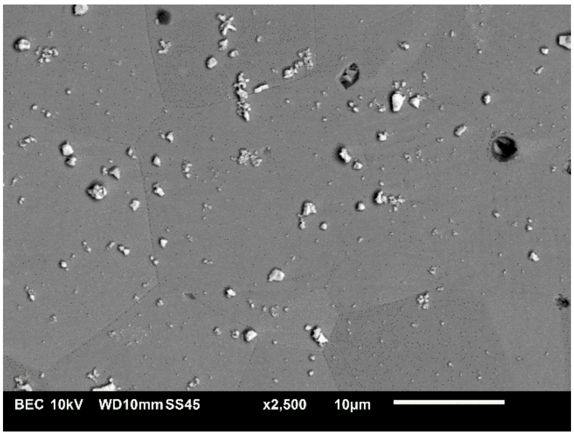

(e) BSE, Batch C, 26.32 mg mL^{-1}, 0h

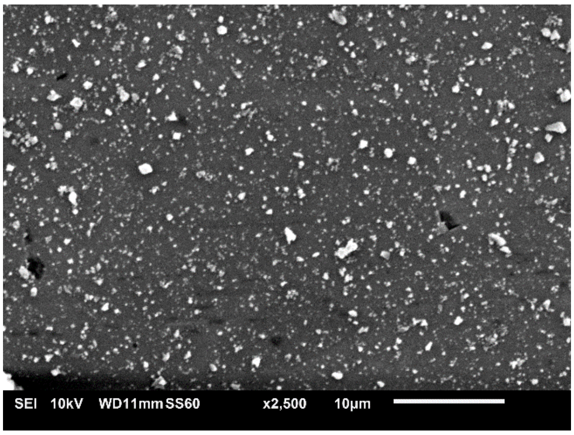

(f) BSE, Batch C, 26.32 mg mL^{-1}, 0h

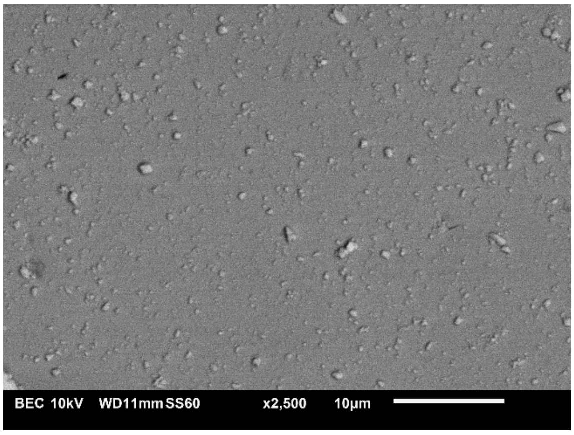

(g) BSE, Batch C, 105.28 mg mL^{-1}, 0h

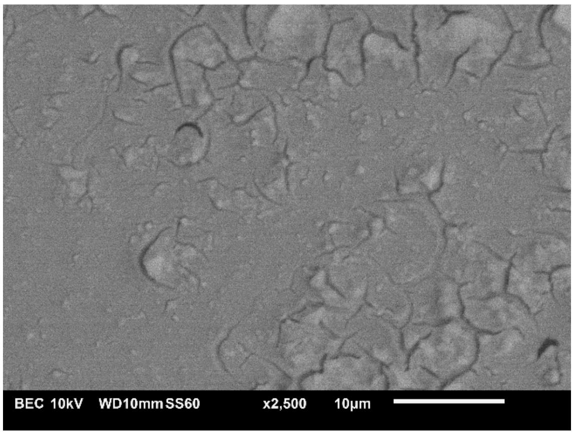

(h) BSE, Batch C, 105.28 mg mL^{-1}, 100h

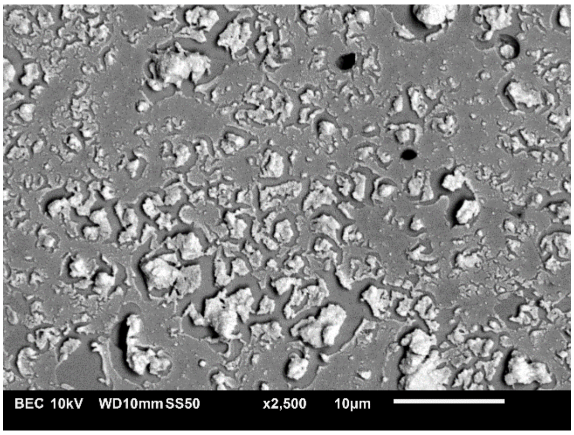

(i) SEM, Batch C, 105.28 mg mL^{-1}, 50h

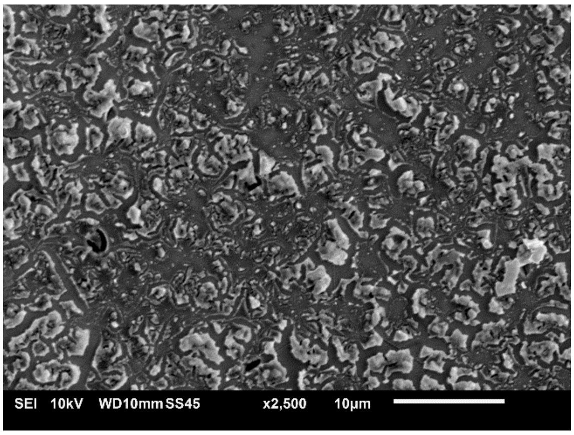

(j) BSE, Batch C, 105.28 mg mL^{-1}, 50h